Effect of Supernovae on ULIRG Spectral Energy Distributions

Clare Elizabeth Jenner

Thesis submitted for the Degree of Doctor of Philosophy of the University of London

Department of Physics & Astronomy

UNIVERSITY COLLEGE LONDON

2008

ProQuest LLC
789 East Eisenhower Parkway
P.O. Box 1346
Ann Arbor, MI 48106-1346

For My Family & Friends

That which we are, we are;
One equal temper of heroic hearts,
Made weak by time and fate, but strong in will
To strive, to seek, to find, and not to yield.
-Alfred, Lord Tennyson (1809-1892)

Acknowledgments

I'd like to thank Jeremy Yates, Mike Barlow, Jenny Thomas & David Mazure for their indefatigable support.

Many thanks also to Jonathan Rawlings for reading the thesis before submission and to Claus Leitherer for the help with STARBURST99.

For the kind use of the DaRT very small grain radiative transfer code I acknowledge: Andreas Efstathiou, Ralph Siebemorgen & Endrik Krügel.

I am grateful for the financial support of the University of London in awarding me a Dixon Studentship and University College London Astronomy Group for a Perrin Fund Studentship.

To Fabrizio Sidoli, your patience and almost encyclopedic knowledge of all things latex was much appreciated!

And finally, but most importantly, to my parents Michael and Jane and my siblings Lucy and Mark: Thank you all, for Everything.

Abstract

This work presents a method for generating synthetic spectra of Ultra-Luminous Infrared Galaxies (ULIRGS) using AGN, HII region and supernovae source functions.

The AGN element represents the far-infrared contribution to the ULIRG spectrum from an energetic central engine. It is modelled using a quasar source embedded in an axi-symmetric dusty torus. The radiative transfer of flux (RT) is then simulated and the AGN emergent spectral energy distributions (SEDs) generated.

The HII region solution is then developed. A stellar evolutionary synthesis code is used to generate instantaneous burst (ISB) source functions which decay in time. The evolution of the gas and dust density in a spherically-symmetric, dense GMC, under the influence of a time-dependent ionizing source flux, is derived. Having irradiated the dust distribution with the source cluster SED, the RT is calculated and the HII region SEDs obtained.

The impact of supernovae energy on a GMC already ionized by stellar flux is then considered. Using the standard pressure-driven expansion model of e.g., Weaver *et al.* (1977) the radial evolution of a superbubble expanding under the influence of a continuous supernovae energy function is derived. The superbubble is modelled in both an adiabatic rapid expansion phase and in an isothermal momentum-conserving phase. As the superbubble expands, upstream gas is swept into a thin shell trapped on its surface and the gas density enhancement is modelled using simple shock physics. Having generated expressions for the evolution of the shell gas temperature, it is linked to the dust density via a temperature dependent condensation factor. Finally expressions are developed to quantify the evolution of the optical depth along a line of sight.

It is found that the star formation efficiency (SFE) has a profound effect on the radial evolution of the optical depth distributions in GMCs; generating marked differences in behaviour between and high and low SFEs. Low SFE models have shells below the dust condensation temperature at the GMC boundary $R2_W$ and the extinction, having initially been in decline, recovers to more substantial values in a dust reformation scenario. These systems tend to be optically thick for most of their evolution. Those models classified high SFE have supershell temperatures in excess of the dust condensation temperature at $R2_W$ and the extinction distribution drops precipitously and reaches very low values ($<$ 1) at $R2_W$. It then remains low for some time before a small recovery in extinction occurs

as the shell dust condenses out. These systems tend to be optically thin for most of their life-times. It is the more powerful supernovae source functions included in the modelled space which generate the high SFE extinction behaviour and vice versa.

Having derived the dust density distributions they are irradiated by the appropriate central source cluster SED and the RT simulated to generate the emergent SEDs. These are similarly categorised as low and high SFE. The low SFE model SEDs appear to be representative of systems where the dust acts as an enshrouding bolometer and most it not all UV and optical radiation is reprocessed and re-emitted into the infrared. Conversely, the high SFE model SEDs are optically revealed and exhibit substantial, only mildly attenuated source flux at short wavelengths for the majority of their evolution.

The emergent AGN and starburst (ISB HII region and supernovae) SEDs are then combined in pairs to form a ULIRG SED Library. These SEDs are matched to the published data for a sample of six nearby (redshift $z \leq 1$) ULIRGS. No model ULIRG SED is found to have a better than 40% probability of belonging to the same population distribution as the published data. This is found to be most likely the result of using an ISB source function. The starburst SED library is therefore extended to approximate constant star formation (CSFRA) using a time decay parameterization and the ULIRGs refitted. In each case a model ULIRG SED was found to match the observations with a better than 5% probability of non-random fit, which suggests that a constant rather than ISB star formation mode is perhaps more appropriate in ULIRGs. Using the CSFRA component of the best-fitting model ULIRG SED, estimates are made for the star formation rate, starburst age and the implied merger and interaction state for each ULIRG. In all case these quantities agree favourably with the literature.

Each ULIRG was fitted with a CSFRA SED element originating in the high SFE group of models. This was found to be a direct result of fitting the upper limits to the short wavelength ($\lambda \leq 3\mu$m) flux data points, as it is the high SFE SEDs that are optically revealed. A thought experiment showed that hypothetical, lower absolute flux values in that region resulted in a best-fit ULIRG SED originating in the low SFE group of models. What this demonstrates is that the model ULIRG SED library can be used in a wide range of environments, from optically thick, to optically thin and good results obtained. However, it was also revealed that estimation of the short wavelength data points must improve before more robust conclusions can be made.

Contents

Acknowledgements 4

Abstract 5

Table of Contents 7

List of Figures 13

List of Tables 16

1 Introduction 18

1.1 Thesis Overview 21

2 Active Galactic Nuclei Model 23

2.1 Optical Spectrum Classification 23

2.1.1 Seyfert I & II 24

2.1.2 LINERS 27

2.2 Review of AGN Modelling 28

2.3 Dust Model 34

2.3.1 Grain Species 35

2.3.2 Extinction Efficiency & Grain Abundance 36

2.3.3 Extinction Curves 41

2.4 PG Quasar Source Function 46

2.4.1 0.01μm - 1.2μm 46

2.4.2 1.2μm - 100μm 47

2.5 Radiative Transfer and Input Variables in DaRT 48

2.5.1 Source Calibration 50

2.5.2 Torus Characteristics 52
2.6 Emergent Spectrum 53
2.6.1 Variation of SED with θ_v 54
2.6.2 Variation of SED with T_{dust} & τ_{uv} 56
2.7 AGN SED Library 57
2.8 Summary of Chapter 2 59

3 HII Region Model **60**
3.1 Starburst Modelling To-Date 61
3.2 Starburst Grain Model 66
3.2.1 Extinction Efficiency & Abundance 67
3.2.2 Extinction Curves 72
3.3 Stellar Population Synthesis Codes 76
3.4 STARBURST99 Input Variables 80
3.4.1 Star Formation Mode 80
3.4.2 Total Stellar Mass 81
3.4.3 The Stellar IMF 83
3.4.4 Metallicity & Mass Loss Tracks 86
3.4.5 Unused Input Variables 86
3.4.6 Summary of Input Parameters 87
3.5 STARBURST99 Central Source Functions 87
3.5.1 Time-Steps for Output 88
3.5.2 Ionizing Photon Output 93
3.6 The HII Region Model 95
3.6.1 The Photoionization Phase 96
3.6.2 The Rapid Expansion Phase 99
3.6.3 Momentum Conservation Phase 102
3.6.4 Boundaries of the System 106
3.6.5 Gas Mass Density 108
3.6.6 Optical Depth 109
3.6.7 Inputs to the Radiative Transfer Code 114
3.7 HII Region Optical Depth Distribution 114
3.8 HII Region Spectral Energy Distributions 117

3.9 Supernovae in ERR00 119

4 Supernovae Model **122**

4.0.1 Supernovae Type Ia, Ib and Type II 122

4.1 Modelling Supernova 123

4.1.1 Standard Pressure-Driven Expansion Model 124

4.1.2 The Standard Model & Starburst Modelling 126

4.1.3 Thesis Modelling 129

4.2 Supernovae Energy Distribution 131

4.3 Adiabatic Phase 132

4.3.1 Equations of Motion 134

4.3.2 Adiabatic Shell 136

4.3.3 Scheme for the Total Supershell Width 139

4.4 Cooling Radius R_c in the GMC 140

4.5 Isothermal Phase 145

4.5.1 Equations of Motion in the GMC 145

4.5.2 Isothermal Shell 146

4.5.3 Width of the Isothermal Shell 146

4.5.4 Equation of Motion in the Ambient Region 147

4.5.5 Cooling Radius in the Ambient Region 149

4.5.6 Cooling Radius in the Ionized HII Region 150

4.6 Evaluation of $R2_{SN}$ 150

4.7 Behaviour of The Radius & Velocity 152

4.7.1 $M_{GMC} = 10^9 M_\odot$ 152

4.7.2 $M_{GMC} = 10^8 M_\odot$ 156

4.7.3 $M_{GMC} = 10^7 M_\odot$ 157

4.7.4 $M_{GMC} = 10^6 M_\odot$ 157

5 Expressions for the Optical Depth **162**

5.1 Evolution of an Example Model System 163

5.2 Review of Gas Density Equations 168

5.2.1 The HII region Phase: $t \leq t_{SNstart}$ 168

5.2.2 The Supernova Phase: $t_{SNstart} < t \leq t_{R2_{SN}}$ 169

5.2.3 Shell Temperature: $R_{SN}(t_{SN})+1\Delta t$ 170

5.2.4 Supershell Temperature: $R_{SN}(t_{SN})+2\Delta t$ . . . 172
5.2.5 Supershell Temperature: $R_{SN}(t_{SN})+3\Delta t$ . . . 172
5.2.6 Supershell Temperature: $R_{SN}(t_{SN})+4\Delta t$ On-wards . . . 175
5.3 Supershell Temperature in Isothermal Phase . . . 176
5.3.1 Dust Condensation . . . 178
5.4 Optical Depth Equations & DaRT Inputs . . . 179
5.5 Behaviour of Optical Depth . . . 183
5.5.1 $M_{GMC} = 10^8 M_\odot$; Low η . . . 184
5.5.2 $M_{GMC} = 10^8 M_\odot$; High η . . . 197
5.5.3 M_{GMC}=10^9-, 10^8-, 10^7- & $10^6 M_\odot$; All η . . . 208

6 Starburst SEDs **215**
6.0.1 $M_{GMC} = 10^8 M_\odot$; Low η . . . 217
6.0.2 $M_{GMC} = 10^8 M_\odot$; High η . . . 231
6.0.3 $M_{GMC} = 10^6$-, 10^7-, 10^8- & $10^9 M_\odot$ SEDs . . . 237
6.0.4 The low η Dust Reformation Scenario . . . 249
6.0.5 Comparison with ERR00 . . . 250
6.1 The Starburst SED Library . . . 252
6.1.1 Instantaneous Burst SED Library . . . 253
6.1.2 Extension to Constant Star Formation Approximation . . . 254

7 Assessment of the ULIRG Model **264**
7.1 ULIRG Sample . . . 265
7.1.1 Published Data . . . 266
7.1.2 Transformation to Rest Frame . . . 268
7.2 Statistical Methodology . . . 269
7.2.1 Generation of the GEM ULIRG SED Library . . . 271
7.2.2 Identification of the Best-fit . . . 276
7.3 Analysis I . . . 291
7.3.1 ULIRG Physical Characteristics I . . . 292
7.3.2 ULIRG Sample Discussion I . . . 296
7.4 Analysis II . . . 311
7.4.1 ULIRG Physical Characteristics II . . . 312
7.4.2 ULIRG Sample Discussion II . . . 317

7.5 Analysis III 320
7.6 Conclusion to the Analyses 328
7.7 Potential Sources of Error in the GEM Approach 329

8 Conclusions & The Future **339**
8.1 Conclusions 339
8.2 The Future 345
8.3 Concluding Remarks 347

A Sampling in Dart **348**
A.1 Initialization of the DaRT System 348
A.1.1 The Radial Grid 348
A.1.2 The Azimuthal & Angular Grids 349
A.1.3 First-Guess Temperature Distribution 350
A.1.4 User-Defined Grid Variables 350
A.2 The Radiative Transfer Equation 350
A.2.1 Validity of the Solution 353
A.3 Input & Output 355
A.4 Grid Integration Variables 357
A.4.1 The ϕ Grid 358
A.4.2 The θ Grid 361
A.4.3 The Radial Grid 363
A.4.4 Summary of Integration Grid Variables 366
A.4.5 Errors on the DaRT Grid 366
A.4.6 Code Convergence to a Single Solution 368

B Gas Dynamics **371**
B.1 The Rankine-Hugoniot Conditions 371
B.1.1 Mass Conservation 372
B.1.2 Momentum Conservation 372
B.1.3 Energy Conservation 373
B.1.4 Summary of the Rankine-Hugoniot Conditions 373
B.2 Density Ratio in Adiabatic Phase 374
B.2.1 Up- and Downstream Gas Velocity 374

B.2.2 Up and Downstream Mach Numbers 375
B.2.3 Velocity Ratio 375
B.2.4 Density Ratio 376
B.3 Density Ratio in the Isothermal Phase 376

Bibliography **379**

List of Figures

2.1 Schematic diagram of a Seyfert Galaxy 25
2.2 Dependence of Q_{ext} on x=$2\pi a/\lambda$ 40
2.3 AGN Dust Model Absorption, Scattering & Extinction Cross-sections . . . 43
2.4 AGN Source Function 49
2.5 Schematic diagram of a Tapered Disc 53
2.6 AGN Spectral Energy Distributions 55

3.1 Starburst Dust Model Individual Grain Cross-sections 73
3.2 Starburst Dust Model Total Cross-sections 74
3.3 STARBURST99 $Z_\odot$ Evolutionary Tracks 79
3.4 STARBURST99 Source Function 91
3.5 STARBURST99 Ionizing Photon Output 94
3.6 Comparison of Time Dependent Radial Solution to the Standard Spitzer Solution 103
3.7 Evolution of the HII Region Optical Depth 112
3.8 A_v^{TOT}(t) Distribution for the HII Region Solution 115
3.9 HII region Spectral Energy Distributions 117

4.1 Supernova Source Function 133
4.2 The Cooling Function 141
4.3 Radius and Velocity curves for $M_{GMC} = 10^9 M_\odot$ 153
4.4 Radius and Velocity curves for $M_{GMC} = 10^8 M_\odot$ 156
4.5 Radius and Velocity curves for $M_{GMC} = 10^7 M_\odot$ 158
4.6 Radius and Velocity curves for $M_{GMC} = 10^7 M_\odot$ 159

5.1 Contributions to A_v^{TOT}(t) at Early Times 164
5.2 Contributions to A_v^{TOT}(t) at Intermediate Times 165

5.3 Contributions to A_v^{TOT}(t) at Late Times 166
5.4 Calculation of Shell Temperature 171
5.5 A_v(t) for M_{GMC}=$10^8 M_\odot$, η=0.01 & η=0.025 186
5.6 Av(t) for M_{GMC}=$10^8 M_\odot$, η=0.05 & η=0.1 192
5.7 Av(t) for M_{GMC}=$10^8 M_\odot$, η=0.15 & η=0.2 201
5.8 Av(t) for M_{GMC}=$10^8 M_\odot$, η=0.25 206
5.9 A_v(t) for all M_{GMC} (a) 209
5.10 A_v(t) for all M_{GMC} (b) 213
5.11 A_v(t) for all M_{GMC} (c) 214

6.1 SEDs for $M_{GMC} = 10^8 M_\odot$, $\eta = 0.01$ & 0.025 218
6.2 SEDs for $M_{GMC} = 10^8 M_\odot$, $\eta = 0.05$ & 0.1 219
6.3 SEDs for $M_{GMC} = 10^8 M_\odot$, $\eta = 0.2$ & 0.25 220
6.4 SEDs for $M_{GMC} = 10^8 M_\odot$, $\eta = 0.25$ 221
6.5 SEDs for $M_{GMC} = 10^9 M_\odot$, $\eta = 0.01$ & 0.025 238
6.6 SEDs for $M_{GMC} = 10^9 M_\odot$, $\eta = 0.05$ & 0.1 239
6.7 SEDs for $M_{GMC} = 10^9 M_\odot$, $\eta = 0.15$ & 0.2 240
6.8 SEDs for $M_{GMC} = 10^9 M_\odot$, $\eta = 0.25$ 241
6.9 SEDs for $M_{GMC} = 10^7 M_\odot$, $\eta = 0.01$, 0.025, & 0.05 242
6.10 SEDs for $M_{GMC} = 10^7 M_\odot$, $\eta = 0.1$ & 0.15 243
6.11 SEDs for $M_{GMC} = 10^7 M_\odot$, $\eta = 0.2$ & 0.25 244
6.12 SEDs for $M_{GMC} = 10^6 M_\odot$, $\eta = 0.15$ & 0.2 245
6.13 SEDs for $M_{GMC} = 10^6 M_\odot$, $\eta = 0.2$ 246
6.14 Comparison of Extinction 251
6.15 Variation of the Constant Star Formation Approximation Half-life 259
6.16 Constant Star Formation Approximation Half-Life Variation SEDs 261

7.1 Reduced χ^2 Testing Flowchart 277
7.2 00262+4251 χ^2 data 279
7.3 12540+5708 χ^2 data 282
7.4 13428+5608 χ^2 data 284
7.5 14348-1447 χ^2 data 286
7.6 15250+3609 χ^2 data 288
7.7 23365+3604 χ^2 data 289

7.8 Best-Fit GEM SEDs 297
7.9 Best-Fit GEM SEDs 298
7.10 13428+5608 Adjusted Flux χ^2 data. 323
7.11 13428+5608 Adjusted SED 324

A.1 Spectra and Maximum Variance for NHPII testing 359
A.2 Model run-time analysis for grid variable NPHII 361
A.3 Spectra and Maximum Variance for NTH testing 362
A.4 Model run-time analysis for grid variable NTH 364
A.5 Normalised Spectra for NSUB testing 367
A.6 Minimum No. Iterations for a Single Solution 369

B.1 Flow Variables of an Adiabatic Shock 372
B.2 Flow Variables of an Isothermal Shock 377

List of Tables

2.1 Ultraluminous infrared galaxy sample 24
2.2 AGN Dust Model Abundances 40
2.3 AGN Model Input Variables for DaRT 54

3.1 Starburst Grain Model Abundances 71
3.2 Principle PAH Infrared Emission Wavelengths & Mechanisms 75
3.3 Input Variables for STARBURST99 87
3.4 Time-Step Variables for STARBURST99 89
3.5 HII Region Solution Models 105
3.6 Fixed Parameters for HII Region Solution 119

5.1 Categorisation of All Models by η 184
5.2 Variation of the Extinction for $\eta = 0.01$, $M_{GMC}=10^8 M_\odot$ 187
5.3 Variation of the Extinction for $\eta = 0.025$, $M_{GMC}=10^8 M_\odot$ 191
5.4 Variation of the Extinction for $\eta = 0.05$, $M_{GMC}=10^8 M_\odot$ 193
5.5 Variation of the Extinction for $\eta = 0.1$, $M_{GMC}=10^8 M_\odot$ 198
5.6 Variation of the Extinction for $\eta = 0.15$, $M_{GMC}=10^8 M_\odot$ 202
5.7 Variation of the Extinction for $\eta = 0.2$, $M_{GMC}=10^8 M_\odot$ 203
5.8 Variation of the extinction for $\eta = 0.25$, $M_{GMC}=10^8 M_\odot$ 207

6.1 Categorisation of all $M_{GMC} = 10^8 M_\odot$ Models by η 217
6.2 Classification of All Models by η 237
6.3 Spectral Characteristics at Early Times 247
6.4 Spectral Characteristics at Late Times 248
6.5 The Rate at which GMC's are Forming Stars at $t' = 0$ 258
6.6 $Av^{TOT}(t)$ for $M_{GMC}=10^8 M_\odot$, η=0.15 263
6.7 The number of GMC's to join the ensemble in a time bin $N_{GMC}(t')\Delta t$ . . 263

7.1 Ultraluminous infrared galaxy sample 266
7.2 Observational Data 267
7.3 Free Parameters of the ULIRG SED 273
7.4 Free Parameters for best-fit ULIRG GEM SED 290
7.5 Luminosity contributions to the best-fit GEM ULIRG SED 299
7.6 Physical Characteristics of the best-fit ULIRG SEDs 300
7.7 Results from the *Analysis II* 318
7.8 13428+5608 Adjusted Fluxes 322
7.9 13428+5608 Adjusted Flux Results 325

A.1 DaRT Integration Grid Variables 367

Chapter 1

Introduction

Ultra-Luminous Infrared Galaxies (ULIRGs) are a class of extragalactic object which emit significant radiation in the infrared. It is the high luminosity of these galaxies which makes them particularly useful as 'laboratories' for studying a broad range of astrophysical processes.

In this introductory chapter, first the nature of ULIRGs and the possible triggering mechanism for starburst activity are briefly examined. An outline of the importance of ULIRGs, both in a local and cosmological context, is followed by a short discussion on modelling such objects. The chapter concludes with an overview of the work undertaken in the thesis.

What Are ULIRGs?

A brief period of intense star formation, where a large amount of gas is rapidly converted into predominantly high mass (>$8M_{\odot}$) stars is, by definition, a starburst (Siebenmorgen & Krügel 2007). Ultra-luminous infrared galaxies (ULIRGs) are one of the brightest categories of starburst galaxy, having a rest-frame 1-1000μm luminosity of $L_{1-1000\mu m} \geq 10^{12}L_{\odot}$ (Farrah *et al.* 2003).

The high mass stars formed in ULRIGs are short-lived (a few million to a few-tens-of-million years) and extremely luminous ($L_{\star}$ > a few thousand $L_{\odot}$), so observed bursts are likely the product of recent star formation (Leitherer *et al.* 1991). It might therefore be expected that the presence of these hot ($T_{\star}$ > 25,000K) high-mass stars means that the luminosity of a ULIRG should peak in the ultraviolet (UV) ($\lambda \sim$ 912 to 3000 $\AA$) region of a galaxy's SED. However the giant molecular clouds (GMCs) which can harbour the

massive stars can also contain significant quantities of dust and the intrinsic SED of a young stellar population peaks in the UV, where the opacity of the grains that permeate the GMC is maximal.

Absorption of UV photons heats the dust grains to temperatures of the order 10 - 100K and longer wavelength, infrared radiation is emitted as the grains cool. Thus, when large numbers of high mass stars are present in the dusty environment of a ULIRG, infrared radiation, not optical and UV radiation dominates.

What Triggers Starburst Activity?

Early theoretical work by Toomre & Toomre (1972) suggested that it was galaxy interactions and mergers which drove huge quantities of gas and dust into the nuclear regions of luminous infrared galaxies, providing an archetypal site for triggering dust enshrouded active galactic nuclei (AGN) and star formation.

The InfraRed Astronomical Satellite (*IRAS*), launched in 1983, carried out four all sky surveys at 12-, 25-, 60- and 100μm and was able to identify $\sim$ 75,000 infrared galaxies, many of which were too faint to have been included in previous optical surveys. The correlation of the luminous infrared sources with catalogues of interacting galaxies showed that starbursts could indeed be triggered by gravitational interaction between galaxies (Kennicutt *et al.* 1987).

This was also confirmed by e.g., Sanders *et al.* (1988), using optical, infrared and millimetre-wave observations of a sample of ten ULIRGs selected from the IRAS Bright Galaxy Survey (Soifer *et al.* 1989). Not only were Sanders *et al.* (1988) able to conclude that all ten were ongoing interactions between two spiral galaxies, but also, that each was powered by a combination of AGN and starburst activity.

Why are ULIRGs Important?

Amongst the other important results from *IRAS* was the construction of the luminosity function. This function describes the number of galaxies having a given absolute magnitude within a luminosity range per cubic parsec and as a general rule locally, luminous galaxies are rare, while intrinsically faint ones are common (Schwarzschild 1965). The luminosity function for galaxies detected by *IRAS* was determined from a compilation of samples with highly complete redshift information and included many nearby low-luminosity galaxies (e.g. Saunders, Rowan-Robinson, Lawrence, Efstathiou, Kaiser,

Ellis & Frenk 1990; Oliver, Rowan-Robinson, Broadhurst, McMahon, Saunders, Taylor, Lawrence, Lonsdale, Hacking & Conrow 1996). The *IRAS* data predicted there would be only one galaxy with $L_{1-1000\mu m} > 10^{12}L_{\odot}$ in the redshift range $0.00 < z < 0.033$; later identified as Arp220 (Heckman 1998). It was therefore estimated that locally, luminous infrared galaxies contributed only around 10% of the integrated bolometric energy density in the Universe (Sanders *et al.* 1988).

However, whilst there did not appear to be evidence for a change in the luminosity function of the local universe, this was not the case as the redshift of the observed objects increased. At faint flux levels, (<1Jy at 60μm, corresponding to sources with $z \geq 0.1$) the derived luminosity function changed to be more strongly biased towards higher luminosity objects. This implied that the contribution to the bolometric luminosity density of the universe from luminous infrared galaxies at higher redshift might greatly exceed that observed for objects located in the more local universe (Farrah 2001).

Further evidence supporting this proposal came from deep sub-mm surveys which discovered a population of sources at high red-shift having rest-frame luminosities of the order $L_{IR} \geq 10^{12}L_{\odot}$ (e.g., Steidel (1996)). The logical conclusion became that the local ULIRGS may be the low-z analogues of these very luminous high-z objects.

In summary, these observations suggest that studying luminous infrared galaxies provides an opportunity not only to examine the interstellar medium under extreme conditions but also the processes involved in the merger, interaction and formation of such galaxies. It would appear that a better understanding of the evolution of ULIRGS is important both locally and in a broader cosmological context.

Modelling ULIRGs

It is therefore vital that infrared observations are interpreted in terms of a self-consistent picture describing the spatial distribution of the stars, and dust over a range of temperatures. This is usually accomplished by simulating the transfer of continuum radiation in a dusty medium using a radiative transfer code and then matching the resultant emergent SEDs to observations.

As suggested by e.g., Sanders *et al.* (1988), most ULIRGs are thought to be powered by a combination of AGN and starburst activity. The AGN element can be modelled by embedding a suitable source function in a dusty torus and then calculating the radiative transfer of flux through the system to generate an emergent SED (e.g., Efsthathiou &

Rowan-Robinson (1990*a*)).

The starburst element is more complex and is often treated by modelling a dusty system evolving under the influence of e.g., a stellar ionizing flux or supernovae energy distribution. Having obtained the dust density distribution, it is irradiated by a stellar SED and the radiative transfer of flux is also calculated. The emergent SEDs generated by the AGN and starburst radiative transfer simulations are then summed to generate a combined ULIRG SED which can be matched to observations (e.g., Farrah *et al.* (2003)).

In this thesis a new method to calculate the evolution of a dusty GMC, under the influence of both a time-dependent ionizing photon flux and the impact of a continuous supernovae energy input is developed. The method incorporates in one package a wide range of physics, including simple shock physics, to determine the structural evolution of the GMCs and hence the dust density distribution and optical depth along a line of sight.

Having conducted the radiative transfer simulations for both the AGN and the new starburst model, a library of ULIRG SEDs in presented and tested against observations of a small sample of local ULIRGs. The properties of the ULIRGs are then constrained, with results generated for, amongst others things, the dust enshrouded star formation rate, the age of the starburst, the galaxy merger and interaction state and the radiating dust mass.

1.1 Thesis Overview

Chapter 2 starts with a brief prècis of modelling AGN's over the last twenty years and then re-generates from the literature, a grain model which has been particularly successful in replicating the highly energetic, optically thick environment of these central engines. A source function suitable for an AGN is then developed, again from the literature and the adopted radiative transfer code is briefly discussed. Finally the emergent AGN SED's are described and illustrated for various combinations of viewing angle, temperature and optical depth in the modelled parameter space.

Chapter 3 develops the first element of the starburst source component - the HII region model - and begins with a brief synopsis of the progress made modelling the emergent SEDs of luminous infrared galaxies to-date. Following this, a grain model suitable for application to a star forming galaxy is described and the evolutionary synthesis code used to generate the instantaneous burst central stellar population is discussed. A model of the thermal evolution of a GMC under the influence of a time-dependent stellar ionizing flux is then

developed, from which the dust density distribution as a function of time is obtained. Irradiating this dust distribution with the appropriate stellar cluster SED and simulating the radiative transfer of flux generates the emergent HII region SEDs. Finally these SEDs are discussed in terms of the central source function and the grain extinction efficiencies.

Chapter 4 considers the second element of the starburst source component - the supernovae model - which describes the impact of supernova energy on a GMC already ionized by the stellar photon flux. First a brief review is given of the physics and assumptions of the standard-pressure driven expansion model (e.g., Weaver *et al.* (1977)) and its application in simulating the effect of supernovae on dusty environs. The motion equations used to describe the expansion of a superbubble under the influence of a continuous supernova energy injection are then derived. The chapter closes with a brief discussion of the behaviour of the derived evolution for all possible parameter combinations on the model grid.

Chapter 5 develops the equations governing the optical depth along a line of sight and derives the input variables needed for the radiative transfer code. The behaviour of the optical depth in all GMCs on the model grid is then illustrated and the key points highlighted. Chapter 6 presents the supernovae solution emergent SEDs and behavioural trends and defining characteristics are identified and discussed. The chapter ends in an in-depth discussion on the extension of the instantaneous burst SED library just developed to approximate constant star formation.

Chapter 7 first considers the manipulation and addition of the SED's from both the AGN and starburst models to generate a library of emergent combined model SEDs suitable for fitting to observational data of a small sample nearby ($z \leq 1$) ULIGRs. Having obtained the SED combination which best matches the observations, results are generated for the ULIRG physical characteristics such as the star formation rate, merger and interaction state, radiating dust mass, the age of the starburst, star formation history and total mass of stars formed. The chapter culminates in a discussion of the potential sources of error in the thesis methodology.

Chapter 8 summarises the results and delivers a conclusion as to the veracity of the adopted modelling approach. The thesis ends in a brief consideration of a potential program of work which might build on the thesis modelling and improve our understanding of these fascinating objects.

Chapter 2

Active Galactic Nuclei Model

In this chapter a library of emergent spectral energy distributions (SEDs) appropriate for the Active Galactic Nuclei (AGN) component of a ULIRG galaxy is presented. The chapter begins by considering some of the basic characteristics of AGN, including an overview of the main physical regions that make up a central engine and the potential effect of varying the viewing angle on the emergent spectrum.

A literature review is then conducted and suitable published models for an AGN central source function, dust composition and radiative transfer computer code are identified. Having discussed the reconstruction and extinction characteristics of the chosen dust model, the central source function is composed. A comprehensive assessment of DaRT, the chosen radiative transfer code has been reserved for Appendix A.

Having examined the three elements required for the AGN modelling, the central source function was then used to irradiate the dust distribution in DaRT and the radiative transfer of flux calculated. The resultant emergent spectra are then considered in terms of the source function and dust model behaviour and a discussion is held on the effect on the SED of changing the viewing angle, dust temperature and optical depth. The chapter concludes by preparing the AGN SED library for fitting to the ULIRG sample

2.1 Optical Spectrum Classification

Table 2.1 gives the name and location of the six local ultraluminous infrared galaxies selected for modelling from the NASA Extragalactic Data base. One classification of AGN can be made on the general characteristics exhibited in the optical part of the spectrum

IRAS Name	Other Name	RA(2000) (hh:mm:ss)	Dec. (° ' ")	z	Optical Spectrum	No.Data Points
00262+4251		00 28 54.2	+43 08 15.3	0.0927	LINER	14
12540+5708	Mrk 231	12 56 14.2	+56 52 25.2	0.0422	SEYFERT 1	29
13428+5608	Mrk 273	13 44 42.1	+55 53 12.6	0.0378	SEYFERT 2	23
14348-1447		14 37 38.4	-15 00 22.8	0.0827	LINER	22
15250+3609		15 26 59.4	+35 58 37.5	0.0552	LINER	21
23365+3604		23 39 01.3	+36 21 08.7	0.0645	HII+LINER	18

Table 2.1: Ultraluminous infrared galaxy sample. Co-ordinates, redshifts, optical spectral classifications and number of data points, taken from the NASA Extragalactic Data base.

and the table shows that the AGN optical spectra in the sample fall into three main classifications: Seyfert 1 and 2 systems and LINERS. As an introduction to modelling Active Galactic Nuclei the physical characteristics of these categories is now be briefly outlined.

2.1.1 Seyfert I & II

Beginning with Mrk 231 & 273, these are Seyfert galaxies, first described as a class by Carl Seyfert in 1943 when 6 galaxies, each with strong, broad emission lines coming from a compact bright galaxy nucleus, were identified (Seyfert 1943). Most Seyferts are located in the nearby universe and emit the bulk of their radiation in the infrared. Seyferts are generally radio-quiet and show distinctly different spectral characteristics depending on the viewing angle. The variable energy output points to the power source as a black hole plus accretion disc, thus qualifying them as AGN (Zeilik & Gregory 1998).

Seyferts fall into two categories: Seyfert 1 and Seyfert 2, essentially defined by the width of their emission lines. The former have permitted emission lines, such as the Balmer series of Hydrogen, which are extremely broad in width and forbidden lines that are only moderately broad. The latter class, Seyfert 2, are fainter in the optical and both their forbidden and permitted lines are of equivalent width, which is remarkably narrow when compared to the width of the permitted lines in Seyfert 1's.

A unification theory has been proposed (e.g. Antonucci 1993; Antonucci & Miller 1985) that suggests these two Seyfert classes are in fact the same type of object, with orientation to-wards the observer being the defining characteristic. The hypothesis is that the radiation from the central nucleus encounters two distinctly different gaseous environments on its journey out-wards through the galaxy. The first region is the Broad

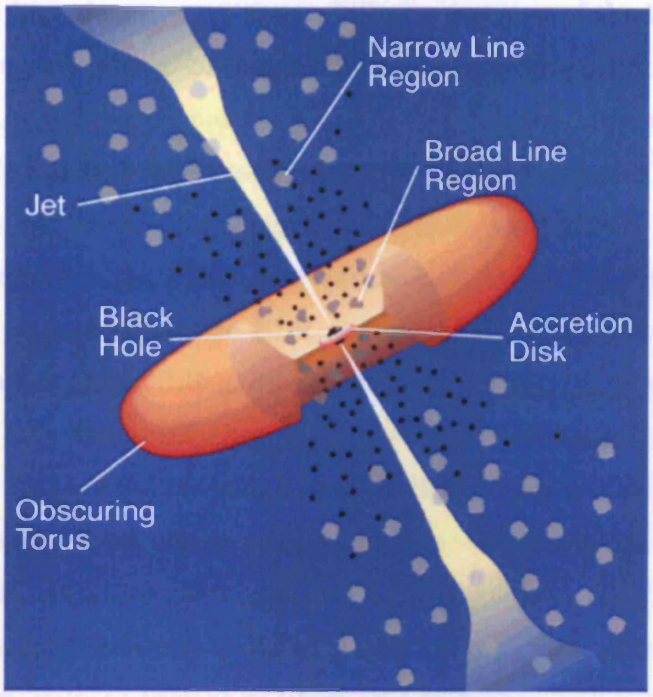

Figure 2.1: Schematic diagram of a Seyfert Galaxy (not to scale), illustrating the effect of viewing angle and the ability to detect the broad line region (BLR) and narrow line region (NLR). An edge-on view will result in the optical spectrum characteristics of a Seyfert 2 due to obscuration of the BLR by cool dust in the outer regions of the torus. Conversely a face-on viewing angle provides a direct view of the BLR and the hot dust at the inner edge of the torus which results in a Seyfert 1 classification. At intermediate angles the BLR is detected only by the scattered light (black dots) and the internal extinction to the BLR will be small relative to an edge-on orientation. That the extinction to the BLR region decreases from the edge-on view is due to the geometric shape of the torus causing a shorter column length of dust to be observed between the viewer and the source as the viewing angle increases. (Diagram taken from Heisler (1998))

Line Region (BLR), which has a typical size of <1parsec and comprises a ring of very hot gas. The region is known to have a very steep temperature gradient and a high density from the unbroadened forbidden lines emanating from this area. Forbidden lines are indicative of a high density and their width is a function of the kinetic temperature.

The BLR is also thought to be responsible for a large proportion of the Seyfert luminosity as the gas in the region has been accelerated to very high speeds by the central black hole. The BLR generates emission features when they appear in the SED and also scatters direct flux out of the line of sight (Zeilik & Gregory 1998).

Moving outwards from the BLR is the Narrow Line Region (NLR), which is often some 1000 times larger in scale than the BLR and considerably less dense, with the density decreasing with radius. The NLR is thought to be composed of huge amounts of cold gas and dust which is only marginally heated, either by re-radiating dust at inner radii or by the central source. Most of the internal heat of the dusty torus is radiated through its upper and lower surfaces and these effects combine to give this area of the cloud a temperature of only around 50K. However, although the NLR contributes little to the spectrum, it can be responsible for obscuring material at shorter radii and therefore for some of the absorption features, such as that at $\approx 10\mu$m, in a spectrum (Zeilik & Gregory 1998).

Finally, the dust on any part of the lower or upper disc surfaces, not just the inner ring region, is likely to be much hotter than the rest of the cloud as it will also be exposed to direct radiation (Zeilik & Gregory 1998; Osterbrock 1989).

Referring to Figure 2.1, it can be seen how the BLR and NLR may be responsible for the orientation dependent spectral characteristics that have led to the two-part classification of Seyferts. When a system is being viewed face-on, the observer has access to emission lines coming from both the BLR and the NLR along with absorption lines from the NLR. Conversely, when the system is being viewed edge on, the dusty torus obscures the BLR and the lines from this area are absent in the observed spectra. Considering the NLR in the edge-on view, emission and absorption lines are still in evidence as this region co-exists with the dusty torus and is thus accessible to the observer in all circumstances (Heisler 1998).

It should be noted that even though the forbidden lines from the NLR are classified as narrow, this is in relation to the broadened lines of a Seyfert 1 rather than in comparison to forbidden lines in normal galaxies which are narrower still than those in a Seyfert 2 (Zeilik & Gregory 1998). Several authors have examined the question of whether the

NLR in Seyferts could be powered by radio jets as Seyfert galaxies containing luminous linear radio sources tend to have broader forbidden emission line widths. It has been suggested (e.g., Bicknell *et al.* 1998; Whittle 1992) that this observation may indicate an additional acceleration mechanism. This could potentially involve interaction of a jet with the circumnuclear interstellar medium, leading to excitation of some fraction of the NLR and hence the increased width of the forbidden emission lines originating there.

Returning to the two-part Seyfert classification, the idea that it may be an issue of orientation is also confirmed by considering one of the main diagnostic characteristics in the emitted infrared spectra of these objects. Seyfert 2 galaxies can be identified by the existence of a silicate spectral feature in absorption at $\lambda \approx 10\mu$m, which indicates the system is being viewed edge on through an optically thick torus. However, the spectra of Seyfert 1 galaxies do not show this feature in emission which is a considerable stumbling block to the unification theory as it would be expected to arise from the inner hot surface of the dusty accretion disk if the BLR was accessible to the observer. Therefore currently, the observation of a silicate absorption feature at 10μm is evidence that the BLR and the system is being viewed edge-on but the absence of that feature is only an *indication* that the system is being viewed edge-on (Zeilik & Gregory 1998).

2.1.2 LINERS

00262+4251, 14348-1447 & 15250+3609 have Low Ionization Nuclear Emission Region (LINER) optical classification whilst 23365+3604 has that of a combination HII region and LINER. Low Ionization Nuclear Emission Regions (LINERS) have optical spectra that are very distinct from AGN although their radio, X-ray and emission line properties may be superficially similar due to hidden 'dwarf' AGN (Nicholson *et al.* 1998). LINERS, as their name implies, have very narrow emission lines of low ionization; the original observational definition of a LINER was a galaxy nucleus with emission-line ratios ([OII]λ3727)/([OIII]λ5007) $\geq$ 1 and ([OI]λ6300)/([OIII]λ5007) $\geq$ 1/3 (Osterbrock 1989). Whilst many HII region galaxies satisfy the first of these conditions they do not satisfy the second.

Another indicator of low-ionization galaxies is that they have stronger [OI]λ6300 and [SII]$\lambda\lambda$ 6716, 6731 than do HII regions and large [NII]/H_α line ratios (Osterbrock 1989). However, the emission lines do not originate in the disk and mechanisms that have been proposed for these lines include shock heating, cooling flows or photoionization by very hot

stars or warmers (Zeilik & Gregory 1998). Among the earlier-type galaxies of the Hubble sequence, Sa and Sb, a large fraction, $\approx$ 80%, are LINERS, with the remainder being HII-region galaxies. However there is an abrupt change at Sc where about 20% are LINERS and 80% HII-region galaxies (Osterbrock 1989). It has been proposed that some LINERS, particularly those potentially containing a 'dwarf' AGN may represent the missing link between low luminosity AGN and nearby 'normal' galaxies (Nicholson *et al.* 1998).

2.2 Review of AGN Modelling

Having ascertained some of the general physics of an AGN, the coming section reviews the research progress that has been made in synthetically regenerating an emergent AGN SED. The community has been considering this problem in particular since the advent of the *InfraRed Astronomical Satellite (IRAS)*, launched in 1983, which was the first observatory to perform an all-sky survey at infrared wavelengths. This instrument gave astronomers access to huge quantities of high quality infrared data which could be used to constrain and improve theoretical models.

Thanks to the ongoing effort, the sophistication of the theoretical AGN models published in the literature has steadily increased until at the time of writing, the choice of possible route for generating an AGN SED library is somewhat numerous. This being so, there was no need to generate a *new* AGN model for the thesis, but simply to identify which published model would be the most appropriate to *re-generate* from the literature. Three elements are required: a dust composition which replicates interstellar extinction, a central source function to irradiate the dust and finally, a computer code capable of calculating the radiative transfer of the flux through a dusty AGN torus.

The primary criteria for the choice of precisely which published dust and central source model would be adopted for the thesis was obviously their suitability and proven success in modelling the AGN element of a ULIRG. However, it was also important to ensure that the chosen models were sufficiently up-to-date to take advantage of the most recent observational and theoretical developments in the research arena. Finally, the degree of detail available in the publishing literature had to be *complete* as both the dust model and the central source function were to be regenerated from scratch, with no help from the originating authors.

In the following research review, particular emphasis has been placed on the methods

that have been adopted by the thesis and provides some justification for the suitability of that choice.

AGN Modelling To-Date

One of the first works to attempt modelling the infrared spectra of *IRAS* galaxies was Rowan-Robinson & Crawford (1989) which presented synthetic SEDs for over 200 galaxies, including the important starburst galaxy Mrk231 and the well studied active galactic nuclei NGC1068. The model required three separate source functions; a normal disc component, a starburst component and a Seyfert component. The luminosity of the normal disc component was well-correlated with the optical luminosity of the galaxy sample and was interpreted as emission from interstellar dust illuminated by galactic starlight (Rowan-Robinson & Crawford 1989). The starburst component was modelled as an optically thick cloud containing a newly formed massive star with a blackbody spectrum. The Seyfert component was assumed to be a power law between $\lambda = 0.1\mu$m and 1mm, with spectral index $\alpha = 0.7$, which was used to illuminate dust in the narrow-line region (NLR). The starburst component was embedded in a spherically symmetric cloud of silicates with the grain properties adopted by Rowan-Robinson & Harris (1982). The emergent starburst SED was obtained using a radiative transfer (RT) code published by Rowan-Robinson (1980) which integrated the equations of RT through a spherical system. When combined with the disc and Seyfert elements satisfactory fits were found to most of the non-Seyfert *IRAS* galaxies in the sample. Other conclusions concerned the composition and geometry of the dust and suggested a better fit to the Seyfert sample could be obtained using a dust spatial distribution more complex than simple spherical symmetry. It was also thought that the incorporation of very small grains into the dust model, in addition to the silicates, might potentially improve the model fits.

The first of these conclusions to be tackled was the issue of non-spherical geometry when *Radiative Transfer in Axi-symmetric Dust Clouds* (Efsthathiou & Rowan-Robinson 1990*b*) [hereafter ERR90] was published which unveiled DaRT - a Dust and Radiative Transfer code developed by Michael Rowan-Robinson's Ph.D. student Andreas Efstathiou. DaRT presented a significant update to the original spherically symmetric RT code published by Rowan-Robinson (1980) due to its ability to calculate flux transfer in dusty, axi-symmetric disk systems, more realistic of AGNs. In this paper the late-type supergiant VYCMa was modelled as a blackbody surrounded by dust distributed in an

equatorial disc. Using the same single grain silicate model published by Rowan-Robinson & Harris (1982), ERR90 were able to reach some important conclusions, foremost amongst which was the affect of orientation on emitted spectra; the FIR spectrum long-ward of 50μm was essentially unaffected by viewing angle θ_v but the rest of the spectrum varied significantly for even a small increment in θ_v. For example the slope of the NIR spectrum decreased with increasing θ_v, as more of the inner hot dust was observed. These conclusions illustrated the importance of viewing angle in an axi-symmetric system and demonstrated that calculation of flux transfer through a disk could be accomplished. This code was used successfully for AGN (e.g Efstathiou *et al.* 2000; Farrah *et al.* 2002; Farrah *et al.* 2003). The axi-symmetric DaRT radiative transfer code was personally requested from its author and obtained for use in the thesis work presented here and hence is described more fully in §2.5.

In addition to a more complex dust spatial geometry, the original conclusions of Rowan-Robinson & Crawford (1989) also made it clear that a grain model more sophisticated than single silicates was needed to improve the model fits (Rowan-Robinson & Crawford 1989). Such a model had been published by Rowan-Robinson (1986) [hereafter RR86] who presented a grain composition designed to fit the interstellar extinction curve. This consisted of small 0.01 and 0.03μm graphite grains, silicate grains of the same radii and 0.1μm amorphous carbon and amorphous silicate grains. This RR86 grain model had originally been used to fit the interstellar 'cirrus' found by *IRAS*, which was presumed to be due to the small graphite grains (RR86). However, the RR86 grain composition was updated for modelling the far-infrared spectra of large, nearby spirals mapped by *IRAS* when *Interstellar Dust in Galaxies* (Rowan-Robinson 1992) [hereafter RR92] was published. In that work the RR86 model was improved with the incorporation of very small grains of radii 0.0005-0.002μm which were included to explain the diffuse mid-infrared emission whist the inclusion of very large grains of radius 30μm was to fit the excess at millimetre wavelengths (RR92). This new grain composition was used by RR92 to model the emission dominated by the cirrus component of the spiral galaxies in their sample and reasonable fits to the 12-100μm spectra were found, with inferred dust extinctions in the visible that were ≤ 1 (RR92).

The RR92 dust model was modified slightly when *Multi-grain Dust Cloud Models of Starburst and Seyfert Galaxies* was published (Rowan-Robinson & Efsthathiou 1993) [hereafter RR93]. Although this work used the RR92 grain model as its root due to its good

agreement with the interstellar extinction curve and with COBE observations of the spectrum of emission from interstellar dust, the very smallest grains (of radii 0.0005-0.002μm) proposed in RR92 were omitted. These very small grains were included in RR92 to model diffuse MIR emission but in the high optical depth starburst and Seyfert environments considered in RR93 these grains were no longer necessary as their contribution was washed out. Having modified the grain composition, RR93 used a source function regime very similar in nature to that used by Rowan-Robinson & Crawford (1989) in that it consisted of a cool disc or cirrus element, a starburst component and a Seyfert component peaking at around at 12-25μm (RR93). Using their improved multi-grain dust model and these source elements, RR93 were able to achieve some very good fits to the infrared spectra of their galaxy sample, specifically for ultra-luminous galaxies at high optical depths. Therefore the RR93 dust model has been replicated in this thesis work to model the composition of the dusty torus within which the central source function will be embedded.

However, despite the ability of DaRT to model axi-symmetric systems, both the starburst and Seyfert source components in RR93 were still modelled as black bodies embedded in spherically symmetric dust-clouds. It was noted that using a more sophisticated AGN source function embedded in a suitable form of axi-symmetric disc might significantly improve the model fits.

Based on these conclusions, it appeared that to progress further the central source function - previously described primarily as a simple black body - needed to evolve in tandem with the grain model and RT code. Some years previously, Sanders *et al.* (1989) had studied an appropriate sample of 109 objects from the Palomar Green survey. This survey targeted quasars (QUASi-stellAR radio source) which are extremely bright and distant active galactic nuclei, thought to consist of a compact halo of matter surrounding the central supermassive black hole of a young galaxy. Sanders *et al.* (1989) found they were able to quantify the form of the SED for around two-thirds of their optically selected sample using power laws.

Using this work, Rowan-Robinson (1995) presented a *A New Model for the IR Emission of Quasars* in which data for a subset of 23 PG quasars, each having 25- and 60μm *IRAS* fluxes of reasonable quality, were used to derive an average PG quasar composite spectrum. This derived spectrum was then used to illuminate isolated clouds composed of the 7 grain dust model of RR93, placed at different distances from the central source. The emission from the narrow-line region at λ = 3-30μm was then modelled as a superposition of

these dust clouds, whilst a starburst component contributed to the emission at 30-100μm. Using the radiative transfer code DaRT (ERR90), the emergent SEDs were calculated. Rowan-Robinson (1995) were able to infer that the broad correlation of luminosities in the starburst and quasar components suggested a common fuelling mechanism, for example via galaxy interactions and mergers (Rowan-Robinson 1995). This AGN source function, derived from the PG quasar sample, has been used successfully many times since (e.g., Efstathiou *et al.* 2000; Farrah *et al.* 2002; Farrah *et al.* 2003) and has been chosen to model the AGN central source function used in this thesis work and is discussed in more depth in §2.4. Having improved the form of the AGN source function, the other main conclusion from RR93 could now be considered; the geometry of the dusty disc.

There are several geometries an axi-symmetric system can take: flared or tapered discs and anisotropic spheres and with *Dusty Discs in AGN*, Efsthathiou & Rowan-Robinson (1990*a*) explored these possibilities. Using a slightly modified version of the ERR90 DaRT code which allowed a variety of density distributions to be tested, infrared spectra for different combinations of dust density and disc geometry were computed. The central source function used followed the broken power law to approximate the average spectrum of the PG quasars. Assuming a dust composition as per the RR93 7-grain model, Efsthathiou & Rowan-Robinson (1990*a*) set three minimum observational requirements for a 'good' fit: the spectrum should be quite broad for face-on views and peak in the mid-IR, absorption features at $\lambda \approx 10\mu$m should be found for edge-on views but be absent for face-on views and finally, that these two requirements should be satisfied across all torus opening angles. After conducting exhaustive tests with combinations of disc geometry and dust density the authors concluded that thick tapered disks, where the height increases with distance from the central source but tapers off to a constant height in the outer part, were the most appropriate. Efsthathiou & Rowan-Robinson (1990*a*) found that a disk opening angle of $\approx 45°$, with the dust following an $n(r) \propto r^{-1}$ density distribution satisfied the observational constraints best, with the remaining combinations being highly inconsistent with published data (Efsthathiou & Rowan-Robinson 1990*a*). Using these conclusions for disc geometry, the derived average spectrum of a PG quasar was then used to model the IR continuum of NGC1068 by Efsthathiou *et al.* (1995) who placed it at the centre of an axi-symmetric thick tapered disc composed of RR93 dust. Having calculated the transfer of flux through the system using the DaRT code of ERR90 a very reasonable fit of the infrared to mm spectrum of this Seyfert galaxy was obtained (Efsthathiou *et al.* 1995).

In 1999, Alexander *et al.* (1999) successfully modelled NIR observations of the infrared continuum of Centaurus A using blackbody cirrus designed to model high latitude clouds in the halo, a starburst source function and a blackbody AGN peaking at 60μm embedded in a thick, tapered disk. On this occasion the cirrus and starburst elements were both surrounded by clouds consisting a new Polycyclic Aromatic Hydrocarbon (PAH) inclusive grain composition. These appeared essential in modelling the distinctive mid-infrared emission bands seen in starburst galaxy spectra (Siebenmorgen & Krügel 1992). As an aside, this latter PAH grain model has been chosen for use with the starburst component of this thesis work and as such is returned to in Chapter 3 where that element is fully developed.

Returning to the AGN, Alexander *et al.* (1999) assumed their disc was also composed of the 7-grain RR93 model which had previously proved so successful. The non-inclusion of PAH clusters in the RR93 dust scheme was considered by those authors a moot point as the transiently heated small grains and PAH's responsible for the starburst mid-IR emission features were presumed to be destroyed on very short times-scales by the hard X-rays present in an AGN (e.g., Voit 1991; Roche *et al.* 1991; Siebenmorgen *et al.* 2004). Alexander *et al.* (1999) found that new ISOSWS, ISOPHOT_S and 8-13μm observations of Centaurus A were fitted very well using the three source component model and importantly, that the AGN component did not require a PAH element. At the time it had been suggested that the *IRAS* 60-to-25μm flux ratio could be used as an indicator of torus inclination, with high and low ratios implying edge-on and face-on inclination respectively (Alexander *et al.* 1999). However, the authors showed that whilst in a small nuclear sized aperture the density ratio may indicate inclination, in a larger aperture, other more powerful IR emitting components like the starburst dominated the torus. Nevertheless Alexander *et al.* (1999) were able to find a best fit to the continuum spectrum with a tapered torus inclined at an angle of 45°. It therefore appeared that an appropriate disc geometry for modelling high energy AGNs was tapered and as such this form was chosen for the dusty tori modelled in this thesis work.

It was now apparent that all three elements needed to successfully model the AGN component of a ULIRG galaxy were in place; a sophisticated radiative transfer code had been developed by ERR90 which was able to trace flux through a variety of disc geometries, of which thick tapered had proved the most applicable. A grain model in the form of the RR93 composition had been tried and tested and shown itself to be a very satisfactory

fit to the interstellar extinction curve. Finally a suitable central source function had been derived from a large number of objects in the PG quasar survey (Rowan-Robinson 1995).

What remained was for this prescription to be applied to a broader range of environments and its efficacy further assessed. This occurred when Farrah *et al.* (2002) presented *Sub-millimetre Observations of Hyper-luminous Infrared Galaxies* which modelled eleven HYLIRGS - those galaxies with $L_{IR} \geq 10^{13.0} h_{65}^{-2} L_{\odot}$, where h_{65} denotes $H_o = 65 kms - 1Mpc^{-1}$ - and employed the prescription discussed above for its AGN component. The paper presented excellent fits to e.g., NGC6090 and the nucleus of M82 and was also able to conclude that where an AGN and starburst were both present, their activities were coeval.

The second paper in the series *Starburst and AGN Activity in Ultraluminous Infrared Galaxies* (Farrah *et al.* 2003) modelled forty-one local ULIRGS - or those galaxies having $10^{12.0} h_{65}^{-2} L_{\odot} \leq L_{IR} \leq 10^{13.0} h_{65}^{-2} L_{\odot}$ - also using the prescription discussed above for the AGN. They found that although each object in the sample required a starburst component, only about half required an AGN and further, that in 90% of the sample the starburst provided over half the IR emission.

These last two papers: Farrah *et al.* (2002) & Farrah *et al.* (2003) [hereafter FH03], present a good example of how modelling synthetic ULIRG SEDs using both an AGN and starburst component has been utilized to interpret observations. This being so, where possible the successful methodology used by FH03 has also been adopted in this thesis.

The choice of the FH03 model as a basis for the thesis proves beneficial in several ways. The six local ULIRGS chosen for this thesis' test sample come from amongst the forty-one objects in the FH03 sample, so the conclusions of this thesis can be compared and contrasted to those of FH03. The model methods used by FH03 to generate the AGN and starburst HII region SED libraries are amongst the more complex and advanced available and are therefore at the forefront of current research. Finally, the success of Farrah *et al.* (2002) & FH03 in interpreting observed ULIRG SEDs means the model provides a solid foundation upon which to build the *new* work undertaken in this thesis.

2.3 Dust Model

As indicated in the previous literature review, the grain model chosen for the thesis is based on the model published by RR92 in *Interstellar Dust in Galaxies*, with the minor

modifications detailed in RR93 incorporated. This dust composition has been used many times to successfully model the environment of AGN (e.g., Rowan-Robinson & Efsthathiou 1993; Rowan-Robinson 1995; Efsthathiou & Rowan-Robinson 1990*a*; Efsthathiou *et al.* 1995; Alexander *et al.* 1999; Farrah *et al.* 2002; Farrah *et al.* 2003).

As mentioned in the introduction, the radiative transfer code to be used for the thesis is DaRT (ERR90). The RR93 dust model therefore had to be replicated from the literature in a form suitable for input into DaRT. To that end, first it was ascertained how and why the constituent grain species had been combined by RR93 to produce the required distribution. A bespoke computer program was then written to prepare the grain extinction efficiencies, apply the correct abundances and output the data for DaRT.

2.3.1 Grain Species

The RR93 model was designed to be the simplest possible that agreed with both COBE observations of the dust emission spectrum and the Milky Way interstellar extinction curve. Seven grains were required to fit that observational data:

- 0.1μm Amorphous Carbon Grains
- 0.03μm Graphite Grains
- 0.01μm Graphite Grains
- 0.1μm Astronomical Silicate Grains
- 0.03μm Silicate Grains
- 0.01μm Silicate Grains
- 30μm Amorphous Grains

As mentioned, the original RR92 model incorporated a species of very small grains of radius a = 5-20$\AA$ to explain the diffuse mid-infrared emission. However RR92 modelled low optical depth media and hence the small grains were necessary to fit the continuum. In RR93, Seyfert galaxies were modelled as high optical depth systems ($A_v \geq 20$) and these very small grains were not required as their contribution would have such a very minor affect on the spectrum. It was therefore presumed by RR93 that for Seyfert systems this very small grain mass was included in the 0.01μm graphite particles, leaving 7 constituent elements in the model (RR93).

2.3.2 Extinction Efficiency & Grain Abundance

The extinction efficiency factor $Q_{\nu,ext}$ can be written as the sum of the corresponding absorption ($Q_{\nu,abs}$) and scattering ($Q_{\nu,scat}$) efficiency factors

$$Q_{\nu,ext} = Q_{\nu,abs} + Q_{\nu,scat} \tag{2.1}$$

where ν is the frequency. The generation of these values for the 7 grains in the dust model is now examined.

0.1μm Grains

Two species of 0.1μm grain are incorporated into the RR93 model; amorphous carbon and amorphous silicate.

The optical properties of the disordered amorphous carbon grains were derived using observations of dust shells surrounding carbon stars, supported by laboratory studies (RR92) - a review of the laboratory studies can be found in e.g., Bussoletti & Colangeli (1990). The extinction factors of these grains were tabulated by Rowan-Robinson & Harris (1983) and originally expressed as

$$Q_{\nu,abs} = 4\pi a/\lambda(\mu m) \qquad log\lambda > 0.14\mu m \tag{2.2}$$

$$Q_{\nu,abs} = 10^{-0.6(log\lambda+0.02)} \qquad 0.14 > log\lambda > -0.4 \tag{2.3}$$

$$Q_{\nu,abs} = 1.69 \qquad log\lambda < -0.4\mu m \tag{2.4}$$

and

$$Q_{\nu,scat} = [4\pi a/\lambda(\mu m)]^4 \qquad log\lambda > 0.14\mu m \tag{2.5}$$

$$Q_{\nu,scat} = Q_{\nu,abs} \qquad log\lambda < 0.14\mu m \tag{2.6}$$

However, RR92 updated the absorption efficiencies for the carbon grains, reducing them by a factor of 1.5 for $\lambda > 0.4\mu$m, which provided a better fit to the interstellar extinction curve between 5-9μm but left the total extinction at $\lambda < 1\mu$m unchanged (RR92). This reduction in absorption efficiency was applied to the Rowan-Robinson & Harris (1983) tabulated values for use in this thesis work. The location of the slope change at $\lambda \approx 1.4\mu$m was determined experimentally by (Rowan-Robinson & Harris 1983) using the visible and NIR observations of the dust shells surrounding carbon stars.

The a =0.1μm amorphous silicate grains had their optical properties derived from *IRAS* observations of circum-stellar dust shells around late-type M-stars undergoing mass-loss (Rowan-Robinson *et al.* 1986). For consistency with that *IRAS* data, $Q_{\nu,abs}$ was presumed proportional to ν for $\lambda > 28\mu$m (Rowan-Robinson *et al.* 1986). For the longer wavelength dust emission, dominated by silicates, the absorption efficiency $Q_{\nu,abs}$ of the grains was assumed to steepen from ν to ν^2 between 100- and 1000μm to get agreement with the Milky Way spectrum between 100-300μm (RR92). However, as the grain properties were empirically derived by Rowan-Robinson *et al.* (1986) their extinction efficiencies did not account for grain radius (RR86).

Therefore to find the extinction cross-section, $C_{\nu,ext} = \pi a^2 Q_{\nu,ext}$, a radius had to be assigned and this was done using evidence from polarization studies; a radius larger than 0.1μm led to inconsistencies with the cosmic abundance of silicon and a radius smaller than 0.1μm led to problems with the Kramers-Kronig relation (Purcell 1969) which implies Q_ν cannot be $\propto \nu$ for arbitrarily long wavelengths. The derived absorption and scattering efficiencies for these 0.1μm silicate grains were tabulated in RR86, Table 1 with the arbitrary normalization that

$$Q_{\nu,abs} = Q_{\nu,abs}(Log\lambda = -0.4) \tag{2.7}$$

and

$$Q_{\nu,scat} = Q_{\nu,scat}(Log\lambda = -0.4) \tag{2.8}$$

0.01μm & 0.03μm Grains

Two species of smaller grains are included in the RR93 model; graphite and silicate. Draine & Lee (1984) used laboratory and astronomical data to construct complex dielectric functions for graphite and silicate and then using Mie theory, were able to tabulate absorption and scattering cross-sections $C_{\nu,abs,scat}$ for particle sizes in the range 0.003-1.0μm. These cross-sections were then converted into extinction efficiencies and used by RR86 and RR92/93 to quantify the extinction profiles of the small grains.

Mie theory describes the scattering and absorption of light by particles (Mie 1908). In this instance *particles* denotes an aggregation of material that constitutes a region with a refractive index which differs from the refractive index of its surroundings. Mie theory utilises the Maxwell equations to derive a wave equation for electromagnetic radiation in three dimensional space and incorporates appropriate boundary equations at the surface of

a spherical particle. The result is a separable partial differential equation, the solution of which is expressed as an infinite series of products of orthogonal basis functions, including sines and cosines (for the dependence on ϕ), spherical Bessel functions (for the dependence on r) and associated Legendre polynomials (for the dependence on cos Θ). Essentially, Mie theory relies on a composition parameter which defines the complex refractive index of the particle material $m = n - ik$. The real part of the complex dielectric function (n), is directly responsible for absorption whilst the imaginary part (k) is responsible for scattering (Whittet 2003). The synthesised dielectric functions also satisfy the Kramers-Kronig dispersion relations which are mathematical properties connecting the real and imaginary parts of any complex function. For example, the integral of $Q_{\nu,ext}$ over all wavelengths can be obtained from the Kramers-Kronig relationship for spherical grains of radius a and refractive index m and then following the method of Purcell (1969) outlined in Whittet (2003), page 83.

Very Large Grains

RR92 introduced 30μm amorphous grains into the original RR86 mixture to account for anomalous observations of Galactic HII regions and star-forming clouds which showed excess absorption efficiency at $\lambda > 300\mu$m. The extinction efficiencies for the 30μm grains were assumed to be

$$Q_{\nu,abs} = 4\pi a/\lambda(\mu m) \qquad \lambda > 4\pi a \tag{2.9}$$

$$Q_{\nu,abs} = 1 \qquad \lambda \leq 4\pi a \tag{2.10}$$

and

$$Q_{\nu,scat} = [Q_{\nu,abs}]^2 \tag{2.11}$$

Grain Abundance

Having prepared the efficiencies for their grain model, RR92 compared them to the interstellar extinction curve tabulated in Mathis (1990). The best least-squares fit to observations of the Mathis (1990) interstellar extinction curve in the wavelength range 0.1-1.25μm was found using the fitting parameter

$$[(B_{\nu,obs} - B_{\nu,pred})/B_{\nu,obs}]^2 \tag{2.12}$$

where $B_{\nu,pred}$ is a fitted parameter and $B_{\nu,obs} = A_\lambda/E(B\text{-}V)$ with A_λ being the extinction at wavelength λ in magnitudes. The term *E(B-V)* quantifies the reddening using the observed colour index.

Thus $B_{\nu,pred} = B_o(Q_{\nu,abs} + Q_{\nu,scat}) = B_o Q_{\nu,ext}$. This expression can then be rearranged and used in conjunction with the following classical relations to find the abundance A_{gr} of the grains

$$\tau_{\nu,ext} = 0.92 A_\lambda \tag{2.13}$$

where $\tau_{\nu,ext}$ is the optical depth for a column of dust

$$\tau_{\nu,ext} = \pi a^2 A_{gr} N_H Q_{\nu,ext} \tag{2.14}$$

$A_{gr} = n_{gr}/n_H$ where n_{gr} is the number density of grains and n_H is the number density of H atoms. N_H is the column density of H atoms, where $N_H = 5.8 \times 10^{21} E(B\text{-}V)$ (Savage & Mathis 1979). Letting

$$E(B-V) = \frac{A_\lambda}{B_o Q_{\nu,ext}} \tag{2.15}$$

it follows that

$$N_H = \frac{A_\lambda \cdot 5.8\text{x}10^{21}}{B_o Q_{\nu,ext}} \tag{2.16}$$

and hence using Equation 2.14

$$A_{gr} = \frac{B_o}{\pi a^2 \cdot 6.3\text{x}10^{21}}. \tag{2.17}$$

The B_o values obtained by fitting this parameter for each grain species to find the best match to the total IS extinction curve are given in Table 2.2. Also tabulated are the percentage of the cosmic abundance accounted for in the grains and the relative abundance values in the form with which DaRT requires them; $A_{gr}/\Sigma A_{gr}$, where $\Sigma A_{gr} = 1.71 \times 10^{-10}$ and is the sum of all seven grain abundances in the model. Table 2.2 shows that 99% of the cosmic interstellar silicon is accounted for in grains, most contained within those of the largest radius and 54% of the cosmic interstellar carbon is available, with 20% in the largest grains.

Dependence of Optical Efficiency Q_{ext} on x=2πa/λ

Finally in this section on the RR93 dust model it is worth considering the dependence of the optical extinction efficiency of a grain, Q_{ext}, on the dimensionless size parameter

GRAIN	a(μm)	B_o	%Cosmic	$A_{gr}/\Sigma A_{gr}$
Amorphous Silicate	0.1	1.36	77	0.00398
Silicate	0.03	1.10	19	0.03567
Silicate	0.01	0.52	3	0.15660
Amorphous Carbon	0.1	0.45	20	0.00122
Graphite	0.03	0.45	9	0.02050
Graphite	0.01	0.24	4.7	0.78108
Amorphous Carbon	30	0.00089	12	2.69e-11

Table 2.2: The AGN Dust Model. Grain radius a, best fitting B_o values, % cosmic abundance and relative grain abundance $A_{gr}/\Sigma A_{gr}$ for the RR93 7-grain dust model (Rowan-Robinson & Efsthathiou 1993).

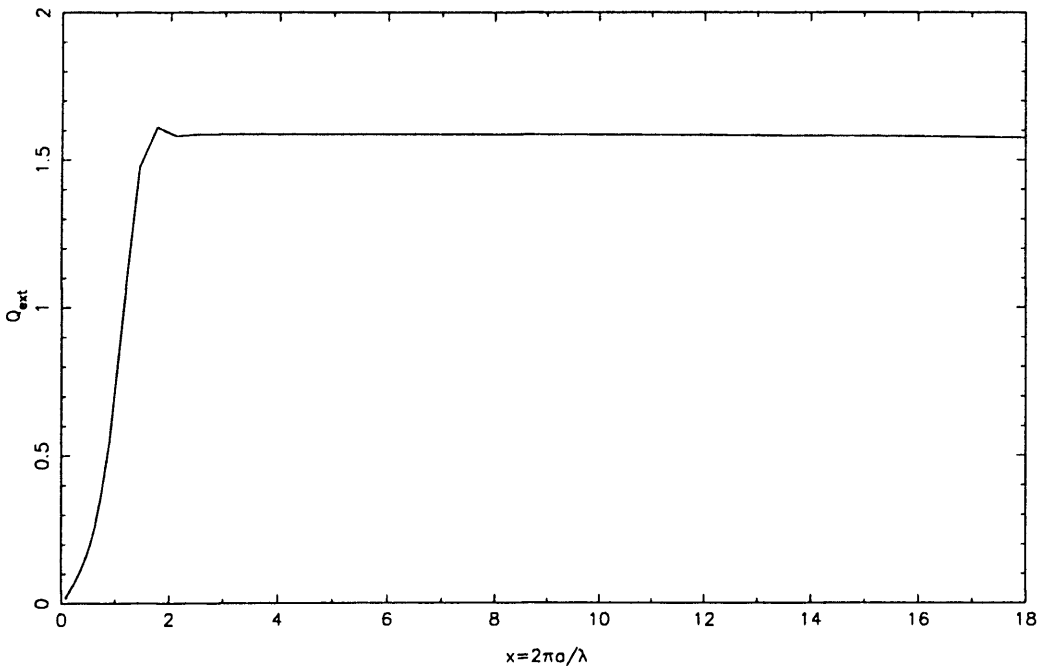

Figure 2.2: Dependence of Q_{ext} on x=2πa/λ for astronomical silicate grains of radius $a = 0.1\mu$m.

x=$2\pi a/\lambda$, where λ is the wavelength of the incident radiation and a is the grain radius. Q_{ext} can be plotted for any of the grains against x, but as the curves have many features in common only the distribution for astronomical silicate grains of radius $a = 0.1\mu$m is illustrated here in Figure 2.2. The primary reason for including this plot is that it is very hard to separate the affect of degenerate quantities such as abundance, efficiency and grain radius in a single plot illustrating e.g., the individual cross-section, $C_{\nu,abs,scat,ext} = \pi a^2 Q_{\nu,abs,scat,ext}$, yet it is important that it is understood.

Figure 2.2 shows that when x is very small ($x << 1$) such that the wavelength of incident radiation is very large compared to the radius a of the grain, the optical efficiency Q_{ext} increases as x increases. The efficiency rises almost linearly as x rises from zero, to reach approximately 1.6 as x approaches 2. The extinction efficiency of the grains rises with increasing x, when x is very small, due primarily to the scattering efficiency of the grains, as in this small x domain, the magnitude of the scattering efficiency is very sensitive to the precise value of x. The grains are the most efficient around $x \approx 2$ due to resonances between the wavelength and grain radii. However, these resonances will most likely be washed out when grains of many different radii are summed (Evans 1994*a*).

As the wavelength of the incident radiation decreases until it is the equivalent of or smaller than the radius a of the grain ($x >> 1$) the optical efficiency maintains its magnitude at $Q_{ext} \approx 1.5$. It might be said therefore that the efficiency distribution levels off when the radius of the grain is approximately $a \geq \lambda/2\pi$. As the efficiency appears to remain approximately constant as x grows large, the extinction is essentially wavelength independent for grains much larger than the wavelength of the incident radiation and the cross-section of scattering or absorption becomes the geometrical cross-section of the grain (Evans 1994*a*)

Having now discussed the constituent elements of the RR93 grain model, their abundance and the general behaviour of the optical efficiency, the grain profiles for absorption, scattering and extinction can be considered.

2.3.3 Extinction Curves

To successfully regenerate the dust model from the literature it was necessary to understand the optical efficiency behaviour of the individual grains and their relative abundance to a sufficient degree that the extinction curves could be programmed and prepared. However, to ultimately relate the impact the individual grain species might have on the

emergent AGN SEDs, the extinction behaviour must be understood across the whole wavelength regime. In that way the grains' response to the central source function and the eventual shape of the emergent SED can be interpreted.

Figure 2.3 gives the individual absorption and scattering cross-sections for all seven grains in the RR93 dust model, along with the extinction cross-section, $Q_{\nu,abs,scat,ext}$. These curves have been multiplied by the relative abundance of each grain $A_{gr_i}/\Sigma A_{gr}$ as listed in Table 2.2. The y-axis scale on each plot is different to provide the best resolution between curves. The plotted wavelength regions can be roughly divided into three regimes: the UV, Optical and NIR between 0.1μm and 4μm, the MIR between 4μm and 30μm and the FIR, submm, mm and cm at $\lambda > 30\mu$m (Mathis 1990) and these are now considered.

UV, Optical & NIR; $0.1\mu m \leq \lambda \leq 4\mu m$

This wavelength region contains one of the most recognisable spectral signatures in the entire interstellar extinction curve - the 2175$\AA$ "bump" (log λ = -0.6). Looking at the top plot of Figure 2.3 illustrating the absorption cross-section, it can be seen that the small graphite particles of $a = 0.01\mu$m, shown in green, are the primary carriers of the 2175$\AA$ absorption feature, with progressively more contribution to absorption from the $a = 0.03\mu$m graphite particles as 2175$\AA$ approaches. However, RR86 noted graphite alone led to a poor fit to the overall shape of the 2175$\AA$ feature and that these single grains could not reproduce the observed extinction over the rise between 0.16-0.1μm (RR86). Hence, at wavelengths shorter than 2175$\AA$ the absorption efficiency of the graphite grains must be supplemented by the two small silicate grains of radius $a = 0.01\mu$m and $a = 0.03\mu$m. Therefore the four silicate and graphite grains together absorb radiation from the line of sight.

Considering the larger $a = 0.1\mu$m silicate and carbon grains in absorption at these short wavelengths, their contribution is somewhat smaller than that of the small graphite grains despite their large size. As mentioned in the previous section §2.3.2 the large grains are efficient interceptors of radiation at shorter wavelengths, but referring to Table 2.2 it can be seen that their abundance is minimal when compared to the abundance of the smaller grains, specifically graphite at $a = 0.01\mu$m, which is $\approx$ 200 times as abundant as e.g., amorphous silicate $a = 0.1\mu$m. However, Figure 2.3 illustrates the considerable geometric cross-section of the larger grains and thus their contribution of the absorption at shorter wavelengths.

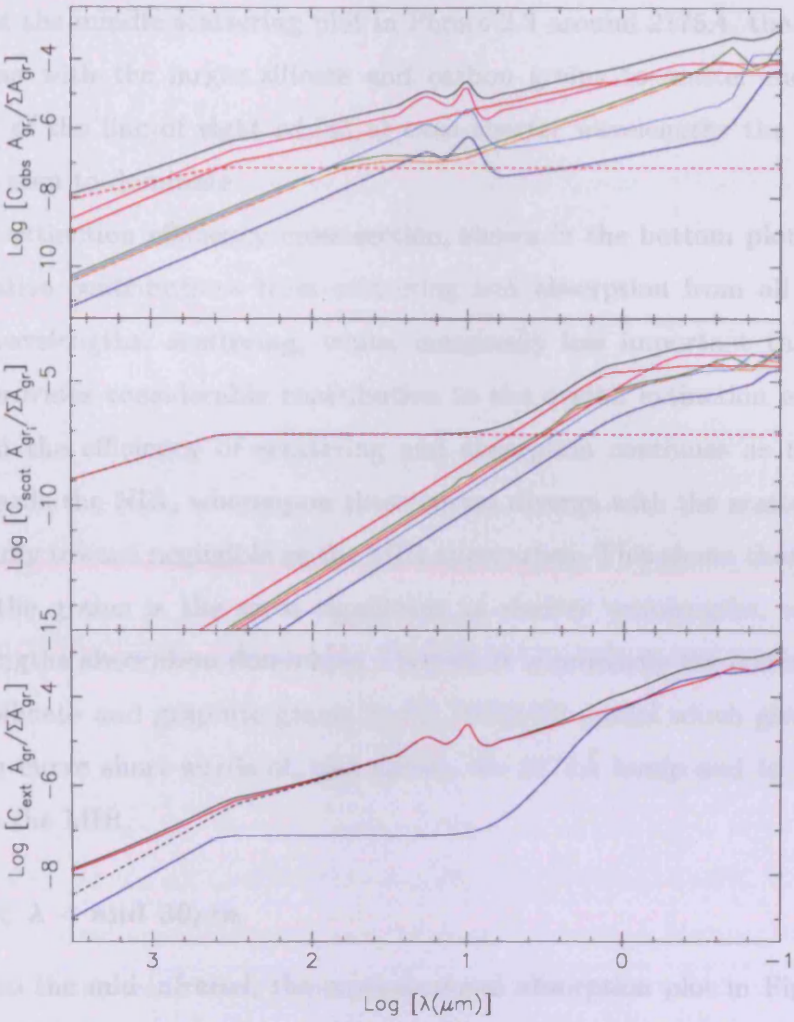

Figure 2.3: Cross-Sections for absorption (top), scattering (middle) and extinction (bottom) of the RR93 grain model. In the two upper plots, the total extinction cross-section of all seven grains is given in black, with the contribution from the 0.1μm silicate and carbon grains and the 30μm carbon grains shown by the pink, red and dashed red lines respectively. The contribution from the 0.03 and 0.01μm silicate grains and the 0.01 and 0.03μm graphite grains are given by the turquoise, dark blue, green and orange curves. Each of the efficiencies in these two plots are multiplied by the appropriate value of $A_{gr_i}/\Sigma A_{gr}$, given in Table 2.2, where the subscript i indicates each of the grains. In the bottom plot the total absorption efficiency, multiplied by the relative abundance $A_{gr}/\Sigma A_{gr}$ is given in red and the scattering in blue, with the solid black line illustrating their sum. The dashed black line in the bottom plot shows the total extinction cross-section in the absence of the 30μm carbon grains.

Looking at the middle scattering plot in Figure 2.3 around 2175$\AA$, the small graphite grains combine with the larger silicate and carbon grains to scatter most of incident radiation out of the line of sight whilst at even shorter wavelengths the small graphite grains can be seen to dominate.

The total extinction efficiency cross-section, shown in the bottom plot of Figure 2.3, gives the relative contributions from scattering and absorption from all grains and at these short wavelengths, scattering, whilst marginally less important than absorption, nonetheless provides considerable contribution to the overall extinction efficiency. This equivalence in the efficiency of scattering and absorption continues as the wavelength increases towards the NIR, whereupon these curves diverge with the scattering efficiency dropping rapidly toward negligible as the MIR approaches. This shows that the scattering efficiency of the grains is the most significant at shorter wavelengths, whilst at much longer wavelengths absorption dominates. Overall, it is primarily the combination of 0.01 and 0.03μm silicate and graphite grains in the RR92/93 model which give a good fit to the extinction curve short-wards of, and across, the 2175$\AA$ bump and to the continuum long-wards to the MIR.

MIR: 4μm < λ < and 30μm

Moving now to the mid-infrared, the cross-sectional absorption plot in Figure 2.3 nicely illustrate two distinct features between 4- and 30μm, which equate to silicate resonance features at 9.7- and 18-μm and originate in magnetic dipole absorption (Evans 1994*a*). The broad, smooth absorption feature at 9.7μm is generated by stretching of the Si-O bond, whilst the shallower peak around 18μm arises from the bending of the O-Si-O bonds, with both peaks corresponding to resonance oscillator frequencies. This provides good evidence for the inclusion of the silicate grains as they are in an amorphous, disordered form which produces smooth broad features - as against crystalline silicates which exhibit narrow, sharp structures (Krätchmer & Huffman 1979). Table 2.2 and the absorption cross-section plot in Figure 2.3 show that of the silicates, the largest grains are amongst the least abundant, but in turn, the cross-sectional plots show that they present the greatest geometric area to the incident radiation. It is these silicate features which provide such an important diagnostic tool for the angle at which an AGN torus is viewed; when the central engine is being viewed edge-on through a significant dust column the MIR silicate features would be expected in deep absorption. As the viewing angle increases, the depth of the

silicate absorption decreases, until for face-on views, the features are essentially absent in the spectra due to the lack of intervening dust.

Although not shown graphite is a highly anisotropic material and has contributions to the efficiency in directions both parallel and perpendicular to the basal plane. The assumption that is often made takes graphite particles as being randomly orientated, with two thirds of the particles having an isotropic dielectric function (perpendicular) and one-third an anisotropic function (parallel) (Whittet 2003).

FIR, submm, mm & cm; $\lambda \geq 30\mu$m

Between 30μm and 60μm the small grains compete to provide the continuum emission with the $a = 0.1\mu$m carbon and silicate grains as these latter grains are large enough to have an almost continuous density of energy states and the efficiency of the smaller grains has dropped off. At $\lambda > 60\mu$m the large grains dominate, which emit long wavelength radiation as they cool. As mentioned, RR92 introduced the 30μm grains to account for observations of excess absorption efficiency at $\lambda > 300\mu$m in Galactic HII regions and star-forming regions (RR92). Further evidence for these grains came from Halpern *et al.* (1988) who examined the diffuse Galactic emission and observed excess, low-temperature emission at millimetre wavelengths (RR92). Rowan-Robinson & Harris (1983) and RR86 suggested that as this high absorption efficiency had been observed in the carbon star IRC+10216 the 30μm grain probably originated in envelope of such stars (RR92).

The top two plots of Figure 2.3 show with the red dashed lines the absorption and scattering profiles of the 30μm grains and it can be seen that, despite their minimal abundance, the large geometric cross section they present to the radiation allows them to significantly contribute at longer wavelengths. The bottom plot of Figure 2.3 shows with the black dashed line the combined extinction cross-section of the six other grains, in the absence of the 30μm grains, with the difference between that dashed curve and the solid total extinction curve primarily arising from 30μm grain absorption.

This concludes the replication of a dust model suitable for the AGN component of a ULIRG. A central source function had to now be prepared to irradiate that dust. In a similar way to the dust model, another bespoke computer program was written to generate the central source function in a form suitable for input to DaRT, the ERR90 radiative transfer code.

2.4 PG Quasar Source Function

The model chosen for the AGN central source function is the derived PG Quasar average continuum used by Rowan-Robinson (1995) to investigate correlations between the continua, accretion disk viewing angle and the dust extinction. The function has also been used by several authors to model the AGN source component of a starburst galaxy (e.g.: Alexander *et al.* 1999; Ruiz *et al.* 2001; Farrah *et al.* 2002; Farrah *et al.* 2003). However, the Rowan-Robinson (1995) PG Quasar source function was found to only be appropriate over the wavelength range 0.01-1.2μm whilst the source function required for the thesis work encompasses the range 0.01-100μm. Therefore the extrapolation of Nenkova *et al.* (2002) was chosen to extend the wavelength region.

2.4.1 0.01μm - 1.2μm

Each quasar in the Rowan-Robinson (1995) set was sampled in its rest-frame at frequency intervals of 0.1dex for log ν = 14.0 to 14.6, 0.005 dex for 14.6 to 15.6 and 0.2dex for 15.6 to 18.00. The quantity ($\nu S_\nu/\nu_B$ S_B) was then estimated, where Log ν_B = 14.84. The power-law fits to the X-ray spectra of Elvis *et al.* (1986) were then extrapolated to 10^{16} Hz and the spectrum between $10^{15.5}$ and 10^{16} Hz was then interpolated on a log-log plot. The data for the average continuum spectrum derived was displayed graphically in Rowan-Robinson (1995) and values for the flux were tabulated in terms of Log ($\nu S_\nu/\nu_B$ S_B). The published values of Log S_B = -10.94 and Log ν_B = 14.84 were then used to convert the original data to λS_λ for use in the thesis.

Mapping this published flux distribution onto the current DaRT wavelength grid was accomplished using a natural cubic spline. A spline interpolates polynomials piecewise between the known data points and makes sure that the functions join up smoothly by causing the first and second derivative of the functions to be equal at the boundaries between the intervals. Thus, spline fitting essentially involved solving a system of simultaneous equations progressively through the Rowan-Robinson (1995) data and then reading off the AGN central source function from the smooth fitted functions at the appropriate current DaRT wavelengths.

The fluxes published by Rowan-Robinson (1995) for the derived average PG quasar continuum spectrum covered the wavelength region up to 3μm. However, it was noted by Rowan-Robinson (1995) and Laor & Draine (1993) that at $\lambda \sim$ 1.2μm, the energy

distributions showed a "break" in the power-law slope where the emission was presumed to change from originating in the central part of the AGN to arising from the reprocessing of radiation by dust in the outer torus (Rowan-Robinson 1995). As it is the latter dust reprocessed element that is to be modelled in this thesis work, the Rowan-Robinson (1995) source function was truncated at 1.2μm to avoid inadvertently including the affect of the source function on the dust, rather than the underlying function itself. Therefore, the spectrum can essentially be decomposed approximately as a power-law continuum at X-ray wavelengths, a 30,000-K blackbody peaking at 0.1μm and Balmer continuum radiation peaking at 3μm Rowan-Robinson (1995).

2.4.2 1.2μm - 100μm

Pier & Krolik (1993), Laor & Draine (1993) and Nenkova *et al.* (2002) also used the PG Quasar survey to study the properties of dust in AGN and designed a variety of power-laws to describe the average continua, generally in the form

$$\lambda_2 S_{\lambda_2} = \lambda_o S_o \left(\frac{\lambda_o}{\lambda_2}\right)^{-\alpha} \tag{2.18}$$

where α is the spectral index, λ_o is the cut-off wavelength, in this instance 1.2μm, S_o is the flux at 1.2μm from the Rowan-Robinson (1995) data and S_{λ_2} is the extrapolated flux. Considering the spectral index, Pier & Krolik (1993) used a radiative transfer algorithm to compute the IR spectra for 23 galaxies and then compared the resulting spectra to observations (Pier & Krolik 1993). They found that the spectra were relatively independent of the high and low energy cut-offs in the continuum power-law and using a value of α = -1 for the entire wavelength range they obtained reasonable fits to their observations(Pier & Krolik 1993) .

Laor & Draine (1993) also analysed galaxies from the PG quasar survey and using a 5 part power-law to cover the range 0.1 - 100μm were able to obtain reasonable fits to their observations. The specific wavelength region 0.03 - 1.2μm was fitted with a spectral index of $\alpha = -0.5$, whereafter it was assumed emission was likely due to dust so the Laor & Draine (1993) spectral indices's reflected that emission source. However, Nenkova *et al.* (2002) used the work of Laor & Draine (1993) to design a two-phase power-law which was employed to model the SEDs of a sample of Seyfert galaxies in the local universe. In that instance Nenkova *et al.* (2002) extrapolated the Laor & Draine (1993) spectral index of $\alpha = -0.5$ from 1.2μm to 100μm to represent the underlying central source function

rather than the emission from the dusty torus. Nenkova *et al.* (2002) then used their own radiative transfer code to model the energy distributions and were able to make some incisive connections between spectral features and the possible distribution of dust through the tori. As such it was decided to adopt the spectral index α =-0.5 in Equation 2.18 for the extrapolation of the Rowan-Robinson (1995) AGN source function to 100μm in this thesis work.

Figure 2.4 illustrates both the shorter wavelength Rowan-Robinson (1995) average continuum and the Nenkova *et al.* (2002) constant extrapolation to 100μm. At first glance it does not appear that this distribution was generated using a natural cubic spline due to its 'jerkiness'. However, this behaviour results from the spline fit being calculated at 1000+ wavelength points, the distribution of which was then mapped to the much grosser 84 point hard-wired DaRT grid used in this thesis. Finally, it should be mentioned that it is not essential to include extrapolations to 3.6cm - the longest wavelength on the DaRT grid - as both Sanders *et al.* (1989) and Laor & Draine (1993) found that beyond 100μm the small amount of rapidly decreasing energy available made very little impact on the emitted flux.

This concludes re-generation of the central source function for the AGN component of the ULIRG modelling. This function will be embedded in a dusty torus and the radiative transfer of flux through the dust calculated to generate the emergent SED. What remains is to therefore scrutinize DaRT, the adopted radiative transfer code (ERR90) and identify appropriate values for its input parameters.

2.5 Radiative Transfer and Input Variables in DaRT

DaRT - a Dust and Radiative Transfer code - was first published by ERR90 and has since been updated to tackle the transfer of flux though a variety of dusty geometries, including flared and tapered discs (Efsthathiou & Rowan-Robinson 1990*a*).

DaRT solves the problem of radiative transfer by ray tracing though a model system and then calculating the contribution to the final emergent spectrum from each point along a ray within that system (ERR90). Analysis of these environments is complex and must take account not only of direct radiation from a central source but also the interaction of that radiation with the dust grains. DaRT can calculate every term in the radiative transfer equation exactly, including multiple isotropic scattering, thermal radiation from

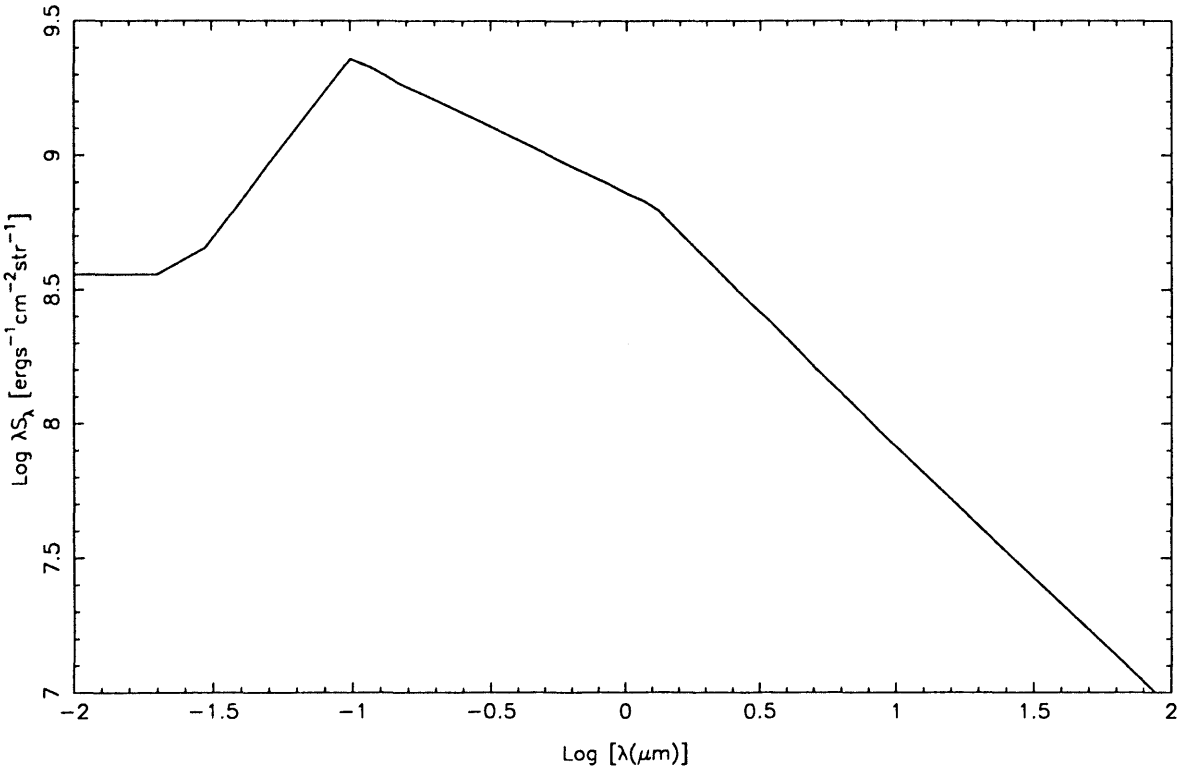

Figure 2.4: Log-Log plot of the AGN source function. 0.01-1.2μm shows the underlying common continuum derived by Rowan-Robinson (1995) from a sample of 23 PG Quasars. The function has been mapped onto the 84 point wavelength grid used in DaRT. Between 1.2-100μm the function is the extrapolation of Nenkova *et al.* (2002) given by Equation 2.18, with α = -0.5.

grains and radiation from the central source (ERR90).

The DaRT code was personally requested and obtained from ERR90 in a *totally uncommented form*, so the first task was to divine the method by which the calculation of the radiative transfer of flux was accomplished and obtain reasonable values for the integration grid variables. During this analysis a serious error was found with the DaRT code whereby around 30° in angle was missed when integrating, which resulted in a substantial lack of flux in the emergent spectra. This error was corrected, ERR90 informed (2004) and the code fully benchmarked to ensure all angles were included in the integration.

Due to the extensive nature of the verification task, full details of the analysis, the radiative transfer equations, assessment of the errors and location of reasonable values for the integration grid variables can be found in Appendix A.

The coming section will therefore be confined to an appraisal of the input variables required to internally calibrate the AGN source function, definition of the dust density distribution and specification of the geometry of the torus, which together characterise a model system.

2.5.1 Source Calibration

In calibration of the central source function, the number of input variables required is kept to a minimum by DaRT's use of the scaling properties of the radiative transfer problem, first described by Rowan-Robinson (1980). In this instance it is the scale-invariance of the radiative transfer problem that allows the user to calibrate a source function using only three parameters; the bolometric luminosity of the source L_{AGN}, the maximum dust temperature at the inner dust radius T_{dust} and the DaRT input variable $ERAT$ which is the *ratio* of the inner dust radius R_1 to the central source radius R_{AGN}. To see how the calibration is accomplished, consider the following equation for the bolometric luminosity or power of the source;

$$L_{AGN} = 4\pi R_1^2 \sigma T_{dust}^4 \tag{2.19}$$

where σ is the Stefan-Boltzman constant; 5.67 x 10^{-8} $Wm^{-2}K^{-4}$. Multiplying both sides by R_{AGN}^2 and rearranging for the source radius leads to

$$R_{AGN}^2 = \left[\frac{R_{AGN}}{R_1}\right]^2 \cdot \frac{L_{AGN}}{T_{dust}^4 4\pi\sigma} \tag{2.20}$$

This equation can now be re-written in terms of the DaRT input variable $ERAT = [R_{AGN}/R_1]$ such that

$$R_{AGN}^2 = \frac{ERAT^2}{T_{dust}^4} \cdot \frac{L_{AGN}}{4\pi\sigma} \tag{2.21}$$

$ERAT$ is a very useful DaRT input variable as it expresses the central source size as a multiple of the inner dust radius and so the need to find explicit values to input as the source and inner dust radii is circumvented. Values for $ERAT$ in the range 0.1 to 0.01 have been investigated by a variety of authors who have also used the DaRT code (e.g.: Efsthathiou & Rowan-Robinson 1990*a*; Efsthathiou, Hough & Young 1995; Alexander, Efstathiou, Hough, Aitken, Lutz, Roche & Sturm 1999), with all achieving good fits to their samples. However, as mentioned, FH03 modelled a large sample of ULIRGS and as good fits to the AGN component of those objects were achieved using a very similar AGN dust model, source function and RT code as described here, it was decided to adopt the same value as FH03 at $ERAT = 0.1$

Having assigned $ERAT$=0.1, to continue with the calibration, an explicit value for L_{AGN} must be selected and $L_{AGN} = L^{12}L_{\odot} = L^{12}$ x 3.9 x 10^{26}W was considered appropriate due to a definition of a luminous or ultra-luminous infrared galaxy being one whose luminosity lies somewhere in the range $L^{11}L_{\odot} < L_{IR} < L^{13}L_{\odot}$ (Condon *et al.* 1991; Farrah *et al.* 2001). However, it should be noted that whilst only one value has been selected by which to pre-calibrate the source function *prior* to its use in DaRT, the emergent AGN SEDs will be extended to cover a much broader luminosity space than simply $L_{AGN} = L^{12}L_{\odot}$ using a multiplication factor mf_{agn} and this is considered in detail at the end of this chapter in §2.7. Substituting the chosen value of L_{AGN} into Equation 2.21, replacing $ERAT = R_{AGN}/R_1$ and resolving for the inner dust radius R_1 gives

$$R_1 = \frac{1}{T_{dust}^2} \cdot \left(L^{12}\right)^{\frac{1}{2}} \cdot 2.34 \times 10^{16}(m) \tag{2.22}$$

So it can be seen that by simply stating the dust temperature T_{dust}, the bolometric luminosity of the central source L_{AGN} and selecting an appropriate value for $ERAT$, an exact position for the inner dust radius R_1 can be obtained. DaRT then places the first non-sublimated dust at that radius and goes on to use the inputted value of $ERAT$ to obtain the relevant source size R_{AGN} that produces the required luminosity at distance R_1. Thus, neither the inner dust radius or the central source radius need to be explicitly identified before calibration, but are a product of the relevant luminosity for the source in hand and the dust temperature at the inner edge of the system's torus.

2.5.2 Torus Characteristics

As DaRT only calculates the dust emission from the system, Table 2.3 shows the input variables needed to define a particular model system. The AGN torus characteristics of a thick tapered disk with an opening angle $\Theta_{max} = 60°$ and 15 viewing angles through the disk have been used successfully not only by FH03 in their ULIRG work but also by Rowan-Robinson (1995) to model NGC1068 and Farrah *et al.* (2002) to model their sample of HYLIRGs. A schematic of a tapered disc is displayed in Figure 2.5 and its defining characteristic is that its thickness, starting with a maximum value of *2h* in the outer part of the disc, decreases gradually in the inner part of the disc. The half-thickness of the disc as a function of *d*, the distance from the source (measured in units of R_{AGN}) is assumed to be

$$\frac{h}{R_2} tanh(h_o d) \tag{2.23}$$

where $h_o = R_2 \tan(\Theta_{max})/h$. Finally, a dust-free envelope within which the density is zero is assumed to surround the tapered dusty torus.

Dust Density Distribution

The radial dust density distribution is described by a power-law $n(R) \propto R^{-\beta}$ where index $\beta = 1$, whilst the index of the θ dust density power law is $\gamma = 0$. These values were taken from FH03.

Radial Variables

Considering the radial inputs of the torus, the ratio of the source radius to the inner dust radius *ERAT*=$[R_{AGN}/R_1]$ used in this thesis work has been discussed in the previous section §2.5.1. DaRT makes use of another ratio $ERO = R_1/R_2$ to find the edge of the dusty system, where R_2 is the outer radius of the torus. FH03 successfully used a value of $ERO = 0.01$ so this was also adopted in the thesis work presented here. Having obtained the inner dust radius R_1, it is a simple procedure for DaRT to use the value of *ERO* to determine the outer radius of the dusty torus.

Optical Depth and Dust Sublimation Temperature

Finally, the values chosen for the equatorial optical depth parameter space in the AGN modelling, at $\tau_{UV} = 1000$, 1250 & 1500, match those of FH03 and the range of dust

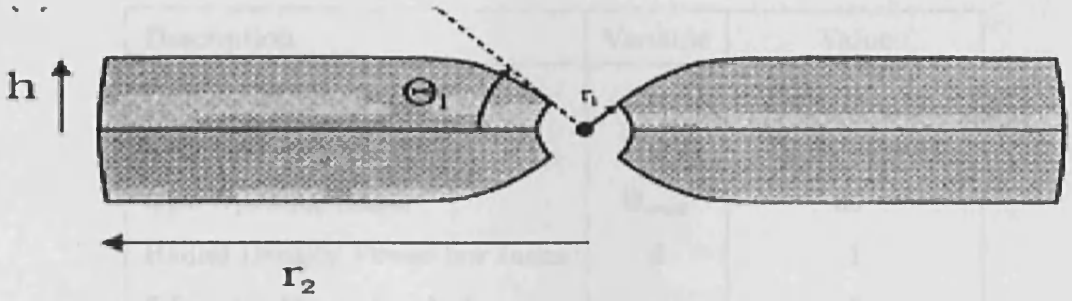

Figure 2.5: Schematic diagram of a Tapered Disc. The defining characteristic of a tapered disc is that its outer thickness, starting with a maximum value of *2h* in the outer part of the disc, decreases gradually in the inner part of the disc. For this diagram $r_1 = R_1$, $r_2 = R_2$ and $\Theta_1 = \Theta_{max}$ in the thesis nomenclature. A dust-free envelope within which the dust density is zero is presumed to surround the dusty torus. (Diagram taken fromEfsthathiou & Rowan-Robinson (1990*a*)).

sublimation temperatures, at T_{dust} = 1000, 1250 & 1500K, whilst not explicitly listed in the FH03, were considered representative of the sublimation temperatures of the constituent species of the grain model.

The ratio *ERO* has been defined such that the outer radius of the system R_2 is always $100R_1$. However, as was shown in section §2.5.1 the inner dust radius R_1 is found using the dust sublimation temperature T_{dust} as that dictates the minimum distance from the central source function at which dust can exist without evaporating. Thus, $R_{1_{1000K}} > R_{1_{1250K}} > R_{1_{1500K}}$ and similarly $R_{2_{1000K}} > R_{2_{1250K}} > R_{2_{1550K}}$. This means that in a system with, for example, $\tau_{UV} = 1000$ and $T_{dust} = 1500$K, the high dust temperature equates to a shorter column length of obscuring material along the observer's line of sight than a system with the same optical depth but a lower dust sublimation temperature e.g., $\tau_{UV} = 1000$, $T_{dust} = 1000$K. Therefore varying both T_{dust} and τ_{UV} in all selected combinations generates nine AGN models which together emulate a wide range of dusty environments.

2.6 Emergent Spectrum

Everything was now in place to generate the library of emergent AGN SEDs. The torus geometry and dust density distribution were defined as in Table 2.3 and the PG quasar central source function was embedded within the torus. The dust was then irradiated by the source function in DaRT and the radiative transfer of flux calculated, convergence

Description	Variable	Value
Number of viewing angles	θ_v	15
Disc Geometry	Mode	Thick Tapered
Disc Opening Angle	Θ_{max}	60°
Radial Density Power-law Index	β	1
θ Density Power-law Index	γ	0
Source Radius/Inner Radius	$ERAT$	$(0.1)^{1/2}$
Inner Radius/Outer Radius	ERO	0.01
Equatorial Optical depth	τ_{UV}	1000,1250,1500
Dust Sublimation Temperature	T_{dust}	1000,1250,1500K

Table 2.3: AGN model input variables for DaRT.

checked and the emergent SEDs produced for the chosen combinations of optical depth, dust sublimation temperature and viewing angle in the parameter space.

It is now possible to interpret the emergent SEDs and relate their behaviour and distinctive spectral features not only to the source function flux distribution but also to the grain model constituents and the extinction curves. The two parameters having the most influence on the spectra are the optical depth through the cloud and the sublimation temperature of the dust and these are now discussed.

2.6.1 Variation of SED with θ_v

Figure 2.6 shows the variation of the AGN emergent spectrum with viewing angle θ_v for the model T=1000K, $\tau_v = 1250$K and $L_{AGN} = 10^{12}L_{\odot}$ and looking first at the UV, Optical and NIR regions between $0.1\mu m \leq \lambda \leq 4\mu m$. As θ_v increases, the AGN's hot inner ring gradually comes into view as the obscuration caused by the dusty torus surrounding the BLR region drops. As mentioned, the inner ring is the region of the cloud responsible for emission and scattering and the plot of extinction cross-section in Figure 2.3 shows that scattering and absorption contribute almost equally to the extinction at $\lambda \approx 1$. So, for viewing angles close to the equator there is little flux to be seen in the SEDs at very short wavelengths due to the high opacity of the cloud and the efficient absorption and scattering of the small grains. This ensures most or all flux is removed from the line-of-sight with the absorbed flux re-emitted by the small grains into the NIR. As the viewing angle increases,

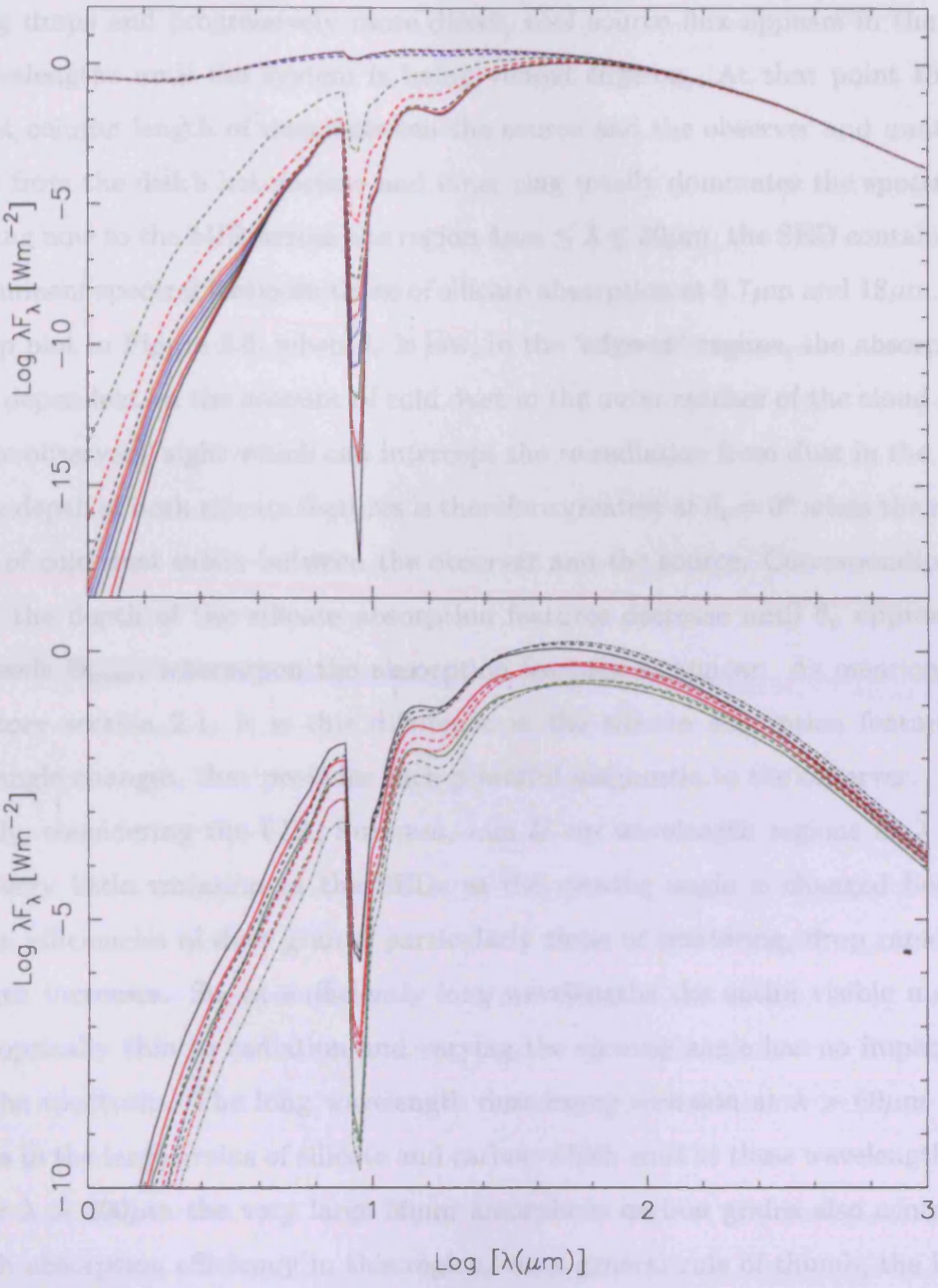

Figure 2.6: AGN Spectral Energy Distributions. The top plot shows the model for T=1000K, τ_v = 1250, $L_{AGN} = 10^{12} L_\odot$. The fifteen viewing angles; 0, 3, 9, 10, 13, 16 & 20° are shown by the solid lines in black, red, green, blue, turquoise, pink & orange respectively. Viewing angles 26, 38, 49, 60, 68, 75, 82 & 90° are shown by the dashed lines in the same colour sequence. The bottom plot shows $\theta_v = 38°$ for all nine models in the parameter space: Black, red and green show T_{dust}=1000K, 1250K & 1500K whilst the solid, dashed and dash-dot lines give τ_v = 1000, 1250 & 1500 respectively.

scattering drops and progressively more direct, cool source flux appears in the SEDs at short wavelengths until the system is being viewed edge-on. At that point there is no significant column length of dust between the source and the observer and unattenuated radiation from the disk's hot surface and inner ring totally dominates the spectrum.

Turning now to the MIR across the region $4\mu m \leq \lambda \leq 30\mu m$, the SED contains the two most prominent spectral features; those of silicate absorption at $9.7\mu m$ and $18\mu m$. Looking at the top plot in Figure 2.6, when θ_v is low, in the 'edge-on' regime, the absorption that occurs is dependent on the amount of cold dust in the outer reaches of the cloud along the line of the observers' sight which can intercept the re-radiation from dust in the hot inner ring. The depth of both silicate features is therefore greatest at $\theta_v = 0°$ when the maximum quantity of cold dust exists between the observer and the source. Correspondingly, as θ_v increases the depth of the silicate absorption features decrease until θ_v approaches and then exceeds Θ_{max}, whereupon the absorption features disappear. As mentioned in the introductory section 2.1, it is this difference in the silicate absorption features as the viewing angle changes, that provides such powerful diagnostic to the observer.

Finally, considering the FIR, Sub-mm, mm & cm wavelength regions at $\lambda \geq 30\mu m$, there is very little variation in the SEDs as the viewing angle is changed because the extinction efficiencies of dust grains, particularly those of scattering, drop rapidly as the wavelength increases. So, at sufficiently long wavelengths the entire visible mass of the cloud is optically thin to radiation and varying the viewing angle has no impact on that part of the spectrum. The long wavelength dust bump emission at $\lambda > 60\mu m$ primarily originates in the large grains of silicate and carbon which emit at these wavelengths as they cool. For $\lambda > 300\mu m$ the very large $30\mu m$ amorphous carbon grains also contribute via their high absorption efficiency in this region. As a general rule of thumb, the broadness of the dust emission for $\theta_v < \Theta_{max}$ is approximately controlled by the ratio of the inner to outer cloud radii, whilst the optical depth controls the NIR slope.

2.6.2 Variation of SED with T_{dust} & τ_{uv}

The bottom plot of Figure 2.6 shows $L_{AGN} = 10^{12} L_{\odot}$, $\theta_v = 38°$ for the nine models in the parameter space: T_{dust} = 1000K, 1250K, 1500K each at τ_{UV} = 1000, 1250 & 1500. That these curves show distinct variation in magnitude and peak wavelength is primarily a function of the dust sublimation temperature T_{dust}. The peak wavelength of the flux is proportional to the temperature of the cool outer dust through Wien's displacement law

$\lambda_{max} = 0.2897/T_{dust}$(cm) and the data is presented in the bottom plot of Figure 2.6 such that the solid line in each group of three represents the varying of the optical depth for the same temperature. Although the resolution in the peak of the three solid curves is very small, due to the close proximity of all three T_{dust}'s, it is possible to just see that the peak of the cool dust bump moves to longer wavelengths as T_{dust} drops - i.e., the top set of black curves for T_{dust} = 1000K peaks at the longest wavelength.

Perhaps counter-intuitively, the magnitude as well as the breadth of the long wavelength flux for the same optical depth is greatest for T_{dust} = 1000K, despite Stephan Boltzmans law $S_\lambda \propto T^4$ implying that the T_{dust} = 1500K spectra would have the greatest peak magnitude. However, setting the outer radius of the system $R_2 = 100R_1$ using the DaRT input variable $ERO = 0.01$ has significant consequence for the column length and density along a line of sight for the same optical depth. Considering the black, red and green solid line in the bottom plot of Figure 2.6 each showing $\tau_{uv} = 1000$ it can be seen that the curve having the greatest magnitude and breadth is the black one T_{dust} = 1000K and this is because the volume $4/3\pi(R_2^3 - R_1^3)$ is also the greatest for the T_{dust} = 1000K system in comparison to those of a higher T_{dust}.

The radial extent of each system is also illustrated in the depth of the silicate absorption feature at 9.7μm for the same optical depth, with those models having T_{dust} = 1500K and consequently the shortest and therefore densest column length of dust along a particular line of sight, exhibiting the deepest absorption. Conversely T_{dust} = 1000K shows the shallowest silicate feature as the column length is longer and therefore sparser than the T_{dust} = 1500K model.

This concludes the analysis of the changes in behaviour of the emergent AGN SEDs under the influence of varying the viewing angle, optical depth and temperature. The final task is to transform this AGN SED library into a form suitable for use when fitting the ULIRG test sample.

2.7 AGN SED Library

It was mentioned in the introduction to this chapter §2.1, that six local ULIRGs have been chosen as a test data set to assess the veracity of the modelling approach. Once the starburst element has been developed, the AGN SEDs will be paired in-turn with the starburst SEDs to generate a combined ULIRG SED and ultimately, those combined

SEDs will be tested against the chosen ULIRG sample, using the reduced χ^2 criteria and the *best-fit* SED found.

With three dust temperatures, three optical depths and one luminosity in the AGN parameter space, the radiative transfer for nine unique models was calculated explicitly by DaRT. As each model has some fifteen viewing angles, the AGN library consists of some 135 SEDs. However, each of these SEDs was generated using a PG quasar source function calibrated to the single luminosity $L_{AGN} = 10^{12}L_{\odot}$, as detailed in §2.4.

An AGN library containing SEDs calibrated at one value of the luminosity is undoubtedly a limitation. The six objects in the sample to be fitted were taken from FH03, but tailoring SEDs to each object using the values for the luminosity found from spectral fitting by FH03 might also have been a restriction. The criteria for a galaxy to be a ULIRG varies between authors who use different minimum luminosities for the classification e.g., Condon *et al.* (1991) uses $L_{40-120\mu m} \geq 10^{11.02}L_{\odot}$, Clements *et al.* (1996) who suggests $L_{60\mu m} \geq 10^{11.77}L_{\odot}$ or the definition of FH03 which takes a rest-frame 1-1000μm luminosity $L_{1-1000\mu m} \geq 10^{12}L_{\odot}$ as representative of ULIRGS in all evolutionary states. Therefore, it would appear that a galaxy can be classified as a ULIRG when the infrared luminosity is as small as $10^{11}L_{\odot}$ or potentially up to a factor of 100 higher at $10^{13}L_{\odot}$ - any galaxy with an infrared luminosity greater than $10^{13}L_{\odot}$ is properly classified a HYLIRG (Farrah *et al.* 2001).

Although the best-fit combined SED for each ULIRG is found from a combination of both a starburst and an AGN SED, it was decided to use the criteria of Condon *et al.* (1991) to set the minimum luminosity in the AGN parameter space and to use the minimum criteria of a HYLIRG according to Farrah *et al.* (2001) as the maximum luminosity. In that way the upper and lower limits have been set at $10^{11}L_{\odot} < L_{AGN} < 10^{13}L_{\odot}$. However, considering each SED *set* contains nine models (T_{dust}, τ_{UV}) and that DaRT in its axi-symmetric form is extremely costly in terms of computer processor time (upwards of five weeks per model), pre-calibrating numerous raw SEDs before running them through DaRT was felt to be prohibitive.

Therefore, an AGN luminosity multiplier mf_{agn} was defined by which the 135, pre-calibrated, emergent AGN SEDs, that were generated explicitly in DaRT, could be multiplied. Selecting $\Delta mf_{agn} = 0.25$ and the minimum and maximum criteria mentioned above led to forty individual values of L_{AGN} in the parameter space, thereby emulating a broader range of luminosity for use in the ULIRG fitting. Thus, for this thesis work, the AGN

SED library consists of 135 SEDs, each multiplied by 40 luminosity values, leading to a total of 5,400 synthetic SEDs covering a broad range of extinction, viewing angle and dust temperature. The number of SEDs in this library and the issue of the uniqueness of the *best-fitting* ULIRG SED will be returned to in greater depth in Chapter 7, where the final χ^2 fitting procedure is discussed.

2.8 Summary of Chapter 2

This chapter began with a brief precis of the basic physics applicable to the three types of AGN thought to reside in the chosen ULIRG sample. A literature review was then conducted to ascertain which of many published central source function and dust recipes would be appropriate for the thesis AGN modelling.

By writing a bespoke computer program, the RR93 dust model was re-generated from the literature and the extinction behaviour of the constituent grains quantified. The PG quasar source function chosen was then replicated from the literature by writing a second bespoke computer program to generate a continuous function across the wavelength regime. The DaRT radiative transfer code was then throughly investigated (See Appendix A) and having ascertained that it was working correctly, the invariance of the integration grid variables was throughly checked. The DaRT input variables which define the dust density distribution and torus geometry where then specified to define the model system.

The PG quasar source function was then used in DaRT to irradiate the dusty torus, the radiative transfer of flux calculated and the emergent SEDs generated. The shape of the spectra were then interpreted in terms of the dust models' extinction and the source function's behaviour. The affect of changing the viewing angle, optical depth and dust sublimation temperature on the SED was examined.

The chapter concluded by noting that the PG quasar source function used in DaRT was calibrated at a single luminosity, $L_{AGN} = 10^{12}L_{\odot}$. The 135 SEDs calculated explicitly by DaRT were therefore extended in luminosity space for the final ULIRG fitting, using the AGN luminosity multiplier mf_{agn}, to encompass $10^{11}L_{\odot} < L_{AGN} < 10^{13}L_{\odot}$ so as not to bias the sample.

The AGN element of the ULIRG modelling is now concluded. As mentioned in the first chapter of the thesis, a starburst source component is also required to model a ULIRG and the next chapter begins to develop this element.

Chapter 3

HII Region Model

This chapter present the HII region emergent SEDs. To facilitate discussion, it is convenient to begin with a very brief review of the evolution of an HII region under the influence of a stellar ionizing flux.

Evolution of an HII Region

A Giant Molecular Cloud can be approximated as a spherical region of molecular gas and dust embedded in ambient interstellar space. Massive stars are assumed to condense from the high density cores of the GMCs and after birth, they undergo a relatively brief period of instability, at the end of which, they reach pressure equilibrium and arrive on the main sequence. As this initial period of instability is usually very short ($\leq 10^5$yrs) when compared to the lifetime of a typical star it is reasonable to ignore the specifics of the unstable state and assume the stars 'switch-on' immediately into a stable state.

Thus at $t \approx 0$, a system can be pictured as a stellar population embedded into a dusty, neutral HI cloud, which is further surrounded by an ambient region of interstellar gas and dust. The cloud is now neutral HI as the remains of the molecular cloud from which the stars condensed has been dissociated before the stars evolved onto the main sequence. There are several sources of energy for this dissociation, including the mean intensity starlight which pervades a galaxy, cosmic rays and X-rays. The mechanism of dissociation occurs when excitation from the ground state X to an excited state B, is followed by a cascade into the vibrational continuum of the ground state X, during which the hydrogen molecule disassociates (Dyson & Williams 1997*a*).

The massive stars birthed in the GMC eject large quantities of ionizing photons and

wind material into the surrounding neutral gas and co-existing dust. In the initial photo-ionization phase, the impact of this stellar radiative flux results in the rapid formation of a Strömgren sphere which encircles the volume within which the recombination rate in the gas balances the stellar photon output rate and the gas is maintained in an ionized state - an HII region is established.

Ionization of the neutral gas considerably increases its pressure and the photoionization phase is followed by an expansion phase as the ionized sphere attempts to adjust to the large increase in internal energy (Franco *et al.* 1990). Expansion can itself be divided into two phases; first a rapid expansion phase where the pressure difference between the neutral region and the bubble of photo-ionized material drives the evolution, rather than the stellar photon output, which ends at t $\approx 10^7$Myrs. The second expansion phase is momentum conserving as the ionized bubble coasts out through the neutral region gradually releasing the pressure accumulated during the photo-ionization phase until it reaches equilibrium with the external medium at around t $\approx 10^8$Myrs (Dyson & Williams 1997*b*).

Photo-ionization and expansion of the HII region heats the gas within its radius, evaporating a proportion of the attendant dust which causes the optical depth through the GMC to vary with the ionization front's progression. The dust density distribution during this evolution can be obtained by tracing the motion of the ionization front through the GMC, determining the associated gas density. The gas density can then be linked to the dust density via a dust condensation factor. This factor determines the fraction of dust that can condense out of the heated gas and contribute to the extinction. Having obtained the dust density distribution, it can be irradiated in DaRT by the central cluster source function and the radiative transfer of flux to be calculated.

Thus, to model an HII region, a dust recipe and method of generating a source function suitable for a starburst must first be identified from the literature. A method of calculating the evolution of the HII region under the influence of the ionizing photon flux and a way to link the resulting gas density to the dust density distribution are then described. The chapter culminates with presentation of the emergent HII region SEDs.

3.1 Starburst Modelling To-Date

As mentioned in the introduction to the AGN element in Chapter 2, it was the advent of the *IRAS* space telescope which prompted many groups to begin modelling infrared galaxies in

earnest. At the forefront of the field, Rowan-Robinson & Crawford (1989) presented model infrared spectra for a sample of over 200 *IRAS* galaxies, using a source function made up of three individual components; a normal disc, a seyfert element and a starburst component. Rowan-Robinson & Crawford (1989) modelled the starburst element of their *IRAS* sample as optically thick silicate clouds (Rowan-Robinson & Harris 1982), surrounding blackbody point sources at 40,000K, which represented newly formed O stars. The spectrum of an optically thick silicate cloud illuminated by a central stellar cluster is readily identifiable primarily because of its distinctive form in the MIR. Here deep absorption is in evidence in the silicate resonance features at 9.7μm and 18μm which originate in magnetic dipole absorption and in the FIR a broad dust bump might be seen - a reflection of the large optical depth of the cloud.

In Rowan-Robinson & Crawford (1989), the starburst component was interpreted as emission due to a burst of star formation and using this model, coupled to the disc and seyfert components, good fits were found for many of the galaxies in their sample (Rowan-Robinson & Crawford 1989). In 1990 the radiative transfer code used here - DaRT - was presented (ERR90) and then in 1992, the root grain model used for the seyfert component discussed in the previous chapter, was published (RR92).

Over the following years much research was directed towards developing a dust model specifically designed for starburst environments and to that end the RR92 grain model, used in the thesis AGN modelling, was slightly modified when Rowan-Robinson & Efsthathiou (1993) [hereafter RR93] published *Multi-grain Dust Cloud Models of Starburst and Seyfert Galaxies.* The RR92 grain recipe had included some very small grains (5-20Å) to explain the diffuse MIR emission in the large spirals that it modelled but RR93 considered high optical depth starburst and seyfert systems and these small grains were no longer needed.

Presuming that all the sample objects were in a very early evolutionary phase, ERR93 deemed it more appropriate to use the radiative transfer code DaRT (ERR90) in its spherically symmetric mode as against the axi-symmetric mode used for the seyfert modelling. Taking a blackbody as the starburst source function and embedding it in a spherical cloud comprising their new, modified, 7-grain dust model, RR93 were able to achieve some very good fits to their sample, particularly to the high optical depth ultra-luminous galaxies (RR93).

The second paper in the series *Multi-grain dust cloud models of compact HII regions*

took advantage of recent observations in the millimetre and sub-millimetre to further constrain the theoretical models (Efsthathiou & Rowan-Robinson 1994) [hereafter ERR94]. One of the important elements of ERR94 was the comparison it carried out between composite and multi-grain dust models. The RR93 multi-grain model consisted of seven individual grains of specific radii (see §2.3) which, when combined together, generated a good representation of the interstellar extinction. ERR94 presented a generalization of the RR93 model which took into account a distribution of grain sizes and species by generating composite grains with average absorption and scattering efficiencies in the form e.g., n(a) $\propto a^{\beta}$; designed to approximate the dust emission of RR93 (ERR94).

Embedding a blackbody source of 40,000K, in a spherical cloud composed of either the RR93 multi-grain model or the ERR94 composite equivalent and calculating the radiative transfer, the authors were able to conclude that the composite grains approximated the multi-grain distribution dust emission very well, contrary to popular opinion at the time (ERR94). ERR94 also noted that the 30μm grains in the RR93 model needed to explain an absorption excess at long wavelengths were not required when modelling starbursts as their inclusion appeared to now predict too much flux at long wavelengths (ERR94).

An important comment on both the RR93 multi-grain and ERR94 composite dust models was their non-inclusion of polycyclic aromatic hydrocarbons (PAHs) which are thought to explain the mid-infrared, narrow emission bands seen in the spectra of many starburst galaxies. Concurrent to development of the RR93 and ERR94 PAH-exclusive dust models, PAH-inclusive dust recipes were also being researched.

Dust Models Containing Polycyclic Aromatic Hydrocarbons in Various Environments (Siebenmorgen & Krügel 1992) [hereafter SK92] analysed infrared spectra and the extinction curve in four environments: the solar neighbourhood, two reflection nebula and an HII region. To fit with the observational data SK92 proposed a dust model similar to that of RR93 in that it contained large ($a = 0.1\mu$m) silicate and carbon grains to account for the FIR emission and the linear rise in the extinction curve. Also included were very small graphite particles ($a \leq 75\AA$) to explain the MIR emission and the 2175$\AA$ extinction bump. Importantly, the model also contained PAHs which SK92 thought responsible for both the MIR emission bands and the non-linear rise in the Far-UV of the extinction curve.

However, SK92 found that the PAH emission was activated only in the environment of very energetic photons ($\geq$7eV) and that due to the small number of constituent atoms their excitation state fluctuated strongly. This led to the assumption of thermal equilibrium be-

ing invalidated, except at very high temperatures (SK92). Consequently new methods of calculating the radiative transfer of flux and the emission from the transiently heated PAHs had to be developed. *Radiative Transfer for Transiently Heated Particles* (Siebenmorgen *et al.* 1992*a*) [hereafter SKM92] considered methods of calculating this emission using self-consistent radiative transfer. By developing a PAH and very small grain extension to the DaRT (ERR90) radiative transfer code, SKM92 were able to present spectra of PAH features in high optical depth media, along with temperature distribution functions for emission from both weak and hard radiation fields (SKM92). The extension to DaRT created by SKM92 to accommodate the very small grains and PAHs was personally requested from Ralph Siebenmorgen and generously provided for use in this thesis.

These papers exploring the role of PAHs in various astronomical environments and the difficulties involved in calculating their emission, were put to practical in 1994 when *The Transfer of Radiation in Galactic Nuclei; Dusty Hot Spots in the Starburst Galaxy M82* was published (Siebenmorgen & Krügel 1994). The inclusion of the very small thermally fluctuating grains in the SK92 dust model and the use of the PAH and very small grain extension to the DaRT radiative transfer code allowed Siebenmorgen & Krügel (1994) to obtain a good fit to the mid-infrared PAH features in the observed spectrum of M82. It was therefore be concluded that whilst the PAH-exclusive grain model of RR93 was appropriate for modelling the highly energetic, optically thick environment of an AGN, a more suitable dust model for starbursts was the PAH-inclusive prescription of SK92. The SK92 dust model was therefore also personally requested from its authors and an approximation of it was kindly received by private communication for use in this thesis. This dust model will be returned to in some depth in coming section 3.2.

Attention could now be turned to the possibility that including central source functions more sophisticated than simple blackbodies might improve the spectral fits. One route to generating such a source function is provided by stellar evolutionary synthesis codes, which use evolutionary tracks and atmospheric grids to produce the emitted spectrum of a stellar population. Leading the development of stellar evolutionary synthesis codes were groups such as Bruzual & Charlot (1993) who wrote GISSEL, Leitherer & Heckman (1995) who developed STARBURST an earlier version of STARBURST99 (Leitherer *et al.* 1999) and Fioc & Rocca-Volmerange (1997) who published PEGASE. Each of these codes produced a stellar spectrum according to a set of user-defined variables including stellar burst mass, initial mass function and star formation rate.

One of the first starburst modelling groups to incorporate stellar spectral synthesis was Gordon *et al.* (1997) who used an improved version of the GISSEL (Bruzual & Charlot 1995) libraries to produce a source population up to the age of $< 2 \times 10^7$ years and STARBURST (Leitherer & Heckman 1995) for the population between 5×10^7 and 1.5×10^{10} years. By embedding these stellar source functions in a 'clumpy' dust-cloud consisting of high and low density regions, Gordon *et al.* (1997) were able to achieve very good fits to a sample of 30 starburst SEDs obtained from the literature.

Over the coming years stellar evolutionary synthesis codes were used successfully by many groups to generate central source functions and good fits were found to the observed IR data of a number of *IRAS* normal and starburst galaxies (e.g., Silva, Granato, Bressan & L. 1998; Alexander, Efstathiou, Hough, Aitken, Lutz, Roche & Sturm 1999; Efstathiou, Rowan-Robinson & Siebenmorgen 2000; Kewley, Dopita, Sutherland, Heisler & Trevena 2001). As such, the stellar evolutionary synthesis code STARBURST99 was chosen to produce the source populations used in this thesis work and will be returned to some depth in future section §3.3.

A dust model, a radiative transfer code and a way of generating a central source function suitable for the successful modelling of a starburst galaxy have now been identified from the literature. What remains is to find a method of describing the evolution of the GMC under the influence of the source function to obtain the dust density distribution.

The progression of an ionization front through a GMC heats the gas, evaporating some of the attendant dust and therefore changing the dust density distribution. Efstathiou *et al.* (2000) [hereafter ERR00] presented a series of expressions to describe the expansion of an ionization front and coupled the gas and dust density distributions together via a dust condensation factor. Using the GISSEL evolutionary synthesis code to generate instantaneous burst central source functions these were embedded in a spherically symmetric cloud composed of SK92 dust and the evolution traced. The radiative transfer of flux was then calculated at time t using the very small grain DaRT extension of (Siebenmorgen & Krügel 1994). The library of SEDs generated was tested against the observed SEDs of the two ULIRGS in their sample and good fits from the NIR to mm were achieved (ERR00)

The same ERR00 description for the evolution of a GMC under the influence of a central source was then employed by amongst others, Farrah *et al.* (2002) & FH03 to successfully model samples of both high-z HYLIRGS and local ULIRGS and more recently

by Siebenmorgen & Krügel (2007) to generate a library of ULIRG SEDs. Based on this prooven success, the ERR00 prescription provides the foundation for the HII region model that is developed and ultimately extended in this thesis and is therefore returned to in depth in section §3.6.

This concludes the review of starburst modelling to-date. In the coming sections the SK92 dust model will be described and the role its various constituents play in the replication of interstellar extinction will be discussed. The inputs needed to the STARBURST99 evolutionary synthesis code (Leitherer *et al.* 1999) to generate an appropriate central source SED and ionizing photon output are then considered and the two functions illustrated and briefly discussed.

3.2 Starburst Grain Model

For the reasons given, the grain model used for the thesis starburst component is based on the PAH-inclusive recipe of SK92. To accompany the SK92 grain model, Siebenmorgen & Krügel (1994) developed the PAH extension to the DaRT radiative transfer code and both this extension and an approximation of the SK92 dust model were provided by Ralph Siebenmorgen. However, as it was understood that the code should be used *solely* for this thesis, only the executable version of the DaRT PAH extension code was delivered, along with a *hard-wired grain* model based on that of SK92 so no alterations could be affected to either component. Nevertheless, to interpret the shape of the starburst SEDs the grain model and its extinction characteristics must still be understood.

SK92 derived the properties of their interstellar grains using 8 contributory factors: (a) constraints on cosmic abundance to the dust forming elements; (b) the interstellar extinction curve; (c) the silicate resonances at 9.7- and 18μm; (d) broadband IR emission from heated dust (e) narrow line emission attributed to PAHs; (f) the wavelength dependence and strength of polarization; (g) observations of scattered light and (h) IR absorption bands from 'ice'-mantles around grains shielded from UV radiation (SK92).

In a similar way to the grain model presented for the AGN component of this thesis (§2.3), the starburst model also consists of larger silicate and amorphous carbon grains designed to fit the mid and far-infrared dust emission. However, in contrast to the AGN model, which included only small graphite grains, the SK92 model includes *very* small graphite grains to account for the 2175$\AA$ feature and PAH clusters to replicate the MIR

narrow line emission.

However, whilst the hard-wired grain model supplied by Ralph Siebenmorgen was based on that published by SK92 it differs in its format. SK92 presents grain size distributions for each species in the form $n(a) \propto a^{\beta}$, where n(a) is the number of grains of radius a, which approximates the *average* size properties of several grains of different radii. The thesis grain model received by private communication consisted of the actual distributions for the different *individual* grains of various radii within a species, which, when summed, generated the species' average size distribution from SK92. That this approach is valid was given weight by ERR94, who compared a composite grain model which approximated the average extinction for each species, to a multi-grain distribution consisting of grains of individual radii and found them to be similarly capable of replicating the galactic extinction. Thus, the dust model consisting of grains of individual radius, hardwired into the DaRT PAH supplemental code reproduces the extinction characteristics of the SK92 model, but employs the grains in a different form.

Having ascertained the origin of the starburst grain model, in the following section the absorption, scattering and extinction cross-sections of the supplied grain constituents are examined.

3.2.1 Extinction Efficiency & Abundance

The supplied dust model contains three species of grain, at four individual radii each, along with a PAH cluster, giving 13 constituents in total:

- Amorphous Carbon at 0.03, 0.06, 0.12 & 0.24μm
- Astronomical Silicate at 0.03, 0.06, 0.12 & 0.24μm
- Graphite at 0.0005, 0.001, 0.002 & 0.01μm
- Polycyclic Aromatic Hydrocarbon cluster

Astronomical Silicate & Amorphous Carbon

The optical constants for the astronomical silicate and amorphous carbon grains were assumed by SK92 to be after Draine & Lee (1984) and Draine (1985)(SK92). Although those published properties were for silicate and graphite, due to their widespread use, SK92 employed the graphite data for their carbon grains rather than using those of e.g.,

Edoh (1983) or Mathis & Whiffen (1989), which were thought quite uncertain at the time (SK92). The scattering and absorption properties of both these grain species were calculated by SK92 using Mie theory (Mie 1908) and then multiplied by the radius square a^2 and the relative abundance $A_{gr}/\Sigma A_{gr}$ to produce the extinction cross-sections +hard-wired into the DaRT supplemental code.

The minimum and maximum radii given in SK92 for these grains are 0.01 and 0.25μm respectively, distributed according to n(a) $\propto a^{-3.5}$ and the four radii (a = 0.03-, 0.06-, 0.12- & 0.24μm) in the supplied hard-wired grain model, when summed together, approximate the average, composite, extinction properties of the distributions for each species. In addition to the extinction cross-sections, the relative abundance of all grains was also hard-wired into the DaRT supplemental code and these are given in Table 3.1. In contrast to the AGN model where the abundances were generated using a fitting parameter B_o, those for the starburst dust model were found explicitly using the following equation

$$A_{gr} = \frac{3Y_{gr}M_x m_H}{4\pi a^3 \sigma_{gr}} \tag{3.1}$$

where Y_{gr} is the abundance of species x relative to hydrogen, σ_{gr} is the mean density of grain material, M_x is the mean molecular weight of material per x atom and m_H is the mass of the hydrogen atom Rowan-Robinson (1986). In a similar way to the AGN dust recipe, the smaller the grain radii a, the more abundant it is in the starburst dust model.

Very Small Graphite Grains

As suggested by Draine (1989) and Sorrell (1990), small graphite grains have been proposed as the primary carriers of the 2175$\AA$ "bump" in SK92, due to their strong resonance around 2200$\AA$. Using a maximum and minimum radius of 0.01 and 0.0005$\AA$ respectively, SK92 gives a distribution n(a) $\propto a^{-4}$ and the four graphite radii in the hard-wired DaRT supplemental code together approximate this distribution. However, due to surface effects, impurities and the irregular shape of small grains, a large degree of uncertainty can be introduced when measuring the optical constants of these small grains and this, added to the unreliability of Mie theory for grains of these radii has resulted in the very small graphites in the SK92 model being represented by a Drude-profile at short wavelengths (SK92). For the absorption efficiency $Q_{\nu,abs}$ in the 2175$\AA$ resonance, for $\lambda < 0.5\mu$m

$$\frac{Q_{\nu,abs}}{a} = c_1 x + \frac{c_2 x^2}{(x - x_o)^2 + \gamma^2 x^2} [cm^{-1}] \tag{3.2}$$

where $c_1 = 6.6 \times 10^4$, $c_2 = 1.92 \times 10^6$ and wavenumber $x_o = \lambda_c^{-1}$, where λ_c is the central wavelength of the resonance and x is in cm^{-1}. γ is the scatter for the half-width of the feature $\gamma = 0.992 \pm 0.12 \mu m^{-1}$ (SK92). For $\lambda > 0.5 \mu m$ the optical constants of Draine (1985) were used, with their absorption and scattering properties calculated using Mie theory (SK92). As will be seen when the extinction distributions are illustrated in the next subsection, the scattering contribution from the very small grains has not been explicitly calculated but rather set constant at $C_{\nu,scat} = 10^{-14}$, which illustrates their inefficiency for scattering radiation and minimal impact on the extinction curve at long wavelengths, due to their small size. The relative grain abundances and associated values for these small graphite grains are also given in Table 3.1 and they are considerably more abundant than the larger grains.

Polycyclic Aromatic Hydrocarbons

PAH clusters consist of a network of carbon atoms with H atoms arranged at the periphery and are subject to transient heating. Leger & Puget (1984) and Allamandola *et al.* (1985) proposed the existence of large PAH molecules not only to explain the family of resonances between 3-14μm seen in e.g., HII regions and planetary nebula but also the discrepancy between observed emission at wavelengths $< 30 \mu m$ and that predicted by standard grain models. PAHs are similar to the more usual grain model components in that they produce infrared radiation after absorption of an ultra-violet photon, but for a PAH the absorption and emission process is strongly constrained by the molecule's discrete energy levels (Evans 1994*b*). When a PAH molecule absorbs a UV photon it undergoes transition to an excited electronic state in the same manner as a more traditional grain. However, rather than de-excitation by cascading down the energy levels to the ground electronic state it experiences isoenergetic internal conversion into a highly excited vibrational state of the ground electronic state (Evans 1994*b*). Having reached this state the molecule is then able to release its energy by cascading down vibrational levels of the ground electronic state with the emission of mid-infrared photons. That the molecule has discrete energy levels means that its UV photon absorption efficiency is sharply peaked at wavelengths specific to the molecule which in turn allows emission to be tightly correlated at corresponding wavelengths in the mid-infrared giving the distinctive narrow bands (Evans 1994*b*).

The PAH cluster used in the hard-wired starburst grain model has 556 carbon atoms, a number Efstathiou *et al.* (2000) found capable of generating the flux seen in M82, one

of the ULIRGS in their sample. The PAH cluster's absorption cross-section $C^{PAH}(\lambda)$ is found by combining the contribution from the larger grains $C^{big}(\lambda)$ and the small graphite particles $C^{grf}(\lambda)$ and assigning the residue to PAHs such that

$$C^{tot}(\lambda) = C^{big}(\lambda) + C^{grf}(\lambda) + C^{PAH}(\lambda) \tag{3.3}$$

from which it follows that

$$C^{PAH}(\lambda) = \frac{C^{tot}(\lambda)}{C^{tot}(V)}[C^{big}(V) + C^{grf}(V) + C^{PAH}(V)] - C^{big}(\lambda) - C^{grf}(\lambda) \tag{3.4}$$

where V indicates visual wavelengths and the ratio $C^{tot}(\lambda)/C^{tot}(V)$ is given by the extinction curve (SK92). As $C^{PAH}(V)$ is so small compared to the other two terms on the right-hand side of Equation 3.4, it can be neglected (SK92). The abundance of PAHs Y_{PAH} is also found from the interstellar extinction curve by taking an estimate for the FUV cross-section of a carbon atom in a PAH to be between 5 x 10^{-18} to 2 x $10^{-17} cm^2$ (Omont 1986) and assuming that $\approx$ 10% of the total carbon abundance is locked up in PAHs, leading to a $Y_{PAH} = 3 \times 10^{-5}$, in agreement with laboratory measurements (Leger *et al.* 1989). Dividing Equation 3.4 by Y_{PAH} gives the absorption cross section of a PAH per C atom (SK92). As with the very small graphite grains the scattering efficiency of these PAH clusters is very small especially at long wavelengths and rather than being explicitly calculated has been set constant at $C_{\nu,scat} = 10^{-14}$ (SK92).

A brief mention should be made of the method by which the DaRT very small grain supplemental code calculates radiative transfer for transiently heated particles, which follows Siebenmorgen *et al.* (1992*b*). A particle can be considered to be transiently heated if the time interval between the absorption of a photon with an energy $h\nu$, which is comparable to the enthalpy of the grain, is much longer than the cooling time of that grain (Siebenmorgen *et al.* 1992*b*). The energy content of a very small grain is variable and it does not attain a steady state temperature which means its temperature fluctuations must be described by a normalized density probability P(T) such that

$$\int P(T)dT = 1 \tag{3.5}$$

so that P(T)dT gives the probability of finding a grain in the temperature interval T...T+dT. If the function P(T) is narrow, the temperature fluctuates very little around an equilibrium value T_{eq}, P(T) approaches a δ-function and the grains are large. However if P(T) is broad, the grains are small and their emission in a radiation field J_ν is found

GRAIN	Radius(μm)	Y_{gr}	$\sigma_{gr}(cm^{-3})$	M_x	$A_{gr}/\Sigma A_{gr}$
Amorphous Carbon	0.03	2.4e-4	2.3	12	0.152
	0.06				0.108
	0.12				0.076
	0.24				0.054
Astronomical Silicate	0.03	3.1e-5	2.5	169	0.183
	0.06				0.129
	0.12				0.091
	0.24				0.064
Graphite	0.0005	5e-5	2.3	12	1.364
	0.001				0.681
	0.002				0.341
	0.01				0.170
PAH Cluster	556 Atoms				13.11

Table 3.1: Grain species, radius, abundance relative to hydrogen, mean density, mean molecular weight and the total relative abundance for the hard-wired starburst grain model. The relative abundance for graphite $a = 0.0005$ and the PAH clusters is > 1 as these are not grains per sè but rather can be viewed as collections of molecules.

from

$$\epsilon = K_\nu \int B_\nu(T) P(T) dT \tag{3.6}$$

where K_ν is the absorption co-efficient and B_ν is the grain Planck function. In order to know when a grain is subject to transient heating, its enthalpy U(T) must also be known and SK92 used the prescription of Chase *et al.* (1985) to find an analytic approximation of U(T) for graphite in erg/atom

$$U(T) = \frac{4.15e^{-22}T^{3.3}}{1 + 6.51e^{-3}T + 1.5e^{-6}T^2 + 8.3e^{-7}T^{2.3}} \tag{3.7}$$

As a general rule, accounting for transient heating shifts the emission from the very small grains in shorter wavelengths. For further information the reader is now referred to Siebenmorgen *et al.* (1992*b*) where this method of calculating the emission from transiently heated grains and PAHs in weak and hard radiation environments is fully described.

3.2.2 Extinction Curves

In contrast to the AGN dust model, it was not necessary to write a bespoke computer program to re-generate the SK92 dust model from the literature as an approximation of it was kindly supplied by those authors. However, to relate the individual grain species to the emergent HII region SEDs, the extinction behaviour must be understood across the entire wavelength regime. As the AGN dust model has several grains in common with the starburst dust model and the extinction behaviour of those grains was thoroughly examined in Chapter 2, attention here will be paid primarily to the very small grains and PAHs characteristic to the starburst dust model.

Figure 3.1 shows the weighted absorption and scattering cross-sections $A_{gr}/\Sigma A_{gr}$ x $C_{\nu,abs,scat}$ for each grain along with the total cross-section for each species. Figure 3.2 shows the weighted absorption, scattering and extinction cross-sections for each species' total and the model total.

UV, Optical & NIR: $0.1\mu m \leq \lambda \leq 4\mu m$

The most prominent feature of the interstellar extinction curve in this region is the 'bump' at 2175$\AA$ which, in a similar way to the AGN dust model, has been assigned primarily to the very small graphite particles by SK92, due to their strong resonance around this wavelength. For the DaRT supplemental code, SK94 assigned abundances $A_{gr}/\Sigma A_{gr}$ to

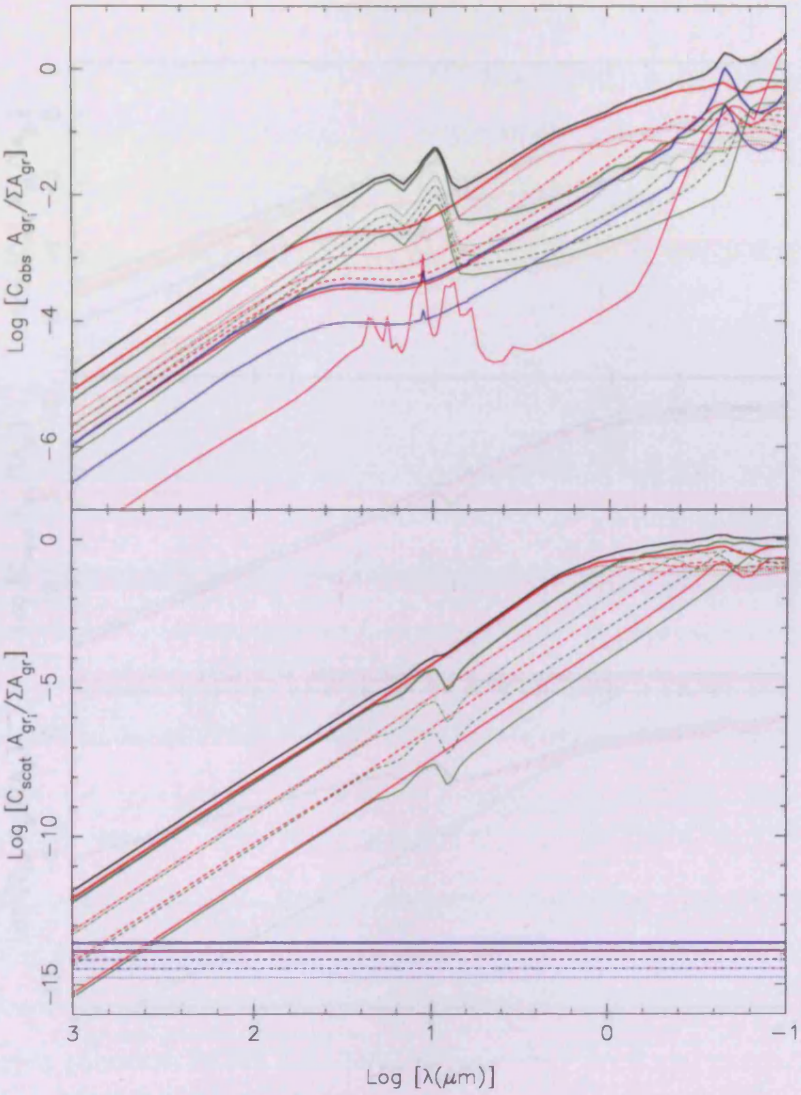

Figure 3.1: The weighted cross-sections for scattering and absorption by silicate, carbon and graphite grains are illustrated in green, red and blue respectively whilst pink shows the cross-section of the PAH cluster. In the first three cases, the largest cross-section is shown by the appropriately colour dotted line, followed by the dot-dash, dashed and thin solid lines as the grain radius decreases. The thick solid line illustrates the total cross-section of all grain radii in a particular species set.

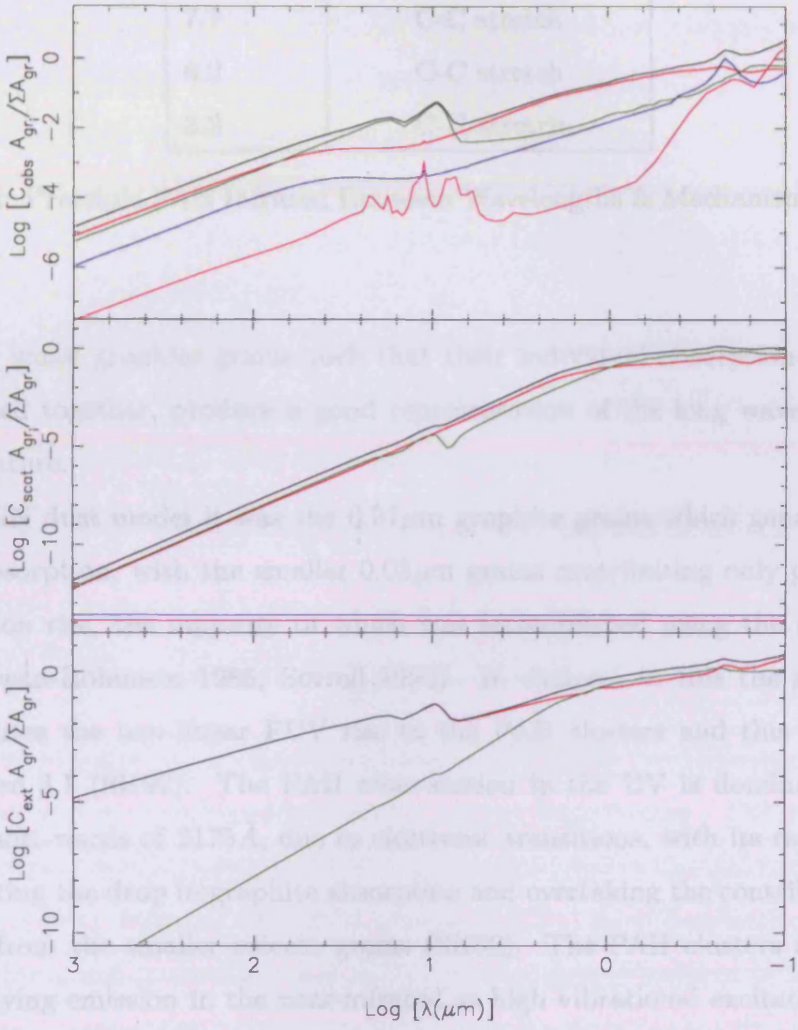

Figure 3.2: The total, weighted, absorption, scattering and extinction cross-sections for each species in the starburst grain model. In the top two plots red, green, blue and pink indicate the carbon, silicate, graphite and PAH clusters respectively with the total shown in black. In the bottom plot the absorption and scattering model totals are shown in red and green respectively with the overall model extinction cross-section shown in black.

$\lambda(\mu m)$	Assignment
11.3, 12.7	C-H out-of-plane bend
8.6	C-H in-plane bend
7.7	C-C stretch
6.2	C-C stretch
3.3	C-H stretch

Table 3.2: Principle PAH Infrared Emission Wavelengths & Mechanism (Whittet 2003).

the four very small graphite grains such that their individual absorption cross-sections, when combined together, produce a good representation of the long wavelength wing of the 2175$\AA$ feature.

In the AGN dust model it was the 0.01μm graphite grains which generated much of the 2175$\AA$ absorption, with the smaller 0.03μm grains contributing only partially to the FUV extinction rise, the majority of which was accomplished using the smaller silicate particles (Rowan-Robinson 1986; Sorrell 1990). In contrast to this the starburst grain model attributes the non-linear FUV rise to the PAH clusters and this can be clearly seen on Figure 3.1 (SK92). The PAH cross-section in the UV is dominated by strong absorption short-wards of 2175$\AA$, due to electronic transitions, with its rapid rise in efficiency mediating the drop in graphite absorption and overtaking the contribution at these wavelengths from the smaller silicate grains (SK92). The PAH clusters also contribute to the underlying emission in the near-infrared as high vibrational excitation produces a quasi-continuum due to the overlapping of many weak absorption bands (SK92).

Considering the scattering at short wavelengths, it is perhaps easier to see the relative contributions of the grains by considering the central plot of Figure 3.2 which shows only the total scattering cross-section for the four grain species. As discussed, the scattering potential of the small graphite grains and the PAH clusters is negligible, as indicated by the blue and pink lines. In a similar way to the AGN dust model, at shorter wavelengths the silicate grains (green) dominate the scattering until the silicate and carbon cross-sections become equivalent around $\lambda = 1\mu$m. From around $\lambda = 1\mu$m scattering diminishes until it becomes insignificant in comparison to absorption at longer wavelengths.

MIR, FIR, Sub-mm, mm & cm: $\lambda \geq 4\mu$m

Perhaps the most striking absorption cross-section as the wavelength increases towards the MIR is the strongly spiked profile of the PAH-clusters. Each of the peaks of this absorption curve correspond to emission features in the MIR SED and the principle wavelengths and mechanisms by which they are generated are detailed in Table 3.2.

The starburst grain model does not include the large 30μm grains that dominate the very longest wavelengths in the AGN dust model. Therefore that region of the extinction in the starburst model it is generated by the large silicate and carbon grains which provide the majority of the absorption profile.

Having considered the unique properties of the starburst dust model, in comparison to the AGN dust model, the starburst grain section is concluded. The next element to be discussed is the generation of the synthesised cluster spectral energy distribution needed to irradiate the dust in DaRT and the stellar ionizing flux output required to drive the HII region evolution.

3.3 Stellar Population Synthesis Codes

Two central source functions must be generated to model the HII region; an ionizing photon output and a central cluster spectral energy distribution. The ionizing photon output is employed as the driving force behind the expansion of the HII region's ionisation front whilst the central cluster SED irradiates the derived dust distribution in DaRT. For the reasons given one convenient way of generating these functions is to use a stellar evolutionary synthesis code.

These codes aim to predict the observable stellar properties of actively star forming galaxies, including the impact of the most massive stars, using stellar evolutionary tracks and atmospheric grids. These evolutionary models have to explain not only pressure and gravity balancing in stellar cores and the associated nuclear processes, but also convection, radiative outflow and chemical mixing within the structure of the star (Norris 2003).

It was not until the late 1980's that processor power evolved sufficiently for complex time evolution solutions to be computed. Thereafter, large libraries (e.g Maeder 1983; Maeder & Meynet 1987; Meynet *et al.* 1994) were built containing stellar tracks describing a wide variety of evolutionary behaviour including for example, the AGB phase of intermediate mass stars, the dynamics of more massive stars as they move from main

sequence to supernova, or the white dwarf cooling sequence of the least massive population (Bruzual & Charlot 1993). Stellar evolutionary synthesis codes then take advantage of these pre-calculated libraries by interpolating smoothly between the stellar tracks to give model isochrones for the evolution of the particular synthetic population required (Norris 2003).

Examples of stellar evolutionary synthesis codes which can be used to generate central source functions are GISSEL (Bruzual & Charlot 1993), STARBURST99 (Leitherer *et al.* 1999) and PEGASE (Fioc & Rocca-Volmerange 1997). Each of these synthesis codes are essentially the same in that the synthetic stellar population is dependent on input variables such as star formation rate, stellar burst mass and the initial stellar mass function. However, the range of output spectra varies considerably due to fundamental differences in input options. For example, STARBURST99 offers a choice of five metallicities and a piece-wise, power-law Initial Mass Function that can be tailored to the users requirements, whereas GISSEL offers only solar metallicity and is restricted to three inbuilt IMF's. GISSEL also consists of a library of model instantaneous burst SEDs pre-run at specific times and for an initial total stellar mass $M_{tot}(t=0) = 1M_{\odot}$, which can then be scaled up to the required population mass. Conversely, STARBURST99 allows the user to define any initial stellar mass and the emitted spectrum is calculated explicitly as it evolves with time.

Despite the differences between these codes, each has been successfully employed to model the source component of starburst galaxies (e.g., Gordon *et al.* 1997; Alexander *et al.* 1999; Efstathiou *et al.* 2000). However, due to its versatility STARBURST99 version 4 has been chosen for use in this thesis and all references to STARBURST99 should be taken as such. This edition of the STARBURST99 evolutionary synthesis code includes continuum metal-blanketing and Wolf-Rayet evolution in the SED modelling (Norris 2003) and is readily available to the community via the Space Telescope Science Institute (STSI) website (http://www.stsci.edu/science/starburst99).

STARBURST99 (v.4)

The central concept of a stellar evolutionary synthesis code is the calculation of accurate isochrones in a colour-magnitude diagram for either an instantaneous burst or a continuous stellar population. A model isochrone is a line which connects points which take the same value at the same time. In general, synthesis codes rely on both evolutionary tracks and

atmospheric stellar theory to compute their populations.

Stellar Evolutionary Tracks

As proposed by Schönberg & Chandrasekhar (1942) stellar evolution is not an homogeneous process but rather, as a star evolves over its lifetime, its physical and observational characteristics undergo significant changes. What form these changes take depends primarily on the initial mass of the star, with the result that the evolutionary sequence it undergoes can be described by a track on a luminosity-temperature plot. Example tracks for stars of 120, 85, 60, 40 and 25$M_{\odot}$ can be found on Figure 3.3. STARBURST99 uses the tracks of Meynet *et al.* (1994), which are based on the previous works of Maeder (e.g Maeder 1983; Maeder & Meynet 1987). These tracks provide information on stellar lifetime, mass loss, temperature, luminosity, surface chemistry abundance and the by-products of nuclear fusion. In order to define the IMF of the central cluster population quantities such as the initial stellar mass, the star formation mode and efficiency, the high and low mass cut-offs and the exponent of the IMF paramertization, the metallicity of the source population and the mass loss of the stellar tracks must be defined by the user. The choice of these values for the thesis work is returned to more fully in the next section.

Upon defining the zero-age population the tracks which describe the user's choice of metallicity, age and mass loss are input into STARBURST99 whereupon the code generates the IMF in mass bins. The resulting evolutionary grid is designed to have variable spacing to give more tracks during periods of fast evolutionary change and fewer tracks during periods of quiescence (Leitherer *et al.* 1999).

The Atmospheric Grid

Once the evolutionary grid has been created, atmospheric grids are then coupled to it by calculating gravity and temperature gradients. The accuracy of the synthetic population depends very heavily on the atmospheric grids used to describe the photospheric properties of stars. The atmospheric grids are coarser than the evolutionary grids and as large changes can occur in quantities like temperature and surface gravity between neighbouring grid solutions, they can produce dramatically different spectra and pure interpolation can introduce uncertainties. In contrast to the evolutionary grids, the atmospheric grids are therefore scaled to fit the luminosity of the each star in the user-defined population (Leitherer *et al.* 1999).

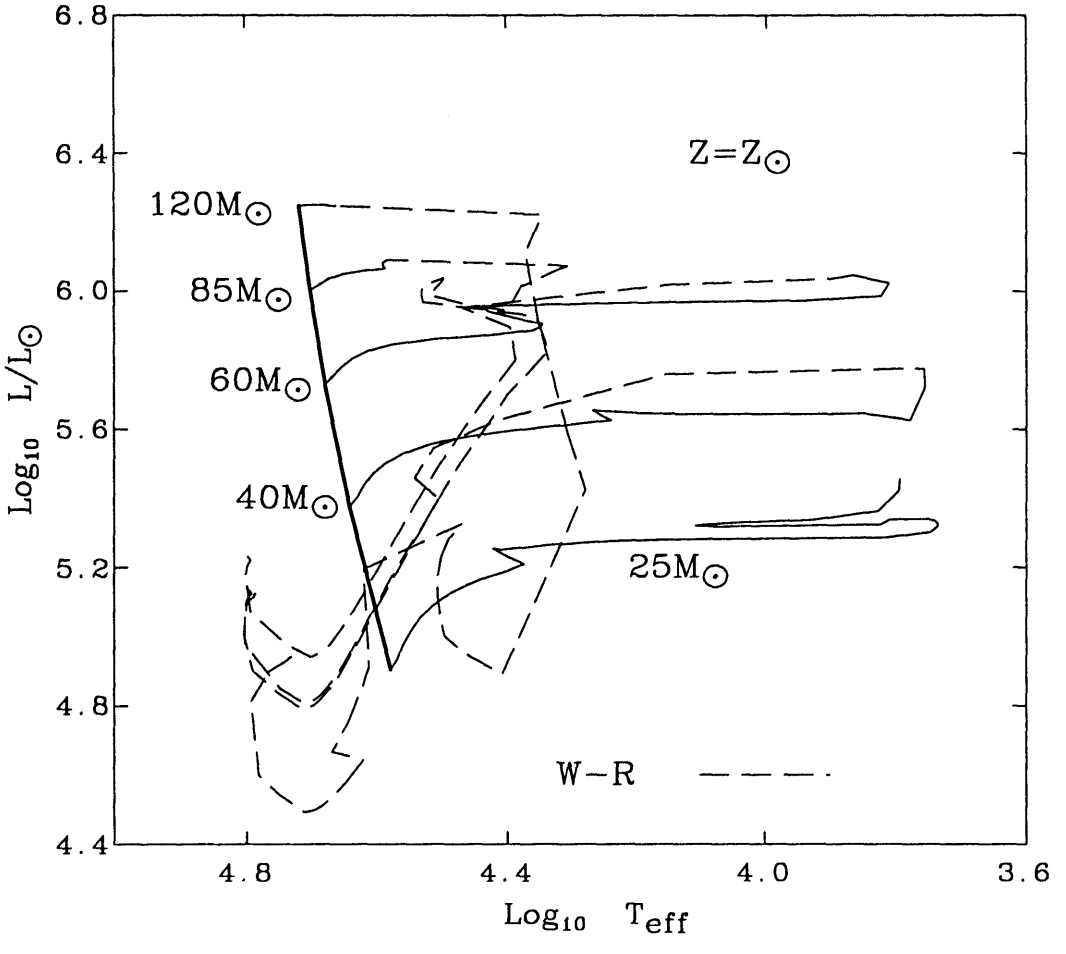

Figure 3.3: The Meynet *et al.* (1994) evolutionary tracks at solar metallicity $Z_{\odot}$, for 120, 85, 60, 40 and 25 $M_{\odot}$. The main sequence is indicated with a thick black line. W-R refers to Wolf-Rayet massive star population. (From Norris (2003) private communication).

Each of these components are then brought together in STARBURST99 by summing the populations' spectra and then re-initialising the flux value at each time step. The product of this procedure is the sum of all the stars in the synthetic population and this output can be used as the central source function for starburst modelling.

3.4 STARBURST99 Input Variables

To give the user a broad range of choice in the parameters defining the synthetic population SED, STARBURST99 has a considerable number of input variables, each capable of taking a wide range of values. All of these input variables must be understood and suitable values identified from the literature if the code is to generate a source function specifically appropriate to illuminate the GMCs in a ULIRG.

To calculate a particular synthetic population the first step is to define the zero-age population so that the correct evolutionary tracks and atmospheric grids can be selected by STARBURST99. This population is specified using the star formation mode, total stellar mass, a form of the IMF, stellar metallicity and the mass-loss rate and the values chosen for these parameters are now reviewed.

3.4.1 Star Formation Mode

STARBURST99 offers two choices of star formation; instantaneous burst or continuous formation mode. The instantaneous burst scenario has all stars forming at the same time which leads to a co-evolution of all components in the population, whereas continuous star formation has stars forming at a constant but lower rate than the instantaneous burst. The stars formed in the continuous mode are added to the population at each time step and distributed across the mass range accordingly. Obviously, with continuous star formation not only will the emission rise during the starburst's life-time but the stars will all evolve at different rates and at different times. However, eventually the output should converge to an equilibrium population (Norris 2003).

It is unclear whether a starburst is best modelled by an instantaneous burst or continuous formation as both have been observed. Kewley *et al.* (2001) generated central source functions for a large number of starburst galaxies using STARBURST99 (Leitherer *et al.* 1999) in both its continuous and instantaneous star formation mode and found their sample was best fitted by the continuous mode. On the other hand Farrah *et al.* (2002) and

FH03 used GISSEL in its instantaneous burst mode to successfully to model the central source functions for both the HYLIRGs and ULIRGs in their sample.

For the reasons given, the foundation of the thesis work is based on FH03 and as such the instantaneous burst star-formation mode was chosen to generate the thesis central source population. However, starbursts will never conform exactly to an 'instantaneous' burst and are much more likely to last anywhere between $\simeq$ 10Myr (Mouhcine & Contini 2002) and 100Myrs (Coziol 1996). Therefore the thesis instantaneous burst emergent starburst SEDs are extended to approximate continuous star formation using an exponential decay parametrization. The constant star formation approximation is returned to more fully at the end of Chapter 6 where the starburst emergent SED library is discussed.

In future work STARBURST99 could be used to generate continuous star formation source functions and the dust distribution and radiative transfer under their influence could be calculated explicitly. The resulting SEDs could be compared to the approximated continuous SEDs generated here and a qualitative estimate of the appropriateness of not only the star formation mode, but also the approximation itself could be obtained. However, this was felt beyond the scope of the thesis work presented here.

3.4.2 Total Stellar Mass

This input option is needed as the instantaneous burst star formation mode has been selected so the total stellar mass essentially determines the breadth of the model on the grid. The mass of a giant molecular cloud M_{GMC} can linked to the efficiency η of the conversion of its gas into stars by the equation

$$M_{\star}(0) = M_{GMC} \cdot \eta \tag{3.8}$$

where $M_{\star}(0)$ is the initial stellar mass. This parametrisation is an approximation as the exact relationship is unlikely to be a function of only mass. An alternative dependence is likely to be highly complex and at present appears undetermined. However, by using Equation 3.8 to quantify the relationship between the molecular cloud mass and star formation efficiency, the mass of stars at t=0 for STARBURST99 can be approximated.

Giant Molecular Cloud (GMC) Mass

The mass of molecular clouds found in the Milky Way Galaxy ranges between 10^2 and $10^7 M_\odot$ and follows a distribution of approximately $M^{-1.5\pm0.1}$ (Dame *et al.* 1986; Solomon *et al.* 1987). Dame *et al.* (1986) used the Columbia CO survey of the first Galactic quadrant to determine power law relations between the line widths and sizes of their molecular complexes and derived a slope of index γ=-1.5 from a section within the Perseus spiral arms. This was in good agreement with previous work by Sanders *et al.* (1985) who found a similar index from 315 discrete CO emission features, also in the first galactic quadrant. Solomon *et al.* (1987) extended the work using CO luminosities from 273 molecular clouds in the galactic disk and by fitting their data above 7 x $10^4 M_\odot$ they found that the mass distribution varied with index γ = -1.5 and also that the mass fraction of clouds per logarithmic mass interval varied with index 0.5. This demonstrated that most of the mass ($\approx$ 70%) of GMCs in the Milky Way is contained within clouds more massive than $10^6 M_\odot$ (Efstathiou *et al.* 2000).

Whilst it is likely that massive star formation in strongly starbursting galaxies also occurs in GMCs, it is by no means certain that the molecular cloud mass and distribution of a starburst galaxy follows a similar form to that of the Milky Way (Efstathiou *et al.* 2000). Indeed Devereux *et al.* (1994) suggested that the high density of O and B stars, along with the attendant high supernovae rate (Reike *et al.* 1980) in the nuclei of starburst galaxies, would make it surprising if these molecular complexes were not significantly different from those in the disk of our Galaxy (Devereux *et al.* 1994). In support of this statement Devereux *et al.* (1994) were able to show that the emission properties of the CO gas in the seven starburst galaxies they observed were measurably different to the average properties of GMCs in the Milky Way (Devereux *et al.* 1994). They also found that the total mass of molecular gas contained within the central 1.2-2.8kpc diameter region of the starburst nuclei in their sample was $\approx 10^9 M_\odot$, but that this only represented a small percentage ($\approx$ 9% - 16%) of the available dynamical mass in the same region (Devereux *et al.* 1994). Similarly Planesas *et al.* (1997) investigated three starburst galaxies; NGC2903, NGC351 and NGC3504 and derived molecular gas masses in the range 10^8-$10^9 M_\odot$ in regions a few hundred parsecs in size and showed that molecular complexes in the circumnuclear regions of these IRAS galaxies have associated HII regions up to a factor of 3 times more massive than those seen in the Milky Way.

Further indirect evidence that strongly starbursting galaxies contain more massive GMCs than those found in the Milky way comes from the luminosity function. Efstathiou *et al.* (2000) suggest that low mass molecular clouds are found to form predominately low mass stars and therefore by analogy, more massive stars would be expected to form in more massive GMCs.

Given the above, four molecular cloud masses were chosen for the modelling in this thesis work: $M_{GMC} = 10^6$, 10^7, 10^8 & $10^9 M_\odot$ to ensure that both the distribution of complexes found in the Milky Way and those inferred from starburst galaxy observations were included in the model parameter space.

Star Formation Efficiency η

As Equation 3.8 shows, the GMC mass by itself does not determine the total stellar mass used as input to the STARBURST99 code and the efficiency of conversion of that gas into stars η must also be defined. Kennicutt (1998) used CO observations of 36 starburst galaxies to find the median rate of gas consumption per 10^8yr to be $\approx$ 30% inferring an average star formation efficiency η of 0.3 (Efstathiou *et al.* 2000). Colbert (1999)also used ISO spectroscopy to estimate a stellar mass of 0.5-1.3 x $10^8 M_\odot$ for the nearby starburst galaxy M82 and in tandem with the results of Hughes *et al.* (1994), who determined an associated molecular gas mass of $\approx$ 2 x $10^8 M_\odot$ for the same galaxy, the implied gas consumption rate was 0.2 - 0.39. Efstathiou *et al.* (2000) consequently chose a mid-range $\eta = 0.25$ as the star formation efficiency for their starburst galaxy modelling. However, in contrast, Planesas *et al.* (1997) used observations of NGC3351, NGC3504 & NGC2903 to estimate that the total gas into stars conversion in these galaxies' molecular clouds was about 10% or less, implying $\eta < 0.1$.

As this thesis work seeks model a wide range of GMCs for testing against the ULIRG sample, seven values of the star formation efficiency were chosen for the model grid at η at 0.01, 0.025, 0.05, 0.1, 0.15, 0.2 & 0.25. Therefore, using Equation 3.8 the total stellar mass range used for the STARBURST99 synthesis code is $1 \times 10^4 M_\odot < M_\star < 2.5 \times 10^8 M_\odot$.

3.4.3 The Stellar IMF

In this case, the Initial Mass Function (IMF) describes the range of masses that stars in the synthetic population take at t=0. Attempts to quantify the IMF began as far back as 1955 when Edwin E. Salpeter published an estimate of the IMF of stars in our neighbourhood

(Salpeter 1955). The parameterisation at which he arrived takes the form:

$$N_{tot} = k_{imf} \int_{M_{min}}^{M_{max}} M_{\star}^{-\alpha} dM_{\star} \tag{3.9}$$

Where N_{tot} is the total number of stars in a system, k_{imf} is a constant, $M_{\star}$ is the stellar mass, M_{max} and M_{min} are the maximum and minimum stellar masses limits and α is the exponent of the power-law. As the population is defined with a negative power-law slope, the number of low mass stars greatly outnumbers the high mass stars. It should be noted that at the very low and high mass the power law approximation of Equation 3.9 is thought to fail (Leitherer *et al.* 1999)..

Lower Mass Limit M_{min}

On a theoretical basis the very smallest value M_{min} can probably take is $0.08M_{\odot}$; a value found from the H-burning limit (Leitherer & Heckman 1995). Perhaps a more reliable value can be estimated from considering the type of stellar population below $0.1M_{\odot}$. Scalo (1998) suggested that young stars would be pre-main sequence and with their high luminosity, would destabilize the inferred mass-luminosity relationship. This means it has not so far been possible to describe the IMF below the $0.1M_{\odot}$ limit leaving it in great uncertainty (Norris 2003). Considering this, the lower mass limit for the IMF input to STARBURST99 has been chosen at $M_{min} = 0.1M_{\odot}$.

Upper Mass Limit M_{max}

In choosing the limiting value of the maximum mass in the stellar population, the evidence has mainly come from spectroscopic measurements of stars in the Milky Way and neighbouring galaxies. Oey & Massey (1995) and Oey (1996) considered ten LMC, one SMC and thirteen Milky Way OB associations with ages between 1 - 11Myr. The most massive star in their survey was $> 120M_{\odot}$, although a $120M_{\odot}$ star is only expected to occur rarely. The maximum value M_{max} can take in STARBURST99 is also $120M_{\odot}$ so this was chosen as the upper mass limit.

IMF Exponent α

Much research has been done into the possibility that the IMF cannot actually be described by one exponent α over all masses but must be split into ranges of masses which describe the probable stellar population in each group. For example in the lowest mass range,

generally considered to be $0.1M_{\odot} < M < 1M_{\odot}$, Mèra *et al.* (1996) and Kroupa (1995) found the slope lies between flat $\alpha = 0$ and $\alpha = -0.5$. More recently (Kroupa 2002) estimated the low mass range IMF at $0.1M_{\odot} < M < 0.5M_{\odot}$ and from brown-dwarf studies determined an exponent of $\alpha = 1.3$. Brown-dwarfs are sub-stellar objects with a mass below that necessary to maintain hydrogen-burning nuclear fusion reactions in their cores, but which have fully convective surfaces and interiors, with no chemical differentiation by depth. Brown dwarfs occupy the mass range between that of large gas giant planets and the lowest mass stars.

Many of the broken power-law models also explore an intermediate mass range, generally between $1M_{\odot} < M < 10\ M_{\odot}$ and a higher mass range $10M_{\odot} < M < 120\ M_{\odot}$. For example Miller & Scalo (1979) used $\alpha = 0.4$, 1.5 & 2.3 for the low ($0.1M_{\odot} < M < 1M_{\odot}$), intermediate and high mass range exponents respectively. Other research has used clusters as laboratories; one of the advantages being that clusters exhaust their supply of pre-main sequence stars in around 10 million years so there is no bias in the mass-luminosity relationship. In the intermediate mass range an average value for the exponent from these surveys is $\alpha = 2.7 \pm 0.5$ (Norris 2003). Perhaps the most famous parameterization of the low-intermediate IMF is the first however, where Salpeter (1955) studied stars in the range $0.3M_{\odot} < M < 10M_{\odot}$ and obtained a value of $\alpha = 2.35$ (Salpeter 1955).

With the higher mass range it is even more difficult to estimate the stellar number density as these stars are so short lived that they are only found in the youngest star forming regions. This rapid evolution means they may be missed out of mass estimates based on very blue main sequence (MS) stars because they have evolved to e.g., cooler, less luminous, post MS super-giants (Norris 2003). However, the work of Elmegreen (1997) and Massey (1998) demonstrated through extensive spectroscopic classification that the result of Salpeter (1955) ($\alpha = 2.35$) is actually valid over the high mass range $10M_{\odot} < M < 120\ M_{\odot}$ too.

Broken Power-Law

STARBURST99 gives the user the option of a broken power-law description of the IMF and the default is the parametization of Kroupa (2002). Combining IMF estimates for different populations in which the stars could be observed individually, Kroupa (2002) was able to conclude that a uniformity of the IMF existed across a very broad range of objects; from ancient, metal-poor, exotic populations, through dense massive clusters

forming in GMCs, to present-day star formation in small molecular clouds (Kroupa 2002). The Salpeter (1955) IMF and its extension (Massey 1998) was used very successfully in the modelling work of Gordon *et al.* (1997), Silva *et al.* (1998) and Efstathiou *et al.* (2000) but the Kroupa (2002) parametization potentially represents an improvement to the very similar single Salpeter (1955) mass range as it contains variation for the very lowest mass brown-dwarfs. The Kroupa (2002) formulation is

$$N_{tot} = k_{imf} \int_{0.1}^{0.5} M_{\star}^{-1.3} dM_{\star} + k_{imf} \int_{0.5}^{120} M_{\star}^{-2.3} dM_{\star} \tag{3.10}$$

and has been chosen as the STARBURST99 IMF parameterisation for the thesis modelling.

3.4.4 Metallicity & Mass Loss Tracks

The metallicity of every star in the synthesized stellar population has been chosen as solar in accordance with the metallicity used by Efstathiou *et al.* (2000). Although the option of five metallicities are available in STARBURST99, using this as an additional free parameter is outside the scope of the present work.

Regarding the mass-loss tracks, STARBURST99 uses the standard mass-loss tracks of Schaller *et al.* (1992), Schaerer *et al.* (1993) and Charbonnel *et al.* (1993) for stellar masses in the range 0.8-12$M_{\odot}$ and the enhanced mass-loss tracks of Meynet *et al.* (1994) for stellar masses of 12-25$M_{\odot}$ and above. Leitherer *et al.* (1999) favoured the enhanced mass-loss models over the standard ones because they generated a better representation of observations of Wolf-Rayet stars. In view of this and because in a starburst galaxy the massive stars account for most of the luminosity, when given the choice between a population undergoing enhanced- or low- mass-loss, the enhanced rate has been adopted in this thesis work.

3.4.5 Unused Input Variables

STARBURST99 in its default mode produces a variety of other outputs which are not required for the thesis. Examples of these are tables of the stellar spectral types generated during each time step or the ultraviolet line spectrum. STARBURST99 has 4 of these variables which need to be specified for the code to run and each has taken the values recommended by the authors of STARBURST99: Supernova Mass cut-off = 120$M_{\odot}$, Blackhole Mass cut-off = 8$M_{\odot}$, Metallicity of UV line spectrum = Solar, Red Super-giant micro turbulence velocity = 0.3 (Leitherer *et al.* 1999).

3.4.6 Summary of Input Parameters

For convenience, the value of STARBURST99 parameters chosen for the thesis modelling are presented in Table 3.3. With four GMC mass values and seven star formation efficiencies, there are 28 model systems in the parameter grid.

Variable	Description	Thesis Value
M_{GMC}	Initial Mass of Starburst	10^6-,10^7-,10^8-,$10^9 M_\odot$
MODE	Star Formation Model	Instantaneous Burst
η	Star Formation Efficiency	0.01,0.025,0.05,0.1,0.15,0.2,025
α	IMF power-law Exponent	Kroupa (2002)
M_{max}	IMF High Mass cut-off	$120 M_\odot$
M_{min}	IMF Low Mass cut-off	$0.1\ M_\odot$
$Z_\star$	Metallicity of Source Population	Solar
M_{loss}	Mass Loss of Stellar Tracks	High
$W_\star$	Wind Model	Theoretical
IG_{mass}	Resolution of the Mass Grid	Full Isochrone
L_{min},L_{min}	Limits for Track Mass Boundaries	All
M_{sn}	Supernova Mass cut-off	$120 M_\odot$
M_{bh}	Blackhole Mass cut-off	$8 M_\odot$
Z_{uv}	Metallicity of UV line spectrum	Solar
V_{rsg}	Red Supergiant turbulence velocity	0.3

Table 3.3: Input Variables chosen for STARBURST99(v.4.)

3.5 STARBURST99 Central Source Functions

The HII region modelling prescription used in this thesis work requires two source functions; the ionizing photon output and the GMC stellar spectral energy distribution.

As mentioned, the cluster's ionizing photon output will be used to drive the expansion of the ionization front through the GMC. The changing gas density under its influence will be linked to the dust density via a dust condensation factor and the dust distribution derived for time t. That distribution is then translated into a form suitable for input into

DaRT, the cloud irradiated with the clusters' stellar SED for the same time t and the radiative transfer of flux calculated.

3.5.1 Time-Steps for Output

An important consideration is the time-steps used by STARBURST99 to calculate the two outputs. The stellar population in the STARBURST99 code can be evolved from an initial time of $t_i = 10^4$yrs to the users preferred age, in this instance chosen as $t_f = 80$Myrs, in an infinite range of time-steps. This is much more flexible than for example GISSEL (Bruzual & Charlot 1993) which is defined in 221 time-steps between 0 and 20Gyrs.

The ionizing photon output should be sampled finely in time to accommodate rapid changes in the clusters population. The value recommended for the ionizing photon output by Leitherer *et al.* (1999) is $\Delta t_{ip} = 0.1$Myr and as substantial changes are unlikely to occur in the source population in timescales less than that value, it seemed reasonable to adopt it for the thesis input.

The source cluster SEDs used to irradiate the derived dust density distribution in DaRT are particularly computer-time intensive and it was deemed unnecessary to generate these SEDs at the 0.1Myr time interval used for the ionizing photon output. In order to provide a comprehensive coverage of all important evolutionary stages it was decided that this thesis work would only generate emergent starburst SEDs at intervals of 1Myrs for 1Myr $< t <$ 10Myr and at intervals of 10Myrs for 10Myr $< t <$ 80Myr; the closer sampling at early times employed to accommodate the more rapid evolution of a younger cluster.

Thus with 28 combinations of GMC mass and star formation efficiency on the parameter grid and with each requiring an emergent starburst SED to be calculated by DaRT at the times stated, approximately 500 individual, synthetic cluster population SEDs were produced by STARBURST99. For convenience all these times are summarised in Table 3.4.

In a similar way to the AGN model it is important to understand the behaviour of these source functions so the shape of the emergent starburst SEDs can be fully interpreted. As the source cluster spectral energy distribution is the root function from which the ionizing photon distribution is derived, it will be considered here first.

Variable	Description	Thesis Value
t_i	Initial Time	10,000yrs
t_f	Final Time	80Myrs
Δt_{SED}	Time-Step for Irradiating Cluster SED:	
	1-10Myrs	1Myrs
	10-80Myrs	10Myrs
Δt_{ip}	Time-Step for Ionizing Photon Output	0.1Myrs

Table 3.4: Time-Step Variables chosen for STARBURST99(v.4.)

Synthetic Population Spectral Energy Distribution

STARBURST99 generates the SEDs of the synthesized population using three components: the stellar, nebular and total specific luminosity, over the wavelength range $0.0912\mu m < \lambda < 160\mu m$ in 1230 steps. Only the stellar component is needed here and the long-wavelength nebulae emission is excluded - this part of the GMC SED is the element calculated by DaRT. In the first instance the outputted STARBURST99 SEDs are converted from the default units of Specific Luminosity($ergs^{-1}\AA^{-1}$) vs. $\lambda(\AA)$ to Specific Flux($ergs^{-1}cm^{-2}sr^{-1}$) vs. $\lambda(\mu m)$ Specific Flux($ergs^{-1}cm^{-2}sr^{-1}$). This procedure requires the location of $R_1(t)$, the inner dust radius and this is accomplished using the following equation

$$R_1(t) = \left(\frac{L_\star(t)}{4\pi\sigma T_{cond}^4}\right)^{\frac{1}{2}} \tag{3.11}$$

where $L_\star(t)$ is the luminosity of the population, σ is the Stefan-Boltzmann constant and T_{cond} is the dust condensation temperature. T_{cond} is taken here as 1600K; a suitable value for the most abundant graphite grains in the dust model. The data is then converted from the 1230 point STARBURST99 wavelength array into the 84 point DART array using the same spline-fitting bespoke computer program written to translate the AGN source function onto the DaRT wavelength array. The spline-fitting program was then extended to extrapolate the STARBURST99 source functions from $160\mu m$ to $1450\mu m$ using a constant source function and a greybody approximation.

STARBURST99 operates scaling, whereby for all other equivalent input variables, the luminosity from e.g.: an $M_\star = 10^9 M_\odot$ population is 10 times that of an $M_\star = 10^8 M_\odot$ population, at all wavelengths, so it is not necessary to illustrate the source function energy

distributions for all values of $M_\star$ run through STARBURST99. Figure 3.4 illustrates the source functions for M_{GMC}=$10^8 M_\odot$ and η=0.2 equating to $M_\star = 2x10^7 M_\odot$, for all years that an SED is to be generated.

Considering the plots in Figure 3.4 perhaps the most obvious comment is that the spline-fitting procedure effectively 'washes out' the atomic spectral lines when converting from the STARBURST99 to the DaRT wavelength grid. For example, in the early spectra dominated by O and B stars, there is little evidence of lines such as HeII, SiIV, OIII or NIII commonly associated with those stars. However, whilst the spline-fitting procedure leaves only the continuum remaining, as the thesis seeks to model the dust, this function is adequate. The primary differences as the population evolves are therefore found in the magnitude and wavelength of the emitted flux (Emerson 1996).

When considering continuum radiation, three processes are responsible for the opacity: electron scattering, photoionization (bound-free) and free-free transitions. Each of these processes is governed by an absorption coefficient which determines how much energy is removed from a beam of photons during its passage through the stellar atmosphere. As stellar atmospheres are predominantly hydrogen (90% by number) the more important of these processes is bound-free or photoionization where for example a neutral H (hydrogen) atom absorbs a photon of energy $h\nu$, where ν is the frequency and h is planck's constant and emits an electron, becoming ionized to H^+ in the process. Only one discrete energy level is involved in this transition - that from which the H atom is ionized - and the associated absorption coefficient increases with wavelength up to a threshold frequency given by $\nu_o = I_n/h$, where I_n is the ionization energy from level n (Emerson 1996).

The first wavelength regime to consider is that short-wards of the Lyman absorption coefficient threshold limit at 0.0912μm in the ultra-violet. Lyman photons have sufficient energy to enable transitions between n=1 and the H^+ continuum and the absorption coefficient is at its maximum at 0.0912μm. As the co-efficient is proportional to ν^{-3} its efficiency drops away towards shorter wavelengths. At early times the most massive OB hot stars produce significant quantities of photons with sufficient energy to ionize hydrogen and short-wards of 0.0912μm there is evidence of this flux as photons are produced in numbers in excess of that required to ionize all available H from its ground state. This short wavelength flux is only seen at early times as the very high mass stars responsible for this excess burn their central hydrogen extremely efficiently and as such have very short lifetimes ($\leq$ 6Myrs).

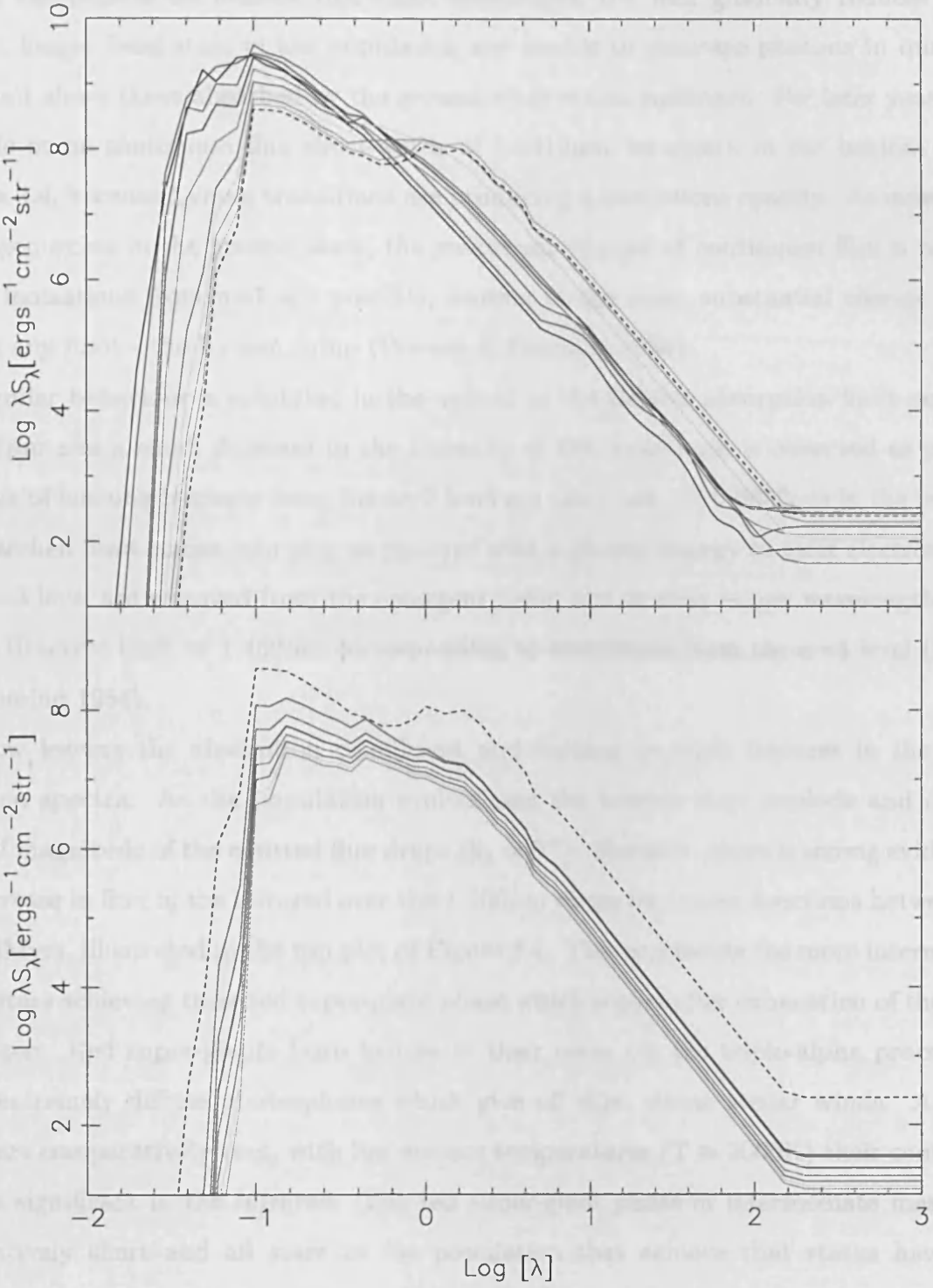

Figure 3.4: STARBURST99 Source Function Spectral Energy Distribution for $M_\star = 2 \times 10^7 M_\odot$. The top plot shows 1-9Myrs as solid lines in black, red, green, blue, cyan, magenta, yellow, orange & light grey respectively whilst the bottom plot shows 20-80Myrs in red, green, blue, cyan, magenta, yellow & orange. The distribution for 10Myrs is shown on both plots as the black dashed line.

As the population evolves this short wavelength UV flux gradually reduces as the cooler, longer lived stars in the population are unable to generate photons in quantities over and above those absorbed by the ground-state stellar hydrogen. For later years there is little or no continuum flux short-wards of 0.0912μm, as shown in the bottom plot of Figure 3.4, because Lyman transitions are producing a continuous opacity. As most of the hydrogen exists in the ground state, the maximum amount of continuum flux is removed when ionizations from n=1 are possible, leading to the most substantial change in flux across any limit - the Lyman jump (Bowers & Deeming 1984).

Similar behaviour is exhibited in the optical as the Balmer absorption limit occurs at 0.3647μm and a small decrease in the intensity of the continuum is observed as photons capable of ionizing H atoms from the n=2 level are absorbed. At 0.8650μm in the infrared, the Paschen limit comes into play as photons with sufficient energy to eject electrons from the n=3 level are removed from the emergent beam and at even longer wavelengths there is the Brackett limit at 1.459μm corresponding to excitations from the n=4 level (Bowers & Deeming 1984).

Now leaving the absorption co-efficient and turning to other features in the source function spectra. As the population evolves and the hottest stars explode and die, the overall magnitude of the emitted flux drops ($S_\lambda \propto T^4$). However, there is strong evidence of an increase in flux in the infrared over the 1-100μm range for source functions between 7 < t < 10Myrs, illustrated in the top plot of Figure 3.4. This represents the more intermediate mass stars achieving their red super-giant phase which occurs after exhaustion of their core hydrogen. Red super-giants burn helium in their cores via the triple-alpha process and have extremely diffuse photospheres which give off slow, dense stellar winds. As these stars are comparatively cool, with low surface temperatures ($T \approx 3000K$) their continuum flux is significant in the infrared. The red super-giant phase of intermediate mass stars is relatively short and all stars in the population that achieve that status have gone supernova by 10Myrs so that by t = 20Myrs, the infrared flux has dropped back to levels more commensurate with those prior to the red super-giant phase (Zeilik & Gregory 1998).

Looking briefly at the bottom plot on Figure 3.4 showing the SEDs for 10-80Myrs, sampled at 10Myrs, less and less difference between each source function is observed as the population now consists of very long lived, cool stars whose evolution is extremely slow. Therefore the primary source of difference at these later times is stellar death and the corresponding drop in emitted flux.

3.5.2 Ionizing Photon Output

STARBURST99 also tabulates the number of ionizing H, HeI and HeII photons in output file *.quanta* and these quantities are plotted in Figure 3.5. The values are calculated by integration of the source cluster spectra below 0.0912μm, 0.0504μm & 0.0228μm respectively and represent the excess of photons not absorbed into the continuum. Perhaps most obviously, those photons capable of ionizing H from the ground-state, as indicated by the red dashed line on Figure 3.5, dominate the total output. As discussed in the previous subsection, short-wards of the 0.0912μm Lyman limit, the absorption coefficient is dominated by transitions from n=1 and has a maximum impact on the spectral energy distribution due to the large amount of hydrogen atoms existing in the ground state. However at early times some excess photons are able to escape the clusters' surface and this leads to the H ionizing photon output seen on the plot. At around 2Myrs this photon flux begins to drop rapidly as the massive O and B stars responsible evolve into their red super-giant phase and eventually go supernova.

Moving to the number of HeI photons, shown on Figure 3.5 as the green dashed line, it is the hottest O and Wolf-Rayet stars which are the dominant contributors of these photons at wavelengths below 0.0504μm. Wolf-Rayet stars begin to form at around 3Myrs and this is shown by the small increase in photons capable of ionizing HeI shown in the plot at that time. The number of photons emitted in the HeII continuum below 0.228μm is also completely dominated by Wolf-Rayet stars and the very few O stars that have extremely high mass-loss rates (Leitherer *et al.* 1999). Helium recombinations in the dense wind can sometimes give a completely opaque HeII continuum (Schmutz *et al.* 1992) and lead to the number of HeII ionizing photons being orders of magnitude lower than the H and HeI values just discussed. However the HeII distribution also shows an increase at around 3Myrs as the more massive Wolf-Rayet stars form, and then drops off as they turn into black holes.

This concludes discussion of the first two STARBURST99 source functions. In the following sections the sum of the ionizing photons $S_\star(t)$, shown on Figure 3.5 as the solid black line, will be used to drive the evolution of the HII region's ionization front, which in turn will be linked to the gas and dust distribution.

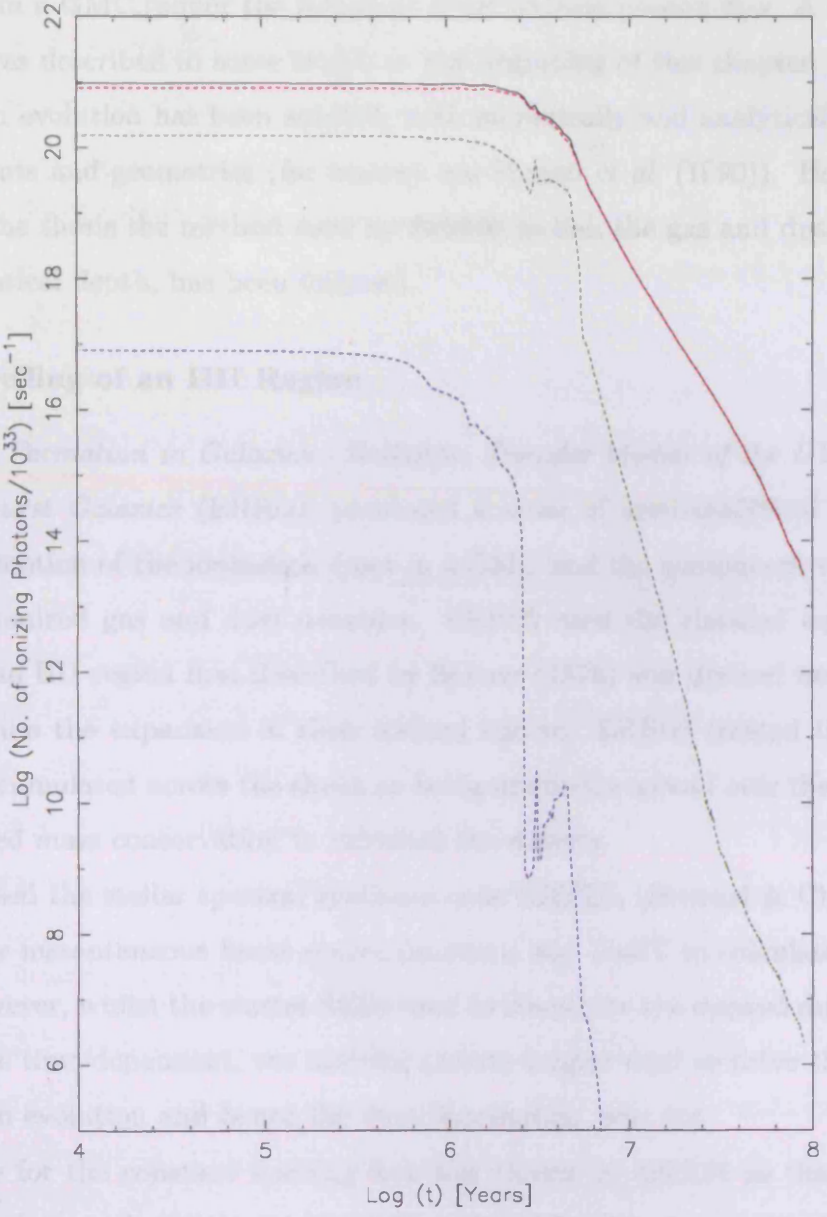

Figure 3.5: STARBURST99 Ionizing Photon Output for an $M_\star = 2 \times 10^7 M_\odot$ stellar cluster. The red, green and blue dashed curves are the number of ionizing photons in the HI, HeI and HeII continuum respectively. The black solid curve is their sum.

3.6 The HII Region Model

In this section a series of expressions are developed to trace the evolution of the gas and dust density in a GMC, under the influence of an ionizing photon flux. A GMC evolving in this way was described in some length at the beginning of this chapter.

HII region evolution has been studied, both numerically and analytically, in a variety of environments and geometries (for reviews see Franco *et al.* (1990)). However, for the purposes of the thesis the method used by ERR00 to link the gas and dust densities and obtain the optical depth, has been followed.

ERR0 Modelling of an HII Region

Massive Star Formation in Galaxies - Radiative Transfer Models of the UV to mm Emission of Starburst Galaxies (ERR00) presented a series of semi-analytical expressions to describe the motion of the ionization front in a GMC and the consequent variation of the neutral and ionized gas and dust densities. ERR00 used the classical equation for the evolution of an HII region first described by Spitzer (1978) and derived here as Equation 3.22 to describe the expansion of their ionized sphere. ERR00 treated the neutral gas which was accumulated across the shock as being uniformly spread over the entire neutral cloud and used mass conservation to calculate the density.

ERR00 used the stellar spectral synthesis code GISSEL (Bruzual & Charlot 1995) to generate their instantaneous burst source functions and DaRT to calculate the radiative transfer. However, whilst the cluster SEDs used to illuminate the derived dust distribution in DaRT were time-dependent, the ionizing photon output used to drive the evolution of the HII region evolution and hence the dust distribution, was not.

The value for the constant ionizing flux was chosen by ERR00 as that emitted at t = 3.3Myrs and as at that time the supergiant O and B stars responsible for most of the ionizing flux are still on the main sequence, the magnitude of the ionizing flux is high. As ERR00 used this value at all times the expansion of their HII region was potentially overestimated as the stellar population dies off and the ionizing flux magnitude decays. By using a constant ionizing flux ERR00 essentially modelled a single ionized bubble which maintains a ionization rate and therefore distorts the affect of a varying ionizing source flux. In reality a series of slower and slower bubbles would actually be generated and this is better modelled with a time-dependent flux.

Extension to ERR00 Modelling

The thesis work therefore extends the ERR00 modelling by incorporating the time-dependent STARBURST99 ionizing photon output discussed in the last section. The new time-dependent radial solution for the expansion of the ionization front was found using a Taylor series expansion to the second order of the ERR00 equation (Spitzer 1978) for HII region the radius. This created a new dynamical model, potentially more realistic for describing the evolution of a GMC. The thesis does not trace the density enhancement across the shock in the HII region phase and follows ERR00 in assuming the gas is spread uniformly over the neutral cloud.

In the coming sections, first the method used by ERR00 will followed to describe the photo-ionization phase and derive the Spitzer (1978) equation for the radius. Diverging then from ERR00, the new time-dependent expression for the radial evolution of the ionization front in the expansion phase is developed. The method of ERR00 is then returned to quantify and link the gas and dust densities to obtain the optical depth.

An important element of the thesis work is the bespoke computer program *GEM*, standing for **G**MC **E**mission **M**odel. This C code contains all the expressions developed in this chapter needed to calculate the optical depth in a form suitable for input into DaRT and was written by the author of the thesis. Beginning then with regenerating the ERR00 prescription for the photo-ionization phase.

3.6.1 The Photoionization Phase

At early times, flux from the clusters' central stars impacts on the surrounding neutral gas cloud, ionizing it to HII. However, recombinations to HI are continuously occurring within the ionized volume, which depletes photons from the stellar flux field. Rather than deriving the equation of motion of the ionization front during the photo-ionization phase, it is more convenient to derive the radius of the HII region at the point at which the stars 'switch-on' into their stable state, - the Strömgren radius - and assume that the two are equal. The Strömgren radius can be obtained by balancing ionizations and recombinations within the volume (Dyson & Williams 1997*b*).

At time t, let $S_\star(t)$ be the rate at which the cluster is producing photons which can ionize hydrogen per second ($h\nu \geq 13.6V$), given by the STARBURST99 ionizing photon output described in §3.5.2. Defining the Strömgren radius $R_s(t)$ as the radius at which

the stellar output photon rate just balances the recombination rate in the volume $V_{wi}(t)$ = $4\pi/3$ $R_s^3(t)$, $S_\star(t)$ becomes

$$S_\star(t) = \dot{N}_R \frac{4\pi}{3} R_s^3(t) \tag{3.12}$$

where $\dot{N}_R$ is the number of recombinations per second per unit volume. The recombination rate $\dot{N}_R$ is determined by two factors. First it is directly proportional to the number density of electrons n_e and protons n_p in the gas which, assuming a pure hydrogen region. gives $n_e = n_p$. Secondly it is dependent on the electron temperature distribution which is determined in part by elastic electron-electron collisions which produce a Maxwellian velocity distribution and transfer energy to all species in the cloud immediately and in part by much slower inelastic collions, which remove energy from the gas. It is the electron temperature which determines not only the probability of recombination into a particular level but also the probability of a proton encountering an electron in the first place (Dyson & Williams 1997*b*). The recombination rate into level n, $\dot{N}_{Rn}$ can be written:

$$\dot{N}_{Rn} = n_e n_p \beta_n (T_e) = n_e^2 \beta_n (T_e) \tag{3.13}$$

where $\beta_n(T_e)$ is the recombination co-efficient from level n and $n_e = n_p$.

When an electron recombines with a proton, photons are emitted as the electron cascades down the atoms' energy levels towards the ground state. Some of these energy level changes produce photons like those of the Balmer series, which have enough energy to ionize any neutral hydrogen in the near-vicinity. In order to take account of these extra photons it is useful to make the approximation that each recombination into the ground-level produces a photon which immediately ionizes a nearby neutral atom in the near neighbourhood, which then in turn recombines into the ground-level and produces a further ionizing photon and so on. Therefore, when balancing Equation 3.12, recombinations into the ground-level effectively cancel each other out and do not need to be included so ionization in the ground-level can essentially be considered to be in equilibrium. Using this 'on-the-spot' approximation, $\beta_n(T_e)$ in Equation 3.13 can be replaced with $\beta_2(T_e)$; the total recombination coefficient to all levels from level n = 2. Thus, the recombination rate $\dot{N}_R$ for the entire ionized region can be found by summing over all the levels excluding the ground-level (Dyson & Williams 1997*b*), such that

$$\dot{N}_R = \sum_{n=2}^{\infty} \dot{N}_n = n_e^2 \beta_2 (T_e) \tag{3.14}$$

Where T_e is the electron temperature and n_e^2 is the product of the number density of electrons and protons; $n_e n_p$. A reasonable numerical approximation of the total recombination coefficient is $\beta_2(T_e) \simeq 2 \times 10^{-17} T_e^{-3/4} cm^3 s^{-1}$ $(T_e/K)^{-3/4}$ (Dyson & Williams 1997*b*). T_e is the electron temperature which is determined by the heating and cooling rates and arbitrary value of $T_e = 10^4 K$ is considered suitable for this kind of environment (Dyson & Williams 1997*b*).

Substituting 3.14 for $\dot{N}_R$ into Equation 3.12 and re-arranging for $R_s(t)$ leads to

$$R_s(t) = \left[\frac{3S^*(t)}{4\pi n_e^2 \beta_2 (T_e)} \right]^{\frac{1}{3}} \tag{3.15}$$

Now considering the number density of electrons n_e in this last equation. The Strömgren radius $R_s(t)$ has been defined as the point at which the number of photons arriving is exactly balanced by the number of recombinations within a sphere of that radius. In its initial stages, the IF moves into the surrounding neutral material at a highly supersonic speed when compared to the speed of sound in ionized gas ($c_i \simeq 10 kms^{-1}$), whilst the best speed at which the gas can react to the changes caused by ionization is c_i (Dyson & Williams 1997*b*). This means that the density of the ionized material internal to the IF n_i, can be considered equal to the initial number density of the neutral material n_o in this phase as the newly ionized material has not yet had time to accommodate the changes caused by ionization (Dyson & Williams 1997*b*), of which pressure is perhaps the most substantial.

Thus, when considering Equation 3.15, the number density of electrons n_e can be thought of as equivalent to the initial number density of HI - n_o - as each HI atom contributes one electron to the gas. However, this is also the number density of the ionized material internal to the IF so n_o can be substituted into 3.15 for n_e

$$R_s(t) = \left[\frac{3S^*(t)}{4\pi n_o^2 \beta_2 (T_e)} \right]^{\frac{1}{3}} \tag{3.16}$$

which is the equation for the Strömgren radius, used by ERR00 to describe the radius of the ionization front at the end of the photo-ionization phase.

Now considering a suitable value for n_o, in Equation 3.16 it is usual for densities in HII regions to be expressed in terms of the molecular Hydrogen density H_2. Downes & Solomon (1998) have shown that the H_2 densities in the cores of the extreme starbursts powering ULIRGS can be much greater than the average density of the giant molecular cloud. Downes & Solomon (1998) assumed a value of around $n_{H_2} = 2 \times 10^3$ cm^{-3} leading

to a value for the number density of HI, $n_o = 4 \times 10^3$ cm^{-3}. This value for n_o was used successfully by ERR00 and has therefore been employed in this thesis work as the initial core number density of the GMCs. It should be noted that there is significant uncertainty not only in the core density but in the radial gas density distribution itself and that, coupled with the assumption that the stars 'switched-on' and instantaneously formed an ionized sphere of radius $R_s(t)$ means Equation 3.16 can only be considered an upper limit of the actual Strömgren sphere radius (ERR00). Whilst it would be possible to investigate varying the value of n_o using the computer code GEM, it was felt this was beyond the scope of the thesis work in hand.

3.6.2 The Rapid Expansion Phase

During the photoionization phase, the dominant factors controlling the radius of the ionization front were the stellar photon output and recombination rates within the ionized volume. However, photo-ionization increases the number of particles per unit volume by a factor of two and feeds energy into the gas in the form of electron kinetic energy, which can also increase its temperature by a factor of up to ~ 100. The combination of these two effects can produce a pressure difference across the boundary between the bubble of hot ionized material and the external, cool, neutral material in excess of a factor of 200. This leads to the hot gas within the ionized sphere attempting to achieve pressure equilibrium by expanding into the surrounding cooler neutral material (Dyson & Williams 1997*c*).

Driven by this substantial pressure difference, the rapid expansion of the ionized sphere is supersonic with respect to the speed of sound in a neutral gas ($c_n \simeq 0.45$kms^{-1} equating to $T_n \simeq 25$K, where T_n is the gas temperature (Dyson & Williams 1997*c*)). The ionized material is forced into the neutral material creating a shock wave ahead of the ionization front. As the expanding bubble pushes the stationary neutral material outwards, a thin, highly compressed layer of neutral gas becomes trapped between the shock and ionization fronts.

The rate at which the ionized bubble expands relies on two conditions: that the pressure in the shocked neutral layer of gas directly behind the shock front is the same as that in the gas interior to the ionization front and that the shock created is strong.

In order for the pressure equality to be valid, the time taken for the gas to react to chemical changes in the ionized and compressed neutral regions must be much shorter than the time taken for the system to undergo appreciable change as a whole. The width

of the compressed neutral layer depends inversely on the square of the ratio of the velocity of the ionization front to the external sound speed. As the sound speed in the neutral region is comparatively low, the pressure equality approximation holds true at all times and infact improves as the expansion slows. (Dyson & Williams 1997*c*)

Establishing that the shock is strong relies on the upstream Mach number. The Mach number is the ratio of the upstream gas velocity and the sound speed in the neutral gas c_n. If the upstream gas is moving faster than the upstream sound speed the shock is moving into the neutral region supersonically, the Mach number is greater than unity and the shock can be considered strong. Due again to the low external sound speed in the neutral material, during the rapid expansion speed the ratio of the gas velocity to the sound speed is >> 1 and the strong shock assumption is valid. However, in contrast to the pressure equality condition, as the expansion slows, the assumption of a strong shock is gradually poorer until it eventually fails (Dyson & Williams 1997*c*).

Thus, taking both the pressure equality and strong shock assumptions as valid, the velocity of the bubble's expansion can be found by balancing the pressure of the ionized region P_{wi} with the pressure of the compressed neutral region behind the shock front P_{ws} such that

$$P_{wi} = P_{ws} = c_i^2 m_H n_{wi} = v_{ws}^2 m_H n_o \tag{3.17}$$

where $c_i = P_{wi}/\rho^{wi}$ is the isothermal speed of sound in the ionized gas and $\rho^{wi} = n_{wi} m_H$ is the density of the ionized region, n_{wi} and n_o being the ionized and initial neutral number densities, m_H is the mass of an hydrogen atom and v_{ws} is the shock velocity.

The width of the compressed neutral layer depends inversely on the square of the ratio of the velocity of the ionization front to the external sound speed. As the velocity of the IF is greater than the neutral sound speed, their ratio is greater than one and the shell can be considered thin in comparison to the radius of the entire system. This allows the approximation that one radius $R_W(t)$ and one velocity $dR_W(t)/dt$ can be applied to both the shock and the ionization fronts. (Dyson & Williams 1997*c*). Thus, the substitution can be made $v_{ws} = dR_W(t_o)/dt$ and Equation 3.17 can be re-arranged to give

$$\left(\frac{dR_W(t_0)}{dt}\right)^2 = \frac{n_{wi}}{n_o} c_i^2 \tag{3.18}$$

Now re-writing the stellar UV output rate $S_\star(t)$ as a function of the radius of the ionized bubble and using the assumption that $S_\star(t)$ balances the recombination rate within the

expanding region

$$S_{\star}(t_o) = \frac{4}{3}\pi n_i^2 \beta_2 R_W^3(t_o) \tag{3.19}$$

which can be re-arranged for ionized gas density n_{wi}. Returning then to Equation 3.16 for the Strömgren radius and re-arranging it for the neutral number density gives n_o. Substituting n_{wi} and n_o into Equation 3.18 and taking the square of both side leads to the final expression for the expansion velocity of the ionized bubble in terms of the ionized radii

$$\frac{dR_W(t_0)}{dt} = c_i \left[\frac{R_s(t_0)}{R_W(t_0)}\right]^{\frac{3}{4}} \tag{3.20}$$

Having derived the expansion velocity it is now possible to integrate it to arrive at the Spitzer (1978) describing the variation of the ionization front radius $R_W(t_0)$. It is now convenient to introduce two dimensionless variables; $\lambda = R_W(t)/R_s(t)$ and $N = c_i t/R_s$. The time t in this latter expression is the ionizing photon output time-step selected for STARBURST99 at $t = \delta t_{ip} = 0.1$Myrs and c_i is the sound speed in the ionized sphere. Rearranging for $R_W(t) = \lambda R_s$, taking $dN/dt = c_i/R_s$ and substituting these into the left-hand-side of equation 3.20 and integrating leads to

$$\lambda^{\frac{7}{4}} = \frac{4}{7}(N + C) \tag{3.21}$$

where C is the constant of integration. The value of C can be found by considering what value N might take at the time the expansion phase begins t_o and it can easily be shown that suitable values are $C = 4/7$ and $N = 1$ (Dyson & Williams 1997*d*). Substituting for C and N in Equation 3.21 gives the classical expression for the radius of the ionized region

$$R_W(t) = \left(1 + \frac{7}{4}\frac{c_i t}{R_s}\right)^{\frac{4}{7}} R_s \tag{3.22}$$

which is the Spitzer (1978) Equation used by ERR00 to describe the rapid expansion phase of their ionization front radius under the influence of a constant ionizing source flux.

Time-dependent HII Region Solution

For the reasons given, it was necessary to extend the time-independent solution of ERR00 to incorporate the time-dependent ionizing photon flux generated by STARBURST99 and used in the thesis modelling. Taking a Taylor series expansion to the second order of Equation 3.22 gives

$$R_W(t) = R_W(t_0) + \Delta t \frac{dR_W(t_0)}{dt} + \frac{\Delta t^2}{2!} \frac{d^2 R_W(t_0)}{dt^2} \tag{3.23}$$

where t_0 is taken to be T_i=10,000yrs - the first time at which STARBURST99 calculates the ionizing flux. This second order expression now contains the ionization front's acceleration and this is found by differentiating the expansion velocity given in Equation 3.20. After taking out common factors and re-arranging the terms, Equation 3.23 becomes

$$\frac{d^2 R_W(t_0)}{dt^2} = \frac{3c_i}{4} \left[R_s^{-\frac{1}{4}}(t_0) \frac{dR_s(t_0)}{dt} R_W(t_0) - R_W^{-\frac{7}{4}}(t_0) \frac{dR_W(t_0)}{dt} R_s^{\frac{3}{4}}(t_0) \right] \tag{3.24}$$

Equation 3.24 contains the term dR_s/dt which is found by by differentiating Equation 3.16

$$\frac{dR_s(t_0)}{dt} = \left[\frac{3}{4\pi (n_o)^2 \beta_2} \right]^{\frac{1}{3}} \frac{1}{3} S_{*-\frac{2}{3}}(t_o) \frac{dS_*(t_o)}{dt} \tag{3.25}$$

where dS_*/dt is determined by fitting a cubic spline to the STARBURST99 ionizing photon output discussed in §3.5.2.

Finally,substituting Equations 3.15, 3.20 and 3.25 into Equation 3.24 finishes the derivation of the terms in Equation 3.23. Thus the new expression for the variation of the radius of the ionization front, under the influence of a time-dependent ionizing source flux, can now be written in full as

$$R_W(t) = R_W(t_0) + c_i \Delta t \left(\frac{R_s(t_0)}{R_W(t_0)} \right)^{\frac{3}{4}} + \frac{3c_i \Delta t^2}{8} \left[\frac{R_W^{-\frac{3}{4}}(t_0)}{R_s^{\frac{1}{4}}(t_0)} \frac{dR_s(t_0)}{dt} - c_i \frac{R_s^{\frac{3}{2}}(t_0)}{R_W^{\frac{5}{2}}(t_0)} \right] \tag{3.26}$$

To ensure that this new time dependent solution essentially reproduces the standard Spitzer solution of Equation 3.22 (Spitzer 1978), the radial distribution given in Equation 3.26 above was calculated using both the first order terms of the Taylor Expansion and then using both the first and second order Talyor series terms. These distributions were then divided by the Spitzer solution and those ratios are plotted in Figure 3.6. Looking at this figure it can be seen then both the first order and the first and second order distributions match to within 0.1 of the Spitzer solution at all times.

The derivation of $R_W(t_0)$ and $dR_W(t_0)/dt$ have been taken from Dyson & Williams (1997*c*) where they have been simply and elegantly derived.

3.6.3 Momentum Conservation Phase

The rapid expansion phase ends at t $\approx 10^7$yrs when most of the stars have moved off the main sequence and Lyman continuum flux has dropped to the point where total

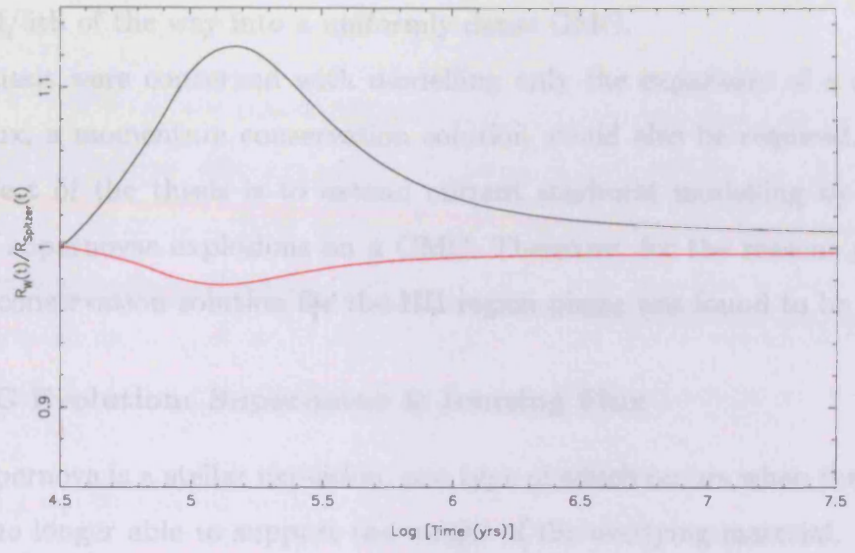

Figure 3.6: Comparison of the new time dependent evolution developed in Equation 3.26 to the standard Spitzer solution of Equation 3.22. The black line represents the time dependent solution using the first order terms of the Taylor expansion only, divided by the Spitzer solution. The red line is the time dependent solution using both the first and second order terms of the Taylor expansion, again divided by the standard Spitzer solution.

recombination can occur within the ionized volume (ERR00). Thereafter the bubble and its narrow neutral shell continue to expand under the momentum the system acquired in the rapid expansion phase, until it reaches pressure equilibrium with the external gas at around 10^8yrs (Dyson & Williams 1997*c*).

Practically this meant that ERR00 continued the rapid expansion of the ionization front into the GMC until the mass of the swept-up material compressed into the thin neutral shell was half the original M_{GMC}. This led to the ERR00 rapid expansion phase ending and the momentum conservation solution beginning when the ionizing front had penetrated 4/5th of the way into a uniformly dense GMC.

If this thesis were concerned with modelling only the expansion of a sphere ionized by stellar flux, a momentum conservation solution would also be required. However the primary object of the thesis is to extend current starburst modelling by incorporating the effect of supernovae explosions on a GMC. Therefore, for the reasons given below, a momentum conservation solution for the HII region phase was found to be unnecessary.

Early GMC Evolution: Supernovae & Ionizing Flux

Briefly, a supernova is a stellar explosion, one type of which occurs when the core pressure of a star is no longer able to support the weight of the overlying material. The explosion expels much or all of a star's material at a high velocity (up to 1/10th the speed of light), driving a shock wave into the surrounding interstellar medium. This shock wave sweeps up a shell of gas and dust on the surface of the expanding superbubble, called a supernova remnant.

The first supernova to explode in a cluster population is a function of mass and with an upper mass limit in the IMF of $M_{max} = 120M_{\odot}$, STARBURST99 shows that this occurs at t = 3.71Myrs in all models. In turn, due to the high velocity of the expanding superbubble, only a short time later, the HII region ionization front is overtaken by the superbubble, which then becomes the driving force behind the system's evolution.

The HII region solution in this chapter has therefore been developed primarily to describe the evolution of the GMC at early times, before the first supernova in the population explodes and thereafter until the superbubble over takes the ionization front. In nearly all cases on the model grid, the HII region IF is overtaken well before the Lyman continuum flux had dropped sufficiently for the rapid expansion phase to end. A momentum conserving solution for the radius of the HII region in this instance is not needed as it is

M_{GMC} ($M_\odot$)	η	$M_\star$ ($M_\odot$)	Break-up Time at R_v (Myrs)
10^6	0.01	1 x 10^4	7.3
10^6	0.025	2.5 x 10^4	8.1
10^6	0.05	5 x 10^5	8.4
10^6	0.1	1 x 10^5	9.5
10^7	0.01	1 x 10^5	9.2
10^7	0.025	2.5 x 10^5	10.2

Table 3.5: HII Region Solution Models. M_{GMC} x $\eta = M_\star$. Each of these models takes the HII region solution at all t because the supernova solution for these parameters generates a shell of insufficient velocity to exit the ionized sphere with the shell intact. However, when the HII region solution is then employed, the ionization front goes on to itself break-up when the IF velocity drops below the sound speed in the neutral region external. This point is indicated by R_v.

superseded by the supernova solution.

Break-Up

There are six instances on the model grid however where the superbubble is unable to catch up and overtake the ionization front. This occurs for parameter combinations of very low star formation efficiency η and small M_{GMC}. In these instances, the superbubble velocity drops below the sound speed in the HII region, c_i, whilst the superbubble is still trapped within the ionization front. This lack of momentum causes the shell on the surface of the superbubble to break-up and disintegrate due to random motions in the external, ionized gas. At that point the modelling is considered ended as it would be unphysical to continue.

When a superbubble breaks up whilst trapped inside the HII region, it is fair to assume that the HII region solution then describes the systems' evolution for all t and the supernova solution is not invoked.

Table 3.5 shows the model systems which revert to the HII region solution for all t. However, for each of these models the expansion velocity of the HII region IF then goes

on to itself drop below the sound speed in the external neutral region, c_n, whereupon the IF also breaks-up. This is a direct result of using a time-dependent ionizing flux for the HII region evolution. As seen in Figure 3.5 as the stellar population dies, the magnitude of the ionizing photon flux plummets, causing the HII region growth to slow.

Table 3.5 also shows the time the HII regions break-up and each is t $\approx 10^7$yrs, which is approximately the time the Lyman continuum flux has dropped sufficiently for the rapid expansion phase to end. This assumption negates the need for a momentum conserving solution. It may be the case that at t $\approx 10^7$yrs the IF is actually expanding due to the momentum acquired in the expansion phase. In that instance its velocity might drop below external sound speed at a later time than the models presented. However, no model which takes the HII region solution at all t was found to have reached 4/5th of the way into the GMC at the point of break-up. Finally, the HII region solution has been developed primarily to account for very early times before the first supernova explodes and overtakes the IF.

Summary of Momentum Conservation Phase

In summary, the HII region solution is either superseded by the model's supernova solution, or the ionization front is assumed to break-up whilst still firmly embedded within the neutral GMC. No modelling of the HII region momentum conservation phase under these assumptions is required.

The supernovae solution is returned to in depth in the next chapter where that element of the modelling is developed. The derivation of the expressions needed to define the radial evolution of the HII region ionization front under the influence of a time-dependent ionizing source flux is now concluded. Each of these expression were programmed into the bespoke computer code GEM.

The next sections returns to the method of ERR00 to derive equations for the outer radii of the GMC and ambient region along with expressions for the evolution of the mass density of ions and neutral material.

3.6.4 Boundaries of the System

The outer radius of the GMC $R2_W$ represents the boundary between the dense neutral region and the ambient interstellar gas within which the GMC is embedded. The outer radius of the system $R2_{SN}$ is the edge of the modelled ambient region.

The Outer Radius of the GMC $R2_W$

The derivation of $R2_W$ relies on the assumption that the mass of both the dust and the gas remaining in the GMC once the stars have formed, can be approximated by the mass of gas only (ERR00). The outer boundary of the GMC $R2_W$ can then be found from

$$M_{GMC} - M_\star = M_{gas} + M_{dust} = \frac{4\pi}{3} R2_W^3 n_{av} m_H \tag{3.27}$$

where $M_\star$ is the mass of stars formed, M_{gas} is the gas mass and M_{dust} is the dust mass, m_H is the mass of the hydrogen atom and n_{av} is the average H_2 density in the cloud. This thesis work has adopted $n_{av} = 300\text{cm}^{-3}$ as Gusten (1989) found that this was within the range of the GMC densities in the centre of the Milky Way galaxy and the value has since been used successfully by others (e.g., Efstathiou *et al.* 2000; Farrah *et al.* 2002). M_{GMC} can be related to the star formation efficiency η approximately as $M_{GMC} = M_\star/\eta$. Equation 3.27 can now be re-written and resolved for the outer boundary of the GMC $R2_W$

$$R2_W = \left[\left(\frac{M_\star}{\eta} - M_\star\right)\left(\frac{3}{4\pi n_{av}} m_H\right)\right]^{\frac{1}{3}} \tag{3.28}$$

The Outer Radius of the System $R2_{SN}$

When the star formation efficiency and M_{GMC} of a model are high, the superbubbles created using the supernovae solution often have sufficient velocity to exit the GMC at $R2_W$ very early in their evolution so it was necessary to extend the modelling region of ERR00 beyond the confines of the GMC and into interstellar space.

In order to compare the emergent SEDs generated by the HII region solution to those from the supernova solution, this volume of interstellar space was also included in the dust density distribution of the HII region models. This is despite the fact that no model which takes the HII region solution at all t reaches the outer boundary of the GMC, but does provide a comparable column length of dust for all models.

It was decided to assign a value to $R2_{SN}$ as the location of each superbubble at 80Myrs, which was pre-calculated and set as the outer boundary of its system such that $4\pi/3[R2_{SN}^3 - R2_W^3]$ is the volume of the ambient external region. The calculation of the radius $R2_{SN}$ is returned to in greater depth in the next chapter where the supernova element is fully discussed.

The derivation of all the radial elements equation for the HII region evolution model is now complete.

3.6.5 Gas Mass Density

The next task towards obtaining the dust density distribution is to use ERR00 to derive the evolution of the mass density of ionized and neutral material under the influence of the ionization front.

Mass Density of Ions

The expression for the mass density of ions ρ_i(t) can be found by equating Equations 3.18 and 3.20 which both contain the term $dR_W(t)/dt$

$$\left(\frac{dR_W(t)}{dt}\right)^2 = c_i^2\frac{n_i}{n_o} = c_i^2\left[\frac{R_s(t)}{R_W(t)}\right]^{\frac{3}{2}} \tag{3.29}$$

taking $n_{Wi} = \rho^{Wi} m_H$ where ρ^{wi} is the mass density of ions internal to the shock front and $n_o = \rho^{n_o} m_H$ where ρ^{n_o} is the initial mass density of neutral material. Hence

$$\rho^{Wi}(t) = \rho^{n_o}\left[\frac{R_W(t)}{R_s(t)}\right]^{-\frac{3}{2}} \tag{3.30}$$

which is Equation (5) of ERR00, used in this thesis to describe the evolution of the ionized mass density.

Mass Density of Neutral Material

ERR00 were unable to trace the density enhancement in the neutral compressed shell analytically, so it was assumed that the neutral gas accumulated in the shock was spread uniformly over the entire neutral cloud. The uniform density of neutral material ρ^n(t) then follows from mass conservation. If the entire mass of the cloud at t = 0, M(0) can be written as

$$M(0) = \frac{4\pi}{3}R2_W^3\rho^{n_o} \tag{3.31}$$

where ρ^{n_o} is the initial mass density of the neutral material, assumed to be equal to the mass density of the ions, mass conservation requires

$$M(t) = \frac{4\pi}{3}R_W^3(t)\rho^{Wi}(t) + \frac{4\pi}{3}\left[R2_W^3 - R_W^3(t)\right]\rho^n(t) \tag{3.32}$$

then substituting for the mass density of ions ρ^{Wi}(t) from Equation 3.30 and equating the result to Equation 3.31 gives after re-arrangement the following expression for

$$\rho^{n}(t) = \rho^{n_o}\left[\frac{1-\left(\frac{R_W(t)}{R2_W}\right)^{\frac{3}{2}}\left(\frac{R_s(t)}{R2_W}\right)^{\frac{3}{2}}}{1-\left(\frac{R_W(t)}{R2_W}\right)^{3}}\right] \tag{3.33}$$

which is Equation (6) of ERR00, used in this thesis to describe the evolution of the neutral mass density.

3.6.6 Optical Depth

Having found the mass density of neutral and ionized material, the next step to obtaining the optical depth is to find the variation in the visual extinction to the centre of the cloud. The solution is developed by considering the environment and hence density of dust in the two regions of the system; internal to the GMC and in the external ambient space.

Visual Extinction through GMC at t = 0

$\tau_{v_{ow}}$ is defined as the visual extinction through the GMC to its centre at t=0 and can be written

$$\tau_{v_{ow}} = n_d \sigma_{gr} R2_W \tag{3.34}$$

where n_d is the number density of dust, σ_{gr} is the cross-section of a generic dust grain and $R2_W$ is the outer radius of the GMC. n_d can be defined in terms of the mass m_{gr} and density ρ_{gr} of the generic grains such that $n_d = \rho_{gr}/m_{gr}$. Assuming that the number density of grains scales in the same was as ρ^{n_o}, the density of grains $\rho_{gr} = dg_r \rho^{n_o}$ where the dust-to-gas ratio $dg_r = \rho_{dust}/\rho_{gas}$ (Mathis 1990). n_d then becomes becomes

$$n_d = \frac{dg_r \rho^{n_o}}{m_{gr}}. \tag{3.35}$$

Using $\rho^{n_o} = 2n_{av}m_H$, where $n_{av} = 300\text{cm}^3$ and is the average H_2 number density. Substituting n_d into Equation 3.34 gives

$$\tau_{v_{ow}} = \left[\sigma_{gr}\frac{dg_r}{m_{gr}}\right] m_H 2n_{av} R2_W \tag{3.36}$$

To progress further the ratio of the total-to-selective extinction, R_v and the wavelength dependence of the extinction $A(\lambda)$ must be considered. R_v depends strongly on the environment along the line of sight and Cardelli *et al.* (1989) used UV and optical/NIR

observations of stars to study galactic extinction laws over a broad range of wavelengths and found a value of $R_v \approx 5$ was appropriate for a dense environment such as that in a GMC.

As the environment so dramatically affects the wavelength dependence of the extinction, Mathis (1990) tabulated values for $A(\lambda)$ scaled to a reference wavelength $A(J)$ for $R_v \approx 5$. J $\approx 1.25\mu$m and was chosen for the reference value as the extinction law is virtually independent of line of sight for wavelengths $\lambda \geq 0.9\mu$m (Mathis 1990). Using $\lambda = 0.55\mu$m - extinction at visual wavelengths - in an $R_v = 5$ environment, the extinction tabulated in the (Mathis 1990) paper is

$$\left|\frac{A(V)}{A(J)}\right|_{R_v=5} = 3.06 \tag{3.37}$$

The legend to this table in Mathis (1990) suggests an estimate of A(V)/N(H) - the visual extinction per hydrogen atom - can be found by multiplying Equation 3.37 by 1.51 x 10^{-22}cm^2(H atom)$^{-1}$; the extinction cross-section per H atom for galactic abundances as N(H) is the number of hydrogen atoms per cm^3. This estimate was arrived at using the work of Bohlin *et al.* (1978) which in turn used measurements from the Copernicus satellite in the spectral region near Lyman-α to obtain column densities of interstellar HI toward 100 stars. Using the Lyman-α equivalent widths they were able to determine a visual extinction per H atom of A(V)/N(H) = 5.3 x 10^{-22} mag cm^2 which leads to the multiplier given in the Mathis (1990) table. $N(H) = \rho^{n_o} R2_W = 2n_{av} m_H \, R2_W$, so replacing these values into Equation 3.37 leads to the visual extinction through the cloud at t=0

$$A(V) = 3.06 \cdot 1.51\text{x}10^{-22} \cdot 2n_{av} m_H R2_W \tag{3.38}$$

It is now possible to use the classic relationship

$$\tau_v = \frac{log_e 10}{2.5} A(V) = 0.92 A(V) \tag{3.39}$$

to change from units of magnitude and to scale Equation 3.38 to the optical depth. By substituting Equation 3.38 into 3.39 for A(V) and then equating the result at t=0 to Equation 3.36, $\tau_{v_{ow}}$, the expression for the visual extinction through the GMC at t = 0 becomes

$$\tau_{v_{ow}} = 4.25\text{x}10^{-22} m_H 2n_{av} R2_W \tag{3.40}$$

Visual Extinction through Ambient Region at t = 0

Each GMC is embedded in a considerable volume of interstellar space that has been included to accommodate the radial solutions of the most powerful supernovae. Therefore a similar procedure must now be carried out to find the optical depth through the ambient region at t=0, $\tau_{v_{osn}}$. Beginning then with the equivalent of Equation 3.36 but for the external ISM

$$\tau_{v_{osn}} = \sigma_{gr}\frac{dg_r}{m_{gr}}m_H 2n_\alpha[R2_{SN} - R2_W] \tag{3.41}$$

Now considering R_v, the best description of the external gas is a diffuse environment and so in contrast to the GMC, the wavelength dependence of the extinction should be evaluated for $R_v = 3.1$ rather than 5 (Mathis 1990). The $A(\lambda)/A(J$ values were also tabulated in Mathis (1990) for $R_v = 3.1$ such that

$$\left|\frac{A(V)}{A(J)}\right|_{R_v=3.1} = 3.55 \tag{3.42}$$

and so the visual extinction $\tau_{v_{osn}}$ from the outer edge of the ambient region $R2_{SN}$ to the boundary of the GMC at $R2_W$ becomes

$$\tau_{v_{osn}} = 4.93\text{x}10^{-22}m_H n_\alpha[R2_{SN} - R2_W] \tag{3.43}$$

where $n_\alpha = 1\text{cm}^{-3}$ is the adopted H_2 number density external to the cloud (Dyson & Williams 1997*b*; Dopita *et al.* 2005).

Evolution of the Visual Extinction

Having now obtained equations to describe the visual extinction through the system at t = 0, the evolution of the extinction under the influence of the ionization front can be derived.

To help compose this expression Figure 3.7 shows in plot (a) a typical system at t $\approx$ 0, with the dusty GMC in the volume $4\pi/3[\text{R2}_W^3\text{-R}_1^3(\text{t})]$ and the ambient region in the volume $4\pi/3[\text{R2}_{SN}^3\text{-R2}_W^3]$. Plot (b) illustrates sometime later, when the ionization front has expanded some way into the GMC, heating the gas and evaporating some of the associated dust. This results in the small magnitude of extinction coming from the ionized sphere of volume $4\pi/3[\text{R}_W^3\text{-R2}_1^3]$ interior to the neutral region.

Referring to Figure 3.7, plot (b) for the column lengths, the optical depth $\tau_{v_w}(\text{t})$ through the GMC once rapid expansion has begun is

$$\tau_{v_w}(t) = Fd^{Wi}\rho^{Wi}(t)\left(R_W(t) - R_1(t)\right) + Fd^n\rho^n(t)\left(R2_W - R_W(t)\right) \tag{3.44}$$

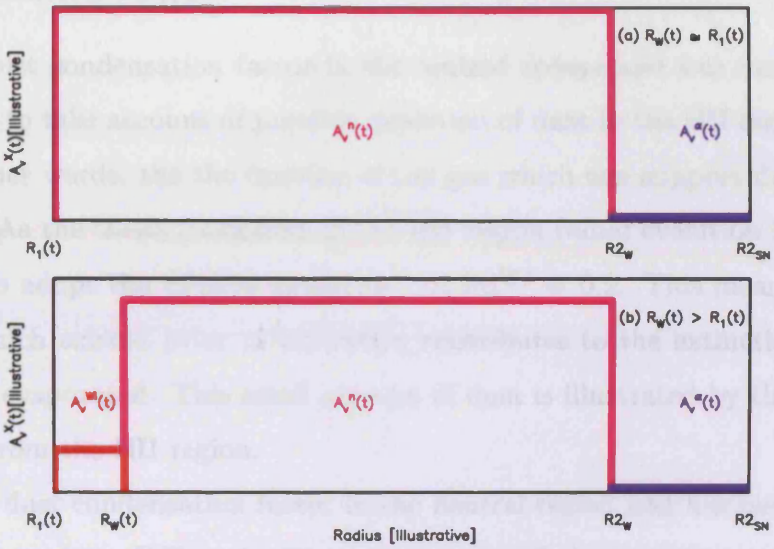

Figure 3.7: Plot (a) shows the system a t ≈ 0 when the stars have just switched on. The pink $A_v^n(t)$ illustrates the magnitude of the extinction from the neutral region whilst the purple $A_v^\alpha(t)$ illustrates that from the external ambient region. Plot (b) shows the HII region some time later, prior to the first supernova explosion, when the ionization front is expanding out through the GMC, ionizing the gas and evaporating the dust. The resulting small magnitude of extinction from the HII region is illustrated in red and indicated by $A_v^W(t)$.

where $R_1(t)$, $R_W(t)$ and $R2_W$ are the dust sublimation, ionization front and GMC outer radii respectively. Fd^{Wi} and Fd^n are the HII region and neutral region dust condensation factors respectively. The first term on the right-hand side of equation 3.44 represents the column density of dust contributing to the extinction from inside the HII region and the second term gives the column density of neutral dust external to the ionization front in the GMC. When multiplied out, this is the equivalent of Equation 8 from ERR00.

Dust Condensation Factors

Fd^{Wi} is the dust condensation factor in the ionized sphere and was incorporated in the ERR00 model to take account of possible depletion of dust in the HII region as a result of shocks - in other words, the the fraction of the gas which can support dust, thanks to its temperature. As the thesis modelling of the HII region radial evolution follows ERR00 it makes sense to adopt the ERR00 assessment of $Fd^{Wi} = 0.2$. This means that only 20% of the dust which existed prior to ionization contributes to the extinction post shock as 80% has been evaporated. This small amount of dust is illustrated by the low magnitude of extinction from the HII region.

Fd^n is the dust condensation factor in the neutral region and has been set by ERR00 and the thesis work to $Fd^n = 1$. The temperature of the neutral region is $T_n \simeq 25K$, corresponding to a sound speed of $c_n \simeq 0.45 kms^{-1}$ (Dyson & Williams 1997*c*). As the dust condensation temperature $T_{cond} = 1600K$, $Fd^n = 1$ ensures that all the cool neutral material external to the ionization front contributes to the extinction at all times.

System Optical Depth

Scaling the evolved extinction of Equation 3.44 to the GMC extinction at $t \approx 0$ and setting $k_w = 4.25 \times 10^{-22}$ from Equation 3.40 gives the optical depth distribution through the GMC.

Taking the total optical depth through the system $\tau_v(t)$ to include $\tau_{vsn}(t)$ from the external ambient region, $\tau_v(t) = \tau_{v_w}(t) + \tau_{vsn}(t)$. Further setting $k_{sn} = 4.93 \times 10^{-22}$ from Equation 3.43 leads to

$$\tau_v(t) = \frac{\tau_{vow}}{k_w 2 n_{av} m_H R2_W} \left[Fd^{Wi} \rho^{Wi}(t) \left[R_W(t) - R_1(t) \right] + \rho^n(t) \left[R2_W - R_W(t) \right] \right] + \frac{\tau_{voSN}}{k_{sn} n_\alpha m_H [R2_{SN} - R2_W]} \left[Fd^\alpha \rho^\alpha [R2_{SN} - R2_W] \right] \quad (3.45)$$

where $\mathrm{Fd}^{\alpha} = 1$ is the dust condensation factor in the ambient region and $\rho^{\alpha}(\mathrm{t}) = 1\mathrm{cm}^{-3}$ is its density (Dyson & Williams 1997*b*; Dopita *et al.* 2005).

3.6.7 Inputs to the Radiative Transfer Code

Finally, it is possible to define the HII region dust density distribution in a form suitable for input to the radiative transfer code. DaRT needs not only the total optical depth along a line of sight at a particular time t but also the precise location at which the density changes. These density breaks occur at the ionization front radius, between the ionized sphere and the neutral region and also at the outer boundary of the GMC, separating the neutral and ambient regions. The location of the density breaks are found from the motion equations derived in §3.6.2 and are expressed as a function of the outer radius of the system $\mathrm{R2}_{SN}$. Thus for the HII region models

$$\mathrm{R}_{B1} = \mathrm{R}_{W}(\mathrm{t})/\mathrm{R2}_{SN} \qquad \mathrm{R}_{B2} = \mathrm{R2}_{W}(\mathrm{t})/\mathrm{R2}_{SN}$$

The optical depth expressions and Figure 3.7 can be used to derive the ratio of the densities in these regions, which are expressed for DaRT as a function of the region closest to the source. Thus, an illustrative example of the DaRT density breaks required at a time when the ionization front is still trapped within the neutral GMC are written

$$\rho_{F1} = \rho^{n}(t)/0.2\rho^{Wi}(t) \qquad \rho_{F2} = \rho^{\alpha}/0.2\rho^{Wi}(t)$$

where ρ^{α} is the ambient density external to the neutral cloud and $\mathrm{Fd}^{wi} = 0.2$.

The four DaRT inputs just described and the total extinction along a line of sight are the quantities generated by the computer program *GEM* and define the dust density distribution of the system at time t.

3.7 HII Region Optical Depth Distribution

Whilst DaRT requires the dust density distribution as a snapshot in time, it is possible to generate the extinction at intervals of $\Delta \mathrm{t}_{ip} = 0.1$Myrs to produce a distribution. Figure

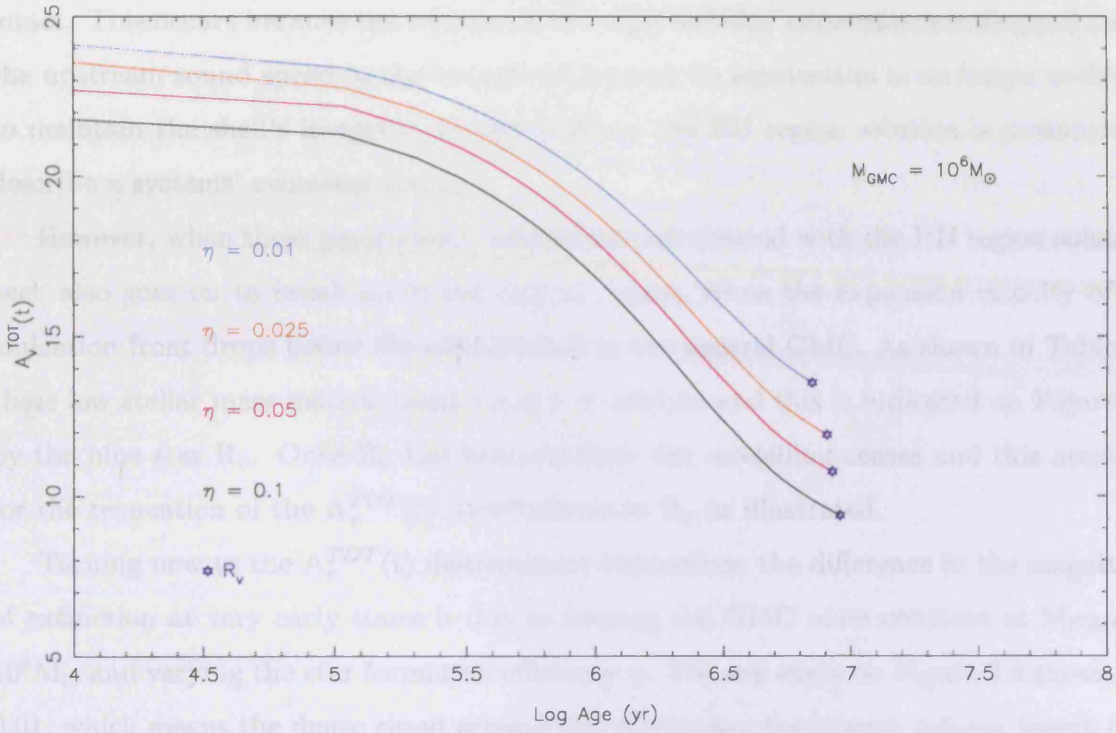

Figure 3.8: $A_v^{TOT}(t)$ distribution for the M_{GMC} = 1e6$M_\odot$ models which take the HII region solution at all t. The turquoise, orange, pink and black lines indicate η = 0.01, 0.025, 0.025 & 0.1 respectively and the blue star indicates R_v which is the point at which the IF fronts break-up in the neutral region.

3.8 shows the extinction $A_v^{TOT}(t)$ for $M_{GMC} = 10^6 M_\odot$, $\eta = 0.01$, 0.025, 0.05 & 0.1. Multiplying these parameter combinations to find the approximate central stellar cluster mass leads to the HII region solution being valid for $M_{GMC} = 10^6 M_\odot$ over the range $10^4 M_\odot < M_\star < 10^5 M_\odot$.

These low stellar mass models revert to the HII region solution at all t because when the supernova solution is applied to these parameter combinations, the superbubbles generated have insufficient velocity to exit the HII region ionization fronts with their supershells' intact. This occurs because the velocity of the superbubbles' expansion has dropped below the upstream sound speed in the ionized sphere and its momentum is no longer sufficient to maintain the shell's integrity. In this instance the HII region solution is presumed to describe a systems' evolution for all t.

However, when these parameter combinations are treated with the HII region solution, each also goes on to break up in the neutral region, when the expansion velocity of the ionization front drops below the sound speed in the neutral GMC. As shown in Table 3.5 these low stellar mass models break up at $t \leq 10$Myrs and this is indicated on Figure 3.8 by the blue star R_v. Once R_v has been reached, the modelling ceases and this accounts for the truncation of the $A_v^{TOT}(t)$ distributions at R_v as illustrated.

Turning now to the $A_v^{TOT}(t)$ distributions themselves, the difference in the magnitude of extinction at very early times is due to keeping the GMC mass constant at $M_{GMC} = 10^6 M_\odot$ and varying the star formation efficiency η. The top curve on Figure 3.8 shows $\eta = 0.01$, which means the dense cloud around this cluster has the longest column length dust in the neutral region along a line of sight. This is because the neutral region is distributed uniformly around the cluster at $t = 0$ and with less of the total system mass trapped in the central cluster, compared to the higher ηs, a greater magnitude extinction is seen through the $\eta = 0.01$ cloud at early times.

After a short period has elapsed, the extinction of all the η models presented in Figure 3.8 appears to vary in what is essentially a volume dilution solution. This is in line with the form of the radial equation, which is in turn driven by the time-dependent STARBURST99 ionizing stellar photon output. This behaviour continues until R_v is reached, which is located closest to the source and occurs earliest for $\eta = 0.01$. This is again directly related to the low star formation efficiency generating an ionization front with the smallest expansion velocity of the η's shown.

Finally, it is possible to use the parameter search to estimate a simple limit on the

maximum mass of stars a system must contain for the HII region solution to be invoked for all t. Using the approximation $M_\star = M_{GMC}.\eta$ it was found that any models on the parameter grid having $M_\star \leq 2.5 \times 10^5 M_\odot$ incur the HII region solution.

Having obtained the dust density distribution through the system for each time t that an emergent HII region SED is required, the value of the total extinction and the density breaks and dust ratios for time t are given to DaRT as its starting conditions. The system is then irradiated with the STARBURST99 stellar cluster SED, also for time t. The radiative transfer of flux is calculated and having achieved convergence, DaRT generates the emergent HII region SEDs.

3.8 HII Region Spectral Energy Distributions

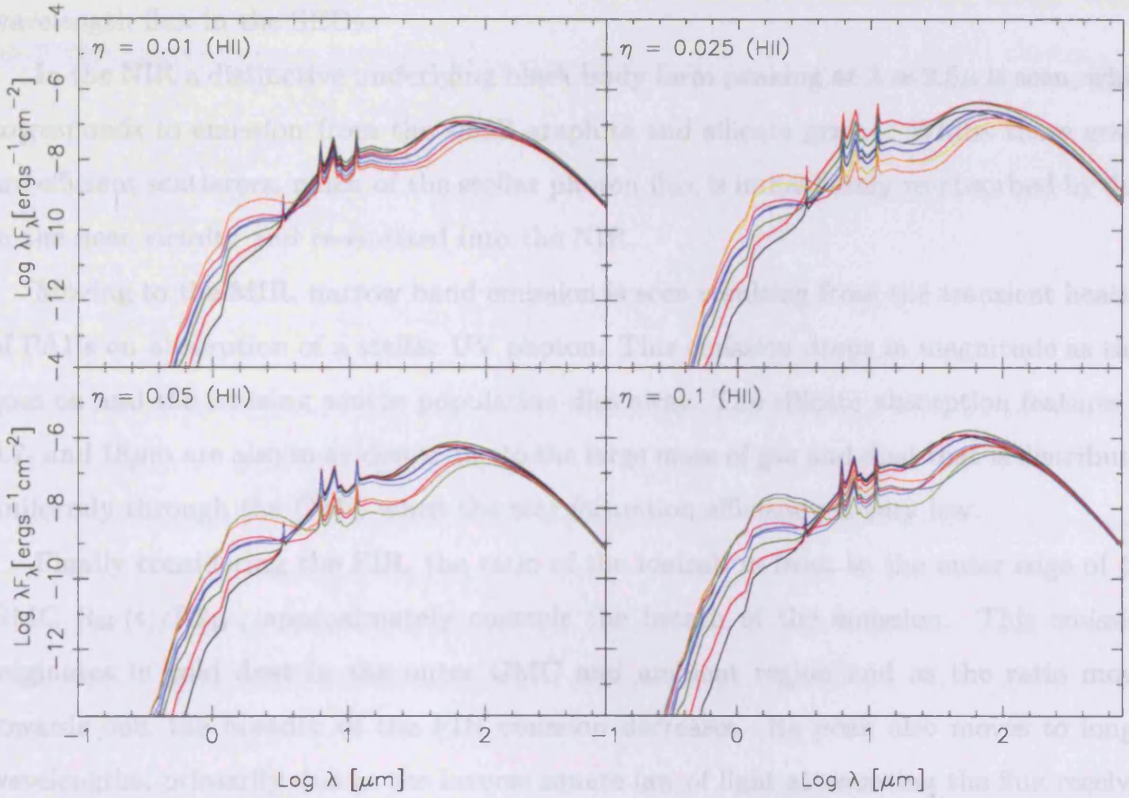

Figure 3.9: Spectral Energy Distributions for M_{GMC} = 1e6$M_\odot$, η = 0.01, 0.025, 0.025 & 0.1 which take the HII region solution at all t. The black, red, green, dark blue, cyan, pink, yellow, orange and light green lines represent t = 1, 2, 3, 4, 5, 6, 7, 8 & 9Myrs respectively.

Figure 3.9 presents the HII region solution SED's for $M_{GMC} = 10^6 M_\odot$, $\eta = 0.01$, 0.025, 0.025 & 0.1. The extinction distribution for these models was illustrated in Figure 3.8. Each of the SED sets presented in Figure 3.9 is generated at 1Myr intervals until R_v is reached and each shows similar attributes.

Beginning with the UV & Optical region, there is little or no flux at these wavelengths at very early times in any of the SEDs. This is a result of the very small graphite and silicate grains and the PAH population in the dust model. The increased absorption efficiency of the PAHs over the FUV rise and that of the very small graphite and silicate grains across the 2175$\AA$ feature, allows this population to absorb much of the direct O and B star radiation out of the line of sight and re-emit it at longer wavelengths. Further, the scattering efficiency of the small graphite and silicate grains is of the same order of magnitude as their absorption efficiency around $\lambda \approx 1$, further depleting the short wavelength flux in the SEDs.

In the NIR a distinctive underlying black body form peaking at $\lambda \approx 2.5\mu$ is seen, which corresponds to emission from the small graphite and silicate grains. Whilst these grains are efficient scatterers, much of the stellar photon flux is immediately re-absorbed by dust in the near vicinity and re-emitted into the NIR.

Moving to the MIR, narrow band emission is seen resulting from the transient heating of PAHs on absorption of a stellar UV photon. This emission drops in magnitude as time goes on and the ionizing source population dies away. The silicate absorption features at 9.7- and 18μm are also in evidence due to the large mass of gas and dust that is distributed uniformly through the GMC when the star formation efficiency is very low.

Finally considering the FIR, the ratio of the ionization front to the outer edge of the GMC $R_W(t)/R2_W$, approximately controls the breath of the emission. This emission originates in cold dust in the outer GMC and ambient region and as the ratio moves towards one, the breadth of the FIR emission decreases. Its peak also moves to longer wavelengths, primarily due to the inverse square law of light attenuating the flux received as the emitting region moves further from the source.

Summary of HII Region SEDs

Some suggestions can now be made as to the spectral form which might be observed in a low stellar mass GMC which has evolved under the influence of a time-dependent ionizing photon flux.

Parameter	Value	Description
n_o	2 x 10^3 cm^{-3}	Core H_2 number density
n_{av}	300cm^{-3}	Average H_2 number density
c_i	10kms^{-1}	Ionized Region Sound Speed
c_n	0.45kms^{-1}	Neutral Region Sound Speed
c_α	1kms^{-1}	Ambient Region Sound Speed

Table 3.6: Fixed Parameters for HII region solution required as inputs for the GEM computer code.

Perhaps the most distinctive characteristic would be the lack of flux at UV and optical wavelengths. Strongly spiking PAH features and silicate absorption at 9.7- and 18μm might be seen in the MIR. In the FIR and sub-mm, cool dust emission, which reduces in breadth with time, is seen at all times. Finally, the mass of the central cluster could potentially have an upper limit of $M_\star = 10^5 M_\odot$.

Table 3.6 lists the values taken by the fixed parameters of the HII region solution, required for the GEM computer code.

3.9 Supernovae in ERR00

Finally, an important question must be asked: why did ERR00 not include the effects of supernovae in their HII region modelling?

ERR00 suggested that after t $\approx 10^7$years, the GMC was likely to consist of a narrow neutral shell still expanding due to the momentum it acquired in the HII region phase. Over the next 3-4 x 10^7 years, ERR00 assumed that supernovae explosions were likely to be the main factor that will influence the evolution of the GMC, eventually leading to its dispersal and return of most of the gas to the HI phase (ERR00).

The momentum conserving phase has been studied extensively both analytically and numerically, but primarily for the 'standard' density case of 1 cm^{-3} (Tenorio-Tagle & Bodenheimer (1988) and references therein). Of these studies ERR00 suggested that the most relevant for their purposes was that of McCray & Kafatos (1987) who presented an analytical solution for the case of frequent multi-supernova explosions in an OB association.

In this instance, the sequence of discrete supernova explosions can be replaced by a

scaled-up stellar wind solution. Using the following equation from McCray & Kafatos (1987), ERR00 were able to estimate the radius of the swept-up shell before the hot interior begins to cool at time t_c and the momentum conservation phase begins

$$t_7 \leq 5\left(\frac{N_{SN}E_{51}}{n_o}\right)^{\frac{1}{2}} \tag{3.46}$$

where t_7 is $t/10^7$, N_{SN} is the number of supernova produced by the association with a mass greater than $7M_\odot$, E_{51} is the energy of one supernova in units of 10^{51} ergs and n_o is the uniform atomic density of the system.

For a Salpeter IMF, the GISSEL evolutionary synthesis code (Bruzual & Charlot 1993) used by ERR00 predicted 8.92 x 10^{-3} supernova explosions per $1M_\odot$ so the ERR00 GMC parameters of $M_{GMC} = 10^7 M_\odot$ and $\eta = 0.25$ implied that $N_\star = 2.23 \times 10^4$. In turn this suggested that the supernova shell remains trapped inside the shell formed by the ionization front at t = 10^7 years, if the density of the medium within which the supernovae are exploding is higher than $10^3 cm^{-3}$ - ERR00 used a core density of $n_{H_2} = 2 \times 10^3$ cm^{-3}, which was also adopted in this thesis. Finally, ERR00 also predicted that the velocity of the supernova shell would drop well below the expansion velocity of the neutral shell by 10^7 yr.

In summary, using McCray & Kafatos (1987), ERR00 were able to assume that any supernova shells formed remained trapped inside the ionization front, which continued to expand until t = 4 x 10^7 yrs, whereupon it breaks-up. Thus, the HII region ionization front was the driving force behind the systems' evolution for all t and modelling the impact of supernova was unnecessary.

Impact of a Time-Dependent Photon Flux

The assumption that the supernova shell remains trapped with the ionization front until it breaks-up at t = 4 x 10^7yrs is valid in ERR00 due to the use of a time-independent ionizing source flux. As mentioned in §3.6, ERR00 chose the ionizing flux emitted by their cluster at t = 3.3Myrs for the constant value. At this time most of the O and B stars in the population are still generating significant amounts of ionizing photons and the magnitude of the flux is very high. It is the use by ERR00 of this high value of photon flux at all times that allows them to make the assumption that the supernova shell remains trapped inside the ionization front at all times and does not require modelling.

This thesis work has updated the ERR00 model by using a potentially more realistic

time-dependent ionizing flux to drive the HII region evolution. The flux function drops in magnitude as the ionizing source population dies away and the expansion of the thesis ionization front slows more rapidly than that of ERR00. In this instance, using Equation 3.46 from McCray & Kafatos (1987) predicts that the supernova shell will overtake the ionization front fairly early on to become the driving force behind the system's gas density evolution. Thus, using a time-dependent ionizing source flux necessitates the inclusion of supernova in the thesis modelling and this is discussed in the next chapter.

Finally it is appropriate to mention that the model parameters of ERR00 at M_{GMC} = $10^7 M_\odot$ and η = 0.25 invoke the supernova solution in the thesis modelling. It is therefore more convenient to compare and contrast the optical depth distributions and the emergent SEDs generated by this work and by ERR00 after the supernova solution has been developed and this is conducted in Chapter 6 §6.0.5.

Chapter 4

Supernovae Model

Using a time-dependent ionizing flux for the HII region solution means that the thesis must now diverge entirely from ERR00 and consider the impact of supernovae on a GMC. It is perhaps convenient to begin this chapter by briefly considering some of the main types of supernova and consequent GMC evolution.

4.0.1 Supernovae Type Ia, Ib and Type II

Type Ib and Type II supernovae are thought to be generated by the more massive stellar population, whilst Type Ia supernovae originate in the intermediate to low mass stars.

Considering Type II supernovae first, these are generated by stars in the mass range 8 - 120$M_{\odot}$ which have lived out their main sequence life-times as O and B stars. In the stellar core, hydrogen is fused into helium and the energy released generates an outward pressure which maintains the core in hydrostatic equilibrium, preventing inward collapse. These more massive stars are able to progressively develop helium, carbon, neon, magnesium and finally iron cores. Eventually the core becomes so dense the degenerate pressure supports the entire weight of the star. However the silicon layer above the iron core continues burning, which adds to the core mass. When this exceeds 1.4$M_{\odot}$ - the Chandrasekhar limit - the core collapses into a neutron star and the accompanying violent rebound from the dramatic compression creates a strong shock wave. This moves out-wards, ejecting the unburned, diffuse outer layers of the star into the surrounding medium, initiating the violent explosions seen as supernovae (Zeilik & Gregory 1998).

Type Ib supernova are also thought to originate from the collapse of more massive stars - in this case Wolf-Rayets. At over 20 solar masses, Wolf-Rayet stars are thought to loose

their mass very rapidly by means of a strong stellar wind. These stars are very evolved and have extremely high surface temperatures in the range 25,000K-50,000K. Having run out of fuel at their centres and lost most of their outer hydrogen envelopes these stars end their lives in supernova explosions similar to Type II.

Type Ia supernova on the other hand involve highly evolved, hydrogen-deficient stars such as white-dwarfs. Stars with initial masses below approximately $8M_{\odot}$ eventually evolve into white-dwarfs. A route to supernova for such stars is when accretion from a binary partner pushes the white-dwarf mass over the Chandrasekhar limit causing it too to collapse into a neutron star, generating a supernova explosion (Zeilik & Gregory 1998).

GMC Evolution

The shock wave generated by each of these types of supernovae expands through the surrounding medium at much greater velocities and involving significantly higher temperatures than an ionization front generated by stellar flux.

Following the initial supernova explosion, the superbubble created first undergoes a period of free expansion which lasts a few centuries. An adiabatic shock wave is then established and the superbubble enters a rapid expansion phase where the shock wave compresses and accelerates the upstream gas into a shell on the superbubble's surface. The adiabatic phase of the supershell continues until radiative cooling becomes important in the hot interior. At that point the supershell becomes thermally unstable and collapses into a thin radiative zone. Having lost its interior pressure, the supershell is then thought to continue expansion according to a zero-pressure snowplow law in a momentum conserving solution.

4.1 Modelling Supernova

In a similar way to development of the HII region solution, a suitable methodology that can be used to incorporate the impact of supernovae in the thesis modelling must now be identified from the literature.

The affect of superbubbles on structure and evolution has been studied extensively, both analytically and numerically since the 1970's. For the purposes of this literature review, first the standard pressure-driven model developed primarily in the 1970's and 1980's to described the evolution of a superbubble will be discussed.

Attention is then turned to more recent research which has made use of the standard pressure-driven model to describe the evolution of supernova when generating starburst emergent SEDs.

The section ends in a description of the methodology adopted in the thesis, with particular emphasis paid both to the assumptions made and the new work undertaken.

4.1.1 Standard Pressure-Driven Expansion Model

Perhaps the seminal series of papers to consider the impact of supernovae on structure and evolution were *Interstellar Bubbles* McCray & Weaver (1975) and *Interstellar Bubbles II* (Weaver *et al.* 1977). The first of these presented a basic theory to describe how an early-type star with a strong stellar wind could blow a large cavity, or bubble, in the ambient interstellar medium. *Interstellar Bubbles* concentrated on describing the 'snowplow' or momentum conservation phase of superbubble evolution as it occupies the majority of the star's lifetime. (McCray & Weaver 1975) were able to use their model to explain O VI column densities in front of early-type stars observed by the *Copernicus* UV telescope and reported by Jenkins & Meloy (1974).

The second paper in the series, *Interstellar Bubbles II*, presented a more detailed theory that eliminated some of the approximations used in *Interstellar Bubbles*, to generate more complex analytic formulae for the bubble's structure and evolution. This paper modelled the free expansion and rapid adiabatic expansion phases and culminated with the momentum conservation phase. *Interstellar Bubbles II* developed both an adiabatic similarity solution for early times and an isothermal similarity solution, which included radiative losses, for later times. The quantitative results of the two *Interstellar Bubbles* papers agreed to within a factor of 2.

Further progress was made in the 1980's by, amongst others, Richard McCray & Mordecai-Mark Mac Low who used the important assumption that the evolution of a superbubble was analogous to that of a wind-driven circum-stellar shell (Spitzer 1968; Woltjer 1972). Essentially, a hot, low-density cavity is the ISM is evacuated by stellar winds from a typical OB association, which lasts longer than the interval between supernova explosions. As the supernova continue, a larger hole is created than that generated either by individual supernova or by the stellar winds. As the cavity expands, a significant volume of the ISM is swept-up into a thin, dense shell, analogous to the shell around a stellar wind bubble. As the mass contained in the shell is sufficient to act as a buffer to

the discrete energy inputs of the supernova, it was found that the dynamics of the system could be described very well by stellar wind bubble theory (McCray & Kafatos 1987) [hereafter MK87].

Using this assumption MK87 were able to present expressions to track the radius of a superbubble and accompanying shell in the adiabatic and isothermal phases. From the results it was suggested that gravitational instabilities in the supershell might form into giant molecular clouds where star formation could be initiated.

The following year Mac Low & McCray (1988) [hereafter MM88] used the assumption of MK87 to also approximate a superbubble as a very large stellar wind bubble. In this instance the bubble was irradiated by a continuous energy source. MM88 were able to make this assumption because consecutive supernovae shock waves were thought to become subsonic, not only before reaching the walls of the shell, but also before the shell underwent significant radiative cooling. In these conditions, the supernovae energy input could be modelled as a continuous luminosity.

MM88 tested the first of these assumptions by presenting an expression for the fractional radius at which a shock wave becomes subsonic and found that all waves in their model met this criteria whilst interior to the shell. Thus, the interior mass of the shell buffered the discrete energy inputs of the supernova and allowed them to be treated as a continuous luminosity.

The second assumption of MM88 used when treating the supernova energy as a continuous luminosity was that a shock wave should become subsonic and dissipate before radiative cooling in the shell became important. MM88 presented expressions to define the cooling time and radius at which the shocked ISM in the shell would become thermally unstable and collapse into the thin shell. The results showed that the supernovae shock waves became subsonic before the shell became fully radiative and the second assumption needed to treat the supernova energy as a continuous luminosity was validated.

In summary, these papers together presented evidence that superbubbles can be approximated as very large stellar wind bubbles and treated using scaled-up wind theory. The supernovae energy input could be treated as continuous function negating the need to model discrete events. Expressions were developed to describe the radial evolution of the superbubble in an adiabatic rapid expansion phase. The location and time at which radiative cooling in the shell caused its collapse into a fully radiative zone were also defined. Finally, expressions were presented to describe the motion of the superbubble in an

isothermal, momentum conservation phase.

4.1.2 The Standard Model & Starburst Modelling

Having briefly described some of the main attributes and assumptions of the standard pressure-driven model, attention can be turned to its more recent application in modelling OB associations and starbursts.

The importance of including the impact of supernovae when describing the evolution of the ISM was recognised by Oey (1995, 1996, 1997, 1998), with *The Dynamics of Superbubbles in the Large Magellanic Cloud* Oey (1996) perhaps being the most appropriate for the thesis. Oey (1996) [hereafter OY96] developed a numerical version of the standard pressure-driven bubble model to investigate superbubbles and their formation.

The Oey models treated the energy input which drove the superbubble as enhancements in the continuous wind energy which was calculated from a numerical integration of

$$\frac{dU}{dt} = L_W - P_i \frac{dV}{dt} \tag{4.1}$$

where U is the internal energy of the bubble, L_W is the wind luminosity, P_i is the internal pressure and V is the bubble volume. OY96 also assumed that the mechanical luminosity dominated by the supernovae remained constant in time until the lowest mass star ($8M_\odot$) that produces a supernova expired at $t_e \approx 40$Myrs and hence the function was continuous.

However, rather than using the cooling radius of MM88 for the location at which the adiabatic bubble collapses into isothermal motion, the growth of the OY96 superbubble was continued into an interstellar medium of density $n_{is} = 1\text{cm}^{-3}$ until the internal pressure of the bubble was equal to the external ambient pressure at R_s, the stall radius.

When pressure equilibrium had been reached at the stall radius, OY96 assumed that radiative losses became so significant that the shell growth was confined and began to disintegrate due to random motions in the up-stream interstellar gas. Any bubbles that did not achieve pressure equilibrium in $t < t_e$ were assumed to continue to grow until t_e (OY96).

To model these bubbles in the momentum conserving phase after the stall radius had been reached, rather than using the standard pressure-driven model of MM88, OY96 used the prescription of Steigman *et al.* (1975) which *conformed* to the standard, zero-pressure snowplow evolution after shell collapse. In this instance the stall radius and stall time

were taken as scaling parameters that correspond to the stall criterion. Thus the shell evolution after collapse was described by OY96 such that

$$\left(\frac{R}{R_e}\right) = \left(\frac{L}{L_e}\right)^{\frac{1}{4}} \left(\frac{t}{t_e}\right)^{\frac{1}{2}} \tag{4.2}$$

where L_e, t_e and R_e are the luminosity, time and radial scaling parameters.

Using this numerical prescription, OY96 modelled a small sample of OB associations in the nearby Small Magellanic Cloud. However, it was found that in comparison to observations, the OY96 models over-estimated the shell growth rate. Essentially, the superbubbles expanded to too large a diameter without reaching the stall condition. This over-estimate was found to be equivalent of up to an order of magnitude increase in the input power and a suggested reason was a discrepancy with the standard model in the shell growth rate. This growth rate discrepancy with observation of OB associations had also been found before by e.g., Saken *et al.* (1992) and Brown *et al.* (1995) who also used an approximate analytic formulation of Weaver's standard model.

More recently DPO5 presented an adapted version of the OY96 model when *Modelling the Pan-Spectral Energy Distribution of Starburst Galaxies* was published. This paper developed a 1-dimensional dynamical evolution model of HII regions around massive clusters of young stars. One unique aspect of the paper was that it linked the derived gas density distribution to the dust density distribution to produce purely theoretical SEDs for starbursts, lasting 10^8years.

In a similar way to OY96, DPO5 used an interstellar density of $n_{is} = 1\text{cm}^{-3}$ and the equations of MM88 for the radial motion of the superbubble. However, in contrast to OY96, DPO5 used a time-dependent luminosity function as the central source function in an attempt to generate superbubbles which did not exhibit the growth rate discrepancy identified by e.g., OY96 or Brown *et al.* (1995).

Like OY96, DPO5 also assumed that the bubble stalled when the external and internal pressure were equal. Following stall, a momentum conserving solution was also employed for the swept-up shell. However, although the DPO5 model did pile up the interstellar medium in front of the expanding superbubble in the momentum conserving phase, it ignored the shock expansion and the consequent density enhancements of the supershell. This allowed DPO5 to combine the momentum phase of the HII region and the momentum phase of the supernova into a simple 1-D hydrodynamic model. DPO5 were then able to couple the temporal evolution of their superbubbles to the dust density distribution using

the MAPPINGS IIIq code (Sutherland & Dopita 1993; Dopita *et al.* 2002) which models the emission line, atomic continuum and dust re-emission spectra of HII regions.

An important parameter in the DPO5 model was the ionization parameter U_{ip} which incorporated the ionizing photon flux and the atomic particle density in the HII region

$$U_{ip} = \frac{S_\star}{4\pi c R_{in}^2 n_{HII}} \tag{4.3}$$

where $S_\star$ is the flux of ionizing photons from cluster stars, c is the speed of light, n_{HII} is the atomic particle density in the H II region, taken to be $n_{HII} = 1\text{cm}^{-3}$, and R_{in} is inner radius of the ionized shell. Equation 4.3 shows that the inner radius determines the ionization parameter, which emphasises the role the pressure of the ISM plays in determining the radius of the DPO5 HII region and its evolution with time.

However, as with OY96 and despite the use of a time-dependent luminosity, the DPO5 superbubbles also exceeded the observed diameters at stall, resulting in a similar growth rate discrepancy to that already observed. This was thought by DPO5 to be because the internal pressure of the model bubbles was too high. Due to this growth rate discrepancy, the DPO5 ionization parameters for the model supershells were also approximately a factor of ten below observed values for HII regions (Kewley *et al.* 2002).

DPO5 proposed a solution to this difficulty by assuming that the mechanical power output of the young stars is less effective than the simple 1-D models suggest. DPO5 empirically determined that the effective power input would have to be decreased by a factor of ten to ensure that the ionization parameters of the model systems matched the observed range. Thus DPO5 modelled their $10^4 M_\odot$ stellar clusters as if they had the mechanical energy luminosity of a $10^3 M_\odot$ cluster and in this way brought their ionization parameters into line.

In summary, the results of both OY96 and DPO5 highlight the difficulties involved when modelling supernova exploding into an interstellar medium of atomic density 1cm^{-3}, ignoring shock expansion and using the pressure equilibrium stall condition to signal the start of the momentum conserving phase. This prescription appears to lead consistently to superbubble radii that exceed those observed, with implied associated growth rate discrepancies.

4.1.3 Thesis Modelling

In the thesis work the standard pressure-driven model is used to describe the radial evolution of the superbubble. First the assumptions of MM88 showing that consecutive supernovae shock waves becomes subsonic before either they reach the shell or the shell undergoes significant cooling, will be used to allow the supernova energy input to be modelled as a continuous function rather than a series of discrete events.

The expressions developed by MK87 will then be used to trace the radial evolution of the superbubble in both an adiabatic, pressure-driven rapid expansion phase and a momentum conservation phase. The derivation of these expressions uses the assumption that supernovae are analogous to a wind-driven circum-stellar shell and can be modelled using scaled-up wind theory. Unlike OY96 or DPO5, simple shock physics will be used to describe the compressional effects on the gas density of passage through the leading supershock.

In contrast to OY96 and DPO5, rather than assuming a pressure equilibrium condition for superbubble stall, the cooling radius and time as described by MM88 are used to find the point at which the thin shell collapses into a fully radiative zone. It is unlikely that the pressure-driven rapid expansion phase ends abruptly and the isothermal phase begins immediately thereafter, as it is more likely that there will be some intermediate transition phase where the system is neither entirely adiabatic or isothermal. However, a location for the radius at which cooling from the shell becomes so overwhelming that it collapses into a fully radiative zone must be found to model the transition. Hence the work of MM88 which showed via the derivation of a cooling radius that the supernova shock wave becomes subsonic before radiative cooling becomes important, will be employed in GEM to delineate the end of the adiabatic phase.

Whilst the thesis superbubbles will initially expand into the low density HII region already ionized by the time-dependent stellar flux, they rapidly overtake the ionization front to enter the GMC. Thus in direct contrast to the work of OY96 and DPO5 who used an HII region density of $n_{is} = 1cm^{-3}$ as their surrounding medium, the thesis superbubbles will spend a proportion of their life-time expanding through an average density of $n_{av_{H_2}}$ = $300cm^3$, which is much more indicative of a GMC than the interstellar medium.

By embedding the thesis superbubbles in an average density more representative of a GMC, an attempt has been made to accommodate superbubble expansion without the

assumption that the power input must be decreased by an order of magnitude to match observation, as in the case of OY96 and DPO5.

In contrast to DP05, the thesis will attempt to trace the gas density of the shell using simple shock physics and hence model the density enhancement across the shock. With the HII region solution, the assumption of ERR00 that the accumulated gas could be modelled as uniformly distributed over the neutral region was suitable. The supernova solution does require the gas density because, for example, when the temperature of the gas drops to the dust condensation temperature, the shell can often provide most of a system's extinction.

Perhaps the primary difficulty with assuming such a high external GMC density is calculating the temperature evolution of the shell, due to the potential invalidation of the assumption of steady state ionization equilibrium (the 'on the spot approximation mentioned in §3.6.1. The thesis uses a 1-d semi-analytical formulation which does not model the hydrodynamic evolution of the shell gas, but an attempt has been made to calculate a supershell temperature appropriate to a system modelling multiple supernova as a single bubble with an expanding supershell. This shell gas temperature calculation is returned to in much depth in §5.3, where the optical depth distributions for the model are developed.

Finally, the assumption and methodology employed in the thesis are tested for efficacy in Chapter 7, where the resultant model emergent SEDs are compared to observations of a small sample of nearby ULIRGs.

In the coming sections, first the STARBURST99 stellar evolutionary synthesis code is used to generate the supernovae function from which the continuous energy input is derived. The equation of MK87 to describe the evolution of the superbubble in the adiabatic phase is then derived. The compression factor across the strong shock and the mass overtaken by the superbubble are then used to find the shell width and hence the shell gas density during rapid expansion.

The expression presented by MM88 for the cooling radius is then derived as is the expression of MK87 which describes the superbubble evolution in the isothermal phase. In a similar way to the rapid expansion phase, the compression factor across the strong shock and the mass overtaken by the superbubble are used to derive the shell width and density. Finally, a new expression is developed to describe the motion of the superbubble and variation of the shell width for expansion through the ambient region ($n_{av_{H_2}} = 1\text{cm}^{-3}$)

within which the GMC is embedded.

The chapter culminates with illustrating the superbubble motion and shell growth and a comparative analysis is carried out over the possible M_{GMC} and η parameter combinations on the model grid.

4.2 Supernovae Energy Distribution

The energy distribution for the supernovae is obtained from the STARBURST99 stellar evolutionary synthesis code and this will now be discussed.

Continuous Supernova Luminosity

STARBURST99 tabulates both the rate and the energy for all supernovae types in the synthetic cluster population at each user-defined time interval; Δt_{ip} =0.1Myrs.

Rather than treating the supernova luminosity as individual energy inputs - a source function that varies with time - they are treated in this thesis work as a continuous energy source. A string of supernova explosions evacuate a significant cavity in the GMC and the gas and dust swept up during this evacuation collapses into a dense shell at the cooling radius R_c. MM88 found that a system of supernova explosions reach a common cooling radius early in the life-time of the stellar association and that the shell acts as a buffer to the discrete supernovae events. It could therefore be modelled as one large superbubble, illuminated by a continuous energy source (MM88).

However, Shull & Saken (1995) suggested that non-coeval star formation and post-main sequence evolution of stellar winds had a significant impact on the amount of energy deposited into the superbubble over time and hence the use of a continuous energy source was a gross approximation. In this thesis work, STARBURST99 has been used in its instantaneous mode and the stellar population is coeval, with no age spread and a fixed IMF so the variations in energy that would arise from a non-coeval population can be discounted.

Regarding the main sequence and subsequent Wolf Rayet phase of the stellar wind evolution on the energy deposited into the superbubble, most of the ionizing radiation available to the system is delivered during the first few million years by O stars with masses greater than $\sim 30M_{\odot}$ and lifetimes less $\sim 10^7$years (MK87). Prior to the first supernova exploding, this variation is provided for by the explicit use of the time-dependent

source functions discussed in Chapter 3, Section §3.3. Although less massive stars may have a strong stellar wind, their energy contribution will be dominated by their terminal supernova explosion and this is accounted for in the supernova energy function. Therefore, in a coeval population, at times greater than t $\sim$ 5Myrs a constant supernova energy source is a fair approximation and has been used in this thesis (Shull & Saken 1995).

STARBURST99 Supernova Source Function

As will be seen in the next section §4.3, the equation describing the radial motion of the superbubble in the adiabatic phase, repeated below for convenience, contains the term $\dot{E}_{SN}$ which is the rate of change of thermal energy due to supernova.

$$\dot{E}_{SN} = \frac{\sum E_{SN}(t)}{t_{OB}} \tag{4.4}$$

where $\Sigma E_{SN}(t)$ is the total energy expended by the supernovae, and t_{OB} is the life time of the OB association. Equation 4.4 has been related to the STARBURST99 supernovae energy output by writing a bespoke computer program to integrate $E_{SN}(t)$ over the life-time of the association using the trapezium rule, to provide $\Sigma E_{SN}(t)$. This was then divided by the life-time t_{OB} to give $\dot{E}_{SN}$. As the initial mass function used to generate the source spectral energy distribution strongly biases it to-wards low mass stars there are many more Type I than Type II supernova in the population. Whilst Type II supernova only contribute until t < 6Myrs, illustrating the short life-time of the heavy OB stars in the population, their energy release dominates that of populations' supernovae.

Figure 4.1 shows this integrated energy $\Sigma E_{SN}(t)$ for each η and M_{GMC} on the model grid, with η and hence $\Sigma E_{SN}(t)$ rising from the left. This plot illustrates the operation of scaling in STARBURST99 that was referred to earlier in section §3.5.1. Having discussed the supernovae energy input, the adiabatic equations of motion can now be presented.

4.3 Adiabatic Phase

The time at which the first supernova explodes is a function of stellar mass. As the Salpeter Initial mass Function (IMF), with the same minimum and maximum mass limits, was used for all the STARBURST99 source functions, the first supernova explodes at $t_{SN_{start}}$ = 3.71Myrs for each model on the parameter grid.

Initially the supernova ejecta freely expands for around t $\sim 10^4$ years, by which time a few solar masses of wind shocked gas has been accumulated around the superbubble.

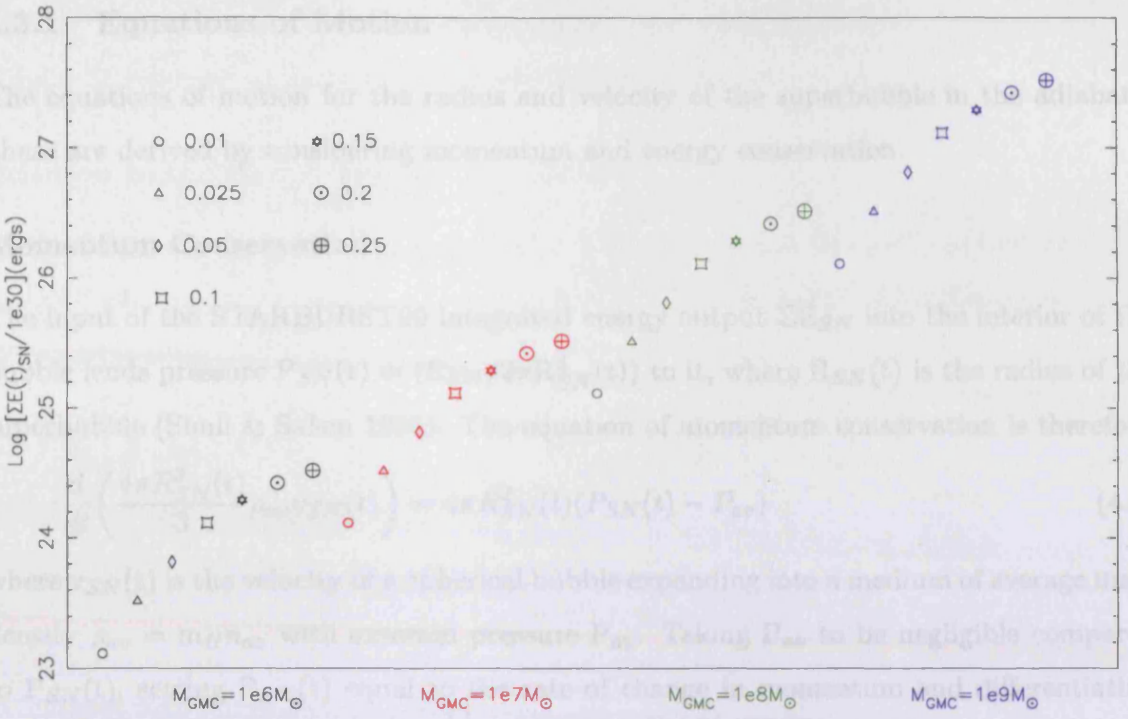

Figure 4.1: Integrated Energy for the STARBURST99 Supernova Distribution. Star formation Efficiency η rises from the left for each M_{GMC}.

The free expansion has then slowed enough for an adiabatic shock wave to be established (MK87).

Once free expansion ends the superbubble is still expanding extremely fast and in a similar way to the HII region model, the shocked gas in its interior, although heated to even higher temperatures ($T \geq 10^5$K), is unable to expand quickly enough to equalise the pressure increase and so remains largely undisturbed from its original position. This means that radiative losses do not greatly affect the system and the interior of the bubble can be considered dynamically to be in adiabatic flow (MK87).

Once the shock wave has formed, it travels outward, sweeping up, compressing and accelerating gas into a supershell trapped on the surface of the expanding superbubble. However, eventually radiative cooling from the supershell becomes so overwhelming that the supershell collapses into a fully radiating zone, the adiabatic pressure-driven expansion phase ends and the isothermal, momentum conservation phase begins.

4.3.1 Equations of Motion

The equations of motion for the radius and velocity of the superbubble in the adiabatic phase are derived by considering momentum and energy conservation.

Momentum Conservation

The input of the STARBURST99 integrated energy output ΣE_{SN} into the interior of the bubble lends pressure $P_{SN}(t) = (E_{SN}/2\pi R_{SN}^3(t))$ to it, where $R_{SN}(t)$ is the radius of the superbubble (Shull & Saken 1995). The equation of momentum conservation is therefore

$$\frac{d}{dt}\left(\frac{4\pi R_{SN}^3(t)}{3}\rho_{av}v_{SN}(t)\right) = 4\pi R_{SN}^2(t)(P_{SN}(t) - P_{av}) \tag{4.5}$$

where $v_{SN}(t)$ is the velocity of a spherical bubble expanding into a medium of average mass density $\rho_{av} = m_H n_{av}$ with external pressure P_{av}. Taking P_{av} to be negligible compared to $P_{SN}(t)$, setting $P_{SN}(t)$ equal to the rate of change in momentum and differentiating $R_{SN}(t)$ allows the pressure of the superbubble to be expressed (Shull & Saken 1995)

$$P_{SN}(t) = \rho_{av}v_{SN}^2(t) + \frac{\rho_{av}}{3}R_{SN}(t)a_{SN}(t) \tag{4.6}$$

where $a_{SN}(t)$ is the acceleration of the superbubble.

Energy Conservation

Moving to the equation of energy conservation for the superbubble, as the bubble is extremely hot the energy is almost totally thermal

$$E_T(t) = \frac{4\pi}{3}R_{SN}^3(t)\left[\frac{3}{2}P_{SN}(t)\right] \tag{4.7}$$

where $E_T(t)$ is the total thermal energy. The conservation of energy requires that the rate of change of thermal energy in the bubble $\dot{E_{SN}}$ is equal to the rate at which energy is given to the gas, less both the rate of work of the expanding gas on the surrounding and the radiative losses of the bubble. Hence the rate of change of the total thermal energy of the bubble can be expressed (Shull & Saken 1995)

$$\frac{d}{dt}\left[\frac{4}{3}R_{SN}^3(t)\left(\frac{3}{2}P_{SN}(t)\right)\right] = \dot{E}_{SN} - P_{SN}(t)\frac{d}{dt}\left[\frac{4\pi}{3}R_{SN}^3(t)\right] - n_{SN}^2\frac{4\pi}{3}R_{SN}^3(t)\Lambda_R(T_{SN})) \tag{4.8}$$

where $\Lambda_R(T_{SN})$ is the cooling function of a superbubble of temperature T_{SN} and n_{SN} is the interior atomic number density. As an adiabatic process is one that takes place with

no heat transfer to or from the system, $\Lambda(T_{SN})$ and hence the last term in Equation 4.8 maybe be assumed to be zero, as no radiative loss occurs.

Solution to the Radial Equation of Motion

To continue with the derivation of $R_{SN}(t)$ it is now convenient to introduce the shorthand $R_{SN}(t) = R$, $v_{SN}(t) = \dot{R}$, $a_{SN}(t) = \ddot{R}$ and $d/dt(\ddot{R}) = \dddot{R}$. Rearranging Equation 4.8 for $\dot{E}_{SN}$ and substituting Equation 4.6 for $P_{SN}(t)$ into it gives

$$\frac{d}{dt}\left[\frac{4\pi}{3}R^3\left(\frac{3}{2}[\rho_{av}\dot{R}^2 + \frac{\rho_{av}}{3}R\ddot{R}]\right)\right] + \left(\rho_{av}\dot{R}^2 + \frac{\rho_{av}}{3}R\ddot{R}\right)\frac{d}{dt}\left[\frac{4\pi}{3}R^3\right] = \dot{E}_{SN} \tag{4.9}$$

which when expanded gives

$$15\dot{R}^3R^2 + 12R^3\dot{R}\ddot{R} + \dddot{R}R^4 = \dot{E}_{SN}\frac{3}{\rho_{av}2\pi} \tag{4.10}$$

As the radius tends to zero when t = 0 and then increases as time goes on, a general solution for the superbubble radius can be expressed in the form

$$R = At^{\alpha} \tag{4.11}$$

where A and α are positive constants (Dyson & Williams 1997*c*). Differentiating this equation three times with respect to time and substituting the expressions into Equation 4.10 leads to

$$A^5[15\alpha^3 + 12\alpha^2(\alpha - 1) + (\alpha - 2)(\alpha - 1)\alpha]t^{5\alpha-3} = \dot{E}_{SN}\frac{3}{\rho_{av}2\pi} \tag{4.12}$$

In the previous subsection §4.2 describing the supernovae element of the starburst source function it was shown that based on the work of MM88, the mechanical energy output of the supernova can be modelled as a continuous energy source. Therefore both the LHS and RHS of Equation 4.12 are time independent and $t^{5\alpha-3} = 1$, 5α- 3 = 0 and $\alpha = \frac{3}{5}$. Substituting for α in Equation 4.12 and using 4.11 gives the solution to Equation 4.10 - the equation of motion of the supernova bubble (Dyson & Williams 1997*c*)

$$R = At^{\alpha} = \left(\frac{125}{154\pi}\right)^{\frac{1}{5}}\left(\frac{\dot{E}_{SN}}{\rho_{av}}\right)^{\frac{1}{5}}t^{\frac{3}{5}} \tag{4.13}$$

The rate of change of thermal energy $\dot{E}_{SN}$ can now be cast in terms of the STARBURST99 supernovae energy output. If ΣE_{SN} is the total integrated energy expended by the supernova and t_{OB} is the life time of the OB association

$$\dot{E}_{SN} = \frac{\sum E_{SN}(t)}{t_{OB}} = L_{SN} \tag{4.14}$$

where L_{SN} is the mechanical luminosity of the supernovae, then

$$R_{SN}(t) = \left(\frac{125}{154\pi}\right)^{\frac{1}{5}} L_{SN}^{\frac{1}{5}} \rho_{av}^{-\frac{1}{5}} t^{\frac{3}{5}} \tag{4.15}$$

where $\rho_{av} = m_H n_{av}$. Equation 4.15 can be thought of as an expression of the balance between the energy density of the external medium and the ram pressure of the expanding supernova shell (MM88). Further defining $L_{38} = L_{SN} 10^{38}$ergs s^{-1}, $t_7 = t/10^7$yrs and multiplying out all the factors gives

$$R_{SN}(t) \approx (267pc)\left(\frac{L_{38} t_7^3}{n_{av}}\right)^{\frac{1}{5}} \tag{4.16}$$

which is Equation 1 of MM88.

Superbubble Velocity

The differential of Equation 4.16 is the velocity of the superbubble in the adiabatic phase

$$v_{SN}(t) \approx (15 kms^{-1}) L_{38}^{\frac{1}{5}} n_{av}^{-\frac{1}{5}} t_7^{-\frac{2}{5}} \tag{4.17}$$

which is Equation 2 of MM88. These last two equations were incorporated into the bespoke GEM computer code and used to describe the radial evolution of the superbubble during the adiabatic phase. The calculation is made for each time-step in the STARBURST99 output; Δt_{ip}. The dynamics of the supershell in the adiabatic phase are now considered.

4.3.2 Adiabatic Shell

As the superbubble expands out through the system, the leading shock wave sweeps-up, compresses and accelerates material into a shell behind the shock front.

It is important to attempt to model the gas density enhancement of the supershell. If computer resources allowed, a fully hydrodynamic, 3-dimensional computer code which calculated e.g.; the transport of ionising radiation and the gas heating and cooling rates, would be able to trace the evolution of the shell density and the shock structure in a formalised manner. However, limited resources meant that this thesis work used a 1-dimensional, semi-analytical code, GEM, to model simply, these effects.

If the assumption is made that all the mass swept-up by the bubble resides in the supershell, then when the gas begins to approach the dust condensation temperature T_{cond}, the dust column through the shell can provide the majority of a system's extinction.

Therefore some way must be found to obtain the gas density of the shell at T_{cond} so it can be linked to the dust density via a temperature dependent dust condensation factor.

It was therefore decided to approximate the shell as adiabatic. An adiabatic process is a thermodynamic process in which no heat is transfered to or from a working system. Adiabatic changes in temperature do occur however, due to changes in the pressure of the gas, but these do not add or subtract heat. Having transferred the gas overtaken by the shock front at each STARBURST99 time-step into a supershell located at the radius of the superbubble, simple shock physics can be used to iteratively calculated the shell width at time t using the density compression ratio across the shock coupled to the mass of gas overtaken.

It should be noted that any shell in the adiabatic phase has a temperature well in excess of the dust condensation temperature and it is not until the superbubble has been in isothermal motion for some time that the shell dust can begin to condense. Therefore the purpose of modelling the adiabatic shell is to attempt to trace the density enhancement of the supershell during the adiabatic phase. In this way no mass is lost to the system and when the supershell gas cools to the dust condensation temperature, all the swept-up mass of the system can contribute to the extinction and mass is conserved.

Calculation of the shell width relies on determining the flow variables on either side of the shock and ultimately the ratio by which the material external to the shock is compressed on its passage through the shock to the shell. The Rankine-Hugoniot jump conditions show how the flow variables are related across the shock to conserve mass, energy and momentum and allow the properties of the individual flow to be examined.

The flow variables are the pressure, density and velocity of the gas on either side of the shock and because the shock is so thin and flow into and out of the shock so fast, the relationship between these variables can be considered time-independent. Hence, the 'jump' conditions are so called because they allow the user to jump straight from knowledge of the gas entry variables to calculation of the exit variables without having to model the discontinuous change taking place whilst the gas travels through the shock.

Full derivation of the Rankine-Hugoniot conditions is reserved for Appendix B so here the expressions for the quantities conserved across the shock: mass and momentum flux and the specific total energy, will simply be stated.

Summary of the Rankine-Hugoniot Conditions

The expression for mass continuity can be written

$$\phi = \rho u \tag{4.18}$$

where ϕ is the mass flux constant, ρ is the density and u is the velocity. That for momentum conservation can be written as

$$\zeta = P + \rho u^2 \tag{4.19}$$

where ζ is the momentum flux constant and P is the pressure. And finally

$$\xi = \frac{1}{2}u^2 + \frac{5}{2}\frac{P}{\rho} \tag{4.20}$$

where ξ is the stagnation enthalpy.

Density Ratio Across the Shock

Having derived the Rankine-Hugoniot conditions, the energy balance equation can be used to find the up and downstream gas velocities. Using these in conjunction with the upstream Mach Number, which is the ratio of the velocity at which gas enters the shock to the sound speed ahead of the shock, allows the velocity ratio across the shock to be obtained.

The Mach number determines if the shock is strong and having made that assumption, the velocity ratio and the mass continuity Rankine-Hugoniot condition can be used to find the density ratio across the shock. Again, full derivation of the density ratio has been reserved for Appendix B, but the result is summarised here as

$$\rho_1 = 4\rho_o \tag{4.21}$$

where ρ_1 is the density of the gas exiting the shock and ρ_o is the density at which gas enters the shock. Equation 4.21 shows that the post-shock compression is limited to four times the pre-shock gas density. This limitation is a function of the pressure in the post-shocked gas as, even if the velocity with which the gas enters the shock is made extremely large, theres is a corresponding exchange of kinetic energy into the translational (thermal kinetic) energy of the post-shocked gas. The high pressure resulting from the exchange then opposes the compression and limits the density ratio to four (Dyson & Williams 1997*d*).

4.3.3 Scheme for the Total Supershell Width

As GEM is a 1-dimensional semi-analytic computer code some method had to be found to model generation of the supershell. The STARBURST99 source functions represent a stellar cluster, within which multiple supernovae explode as the population evolves. However, the energy input E_{SN} has been integrated into a continuous source function for use in GEM, as discussed in §4.2 (MM88). The calculations for the systems' radial evolution are also made at each t_{ip} = 0.1Myrs and it therefore seemed appropriate to generate a new shell at each time-step and assume that each shell formed merges with the pre-existing shells to generate one supershell. As mentioned,MK87 to assumed that the supershell acts as a buffer to discrete energy inputs and therefore by forming successive shells the thesis employs the numerical method of MK87 in an analytical form.

The assumption is made that the first shell forms behind $R_{SN}(t)$ such that the width of the shell $\Delta R_{shell}(t)$ could also be expressed

$$\Delta R_{shell}(t) = R_{SN}(t) - R_{cav}(t) \tag{4.22}$$

where $R_{cav}(t)$ represents the inner edge of the shell. The equations of MM88 used to derive the form of motion of the superbubble assumed that $R_{SN}(t)$ was the outer radius of the gas shell trapped on the bubbles surface, so placing the first shell formed behind $R_{SN}(t)$ appears a reasonable assumption.

The width of the first shell formed is then calculated using the compression ratio across a strong adiabatic shock and mass conservation of the material overtaken by the shock. The question then becomes where to place the succeeding shells? As was mentioned in §4.2 MM88 showed using numerical techniques that after approximately 5-10 supernovas had exploded their cooling radii had all converged on the same radius. This implies that successive shells formed catch up with each other and merge into a single supershell. Therefore it was decided to place each shell formed behind the previous shell such that the total shell width $R_{SH}(t)$ becomes

$$R_{SH}(t) = \sum_{R_{SN_{start}}+1\Delta R}^{R_{SN}(t)} \Delta R_{shell}(t) \tag{4.23}$$

Finally, all supershell widths $R_{SH}(t)$ are only a tiny fraction of the superbubble radius at any time.

Width of Each Shell Formed

The equation for the width of each shell formed, ΔR_{shell}(t), can now be determined using mass conservation and the compression ratio across a strong shock. This method of finding the shell width is used in the absence of a fully 3-dimensional hydro-dynamic code, which is beyond the computational resources available.

Expressing the mass of the gas swept-up into the approximated adiabatic shell as the left-hand side of Equation 4.24 and balancing that with the mass of gas originally contained within R_{SN}(t) gives

$$4\pi R_{SN}^2(t)\Delta R_{shell}(t)\rho^{SH}(t) = \frac{4\pi}{3}\rho^{Wi}[R_{SN}^3(t) - R_{SN}^3(t-\Delta t)] \tag{4.24}$$

where ρ^{SH}(t) is the downstream density of the shell and ρ^{Wi} is the upstream density in in the ionized HII region. Re-arranging for ΔR_{shell}(t) and substituting the compression ratio from Equation 4.21 with ρ^{SH}(t) = ρ_1 and ρ^{Wi}(t) = ρ_o gives

$$\Delta R_{shell}(t) = \frac{[R_{SN}^3(t) - R_{SN}^3(t-\Delta t)]}{12R_{SN}^2(t)} \tag{4.25}$$

For all times when the superbubble is trapped within the ionization front formed by the impact of the time-dependent stellar flux, the upstream density ρ_o is given by the density in the HII region ρ^{Wi}(t). Once the superbubble has overtaken the ionization front, the upstream density changes to be the neutral density ρ^n(t). Similarly, when the superbubble exits the GMC, the upstream density again changes to the ambient density ρ^α(t) until the modelling ends. Thus, as a system evolves, each new shell ΔR_{shell}(t) formed merges with all existing shells to form one large supershell of width $R_{SH}(t)$, which is the column length over which dust will condense as the gas temperature approaches the dust condensation temperature.

Having derived the equations of motion determining the radius of the superbubble and the width of the supershell formed, it is now possible to consider the changes occurring when the system moves from the adiabatic form of motion, given by Equation 4.16, to isothermal motion.

4.4 Cooling Radius R_c in the GMC

As already described, the shock wave passes through the upstream gas compressing it into a thin shell. The temperature the gas achieves is dependent on both the shock velocity

and the molecular weight of the gas (Dyson & Williams 1997*d*). In the adiabatic phase the shock velocity is considerable, leading to high shell gas temperatures and no dust.

However, using MM88, a radius can be located at which removal of energy via radiation becomes so overwhelming that the shell undergoes runaway cooling and collapses into fully radiative zone. This radius is the cooling radius R_c and signals the change from adiabatic to isothermal superbubble motion. Although gas is not explicitly modelled here, it is worth briefly considering the processes by which it cools at various temperatures in order to realistically couple the dust condensation in the shell to its gas temperature.

Radiative Mechanisms

The cooling function discussed is illustrated pictorially in Figure 4.2. At temperatures $\geq$

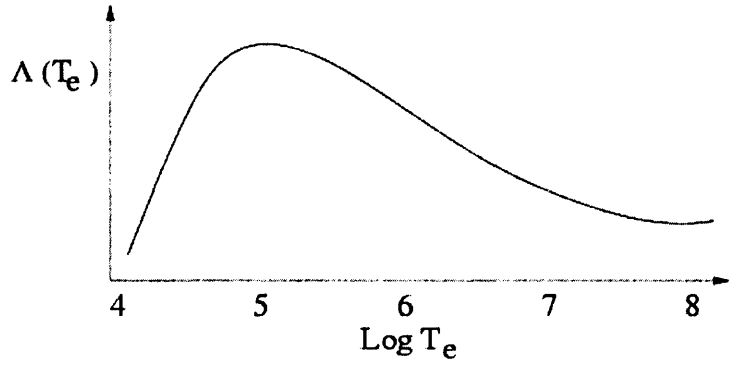

Figure 4.2: The Cooling function $\Lambda(T_e)$ for shocked interstellar gas (Dyson & Williams 1997*d*).

10^8K the gas is made up of electrons, protons and the bare nuclei so the only process by which cooling can occur is via bremsstrahlung or free-free emission.

Between around 10^5K and 10^8K the gas starts to contain highly ionized species of Oxygen and Carbon, e.g., C^{3+}, O^4. These have energy levels which can be collisionally excited and that subsequently decay radiatively. As these very high energy levels are not metastable and the radiative transitions have very high probabilities, cooling proceeds via 'resonance' lines seen in the far UV and soft X-rays part of the spectrum. Between temperatures of 10^4K and 10^5K cooling occurs via forbidden line excitation from heavy elements like O^+ and O^{++}. Despite the low abundance and low transitional probabilities of these ions this is a highly efficient process and so forbidden line cooling is the dominant

cooling mechanism at these temperatures (Dyson & Williams 1997*d*). As the temperature drops to below 10^5K cooling proceeds via bound-bound emission with electrons excited from the ground level to a higher energy level radiatively decaying and by mechanical energy loss which occurs when the most energetic electrons undergo collisional ionisation. These processes dominate below T $\simeq$ 10^5K as the mean thermal energy of a particle becomes equal to the ionization potential of hydrogen at a temperature of T $\simeq$ 1.6 x 10^5K and both processes require neutral hydrogen to be present in the shell (Dyson & Williams 1997*d*).

Equation For The Cooling Radius

Collapse into an emitting shell occurs at the time the total energy radiated from the bubble balances the total energy in its interior (MM88). Cooling in the shell via bremsstrahlung, forbidden or resonance lines occurs in the temperature range 10^5K < T < 10^8K. Once gas at these temperatures starts to cool, its cooling rate increases, resulting in a runaway process as the gas becomes thermally unstable. The point of collapse occurs at the cooling time t_{cool} and having found this time, the collapse or cooling radius R_c can be determined.

Beginning then with an implicit equation to describe the total energy radiated from the superbubble per unit volume (MM88)

$$U(t_{cool}) = \int_0^{t_{cool}} dt \int_0^{R_{SN}} d^3r C_{SN}\,[n_{SN}(r,t),\ T_{SN}(r,t)] \tag{4.26}$$

where $U(t_{cool})$ is the fraction of supernova luminosity radiated from the superbubble at t_{cool}, $C_{SN}[n_{SN}(r,t),T_{SN}(r,t)]$ is the rate of cooling per unit volume of the interior and d^3r is the volume element. Considering the cooling rate per unit volume C_{SN} first, MM88 equated this to

$$C_{SN} = n_e n_{SN} \Lambda_R(T_{SN}) \tag{4.27}$$

where n_e is the electron number, n_{SN} is the central interior atomic number density, T_{SN} the central temperature of the bubble and $\Lambda_R(T_{SN})$ is its cooling function. To estimate n_{SN}, an approximate solution can be found in terms of the self similarity variable $x = r/R_{SN}(t)$ and MM88 followed Weaver *et al.* (1977) to find n_{SN} in terms of x

$$n(x) = n_{SN}(1-x)^{-2/5} = \gamma L_{38}^{\frac{6}{35}} n_{av}^{\frac{19}{35}} t_6^{-\frac{22}{35}} (1-x)^{-\frac{2}{5}} \tag{4.28}$$

where $\gamma = 4.0 \times 10^{-3}\mathrm{cm}^{-3}$. As the electron density n_e is equal to the atomic density n(x), $n_e n_{SN} = n(x)^2$ so squaring Equation 4.28 and replacing it in Equation 4.27 gives

$$C_{SN} = n_e n_{SN} \Lambda_R(T_{SN}) = \gamma^2 L_{38}^{\frac{12}{35}} n_{av}^{\frac{38}{35}} t_6^{-\frac{44}{35}} (1-x)^{-\frac{4}{5}} \Lambda_R(T_{SN}) \tag{4.29}$$

In order to make an analytic estimate of the cooling of the interior gas, MM88 used a cooling function in the form

$$\Lambda_R(T_{SN}) = \beta T_6^{-0.7} \zeta \tag{4.30}$$

where ζ is the metallicity of the interstellar medium - taken here in all models to be cosmic (ζ=1), $\beta = 1.0 \times 10^{-22}$ ergs $\mathrm{cm}^3\mathrm{s}^{-1}$ and $T_6 = T_{SN}(\mathrm{K})/10^6$. MM88 then followed Weaver *et al.* (1977) to find a self similarity solution for the interior central temperature of the superbubble in the form

$$T(x) = T_{SN}(1-x)^{2/5} = \alpha L_{38}^{\frac{8}{35}} n_{av}^{\frac{2}{35}} t_6^{-\frac{6}{35}} (1-x)^{\frac{2}{5}} \tag{4.31}$$

where $\alpha = 3.5 \times 10^6$K. Raising Equation 4.31 to the power of -0.7 and replacing it equation 4.30 gives

$$\Lambda_R(T_{SN}) = \beta \alpha^{-\frac{7}{10}} L_{38}^{-\frac{56}{350}} n_{av}^{-\frac{14}{350}} t_6^{-\frac{42}{350}} (1-x)^{-\frac{14}{50}} \tag{4.32}$$

The cooling rate of Equation 4.27 has now been found in terms of the supernova luminosity, the average density of the GMC and the time *t*. Referring back to Equation 4.26 the similarity variables *x* and dx = dr/R_{SN}(t) can be used to express the volume element d^3r as

$$\int_0^{R_{SN}} d^3r = \int_0^1 4\pi r^2 dr = \int_0^1 4\pi x^2 R_{SN}^2 R_{SN} dx = \int_0^1 4\pi x^2 R_{SN}^3(t) dx \tag{4.33}$$

and so replacing Equation 4.32 for $\Lambda_R(T_{SN})$ into equation 4.29 and then replacing that into Equation 4.26 for the cooling rate $C_{SN}[n_{SN}(r,t), T_{SN}(r,t)]$ and using the volume element in Equation 4.33 leads to

$$\frac{U(t_{cool})}{\beta \alpha^{-0.7} \gamma^2} = \int_0^{t_{cool}} t_6^{-\frac{44}{35}} t_6^{\frac{42}{350}} dt \int_0^1 L_{38}^{\frac{12}{35}} n_{av}^{\frac{38}{35}} (1-x)^{-\frac{4}{5}} L_{38}^{-\frac{56}{350}} n_{av}^{-\frac{14}{350}} (1-x)^{-\frac{14}{50}} 4\pi x^2 R_{SN}^3(t) dx \tag{4.34}$$

then gathering like terms

$$\frac{U(t_{cool})}{4\pi \beta \alpha^{-0.7} \gamma^2} = R_{SN}^3(t) \int_0^{t_{cool}} t_6^{-\frac{398}{350}} dt \int_0^1 L_{38}^{\frac{64}{350}} n_{av}^{\frac{366}{350}} x^2 (1-x)^{-\frac{56}{50}} dx \tag{4.35}$$

Now considering the $R_{SN}(t)$ term of Equation 4.35, the equation for the radius R_c at which catastrophic cooling causes collapse into the thin shell must have the same form as Equation 4.16 for the radius of the superbubble $R_{SN}(t)$, so the variable can be changed by setting $R_{SN}(t_{cool}) = R_c$ and cubing Equation 4.16 to give

$$R_{SN}^3(t) = R_c^3 = \xi^3 L_{38}^{\frac{3}{5}} n_{av}^{-\frac{3}{5}} t_6^{\frac{9}{5}} \tag{4.36}$$

where $\xi = 267$pc and is the constant from Equation 4.16. Substituting Equation 4.36 for $R_{SN}^3(t)$ in Equation 4.35 leads to

$$\frac{U(t_{cool})}{4\pi\beta\alpha^{-0.7}\gamma^2\xi^3} = L_{38}^{\frac{274}{350}} n_{av}^{\frac{156}{350}} \int_0^{t_{cool}} t_6^{\frac{232}{350}} dt \tag{4.37}$$

The term t_6 can now be integrated to cast Equation 4.37 in terms of t_{6cool}, the time at which collapse occurs

$$\frac{U(t_{cool})}{4\pi\beta\alpha^{-0.7}\gamma^2\xi^3}\frac{350}{582} = L_{38}^{\frac{274}{350}} n_{av}^{\frac{156}{350}} t_{6cool}^{\frac{582}{350}} \tag{4.38}$$

which is the equation to describe the energy radiated from the bubble at the time t_{cool} it collapses into the thin shell. It is now necessary to balance this with the energy U(t) remaining in the interior of the bubble at $t=t_{cool}$. Assuming that the interior thermal energy is given by $U(t) = (3/2)P_{SN}V_{SN}$ and equating the pressure to the change in shell momentum per unit area, MM88 followed Weaver *et al.* (1977) to find

$$U(t) = \frac{5}{11} L_{SN} t \tag{4.39}$$

to be the internal thermal energy of a spherical superbubble with an adiabatic interior (Weaver *et al.* 1977). Rearranging and reducing Equation 4.38 for $U(t_{cool})$, setting it equal to Equation 4.39 and taking $t = t_{cool}$, then resolving for the cooling time gives

$$t_{6cool} \approx (16 Myrs) L_{38}^{\frac{8}{23}} n_{av}^{-\frac{16}{23}} \tag{4.40}$$

where the value 16Myrs incorporates quantities such as e.g., β, α and γ from Equation 4.38. This latter Equation 4.40 is Equation 14 of MM88 and gives the time at which collapse is taken to occur in this thesis work. Having obtained the cooling time it is a simple procedure to obtain the corresponding cooling radius by taking the cube root of Equation 4.36 for R_c^3

$$R_c \approx \xi L_{38}^{\frac{1}{5}} t_{6cool}^{\frac{3}{5}} n_{av}^{-\frac{1}{5}} \tag{4.41}$$

and substituting Equation 4.40 for t_{6cool} into Equation 4.41, gathering like terms and replacing the constants gives

$$R_c \approx (350pc) L_{38}^{\frac{47}{115}} n_{av}^{-\frac{71}{115}} \tag{4.42}$$

which is Equation 15 of MM88 for the cooling radius of a superbubble powered by an OB association of luminosity L_{SN} and is by GEM to find that location. The cooling time signals the start of the isothermal phase and the next sections develop expressions for the superbubble motion and width of the isothermal shell.

4.5 Isothermal Phase

At R_c, the adiabatic phase ceases because the region of shocked gas directly behind the front has radiated heat with sufficient efficiency for the cool, thin shell to form. The equation of motion of the superbubble changes then from one driven by the pressure gradient across $R_{SN}(t)$ to a momentum conserving solution - often referred to as the zero-pressure snow-plow solution.

4.5.1 Equations of Motion in the GMC

Assuming that all mass originally contained within R_c now resides in the shell, momentum conservation can be written

$$\frac{4\pi}{3}\rho_{av}R_c^3\frac{dR_c}{dt} = constant = \frac{4\pi}{3}\rho_{av}R_{SN}^3(t)\frac{dR_{SN}(t)}{dt} \tag{4.43}$$

where ρ_{av} is the average density of the GMC. Integrating with respect to time and solving for $R_{SN}(t)$

$$R_{SN}(t) = R_c\left[1 + 4\frac{\dot{R}_c}{R_c}[t - t_c]\right]^{\frac{1}{4}} \tag{4.44}$$

where $\dot{R}_{SN}(t)$ is the superbubble velocity. However for very late times $t \gg t_{cool}$ so $t - t_{cool} \rightarrow t$. In this limit $4t\dot{R}/R_c \gg 1$ and $t \gg R_c/\dot{R}$. Therefore $R_{SN}(t) \propto t^{1/4}$. Hence

$$R_{SN}(t) \approx R_c(\frac{t}{t_c})^{\frac{1}{4}} \tag{4.45}$$

which is Equation 13 from MK87 and used in GEM to describe the motion of the superbubble in the isothermal phase after R_c.

Superbubble Velocity

The simple differential of Equation 4.45 is the corresponding velocity of the superbubble in the isothermal phase for all times when the superbubble is trapped within a GMC of average density n_{av}

$$\dot{R}_{SN}(t) = v_{SN}(t) \approx \frac{R_c}{4t_c}\left(\frac{t}{t_c}\right)^{-\frac{3}{4}} \tag{4.46}$$

Equations 4.45 and 4.46 show that the superbubble velocity drops much more rapidly and the radius increases far more slowly in this isothermal phase than during the adiabatic phase (Dyson & Williams 1997*c*).

4.5.2 Isothermal Shell

In a similar way to the adiabatic phase, the width of the shells formed in the isothermal phase are also inversely dependent on the compression ratio across the shock. The derivation of these quantities are reserved for Appendix A and the results will simply be summarised here.

The density ratio across an isothermal shock is

$$\frac{\rho_2}{\rho_o} = \frac{u_o^2}{c_o^2} \tag{4.47}$$

where density and velocity in the pre-shock region are ρ_o and u_o and the downstream density and velocity in the shocked, but cooled gas are ρ_2 and u_2 respectively. Equation 4.47 shows that the compression ratio in the isothermal phase is unlimited. This is because once the cooling becomes catastrophic, the shocked gas must radiate the energy it has gained in order to maintain isothermality. As that energy is mostly in the form of translational energy the pressure in the post shocked gas plummets and is no longer able to oppose compression (Dyson & Williams 1997*d*).

4.5.3 Width of the Isothermal Shell

Having obtained the compression ratio it is now possible to use that to find the width of the thin shell $\Delta R_{shell}(t)$ formed at this step $R_{SN}(t) = R_c + 1\Delta R$. Writing the mass of the shell as the LHS of Equation 4.48 and balancing that with the mass of gas originally contained with the radius $R_{SN}(t)$ since the isothermal shell formed at $R_c = R^3_{SN}(t\text{-}\Delta t)$

$$4\pi R^2_{SN}(t)\Delta R_{shell}(t)\rho^{SH}(t) = \frac{4\pi}{3}\rho^n(t)[R^3_{SN}(t) - R^3_{SN}(t-\Delta t)] \tag{4.48}$$

where ρ^{SH}(t) is the shell density and ρ^n is the neutral density. Re-arranging the compression ratio of Equation 4.47 for the density in the shell leads to

$$\rho^{SH}(t) = \left[\frac{v^{SH}(t)}{c_n}\right]^2 \rho^n \tag{4.49}$$

and solving for R_{SN}(t) gives

$$\Delta R_{shell}(t) = \frac{[R^3_{SN}(t) - R^3_{SN}(t-\Delta t)]}{3R^2_{SN}(t)\left[\frac{v_{SN}(t)}{c_n}\right]^2} \tag{4.50}$$

which describes the width of all isothermal shells formed whilst the superbubble is inside the GMC. In the same way as for the adiabatic shell and repeated here for convenience, each new shell formed is merged into the existing supershell width to make a new total supershell width of R_{SH}(t)

$$R_{SH}(t) = \sum_{SN_{start}+1\Delta R}^{R_{SN}(t)} \Delta R_{shell}(t) \tag{4.51}$$

R_{SH}(t) is the column length over which the optical depth calculation for the shell is made.

4.5.4 Equation of Motion in the Ambient Region

As can be seen from the derivation of the form of motion for momentum conservation, given by Equation 4.45, the equation is only valid whilst the superbubble is within the giant molecular cloud and travelling through an average density $n_{av_{H_2}} = 300\text{cm}^{-3}$ (ERR00). To continue this form of motion once the superbubble has exited the GMC, the momentum of the system must be conserved by considering the decrease in the external density upon entering the ambient region. Therefore, for all radii greater than the outer edge of the dense GMC, given by $R2_W$, a new equation of motion must be derived.

If momentum is conserved at the outer radius of the GMC, the mass of the shell multiplied by its velocity at $R2_W$ is a constant. Taking the mass of the swept up shell at $R2_W$ to be M_o at t_o, setting $R2_W = R_o$ and taking M_{SH+G}(t) to be the mass of the swept up shell at time t where $t_{R2_W} < t < t_{R2_{SN}}$, this momentum conservation relationship can be written

$$M_{SH+G}(t)\frac{dR(t)}{dt} = constant = M_o\frac{dR_o}{dt_o} \tag{4.52}$$

where the mass of the shell M_{SH+G}(t) is given in terms of the ambient density ρ^α by

$$M_{SH+G}(t) = M_o + \frac{4\pi}{3}\rho_\alpha R(t)^3 \tag{4.53}$$

Substituting this expression for into Equation 4.52, separating the variables, integrating and resolving for $R_{SN}(t)$ gives the equation describing the motion of the superbubble upon entering the ambient region outside the giant molecular cloud

$$R_{SN}(t) = \frac{M_o \frac{dR_o}{dt_o}[t - t_o] + M_o R_o + \frac{\pi}{3}\rho_\alpha R_o^4}{\left[M_o + \frac{\pi}{3}\rho_\alpha R_{SN}^3(t)\right]} \tag{4.54}$$

However, a numerical method must be applied to extract the solution to Equation 4.54 as it cannot be evaluated directly due to the quantity $R_{SN}(t)$ occurring both as the subject and in the denominator.

Therefore the 'rearrangement of the equation' iterative scheme has been employed in which successive approximations are obtained for value $R_{SN}(t)$ and then tested against a convergence measure. Ideally, each approximation is better than the preceding one and the solution to Equation 4.54 can then be found. Thus, Equation 4.54 is rearranged

$$R_{SN}(t) = \frac{M_o \frac{dR_o}{dt_o}[t - t_o] + M_o R_o + \frac{\pi}{3}\rho_\alpha R_o^4}{\left[M_o + \frac{\pi}{3}\rho_\alpha R_{SNguess}^3(t)\right]} \tag{4.55}$$

with $R_{SNguess}(t)$ set as $R2_W$ at $t = t_o+1\Delta t$ and then tested for convergence using the relationship

$$R_{SNtest}(t) = \frac{R_{SN}(t) - R_{SNguess}}{R_{SNguess}} \tag{4.56}$$

Should the outcome of Equation 4.56 at $t = t_o+1\Delta t$ be less than the convergence measure, in this case chosen as 0.0001, $R_{SNguess}(t_o+2\Delta t)$ is set at $R_{SNguess}(t_o+1\Delta t)$. Should the result of Equation 4.56 be greater than the convergence measure, $R_{SNguess}(t_o+2\Delta t)$ is set at $R_{SN}(t-\Delta t)$. Put simply this translates to

$$\text{if} \quad R_{SNtest}(t_o + 1\Delta t) < 0.0001, \quad R_{SNguess}(t_o + 2\Delta t) = R_{SNguess}(t_o + 1\Delta t)$$

and

$$\text{if} \quad R_{SNtest}(t_o + 1\Delta t) > 0.0001, \quad R_{SNguess}(t_o + 2\Delta t) = R_{SN}(t_o + 1\Delta t)$$

and so on as t increases.

It is a simple procedure to obtain the velocity of the superbubble whilst it is travelling through the ambient region, by differentiation of Equation 4.54

$$\frac{dR_{SN}(t)}{dt} = \frac{M_o \frac{dR_o}{dt_o}}{M_o + \frac{4\pi}{3}\rho_\alpha R_{SN}^3(t)} = v_{SN}(t) \tag{4.57}$$

where t $\geq$ t_o. and finally, the width of each new isothermal shell formed in the ambient region now becomes dependent on the ratio of the supernova velocity to the ambient sound speed c_α squared

$$\Delta R_{shell}(t) = \frac{[R^3_{SN}(t) - R^3_{SN}(t - \Delta t)]}{3R^2_{SN}(t)\left[\frac{v)_{SN}(t)}{c_\alpha}\right]^2} \tag{4.58}$$

This concludes the derivation of the isothermal phase equations, when the cooling radius R_c occurs in the neutral region internal to the GMC boundary, needed for the GEM computer code. However, as mentioned, given the very large M_{GMC} and η parameter space modelled in this work, some parameter combinations produce cooling radii which occur in the HII region internal to the ionization front or external to the GMC in the ambient region and these can now be briefly discussed.

4.5.5 Cooling Radius in the Ambient Region

The cooling radius R_c occurs in the ambient region for two of the models presented here; $M_{GMC} = 10^8 M_\odot$, $\eta = 0.25$ and $M_{GMC} = 10^9 M_\odot$, $\eta = 0.25$. This is due to the high proportion of the GMC mass that has been converted into stars for the source function and therefore the comparatively small quantity of gas and dust available to provide resistance to the very powerful expansion of the superbubble. Unfortunately in these instances it is not possible to use Equation 4.42 to calculate the cooling radius as this relationship is derived using the average density of the GMC, ρ_{av} and cannot easily be extended into the ambient region.

However, a best guess estimate as to how far these superbubbles might travel into the ambient region before collapsing into a thin shell was obtained by artificially extrapolating the neutral density beyond the edge of the GMC and using Equation 4.42 to continue the isothermal motion to R_c. This analysis showed that in both instances where the superbubble had sufficient velocity to exit the GMC whilst still in adiabatic motion, R_c must be located close to $R2_W$ and occur very early in these systems' lifetimes. If the neutral region is hypothetically extended, $M_{GMC} = 10^8 M_\odot$, $\eta = 0.25$ has $R_c = R2_W + 1\Delta R$ at 5Myrs and for $M_{GMC} = 10^9 M_\odot$, $\eta = 0.25$, $R_c = R2_W + 3\Delta R$ at 6Myrs. That being so, it appears that if these superbubbles were continued into the ambient region using a form of motion appropriate to that lower density, they would still only travel a *relatively* small distance into interstellar space before reaching their cooling radius. It

would therefore seem reasonable for this thesis work to set $R_c = R2_W$. Having reached $R_c = R2_W$ the form of motion then assumed is that given by Equation 4.54 with M_o, the mass swept-up by the supershell, being equal to the mass of the M_{GMC}, less that contained in the stars.

For future work it may well be possible to determine R_c when it occurs in the ambient region by splitting the problem into two parts; first using the average density in Equation 4.42 between R1(t) and $R2_W$ and then adding a component using the ambient density between $R2_W$ and R_c and finally re-calculating Equation 4.40 to find time at which the shell formed in much the same way as for when the cooling radius occurs within the GMC.

4.5.6 Cooling Radius in the Ionized HII Region

The cooling radius R_c occurs inside or at the ionized HII region radius for two of the models in the parameter grid which invoke the supernova solution. The changes in the equations just discussed to accommodate collapse in the HII region bubble mainly involve the expressions for the shell width and density. For example, the compression factor in the isothermal shell, given by Equation 4.49, is dependent on the upstream sound speed and when R_c occurs within the neutral region this quantity is c_n. When collapse occurs in the HII region, the upstream sound speed is that of the ionized gas, c_i, so the shell density then depends of the ratio of the shell velocity to the ionized sound speed squared rather than on the ratio of the shell velocity to the neutral sound speed squared.

4.6 Evaluation of $R2_{SN}$

Now the scheme used to define $R2_{SN}$ - the outer edge of the system - can be discussed. Many of the models in the parameter space provide for superbubbles that are powerful enough to still be expanding into the ambient region external to the GMC at 80Myrs. So for these models, ($M_{GMC} = 10^7 M_\odot$, η = 0.05, 0.1, 0.15, 0.2 & 0.25, $M_{GMC} = 10^8 M_\odot$, η = 0.05, 0.1, 0.15 & 0.2 and $M_{GMC} = 10^9 M_\odot$, η = 0.025, 0.05, 0.1, 0.15 & 0.2) R2SN is taken as the radius of the superbubble at t = 80Myrs. Pre-calculation of this variable is possible because having found the HII region ionized bubble radius R_W(t) and the outer edge of the GMC, $R2_W$, the equations of motion can be run through the system in the first instance to find the radius achieved by the leading edge of the superbubble at t = 80Myrs, without considering the attendant dust density distribution. $R2_{SN}$ determines

the column length of ambient material through which each GMC would be observed at any time prior to the superbubble reaching interstellar space and $R2_{SN}$ was pre-calculated in this way where possible, in an attempt to introduce some scaling in the volume of ambient region included for each combination of M_{GMC} and η on the grid. Once the superbubble has entered interstellar space, the column length of ambient material is gradually reduced to eventually reach zero at t=80Myrs.

However, as mentioned in Chapter 3, $M_{GMC} = 10^6 M_\odot$, η = 0.01, 0.025, 0.05 & 0.1 models revert to the HII region solution for all t as the superbubbles corresponding to these models break-up whilst internal to the HII region IF. However, these HII region solution IF velocities drop below the neutral sound speed and break-up at R_v themselves, whilst the HII region is still trapped within the confines of the GMC. In order to also compare these HII region solution models across the board at early times a reasonable column length of ambient material must still be included but it was not possible to pre-calculate a value of $R2_{SN}$ for these systems as they do not invoke the supernova solution. Amongst those parameter combinations which do invoke the supernova solution, $M_{GMC} = 10^7 M_\odot$, η = 0.01 & 0.025 and $M_{GMC} = 10^8 M_\odot$, η = 0.01, 0.025 also break up whilst within the GMC and it is not physical to continue motion after R_v. Thus, in these instances, where the bubble's loose their integrity whilst internal to the GMC, the outer radius of the ambient region is set at double the GMC outer radius such that $R2_{SN} = 2R2_W$.

In the case where the dust content is low and the quantity of mass converted into stars is relatively large, some models break-up in the ambient region; $M_{GMC} = 10^6 M_\odot$ η = 0.15, 0.2 & 0.25. In these instances R_v is located at radii much greater than twice the extent of the GMC. As it is not possible to extend any of the forms of motion after break-up the point of break-up, R_v has been taken as the outer edge of the system R2SN for these models.

Regarding $M_{GMC} = 10^8 M_\odot$, η = 0.25 and $M_{GMC} = 10^9 M_\odot$, η = 0.25, these models reach R_v and break-up whilst in the ambient region at t < 80Myrs, despite their powerful source functions and comparatively small gas and dust components. This is because the huge compression undergone by the gas and dust entering the shell dramatically slows the superbubble down, so in these models also, $R2_{SN}$ has been taken as R_v.

One further situation occurs where the mass available is considerable at M_{GMC} = $10^9 M_\odot$ and the SFE η is low at 0.01. As there is such a large quantity of dust in this system yet a very weak power source, the bubble exists intact to 100Myrs whilst still

trapped inside the GMC and so $R2_W$ has been taken as $R2_{SN}$ and no ambient material has been included.

The equations governing the superbubble and shell in both the adiabatic and isothermal phases have now been defined. It is now possible to look at the behaviour of these quantities over the entire parameter space.

4.7 Behaviour of The Radius & Velocity

Figures 4.3, 4.4, 4.5 & 4.6 show the behaviour of the HII region ionization front (IF) $R_W(t)$ and superbubble radii $R_{SN}(t)$ along with the superbubble or HII region IF velocity and the width of the supershell $R_{SH}(t)$ for all M_{GMC} and SFE η. Also marked are the outer radius of the GMC, $R2_W$ and if applicable, the break-up radius R_v, where the velocity of the superbubble drops below the sound speed in the external gas and loses its integrity. The lower panels of Figures 4.3, 4.4, 4.5 & 4.6 show the corresponding superbubble and where appropriate HII region IF velocity distributions for all star formation efficiencies η.

4.7.1 $M_{GMC} = 10^9 M_\odot$

Beginning with $M_{GMC} = 10^9 M_\odot$ and looking at the curves in the left-hand panel of Figure 4.3 showing motion and velocity for $\eta = 0.01$, 0.025, 0.05 and 0.1. In the upper panel, the HII region IF radii show steady growth at early times when the associations massive OB stars are able to deliver considerable ionizing radiation, but which then slows over time as the source function dwindles.

Turning to the superbubble radial and velocity distributions for the same η, the superbubble radial curves show very rapid growth at early times which is mirrored in the relatively steep gradient of the velocity curves, prior to their first break. This rapid growth is a function of the adiabatic expansion discussed earlier in this chapter. Although not explicitly indicated, the cooling radius is easy to spot on the superbubble curves as a sudden levelling off in growth which marks the change from adiabatic to isothermal motion. The superbubble for the $\eta = 0.1$ model spends the longest time in the adiabatic phase as this model has the most luminous source function and the smallest proportion of dust and gas available in the GMC to slow the superbubble down. Looking at the shell width distributions prior to R_c, these also show rapid growth before the first break as the shell width formed at each time-step is inversely dependent on the compression factor, which

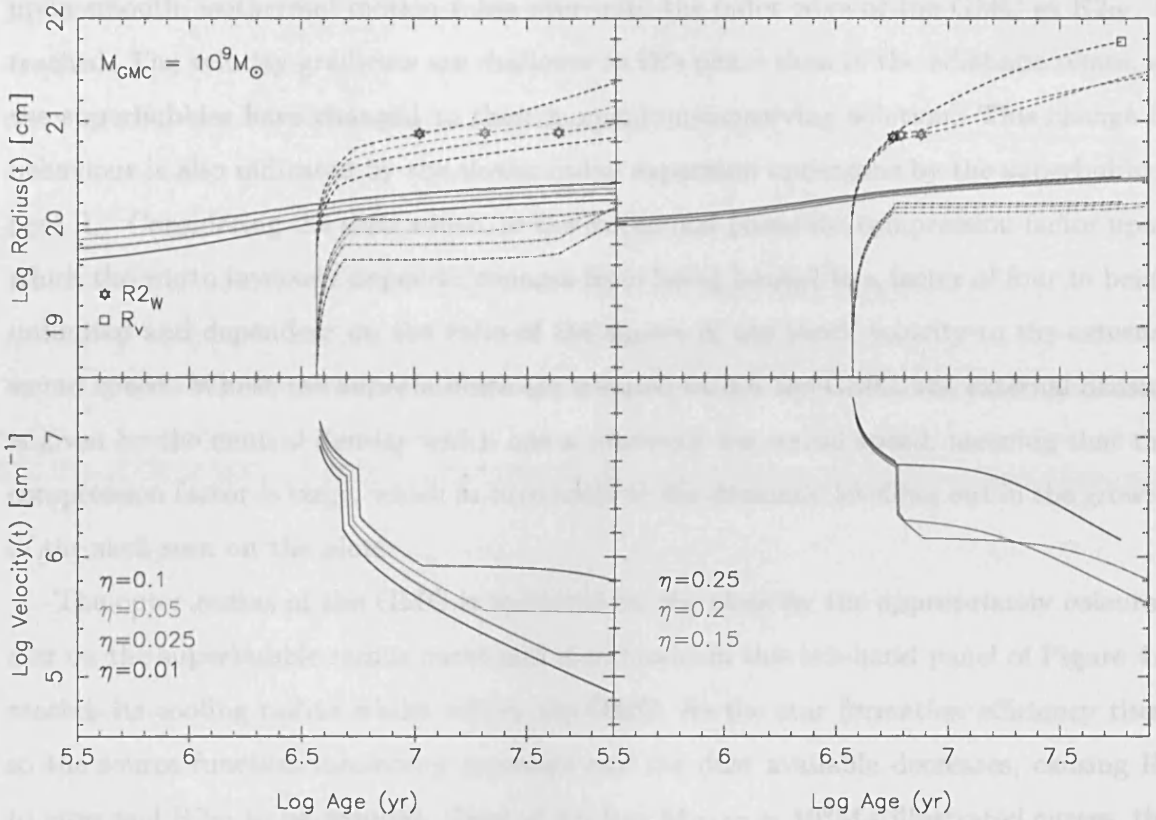

Figure 4.3: Radius and Velocity curves for $M_{GMC} = 10^9 M_\odot$, all η. The HII region IF radius $R_W(t)$, superbubble radius $R_{SN}(t)$ and the growth of the shell $R_{SH}(t)$ are shown by the solid, dashed and dot-dashed lines respectively. The left-hand panel gives distributions for $\eta = 0.01$, 0.025, 0.05 and 0.1 in black, red, turquoise and blue respectively. The left hand panel shows $\eta = 0.15$, 0.2 & 0.25 in green, pink and black respectively. Where applicable, the outer radius of the GMC, $R2_W$ and the break-up radius R_v have been indicated by the appropriately coloured star or box respectively for each curve.

is limited in the adiabatic phase to a factor of four.

Staying with the left-hand side of Figure 4.3, the cooling radius can also be easily identified on the velocity curves as the straight drop between the first and second breaks. This illustrates the de-acceleration occurring between R_c and $R_c + 1\Delta R$ only, whereupon smooth, isothermal motion takes over until the outer edge of the GMC at $R2_W$, is reached. The velocity gradients are shallower in this phase than in the adiabatic phase, as the superbubbles have changed to their momentum-conserving solution. This change in behaviour is also indicated by the slower radial expansion undergone by the superbubbles post R_c. Considering the shell width, in the isothermal phase the compression factor upon which the width inversely depends, changes from being limited to a factor of four to being unlimited and dependent on the ratio of the square of the shock velocity to the external sound speed. Whilst the superbubbles are trapped within the GMC, the external density is given by the neutral density which has a relatively low sound speed, meaning that the compression factor is large, which in turn leads to the dramatic levelling out in the growth of the shell seen on the plots.

The outer radius of the GMC is indicated on the plots by the appropriately coloured star on the superbubble radius curve and each model in this left-hand panel of Figure 4.3 reaches its cooling radius whilst within the GMC. As the star formation efficiency rises, so the source function luminosity increases and the dust available decreases, causing R_c to grow and $R2_W$ to be reduced. Thus of the four $M_{GMC} = 10^9 M_\odot$ illustrated curves, the $\eta = 0.1$, superbubble spends least time in the neutral region of the GMC, having reached $R2_W$ first, whilst conversely for $\eta = 0.01$ the superbubble does not reach the outer radius of the GMC at all and isothermal growth continues uninterrupted, within the GMC, to 80Myrs.

Continuing with the distributions for $M_{GMC} = 10^9 M_\odot$, $\eta = 0.01$, 0.025, 0.05 & 0.1, once the superbubbles have entered the ambient region, the radius curves again show more substantial growth as the reduced density in the ambient region allows the superbubble to overtake a larger volume per time step than whilst in the GMC. This levelling off in the deceleration undergone by the superbubble is shown in the gradient of the velocity curves which also drop substantially upon exit from the GMC. Of those models which reach $R2_W$, the curves for the shell width also show a volume increase on exit from the GMC as in the ambient region, the isothermal phase compression factor becomes proportional to the ratio of the square of the velocity of the superbubble to the ambient sound speed, which at

$c_\alpha = 1 \times 10^5 cms^{-1}$ is higher than the neutral sound speed at $c_n = 4.5 \times 10^4 cms^{-1}$ (Dyson & Williams 1997*c*).

Turning now to the right-hand panels of Figure 4.3 showing curves for $M_{GMC} = 10^9 M_\odot$ $\eta = 0.15$, 0.2 & 0.25. The superbubble radius, velocity and shell width curves for these higher star formation efficiencies show the same rapid growth in the adiabatic phase as the lower star formation efficiencies already described. The radial curves for these models show that R_c occurs closer and closer to the outer radius of the GMC, until for $\eta = 0.25$ it occurs just inside the ambient region. However, it should be remembered that due to the difficulty in finding the exact cooling radius within the ambient region, for $\eta = 0.25$, R_c was set at $R2_W$. $\eta = 0.25$ is the only model on the $M_{GMC} = 10^9 M_\odot$ parameter grid which breaks-up in the ambient region and this in indicated by the square box at t = 57Myrs.

Upon exit from the GMC the radial curves for $\eta = 0.15$ & 0.2 show smooth isothermal growth to R2SN; the outer radius of the system. For the $\eta = 0.25$ model, the radial growth upon entering the ambient region is greater than the two curves for $\eta = 0.15$ & 0.2 as the $\eta = 0.25$ model spends no time in isothermal motion in the GMC and therefore has a very high velocity at $R2_W$. Equation 4.54 for the isothermal motion of the superbubble in the ambient region is dependent on the velocity at $R2_W$ and as that value is in the numerator this has a knock-on effect for all t thereafter, leading to the additional volume growth of the $\eta = 0.25$ superbubble.

For these higher star formation efficiency models, the close proximity of the cooling radius to the outer radius of the GMC means that the superbubbles for $\eta = 0.15$ & 0.2 spend very little in isothermal motion whilst within the GMC. This is illustrated on the velocity curves; the drop in velocity between the first and second breaks marks the change between R_c and $R_c + 1\Delta R$, whilst the third break indicates the levelling off in the drop in velocity which occurs in the ambient region thanks to its reduced density. The velocity curve for $\eta = 0.25$ shows no third break as the time it enters the ambient region co-incides with the change from adiabatic to isothermal motion. At later times, the velocity curve for $\eta = 0.2$ drops below that of $\eta = 0.15$ at approximately t= 20Myrs due to the difference in dust mass and source function luminosity of these models. i.e., the $\eta = 0.2$ was not slowed as much as the $\eta = 0.15$ model during its passage through the neutral region due to the lesser extent of the former GMC coupled to the more powerful source function. Equation 4.57 for the velocity for the superbubble shows that it is inversely dependent on the radius cubed which means that the velocity for the $\eta = 0.2$ model eventually drops

below that of $\eta = 0.15$.

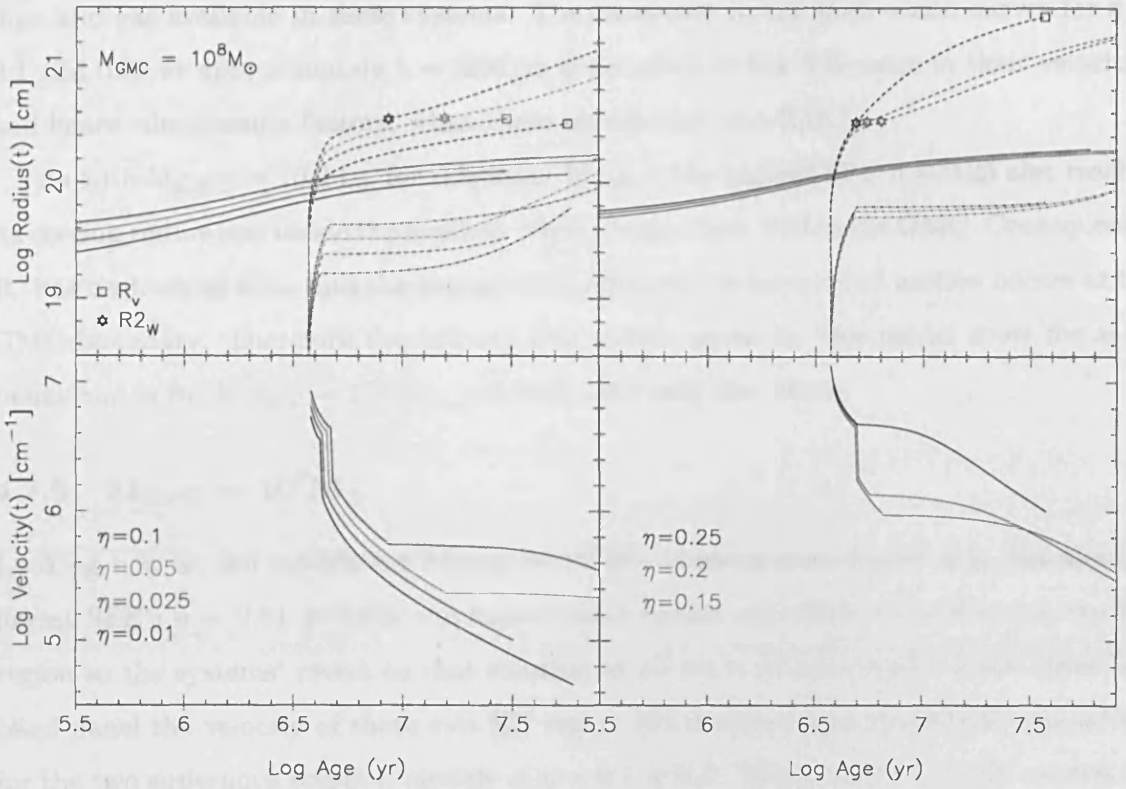

Figure 4.4: Radius and Velocity curves for $M_{GMC} = 10^8 M_\odot$, all η. The HII region IF radius $R_W(t)$, superbubble radius $R_{SN}(t)$ and the growth of the shell $R_{SH}(t)$ are shown by the solid, dashed and dot-dashed lines respectively. The left-hand panel gives distributions for $\eta = 0.01$, 0.025, 0.05 and 0.1 in black, red, turquoise and blue respectively. The left hand panel shows $\eta = 0.15$, 0.2 & 0.25 in green, pink and black respectively. Where applicable, the outer radius of the GMC, $R2_W$ and the break-up radius R_v have been indicated by the appropriately coloured star or box respectively for each curve.

4.7.2 $M_{GMC} = 10^8 M_\odot$

Moving to Figure 4.4, for $M_{GMC} = 10^8 M_\odot$, much the same behaviour is seen at all η as that for $M_{GMC} = 10^9 M_\odot$. However, for both $\eta = 0.01$ and 0.025 the superbubbles break-up whilst inside the GMC so there is no third break in the velocity curves or rise in the superbubble radius upon entering the ambient region. The magnitude of the HII region IF radius, superbubble radius and the shell width, along with the location of $R2_W$

are all proportionally smaller than those for $M_{GMC} = 10^9 M_\odot$ due to the lower amount of dust and gas available in these systems. The cross-over in the shell width curves for $\eta =$ 0.1 and 0.05 at approximately t = 30Myrs is an affect of the difference in their velocities and hence compression factors, when these models exit the GMC.

As with $M_{GMC} = 10^9 M_\odot$, for this lower M_{GMC}, the highest SFE $\eta = 0.25$ also reaches its cooling radius just inside the ambient region rather than within the GMC. Consequently R_c has been set as $R2_W$ and the change from adiabatic to isothermal motion occurs at the GMC boundary. Therefore the velocity and radial curves for this model show the same behaviour as for $M_{GMC} = 10^9 M_\odot$, $\eta = 0.25$ with only one break.

4.7.3 $M_{GMC} = 10^7 M_\odot$

Looking now at the models for $M_{GMC} = 10^7 M_\odot$ illustrated in Figure 4.5. For the two lowest SFE's $\eta = 0.01$ & 0.025 the superbubble breaks up whilst trapped inside the HII region so the systems' revert to that solution at all em t. Consequently in the lower left-hand panel the velocity of these two HII region IFs is shown as a magnitude comparison for the two supernova solution models of $\eta = 0.1$ & 0.5. The $\eta = 0.01$ & 0.025 models are also truncated at 9- & 10Myrs respectively as at those times the IF velocity drops below the sound speed in the neutral region and the front breaks-up.

Considering the supernova solutions, the behaviour of the superbubbles mirror those of the higher M_{GMC}s, with the exception of $\eta = 0.25$ as, unlike $\eta = 0.25$ for M_{GMC}'s $= 10^8$- & $10^9 M_\odot$, this model reaches the cooling radius whilst within the GMC so the behaviour in the ambient region is described by Equation 4.54 and there is no need to set $R_c = R2_W$. The velocity curve for $\eta = 0.25$ drops faster at later times than that for $\eta =$ 0.2, which in turns drops faster than that for $\eta = 0.15$ as Equation 4.57 shows the velocity is inversely dependent on the superbubble radius which is greater for eg., $\eta = 0.25$ than η $= 0.2$ at the same time t.

4.7.4 $M_{GMC} = 10^6 M_\odot$

Looking finally at the plots for $M_{GMC} = 10^6 M_\odot$ in Figure 4.6, those curves in the left hand panels show HII region solutions for all t as for these parameters, the superbubble formed breaks-up whilst still confined within the IF. In turn the HII region solution bubbles also go on to break-up within the GMC and so all are truncated at t = 7-, 8-, 8- & 9Myrs for $\eta = 0.01$, 0.025, 0.05 & 0.1 respectively.

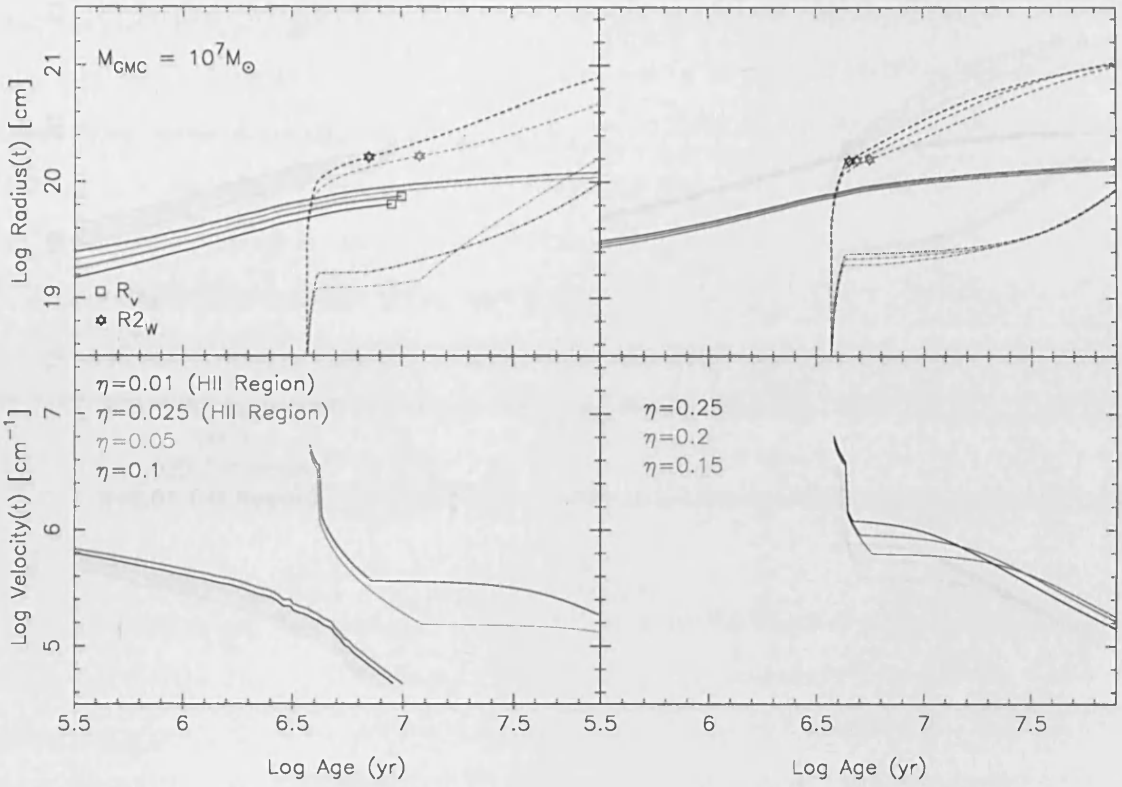

Figure 4.5: Radius and Velocity curves for $M_{GMC} = 10^7 M_\odot$, all η. The HII region IF radius $R_W(t)$, superbubble radius $R_{SN}(t)$ and the growth of the shell $R_{SH}(t)$ are shown by the solid, dashed and dot-dashed lines respectively. The left-hand panel gives distributions for $\eta = 0.01$, 0.025, 0.05 and 0.1 in black, red, turquoise and blue respectively with the former two efficiencies invoking the HII region solution for all t. The left hand panel shows $\eta = 0.15$, 0.2 & 0.25 in green, pink and black respectively. Where applicable, the outer radius of the GMC, $R2_W$ and the break-up radius R_v have been indicated by the appropriately coloured star or box respectively for each curve.

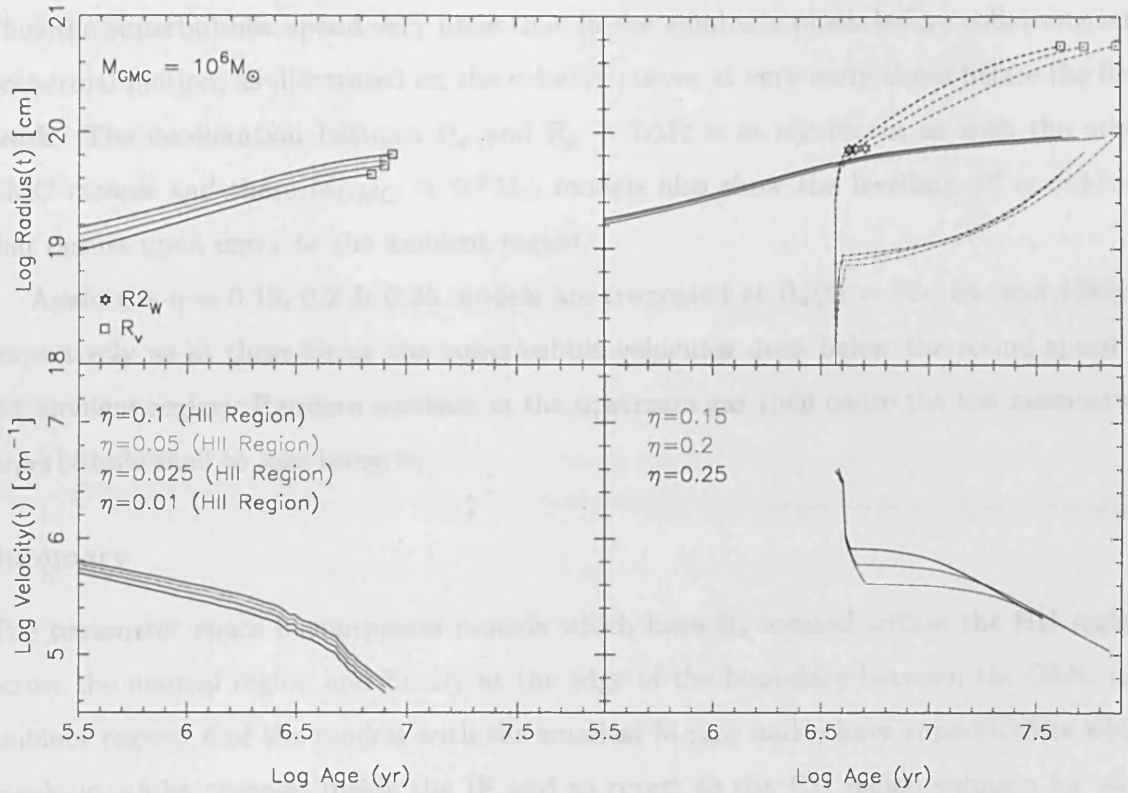

Figure 4.6: Radius and Velocity curves for $M_{GMC} = 10^7 M_\odot$, all η. The HII region IF radius $R_W(t)$, superbubble radius $R_{SN}(t)$ and the growth of the shell $R_{SH}(t)$ are shown by the solid, dashed and dot-dashed lines respectively. The left-hand panel gives distributions for η = 0.01, 0.025, 0.05 and 0.1 in black, red, turquoise and blue respectively with each of these efficiencies invoking the HII region solution for all t. The left hand panel shows η = 0.15, 0.2 & 0.25 in green, pink and black respectively. Where applicable, the outer radius of the GMC, $R2_W$ and the break-up radius R_v have been indicated by the appropriately coloured star or box respectively for each curve.

In the right-hand panel, superbubble radii for $\eta = 0.2$ and 0.25 reach R_c having only just overtaken their IFs, whilst for $\eta = 0.15$, R_c actually occurs inside the HII region. Due to the very low dust and gas mass available to these models, the outer radii of the GMC, the point at which the IFs are overtaken and the cooling radii are all very close. Thus the superbubbles spend very little time in the adiabatic phase before collapsing into isothermal motion, as illustrated on the velocity curves at very early times before the first break. The deceleration between R_c and $R_c + 1\Delta R$ is as significant as with the other GMC masses and these $M_{GMC} = 10^6 M_\odot$ models also show the levelling off in velocity that occurs upon entry to the ambient region.

Again the $\eta = 0.15$, 0.2 & 0.25 models are truncated at $R_v(t) =$ 76-, 54- and 42Myrs respectively as at these times the superbubble velocities drop below the sound speed in the ambient region. Random motions in the upstream gas then cause the low momentum superbubble shell to lose integrity.

Summary

The parameter space encompasses models which have R_c located within the HII region, across the neutral region and finally at the edge of the boundary between the GMC and ambient region. 6 of the models with the smallest M_{GMC} and η have superbubbles which break-up whilst trapped inside the IF and so revert to the HII region solution for all t. These latter models are small M_{GMC} & η and all go on to break up in the neutral region. This shows that with very little dust and a low luminosity source function, clouds can be modelled as HII regions with no accommodation made for supernovae, but that at higher M_{GMC} & η supernova should be considered.

As expected, for the supernovae solution models, all superbubbles show rapid growth in the adiabatic phase until the cooling radius has been reached, whilst in the isothermal phase the velocity drops less rapidly and superbubble growth slows. Upon exit from the GMC the superbubble again grows in volume due to the sparse density of the ambient region providing little resistance to its expansion. As M_{GMC} rises so does $R2_W$ for the same η and within an M_{GMC}, $R2_W$ drops as η rises. Models at high η spend longest in adiabatic motion and reach $R2_W$ first due to the luminosity of the source function coupled to the paucity of gas and dust. As η drops, the density increases and on occasion the superbubble does not reach $R2_W$ within the 80Myrs. Thus the lower η models, which reach their cooling radii first and $R2_W$ last, spend the most time in isothermal motion

whilst in the dense neutral region. These lower η models also have the greatest GMC radii, which allows significant quantities of neutral gas and dust to accumulate in the shell over their lifetimes. This also means these lower η models will have the highest opacity at early times and conversely, dust in higher η models will not contribute until later times.

The supershell growth is the partner of the superbubble growth due to the relative compression factors in the adiabatic and isothermal phases. At early times the shells show rapid growth as the density ratio across the shock is limited to 4 and this is inversely proportional to the supershell width. However, once the cooling radius has been reached the shell growth slows as the compression factor becomes unlimited and a function of the dropping velocity. On exit from the ambient region the shell again undergoes volume growth due to the increase in the external ambient sound speed and the consequent affect on the compression factor.

This concludes the chapter developing the supernovae solution relationships required by GEM to calculate the evolution of superbubble under the influence of a continuous energy input. It is now possible to consider the potential affect of the superbubble expansion on a system's gas and dust density distribution and calculation of the optical depth along a line of sight required for the radiative transfer code.

Chapter 5

Expressions for the Optical Depth

As the superbubble progresses through the giant molecular cloud, it heats, accelerates and compresses the overtaken gas and attendant dust into the supershell, thereby altering the optical depth along a line of sight as it evolves.

To better understand the evolution of the optical depth, this chapter begins with a brief overview of the entire evolution of an example model system, beginning at t = 0 and ending when the superbubble reaches the outer radius of the ambient region at $R2_{SN}$. This overview is accompanied by a series of *sketches* depicting the contribution to the total extinction from each region of the system: the HII, neutral and ambient regions and the supershell, to the total optical depth, illustrated as snapshots in time.

The optical depth and the gas density are intimately linked so the expressions describing the density of the HII region, supershell, neutral and ambient regions are then briefly re-iterated for easy reference purposes.

As the supershell contains the entire swept up mass of the system, its temperature is an important quantity as this essentially determines the amount of dust that can condense out of the gas and contribute to the opacity. The three step process developed by the thesis author for calculating the supershell temperature is therefore considered in some depth, with accompanying figures, for the adiabatic and isothermal motion phases.

Having obtained expressions for the shell temperature and dust condensation, the optical depth equations developed by the thesis author are compiled and the inputs required by DaRT to define the dust density distribution generated. These expressions were programmed into the bespoke *GEM* computer code and the variation of the extinction with time obtained.

The second section of this chapter considers the behaviour of these distributions for different combinations of the η and M_{GMC} parameters on the model grid.

5.1 Evolution of an Example Model System

Each of the models in the parameter space has a different stellar luminosity and Equation 4.42 for the cooling radius R_c shows this has a considerable effect on the location of the R_c. For example, collapse of the adiabatic shell into the radiating shell can occur inside the ionized HII region, within the neutral region or outside the GMC altogether, depending on the particular balance of stellar luminosity to cloud mass. R_c is therefore pivotal in determining which form of motion for $R_{SN}(t)$ must be applied, and into what density, for the system to be modelled successfully over its evolution.

For simplicity the model system evolution discussed in this section will describe a situation where R_c occurs between $R_W(t)$, the HII region boundary and $R2_W$, the edge of the neutral cloud. The discussion is augmented by Figures 5.1, 5.2 & 5.3, which are *sketches* depicting the contribution from each region of the system to the optical depth, as snapshots in time. It is important to note that these sketches are simply *illustrative*: the magnitude of each component and its radius only *reflects* the correct values, as very small contributions from, for example, the ambient region have been amplified so that the general scheme adopted may be established. The behaviour of the optical depth and regional density is examined in a more rigorous and quantitative manner later in this chapter.

Beginning with Figure 5.1, plot (a) shows the state of the system at $t \approx 0$. The stars have only just switched on and the major contribution to the optical depth is shown in pink as $A_v^n(t)$; being the extinction due to dust in the neutral region. $A_v^\alpha(t)$ is the extinction due to sparse dust in the ambient region outside the GMC ie., over the column length [$R2_{SN}$ - $R2_W$] with $R2_W$ and $R2_{SN}$ the outer radii of the GMC and system respectively. $R_1(t)$ is the inner dust radius.

On plot (b), the ionization front has now moved into the cloud and its passage has heated the gas and evaporated the dust, resulting in the small contribution shown in red $A_v^{Wi}(t)$, this being the dust density in the ionized region multiplied by its column length [$R_W(t)$ - $R_1(t)$]. The constant dust condensation factor for the HII region, at $Fd^{Wi} = 0.2$, ensures 20% of the dust condenses out of the bubble at all times. Plot (c) shows a time

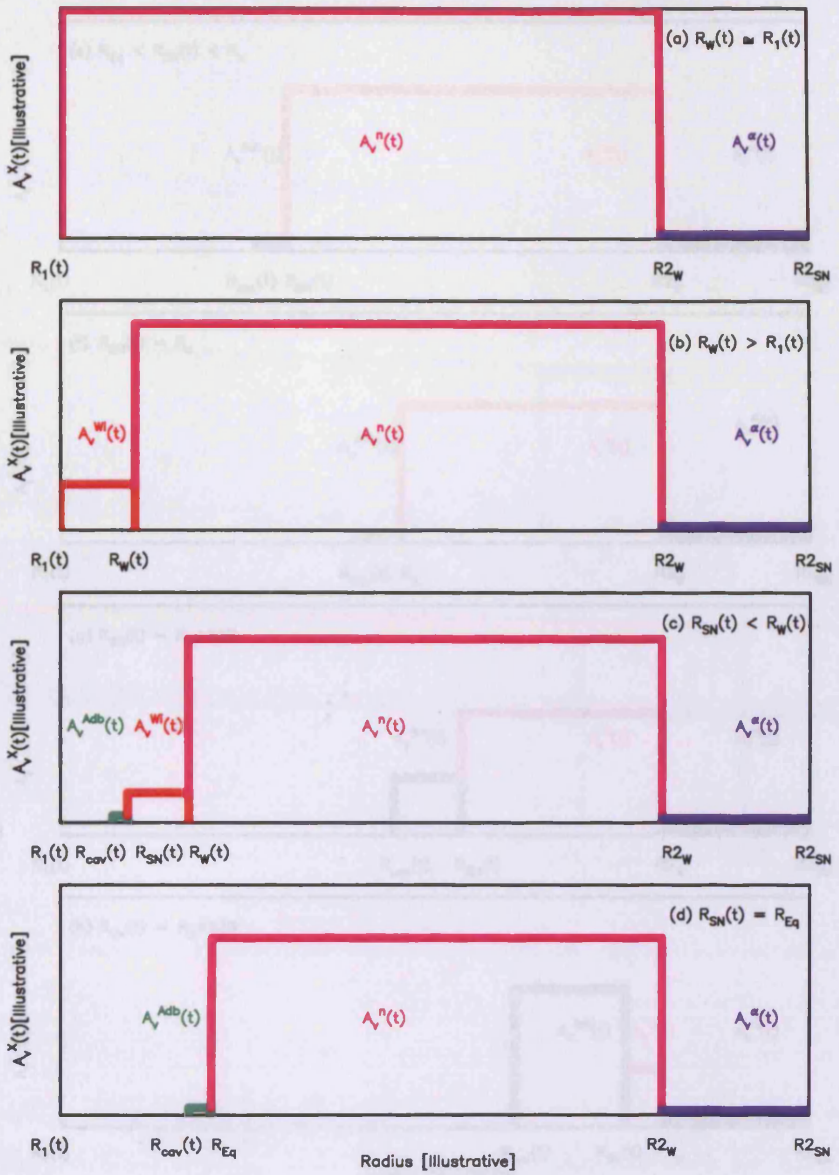

Figure 5.1: Contributions to $A_v^{TOT}(t)$ from different regions of the system as it evolves. $A_v^n(t)$ and $A_v^\alpha(t)$ represent the extinction due to the neutral and ambient regions respectively whilst $A_v^{Wi}(t)$ and $A_v^{SH}(t)$ illustrate the visual extinction from the ionized HII region and adiabatic shell respectively. Plot (a) shows the system at very early times, where the HII region IF has yet to make significant impact on the neutral cloud and lot (b) shows the HII region beginning to contribute. In plot (c) the adiabatic shell is trapped within the IF and whilst its volume is growing rapidly, it is essentially a dust-free cavity. Plot (d) shows the point at which the IF is overtaken by the superbubble and the original HII region ceases to contribute to $A_v^{TOT}(t)$.

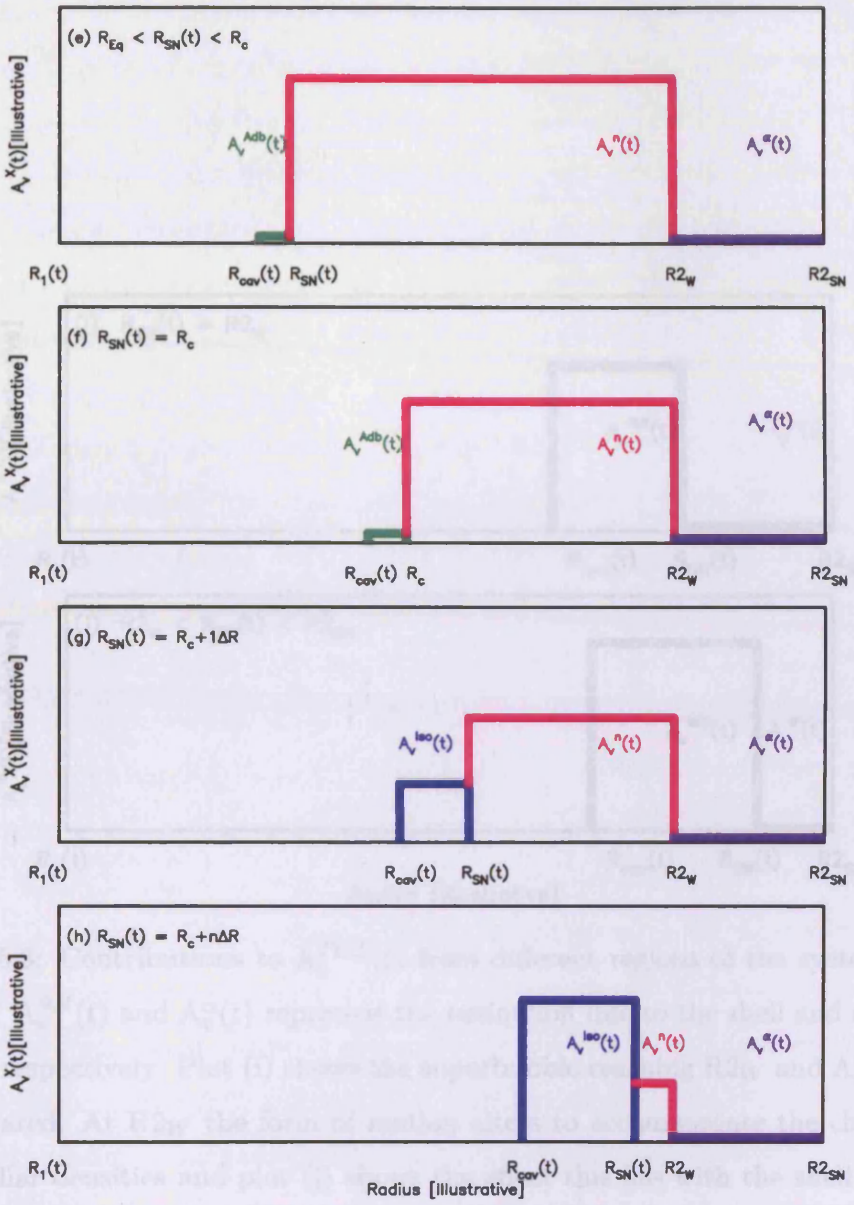

Figure 5.2: Contributions to $A_v^{TOT}(t)$ from different regions of the system as it evolves. $A_v^{SH}(t)$, $A_v^n(t)$ and $A_v^\alpha(t)$ represent the extinction due to the shell, neutral and ambient regions respectively. Plot (e) shows the superbubble expanding adiabatically through the neutral GMC without contributing to the extinction and $A_v^n(t)$ dropping rapidly. Plot (f) shows R_c, where the supershell collapses, begins isothermal motion and becomes an emitting region, whilst plot (g) illustrates the rise in extinction this provides. Plot (h) shows the superbubble approaching $R2_W$, with all the dust previously contained within $R_{SN}(t)$ now contained in the optically thick shell.

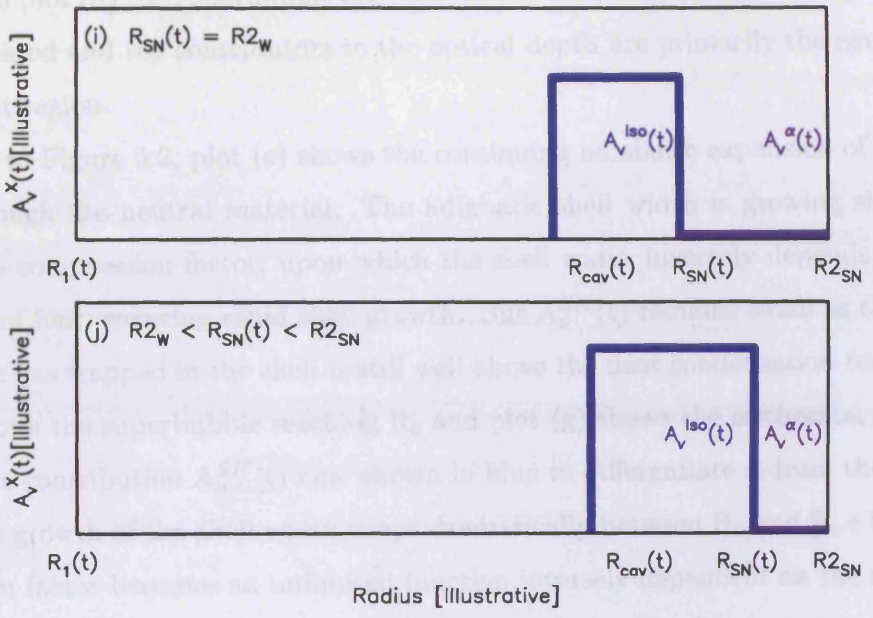

Figure 5.3: Contributions to $A_v^{TOT}(t)$ from different regions of the system as it evolves. $A_v^{SH}(t)$ and $A_v^{\alpha}(t)$ represent the extinction due to the shell and ambient regions respectively. Plot (i) shows the superbubble reaching $R2_W$ and $A_v^n(t)$ has disappeared. At $R2_W$ the form of motion alters to accommodate the change to interstellar densities and plot (j) shows the effect this has with the shell volume growing more rapidly than previously and the consequent drop in the extinction due both to volume dilution and the sparsity of the upstream density. The contribution $A_v^{\alpha}(t)$ begins to falls once the superbubble has exited the GMC, reaching zero at $R2_{SN}$(t=80Myrs).

after the first supernova has exploded and the superbubble has begun its expansion into the HII region. The contribution from the adiabatic shell, shown in green as $A_v^{SH}(t)$, is the total merged supershell width $R_{SH}(t) = [R_{SN}(t) - R_{cav}(t)]$, where $R_{cav}(t)$ is the inner shell radius, multiplied by its dust density. In this initial hot, energetic phase the supershell width grows rapidly but contributes essentially zero to the dust extinction. Finally, on Figure 5.1 in plot (d) the superbubble has reached the outer edge of the HII region, $A_v^{Wi}(t)$ has disappeared and the contributors to the optical depth are primarily the neutral cloud and ambient region.

Moving to Figure 5.2, plot (e) shows the continuing adiabatic expansion of the superbubble through the neutral material. The adiabatic shell width is growing significantly because the compression factor, upon which the shell width inversely depends, is limited to a factor of four, ensuring rapid shell growth. But $A_v^{SH}(t)$ remains small as the temperature of the gas trapped in the shell is still well above the dust condensation temperature. Plot (f) shows the superbubble reaching R_c and plot (g) shows the isothermal shell forming, with its contribution $A_v^{SH}(t)$ now shown in blue to differentiate it from the adiabatic phase. The growth of the shell width drops dramatically between R_c and $R_c+1\Delta R$ as the compression factor becomes an unlimited function inversely dependent on the ratio of the square of the velocity of the superbubble to the sound speed in the neutral material. The magnitude of the shell contribution $A_v^{SH}(t)$ therefore continues to grow as radiation of heat allows the shell temperature to drop and the shell becomes increasingly dust-dense. Plot (h) shows the isothermal shell at a later time whilst still contained within the neutral region. Its contribution has now grown such that it dwarfs that from the neutral dust and has become the primary contributor to the opacity.

Finally on Figure 5.3, plot (i), the leading front of the superbubble has reached the outer edge of the GMC and all material that was in the cloud at $t \approx 0$ years is now contained within the supershell. Plot (j) shows the shell volume again undergoing more rapid growth upon entry to the ambient region as the external sound speed in the ambient interstellar gas at $c_\alpha = 1 \times 10^5 cm^{-1}$ is higher than that in the neutral region at $c_n = 4.5 \times 10^4 cm^{-1}$, so that the compression factor for the forming shell width reduces (Dyson & Williams 1997*b*). However this also volume dilutes the material within the shell leading to a drop in dust density and hence extinction. Eventually the superbubble velocity will either drop below the ambient sound speed and the shell will lose integrity and break up (R_v) or the superbubble will continue intact until $t = 80$Myrs when the modelling ends.

5.2 Review of Gas Density Equations

As the optical depth equations developed in this chapter reply on the density of the different regions of a model system, it is perhaps convenient to briefly re-iterate those expressions given in Chapter 3 which define the density of the neutral and ionized regions in the HII region phase. Also re-iterated are the equations given in Chapter 4 for the supershell density in both the adiabatic and isothermal phases.

5.2.1 The HII region Phase: $t \leq t_{SNstart}$

The first supernova explodes at $t_{SNstart} = 3.71$Myrs so at all prior times the ionized, neutral and ambient densities along a line of sight are governed by the HII region solution.

Ionized Density

The uniform density of the ionized HII region $\rho^{Wi}(t)$ is given at these times by Equation 3.30, derived in section §3.6 using Efstathiou *et al.* (2000)

$$\rho^{Wi}(t) = \rho^{n_o}\left[\frac{R_W(t)}{R_s(t)}\right]^{-\frac{3}{2}} \tag{5.1}$$

ρ^{n_o} is the initial density of the neutral material, with $\rho^{n_o} = m_H n_o$ where n_o is the initial number density of neutral material, m_H is the mass of the hydrogen atom, $R_W(t)$ is the radius of the HII region and $R_S(t)$ is the Stromgren radius ERR00.

Neutral Density

The neutral density $\rho^n(t)$ is given by Equation 3.33, also derived in section §3.6

$$\rho^n(t) = \rho^{n_o}\left[\frac{1-\left(\frac{R_W(t)}{R2_W}\right)^{\frac{3}{2}}\left(\frac{R_s(t)}{R2_W}\right)^{\frac{3}{2}}}{1-\left(\frac{R_W(t)}{R2_W}\right)^{3}}\right] \tag{5.2}$$

where $R2_W$ is the outer radius of the GMC (ERR00).

Ambient Density

The ambient density is given by $\rho^{\alpha}(t) = 1 m_H cm^{-3}$ (Dyson & Williams 1997*b*). The location of the density breaks and the ratio of densities across those breaks needed for DaRT in the HII region phase were discussed in §3.6.6

5.2.2 The Supernova Phase: $t_{SNstart} < t \leq t_{R2_{SN}}$

Once the supernova energy injection has begun at $t_{SNstart}$, the adiabatic equation of motion governing $R_{SN}(t)$ is given by 4.16, which remains valid until the cooling radius R_c is reached. Thereafter, isothermal motion in the neutral region is described by Equation 4.45 and in the ambient region by Equation 4.54.

Density of First Shell Formed

The density of the first shell only formed whilst the superbubble is trapped within the ionized HII region, is easily found by re-arranging the mass conservation expression of Equation 4.24

$$\rho^{SH}(t) = \frac{4\pi}{3} \frac{\rho^{Wi}(t-\Delta t)[R_{SN}^3(t) - R_{SN}^3(t-\Delta t)]}{3R_{SN}^2(t)\Delta R_{shell}(t)} \tag{5.3}$$

where ΔR_{SH} is the width of the first shell formed.

Supershell Density for Motion in the HII Region

Moving to the second and all future times when the supershell is in adiabatic motion through the ionized HII region, the entire mass swept-up by the superbubble resides in the supershell and mass conservation allows its density $\rho^{SH}(t)$ to be derived

$$\rho^{SH}(t) = \frac{M^{SH}(t-\Delta t) + \rho^{Wi}(t-\Delta t)[R_{SN}^3(t) - R_{SN}^3(t-\Delta t)]}{R_{SN}^3(t) - R_{cav}^3(t)} \tag{5.4}$$

where $R_{cav}(t)$ is the inner shell radius given by $R_{cav}(t) = R_{SN}(t)$ - $R_{SH}(t)$.

Supershell Density at the HII Region Boundary

The equations quantifying the radius of the HII region $R_W(t)$ and that of the superbubble $R_{SN}(t)$ are never equivalent due to the restriction of a 0.1Myr time-step in the STARBURST99 output. Hence R_{Eq} is taken as the last point where $R_{SN}(t\text{-}\Delta t) < R_W(t)$ - inside the HII region - and $R_{SN}(t) > R_W(t)$ - outside the HII region. Thus is the step when the superbubble overtakes the HII region boundary the supershell density must be altered to include the contribution both from the ionized region and the neutral region.

$$\rho^{SH}(t) = \frac{\rho^{Wi}(t-\Delta t)[R_W^3(t) - R_{SN}^3(t-\Delta t)] + \rho^{n}(t)[R_{SN}^3(t) - R_W^3(t)]}{[R_{SN}^3(t) - R_{cav}^3(t)]} \tag{5.5}$$

Supershell Density For Motion In Neutral Region

Once the supernova bubble has exited the HII region and entered the neutral region, Equation 5.4 for the supershell density becomes

$$\rho^{SH}(t) = \frac{M^{SH}(t-\Delta t) + \rho^{n}(t-\Delta t)[R^{3}_{SN}(t) - R^{3}_{SN}(t-\Delta t)]}{R^{3}_{SN}(t) - R^{3}_{cav}(t)} \tag{5.6}$$

Supershell Density for Motion in Ambient Region

The final variation to the supershell density occurs when the superbubble enters the rarefied ambient region external to the giant molecular cloud

$$\rho^{SH}(t) = \frac{M^{SH}(t-\Delta t) + \rho^{\alpha}(t-\Delta t)[R^{3}_{SN}(t) - R^{3}_{SN}(t-\Delta t)]}{R^{3}_{SN}(t) - R^{3}_{cav}(t)} \tag{5.7}$$

where ρ^{α} is the ambient region density.

Scheme for the Total Shell Width

As discussed in §4.1 and reiterated here for ease of reference, the paradigm for the supershell is that at each time-step, the shell width formed $\Delta R_{shell}(t)$ is calculated using Equation 4.25 and Equation 4.50 in the adiabatic and isothermal phases respectively. This new shell is then merged with all pre-existing shells to generate a supershell of total width $R_{SH}(t)$

$$R_{SH}(t) = \sum_{R_{SN_{Start}}+1\Delta R}^{R_{SN}(t)} \Delta R_{shell}(t) \tag{5.8}$$

The inner radius of the supershell $R_{cav}(t)$, is given by

$$R_{cav}(t) = R_{SN}(t) - R_{SH}(t) \tag{5.9}$$

5.2.3 Shell Temperature: $R_{SN}(t_{SN})+1\Delta t$

On the **first step** of the superbubble into the HII region, the number density of the gas $n_G(1\Delta t)$ overtaken by the leading edge of the supernova bubble, given on Figure 5.4 by the red stripes on plot (a), is

$$n_G(1\Delta t) = \frac{4\pi}{3}\frac{\rho^{Wi}(t_{SN})[R^{3}_{SN}(1\Delta t) - R^{3}_{SN}(t_{SN})]}{V_G(1\Delta t)m_H} \tag{5.10}$$

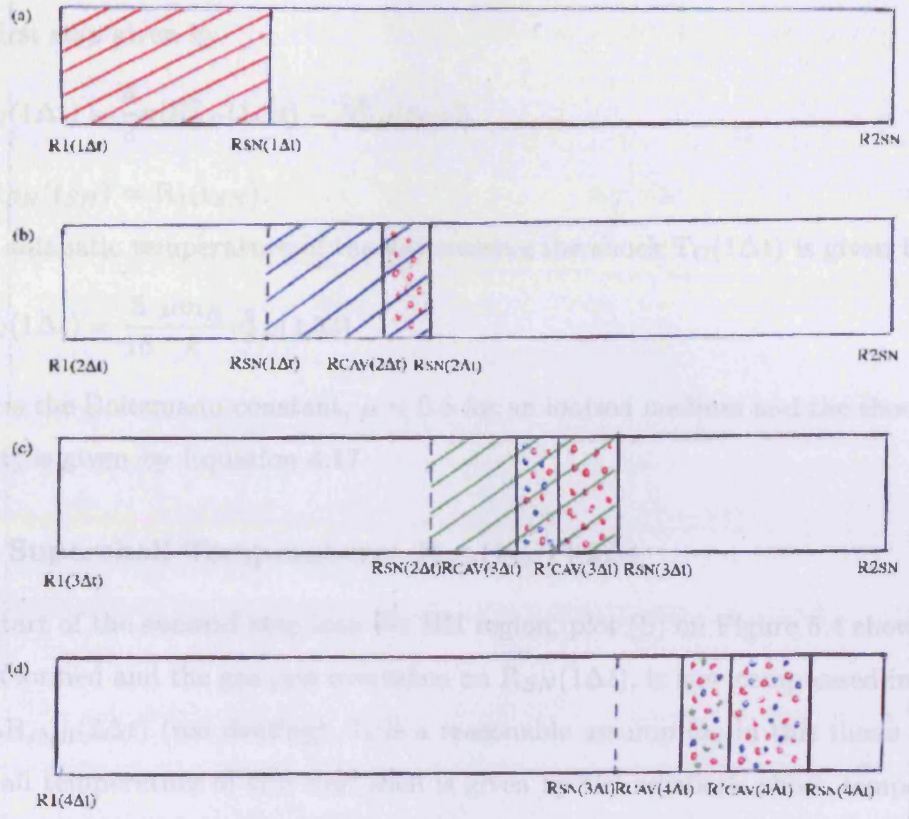

Figure 5.4: Calculation of Shell Temperature: In plot (a) the gas overtaken in the first step is given by the red stripes and has the adiabatic shock temperature $T_G(t)$. In plot (b) the first shell has formed and the gas just overtaken on $R_{SN}(1\Delta t)$ is now compressed into the shell of width $\Delta R_{shell}(2\Delta t)$, indicated by the red dotting. The blue stripes on plot (b) show the gas overtaken at the second step $R_{SN}(2\Delta t)$. In plot (c) the gas overtaken at $R_{SN}(2\Delta t)$ is now assumed to form a new shell of width $\Delta R_{shell}(3\Delta t)$, shown by the blue dotting. This new shell has also merged with the shell formed at the first step and the gas overtaken on the first step is now assumed to occupy its entire volume, indicated by the red dotting. The gas overtaken on the third step is shown on plot (c) by the green stripes. In plot (d) the blue and red gas overtaken at steps two and one is now assumed to occupy the entire merged shell volume, whilst that overtaken at step three is now given by the green dotting. The system then iterates.

where m_H is the mass of an hydrogen atom, $\rho^{Wi}(t_{SN})$ is the density of the ionized HII region that the supernova is expanding into and $V_G(1\Delta t)$ is the volume of the gas overtaken on the first step given by

$$V_G(1\Delta t) = \frac{4}{3}\pi[R^3_{SN}(1\Delta t) - R^3_{SN}(t_{SN})] \tag{5.11}$$

where $R_{SN}(t_{SN}) = R_1(t_{SN})$.

The adiabatic temperature of the gas crossing the shock $T_G(1\Delta t)$ is given by

$$T_G(1\Delta t) = \frac{3}{16}\frac{\mu m_H}{k} v^2_{SN}(1\Delta t) \tag{5.12}$$

where k is the Boltzmann constant, $\mu = 0.5$ for an ionized medium and the shock velocity $v_{SN}(1\Delta t)$ is given by Equation 4.17.

5.2.4 Supershell Temperature: $R_{SN}(t_{SN})+2\Delta t$

At the start of the **second** step into the HII region, plot (b) on Figure 5.4 shows the first shell has formed and the gas just overtaken on $R_{SN}(1\Delta t)$, is now compressed into shell of width $\Delta R_{shell}(2\Delta t)$ (red dotting). It is a reasonable assumption in this thesis work that the overall temperature of this first shell is given by the adiabatic shock temperature as the supershell contains only the shocked gas overtaken on the first step and no dust has been able to condense out. Thus

$$T_G(2\Delta t) = \frac{3}{16}\frac{\mu m_H}{k} v_{SN}(2\Delta t) \tag{5.13}$$

The number density $n_G(2\Delta t)$ of the gas compressed into this first shell is given by

$$n_G(2\Delta t) = \frac{4\pi}{3}\frac{\rho^{Wi}(1\Delta t)[R^3_{SN}(2\Delta t) - R^3_{SN}(1\Delta t)]}{V_G(2\Delta t)m_H} \tag{5.14}$$

The volume of the shell which this overtaken gas occupies is now given by

$$V_G(2\Delta t) = \frac{4}{3}\pi[R^3_{SN}(2\Delta t) - R^3_{cav}(2\Delta t)] \tag{5.15}$$

where $R_{cav}(2\Delta t) = R_{SN}(2\Delta t) - R_{SH}(2\Delta t)$ where at this time only $R_{SH}(2\Delta t) = \Delta R_{shell}(2\Delta t)$ with $\Delta R_{shell}(2\Delta t)$ being the width of the first shell formed.

5.2.5 Supershell Temperature: $R_{SN}(t_{SN})+3\Delta t$

At the start of the **third** expansion step, the gas overtaken at the second step (blue stripes) is assumed to form a new shell of width $\Delta R_{shell}(3\Delta t)$ (blue dots). This shell has

now merged with the shell formed at the second step $\Delta R_{shell}(2\Delta t)$ and assuming that the newly formed shell volume is small compared to the total merged volume, simply, these shell can be added to find the total merged shell width $R_{SH}(3\Delta t)$ which is given by $R_{SH}(3\Delta t) = \Delta R_{shell}(1\Delta t) + \Delta R_{shell}(2\Delta t)$.

The first gas component to consider is that accumulated at $R_{SN}(1\Delta t)$ (red stripes) and compressed into the shell formed at the second step $\Delta R_{shell}(2\Delta t)$. As the shell is trapped on the surface of the superbubble, as the bubble expands the volume of the shell increases. Additionally, as the two shells formed so far are assumed to merge into one smooth supershell, it is likely that the second shell would be backfilled by the gas contained in the first shell. In order to take some account of this dynamic, the simple assumption is made that this compressed gas is volume diluted into the new, total, merged supershell volume $V_{SH}(3\Delta t)$ (red dots on plot (c)). This is accomplished using the first law of thermodynamics together with the adiabatic equation of state

$$n_G(2\Delta t)T_G(2\Delta t)V_G^{\gamma}(2\Delta t) = constant = n_{SH}(3\Delta t)T_{SH}(3\Delta t)V_{SH}^{\gamma}(3\Delta t) \tag{5.16}$$

where on the left hand side the values represent the compressed number density, temperature and volume of the shell formed at $R_{SN}(2\Delta t)$, ($V_G(2\Delta t)$ and on the right hand side, the variables $n_{SH}(3\Delta t), T_{SH}(3\Delta t)$ and $V_{SH}^{\gamma}(3\Delta t)$ are the new diluted number density, temperature and volume of this gas at $R_{SN}(3\Delta t)$. In Equation 5.16, $\gamma = 5/3$ which is the adiabatic index for atomic species. The shell temperature $T_G(2\Delta t)$ is given by the adiabatic gas temperature of Equation 5.12 and this temperature then drops via volume dilution to $T_{SH}(3\Delta t)$. For convenience this temperature has been named the 'wolume diluted temperature' to identify it as that obtained after the shell has expanded in a step and to differentiate it from the overtaken shocked gas temperature and the overall gas temperature used for the dust density distribution.

Thus rearranging Equation 5.16 for $T_{SH}(3\Delta t)$ gives the new volume diluted temperature of the gas

$$T_{SH}(3\Delta t) = \left(\frac{n_G(2\Delta t)}{n_{SH}(3\Delta t)}\right) T_G(2\Delta t) \left(\frac{V_G(2\Delta t)}{V_{SH}(3\Delta t)}\right)^{\gamma} \tag{5.17}$$

where $V_{SH}(3\Delta t)$ is the volume of the merged supershell such that

$$V_{SH}(3\Delta t) = \frac{4}{3}\pi[R_{SN}^3(3\Delta t) - R_{cav}^3(3\Delta t)] \tag{5.18}$$

Now considering the number density of this volume diluted gas. As the only material being volume diluted into the new total merged shell volume is that from the shell formed

at the second step, ($\Delta R_{shell}(2\Delta t)$), the number density can be written

$$n_{SH}(3\Delta t) = \frac{\rho^{SH}(2\Delta t)[R^3_{SN}(2\Delta t) - R^3_{cav}(2\Delta t)]}{[R^3_{SN}(3\Delta t) - R^3_{cav}(3\Delta t)]m_H} \tag{5.19}$$

where $\rho^{SH}(2\Delta t)$ is given by Equation 5.4 and m_H is the mass of the hydrogen atom. Now considering the energy of the volume diluted gas $E_{SH}(3\Delta t)$, this can be written

$$E_{SH}(3\Delta t) = n_{SH}(3\Delta t)V_{SH}(3\Delta t)\frac{3}{2}kT_{SH}(3\Delta t) \tag{5.20}$$

Setting $N_{SH}(3\Delta t) = n_{SH}(3\Delta t).V_{SH}(3\Delta t)$ to be the volume diluted number of hydrogen atoms, Equation 5.20 becomes

$$E_{SH}(3\Delta t) = N_{SH}(3\Delta t)\frac{3}{2}kT_{SH}(3\Delta t) \tag{5.21}$$

Now considering the second component of the gas; that *overtaken* at the second step ($R_{SN}(2\Delta t)$) (blue stripes) and compressed into the small shell formed at this third step $\Delta R_{shell}(3\Delta t)$ shown on plot (c) by the blue dotting. The number density of this gas is given by

$$n_G(3\Delta t) = \frac{4\pi}{3}\frac{\rho^{Wi}(2\Delta t)[R^3_{SN}(2\Delta t) - R^3_{SN}(1\Delta t)]}{V_G(3\Delta t)m_H} \tag{5.22}$$

where m_H is the mass of an hydrogen atom, $\rho^{Wi}(2\Delta t)$ is the density of the ionized HII region that the supernova expanded into and $V_G(3\Delta t)$ is the volume of the small shell formed at the third step such that

$$V_G(3\Delta t) = \frac{4}{3}\pi[R^{3'}_{cav}(3\Delta t) - R^3_{cav}(3\Delta t)] \tag{5.23}$$

where $R^{3'}_{cav}(3\Delta t)$ gives the inner radius of the first shell such that Equation 5.23 gives the volume of the second shell only.

The temperature of this gas is given by the adiabatic gas temperature such that

$$T_G(3\Delta t) = \frac{3}{16}\frac{\mu m_H}{k}v_{SN}(3\Delta t) \tag{5.24}$$

The energy of this compressed gas can now be written

$$E_G(3\Delta t) = n_G(3\Delta t)V_G(3\Delta t)\frac{3}{2}kT_G(3\Delta t) \tag{5.25}$$

And taking $N_G(3\Delta t) = n_G(3\Delta t).V_G(3\Delta t)$ to be the compressed number of hydrogen atoms, Equation 5.25 becomes

$$E_G(3\Delta t) = N_G(3\Delta t)\frac{3}{2}kT_G(3\Delta t) \tag{5.26}$$

Now it is possible to equate the energies of the volume diluted and the compressed gas to get the overall temperature of the merged supershell $T_{SH+G}(3\Delta t)$ such that

$$E_{SH+G}(3\Delta t) = n_{SH+G}(3\Delta t)V_{SH+G}(3\Delta t)\frac{3}{2}kT_{SH+G}(3\Delta t) \tag{5.27}$$

and substituting using equations 5.21 and 5.26, the overall supershell temperature becomes

$$T_{SH+G}(3\Delta t) = \frac{N_{SH}(3\Delta t)T_{SH}(3\Delta t) + N_G(3\Delta t)T_G(3\Delta t)}{N_{SH+G}(3\Delta t)} \tag{5.28}$$

where

$$N_{SH+G}(3\Delta t) = n_{SH+G}(3\Delta t).V_{SH+G}(3\Delta t) \tag{5.29}$$

and

$$n_{SH+G}(3\Delta t) = \frac{M^{SH}(2\Delta t) + \rho^{SH}(2\Delta t)[R^3_{SN}(2\Delta t) - R^3_{SN}(1\Delta t)]}{[R^3_{SN}(3\Delta t) - R^3_{cav}(3\Delta t)]m_H} \tag{5.30}$$

and

$$V_{SH+G}(3\Delta t) = \frac{4}{3}[R^3_{SN}(3\Delta t) - R^3_{cav}(3\Delta t)] \tag{5.31}$$

such that Equation 5.31 is the volume of the merged supershell.

Equation 5.28 is essentially the mass weighted particle temperature of all the gas in the merged supershell, at the third step, assuming that all particles in the shell are hydrogen.

5.2.6 Supershell Temperature: $R_{SN}(t_{SN})+4\Delta t$ On-wards

The gas overtaken on the third step into the ionized sphere, given on plot (c) by the green stripes, is accounted for at the start of the fourth step in a similar way to the previous gas components just described. Thus, the expressions derived are now be generalized for all times when the supershell is in adiabatic motion.

Beginning with the variables for the overtaken gas in each time step, the number density $n_G(t)$ is given by Equation 5.22, the volume $V_G(t)$ is given by Equation 5.23 and the adiabatic shock temperature $T_G(t)$ by Equation 5.24 where in each of these equations Δt is iterated ($t_{SN} = 0$).

Considering $T_{SH}(t)$, the temperature of the gas which was compressed into the shell at the previous step and is now diluted into the merged current shell volume. Because the shells are formed in arrears, the reference number density, volume and temperature in Equation 5.17 for $T_{SH}(t)$ were given by the overtaken gas adiabatic temperature for

the second step into the cloud. However, from the third step the reference variables are changed to be a function of the overall number density, temperature and volume calculated for the previous shell, so Equation 5.17 becomes

$$T_{SH}(t) = \left(\frac{n_{SH+G}(t-\Delta t)}{n_{SH}(t)}\right) T_{SH+G}(t-\Delta t) \left(\frac{V_{SH+G}(t-\Delta t)}{V_{SH}(t)}\right)^{\gamma} \tag{5.32}$$

which is the diluted gas temperature at all future times in a system's evolution. This gas has a volume V_{SH}(t) given by Equation 5.18 and the number density n_{SH}(t) is given by Equation 5.19 with Δt iterated.

Similarly the variables for the new merged shell T_{SH+G}(t), N_{SH+G}(t), n_{SH+G}(t) and V_{SH+G}(t) are given by Equations 5.28 to 5.31, again, with Δt iterated.

Nearly all the equations listed in the last three paragraphs remain valid for a system's entire adiabatic evolution, but those that have been couched in terms of the ionised density ρ^{Wi}(t) change to be in terms of the neutral density ρ^{n}(t) once the IF has been overtaken.

5.3 Supershell Temperature in Isothermal Phase

The end of the adiabatic phase is reached when the supershell has lost sufficient heat for it to catastrophically collapse into a radiating zone at the cooling radius R_c, whereupon the isothermal phase begins (MM88).

However, a difficulty occurs with assuming that the shell achieves e.g., $T_{SH+G}(t) \leq T_{cond}$ immediately upon R_c in the thesis work. As mentioned in §4.1, the equations for the superbubble and shell were developed by MK87 and MM88 assuming a uniform neutral density of $n_o = 1\text{cm}^{-3}$ which is indicative of the interstellar medium. This assumption ensures that the shell is able to cool radiatively.

First mentioned in §3.6.1, the assumption of equilibrium presumes that although ionization of the neutral gas generates more photons capable of ionizing HI, these are absorbed by further neutral HI in the near vicinity and recombinations balance ionization - the 'on-the-spot' approximation. This means that once the supershell has collapsed at the cooling radius, it is able to maintain a low temperature via e.g., forbidden line or bound-bound cooling.

However, the thesis has used an average density of $n_o = 300\text{cm}^{-3}$ and central sources having very strong UV radiation which is more representative of a GMC. Thus, the supershell is extremely dense at R_c so it is likely that ionization and recombination within

the shell will not balance. In turn this implies that photons will be unable to escape due to the very short mean free path length through the dense shell. This could lead to heat retention as radiative loss will be diminished and therefore the thesis supershells will be hotter than those calculated assuming ionization equilibrium.

Thus, in the isothermal phase, the supershell temperature calculation needs to now take some account of this lack of heat loss from the shell as well as the accommodating the temperature of the gas already existing in the supershell from the adiabatic phase. Whilst he neutral gas overtaken in the isothermal phase can now cross the shock and maintain its cool entry temperature, the cooling via the volume dilution is reduced due to the increase in the shock compression factor.

The temperature of the supershell in the isothermal phase is therefore modelled in the same way as in the adiabatic phase, with the exception that the gas crossing the shock T_G is no longer heated by its passage through the shock, but rather retains its pre-shock temperature. This coupled to the volume dilution is presumed to cool the shell down and thus the supershell cools more slowly after collapse, rather than experiencing a dramatic and permanent drop in temperature at the cooling radius. In this way an attempt has been made to accommodate the large density of the shell and the effect this has on radiation of its heat.

Therefore, for all times whilst the superbubble is travelling though the neutral region in the isothermal phase, the material accumulated in each shell travels across the discontinuity and emerges with the same temperature it had when it entered. The sound speed in the neutral region is given by

$$c_n^2 = \frac{T_n k}{\mu m_H} \tag{5.33}$$

with $c_n = 4.5 \text{ x } 10^4$ cms^{-1} (Dyson & Williams 1997*b*), $\mu = 1$, the mass of the hydrogen atom $m_H = 1.67 \text{ x } 10^{-24}$gm and the Boltzmann constant k = 1.381x10^{-16}ergK^{-1}. Resolving Equation 5.33 and referring back to Equation 5.12, the temperature of the gas overtaken by the shock front and entering the shell is now given by

$$T_G(t) = T_n (= 25K \tag{5.34}$$

Finally, when the superbubble exits the neutral GMC and enters the ambient, the temperature of the gas overtaken by the shock front again changes to reflect the ambient

gas temperature. The sound speed in the ambient region is given by

$$c_\alpha^2 = \frac{T_\alpha(t)k}{\mu m_H} \tag{5.35}$$

with c_α = 1 x 10^5 cms^{-1} (Dyson & Williams 1997*b*). The temperature of gas transferred to the shell in Equation 5.12 therefore becomes

$$T_G(t) = T_\alpha = 120K \tag{5.36}$$

which is hotter than the neutral region due to the change in gas density (Dyson & Williams 1997*b*).

5.3.1 Dust Condensation

Finally in this section, the supershell temperature can now be related to the quantity of dust that can reform to contribute to the opacity. For this calculation the work of Bowen (1988) was used. This author considered the difficult problem of dust formation and dynamics and assumed, under the conditions of a strong radiation field with grains at the local equilibrium temperature, that the fraction of dust which could condense out of a field at temperature $T_{SH+G}(t)$ would be given by

$$Fd^{SH}(t) = \frac{1}{\left[1 + exp\left(\frac{T_{SH+G}(t) - T_{cond}}{\Delta T}\right)\right]} \tag{5.37}$$

where T_{cond} is the condensation temperature, taken here as 1600K for a dust mixture of primarily silicate and carbon with PAHs, ΔT describes the width of the condensation range set at 100K and $Fd^{SH}(t)$ is the fraction of dust which condenses out of the gas.

This empirical law essentially mimics the condensation curve and has 50% of the dust condensing out at $T_{SH+G}(t)$ = 1600K, $Fd^{SH}(t)$ = 0.5 and considerably less at higher temperatures. The behaviour of the dust condensation parameters for all star formation efficiencies on the $M_{GMC} = 10^8 M_\odot$ parameter grid are also shown graphically in the next section §5.5 where the behaviour of the optical depth is more rigorously discussed.

The temperature distributions for $T_G(t)$, $T_{SH}(t)$ and $T_{SH+G}(t)$ as a system evolves, for each η on the $M_{GMC} = 10^8 M_\odot$ model grid are shown graphically in the next section §5.5 as is the behaviour of the dust condensation parameter just discussed.

Having now considered the temperature calculation in some depth, attention can be returned to the remainder of the expression needed to generate the dust density distribution and input variables needed for the DaRT radiative code.

5.4 Optical Depth Equations & DaRT Inputs

In order to generate the emergent spectral energy distributions for the starburst component, the optical depth along a line of sight must be obtained for all times at which an SED will be generated. The model SED's are to be sampled at Δt_{SED} = 1Myr for the first 10Myrs and Δt_{SED} = 10Myr between 10- and 80Myrs, with this preferential sampling accounting for early times when most source variation is observed. Having obtained the dust density distribution, it is irradiated in DaRT by the appropriate STARBURST99 source function, the radiative transfer of flux calculated and the SEDs produced.

As first discussed in §3.6.7 DaRT requires not only the dust-density in a particular region i.e.: the ionized HII region or the supershell, but also the boundaries between those regions. As such, Figure 5.1 can be used initially as a reference to compose the total optical depth along a line of sight and locate the regional boundaries which define the radial density distribution for input to DaRT.

Optical Depth whilst in Motion through the HII Region

As a first example it is convenient to begin with the optical depth equation for all times when the superbubble is trapped within the HII region, as illustrated on Plot (c) Figure 5.1. The adiabatic shell has formed, as indicated by the green line and although the shell has little to contribute to the optical depth at this time due to its high temperature, it must still be included in the opacity calculation along the line of sight for DaRT. The extinction from the supershell can be written

$$A_v^{SH}(t) = 1.086 \frac{\tau_{voW}}{k_w 2 n_{av} m_H R2_W} (F d^{SH}(t) \rho^{SH}(t) [R_{SN}(t) - R_{cav}(t)]) \tag{5.38}$$

where k_w = 4.25 x 10^{-22}. τ_{voW} is the reference τ and is the radial optical depth in the visual from the centre of the GMC to its surface. Both these quantities were fully discussed in §3.6 with Equation 3.36 now re-iterated for convenience

$$\tau_{v_oW} = \frac{\sigma_{gr}}{m_{gr}} dg_r \rho_{n_o} R2_W \tag{5.39}$$

where σ_{gr} is the cross-section of a generic dust grain, m_{gr} is the mass of the generic dust grain, $dg_r = \rho_{dust}/\rho_{gas}$ is the dust-to-gas ratio and $R2_W$ is the outer radius of the GMC.

Moving radially outwards, the extinction due to the ionized HII region, shown on Figure 5.1 plot (c) in red, can be similarly composed

$$A_v^{Wi}(t) = 1.086 \frac{\tau_{voW}}{k_w 2 n_{av} m_H R2_W} (F d^{Wi} \rho^{Wi}(t) [R_W(t) - R_{SN}(t)]) \tag{5.40}$$

The neutral region extinction is given by

$$A_v^{Wi}(t) = 1.086 \frac{\tau_{voW}}{k_w 2 n_{av} m_H R2_W} (Fd^n \rho^n(t)[R2_W - R_{SN}(t)]) \quad (5.41)$$

whilst the final component of the total optical depth is provided by the ambient region external to the GMC

$$A_v^{\alpha}(t) = \frac{\tau_{voSN}}{k_{sn} n_\alpha m_H [R2_{SN} - R2_W]} (Fd^\alpha \rho^\alpha [R2_{SN} - R2_W]) \quad (5.42)$$

where k_{sn} = 4.93 x 10^{-22}, which was fully discussed in §3.6.6 and τ_{voSN} is the reference opacity in the ambient region.

It is then a simple task to set

$$\tau_v(t) = \frac{A_v(t)}{1.086} \quad (5.43)$$

and add the extinction from these four regions along the line of sight to generate the equation for the total optical depth at visual wavelengths, τ_v(t) for all times when the superbubble is trapped within the HII region

$$\tau_v(t) = \frac{\tau_{voW}}{k_w 2 n_{av} m_H R2_W} (Fd^{SH}(t) \rho^{SH}(t)[R_{SN}(t) - R_{cav}(t)] + Fd^{Wi} \rho^{Wi}(t)[R_W(t) - R_{SN}(t)]$$
$$+ Fd^n \rho^n(t)[R2_W - R_{SN}(t)]) + \frac{\tau_{voSN}}{k_{sn} n_\alpha m_H [R2_{SN} - R2_W]} (Fd^\alpha \rho^\alpha [R2_{SN} - R2_W]) \quad (5.44)$$

As described in §3.6 Fd^{Wi} = 0.2, Fd^n = 1 and Fd^α = 1 in all cases. The value Fd^{Wi} = 0.2 is taken directly from ERR00 while values of $Fd^n = Fd^\alpha$ = 1 at all times ensures that 100% of the dust contained in the shell condenses out of the gas. Fd^{SH}(t) is given by the temperature dependent formalisation of Bowen (1988) in Equation 5.37.

It can be seen from these equations that 100% of the neutral gas overtaken by the superbubble is transferred into the shell on a one-to-one basis, with no accommodation taken for possible ionization and hence, the doubling of the number of gas particles available that would entail. This is a reasonable assumption in this thesis work as substantial dust does not condense out of the hot gas until the temperature drops to T $\approx$ 1600K and any gas at that temperature would be in a neutral state. In essence therefore, the step whereby the gas is heated and potentially ionized, before cooling and returning to neutral, has been omitted and the material has been transferred to the supershell in its neutral state, where it remains. In future work where a fully 3-dimensional hydrodynamic treatment could be developed the proportion of ionized gas and the corresponding increase in density could be modelled.

DaRT Inputs whilst in Motion through the HII Region

DaRT requires the location of the density breaks R_{B_x}, or boundaries between the individual regions along a line of sight and these are given as a function of the outer radius of the system $R2_{SN}$. The density ratios ρ_{F_x} over those breaks are a function of the dust density in the region closest to the source - in this instance that of the adiabatic shell $Fd^{SH}(t)\rho^{SH}(t)$. Thus with reference to Figure 5.1, plot (c) the density breaks and ratios for all times when the superbubble is travelling in adiabatic motion through the ionized HII region can be written

$$R_{B1} = R_{SN}(t)/R2_{SN} \qquad \rho_{F1} = 0.2\rho^{Wi}(t)/Fd^{SH}(t)\rho^{SH}(t)$$
$$R_{B2} = R_{W}(t)/R2_{SN} \qquad \rho_{F2} = \rho^{n}(t)/Fd^{SH}(t)\rho^{SH}(t)$$
$$R_{B3} = R2_{W}(t)/R2_{SN} \qquad \rho_{F3} = \rho^{\alpha}(t)/Fd^{SH}(t)\rho^{SH}(t)$$

R_{B1} represents the change in density that occurs between the outer edge of the adiabatic shell and the ionized medium with the corresponding densities of those two regions providing the ratio over the break ρ_{F1}. R_{B2} describes the discontinuity between the outer edge of the HII region and the neutral region, with ρ_{F2} giving the HII region density as a function of the shell density. Finally R_{B3} characterises the boundary between the GMC and the ambient region, with the density ratio again given as a function of the shell density. Two more parameters complete the entries for DaRT and give the relationship between the source and the inner and outer dust radii such that

$$ERAT = R^{\star}(t)/R_{cav}(t) \qquad E = R_{cav}(t)/R2_{SN}$$

where $R^{\star}(t)$ is the source radius, which, in a similar way to calculation of the AGN model source radius R_{AGN}, is given as a function of the inner dust radius $R_1(t)$ by $R_{\star}(t) = 0.1^{1/2}R_1(t)$.

Thus, by specifying the total optical depth along a line of sight and then defining that in terms of the location of the regional boundaries or density breaks, along with the ratio of the dust density across those breaks, the radial dust distribution is translated into starting variables for input into the DaRT code.

Optical Depth whilst in Motion through the Neutral Region

The location $R_{SN}(t) = R_{Eq}$ is illustrated in Figure 5.1 plot (d) and the equation for the optical depth $\tau_v(t)$ no longer contain an ionized component as the entire HII region has been accumulated into the supershell

$$\tau_v(t) = \frac{\tau_{voW}}{k_w 2 n_{av} m_H R2_W}\left(Fd^{SH}(t)\rho^{SH}(t)[R_{SN}(t) - R_{cav}(t)] + \rho^n(t)[R2_W - R_{SN}(t)]\right) + \frac{\tau_{voSN}}{k_{sn} n_\alpha m_H [R2_{SN} - R2_W]}(\rho^\alpha [R2_{SN} - R2_W]) \quad (5.45)$$

DaRT Inputs whilst in Motion through the Neutral region

The DaRT inputs to describe the location of the regional boundaries and the ratio of densities across those boundaries are obtained in precisely the same manner as those from times when the superbubble is travelling through the HII region. Using plot (e) on Figure 5.2 as a reference

$$\mathrm{R}_{B1} = \mathrm{R}_{SN}(\mathrm{t})/\mathrm{R2}_{SN} \qquad \rho_{F1} = \rho^n(t)/\mathrm{Fd}^{SH}(\mathrm{t})\rho^{SH}(\mathrm{t})$$
$$\mathrm{R}_{B2} = \mathrm{R2}_W(\mathrm{t})/\mathrm{R2}_{SN} \qquad \rho_{F3} = \rho^\alpha(t)/\mathrm{Fd}^{SH}(\mathrm{t})\rho^{SH}(\mathrm{t})$$
$$\mathrm{ERAT} = \mathrm{R}^\star(\mathrm{t})/\mathrm{R}_{cav}(\mathrm{t}) \qquad \mathrm{E} = \mathrm{R}_{cav}(\mathrm{t})/\mathrm{R2}_{SN}$$

Momentum Conservation at the GMC Boundary

Several constants must be set at $R2_W$ for use in the momentum conserving solution given by Equation 4.54 for all radii $R_{SN}(t) > R2_W$. These values are t_o which is simply the STARBURST99 time, Δt_{ip}, that $R_{SN}(t)$ reaches $R2_W$, M_o which is the mass of the swept up supershell at t_o, given by $M_o = \rho^{SH}(t_{R2_W})V_{SH+G}(t_{R2_W})$, R_o is the radius $R2_W$ and dR_o/dt is given by the isothermal velocity of Equation 4.46.

Optical Depth whilst in Motion through the Ambient Region

Plot (i) of Figure 5.3 shows the superbubble reaching the outer boundary of the GMC, whereupon the contribution from dust in the neutral region disappears and only the supershell and ambient regions remain. Plot (j) shows the superbubble continuing its isothermal motion through the ambient region. The optical depth expression for this phase is

$$\tau_v(t) = \frac{\tau_{voW}}{k_w 2 n_{av} m_H R2_W} F d^{SH} \rho^{SH}(t)[R_{SH}(t)] + \frac{\tau_{voSN}}{k_{sn} n_\alpha m_H [R2_{SN} - R2_W]} \rho_\alpha [R2_{SN} - R_{SN}(t)] \tag{5.46}$$

DaRT Inputs whilst in Motion through the Ambient Region

Similarly, the DaRT inputs for all times when the superbubble has excited the GMC and entered interstellar space becomes

$$\mathrm{R}_{B1} = \mathrm{R}_{SN}(\mathrm{t})/\mathrm{R2}_{SN} \qquad \rho_{F1} = \rho^{\alpha}(t)/\mathrm{Fd}^{SH}(\mathrm{t})\rho^{SH}(\mathrm{t})$$
$$\mathrm{ERAT} = \mathrm{R}^{\star}(\mathrm{t})/\mathrm{R}_{cav}(\mathrm{t}) \qquad \mathrm{E} = \mathrm{R}_{cav}(\mathrm{t})/\mathrm{R2}_{SN}$$

This concludes development of the expressions required to specify the optical depth. Each expression was programmed into GEM and the evolution of the extinction was obtained both as a distribution and as the snapshot at t suitable for input to DaRT. The behaviour of the extinction distributions can now be examined.

5.5 Behaviour of Optical Depth

With 28 models on the parameter grid; η = 0.01, 0.025, 0.05, 0.1 0.15, 0.2 & 0.25, at four $\mathrm{M}_{GMC} = 10^6$-, 10^7-, 10^8- & $10^9 \mathrm{M}_\odot$ it is now convenient to attempt to categorise the behaviour of the extinction distributions based on defining characteristics.

With the supernova solution, when a supershell reaches the outer boundary of the GMC at $\mathrm{R2}_W$, it contains the GMC's entire mass of swept up gas and dust. The supershell temperature at $\mathrm{R2}_W$ can therefore be used as a useful guide to generalise the behaviour of a system's extinction over its evolution.

In summary, if the overall supershell temperature $\mathrm{T}_{SH+G}(\mathrm{t})$ is above T_{cond}, the condensation temperature, at the boundary of the GMC, the extinction will drop precipitously from an initially high value to reach a minimum after $\mathrm{R2}_W$ ($\mathrm{A}_v^{TOT} \leq 2$). The extinction will then remain very low for some time before exhibiting a small recovery at later times. These systems have been classified as *high* η.

In contrast, if the overall supershell temperature $\mathrm{T}_{SH+G}(\mathrm{t})$ is below T_{cond} at the boundary of the GMC, the extinction distribution, having initially been in decline, will

M_{GMC} ($M_\odot$)	HII Region Solution	Low η	High η
10^9	-	0.01, 0.025, 0.05	0.1, 0.15, 0.2, 0.25
10^8	-	0.01, 0.025, 0.05	0.1, 0.15, 0.2, 0.25
10^7	0.01, 0.025	0.05	0.1, 0.15, 0.2, 0.25
10^6	0.01, 0.025, 0.05, 0.1,	0.15, 0.2, 0.25	-

Table 5.1: Categorisation of Models by Star Formation Efficiency

exhibit a recovery to much more substantial values in a dust reformation scenario . These models have been classified as *low* η.

The 22 models in the parameter space which trigger the supernova solution and their *high* or *low* η classifications are detailed in Table 5.1. Also shown for reference are the 6 models whose supernova bubbles have insufficient velocity to overtake their HII ionization fronts with their supershells' intact and therefore revert to the HII region solution, thoroughly discussed in Chapter 3, at all times.

To illustrate how these *high* or *low* η classifications have been arrived at, it is convenient to begin by considering all seven star formation efficiencies for $M_{GMC} = 10^8 M_\odot$ in some depth, as they provide good examples to which the extinction distributions for the remaining GMC masses on the parameter grid can be compared.

5.5.1 $M_{GMC} = 10^8 M_\odot$; Low η

Figures 5.5 & 5.6 show the total extinction at the visual wavelength, $A_v^{TOT}(t) = 1.086\tau_v(t)$, along with the individual contributions to that total from the HII region $A_v^{Wi}(t)$, supershell $A_v^{SH}(t)$, neutral $A_v^n(t)$ and ambient $A_v^\alpha(t)$ regions for $M_{GMC} = 10^8 M_\odot$, $\eta = 0.01$, 0.025 & 0.05. Shown below the extinction plots are the corresponding distributions for the volume diluted temperature of the supershell $T_{SH}(t)$ from Equation 5.32, along with the temperature of the overtaken gas $T_G(t)$ which is given in the adiabatic phase by Equation 5.12 and in the isothermal phase by 25K and 120K in the neutral and ambient regions respectively. Also shown is the overall supershell temperature $T_{SH+G}(t)$ of Equation 5.28 and in the bottom plot, the corresponding behaviour of the supershell dust condensation factor $Fd^{SH}(t)$. Where applicable the points R_{Eq}, R_c, $R2_W$ and R_v have also been indicated.

Tables 5.2, 5.3 & 5.4 give numerically the total and regional contributions to the extinction for η=0.01, 0.025 & 0.5, along with the phase of the system at time t. An example of the phase is $R_{Eq} < R_{SN}(t) \leq R_c$ which refers to times when the superbubble has overtaken the HII region at R_{Eq} but is still travelling adiabatically through the neutral region towards the cooling radius R_c. The tables give the contributions at each year an SED is produced i.e., Δt_{SED}=1Myr for 1Myr < t < 10Myr and at Δt_{SED}=10Myr for 10Myr < t < 80Myr, along with values at $R_{SN_{start}}+1\Delta R$, R_{Eq}, R_c, $R2_W$ and R_v where reached.

Star Formation Efficiency η=0.01

The first thing to note for η = 0.01 is that the cloud surrounding this stellar cluster has the largest proportion of gas and dust coupled to the lowest luminosity source function on the $M_{GMC}=10^8 M_\odot$ parameter grid. This leads to the largest value of $A_v^{TOT}(t) = 104.86$ at t $\approx$ 1Myrs as shown on table 5.2. This model also has the largest value of $R2_W$, but R_V occurs in the neutral region at $t(R_v)$ = 62Myrs and so the outer boundary of the GMC is not reached by the superbubble. The shell reaches the condensation temperature early in the systems' life-time with $T_{SH+G}(7\text{Myrs}) \leq T_{cond}$.

The HII Region Phase

$R_W(t) < R_{SN}(t_{SNstart})$

This phase runs from t = 0 to t = $t_{SN_{start}}$ - before the supernovae energy injection begins. The extinction distribution due to the HII region $A_v^{Wi}(t)$ and neutral region $A_v^n(t)$ are shown on Figure 5.5 in red and blue respectively. During this phase $A_v^{TOT}(t)$ drops gradually, in parallel with $A_v^n(t)$, as the IF expands into the GMC, ionizing the neutral gas and evaporating dust in its passage. The contribution from the HII region $A_v^{Wi}(t)$ is very small because $R_W(t)$ at these early times is also small due to this model's low luminosity and hence expansion velocity. However 1/5th of the dust does condense out of the ionized region, regardless of the gas temperature, due to Fd^{Wi} being held constant at 0.2. The ambient contribution $A_v^\alpha(t)$ does not vary whilst the HII region is trapped within the GMC.

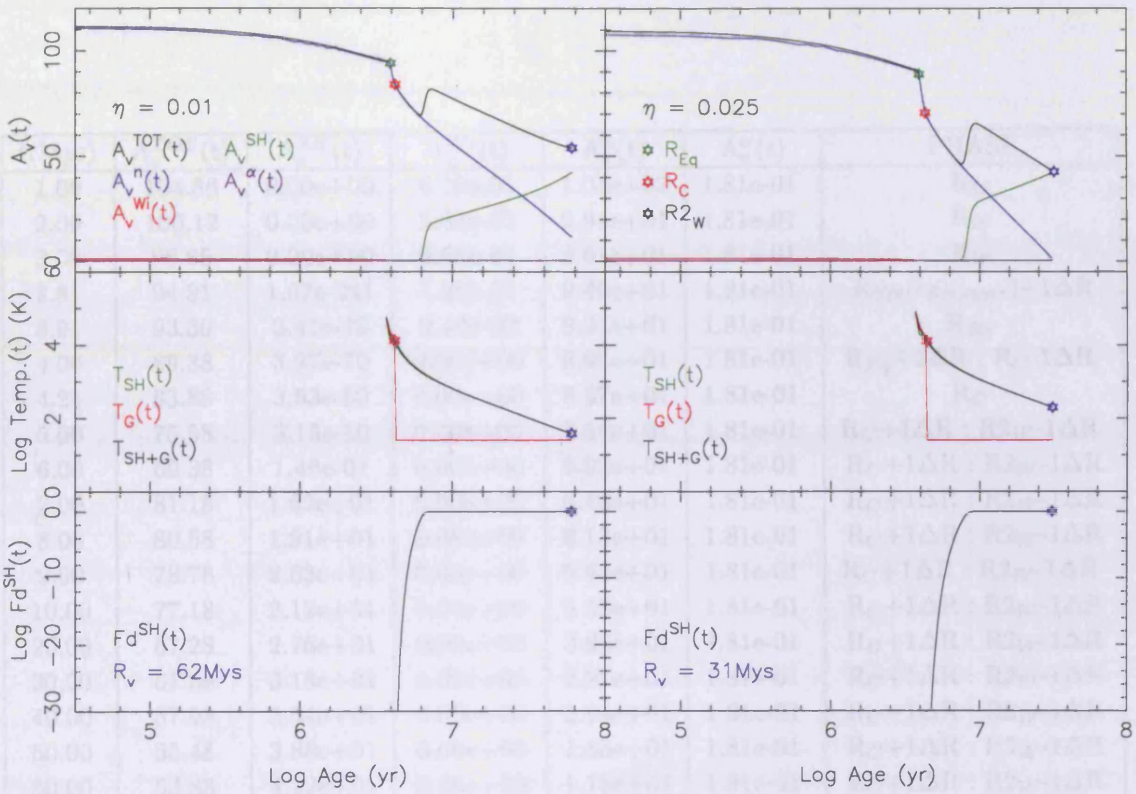

Figure 5.5: $A_v(t)$ contributions for $M_{GMC}=10^8 M_\odot$. η=0.01 is on the LHS whilst η=0.025 is on the RHS. In the top plots the extinctions from each region of the GMC are indicated by: the sum $A_v^{TOT}(t)$(black); neutral $A_v^n(t)$ (blue); HII Region $A_v^{Wi}(t)$ (red); supershell $A_v^{SH}(t)$ (green) and ambient $A_v^{\alpha}(t)$ (purple). In the middle plots the pre-existing volume diluted gas temperature $T_{SH}(t)$ (green) and the new overtaken gas temperature $T_G(t)$ (red) along with the supershell temperature $T_{SH+G}(t)$ (black) are given. The bottom plots show the behaviour of the dust condensation factor. Where appropriate the green, red, black and blue stars represent R_{Eq}, R_c, $R2_W$ and R_v respectively.

t(Myr)	A_v^{TOT}(t)	A_v^{SH}(t)	A_v^{Wi}(t)	A_v^{n}(t)	A_v^{α}(t)	PHASE
1.00	104.86	0.00e+00	6.79e-01	1.04e+02	1.81e-01	R_W
2.00	100.12	0.00e+00	5.35e-01	9.94e+01	1.81e-01	R_W
3.00	96.65	0.00e+00	3.68e-01	9.61e+01	1.81e-01	R_W
3.81	94.91	1.97e-241	1.30e-01	9.46e+01	1.81e-01	$R_{SN}(t_{SNstart})$+1ΔR
3.91	93.30	3.41e-75	2.10e-02	9.31e+01	1.81e-01	R_{Eq}
4.00	89.38	3.27e-70	0.00e+00	8.92e+01	1.81e-01	R_{Eq}+1ΔR : R_C-1ΔR
4.21	83.88	3.53e-50	0.00e+00	8.37e+01	1.81e-01	R_C
5.00	75.58	3.15e-10	0.00e+00	7.54e+01	1.81e-01	R_C+1ΔR : R2$_W$-1ΔR
6.00	69.38	1.46e-01	0.00e+00	6.92e+01	1.81e-01	R_C+1ΔR : R2$_W$-1ΔR
7.00	81.18	1.62e+01	0.00e+00	6.48e+01	1.81e-01	R_C+1ΔR : R2$_W$-1ΔR
8.00	80.58	1.91e+01	0.00e+00	6.13e+01	1.81e-01	R_C+1ΔR : R2$_W$-1ΔR
9.00	78.78	2.03e+01	0.00e+00	5.83e+01	1.81e-01	R_C+1ΔR : R2$_W$-1ΔR
10.00	77.18	2.12e+01	0.00e+00	5.58e+01	1.81e-01	R_C+1ΔR : R2$_W$-1ΔR
20.00	67.28	2.76e+01	0.00e+00	3.95e+01	1.81e-01	R_C+1ΔR : R2$_W$-1ΔR
30.00	61.68	3.18e+01	0.00e+00	2.97e+01	1.81e-01	R_C+1ΔR : R2$_W$-1ΔR
40.00	57.98	3.54e+01	0.00e+00	2.24e+01	1.81e-01	R_C+1ΔR : R2$_W$-1ΔR
50.00	55.48	3.88e+01	0.00e+00	1.65e+01	1.81e-01	R_C+1ΔR : R2$_W$-1ΔR
60.00	53.88	4.22e+01	0.00e+00	1.15e+01	1.81e-01	R_C+1ΔR : R2$_W$-1ΔR
61.00	53.78	4.27e+01	0.00e+00	1.09e+01	1.81e-01	R_V

Table 5.2: Contributions to the extinction from various regions of the cloud as the η = 0.01, M_{GMC}=$10^8 M_\odot$ system evolves. A_v^{TOT}(t) is the total extinction along a line of sight, A_v^{Wi}(t), A_v^{SH}(t), A_v^{n}(t) and A_v^{α}(t) are the contributions to that extinction from the HII region, supershell, neutral and ambient regions respectively. The final column gives the phase of the system at the time the extinction is calculated.

Extinction whilst in Adiabatic Motion through the HII Region

$R_{SN}(t_{SNstart}) < R_{SN}(t) < R_{Eq}$

At $t_{SNstart}$ = 3.71Myrs the supernova energy injection starts and the superbubble begins to travel outwards through the GMC. The temperature distribution for the supershell is shown in the middle panel on the left-hand side of Figure 5.5.

During adiabatic motion, the temperature of the gas overtaken by the superbubble and compressed into the supershell, $T_G(t)$ slightly exceeds the volume dilution temperature $T_{SH}(t)$ because the shell growth is extremely rapid and the overall supershell temperature $T_{SH+G}(t)$ tracks between them. However, the extinction from the supershell $A_v^{SH}(t)$ is effectively zero whilst the superbubble is in adiabatic motion due to the high shock velocity and hence $T_G(t)$, coupled to the temperature-dependence of the shell condensation law for $Fd^{SH}(t)$.

Extinction whilst in Adiabatic Motion through the Neutral Region

$R_{Eq} \leq R_{SN}(t) \leq R_c$

Once the superbubble has excited the HII region at radius R_{Eq}, as indicated on the plots by the green star, the contribution to the extinction from the HII region $A_v^{Wi}(t)$ disappears. The supershell has yet to contribute to the extinction as although it has now entered the neutral region and the shell density can begin to grow more substantially, the post-shock temperature $T_G(t)$ is still a function of the high shock velocity. This leads to the overall shell temperature $T_{SH+G}(t)$ maintaining a value which is still considerably in excess of the dust condensation temperature.

The neutral contribution to the extinction $A_v^n(t)$ begins to drop abruptly once the superbubble has exited the HII region, as shown by the steep gradient of the neutral and total curves between R_{Eq} and R_c (red star). This effect is also a function of the luminosity and hence shock velocity. As the superbubble expands rapidly through the dense cloud, its passage evaporates the any co-existing with the cool neutral gas and destroys the main contributor to the extinction at this time.

Extinction whilst in Isothermal Motion through the Neutral Region

$R_c + 1\Delta t \leq R_{SN}(t) \leq R_V$

The $\eta = 0.01$ superbubble is the first of the $M_{GMC} = 10^8 M_\odot$ models to reach R_c as it has the lowest expansion velocity. The $\eta = 0.01$ superbubble therefore enters isothermal motion whilst firmly trapped within the GMC. Prior to R_c, the temperature of the overtaken gas $T_G(t)$ was greater than the volume diluted temperature of the shell $T_{SH}(t)$ due to the adiabatic high shock velocity. However, once R_c has been reached, this relationship is inverted as the temperature of the material crossing the shock $T_G(t)$ is no longer a function of the shock velocity but becomes equivalent to the external gas temperature; 25K (Dyson & Williams 1997*b*).

The drop in post-shock gas temperature is illustrated in the middle panel of Figure 5.5 where $T_G(t)$ drops sharply to 25K from R_c. However, despite the now low temperature of gas added to the supershell with each new shell formed, the overall temperature of the supershell $T_{SH+G}(t)$ continues to track the volume dilution temperature $T_{SH}(t)$ quite closely. This effect was fully discussed earlier in this chapter §5.3 where it was mentioned that it was potentially unrealistic to cool the supershell dramatically at R_c due to the possibility of non-equilibrium ionization affects inhibiting the radiation of heat from the a very dense supershell. Therefore, following R_c, the overall supershell temperature $T_{SH+G}(t)$ does drop due to the ingress of new neutral gas which maintains its cool pre-shock temperature, but due to the increase in the compression factor for shells formed after R_c the cooling via volume expansion is more limited and the drop in the overall shell temperature $T_{SH+G}(t)$ is perhaps more gradual than a catastrophic collapse would imply.

Shortly after R_c the dust condensation factor $Fd^{SH}(t)$, illustrated in the bottom LHS panel of Figure 5.5, does begin to rise. However, the overall shell temperature is still somewhat greater than the dust condensation temperature so the total extinction continues to drop in line with $A_v^n(t)$ as the dust in the neutral region is transferred to a shell too hot to contribute to the extinction.

Eventually, the overall supershell temperature $T_{SH+G}(t)$ reaches the dust condensation temperature, $T_{cond} \approx 1600$K, leading to $Fd^{SH}(t) \approx 0.50$ and 50% of the dust compressed in the shell can contribute to the extinction. Achieving the dust condensation temperature in the shell is a very important point in a system's evolution as it coincides with the trough in $A_v^{TOT}(t)$ which signals the end of its decline from R_{Eq}.

As the supershell temperature continues due to drop, $Fd^{SH}(t)$ continues to rise rapidly until it reaches a maximum value of $Fd^{SH}(t) \approx 1$, whereupon 100% of the supershell dust is contributing to the extinction. $Fd^{SH}(t) \approx 1$ ($T_{cond} \approx 1200K$) coincides with the peak in extinction recovery. Having reached $Fd^{SH}(t) \approx 1$, $A_v^{SH}(t)$ continues to grow but at a rate proportional to the density and width of each new shell now formed.

The $A_v^{TOT}(t)$ and $A_v^n(t)$ curves diverge dramatically once the supershell starts to contribute as $A_v^{TOT}(t)$ ceases to be so heavily dependent on the neutral density and becomes a function of the supershell density as well. After the peak at $Fd^{SH}(t) \approx 1$, the gradient of the drop in $A_v^{TOT}(t)$ is shallower than that between e.g., R_c and the trough, due to the growing contribution from the supershell compensating for the on-going destruction of the neutral material. As the superbubble continues to expand through the neutral region, the contribution to the extinction from the shell $A_v^{SH}(t)$ eventually overtakes $A_v^n(t)$ as the neutral region is exhausted.

Due to the significant quantity of dust in the $\eta = 0.01$ system coupled to the low luminosity of the source function, the velocity of the superbubble drops below the sound speed in the neutral region and breaks up at $t(R_v) = 62$Myrs. At this point the dust modelling ceases as it would be unphysical to continue.

Therefore in summary, the extinction distribution generated by the $M_{GMC}=10^8 M_\odot$, $\eta = 0.01$ system initially declines as the superbubble expands through both the ionized HII region and the neutral dusty GMC in adiabatic motion, transferring the gas and dust to a very hot supershell. Once the cooling radius has been reached, isothermal motion begins and the supershell temperature drops. The trough in the total extinction $A_v^{TOT}(t)$ signals that the dust condensation temperature has been reached in the supershell and that 50% of the dust is contributing to the extinction. As the supershell continues to rapidly cool, more dust is able to condense out of the gas until the peak in recovery of $A_v^{TOT}(t)$ is reached when 100% of the supershell dust contributes to the opacity. The extinction then continues to drop essentially in line with the radial solution until break up occurs and the modelling ceases.

Star Formation Efficiencies η=0.025 & 0.05

Table 5.3 gives the extinction data numerically for $\eta = 0.025$, whilst the right-hand side of Figure 5.5 illustrates the distributions. For $\eta = 0.025$, R_c again occurs in the neutral region where the model also breaks-up, reaching $R2_W$ at $t(R_v) = 31$Myrs.

t(Myr)	A_v^{TOT}(t)	A_v^{SH}(t)	A_v^{Wi}(t)	A_v^{n}(t)	A_v^{α}(t)	PHASE
1.00	102.16	0.00e+00	9.83e-01	1.01e+02	1.80e-01	R_W
2.00	96.96	0.00e+00	7.82e-01	9.60e+01	1.80e-01	R_W
3.00	93.12	0.00e+00	5.40e-01	9.24e+01	1.80e-01	R_W
3.81	91.16	0.00e+00	1.83e-01	9.08e+01	1.80e-01	$R_{SN}(t_{SNstart})$+1ΔR
3.91	90.52	6.27e-111	4.19e-02	9.03e+01	1.80e-01	R_{Eq}
4.00	83.58	1.56e-100	0.00e+00	8.34e+01	1.80e-01	R_{Eq}+1ΔR : R_c-1ΔR
4.31	70.48	1.17e-57	0.00e+00	7.03e+01	1.80e-01	R_c
5.00	61.78	1.45e-20	0.00e+00	6.16e+01	1.80e-01	R_c+1ΔR : $R2_W$-1ΔR
6.00	53.78	2.19e-07	0.00e+00	5.36e+01	1.80e-01	R_c+1ΔR : $R2_W$-1ΔR
7.00	48.10	2.05e-02	0.00e+00	4.79e+01	1.80e-01	R_c+1ΔR : $R2_W$-1ΔR
8.00	49.63	6.05e+00	0.00e+00	4.34e+01	1.80e-01	R_c+1ΔR : $R2_W$-1ΔR
9.00	64.88	2.52e+01	0.00e+00	3.95e+01	1.80e-01	R_c+1ΔR : $R2_W$-1ΔR
10.00	58.88	2.85e+01	0.00e+00	3.02e+01	1.80e-01	R_c+1ΔR : $R2_W$-1ΔR
20.00	51.28	3.66e+01	0.00e+00	1.48e+01	1.80e-01	R_c+1ΔR : $R2_W$-1ΔR
30.00	43.75	4.16e+01	0.00e+00	1.97e+00	1.80e-01	R_c+1ΔR : $R2_W$-1ΔR
32.00	42.58	4.24e+01	0.00e+00	0.00e+00	1.80e-01	$R_V = R2_W$

Table 5.3: Contributions to the extinction from various regions of the cloud as the η = 0.025, $M_{GMC}=10^8 M_\odot$ system evolves. A_v^{TOT}(t) is the total extinction along a line of sight, A_v^{Wi}(t), A_v^{SH}(t), A_v^{n}(t) and A_v^{α}(t) are the contributions to that extinction from the HII region, supershell, neutral and ambient regions respectively. The final column gives the phase of the system at the time the extinction is calculated.

Table 5.4 gives the numerical data for η=0.05 with the left-hand side of Figure 5.6 shows the extinction data graphically. For η = 0.05, R_c is also located inside the GMC but in contrast to η=0.01 and η=0.025, the η = 0.05 superbubble is able to exit the GMC and reach the outer edge of the ambient region at R2SN with its supershell intact; the R_v break-up condition is not invoked and the modelling continues to 80Myrs. For η = 0.05 the supershell temperature at $R2_W$ is $T_{SH+G}(t_{R2_W}) \approx$ 800K - well below T_{cond}.

Extinction whilst in Adiabatic Motion through HII & Neutral Regions $R_W(t) < R_c$

Looking first at the adiabatic phase extinction behaviour, prior to the cooling radius R_c being reached. Perhaps the first thing to note is that because the GMC mass is being held constant, the initial A_v^{TOT}(t) for e.g., η = 0.05 is lower than for η = 0.025 or 0.01. This illustrates the proportionately greater quantity of the initial GMC mass that is converted in the central cluster as η rises. As the systems evolve, in turn this leads to a larger HII region IF velocity for η=0.05 and therefore a bigger magnitude of A_v^{Wi}(t) at the same t than for either η = 0.01 or 0.025. This is because one-fifth of the dust accumulated in the

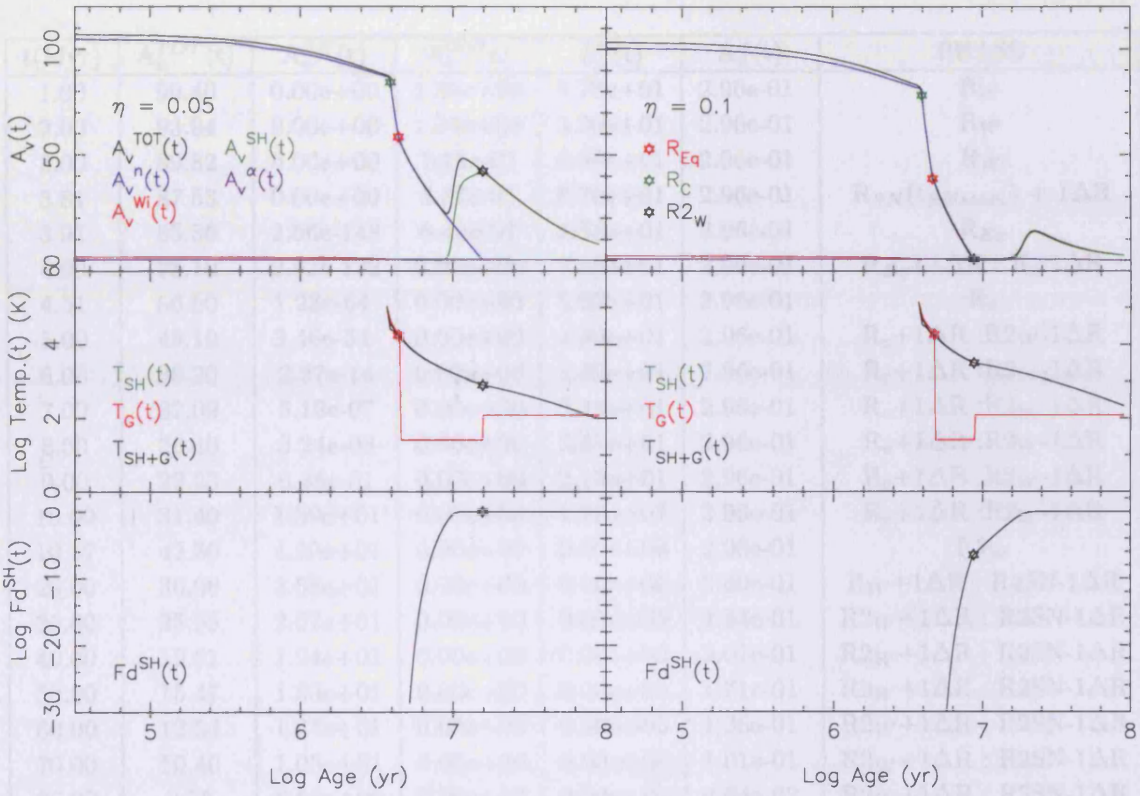

Figure 5.6: Av(t) contributions for $M_{GMC}=10^8 M_\odot$. η=0.05 is on the LHS whilst η=0.1 is on the RHS. In the top plots the extinctions from each region of the GMC are indicated by: the sum A_v^{TOT}(t)(black); neutral A_v^n(t) (blue); HII Region A_v^{Wi}(t) (red); supershell A_v^{SH}(t) (green) and ambient A_v^α(t) (purple). In the middle plots the pre-existing volume diluted gas temperature T_{SH}(t) (green) and the new overtaken gas temperature T_G(t) (red) along with the supershell temperature T_{SH+G}(t) (black) are given. The bottom plots show the behaviour of the dust condensation factor. Where appropriate the green, red, black and blue stars represent R_{Eq}, R_c, $R2_W$ and R_v respectively.

t(Myr)	A_v^{TOT}(t)	A_v^{SH}(t)	A_v^{Wi}(t)	A_v^{n}(t)	A_v^{α}(t)	PHASE
1.00	99.40	0.00e+00	1.30e+00	9.78e+01	2.96e-01	R_W
2.00	93.94	0.00e+00	1.04e+00	9.26e+01	2.96e-01	R_W
3.00	89.82	0.00e+00	7.19e-01	8.88e+01	2.96e-01	R_W
3.81	87.53	0.00e+00	2.37e-01	8.70e+01	2.96e-01	$R_{SN}(t_{SNstart})$ + 1ΔR
3.91	85.86	2.56e-148	6.43e-02	8.55e+01	2.96e-01	R_{Eq}
4.00	78.10	2.82e-132	0.00e+00	7.78e+01	2.96e-01	R_{Eq}+1ΔR : R_c-1ΔR
4.51	56.50	1.23e-64	0.00e+00	5.62e+01	2.96e-01	R_c
5.00	49.19	3.46e-34	0.00e+00	4.89e+01	2.96e-01	R_c+1ΔR :$R2_W$-1ΔR
6.00	39.20	2.27e-14	0.00e+00	3.89e+01	2.96e-01	R_c+1ΔR :$R2_W$-1ΔR
7.00	32.09	5.19e-07	0.00e+00	3.18e+01	2.96e-01	R_c+1ΔR :$R2_W$-1ΔR
8.00	26.40	3.24e-03	0.00e+00	2.61e+01	2.96e-01	R_c+1ΔR :$R2_W$-1ΔR
9.00	22.23	6.38e-01	0.00e+00	2.13e+01	2.96e-01	R_c+1ΔR :$R2_W$-1ΔR
10.00	31.40	1.39e+01	0.00e+00	1.72e+01	2.96e-01	R_c+1ΔR :$R2_W$-1ΔR
10.57	42.30	4.20e+01	0.00e+00	0.00e+00	2.96e-01	$R2_W$
20.00	36.08	3.58e+01	0.00e+00	0.00e+00	2.80e-01	R_W+1ΔR : R2SN-1ΔR
30.00	25.95	2.57e+01	0.00e+00	0.00e+00	2.44e-01	$R2_W$+1ΔR : R2SN-1ΔR
40.00	19.61	1.94e+01	0.00e+00	0.00e+00	2.07e-01	$R2_W$+1ΔR : R2SN-1ΔR
50.00	15.47	1.53e+01	0.00e+00	0.00e+00	1.71e-01	$R2_W$+1ΔR : R2SN-1ΔR
60.00	12.54	1.24e+01	0.00e+00	0.00e+00	1.36e-01	$R2_W$+1ΔR : R2SN-1ΔR
70.00	10.40	1.03e+01	0.00e+00	0.00e+00	1.01e-01	$R2_W$+1ΔR : R2SN-1ΔR
80.00	8.75	8.68e+00	0.00e+00	0.00e+00	6.64e-02	$R2_W$+1ΔR : R2SN-1ΔR

Table 5.4: Contributions to the Extinction from various regions of the cloud as the η = 0.05, M_{GMC}=$10^8 M_\odot$ system evolves. A_v^{TOT}(t) is the total extinction along a line of sight, A_v^{Wi}(t), A_v^{SH}(t), A_v^{n}(t) and A_v^{α}(t) are the contributions to that extinction from the HII region, supershell, neutral and ambient regions respectively. The final column gives the phase of the system at the time the extinction is calculated.

HII region condenses out regardless of the gas temperature and the up-stream neutral gas is uniformly distributed.

In a similar way to $\eta = 0.01$, once the supernova energy injection begins for $\eta = 0.025$ & 0.05, the hot, rapidly expanding superbubbles quickly evaporate any dust that has condensed out of the HII region and transfers the ionized gas to their supershells.

Once the IF has been overtaken at R_{Eq}, the neutral contributions to the extinction drop rapidly as the superbubbles expand through the neutral region. The gradient of the drop from R_{Eq} is the steepest for $\eta = 0.05$ of all models discussed as that superbubble has the greatest velocity at the same time t. As superbubble velocity rises with η this is easy to understand as the $\eta = 0.05$ superbubble is transferring neutral gas and dust to its shell at the fastest rate and that dust has a post-shock temperature which is dependent on the shock velocity.

Extinction whilst in Isothermal Motion through the Neutral Region
$R_c \leq R_{SN}(t) \leq R_v$ or $R2_W$

Each of these low η models discussed reaches R_c in the neutral region. The higher velocity $\eta = 0.05$ supershell therefore reaches R_c and collapses last and is the most gas-rich at that collapse.

Figures 5.5 and 5.6 show that the total extinction for $\eta = 0.05$ behaves in a similar way to that of $\eta = 0.01$ & 0.025 with the overall supershell temperature $T_{SH+G}(t)$ dropping gradually from R_c, in line with the radial solution modified by the accumulation of the cool, 25K, neutral gas. Volume growth of the superbubble and shell now slows because the gas compression across the shock is unlimited and the shell density can begin to rise more substantially.

In the same way as for $\eta = 0.01$, $T_{SH+G}(t) = T_{cond}$ also signals the end of the trough in extinction for the $\eta = 0.025$ & 0.05 systems. $Fd^{SH}(t) \approx 0.5$ occurs progressively later as η rises - t = 7-, 9- & 10Myrs for $\eta = 0.01$, 0.025 & 0.05 respectively, due to the increase in superbubble velocity and hence shell temperature as the cluster mass increases.

Upon reaching the trough in $A_v^{TOT}(t)$ both the $\eta = 0.025$ & 0.05 models exhibit a resurgence in extinction as dust re-forms in the supershells. In the same manner as $\eta = 0.01$, the peak in $A_v^{TOT}(t)$ occurs a short while later when $Fd^{SH}(t) \approx 1$ and 100% of the dust condenses out across the supershell width. This substantial recovery in extinction at earlier times is indicative of all low η models.

Following the peak in $A_v^{TOT}(t)$, $A_v^{SH}(t)$ continues to grow, but much more slowly and in proportion to the density and width of each new shell formed. $A_v^{TOT}(t)$ drops gradually after the peak with its gradient slightly shallower than prior to the trough due to the added contribution to the extinction from the supershell.

The $\eta = 0.01$ & 0.025 shell extinction are both still rising when R_v is reached. R_v for these models occurs inside the neutral region when the supershells break up due to random motions in the upstream gas.

Illustration of Break-up

As an aside, the particulars of the $\eta = 0.01$ and $\eta = 0.025$ models provide a good illustration on the effect of the break-up condition, first mentioned in Chapter 3, §3.6.3 and demonstrates the importance of the fine balance between source luminosity and dust mass at these low star formation efficiencies.

The $\eta = 0.025$ model breaks-up and loses its integrity at $t(R_v) = 31$Myrs, which is almost half the break-up time of the $\eta = 0.01$ model at $t(R_v) = 61$Myrs. The $\eta = 0.01$ model, with its small source luminosity and large proportion of dust, breaks up while still firmly embedded in the GMC, with the break-up velocity determined by the sound speed in the cool neutral region; $c_n = 4.5 \times 10^4 \mathrm{cms}^{-1}$ ($T_n = 25$K) (Dyson & Williams 1997*b*). The $\eta = 0.025$ model, with its greater source luminosity and hence smaller proportion of dust is able to exhaust its neutral region entirely and actually reaches the outer edge of the GMC at $R2_W$. However, upon entering the ambient region the break-up velocity becomes a function of the external sound speed and the ambient region is considerably hotter than the neutral region $c_\alpha = 1 \times 10^5 \mathrm{cms}^{-1}$ ($T_\alpha = 120$K) (Dyson & Williams 1997*b*). Thus at $R2_W$, $\eta = 0.025$ has $v_{SN}(t) = 1.01 \times 10^5 \mathrm{cms}^{-1}$ - sufficient for the shell to have maintained its integrity whilst in the GMC, but insufficient for any progress to be made in the ambient region.

Therefore it is the proportionately greater radius of $R2_W$ coupled to the lower source luminosity and hence velocity of the $\eta = 0.01$ model over the $\eta = 0.025$ model, which allows the former supershell to survive for 62Myrs yet still not exit the GMC intact. Conversely, the proportionately greater luminosity and smaller $R2_W$ of the $\eta = 0.025$ model allows that supershell to reach the edge of the GMC intact, in a considerably reduced amount of time, but still does not allow it to enter the ambient region and also maintain its integrity.

Extinction whilst in Isothermal Motion through the Ambient Region $R2_W < R_{SN}(t) \leq R2_{SN}$ ($\eta = 0.05$ only)

Returning to the extinction distributions, of the low η models, only $\eta = 0.05$ is able to make any progress through the ambient region. At $R2_W$ the form of motion of the superbubble changes from the classical momentum conserving solution given by Equation 4.42 to that given by Equation 4.54. Figure 4.4 in §4.7, gives the radius and velocity curves for $M_{GMC} = 10^8 M_\odot$, η=0.05. These curves show a break in the superbubble radius and velocity behaviour at $R2_W$ when this new form of motion takes over with the velocity levelling off and the shell volume growing. The shell experiences this volume increase after $R2_W$ as $\Delta R_{shell}(t)$ becomes inversely dependent on the ratio of the square of the superbubble velocity to the ambient sound speed rather than to the neutral sound speed, giving a correspondingly smaller compression factor.

The effect of this increase in supershell volume can be seen for $\eta = 0.05$ on the left-hand side of Figure 5.6 where the shell contribution, $A_v^{SH}(t)$, reaches a peak at $R2_W$, whereafter it drops in what is essentially a volume dilution solution to $R2_{SN}$. Although the supershell does continue to sweep up the gas and dust ahead of it, the sparse ambient material accumulated does little to counteract the increased volume overtaken at each step, causing $A_v^{SH}(t)$ to drop smoothly and substantially as times goes on.

The middle plot on the LHS of Figure 5.6 also shows the effect of the increased volume growth of the supershell after $R2_W$, with the gradient of the overall supershell temperature $T_{SH+G}(t)$ levelling out and dropping less rapidly than prior to $R2_W$. Although the cooling via volume dilution of the neutral material trapped in the supershell is now occurring faster due to the increased shell volume growth, the temperature of the overtaken gas has increased from 25K in the neutral region to 125K in the ambient region, slightly mitigating the cooling via volume expansion.

Finally, it is worth mentioning that when the $\eta = 0.05$ superbubble exits the GMC, the contribution $A_v^{\alpha}(t)$ begins to drop steadily as the overtaken ambient material is transferred into the shell.

Summary of low η Models

$\eta = 0.025$ and 0.05 model systems therefore show essentially the equivalent extinction behaviour to the $\eta = 0.01$ model. The distributions initially decline from their maximum value at t = 0 as the superbubbles expand in adiabatic motion through both the ionized

HII region and the neutral regions.

When isothermal motion begins the supershell temperatures start to drop substantially, eventually achieving the dust condensation temperature, T_{cond}, which co-incides with the trough in the total extinction and the end of its initial decline. As the supershell dust cools further, the total extinction begins to rapidly rise again until it reaches a peak, when 100% of the supershell dust contributes to the extinction. The trough and peak in extinction of these low η systems occurs relatively early in the system's life time ($\leq$ 10Myrs).

Following the peak, the total extinction drops in a volume dilution solution, mitigated by the ingress of shocked, but cool neutral gas, until R_v where a model breaks up, or the edge of the GMC $R2_W$ is reached. Where a model exits the GMC with its supershell intact, its overall gas temperature is below the dust condensation temperature at $R2_W$. The total extinction then drops more rapidly in the ambient region than in the neutral region due primarily to the lower external density and the higher ambient sound speed.

5.5.2 $M_{GMC} = 10^8 M_\odot$; High η

η = 0.1, 0.15, 0.2 & 0.25 on the M_{GMC}=$10^8 M_\odot$ model grid have been categorized as high star formation efficiencies because the overall temperature of these supershells, $T_{SH+G}(t)$ at $R2_W$ is above the condensation temperature. Figures 5.6, 5.7 & 5.8 show the total and regional contributions to the extinction at the visual wavelength and the behaviour of the shell temperature and the dust condensation factor for these η's respectively. Tables 5.5, 5.6, 5.7 & 5.8 give that extinction data numerically along with the phase of the system. In a similar way to the lower efficiencies, η = 0.1 will be discussed in some depth and then η = 0.15 & 0.2 will be compared. The extinction distribution for η = 0.25 will be discussed at the end due to the difference in this model caused by the cooling radius being set as the outer boundary of the GMC, $R_{c_{\eta=0.25}} = R2_W$.

Star Formation Efficiency η=0.1

Looking then at the plots on the right-hand side of Figure 5.6 and Table 5.5 for η = 0.1. Again this model reaches R_c whilst the superbubble is trapped within the neutral region, has $T_{SH+G}(t_{R2_W}) \approx$ 3000K and also has sufficient velocity to reach $R2_{SN}$ with its shell intact. The phase headings on the forthcoming paragraphs now change to be biased towards later rather than early times to accommodate the more interesting features in the extinction at these higher cluster luminosities.

t(Myr)	A_v^{TOT}(t)	A_v^{SH}(t)	A_v^{Wi}(t)	A_v^n(t)	A_v^α(t)	PHASE
1.00	95.52	0.00e+00	1.70e+00	9.32e+01	6.19e-01	R_W
2.00	89.70	0.00e+00	1.38e+00	8.77e+01	6.19e-01	R_W
3.00	85.28	0.00e+00	9.57e-01	8.37e+01	6.19e-01	R_W
3.81	82.73	0.00e+00	3.07e-01	8.18e+01	6.19e-01	$R_{SN}(t_{SNstart})$+1ΔR
3.91	81.97	9.56e-198	5.06e-02	8.13e+01	6.19e-01	R_{Eq}
4.00	71.12	2.50e-174	0.00e+00	7.05e+01	6.19e-01	R_{Eq}+1ΔR : R_c-1ΔR
4.71	37.82	4.14e-73	0.00e+00	3.72e+01	6.19e-01	R_c
5.00	32.72	2.52e-52	0.00e+00	3.21e+01	6.19e-01	R_c+1ΔR : $R2_W$-1ΔR
6.00	20.22	7.80e-24	0.00e+00	1.96e+01	6.19e-01	R_c+1ΔR : $R2_W$-1ΔR
7.00	11.42	2.72e-13	0.00e+00	1.08e+01	6.19e-01	R_c+1ΔR : $R2_W$-1ΔR
8.00	4.31	7.25e-08	0.00e+00	3.69e+00	6.19e-01	R_c+1ΔR : $R2_W$-1ΔR
8.71	0.62	1.29e-05	0.00e+00	0.00e+00	6.19e-01	$R2_W$
9.00	0.62	2.55e-05	0.00e+00	0.00e+00	6.16e-01	$R2_W$+1ΔR : R2SN-1ΔR
10.00	0.61	2.06e-04	0.00e+00	0.00e+00	6.07e-01	$R2_W$+1ΔR : R2SN-1ΔR
20.00	11.92	1.14e+01	0.00e+00	0.00e+00	5.21e-01	$R2_W$+1ΔR : R2SN-1ΔR
30.00	10.31	9.87e+00	0.00e+00	0.00e+00	4.39e-01	$R2_W$+1ΔR : R2SN-1ΔR
40.00	6.97	6.61e+00	0.00e+00	0.00e+00	3.60e-01	$R2_W$+1ΔR : R2SN-1ΔR
50.00	5.13	4.84e+00	0.00e+00	0.00e+00	2.87e-01	$R2_W$+1ΔR : R2SN-1ΔR
60.00	4.00	3.79e+00	0.00e+00	0.00e+00	2.19e-01	$R2_W$+1ΔR : R2SN-1ΔR
70.00	3.28	3.12e+00	0.00e+00	0.00e+00	1.56e-01	$R2_W$+1ΔR : R2SN-1ΔR
80.00	2.77	2.67e+00	0.00e+00	0.00e+00	9.92e-02	$R2_W$+1ΔR : R2SN-1ΔR

Table 5.5: Contributions to the extinction from various regions of the cloud as the $\eta = 0.1$, $M_{GMC}=10^8 M_\odot$ system evolves. A_v^{TOT}(t) is the total extinction along a line of sight, A_v^{Wi}(t), A_v^{SH}(t), A_v^n(t) and A_v^α(t) are the contributions to that extinction from the HII region, supershell, neutral and ambient regions respectively. The final column gives the phase of the system at the time the extinction is calculated.

Extinction for Motion in the HII & Neutral Region
$R_W(t) < R_{SN}(t) \leq R2_W$

The extinction curve for $\eta = 0.1$ shows the same behaviour prior to R_c as the low η's discussed. As the star formation efficiency rises, so does the superbubble velocity and the extent of the associated neutral region diminishes. At $\eta = 0.1$, the mass tied up in the stellar cluster is 10% of the GMC and as such the velocity imparted to the superbubble during the adiabatic phase is considerable. Looking at all models considered so far, the gradient of the drop in extinction between R_{Eq} and R_c is therefore steepest for $\eta = 0.1$ and R_c occurs latest and closest to $R2_W$.

The correspondingly smaller extent of the neutral cloud means this supershell spends very little time in the neutral region in isothermal motion and the cooling affect of the accumulation of that low temperature, shocked gas is diminished. Upon reaching $R2_W$ therefore, the overall temperature of the supershell is well in excess of the dust condensation temperature. This means the GMC's entire compliment of swept-up gas and dust, is contained in a supershell far too hot to contribute to the extinction. This is illustrated by the steep drop in $A_v^{TOT}(t)$ and $A_v^n(t)$ after R_c to almost zero when the superbubble reaches $R2_W$ (black star) and the very small magnitude of $Fd^{SH}(t)$ at this time - a function of its exponential form. Thus, in contrast to the lower η models, at $R2_W$ the only region contributing to the extinction is the sparse ambient region.

Extinction for Motion in the Ambient Region
$R2_W < R_{SN}(t) \leq R2_{SN}$

Once the ambient region has been reached, not only does the form of motion of the superbubble change as previously described, but each new shell formed is larger than those formed in the GMC due to the change in upstream density and temperature and hence the compression factor. However, looking at the bottom plot on the right-hand side of Figure 5.6 the volume expansion does cause $Fd^{SH}(t)$ to begin to rise upon the superbubbles' exit from the GMC.

After $R2_W$ the rise in $Fd^{SH}(t)$ is not as rapid as it might be as the cooling affect caused by the volume increase is somewhat mollified by the ingress of the hotter ambient gas, as compared to the cooler gas that existed in the neutral region.

Thus, as the superbubble continues its motion into the ambient region, the supershell temperature is still above the dust condensation temperature and whilst $Fd_{SH}(t)$ is rising,

it takes some time to approach unity. Therefore $A_v^{TOT}(t)$ and $A_v^{SH}(t)$ remain low at approximately zero, as the superbubble initially travels out into the ambient region.

In the same way as for the low η's, as the $\eta = 0.1$ supershell temperature continues to drop, the shell dust begins to contribute to the extinction, reaching a trough at $Fd_{SH}(t) = 0.05$, $T_{SH+G}(t) \approx T_{dust}$. $A_v^{TOT}(t)$ then rises, reaching a peak at $Fd_{SH}(t) = 1$.

However the peak achieved by this high η model is minimal compared to that of the low η models as by the time the $\eta = 0.1$ supershell has cooled sufficiently for the dust condensation temperature to be achieved, its volume is significant. This means that when the shell does begin to contribute to the extinction, its dust is distributed over a considerable column length. The resulting low dust density means that only a small recovery in the $A_v^{TOT}(t)$ extinction distribution is achieved.

After reaching its peak, $A_v^{TOT}(t)$ again begins to drop in a volume dilution solution dependent on the width of each new shell formed. As an aside, the contribution from the ambient region to the extinction drops in tandem.

Therefore, the extinction distribution for a high η model is considerably different to that obtained over a low η model's evolution. For the high η model, the extinction appears to drop precipitously once the HII region is overtaken, reaching a minimum of $A_v^{TOT}(t) \leq 2$ at the boundary of the GMC $R2_W$. Due to the high supershell temperature the extinction remains very low for sometime, until volume cooling of the shell allows Fd^{SH} to gradually rise and eventually reach unity. At that point a small peak in the extinction is seen, whereafter the extinction drops in what is essentially a volume dilution solution until the outer edge of the system is reached at $R2_{SN}$.

Star Formation Efficiencies η=0.15, & 0.2

It is now possible to compare these observations for $\eta = 0.1$ to those for $\eta = 0.15$ & 0.2 and generalise the high η model behaviour. The extinction curves for $\eta = 0.15$ & 0.2 are shown on Figure 5.7, with the numerical values given in Tables 5.6 and 5.7. Both these models reach their cooling radii R_c whilst trapped within the neutral region, have shell temperatures in excess of the condensation temperature at $R2_W$ and have sufficient momentum to reach $R2_{SN}$ with their shells intact.

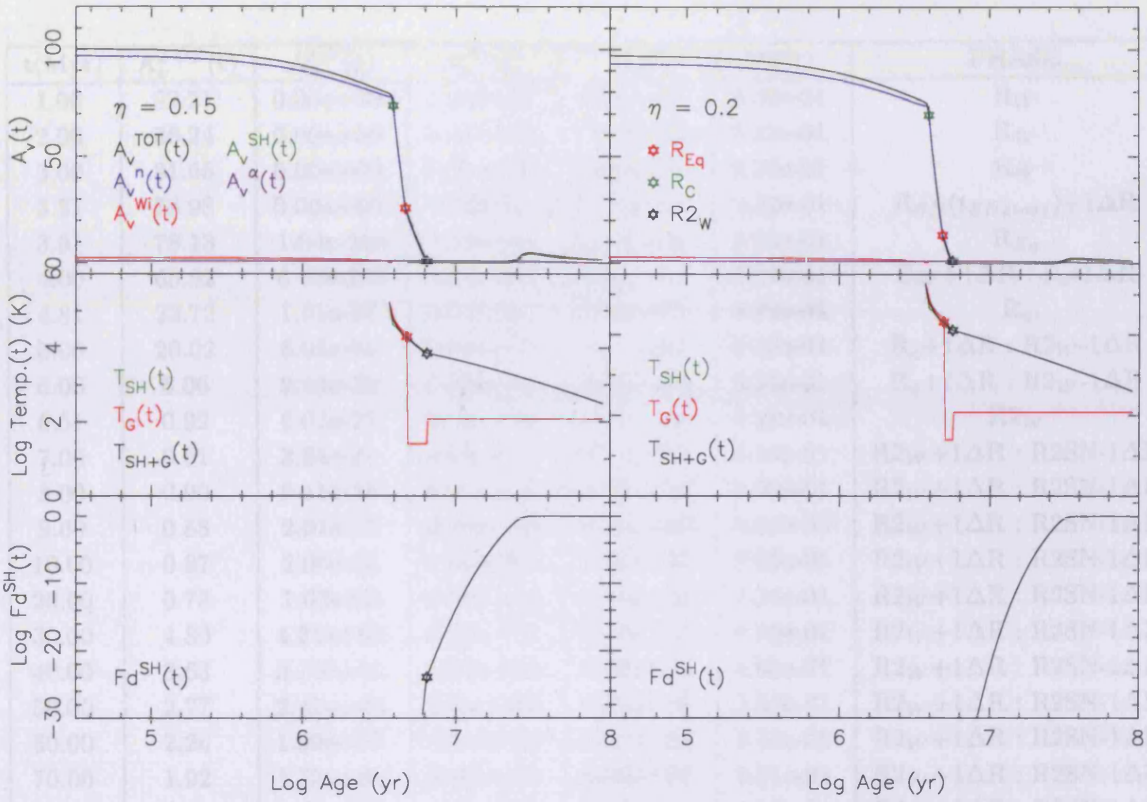

Figure 5.7: $A_v(t)$ contributions for $M_{GMC}=10^8 M_\odot$. η=0.15 is on the LHS whilst η=0.2 is on the RHS. In the top plots the extinctions from each region of the GMC are indicated by: the sum $A_v^{TOT}(t)$(black); neutral $A_v^n(t)$ (blue); HII Region $A_v^{Wi}(t)$ (red); supershell $A_v^{SH}(t)$ (green) and ambient $A_v^\alpha(t)$ (purple). In the middle plots the pre-existing volume diluted gas temperature $T_{SH}(t)$ (green) and the new overtaken gas temperature $T_G(t)$ (red) along with the supershell temperature $T_{SH+G}(t)$ (black) are given. The bottom plots show the behaviour of the dust condensation factor. Where appropriate the green, red, black and blue stars represent R_{Eq}, R_c, $R2_W$ and R_v respectively.

t(Myr)	A_v^{TOT}(t)	A_v^{SH}(t)	A_v^{Wi}(t)	A_v^{n}(t)	A_v^{α}(t)	PHASE
1.00	92.21	0.00e+00	1.99e+00	8.93e+01	9.22e-01	R_W
2.00	86.24	0.00e+00	1.62e+00	8.37e+01	9.22e-01	R_W
3.00	81.65	0.00e+00	1.13e+00	7.96e+01	9.22e-01	R_W
3.81	78.98	0.00e+00	3.58e-01	7.77e+01	9.22e-01	$R_{SN}(t_{SNstart})$+1ΔR
3.91	78.13	1.04e-233	1.03e-02	7.72e+01	9.22e-01	R_{Eq}
4.00	65.92	6.43e-205	0.00e+00	6.50e+01	9.22e-01	R_W+1ΔR : R_c-1ΔR
4.81	23.72	1.61e-78	0.00e+00	2.28e+01	9.22e-01	R_c
5.00	20.02	6.03e-64	0.00e+00	1.91e+01	9.22e-01	R_c+1ΔR : $R2_W$-1ΔR
6.00	6.06	2.44e-30	0.00e+00	5.14e+00	9.22e-01	R_c+1ΔR : $R2_W$-1ΔR
6.51	0.92	5.03e-23	0.00e+00	0.00e+00	9.22e-01	$R2_W$
7.00	0.91	3.54e-21	0.00e+00	0.00e+00	9.14e-01	$R2_W$+1ΔR : R2SN-1ΔR
8.00	0.90	5.11e-18	0.00e+00	0.00e+00	8.99e-01	$R2_W$+1ΔR : R2SN-1ΔR
9.00	0.88	2.01e-15	0.00e+00	0.00e+00	8.84e-01	$R2_W$+1ΔR : R2SN-1ΔR
10.00	0.87	2.95e-13	0.00e+00	0.00e+00	8.69e-01	$R2_W$+1ΔR : R2SN-1ΔR
20.00	0.73	1.03e-02	0.00e+00	0.00e+00	7.24e-01	$R2_W$+1ΔR : R2SN-1ΔR
30.00	4.80	4.21e+00	0.00e+00	0.00e+00	5.89e-01	$R2_W$+1ΔR : R2SN-1ΔR
40.00	3.63	3.16e+00	0.00e+00	0.00e+00	4.68e-01	$R2_W$+1ΔR : R2SN-1ΔR
50.00	2.77	2.41e+00	0.00e+00	0.00e+00	3.63e-01	$R2_W$+1ΔR : R2SN-1ΔR
60.00	2.26	1.99e+00	0.00e+00	0.00e+00	2.71e-01	$R2_W$+1ΔR : R2SN-1ΔR
70.00	1.92	1.73e+00	0.00e+00	0.00e+00	1.91e-01	$R2_W$+1ΔR : R2SN-1ΔR
80.00	1.68	1.56e+00	0.00e+00	0.00e+00	1.20e-01	$R2_W$+1ΔR : R2SN-1ΔR

Table 5.6: Contributions to the extinction from various regions of the cloud as the η = 0.15, M_{GMC}=$10^8 M_\odot$ system evolves. A_v^{TOT}(t) is the total extinction along a line of sight, A_v^{Wi}(t), A_v^{SH}(t), A_v^{n}(t) and A_v^{α}(t) are the contributions to that extinction from the HII region, supershell, neutral and ambient regions respectively. The final column gives the phase of the system at the time the extinction is calculated.

t(Myr)	A_v^{TOT}(t)	A_v^{SH}(t)	A_v^{Wi}(t)	A_v^{n}(t)	A_v^{α}(t)	PHASE
1.00	89.13	0.00e+00	2.23e+00	8.58e+01	1.10e+00	R_W
2.00	82.92	0.00e+00	1.82e+00	8.00e+01	1.10e+00	R_W
3.00	77.28	0.00e+00	1.27e+00	7.59e+01	1.10e+00	R_W
3.81	75.60	0.00e+00	3.99e-01	7.41e+01	1.10e+00	$R_{SN}(t_{SNstart})+1\Delta R$
3.90	74.61	4.86e-263	2.67e-02	7.35e+01	1.10e+00	R_{Eq}
4.00	61.40	8.95e-230	0.00e+00	6.03e+01	1.10e+00	$R_W+1\Delta R$: R_c-$1\Delta R$
4.91	11.70	8.85e-83	0.00e+00	1.06e+01	1.10e+00	R_c
5.00	9.74	4.80e-75	0.00e+00	8.64e+00	1.10e+00	$R_c+1\Delta R$
5.61	1.10	1.22e-48	0.00e+00	0.00e+00	1.10e+00	$R2_W$
6.00	1.09	1.05e-44	0.00e+00	0.00e+00	1.09e+00	$R2_W+1\Delta R$: R2SN-$1\Delta R$
7.00	1.07	9.79e-37	0.00e+00	0.00e+00	1.07e+00	$R2_W+1\Delta R$: R2SN-$1\Delta R$
8.00	1.05	1.10e-30	0.00e+00	0.00e+00	1.05e+00	$R2_W+1\Delta R$: R2SN-$1\Delta R$
9.00	1.03	5.82e-26	0.00e+00	0.00e+00	1.03e+00	$R2_W+1\Delta R$: R2SN-$1\Delta R$
10.00	1.00	3.47e-22	0.00e+00	0.00e+00	1.00e+00	$R2_W+1\Delta R$: R2SN-$1\Delta R$
20.00	0.80	8.35e-06	0.00e+00	0.00e+00	8.01e-01	$R2_W+1\Delta R$: R2SN-$1\Delta R$
30.00	1.12	4.97e-01	0.00e+00	0.00e+00	6.27e-01	$R2_W+1\Delta R$: R2SN-$1\Delta R$
40.00	2.47	1.99e+00	0.00e+00	0.00e+00	4.84e-01	$R2_W+1\Delta R$: R2SN-$1\Delta R$
50.00	2.02	1.65e+00	0.00e+00	0.00e+00	3.67e-01	$R2_W+1\Delta R$: R2SN-$1\Delta R$
60.00	1.71	1.44e+00	0.00e+00	0.00e+00	2.70e-01	$R2_W+1\Delta R$: R2SN-$1\Delta R$
70.00	1.50	1.31e+00	0.00e+00	0.00e+00	1.87e-01	$R2_W+1\Delta R$: R2SN-$1\Delta R$
80.00	1.34	1.23e+00	0.00e+00	0.00e+00	1.15e-01	$R2_W+1\Delta R$: R2SN-$1\Delta R$

Table 5.7: Contributions to the extinction from various regions of the cloud as the η = 0.2, $M_{GMC}=10^8 M_\odot$ system evolves. A_v^{TOT}(t) is the total extinction along a line of sight, A_v^{Wi}(t), A_v^{SH}(t), A_v^{n}(t) and A_v^{α}(t) are the contributions to that extinction from the HII region, supershell, neutral and ambient regions respectively. The final column gives the phase of the system at the time the extinction is calculated.

Extinction for Motion in the HII & Neutral Regions
$R_W(t) < R_{SN}(t) \leq R2_W$

The extinction distributions for both η=0.15 & 0.2 behave in a similar manner during the adiabatic phase to all models discussed so far. As the star formation efficiency η rises R_c occurs later and closest to $R2_W$. Neither of the models show a recovery in total extinction after R_c because there has been insufficient time for the gas rapidly accumulated in the supershell to cool to the condensation temperature before $R2_W$. This leads to an optical depth at $R2_W$ of $A_v^{TOT}(t) \leq 2$. This is illustrated in the bottom panels of Figure 5.7 which shows the dust condensation factors do not make any appreciable rise whilst the superbubbles are trapped within the GMC.

Extinction for Motion in the Ambient Region
$R2_W + 1\Delta t \leq R_{SN}(t) \leq R2_{SN}$

From $R2_W$ the total extinction distributions for η = 0.15 & 0.2 initially remain almost constant at essentially zero as the superbubbles continue out into the ambient region. After some time, the supershells cool sufficiently under the influence of volume expansion for the condensation factors to undergo a gradual rise. As Fd^{SH} approaches unity, the $A_v^{TOT}(t)$ of both models does begin a slight recovery to reach a small peak at $T_{SH+G}(t) \approx 1200K$. However, as with η = 0.1, the peak in extinction recovery for both the η = 0.15 & 0.2 models is very minor in comparison to those seen in the low η models.

With the low η's that reached $T_{SH+G}(t) = T_{cond}$ whilst inside the GMC, the difference between the peak and trough in $A_v^{TOT}(t)$ grew as the SFE rose, due to the increased velocity allowing more neutral material to be accumulated in the supershell before T_{cond} is reached. With these higher star formation efficiencies which do not reach $T_{SH+G}(t) = T_{cond}$ internally to $R2_W$, this relationship is inverted and the magnitude of the peak with respect to the trough drops with increasing SFE.

This effect can be explained in part by considering the distance a superbubble has travelled into the ambient region when the dust condensation temperature is reached. The further from $R2_W$ that $T_{SH+G}(t) = T_{cond}$, the broader the supershell width over which the dust contributes tends to be. This increase in volume drops the extinction contribution from the shell. Coupling this to the fact a system contains less gas and dust in the GMC as SFE rises, explains the corresponding drop in peak magnitude of the $A_v^{TOT}(t)$ recovery in the high η models.

Having reached their $A_v^{TOT}(t)$ peak the extinction for both η = 0.15 & 0.2 continues to drop down smoothly in line with the radial solution. The ambient contribution $A_v^{\alpha}(t)$ also begins to decrease as soon as the superbubble exits the GMC.

Star Formation Efficiency 0.25

Finally in this subsection Figure 5.8 and Table 5.8 show the dust extinction for η=0.25.

Extinction for Motion in the HII & Neutral Regions
$R_W(t) < R_{SN}(t) \leq R_c = R2_W$

The model has the highest luminosity of the SFEs considered here and consequently shows the most extreme behaviour in the adiabatic phase. η=0.25 is unique on the M_{GMC}=$10^8 M_\odot$ grid in that R_c actually occurs just inside the ambient region. 4.5.5 discusses the difficulties in accurately locating R_c when it occurs outside the GMC and justifies the use of $R_c = R2_W$ for this thesis work.

The behaviour of the η = 0.25 distribution mimics that of the other three high η models whilst internal to $R2_W$, with the extinction dropping very rapidly from R_{Eq} to $R2_W$ and no recovery in the optical depth exhibited.

The effect of setting $R_c = R2_W$ is clearly illustrated on Figure 5.8. In the middle temperature plot there is only one break in the $T_{SH+G}(t)$ distribution at $R_c = R2_W$ and correspondingly only one break in the temperature of the overtaken gas $T_G(t)$ where it drops to the external ambient temperature - and the cooling effect of accumulating neutral GMC material whilst in the isothermal phase is absent.

Extinction for Motion in the Ambient Region
$R_c + 1\Delta t \leq R_{SN}(t) \leq R2_{SN}$

The η = 0.25 superbubble must also continue into the ambient region some distance before $T_{SH+G}(t) = T_{cond}$. However, with η = 0.1, 0.15 & 0.2, as the SFE rose, the further the superbubble had to travel into the ambient region before $T_{SH+G}(t) = T_{cond}$ was achieved. η = 0.25 therefore presents some unique behaviour as it appears to reach $T_{SH+G}(t) = T_{cond}$ at a smaller radius than even η = 0.1.

Figure 3.28 in §4.7, gives the radius and velocity curves for $M_{GMC} = 10^8 M_\odot$ and this shows that because $R_c = R2_W$ the velocity $v_{SN}(t_{R2_W})$ is also very high. This has a knock-on effect for the motion of the superbubble after it exits the GMC as the velocity of the

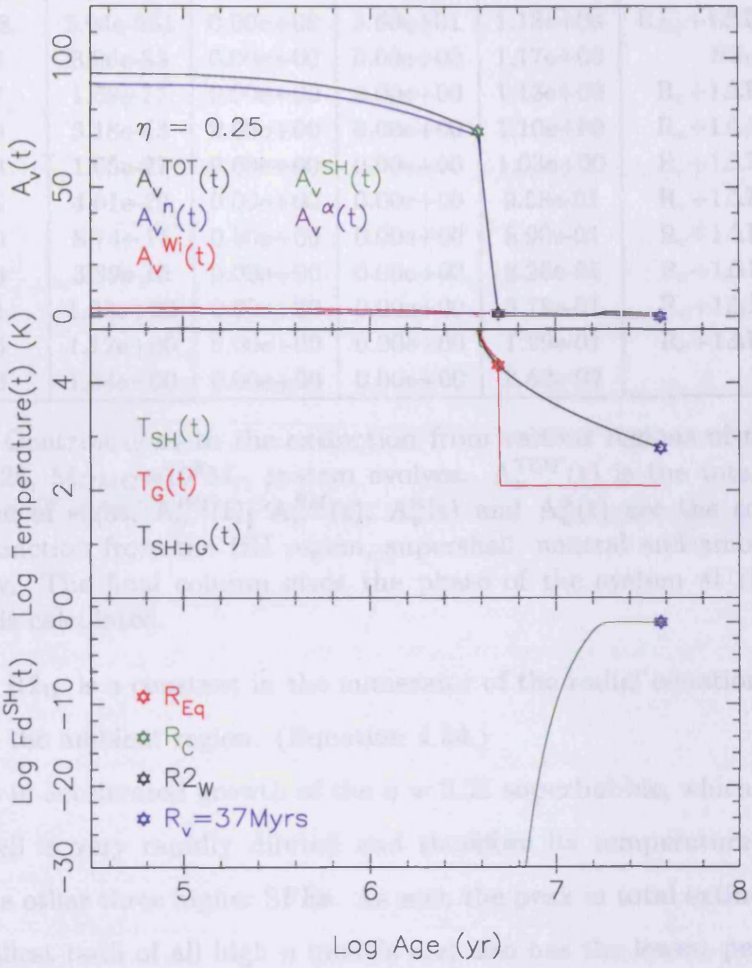

Figure 5.8: Av(t) contributions for $M_{GMC}=10^8 M_\odot$, η=0.25. In the top plot the extinction from each region of the GMC is indicated by: the sum A_v^{TOT}(t)(black); neutral A_v^n(t) (blue); HII Region A_v^{Wi}(t) (red); supershell A_v^{SH}(t) (green) and ambient A_v^α(t) (purple). In the middle plot the pre-existing volume diluted gas temperature T_{SH}(t) (green) and the new overtaken gas temperature T_G(t) (red) along with the supershell temperature T_{SH+G}(t) (black) are given. The bottom plot shows the behaviour of the dust condensation factor. Where appropriate the green, red, black and blue stars represent R_{Eq}, R_c, $R2_W$ and R_v respectively.

t(Myr)	A_v^{TOT}(t)	A_v^{SH}(t)	A_v^{Wi}(t)	A_v^n(t)	A_v^α(t)	PHASE
1.00	85.91	0.00e+00	2.43e+00	8.23e+01	1.18e+00	R_W
2.00	79.77	0.00e+00	1.99e+00	7.66e+01	1.18e+00	R_W
3.00	75.00	0.00e+00	1.39e+00	7.24e+01	1.18e+00	R_W
3.81	72.22	0.00e+00	4.35e-01	7.06e+01	1.18e+00	$R_{SN}(t_{SNstart})$+1ΔR
3.91	71.22	2.97e-288	3.59e-02	7.00e+01	1.18e+00	R_{Eq}
4.00	57.18	2.04e-251	0.00e+00	5.60e+01	1.18e+00	R_{Eq}+1ΔR : $R2_W$-1ΔR
4.91	1.18	3.06e-83	0.00e+00	0.00e+00	1.17e+00	$R2_W = R_c$
5.00	1.17	1.69e-77	0.00e+00	0.00e+00	1.13e+00	R_c+1ΔR : R_V-1ΔR
6.00	1.10	3.18e-43	0.00e+00	0.00e+00	1.10e+00	R_c+1ΔR : R_V-1ΔR
7.00	1.03	1.05e-27	0.00e+00	0.00e+00	1.03e+00	R_c+1ΔR : R_V-1ΔR
8.00	0.96	4.01e-19	0.00e+00	0.00e+00	9.58e-01	R_c+1ΔR : R_V-1ΔR
9.00	0.89	8.74e-14	0.00e+00	0.00e+00	8.90e-01	R_c+1ΔR : R_V-1ΔR
10.00	0.83	3.39e-10	0.00e+00	0.00e+00	8.26e-01	R_c+1ΔR : R_V-1ΔR
20.00	1.71	1.33e+00	0.00e+00	0.00e+00	3.78e-01	R_c+1ΔR : R_V-1ΔR
30.00	1.25	1.12e+00	0.00e+00	0.00e+00	1.29e-01	R_c+1ΔR : R_V-1ΔR
37.00	1.13	1.04e+00	0.00e+00	0.00e+00	8.62e-02	R_V

Table 5.8: Contributions to the extinction from various regions of the cloud as the $\eta = 0.25$, $M_{GMC}=10^8 M_\odot$ system evolves. A_v^{TOT}(t) is the total extinction along a line of sight, A_v^{Wi}(t), A_v^{SH}(t), A_v^n(t) and A_v^α(t) are the contributions to that extinction from the HII region, supershell, neutral and ambient regions respectively. The final column gives the phase of the system at the time the extinction is calculated.

superbubble at $R2_W$ is a constant in the numerator of the radial equation for momentum conservation in the ambient region. (Equation 4.54.)

This results in accelerated growth of the $\eta = 0.25$ superbubble, which means any dust in the supershell is very rapidly diluted and therefore its temperature drops far more quickly than the other three higher SFEs. As such the peak in total extinction occurs first and at the smallest radii of all high η models and also has the lowest peak magnitude of A_v^{TOT}(t). This latter observation is a result of a combination of large supershell volume at T_{cond} and low initial cloud mass. As the total extinction for $\eta = 0.25$ does not rise above 1.71 once the superbubble has exited the GMC the peak achieved in A_v^{TOT}(t) is barely discernible.

Having reached this peak the extinction dilutes in proportion to the radial solution but again in contrast to the other three higher SFEs this model is unable to reach $R2_{SN}$ with its shell intact. This is also due to the effect of $R_c = R2_W$ on the radial solution as the volume cooling experienced by the shell rapidly drops T_{SH+G}(t) to below the external ambient temperature and the shell breaks up and looses its integrity at t(R_V) = 37Myrs.

This last results suggests that perhaps in future work it would be beneficial to develop

a method of determining the cooling radius within the ambient region. This would be particularly relevant if e.g., higher mass GMCs or greater values of the star formation efficiency were to be tested. However, the logical successor to the 1-d semi-analytical code GEM is a fully 3-d hydrodynamic code, in which case a location of R_c would not have to be imposed as the heating and cooling rates would dictate the shell's collapse.

Summary of High η Models

The behaviour of the extinction for all high η models exhibits the same general trends. The extinction appears to drop precipitously from the maximum value once the superbubble has exited the HII region and entered the neutral cloud. The cooling radius occurs progressively further from the source as the star formation efficiency η rises, with R_c for the most luminous model, $\eta = 0.25$, actually being located in the ambient region.

Due to the supershell temperature being well in excess of the dust condensation temperature at the outer boundary of the GMC, the extinction tends to be nominal ($A_v^{TOT}(t) \leq 2$) at $R2_W$ because the entire mass of the neutral GMC is now contained in a supershell too hot to contribute to the extinction.

As the superbubble continues into the ambient region the increase in shell growth due to the change in the upstream density, causes the shell temperature to drop so that some time later the dust condensation temperature is reached. However, in contrast to the lower η models where a substantial peak magnitude recovery was seen in the optical depth when $T_{SH+G}(t) = T_{cond}$, the high η model show no such substantial recovery. This is because by the time the condensation temperature has been reached the shell volume is so large that the dust is distributed very sparsely within it.

Thus in a high η model it could be said that the extinction drops rapidly to low values where it remains for the majority of the system's evolution.

5.5.3 M_{GMC}=10^9-, 10^8-, 10^7- & $10^6M_\odot$; All η

Having discussed the regional contribution to the extinction as a system evolves for the M_{GMC}=$10^8M_\odot$ η grid, variation in η for the other giant molecular cloud masses; M_{GMC}= 10^9-, 10^7- & $10^6M_\odot$ can now be compared. The total extinction distribution $A_v^{TOT}(t)$, only, for each η at all GMC masses is illustrated in Figure 5.9.

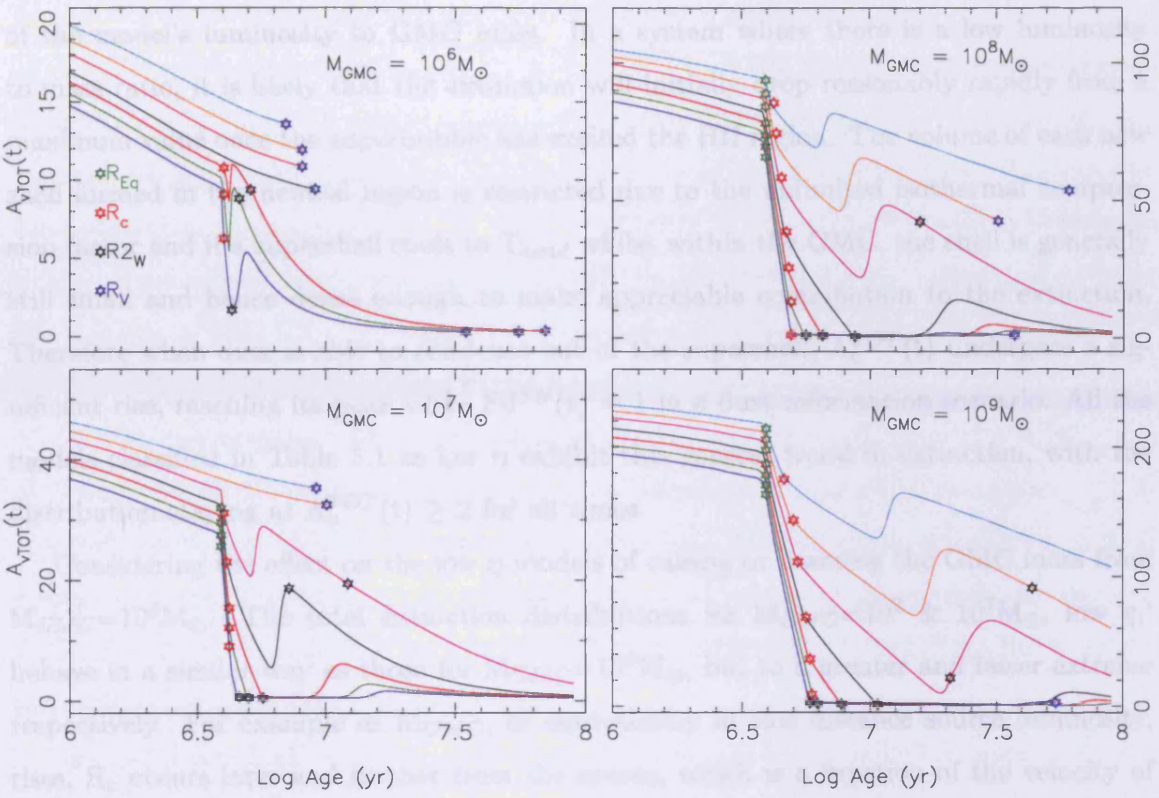

Figure 5.9: $A_v(t)$ distributions for all M_{GMC}. $\eta = 0.01$, 0.025, 0.05, 0.1, 0.15, 0.2 & 0.25 are given in cyan, orange, pink, black, red, green & blue respectively. the green star represents the point at which superbubble overtakes its HII region IF R_{Eq}, the red star indicates the cooling radius R_c, the black star gives the outer edge of the dense GMC, $R2_W$ and the blue star shows the break up radius R_v where applicable. M_{GMC}=1e6$M_\odot$ η = 0.01, 0.025, 0.5, 0.1 and M_{GMC}=$10^7 M_\odot$ $\eta = 0.01$ & 0.025 are given by the HII region solution at all t.

Discussion

As mentioned, the defining characteristic leading to the categorization of a model as either high or low η is the temperature of the supershell at the outer boundary of the GMC; when a supershell exits the GMC with a shell temperature in excess of the condensation temperature it has been categorised as *higher* η and vice versa.

The factor which in turn determines the supershell temperature at $R2_W$ is the ratio of the model's luminosity to GMC mass. In a system where there is a low luminosity to mass ratio, it is likely that the extinction will initially drop reasonably rapidly from a maximum value once the superbubble has excited the HII region. The volume of each new shell formed in the neutral region is restricted due to the unlimited isothermal compression factor and if a supershell cools to T_{cond} whilst within the GMC, the shell is generally still small and hence dense enough to make appreciable contribution to the extinction. Therefore when dust is able to condense out of the supershell, $A_v^{TOT}(t)$ undergoes a significant rise, reaching its peak when $Fd^{SH}(t) = 1$ in a dust-reformation scenario. All the models classified in Table 5.1 as low η exhibit this general trend in extinction, with the distribution staying at $A_v^{TOT}(t) \geq 2$ for all times.

Considering the effect on the low η models of raising or lowering the GMC mass from $M_{GMC}=10^8 M_\odot$. The total extinction distributions for $M_{GMC}=10^9$ & $10^7 M_\odot$, low η,' behave in a similar way as those for $M_{GMC}=10^8 M_\odot$, but to a greater and lesser extreme respectively. For example as M_{GMC}, or equivalently in this instance source luminosity, rises, R_c occurs later and further from the source, which is a function of the velocity of the supershell governing its temperature in the adiabatic phase and the smaller extent of the neutral region as the SFE rises.

The effect of this increasing outflow velocity is illustrated on Figure 5.9 by the gradient and time these systems' extinction spends in decline before dust reforms, coupled to the difference between their tough and peak in $A_v^{TOT}(t)$. As M_{GMC} rises for the same η so does the amount of time spent accumulating neutral material in the adiabatic phase and the time a supershell needs to cool to the dust condensation temperature T_{cond}. In turn this leads to the increase in the gradient and time over which the extinction drops as well as the difference in $A_v^{TOT}(t)$ trough and peak. This behaviour is familiar as it is the same trend seen in the $M_{GMC}=10^8 M_\odot$ models as η rises from 0.01 through 0.025 to 0.05. This is to be expected as the neutral material is distributed uniformly in each cloud; raising

the mass converted into stars either via M_{GMC} or η just increases the luminosity.

Conversely, models classified as high η tend to have $T_{SH+G}(t_{R2_W}) >> T_{cond}$. The optical depths of these models appears to drop precipitously to approximately zero at $R2_W$, which is reached early in the system's life-time, whereupon the extinction remains low for the entire evolution. Whilst these high η models do show a small recovery in their extinction at late times, the magnitude of the peak is minimal compared to that achieved by the low η models due to the large shell volume at $T_{SH+G} = T_{cond}$.

That the difference between the low and high η models is a function of the ratio of the luminosity to the gas and dust mass contained in the surrounding cloud can be illustrated by considering $M_{GMC}=10^8 M_\odot$ $\eta = 0.25$ and $M_{GMC}=10^9 M_\odot$ $\eta = 0.025$. Both these models have equivalent masses tied up in their source clusters at $M_\star = 2.5 \times 10^7 M_\odot$, but the mass of the surrounding neutral clouds are $7.5 \times 10^7 M_\odot$ and $9.75 \times 10^8 M_\odot$ respectively. Hence for $M_{GMC}=10^8 M_\odot$, $R2_{W_{0.25}} = 3.30 \times 10^{20}$cm and for $M_{GMC}=10^9 M_\odot$, $R2_{W_{0.025}} = 7.73 \times 10^{20}$cm; well over twice the radius of the lower M_{GMC} system.

Due to the extent of the individual clouds, $t(R2_{W_{0.25}}) = 5$Myrs, whilst $t(R2_{W_{0.025}}) = 44$Myrs which leads to $T_{SH+G}(t_{R2_{W_{0.025}}}) = 458\text{K} << T_{cond}$ but $T_{SH+G}(t_{R2_{W_{0.25}}}) = 15{,}000\text{K} >> T_{cond}$. Therefore, despite both supershells containing the entire mass of their respective systems at $R2_W$, a considerable amount of heat must be radiated by the $\eta = 0.25$ supershell before its dust can contribute to the extinction because $R2_W$ has occurred so much earlier in the systems evolution.

Having reached $R2_W$, heat radiation from the $\eta = 0.25$ supershell is assisted by the additional volume dilution that occurs in the ambient region due to the change in the external sound speed along with the sparsity of new material added to the supershell at each step. Thus, in comparison, the width of the $\eta = 0.025$ supershell at T_{cond} is $R_{SH}(t_{T_{cond}}) = 9.5 \times 10^{18}$cm but for the $\eta = 0.25$ supershell at T_{cond}, $R_{SH}(t_{T_{cond}}) = 2 \times 10^{19}$cm. So, not only does the $\eta = 0.25$ supershell contain considerably less mass when it reaches the condensation temperature - the additional material accumulated in the ambient region does little to mitigate the difference in GMC starting conditions - but it is also significantly broader than the $\eta = 0.25$ supershell at the same temperature. This difference in shell volume and hence density at $T_{SH+G}(t_{T_{cond}})$ results in the almost non-existent peak in $A_v^{TOT}(t)$ seen on the $\eta = 0.25$ extinction curve and the significant recovery in $A_v^{TOT}(t)$ for $\eta = 0.025$. As these two models have equivalent luminosity, it can be seen it is the ratio of luminosity to available dust and gas - the SFE - and the adoption

of a common condensation temperature T_{cond} which has determined the behaviour of the extinction.

In summary, the range of SFE on the entire supernovae parameter grid has between 1% and 25% of the GMC mass converted into the source function and a break in the behaviour of the extinction is seen at around $\eta = 0.1$. In general, if $M_\star$ represents between 1%- 10% of the total cloud mass the supershell is able to cool to $T_{SH+G}(t) = T_{cond}$ whilst trapped within the confines of the GMC and the extinction distribution, having been in decline, exhibits a recovery to more substantial values in a dust reformation scenario. These can be classified as low η. Conversely in a system where between 10% and 25% of the GMC mass has been converted into the central source function, the supershell temperature is in excess of the dust condensation temperature at $R2_W$, the extinction declines to reach a minimum after $R2_W$, where it remains for some time, before exhibiting a much smaller peak in recovery at late times and these have been classified as high η.

This distinction is illustrated in Figures 5.10 and 5.11 which shows all seven star formation efficiencies as a function of giant molecular cloud mass. Of those models which invoke the supernova solution, the extinction distributions for the low η models show the recovery of $A_v^{TOT}(t)$ after it reaches a minimum at all four M_{GMC}'s. Conversely, for the high η's there is almost no appreciable $A_v^{TOT}(t)$ at any M_{GMC} after $R2_W$. What is also illustrated is that those models at the very lowest M_{GMC} and η revert to the HII region solution at all times t.

This concludes development of the optical depth distributions. The dust density ratios and the location of the density breaks, along with the total optical depth along a line of sight at time t are now used in DaRT to define the GMC's dust starting conditions. The dust distribution is irradiated by the appropriate STARBURST99 source cluster SED, also for time t. The radiative transfer of the source flux is then calculated in a series of iterations until convergence of the model system is achieved. The emergent starburst supernovae SEDs are then generated and these are examined in the next chapter.

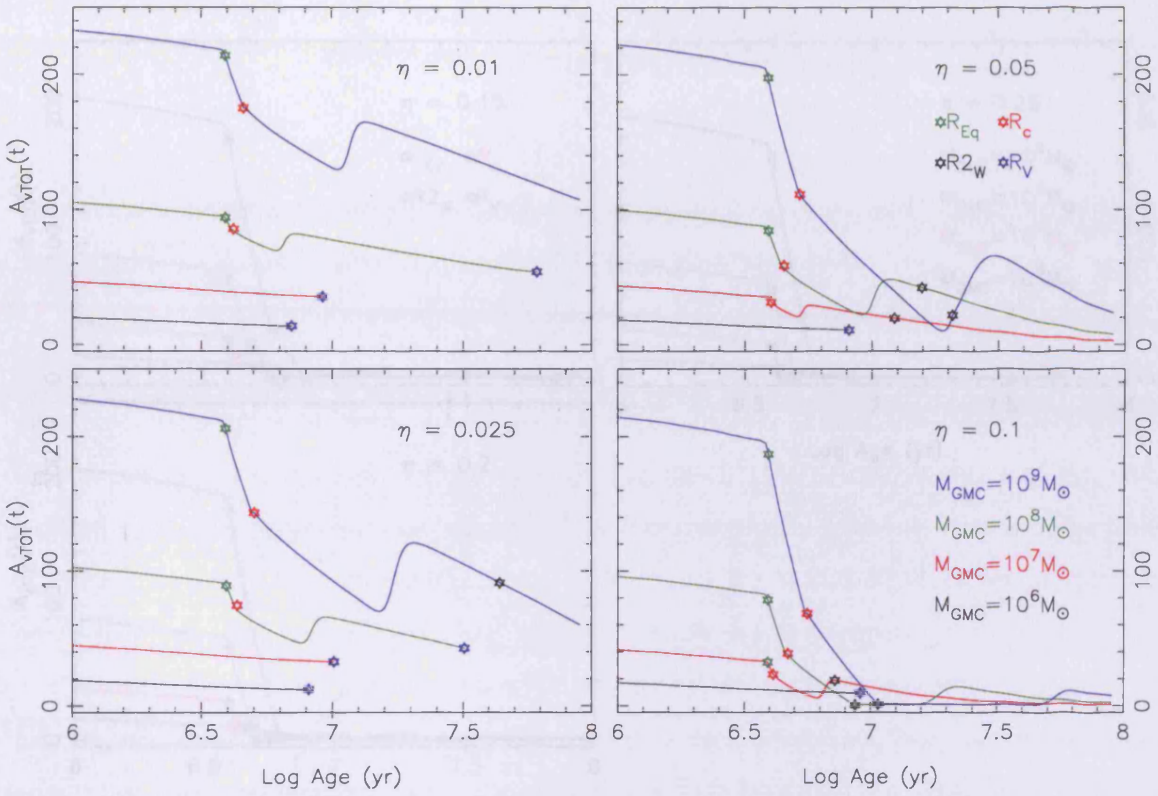

Figure 5.10: $A_v(t)$ contributions from all M_{GMC} at $\eta = 0.01$, 0.025, 0.05 & 0.1. M_{GMC}=1e6$M_\odot$ $\eta = 0.01$, 0.025, 0.5, 0.1 and M_{GMC}=$10^7 M_\odot$ $\eta = 0.01$ & 0.025 are given by the HII region solution. Each plot shows $A_v^{TOT}(t)$ for all four M_{GMC}'s per η. M_{GMC}=10^6-, 10^7-,10^6-,10^8- & $M_\odot$ given in black, red, green and blue respectively. The top and bottom LHS plots show $\eta = 0.01$ & 0.025 whilst those on the RHS give $\eta = 0.05$ at the top & $\eta = 0.1$ at the bottom. Where appropriate the green, red, black and blue stars represent R_{Eq}, R_c, $R2_W$ and R_v respectively.

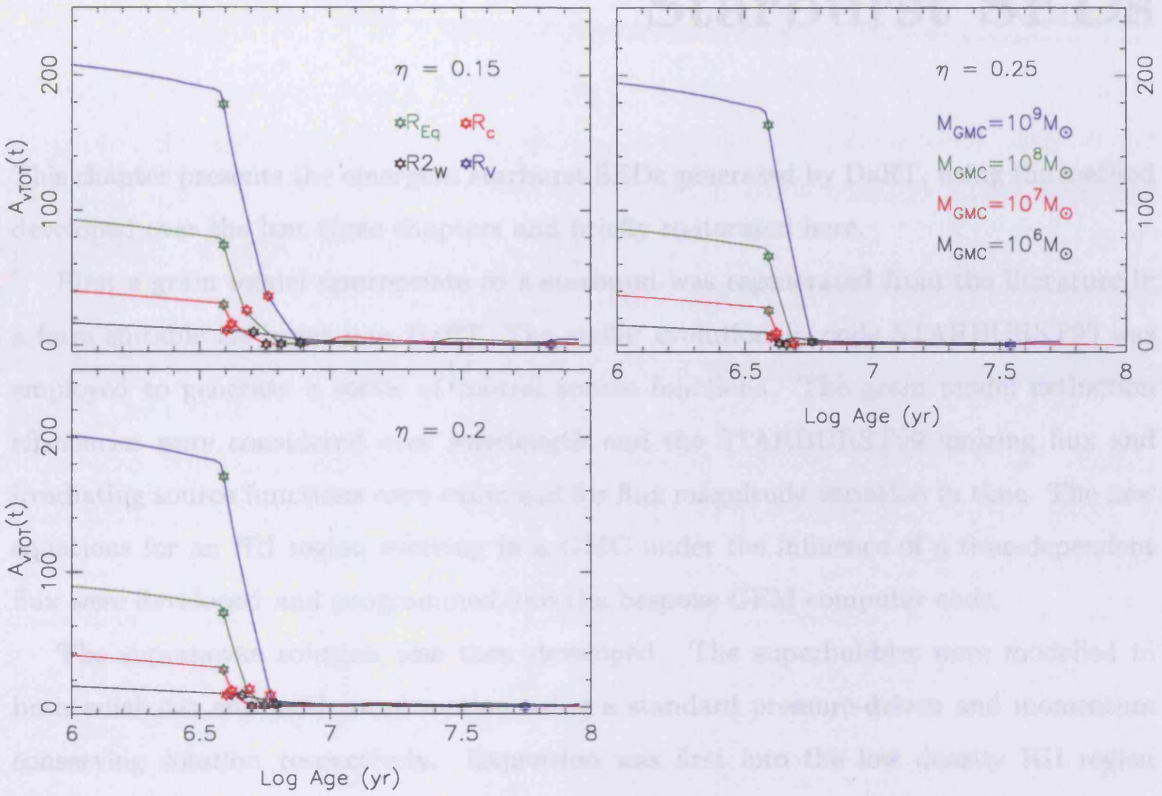

Figure 5.11: $A_v(t)$ contributions from all M_{GMC} at $\eta = 0.15$, 0.2 & 0.25. Each plot shows $A_v^{TOT}(t)$ for all four M_{GMC}'s per η; M_{GMC}=10^6-, 10^7-,10^6-,10^8- & $M_\odot$ given in black, red, green and blue respectively. The top and bottom LHS plots show $\eta = 0.15$ & 0.2 whilst that on the RHS gives $\eta = 0.25$. Where appropriate the green, red, black and blue stars represent R_{Eq}, R_c, $R2_W$ and R_v respectively.

Chapter 6

Starburst SEDs

This chapter presents the emergent starburst SEDs generated by DaRT, using the method developed over the last three chapters and briefly re-iterated here.

First a grain model appropriate to a starburst was regenerated from the literature in a form suitable for input into DaRT. The stellar evolutionary code STARBURST99 was employed to generate a series of central source functions. The grain model extinction efficiencies were considered over wavelength and the STARBURST99 ionizing flux and irradiating source functions were examined for flux magnitude variation in time. The new equations for an HII region evolving in a GMC under the influence of a time-dependent flux were developed and programmed into the bespoke GEM computer code.

The supernovae solution was then developed. The superbubbles were modelled in both adiabatic and isothermal motion using a standard pressure-driven and momentum conserving solution respectively. Expansion was first into the low density HII region generated by the impact of the ionizing stellar flux, then into a GMC of average density 300cm^{-3} and finally into an ambient interstellar region of average density 1cm^{-3}. The accumulation of up-stream gas into a narrow shell trapped on the bubble's surface was also modelled using simple shock physics. The gas density of the shell was linked to the dust density via a temperature dependent dust condensation factor. These expressions were also programmed into GEM.

Optical depth equations were then developed to quantify the evolution of the extinction with time. These expressions were programmed into GEM, along with the DaRT relationships defining the ratio of regional densities and the location of the density breaks. GEM was then run 28 times to model systems with each combination of M_{GMC} and η on the parameter grid. This generated the final product; the dust density distribution

as a function of time, for a wide range of GMCs evolving under the influence of both time-dependent stellar flux and supernovae continuous luminosity, in a form suitable for input into DaRT.

For each of the 28 models, the dust density distribution for a particular time t was then irradiated in DaRT by the appropriate time-dependent STARBURST99 source function SED for the same time t. The radiative transfer of flux was calculated, the system brought to convergence via a series of iterations and the emergent supernovae SEDs generated.

The DaRT code was run for each model combination of η and M_{GMC} at Δt_{SED} = 1Myr for the first 10Myrs and Δt_{SED} = 10Myr between 10- and 80Myrs, with the preferential sampling accounting for early times when most source variation is observed. Each of the 28 models produces approximately 17 individual SEDs, which together give a picture of the system's evolution with time.

As the extinction was discussed and illustrated in depth first with respect to the output for $M_{GMC} = 10^8 M_\odot$, it is convenient to continue in a similar manner with the emergent spectra. The SEDs for $M_{GMC} = 10^9$-, 10^7- & $10^6 M_\odot$ can then be briefly compared.

At the end of the previous chapter it was found that the models for each M_{GMC} exhibited bi-polar activity and could be divided into low and high star formation efficiency η, based on the temperature of the supershell at $R2_W$. The SEDs have therefore been categorised into four regimes; above or below the dust condensation temperature, whilst internal or external to $R2_W$. These have been indicated on the SED plots displayed in this chapter with a different line type:

- Solid Line: $T_{SH+G}(t) \geq T_{cond}$ whilst $R_{SN}(t) \leq R2_W$
- Dashed Line: $T_{SH+G}(t) \leq T_{cond}$ whilst $R_{SN}(t) \leq R2_W$
- Dash-Dot Line: $T_{SH+G}(t) \geq T_{cond}$ whilst $R_{SN}(t) \geq R2_W$
- Dotted Line: $T_{SH+G}(t) \leq T_{cond}$ whilst $R_{SN}(t) \geq R2_W$

In all cases the SEDs for t = 1, 2 & 3Myrs, prior to the first supernova explosion, are given by the HII region solution and as such were considered at the end of Chapter 3. Referring to Figure 3.8 each of these very early SEDs has a similar form. No flux is visible in any HII region spectra at wavelengths shorter than $\lambda = 1\mu$m. Strongly spiking MIR PAH emission and NIR very small grain emission emanates from the low optical depth

M_{GMC}	η	Category
$10^8 M_\odot$	0.1, 0.15, 0.2, 0.25	High
$10^8 M_\odot$	0.01, 0.025, 0.05	Low

Table 6.1: η Classification of $M_{GMC} = 10^8 M_\odot$ All Models. Models have been categorised as Low η if $T_{SH+G} < T_{cond}$ at $R2_W$, whilst those categorised as High η have $T_{SH+G} \geq T_{cond}$ at $R2_W$.

ionized sphere. And in the FIR, broad cool emission is seen from dust in the neutral region.

For this discussion on the supernovae solution SEDs, these early HII region solutions have not been illustrated as their inclusion somewhat confuses the behaviour of the supernovae solutions. However $M_{GMC} = 10^7 M_\odot$, $\eta = 0.01$ & 0.025 revert to the HII region solution at all times t and these SEDs have been illustrated later in this section in Figure 6.9 for easy comparison.

6.0.1 $M_{GMC} = 10^8 M_\odot$; Low η

As Table 6.1 shows, for $M_{GMC} = 10^8 M_\odot$ the models in the low efficiency category are $\eta =$ 0.01, 0.025 & 0.05. These SEDs are illustrated in Figures 6.1 & 6.2. The numerical optical depth data for each region of these systems were shown in the previous chapter in Tables 5.2, 5.3 & 5.4 respectively, whilst Figures 5.5 & 5.6 showed the extinction contributions graphically. Also shown on those plots was the corresponding temperatures $T_{SH}(t)$, $T_G(t)$ and $T_{SH+G}(t)$ and the dust condensation factor for the supershell $Fd^{SH}(t)$.

$\eta = 0.01$: $T_{SH+G}(t) \geq T_{cond}$ whilst $R_{SN}(t) \leq R2_W$
Supershell above T_{cond} whilst inside the GMC

Three SEDs from the $\eta = 0.01$ model set originate in this regime: t = 4-, 5- & 6Myrs. These are depicted on Figure 6.1 by the solid lines. Each of these SEDs is representative of a phase of the early superbubble and shell evolution.

t = 4Myrs

At t=4Myrs, the superbubble has only just overtaken the HII region IF and as such contains all the gas that previously occupied the volume $4\pi/3[R_{SN}(t)^3 - R_1(t_{SN_{start}})^3]$. As

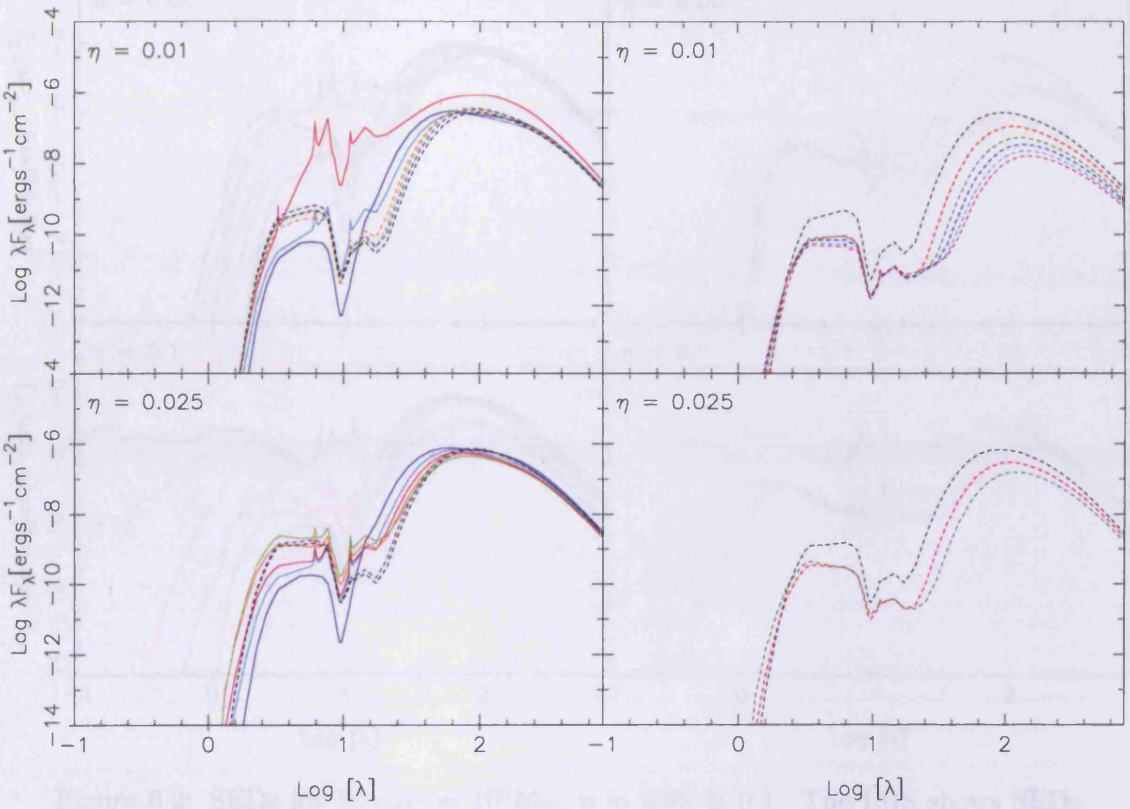

Figure 6.1: SEDs for $M_{GMC} = 10^8 M_\odot$, $\eta = 0.01$ & 0.025. The LHS shows SEDs for 4, 5, 6, 7, 8, 9 & 10 Myrs in blue, cyan, magenta, orange, light green, purple and black respectively. The RHS shows SEDs for 10, 20, 30, 40, 50 & 60Myrs in black, red, dark green, blue, cyan and magenta respectively. Solid lines indicate that $T_{SH+G}(t) > T_{cond}$ whilst $R_{SN}(t) < R2_W$ and Dashed Lines illustrate $T_{SH+G}(t) < T_{cond}$ whilst $R_{SN}(t) < R2_W$

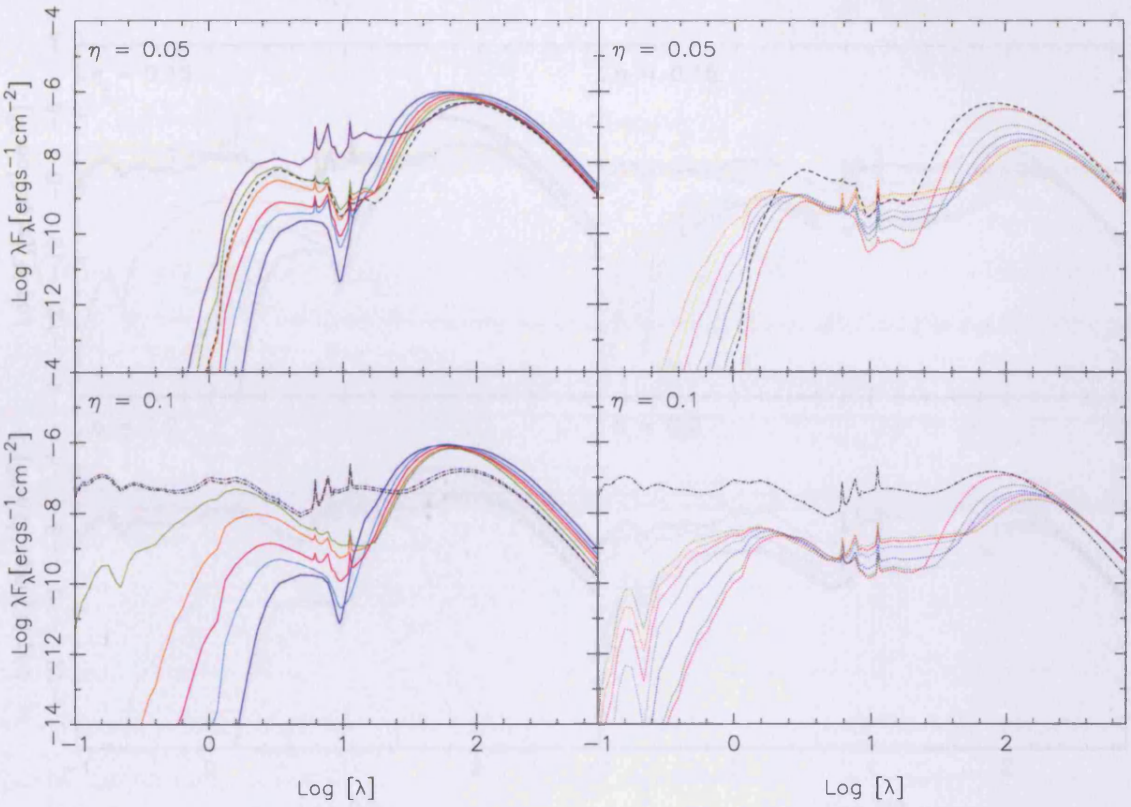

Figure 6.2: SEDs for $M_{GMC} = 10^8 M_\odot$, $\eta = 0.05$ & 0.1. The LHS shows SEDs for 4, 5, 6, 7, 8, 9 & 10 Myrs in blue, cyan, magenta, orange, light green, purple and black respectively. The RHS shows SEDs for 10, 20, 30, 40, 50, 60, 70 & 80Myrs in black, red, dark green, blue, cyan and magenta respectively. Solid lines indicate that $T_{SH+G}(t) > T_{cond}$ whilst $R_{SN}(t) < R2_W$, Dashed Lines illustrate $T_{SH+G}(t) < T_{cond}$ whilst $R_{SN}(t) < R2_W$, Dash-Dot Lines show $T_{SH+G}(t) > T_{cond}$ whilst $R_{SN}(t) > R2_W$ and Dotted lines show $T_{SH+G}(t) < T_{cond}$ whilst $R_{SN}(t) > R2_W$

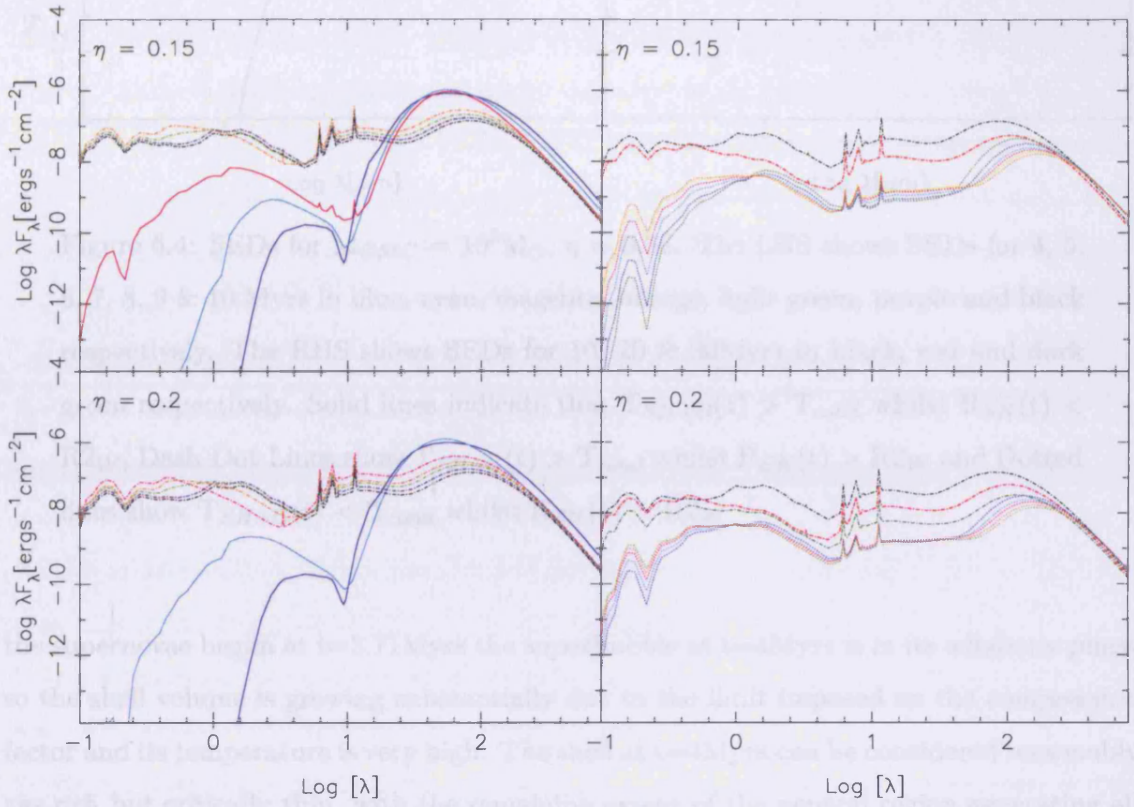

Figure 6.3: SEDs for $M_{GMC} = 10^8 M_\odot$, $\eta = 0.2$ & 0.25. The LHS shows SEDs for 4, 5, 6, 7, 8, 9 & 10 Myrs in blue, cyan, magenta, orange, light green, purple and black respectively. The RHS shows SEDs for 10, 20, 30, 40, 50, 60, 70, 80Myrs in black, red, dark green, blue, cyan, magenta, orange and light green respectively. Solid lines indicate that $T_{SH+G}(t) > T_{cond}$ whilst $R_{SN}(t) < R2_W$, Dash-Dot Lines show $T_{SH+G}(t) > T_{cond}$ whilst $R_{SN}(t) > R2_W$ and Dotted lines show $T_{SH+G}(t) < T_{cond}$ whilst $R_{SN}(t) > R2_W$

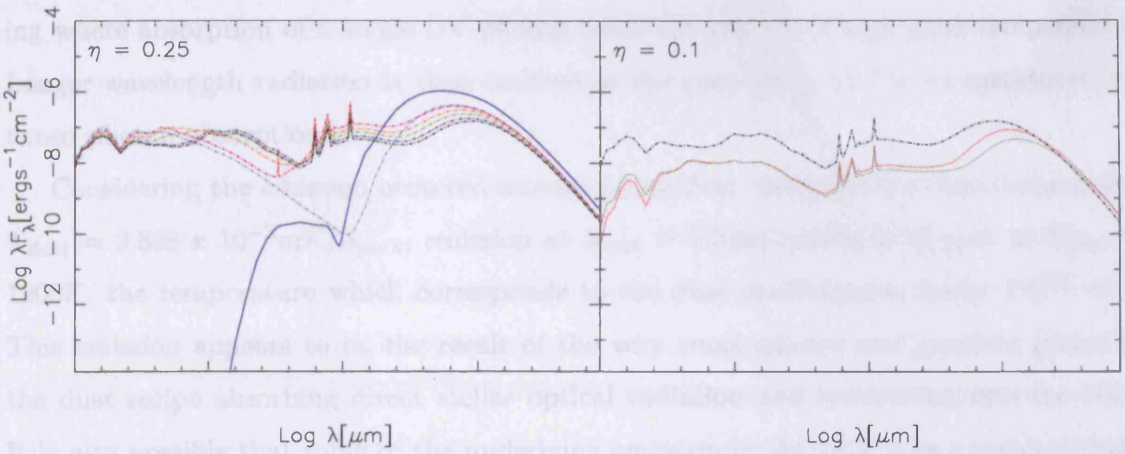

Figure 6.4: SEDs for $M_{GMC} = 10^8 M_\odot$, $\eta = 0.25$. The LHS shows SEDs for 4, 5, 6, 7, 8, 9 & 10 Myrs in blue, cyan, magenta, orange, light green, purple and black respectively. The RHS shows SEDs for 10, 20 & 30Myrs in black, red and dark green respectively. Solid lines indicate that $T_{SH+G}(t) > T_{cond}$ whilst $R_{SN}(t) < R2_W$, Dash-Dot Lines show $T_{SH+G}(t) > T_{cond}$ whilst $R_{SN}(t) > R2_W$ and Dotted lines show $T_{SH+G}(t) < T_{cond}$ whilst $R_{SN}(t) > R2_W$

the supernovae began at t=3.71Myrs the superbubble at t=4Myrs is in its adiabatic phase so the shell volume is growing substantially due to the limit imposed on the compression factor and its temperature is very high. The shell at t=4Myrs can be considered reasonably gas-rich but optically thin, with the remaining extent of the neutral region generating all the opacity.

The influence of the extinction from the neutral region is shown by the steep gradient of the short wavelength side of the NIR spectrum and effectively zero emission short-wards of $\lambda = 1\mu$m, where attenuated stellar source flux might be expected.

As mentioned when the HII region SEDs were illustrated, the absorption at these very short wavelengths is generated by the highly efficient very small graphite and silicate grains across the 2175$\AA$ feature and by PAHs over the non-linear FUV rise. Around $\lambda = 1\mu$m, scattering by the very small grains is also an important component of the extinction. Therefore not only are photons being absorbed directly out of the line of sight by the very small grains, but they are also being scattered and then immediately re-absorbed by dust in the near vicinity.

The very small grain and PAH population undergoes transient stochastic (nLTE) heat-

ing where absorption of a single UV photon heats the grain to a high peak temperature. Longer wavelength radiation is then emitted as the grain cools to low temperatures between photon absorptions.

Considering the emission centered around 2.5μm first, using Wein's displacement law T_{dust} = 2.898 x 10^{-3}mK/λ_{peak}, emission at λ_{peak} = 2.5μm results from dust at $T_{dust} \approx$ 1200K, the temperature which corresponds to the dust condensation factor $Fd^{SH} = 1$. This emission appears to be the result of the very small silicate and graphite grains in the dust recipe absorbing direct stellar optical radiation and re-emitting into the NIR. It is also possible that some of the underlying emission in the NIR is as a result of high vibrational excitation of PAHs by UV radiation producing a quasi-continuum due to the overlapping of many weak absorption bands (SK92).

Looking in the MIR, the t = 4Myr spectra does not exhibit any characteristic PAH features. As mentioned, the SEDs for t $\leq$ 3Myrs, given by the HII region solution, show strongly spiking PAH emission in the MIR coming from dust in the low optical depth ionized sphere. However, the η = 0.01 superbubble overtook the HII region at $t(R_{Eq})$ = 3.91Myrs and at t = 4Myrs the PAH features are absent. This can be understood by considering the free path length of the exciting radiation.

One criteria for single photon absorption by either very small grains or PAHs is that they can see the hard radiation field. As the supershell is very hot during the adiabatic phase no dust is able to condense and at early times the stellar radiation can pass straight through the shell into the ionized sphere to excite the PAHs and very small grains giving the distinctive spectra.

Once the superbubble has overtaken the HII region IF the stellar radiation falls on the face of the neutral region. The very small grains located there are excited into the NIR 2.5μm emission primarily by optical photons and in the process the neutral gas and dust warms. The optical depth of the neutral region is very high at this early time and the free path length of an optical photon is relatively small which leads to the low magnitude of the 2.5μm dust emission

However, it is the UV photons which excite the PAH population and the free path length of a UV photon in a high optical depth medium like the neutral region is smaller still than an optical photon. Thus, the 100,000yrs that have elapsed between the IF front being overtaken and the SED being generated are insufficient for an emitting column length of PAHs to be excited. Secondly, the high optical depth of the neutral region also

means the free path length of the re-emitted photons is short. This dynamic explains the small magnitude very small grain emission and the absence of MIR PAH features in the t = 4Myrs spectra.

Therefore is it primarily the very small grain population undergoing single photon absorption, coupled to highly efficient scattering, which removes all the hard stellar radiation generated by the young O and B stars in the weak source population, out of the line of sight. Whilst there may be a contribution to the very NIR continuum from the PAHs, the column length of excited PAHs is as yet insufficient to generate substantial MIR features, despite the stellar source population generating a surfeit of high energy UV photons at this time.

Moving to absorption in the MIR, the influence of the long column length of dust in the neutral region at t = 4Myrs is illustrated by the significant depth of the absorption feature at 9.7μm. This absorption originates in the large, cold, silicate grains in the dusty neutral region.

The extent of the cold dust is also demonstrated by the magnitude of the long wavelength FIR emission. As a general rule of thumb it is the optical depth which controls the gradient of the slope on the MIR side of the FIR dust emission, with a high optical depth producing a steep gradient and considerable peak magnitude and vice versa.

The breadth of the long wavelength emission is dependent on the ratio of the inner dust radius $R_1(t)$ and the outer GMC radius $R2_W$. A small $R_1(t)/R2_W$ equates to a long column length of dust being available to reprocess the stellar radiation. At t=4Myrs, the superbubble has only just begun its expansion into the GMC and its radius is relatively small. As there is effectively zero dust in the supershell, $R_1(t)$ is given by $R_{SN}(t)$ and the ratio $R_1(t)/R2_W$ is comparatively small, leading to the broad FIR dust bump.

t = 5Myrs

The SED for η = 0.01, t = 5Myrs, is very different to that of t = 4Myrs, particularly in the MIR. The superbubble reached its cooling radius at t(Rc) = 4.21Myrs whereupon the adiabatic phase ends and the isothermal phase begins. Whilst the supershell temperature has dropped from $T_{SH+G}(t_{R_c})$ = 13,200K to T_{SH+G}(5Myrs) = 4050K in the intervening period, the shell has yet to condense any dust, so again most of the dust opacity is generated in the neutral region. At t = 5Myrs many of the more massive stars are still on the main sequence and the large amount of UV and optical photons generated are able to

pass directly through the shell to penetrate the front of the neutral region.

The 2.5μm very small grain continuum emission shown in the t = 5Myrs spectra is therefore still emanating from the face of the neutral region, but it is now accompanied by MIR narrow-band PAH features. This is because the column length of excited PAHs is now sufficient for emitted photons to escape the system and appear in the spectra. The large optical depth through the neutral region means that it is only grains at the front face closest to the source function that can see the UV radiation field and this, coupled to the short free path length of emitted photons explains the small magnitude of the MIR PAH features.

The superbubble is still expanding through the neutral region reasonably rapidly as the adiabatic phase has only just ended. This is illustrated by the reduction in the depth of the MIR the silicate absorption features at 9.7- & 18μm as the neutral region is transferred to the hot shell.

The breadth of the t = 5Myr long wavelength cool dust emission has also reduced in comparison to t = 4Myrs but maintains its peak magnitude and wavelength. This is because the inner dust radius $R_1(t)$ is still given by the superbubble radius $R_{SN}(t)$ so the ratio $R_1(t)/R2_W$ is larger at this time than for t = 4Myrs, leading to the reduced breadth. The peak magnitude and wavelength of the emission remain approximately the same as for t = 4Myrs suggesting that the source function appears approximately constant.

t = 6Myrs

Now considering the SED for η = 0.01, t = 6Myrs which again in contrast to the earlier two SEDs discussed exhibits very significant MIR narrow band emission, along with the broadest FIR emission of all SEDs in the η = 0.01 set.

The overall supershell temperature at t = 6Myrs is still some way above T_{cond} at T_{SH+G}(6Myrs) = 2070K but the exponential form of the dust condensation factor $Fd^{SH}(t)$, given by Equation 5.37, shows that dust is able to reform and contribute to the supershell opacity when $T_{SH+G}(t)$ is *approaching* T_{cond} and $Fd^{SH}(t)$ rises towards 0.5. Table 5.2 shows that A_v^{SH}(6Myrs) = 0.15 - a value which is just above what might be considered as canonical for a significant emitting dust column at $A_v(t)$ = 0.1. So, although $Av^{SH}(t)$ is not yet great enough to ameliorate the drop in $Av^{TOT}(t)$ caused by the transfer of the dust in the neutral region to the supershell, the shell does contain a small amount of dust at a temperature in the upper end of the condensation range.

Whilst the large and small grains and the PAHs are all reasonably efficient absorbers of short-wavelength radiation, in a low optical depth environment, the PAHs and very small grains interact preferentially with the stellar radiation due to their high abundance. Additionally, in a low optical depth environment a longer column length of small grains or PAHs can see the UV radiation field than in e.g.; the high optical depth neutral region and the free path length of the re-emitted photons is longer.

Thus, the NIR and MIR SED at t=6Myrs represents the combined emission from the PAH clusters and the very small grains located in both the very dust-sparse shell and those which can still see the hard radiation field in the warm, dust-rich face of the neutral region. However, it is the PAH population in the shell that are able to condense out of gas at the very top of the condensation temperature range which generate the dramatic increase in the magnitude of the MIR continuum and narrow-band emission between t = 5- and t = 6Myrs.

Finally considering the long wavelength FIR emission for t = 6Myrs, as the shell can be considered emitting, the inner dust radius is now given by the inner shell radius $R_{SH}(t)$ and consequently the ratio $R_1(t)/R2_W$ has dropped with respect to its value at t=5Myrs, accounting for the greater breadth of the emission. However, there is contamination of this relationship on the short wavelength side of the FIR emission by the elevated magnitude of the MIR continuum resulting in a breadth over and above what might perhaps be expected using only the $R_1(t)/R2_W$ ratio as the determining factor.

Summary of t = 4-, 5- & 6-Myr SEDs

Thus the first three SEDs of $\eta = 0.01$ demonstrate emission from three different phases of early superbubble evolution.

The t = 4Myrs SED is generated when the superbubble has only just overtaken the HII region IF, the shell is extremely hot and the optical depth through the neutral region high. There is no direct stellar flux in evidence at very short wavelengths as this has been absorbed or scattered out of the line of sight, primarily by the very small silicate and graphite grains. These very small grains re-emit at longer wavelengths and this is seen by the emission peaking at 2.5μm, corresponding to dust around the dust condensation temperature. The equivalent behaviour is seen for the t = 5- & 6-Myrs with no short wavelength flux in evidence at either time. The t = 4Myrs spectra also exhibits deep silicate absorption in the MIR and substantial cool grain emission in the FIR, illustrating

the large extent of the cold dust in the neutral region.

The t = 5Myrs exhibits MIR PAH features as the column length of excited PAHs is now sufficient for emission to be seen. However, due to the small path length of both the UV and re-emitted photons in the high optical depth neutral region, the MIR PAH emission is of relatively low magnitude. At t = 6Myrs, for the first time the shell can contain dust at the upper limit of the condensation temperature range and very high level, MIR narrow-band PAH emission appears in the SED. This emission is now emanating from both the warm neutral face and the low optical depth shell with the latter population accounting for the enhanced MIR flux magnitude.

For both t = 5 and 6-Myrs the FIR emission progressively narrows, it magnitude drops and the peak wavelength lengthens. This illustrates the destruction of the neutral region as it is transferred to the shell along with inverse square law attenuation as the region moves further from the source.

η = 0.01: $T_{SH+G}(t) \leq T_{cond}$ whilst $R_{SN}(t) \leq R2_W$
Supershell above T_{cond} whilst inside the GMC

As the η = 0.01 model breaks-up within the GMC, the remaining SEDs all achieve the dust condensation temperature T_{cond} = 1600K whilst internal to $R2_W$.

t = 7-, 8- & 9Myrs

The SEDs for t = 7-, 8- & 9Myrs are illustrated on the left-hand-side of Figure 6.1 by the dashed lines. These SEDs also exhibit a very different form to the SEDs discussed in the previous subsection, with strong NIR small grain emission, no MIR PAH features and FIR emission reducing in breadth.

The superbubble has been travelling though the neutral region in isothermal motion for some time now and because the compression factor is unlimited in the isothermal phase, the shell volume is growing at a slower rate than in the adiabatic phase. This leads to a denser shell and accelerated cooling. Figure 5.5 shows the total extinction is therefore undergoing recovery as the dust rich shell is now compensating for the destruction of the external neutral material.

Looking at the NIR, the t = 7-, 8- & 9Myr SEDs all show significant small grain emission around $\lambda = 2.5\mu$m, which is now emanating from both the shell and the neutral

region. Looking closely at Figure 6.1 it can be seen that this emission rises in magnitude over t = 7-, 8- & 9Myrs before dropping back at t $\geq$ 10Myrs.

The initial rise occurs because the supershell temperature is dropping rapidly toward the condensation temperature causing $Fd^{SH}(t)$ to rise. By t = 8.8Myrs, $T_{SH+G}(t) = T_{cond}$, at which point $Fd^{SH}(t) = 0.5$ and 50% of accumulated supershell dust contributes to the opacity. By t = 9Myrs, $T_{SH+G}(t) < T_{cond}$, $Fd^{SH}(t) = 1$ and all the shell dust contributes to the opacity, accounting for the high flux magnitude of the 2.5μm flux of the t = 9Myrs SED.

That the very small grain flux magnitude drops back down again at t $\geq$ 10Myrs is degenerate in reason; first the UV luminosity of the source population has dropped significantly as the most massive stars die and only the tail end of the O star population and the B stars are able to generate the UV flux. Additionally, the shell is now located quite some considerable distance from the source, which dilutes the quantity of flux received.

Considering the absence of the PAH features in the MIR, the shell is now so optically thick that the larger grains are also able to significantly intercept the radiation washing out the PAHs' advantage due to their high abundance. Essentially the excitable column length of PAH molecules is now so short that the emission is no longer visible. Finally, deep MIR silicate absorption is in evidence caused by the cold large gains in the outer reaches of the cloud.

t = 10-, 20-, 30-, 40-, 50- & 60Myrs

Turning now to the later SEDs for $\eta = 0.01$, the most significant variation in time is seen in the FIR. This is because the accumulation of neutral gas and dust into the supershell has a significant impact in this region.

As mentioned, the breadth of the FIR emission is determined by the ratio $R_1(t)/R2_W$ with $R_1(t)$ now given by the inner supershell radius. As the incremental shell volume is never large in comparison to the distance overtaken by the superbubble in a time-step, the breadth of the FIR emission reduces as the superbubble expands through the neutral region increasing $R_1(t)$.

The FIR peak flux is also dropping in magnitude and moving to longer wavelengths as time goes on and the indication is that the temperature of the emitting region is also dropping. This is due primarily to the increasing distance between the remaining neutral region and the source.

Having thoroughly considered the SEDs for $\eta = 0.01$, those for $\eta = 0.025$ & 0.05 can be compared.

Comparison with $\eta = 0.025$ & 0.05

The SEDs for $\eta = 0.025$ are shown in the bottom half of Figure 6.1, with the numerical and graphical extinction data displayed in the last chapter in Table 5.3 and Figure 5.5 respectively. The model for $\eta = 0.025$ also breaks up within $R2_W$ and therefore only two regimes are indicated on the plot: above and below the condensation temperature.

Figure 6.2 shows the SEDs for $\eta = 0.05$ with the numerical and graphical extinction data is displayed in Table 5.4. $\eta = 0.05$ has sufficient velocity to exit the GMC with its supershell intact and therefore three temperature regimes are indicated on the plot: above and below the condensation temperature for motion inside the GMC and below the condensation temperature whilst in motion through the ambient region. $\eta = 0.05$ is modelled to t = 80Myrs.

$\eta = 0.025$ & 0.05: $T_{SH+G}(t) \geq T_{cond}$ whilst $R_{SN}(t) \leq R2_W$

Supershell Above T_{cond} whilst inside GMC

The SEDs in this regime are 4Myrs $\leq$ t $\leq$ 8Myrs for $\eta = 0.025$ and 4Myrs $\leq$ t $\leq$ 9Myrs for $\eta = 0.05$. The SEDs for both η at t = 4Myrs have the equivalent form as t = 4Myrs for $\eta = 0.01$ and are generated by the same dynamic.

The t = 5-, 6-, 7- & 8Myrs SEDs for both $\eta = 0.025$ and $\eta = 0.05$ and have the same form as $\eta = 0.01$, t = 5Myrs./

These SEDs illustrate NIR very small grain emission, MIR narrow-band PAH emission, deep silicate absorption in the MIR and broad FIR emission.

Looking closely it can be seen that the magnitude of the NIR continuum emission and narrow-band MIR PAH emission rises in time as the neutral gas is transferred to the shell. As the shell is too hot to contain substantial dust, this occurs because the gradually reducing optical depth of the neutral region allows grains located progressively deeper into the neutral cloud to also see any UV and optical stellar flux. Thus the excited column length increases and the emission rises as the optical depth of the neutral region decreases.

Considering the SED in this regime which for each η achieves the highest magnitude of MIR flux. These are $\eta = 0.01$, $t_{0.01}$ = 6Myrs, $\eta = 0.025$, $t_{0.025}$ = 8Myrs and $\eta = 0.05$, $t_{0.05}$ = 9Myrs.

Comparison reveals that the $t_{0.01}$ = 6Myrs SED and the $t_{0.05}$ = 9Myrs both exhibit a significantly enhanced magnitude of NIR and MIR emission over and above the previous years. Conversely, the $t_{0.025}$ = 8Myrs SED shows no such jump in flux magnitude and remains consistent with earlier times.

As with $\eta = 0.01$, this is an effect of the shell temperature and optical depth at the time the SED is generated. The $\eta = 0.01$ supershell achieved T_{SH+G}(6Myrs) = 2070K and A_v^{SH}(6Myrs) = 0.15 to become a significant emitting column whilst containing dust at the very top of the condensation range. Similarly, the $\eta = 0.05$ supershell achieved T_{SH+G}(8Myrs) = 2000K and A_v^{SH}(9Myrs) = 0.63. For $\eta = 0.025$ however, the supershell achieved T_{SH+G}(8Myrs) = 1620K and A_v^{SH}(8Myrs) = 6, so the SED shows emission more indicative of dust at the condensation temperature.

Thus, it is the difference in temperature and hence opacity at the time of the SED which accounts for the dramatic fluctuation in flux magnitude in the MIR. As it is a sampling effect, perhaps this suggests that the model SEDs would benefit from closer sampling than Δt = 1Myrs, particularly once the cooling radius has been reached and until $Fd^{SH} = 1$.

Finally in the MIR the reduction in neutral extinction is also illustrated by the drop in the depth of the silicate absorption features as the cold material responsible for that emission is transferred in the shell. And in the FIR, the breadth of the emission drops and the peak moves to longer wavelengths as the emitting region moves further from the source and the ratio $R_1(t)/R2_W$ increases.

η = 0.025 & 0.05: $T_{SH+G}(t) \leq T_{cond}$ whilst $R_{SN}(t) \leq R2_W$
Supershell below T_{cond} whilst inside GMC

The $\eta = 0.025$ superbubble velocity drops below the sound speed in the neutral region and the supershell breaks up at $t(R_v)$ = 32Myrs, so SEDs for **t = 9-, 10-, 20-, & 30Myrs** reach the condensation temperature whilst internal to the GMC.

For the $\eta = 0.05$ system, only **t = 10Myrs** occurs in this regime as this superbubble has sufficient velocity to exit the GMC and progress through the ambient region with the supershell intact at $t(R2_W)$ = 10.57Myrs. Each of these SEDs has the same form as those of $\eta = 0.01$ at $t = 8 \leq t \leq 60$Myrs.

η = 0.05: $T_{SH+G}(t) \leq T_{cond}$ whilst $R_{SN}(t) \leq R2_W$

Supershell below T_{cond} whilst outside GMC

η = 0.05 is able to exit the GMC with its shell intact so SEDs for 20Myrs $\leq$ t $\leq$ 80Myrs are indicated on the right hand side of Figure 6.2 by dotted lines.

The form of superbubble motion changes when it enters the ambient region due to the sparsity of the external interstellar density. The corresponding drop in the shell compression factor, due to the change in upstream sound speed, causes an increase in the merged shell volume per time step $\Delta R^3_{shell}(t)$. This volume increase causes the shell optical depth to drop steadily from $R2_W$.

As the extinction from the shell drops, the NIR small grain emission also decreases in magnitude as the shell moves further from the source and its temperature drops well below the condensation temperature. Strongly spiking PAH features appear in the MIR as their high abundance in the low optical depth, broad shell and ambient region allows their interaction with any short wavelength radiation still being produced by, for example, the cluster's B stars.

In the FIR broad cool dust emission is seen and the emission drops in breadth and peak magnitude as the superbubble expands further until it achieves its minimum at t = 80Myrs when the shell is very close to the outer edge of the system $R2_{SN}$.

Summary: Low η: 1Myrs $\leq$ t $\leq$ 10Myrs

The supershell for each of the low η models achieves the condensation temperature whilst internal to the GMC. In the UV, optical and very NIR short-wards of $\lambda \approx 1\mu$m there is essentially no sign of any attenuated stellar flux in any of the SEDs. This is because the highly efficient very small silicate and graphite grains and the PAH population located at the face of the neutral region are able to absorb or scatter all the direct flux out of the line of sight, re-emitting it at longer wavelengths.

In the NIR emission is seen at 2.5μm, which corresponds to dust at approximately the condensation temperature. This 2.5μm continuum emission originates in the very small silicate and graphite grain population which undergo transient stochastic heating. As the neutral region optical depth reduces, grains progressively further back in the dusty cloud are able to see the UV radiation and the NIR emission rises in magnitude with time.

For the same reasons, in the MIR narrow-band PAH features are also seen, growing in

magnitude as time progresses. However once the shell begins to approach the condensation temperature, its optical depth rises and the PAHs are no longer excited into emission. The NIR emission exited by the tail end of the O star and B stars in the cluster, remains at an approximately constant magnitude once the shell has condensed.

Also in the mid-infrared, deep silicate absorption at 9.7 & 18μm illustrates the large radial extent of the neutral region at early times. Similarly at longer FIR wavelengths, broad cool dust emission drops away with time as the superbubble expands and the ratio $R_1(t)/R2_W$ increases.

Summary: Low η: 20Myrs $\leq$ t $\leq$ 80Myrs

For the low η's at later times there is still very little or no flux in the spectra at short-wavelengths at any times, which reflects the low source luminosity to dust and gas mass ratio.

In the MIR silicate absorption at 9.7- and 18μm is in evidence from any dust in the remaining neutral and ambient regions. The low magnitude small grain emission at 2.5μm reduces as the source function drops away, the emitting region moves further from the source and the shell temperature drops to well below the condensation temperature.

For those models which are able to exit the GMC with the supershell intact, PAH features begin appear, originating in the very low optical depth ambient region and the now broad, low optical depth, but nonetheless emitting shell.

In the FIR at late times there is substantial narrowing of the breadth of the emission, with the peak wavelength lengthening and the magnitude of emission dropping.

6.0.2 $M_{GMC} = 10^8 M_\odot$; High η

Turning now to the SEDs for the high star formation efficiencies. These are: $\eta = 0.1$ illustrated on the bottom half of Figure 6.2, $\eta = 0.15$ & 0.2 on Figure 6.3 and $\eta = 0.25$ shown on Figure 6.4. $\eta = 0.1$, 0.15 & 0.2 are modelled to t=80Myrs whilst $\eta = 0.25$ reaches R_v and breaks-up at t($R_{v(0.25)}$)=37Myrs.

The supershell of each of these models has an overall shell temperature well in excess of the condensation temperature at $R2_W$, classifying them as high η. The SEDs for $\eta = 0.1$ will be considered first, concentrating on the more unique properties of a high η model. $\eta = 0.15$, 0.2 & 0.25 will then be briefly compared.

η = 0.1: $T_{SH+G}(t) \geq T_{cond}$ whilst $R_{SN}(t) \leq R2_W$
Supershell above T_{cond} whilst inside GMC

The SEDs for η = 0.1 in this regime are 4Myrs $\leq$ t $\leq$ 8Myrs. Those for t = 4- & 5-Myrs have the equivalent form as for the low η's at t = 4Myrs. Having overtaken the IF front, the η = 0.1 superbubble at both times has a shell which is far too hot to generate any opacity, whilst a significant emitting column of PAHs has yet to be excited. Consequently the η = 0.1 SEDs for t = 4- & 5Myrs show increasing 2.5μm small grain emission, no MIR PAH emission, reducing deep silicate absorption and gradually decreasing, but broad, FIR emission.

Due to the balance between source luminosity and the dust and gas mass in the GMC, in a high η model the extent of the neutral region, or the value of $R2_W$, is much smaller than the low η models. Over the period 6- to 8-Myrs the η = 0.1 superbubble is travelling through the GMC in isothermal motion and the optical depth is dropping rapidly. Perhaps the most obvious indication in the η = 0.1 SED of this reduced neutral extent is the quantity of stellar flux seen at optical and UV wavelengths from t $\geq$ 6Myrs.

Figure 3.2 in §3.2 showed the starburst grain model extinction efficiencies and illustrated the high absorption and scattering efficiency of the very small silicate and graphite grains and the PAHs at short wavelengths. However, for the η = 0.1 model, even at earlier times, the column length of dust in the neutral region which is able to see the weak source UV radiation field is insufficient to absorb or scatter all the stellar flux out of the line of sight.

Thus, as the superbubble expands towards $R2_W$, the quantity of mildly attenuated and less processed direct, short wavelength source flux seen in the spectra increases as the column length of absorbing and scattering material reduces. In fact by t = 8Myrs the optical depth for η = 0.1 has dropped so much that for the first time the high absorption efficiency across the 2175$\AA$ feature of the very small graphite grains in the remaining neutral and ambient regions is insufficient to absorb all the UV stellar flux out out of the line of sight. However, sufficient numbers do remain to generate the shallow absorption feature seen at Log $\lambda \approx$ -0.6.

This model is able to exit the GMC with its shell intact and at a temperature T_{SH+G} >> T_{cond}. The total optical depth is therefore in rapid decline to reach $Av^{TOT}(t) \leq 1$ at $R2_W$. The extinction remains low and does not exhibit an $Av^{TOT}(t)$ recovery as the dust

re-forms in the shell until the supershell has been in the ambient region for some time.

η = 0.1: $T_{SH+G}(t) \geq T_{cond}$ whilst $R_{SN}(t) \geq R2_W$
Supershell above T_{cond} whilst inside Ambient Region

The SEDs for t = 9- & 10Myrs are shown by dash-dot lines indicating they have supershell temperatures well above the condensation temperature whilst expanding through the ambient region. These SEDs have a very different spectral shape at all wavelengths to earlier years. The total optical depth has been in rapid decline to reach $Av^{TOT}(t) \leq 1$ at $R2_W$. In contrast to the low η models, the extinction then remains low and does not exhibit an $Av^{TOT}(t)$ recovery as the dust re-forms in the shell, until the supershell has been in the ambient region for some time.

Table 5.5 shows that $t(R2_W)$ = 8.71Myrs the ambient region has an optical depth of $Av^{\alpha}(t)$ = 0.62 and the shell is still optically thin. Thus the only emitting region over these years is the ambient region which is extremely sparse in comparison to the dense neutral region. At t = 9 & 10Myrs the direct source flux evident at short wavelengths achieves the greatest magnitude of all SEDs so far and this is an expression of the very mild attenuation of flux in the ambient region.

As the shell is optically thin, any UV radiation generated by e.g., the cluster's B stars can impact directly onto the ambient region. Due to the low optical depth, the free path length for UV and optical photons is long and a significant column length of PAHs and very small grains can see the radiation. This accounts for the high magnitude, strongly spiking MIR PAH narrow-band emission seen in the spectra for all times when the supershell is above T_{cond} whilst in the ambient region.

As mentioned, the long wavelength emission originates in silicate and carbon grains located both in the cold outer GMC and in the sparse ambient region in which the GMC is embedded. For the low star formation efficiency models which spent all or most of their lifetime trapped inside the GMC and in consideration of the overwhelming GMC density in comparison to the ambient region it was appropriate to couch the ratio of the inner to outer dust radii in terms of the outer edge of the GMC - $R2_W$. The high η models on the other hand spend the majority of their lifetime in the ambient region external to the GMC so now the appropriate ratio when considering the breadth of the long wavelength emission is the inner dust radius to the outer *system* radius $R_1(t)/R2_{SN}$. For information on the calculation of $R2_{SN}$ for each supernova model the reader is referred to §4.6.

Looking at Figure 6.2 the breadth and magnitude of the long wavelength emission for t = 9- & 10Myrs has dropped dramatically compared to earlier years when the cold, dense neutral region existed between the observer and the source. This is illustrates the increase in the ratio $R_1(t)/R2_{SN}$, whilst the shallow slope on the short wavelength side of the FIR emission demonstrates the low optical depth of the ambient region.

η = 0.1: $T_{SH+G}(t) \leq T_{cond}$ whilst $R_{SN}(t) \geq R2_W$
Supershell below T_{cond} whilst inside Ambient Region

The SEDs for η = 0.1 in this regime are 20Myrs $\leq$ t $\leq$ 80Myrs - indicated on the plot by the dotted lines. Figure 5.6 shows the total extinction reaches its minimum at $R2_W$ and plateaus at $Av^{TOT}(t) < 1$ until around t $\approx$ 14Myrs. After this, the total extinction gradually begins to rise as the supershell temperature approaches T_{cond} and its dust condenses so that by t = 20Myrs $Av^{TOT}(t) = 11.92$.

This movement of the shell to optically thick is demonstrated by the dramatic drop in the magnitude of the direct stellar source flux at short wavelengths between 10- and 20Myrs as the grain density is again able to scatter and absorb more source flux from the line of sight. Also seen is a a steepening of the gradient of the short wavelength side of the FIR emission and an increase in its breadth as $R_1(t)$ changes from being given by the superbubble radius $R_{SN}(t)$ to the inner shell radius $R_{SH}(t)$ as the shell condenses.

However, the late resurgence in $Av^{TOT}(t)$ is minimal and the extinction drops steadily again from t = 20Myrs as once external to the GMC, the accumulated shell volume at each timestep increases, leading to a drop in shell density. The short-wavelength flux visible in the optical and UV increases as the optical depth through the shell and in the ambient region reduces and less and less stellar flux is scattered and absorbed out of the line of sight.

By t = 50Myrs the optical depth has dropped sufficiently for flux to be seen in the spectra across the 2175$\AA$ feature and in the FUV. The implication is that the grain density of PAHs and very small grains in the shell has now dropped so much that mildly attenuated stellar flux is able to escape the system entirely again. In the MIR at late times shallow PAH features are also in evidence, again due to the reduction in the optical depth of the shell and ambient region.

Having considered the η = 0.1 SEDs in depth it is now appropriate to examine the three higher star formation efficiencies together as the behaviour of these SEDs are not

only very similar to that of $\eta = 0.1$ but also to each other.

η = 0.15, 0.2 & 0.25: $T_{SH+G}(t) \geq T_{cond}$ whilst $R_{SN}(t) \leq R2_W$
Supershell above T_{cond} whilst inside GMC

Figures 6.3 and 6.4 show that for $\eta = 0.15$ the SEDs in this regime are t = 4-, 5- & 6Myrs, for $\eta = 0.2$ the SEDs are t = 4- & 5Myrs and for $\eta = 0.25$ the SED is t = 4Myrs. These SEDs are very similar in form to the SEDs from those years in the same regime for η = 0.1, with the exception of more stellar source flux being in evidence at optical and UV wavelengths as the low optical depth of the narrower neutral regions allows more direct flux to exit the cloud without significant reprocessing.

η = 0.15, 0.2 & 0.25: $T_{SH+G}(t) \geq T_{cond}$ whilst $R_{SN}(t) \geq R2_W$
Supershell above T_{cond} whilst inside Ambient Region

The SEDs in this regime for $\eta = 0.15$ are 7Myrs $\leq$ t $\leq$ 20Myrs, for $\eta = 0.2$, 6Myrs $\leq$ t $\leq$ 30Myrs and for $\eta = 0.25$ 5Myrs $\leq$ t $\leq$ 10Myrs. These SEDs are indicated on the plots by the dot-dash lines.

The decrease in the time the superbubble can spend in the neutral region is an expression of the reduced radial dust extent and increased source function luminosity and hence superbubble velocity, as η rises. These curves have the same form as their equivalent in the same regime for $\eta = 0.1$ with significant, mildly attenuated, cool source flux visible across UV and optical wavelengths, strong MIR PAH emission and a narrow FIR dust bump.

η = 0.15, 0.2 & 0.25: $T_{SH+G}(t) \leq T_{cond}$ whilst $R_{SN}(t) \geq R2_W$
Supershell below T_{cond} whilst inside Ambient Region

The remainder of the SEDs for each of these η models are in this regime and again are very similar to those of $\eta = 0.1$. The magnitude of direct, attenuated, source flux drops as the shell optical depth rises and provides absorbing and scattering sites for any remaining UV and optical radiation from the central cluster. The source flux is provided at these late times by the B stars as all the O stars are dead by t $\approx$ 7 Myrs. The deep absorption across the 2175$\AA$ feature is decreasing with time as the optical depth of the shell reduces due to its increasing volume and the low density of the overtaken ambient gas. Significant MIR PAH features are also seen due to the low shell optical depth whilst very slim FIR

emission illustrates the larger value of the ratio $R_1(t)/R2_{SN}(t)$. Direct, mildly attenuated, source flux rises with time after the shell has condensed out also due to the reduction in shell optical depth as time progresses.

Summary: High η: 1Myrs $\leq$ t $\leq$ 10Myrs

Each of these systems have supershells which exit the GMC with temperatures in excess of the condensation temperature. The source function in these high η models is significant and the radial dust extent small in comparison to the low η models. Thus it is only at very early times that a model system is optically thick enough to produce silicate absorption in the MIR and very small grain emission in the NIR. Weak narrow-band MIR PAH features are also in evidence, emanating from the warmed neutral dust face, accompanied by broad FIR emission.

As time goes on, the rapidly reducing optical depth means short wavelength optical, UV and very NIR radiation is seen in the SEDs as some mildly attenuated stellar flux is able to escape a system. However, the high efficiency of the PAH's and small graphite and silicate grain population in the low opacity system ensures that any flux which can be removed from the line of sight is and this is illustrated by shallow absorption across the $2175\mathring{A}$.

Once the supershell has exited the GMC, the entire neutral region has been accumulated into a shell too hot to contribute to the extinction. This change is illustrated by high magnitude direct source flux at very short wavelengths, strongly spiking MIR PAH features and very narrow, cool, low magnitude FIR emission from the low-optical depth ambient region.

Summary: High η: 20Myrs $\leq$ t $\leq$ 80Myrs

Despite entering the ambient region, the luminosity of these high η models is so great that the supershells take a considerable time to cool towards T_{cond}. Thus, when the shell does eventually condense out, it is very broad and the peak recovery in extinction is extremely minimal when compared to the low η models.

However, the high η supershell's do provide opacity and the magnitude of the short-wavelength flux seen in the SEDs drops substantially when the shell's become a significant emitting column. Deep absorption across the $2175\mathring{A}$ feature appears as the grains in the shell are able to scatter and absorb the stellar flux out of the line of sight. The absorption

M_{GMC}	η	Category
$10^9 M_\odot$	0.1, 0.15, 0.2, 0.25	High
$10^9 M_\odot$	0.01, 0.025, 0.05	Low
$10^8 M_\odot$	0.1, 0.15, 0.2, 0.25	High
$10^8 M_\odot$	0.01, 0.025, 0.05	Low
$10^7 M_\odot$	0.1, 0.15, 0.2, 0.25	High
$10^7 M_\odot$	0.05	Low
$10^7 M_\odot$	0.01, 0.025	HII Region
$10^6 M_\odot$	0.15, 0.2, 0.25	Low
$10^6 M_\odot$	0.01, 0.025, 0.05, 0.1	HII Region

Table 6.2: η Classification of All Models. Those models which take the supernova solution have been categorised as Low η if $T_{SH+G} < T_{cond}$ at $R2_W$, whilst those categorised as High η have $T_{SH+G} \geq T_{cond}$ at $R2_W$. Those models where the superbubble has insufficient velocity to overtake the ionization front with the supershell intact and therefore revert to the HII Region solution at all times, have also been indicated.

and scattering reduces as time progresses because the optical depth of the shell is dropping as its volume grows quite rapidly in the ambient region.

Eventually at very late times the optical depth of the shell falls to the point where absorption and scattering is unable to remove substantial quantities of short wavelength flux from the line of sight and high magnitude, only mildly processed source flux appears in the spectra. At FIR wavelengths at late times, narrow, low magnitude emission is seen, increasing in breadth as the shell gradually broadens and its temperature drops.

This concludes the analysis of the seven star formation efficiency models at $M_{GMC} = 10^8 M_\odot$.

6.0.3 $M_{GMC} = 10^6$-, 10^7-, 10^8- & $10^9 M_\odot$ SEDs

It is now possible to consider the remaining spectra in the modelled parameter space. The SEDs for $M_{GMC} = 10^6 M_\odot$ are shown in Figures 6.12 & 6.13, those for $M_{GMC} = 10^7 M_\odot$ in Figures 6.9, 6.10 & 6.11 and for $M_{GMC} = 10^9 M_\odot$ in Figures 6.5, 6.6, 6.7 & 6.8. The η categorisation of the SEDs from each model is re-iterated in Table 6.2.

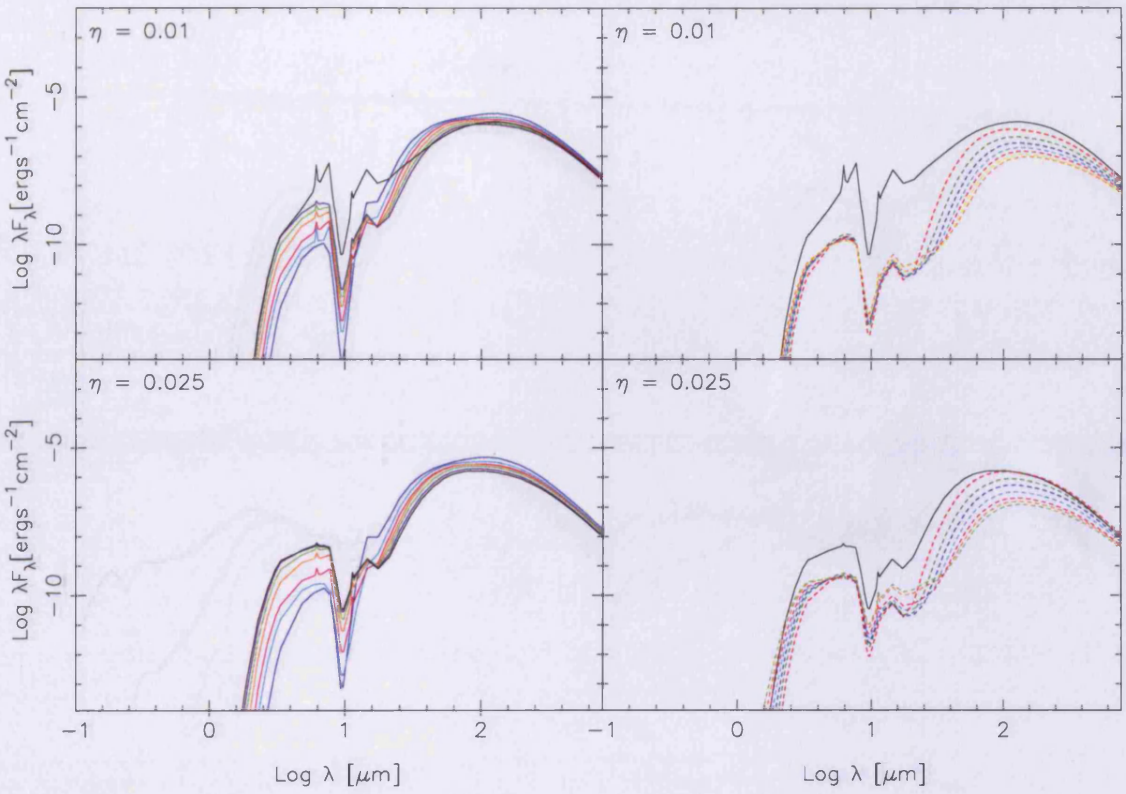

Figure 6.5: SEDs for $M_{GMC} = 10^9 M_\odot$, $\eta = 0.01$ & 0.025. The LHS shows SEDs for 4, 5, 6, 7, 8, 9 & 10 Myrs in blue, cyan, magenta, orange, light green, purple and black respectively. The RHS shows SEDs for 10, 20, 30, 40, 50, 60, 70 & 80Myrs in black, red, dark green, blue, cyan, orange and light green respectively. Solid lines indicate that $T_{SH+G}(t) > T_{cond}$ whilst $R_{SN}(t) < R2_W$ and Dashed Lines illustrate $T_{SH+G}(t) < T_{cond}$ whilst $R_{SN}(t) < R2_W$

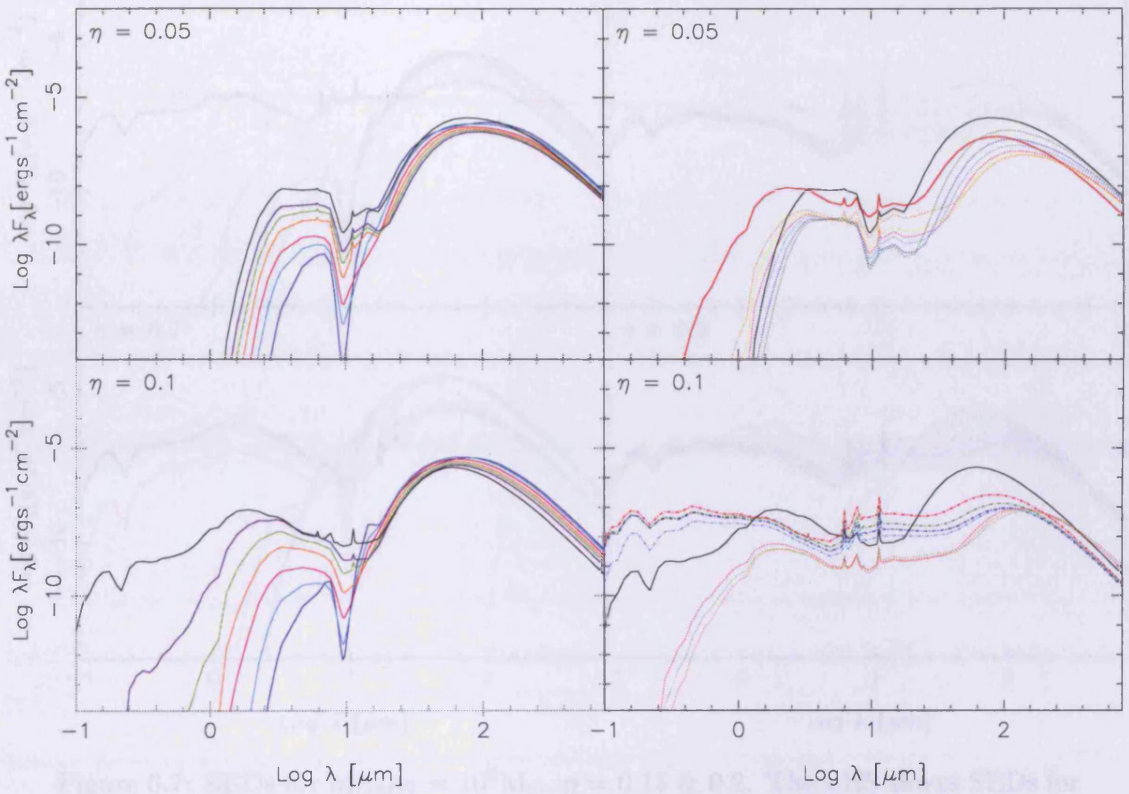

Figure 6.6: SEDs for $M_{GMC} = 10^9 M_\odot$, $\eta = 0.05$ & 0.1. The LHS shows SEDs for 4, 5, 6, 7, 8, 9 & 10 Myrs in blue, cyan, magenta, orange, light green, purple and black respectively. The RHS shows SEDs for 10, 20, 30, 40, 50, 60, 70 & 80Myrs in black, red, dark green, blue, cyan, orange and light green respectively. Solid lines indicate that $T_{SH+G}(t) > T_{cond}$ whilst $R_{SN}(t) < R2_W$ and Dashed Lines illustrate $T_{SH+G}(t) < T_{cond}$ whilst $R_{SN}(t) < R2_W$

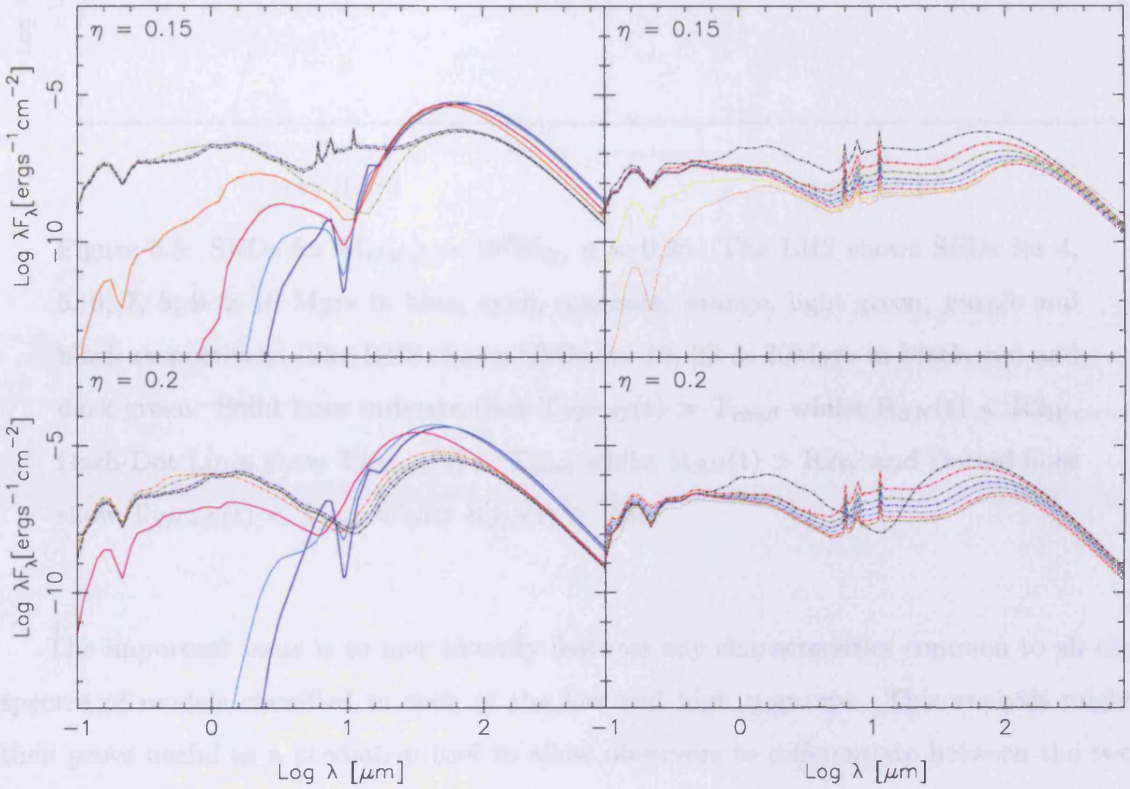

Figure 6.7: SEDs for $M_{GMC} = 10^9 M_\odot$, $\eta = 0.15$ & 0.2. The LHS shows SEDs for 4, 5, 6, 7, 8, 9 & 10 Myrs in blue, cyan, magenta, orange, light green, purple and black respectively. The RHS shows SEDs for 10, 20, 30, 40, 50, 60, 70 & 80Myrs in black, red, dark green, blue, cyan, orange and light green respectively. Solid lines indicate that $T_{SH+G}(t) > T_{cond}$ whilst $R_{SN}(t) < R2_W$, Dashed Lines illustrate $T_{SH+G}(t) < T_{cond}$ whilst $R_{SN}(t) < R2_W$, Dash-Dot Lines show $T_{SH+G}(t) > T_{cond}$ whilst $R_{SN}(t) > R2_W$ and Dotted lines show $T_{SH+G}(t) < T_{cond}$ whilst $R_{SN}(t) > R2_W$

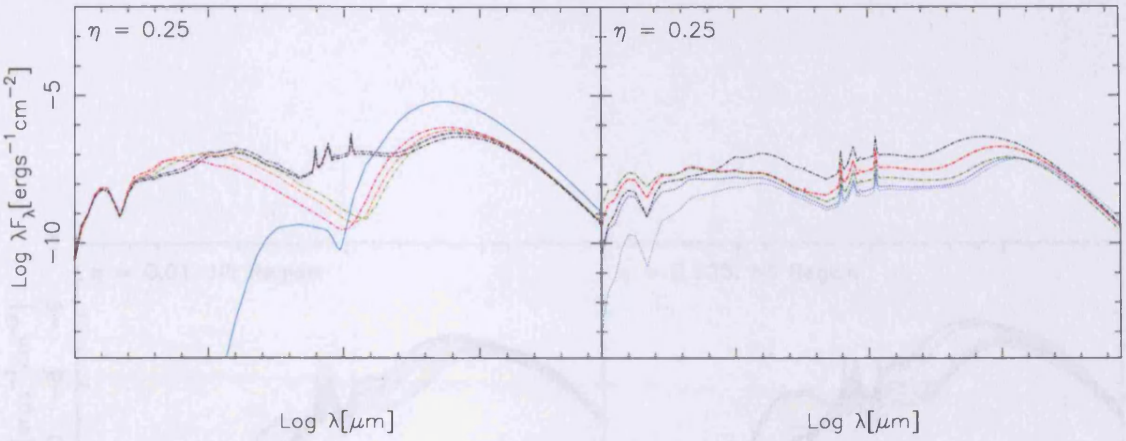

Figure 6.8: SEDs for $M_{GMC} = 10^9 M_\odot$, $\eta = 0.25$. The LHS shows SEDs for 4, 5, 6, 7, 8, 9 & 10 Myrs in blue, cyan, magenta, orange, light green, purple and black respectively. The RHS shows SEDs for 10, 20 & 30Myrs in black, red and dark green. Solid lines indicate that $T_{SH+G}(t) > T_{cond}$ whilst $R_{SN}(t) < R2_W$, Dash-Dot Lines show $T_{SH+G}(t) > T_{cond}$ whilst $R_{SN}(t) > R2_W$ and Dotted lines show $T_{SH+G}(t) < T_{cond}$ whilst $R_{SN}(t) > R2_W$

The important issue is to now identify features any characteristics common to all the spectra of models classified in each of the low and high η groups. This analysis might then prove useful as a predictive tool to allow observers to differentiate between the two categories and potentially infer the approximate ratio of the luminosity to dust and gas mass.

Using the approximate relationship $M_\star = M_{GMC}.\eta$, if between 1 - 10% of a GMC's mass of gas and dust at t = 0 is converted into the stellar source function, the system can be considered low η. Having initially been in decline, the extinction will exhibit a significant recovery after reaching its trough, as dust condenses out of the supershell in a dust reformation scenario. The SEDs from the low η models are unlikely to exhibit any flux at short-wavelengths due to their large optical depths at all times. This is also demonstrated by broad cool FIR dust emission.

On the other hand, it could be proposed that if between 10 - 25% of a GMC's initial mass be converted into stars, the system might be classified high η. The extinction will decline rapidly to approximately zero at the edge of the GMC $R2_W$. Whilst the extinction does undergo a small resurgence in magnitude at later times when the shell approaches the dust condensation temperature, that recovery is minimal and the extinction remains

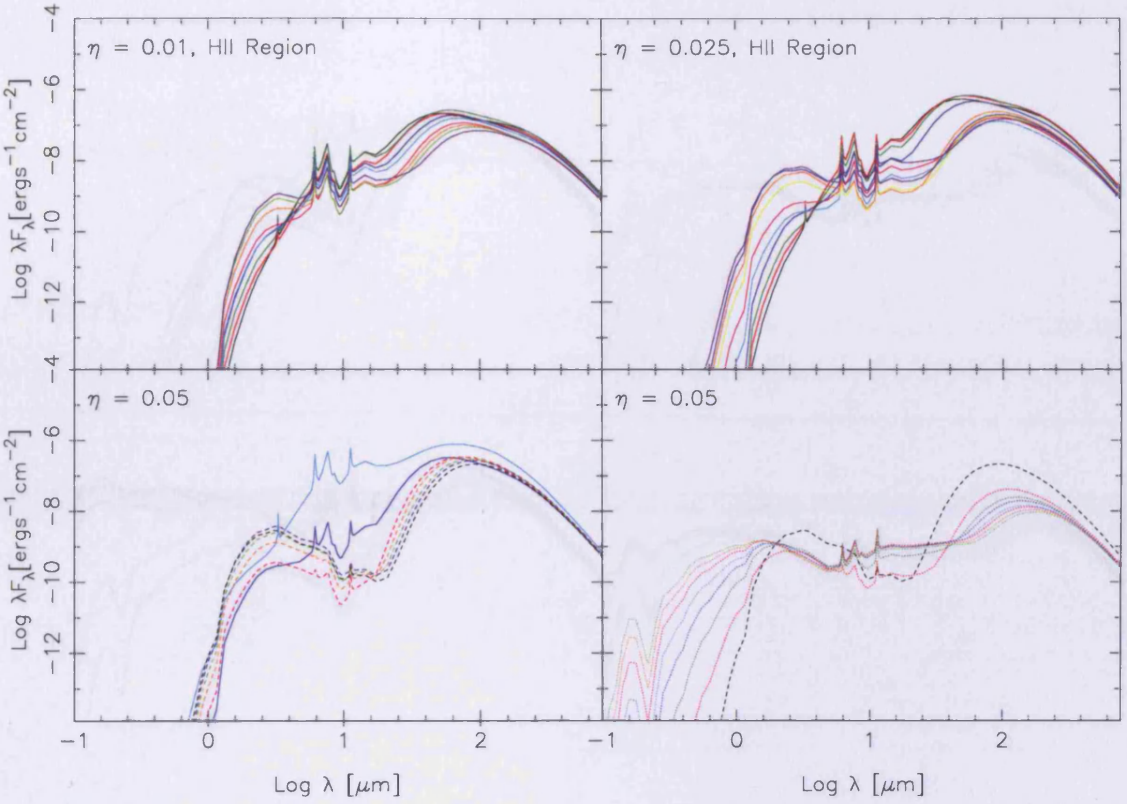

Figure 6.9: SEDs for $M_{GMC} = 10^7 M_\odot$, $\eta = 0.01$, 0.025, & 0.05. $\eta = 0.01$ & 0.025 are given by the wind solution whilst $\eta = 0.05$ is given by the supernova solution. The LHS of $\eta = 0.05$ shows SEDs for 4, 5, 6, 7, 8, 9 & 10 Myrs in blue, cyan, magenta, orange, light green, purple and black respectively. The RHS shows SEDs for 10, 20, 30, 40, 50, 60, 70 & 80Myrs in black, red, dark green, blue, cyan, orange and light green respectively. Solid lines indicate that $T_{SH+G}(t) > T_{cond}$ whilst $R_{SN}(t) < R2_W$, Dashed Lines illustrate $T_{SH+G}(t) < T_{cond}$ whilst $R_{SN}(t) < R2_W$ and Dotted lines show $T_{SH+G}(t) < T_{cond}$ whilst $R_{SN}(t) > R2_W$

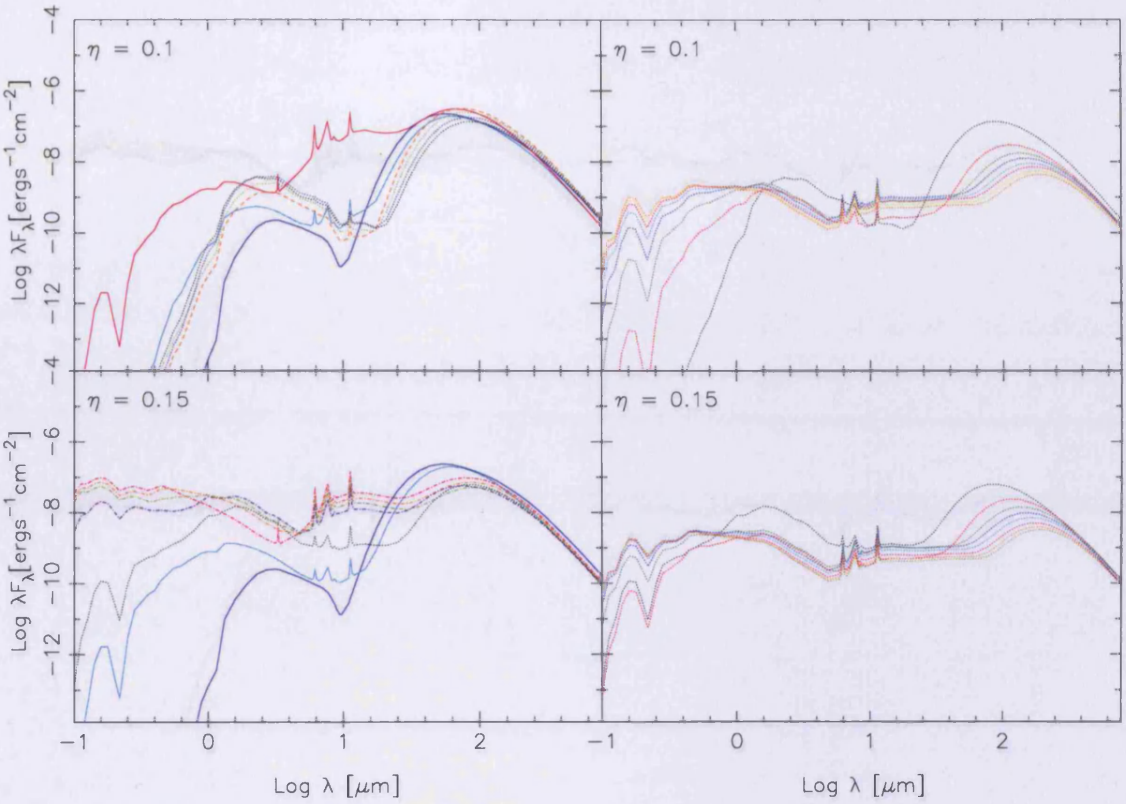

Figure 6.10: SEDs for $M_{GMC} = 10^7 M_\odot$, $\eta = 0.1$ & 0.15. The LHS shows SEDs for 5, 6, 7, 8, 9 & 10 Myrs in blue, cyan, magenta, orange, light green, purple and black respectively. The RHS shows SEDs for 10, 20, 30, 40, 50, 60, 70 & 80Myrs in black, red, dark green, blue, cyan, orange and light green respectively. Solid lines indicate that $T_{SH+G}(t) > T_{cond}$ whilst $R_{SN}(t) < R2_W$, Dashed Lines illustrate $T_{SH+G}(t) < T_{cond}$ whilst $R_{SN}(t) < R2_W$, Dash-Dot Lines show $T_{SH+G}(t) > T_{cond}$ whilst $R_{SN}(t) > R2_W$ and Dotted lines show $T_{SH+G}(t) < T_{cond}$ whilst $R_{SN}(t) > R2_W$

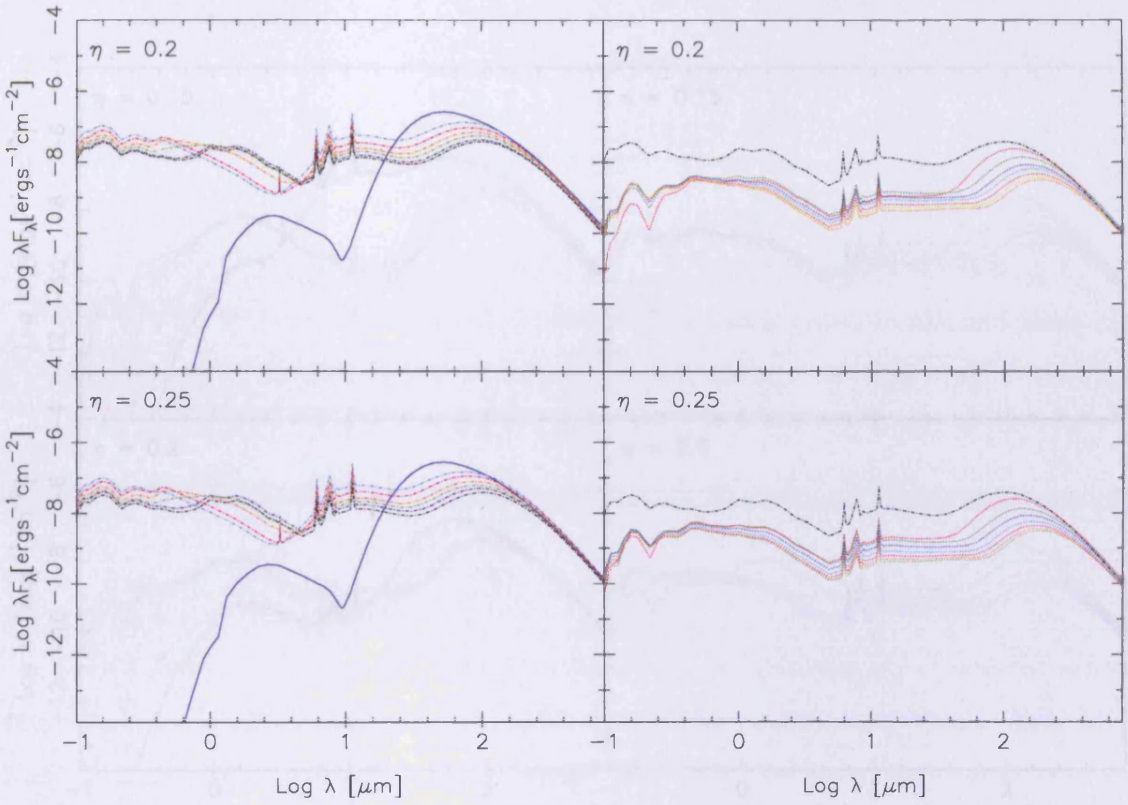

Figure 6.11: SEDs for $M_{GMC} = 10^7 M_\odot$, $\eta = 0.2$ & 0.25. The LHS shows SEDs for 4, 5, 6, 7, 8, 9 & 10 Myrs in blue, cyan, magenta, orange, light green, purple and black respectively. The RHS shows SEDs for 10, 20, 30, 40, 50, 60, 70 & 80Myrs in black, red, dark green, blue, cyan, orange and light green respectively. Solid lines indicate that $T_{SH+G}(t) > T_{cond}$ whilst $R_{SN}(t) < R2_W$, Dashed Lines illustrate $T_{SH+G}(t) < T_{cond}$ whilst $R_{SN}(t) < R2_W$, Dash-Dot Lines show $T_{SH+G}(t) > T_{cond}$ whilst $R_{SN}(t) > R2_W$ and Dotted lines show $T_{SH+G}(t) < T_{cond}$ whilst $R_{SN}(t) > R2_W$

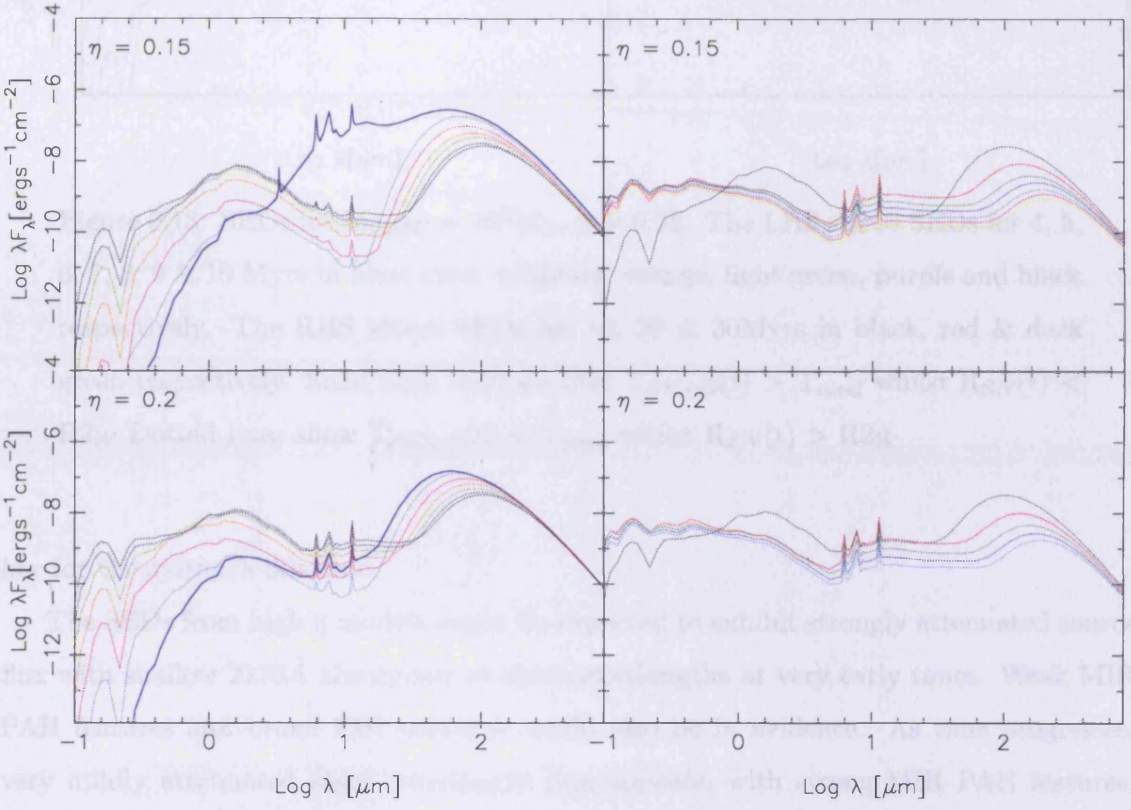

Figure 6.12: SEDs for $M_{GMC} = 10^6 M_\odot$, $\eta = 0.15$ & 0.2. The LHS shows SEDs for 4, 5, 6, 7, 8, 9 & 10 Myrs in blue, cyan, magenta, orange, light green, purple and black respectively. The RHS shows SEDs for 10, 20, 30, 40, 50, & 60Myrs in black, red, dark green, blue, cyan and magenta respectively. Solid lines indicate that $T_{SH+G}(t) > T_{cond}$ whilst $R_{SN}(t) < R2_W$ and Dotted lines show $T_{SH+G}(t) < T_{cond}$ whilst $R_{SN}(t) > R2_W$

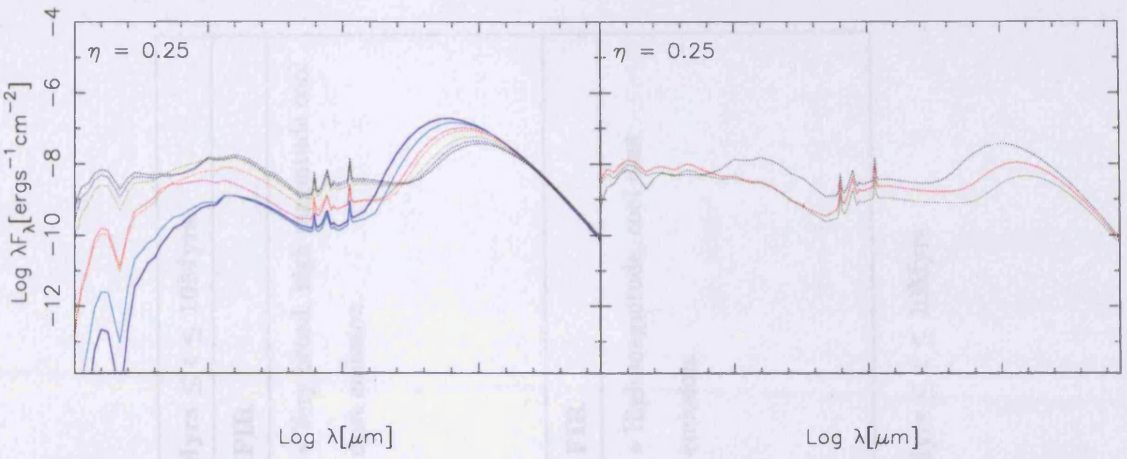

Figure 6.13: SEDs for $M_{GMC} = 10^6 M_\odot$, $\eta = 0.25$. The LHS shows SEDs for 4, 5, 6, 7, 8, 9 & 10 Myrs in blue, cyan, magenta, orange, light green, purple and black respectively. The RHS shows SEDs for 10, 20 & 30Myrs in black, red & dark green respectively. Solid lines indicate that $T_{SH+G}(t) > T_{cond}$ whilst $R_{SN}(t) < R2_W$ Dotted lines show $T_{SH+G}(t) < T_{cond}$ whilst $R_{SN}(t) > R2_W$

low for the system's life-time.

The SEDs from high η models might be expected to exhibit strongly attenuated source flux with shallow 2175$\mathring{A}$ absorption at short-wavelengths at very early times. Weak MIR PAH features and broad FIR emission would also be in evidence. As time progresses, very mildly attenuated short wavelength flux appears, with strong MIR PAH features, and narrow FIR emission. At even later times, the short wavelength flux magnitude drops substantially and deep absorption over the 2175$\mathring{A}$ is seen.

In summary, perhaps the most distinctive defining spectral characteristic of these categories is the magnitude and quantity of flux seen in the spectra at UV, optical and NIR wavelengths. However, observations are often taken at many wavelengths so the characteristics expected in the SEDs of objects in these two classes have been generally categorised in the three wavelength regimes: Optical & UV, NIR & MIR and FIR, at early (1Myrs $\leq$ t $\leq$ 10Myrs) and late times (20Myrs $\leq$ t $\leq$ 80Myrs). The generalised results are presented in Tables 6.3 and 6.4 for easy reference.

Model		Predicted Spectral Characteristics at Early Times: 1Myrs $\leq$ t $\leq$ 10Myrs		
M_{GMC}	Low η	Optical & UV	NIR & MIR	FIR
$10^9 M_\odot$ $10^8 M_\odot$ $10^7 M_\odot$ $10^6 M_\odot$	0.01, 0.025, 0.05 0.01, 0.025, 0.05 0.05 0.15, 0.2, 0.25	• No flux in spectra due to large optical depth at all times.	• Small grain emission peaking at 2.5μm. • Weak narrow-band PAH emission. • Deep silicate absorption at 9.7- & 18-μm.	• Very broad, high magnitude cool dust emission.
M_{GMC}	High η	Optical & UV	NIR & MIR	FIR
$10^9 M_\odot$ $10^8 M_\odot$ $10^7 M_\odot$	0.1, 0.15, 0.2, 0.25 0.1, 0.15, 0.2, 0.25 0.1, 0.15, 0.2, 0.25	• Strongly attenuated source flux & deep absorption across 2175$\AA$.	• Strong small grain emission peaking at 2.5μm. • Narrow-band PAH emission. • Shallow or absent silicate absorption at 9.7- & 18-μm.	• High magnitude, cool dust emission.

Table 6.3: Generalised spectral characteristics of low and high η models, between 1Myrs $\leq$ t $\leq$ 10Myrs

Model		Spectral Characteristics: **20Myrs $\leq$ t $\leq$ 80Myrs**		
M_{GMC}	Low η	Optical & UV	NIR & MIR	FIR
$10^9 M_\odot$ $10^8 M_\odot$ $10^7 M_\odot$ $10^6 M_\odot$	0.01, 0.025, 0.05 0.01, 0.025, 0.05 0.05 0.15, 0.2, 0.25	• No Flux due to large optical depth at all times	• Small grain emission peaking at 2.5μm. • Weak narrow-band PAH emission. • Shallow silicate absorption at 9.7- & 18-μm.	• Very broad, high magnitude emission from cool dust.
M_{GMC}	High η	Optical & UV	NIR & MIR	FIR
$10^9 M_\odot$ $10^8 M_\odot$ $10^7 M_\odot$	0.1, 0.15, 0.2, 0.25 0.1, 0.15, 0.2, 0.25 0.1, 0.15, 0.2, 0.25	• High magnitude, cool direct source flux	• Small grain emission peaking at 2.5μm. • Strong narrow-band PAH emission. • Very shallow or absent silicate absorption at 9.7- & 18-μm	• Low magnitude, narrow emission from cool dust.

Table 6.4: Generalised spectral characteristics of low and high η models, between 20Myrs $\leq$ t $\leq$ 80Myrs

6.0.4 The low η Dust Reformation Scenario

Before concluding this section on the SED analysis, there is some evidence for the dust reformation scenario indicated by the low η models, as the presence of dust in supernovae systems has been observed in a number of instances.

Very well-studied is the nearby Type IIP supernova 1987A, in the LMC, which was estimated to have formed a modest amount of dust in its ejecta (Wooden et al. 1993); the dust is believed to have first condensed about 530 days after outburst (Danziger et al. 1991). More recently, Sugerman *et al.* (2006) suggested that late-time MIR observations of the Type II supernova 2003gd, taken between 499 and 678 days after the outburst, were consistent with ejecta-condensed dust. Finally, Barlow *et al.* (2005) used MIR *Spitzer Space Telescope* and Gemini observations of the Type IIP supernova SN 2002hh taken between 590 and 758 days after outburst to also imply the presence of dust.

In contrast to the work of Sugerman *et al.* (2006), the dust SED modelling of Barlow *et al.* (2005) suggested that the emitting radius of the dust was too large for it to have formed in the supernova ejecta and therefore concluded that the emission was from an optically thick circumstellar shell, which pre-existed the supernova, possibly generated in the mass-loss phase of the massive star progenitor of the supernova.

This Barlow *et al.* (2005) case is perhaps analogous to early time models in this thesis where the supernovae have exploded into an HII region already ionized by the stellar flux. There, dust emission is seen prior to the IF being overtaken by the superbubble. Alternatively, the very lowest luminosity to mass ratio thesis systems have superbubbles with insufficient velocity to overcome the random gas motions in the upstream HII region and therefore loose their integrity and break-up inside the IF front, in which case the dusty HII region solution holds for all t.

Regarding the dust reformation timescales, both Sugerman *et al.* (2006) and Barlow *et al.* (2005) observed single supernova systems and this thesis work considers a central source cluster generating multiple supernovae, modelled with a continuous supernova energy function. This might explain the considerably longer period between the first outburst and dust being seen in the *low* η thesis systems compared to that observed in the single supernova systems.

However what both Sugerman *et al.* (2006) and Barlow *et al.* (2005) do demonstrate is that dust can be available to provide MIR emission in systems recently impacted by

supernova which is in line with some of the results indicated by this thesis.

6.0.5 Comparison with ERR00

It was mentioned at the very end of Chapter 3 that the ERR00 constant ionizing flux HII region model would be considered in comparison to the thesis models after the development of the starburst solution. The parameters used by ERR00 at $M_{GMC} = 10^7 M_\odot$, $\eta = 0.2$ for their HII region solution invoke the supernova solution in the thesis modelling. This is because the $M_{GMC} = 10^7 M_\odot$, $\eta = 0.2$ thesis supershell has sufficient velocity to overtake the HII region ionization front with its shell intact to become the driving force behind the system's evolution.

Optical Depth Distribution

Figure 6.14 illustrates the optical depth distribution generated by both the ERR00 constant ionizing flux model (dashed-line) and the thesis supernovae solution (solid line) for $M_{GMC} = 10^7 M_\odot$, $\eta = 0.2$. It should be noted that although this thesis work extended the ERR00 model to accommodate a time-dependent flux, it is the constant ionizing flux solution from ERR00, which is illustrated in Figure 6.14.

Looking at the plot, as to be expected from what is essentially a quasi-constant star formation scenario, the ERR00 extinction follows an almost volume dilution solution, dropping steadily as the IF moves towards the outer boundary of the GMC. The supernova model on the other hand has a high η solution and the extinction drops very rapidly to approximately zero at $R2_W$ and does not rise again substantially for the rest of the systems' evolution. At very late times the two solutions do begin to converge as after the small resurgence in the total optical depth of the supernova model after $R2_W$, also follows volume dilution.

It is therefore easy to see how the ERR00 superbubbles would have remained trapped inside the IF for the systems' evolution. The gradual drop in the ERR00 extinction is also essentially an expression of the velocity of an ionization front driven at all times t by a constant stellar flux.

Spectral Energy Distributions

It might therefore be supposed that very different spectral forms would be generated by the ERR00 HII region solution and the thesis supernova solution using the same model

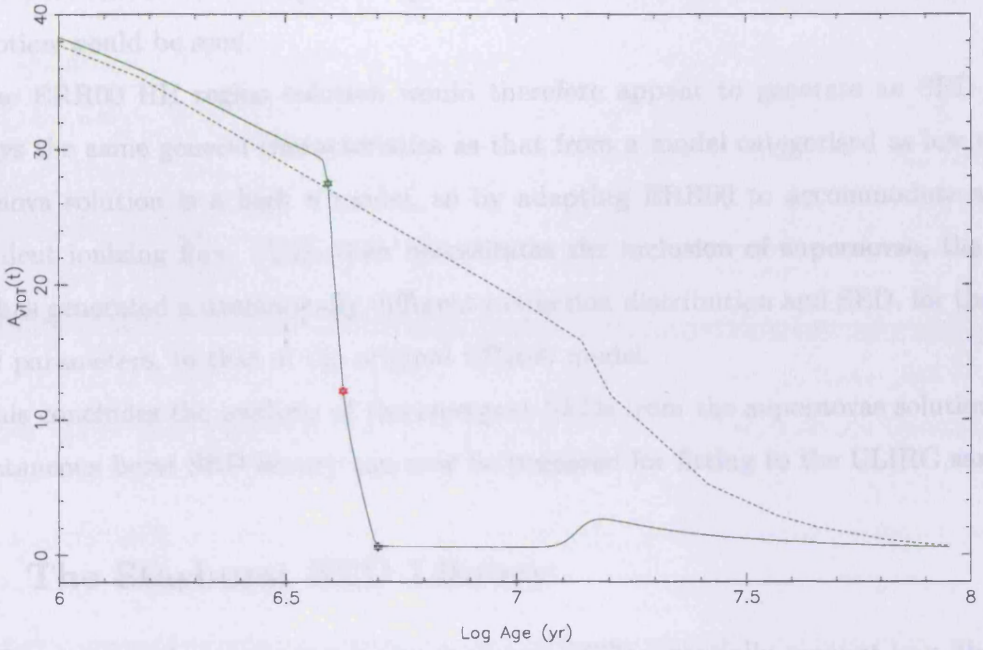

Figure 6.14: The extinction distributions for $M_{GMC} = 10^7 M_\odot$ $\eta = 0.2$, following (Efstathiou *et al.* 2000) (dashed line) and the supernova solution developed here (solid line). R_{eq}, R_c and $R2_W$ are shown by the green, red and black stars respectively

parameters.

The ERR00 model would essentially have a source function which is enshrouded at all times, whilst the supernova solution would have it exposed from early times. In the ERR00 model, practically no reprocessed stellar flux would be seen at short wavelengths and the FIR emission would be broad and of high magnitude.

On the other hand, the thesis model generates a supernova solution SED which would exhibit reprocessed stellar flux from fairly early times. At later times, low magnitude, narrow FIR emission, accompanied by strong MIR PAH narrow-band and deep 2175$\AA$ absorption would be seen.

The ERR00 HII region solution would therefore appear to generate an SED which displays the same general characteristics as that from a model categorised as low η. The supernova solution is a high η model, so by adapting ERR00 to accommodate a time-dependent ionizing flux, which then necessitates the inclusion of supernovae, the thesis work has generated a dramatically different extinction distribution and SED, for the same model parameters, to that of the original ERR00 model.

This concludes the analysis of the emergent SEDs from the supernovae solution. The instantaneous burst SED library can now be prepared for fitting to the ULIRG sample.

6.1 The Starburst SED Library

The HII region and supernova solution starburst SEDs essentially amount to a library of spectra which describe the evolution of giant molecular clouds under the influence of an *instantaneous* burst of star formation.

There are seven star formation efficiencies in the parameter space and when these are coupled to the four GMC masses, a total of 28 individual systems have been modelled. The mass of the central clusters $M_\star$ has a range of $2.5 \times 10^8 M_\odot \geq M_\star \geq 1 \times 10^4 M_\odot$, whilst the mass of gas and dust $M_{gas}+M_{dust}$ surrounding these clusters runs from $7.5 \times 10^8 M_\odot \geq M_{gas}+M_{dust} \geq 9.9 \times 10^6 M_\odot$.

Of these 28 models, 6 reverted to the time-dependent HII region solution for all t whilst the remaining 22 invoke the supernova solution. For all models which reach $R2_{SN}$, 17 SEDs are generated. However, some of the lowest cluster masses in the parameter space produced supershells which broke-up before reaching $R2_{SN}$, in which case the modelling ends. Therefore the instantaneous burst library contains over 400 SEDs.

6.1.1 Instantaneous Burst SED Library

One object of the thesis is to sum each starburst SED in turn with each of the AGN SED's generated in Chapter 2. The resultant *combined* ULIRG SEDs can then matched to the published SED data of a small sample of nearby ($z \leq 1$) ULIRG galaxies.

A fitting process to accomplish this was developed and this is discussed in some depth in the next chapter. For this discussion suffice it to say that the goodness-of-fit of each combined instantaneous burst and AGN ULIRG SED was assessed using the reduced χ^2 criterion.

It was found in this rigorous fitting procedure that no instantaneous burst and AGN SED combination was able to match any of the ULIRG samples' SEDs to better than an $\approx 40\%$ probability that the model SED belonged to the same population distribution as the published data.

This result suggests that perhaps the constraint of instantaneous star formation in the starburst library has rendered the ULIRG fitting results biased. This is particularly interesting as it is unknown whether an instantaneous or more constant star formation scenario better fits the observational data from local starburst galaxies (Kewley *et al.* 2002).

It was therefore decided to follow FH03 and ERR00 and extend the instantaneous burst SED library to approximate constant star formation. These constant star formation SEDs can then be paired with the AGN SED Library and the new combined ULIRG SED fitted to the published ULIRG data. If the results indicate a better than $\approx 40\%$ probability that the model SED belongs to the same population distribution as the published data, it might be suggested that continuous star formation is more appropriate for nearby ULIRGs. This re-fitting is carried out in the next chapter.

Extending instantaneous burst SEDs to approximate constant star formation when fitting starbursts appears fairly common. Several authors besides ERR00 and FH03 have used the approximation (e.g. Reike *et al.* 1980; Genzel *et al.* 1998; Siebenmorgen & Krügel 2007) to generate good fits to observational data; these were briefly reviewed in chapter 3.

6.1.2 Extension to Constant Star Formation Approximation

The extension to approximate constant star formation assumes that the star formation rate can be parameterised as a function which exponentially decays according to a range of e-folding times τ.

The approximation begins by assuming that at time t_{sb} after the onset of the starburst, the observed star formation rate (or in this instance the number of GMC's forming stars with efficiency η ERR00) is given by $\dot{M}_{\star}(t_{sb})$ and assuming that the clouds do not overshadow each other, the monochromatic flux from that burst can be written

$$F_{\nu}(t_{sb}) = \int_{o}^{t_{sb}} \dot{M}_{\star}(t')F_{\nu}(t_{sb} - t')dt' \tag{6.1}$$

where $F_{\nu}(t_{sb} - t')$ is the flux from a GMC t_{sb} - t' years after the onset of star formation at its centre (ERR00). $\dot{M}_{\star}(t')$ is the global starburst star formation rate per year at t', which can be approximated by

$$\dot{M}_{\star}(t') = \dot{M}_{\star}(0)e^{-\frac{t'}{\tau}} \tag{6.2}$$

where $\dot{M}_{\star}(0)$ is the rate at which stars are forming per year at $t' = 0$ and τ represents the ability of a GMC to support star formation i.e., the time it takes for the material and energy available for star formation to be exhausted. Although Equation 6.1 can be solved analytically, only the numerical terms on the right hand side are available, so the integral had to be solved numerically.

This appears to be the limit of the information available in the literature on conducting a constant star formation approximation from a set of instantaneous burst SEDs. The suggestion is that the approximation must therefore be tailored to the input variables of each modelling method. Therefore the coming equations have been deduced for particular application to the GEM modelling approach developed in this thesis.

Considering the rate at which stars are forming per year at $t' = 0$, this can be equated to

$$\dot{M}_{\star}(0) = mf_{sb} \cdot \eta \cdot M_{GMC} \tag{6.3}$$

where mf_{sb} is a multiplication factor which gives the rate at which GMC's are forming stars per year at $t' = 0$ and the product of η . M_{GMC} is the mass of stars formed in each GMC. The rate at which GMCs are forming stars per year at $t' = 0$, mf_{sb}, is considered in some depth in the next subsection *'Determination of the Fitting Range for mf_{sb}'* as this

is a free parameter in the modelling for which upper and lower limits must be set. Thus, with reference to Equations 6.2 and 6.3, both of which are expressed in terms of $\dot{M}_{\star}$, the global star formation rate per year can be expressed

$$\dot{M}_{\star}(t') = mf_{sb} \cdot \eta \cdot M_{GMC} \cdot e^{-\frac{t'}{\tau}} \tag{6.4}$$

where τ is the e-folding time decay constant parameterisation or the half-life of the GMC ensemble.

To illustrate how Equation 6.4 also represents the number of GMCs forming stars at t', $N_{GMC}(t')$ (Efstathiou *et al.* 2000), this annual star formation rate can be summed over the elapsed period since star formation began to give the total mass of stars formed $M_{\star}^{TOT}(t_{sb})$ at $t' = t_{sb}$

$$M_{\star}^{TOT}(t_{sb}) = \sum_{0}^{t_{sb}} \dot{M}_{\star}(t')\Delta t \tag{6.5}$$

where the summation is carried out using the trapezium rule and Δt is the width of a time bin in years, such that $\Delta t=10^6$Myrs for t' = 1-10Myrs and $\Delta t=10^7$Myrs for t' = 20-80Myrs. Having obtained the total mass of stars formed, it can be divided by the mass of stars formed per GMC to find the number of GMC's, $N_{GMC}^{TOT}(t_{sb})$ that have joined the starbursting ensemble to t_{sb} such that

$$N_{GMC}^{TOT}(t_{sb}) = \frac{M_{\star}^{TOT}(t_{sb})}{\eta \cdot M_{GMC}} \tag{6.6}$$

Similarly, t_{sb} in Equation 6.5 can be replaced with t' and the trapezium rule used to find the mass of stars $M_{\star}(t')$ formed in a time bin and this can also be divided by the stellar mass of each GMC. This gives the number of GMCs forming stars with efficiency η, which joined the starbursting ensemble in the time bin

$$N_{GMC}(t')\Delta t = \frac{\dot{M}_{\star}(t')\Delta t}{\eta \cdot M_{GMC}} = mf_{sb}e^{-\frac{t'}{\tau}}\Delta t \tag{6.7}$$

This is also the global star formation rate at efficiency η, at t', from Equation 6.4, in a time bin Δt.

Having obtained the number of GMC's joining the starbursting ensemble in a time bin the question becomes, given a particular combination of M_{GMC} and η, how should the fluxes from those SEDs in the instantaneous burst library set be distributed to generate the constant star formation rate approximation SED for time t_{sb}.

Equation 6.1 can be interpreted as a superposition of instantaneous burst SEDs at different times e.g., $t' \leq t_{sb}$ = 3Myrs such that

$$F_\nu(t_{sb}) = \Delta t[\dot{M}_\star(0)F_\nu(t_{sb})+\dot{M}_\star(t_1)F_\nu(t_{sb}-t_1)+\dot{M}_\star(t_2)F_\nu(t_{sb}-t_2)+\dot{M}_\star(t_{sb})F_\nu(0)] \quad (6.8)$$

Using Equation 6.2, Equation 6.8 can be re-written

$$F_\nu(t_{sb}) = \Delta t\dot{M}_\star(0)[e^{-\frac{t_o}{\tau}}F_\nu(t_{sb})+e^{-\frac{t_1}{\tau}}F_\nu(t_{sb}-t_1)+e^{-\frac{t_2}{\tau}}(t_2)F_\nu(t_{sb}-t_2)+e^{-\frac{t_{sb}}{\tau}}F_\nu(0)] \quad (6.9)$$

and noting that $t_3 = t_{sb}$ - t_2, $t_2 = t_{sb}$ - t_1, $t_1 = t_{sb}$ - t_2 and $t_{sb} = t_{sb}$ - t_0, Equation 6.9 becomes

$$F_\nu(t_{sb}) = \Delta t\dot{M}_\star(0)[e^{-\frac{t_3-t_o}{\tau}}F_\nu(t_{sb}) + e^{-\frac{t_2-t_{sb}}{\tau}}F_\nu(t_2) + e^{-\frac{t_1-t_{sb}}{\tau}}(t_1)F_\nu(t_1) + e^{-\frac{t_o-t_{sb}}{\tau}}F_\nu(0)] \quad (6.10)$$

which shows that the largest number of GMC's to join the starbursting ensemble - i.e., those which formed between t_{sb} = 0 and 1Myrs are assigned the flux of the most evolved SED in an M_{GMC} and η set. Correspondingly, it is smallest number of GMC's to join the ensemble, i.e., those between t_{sb} - Δt and t_{sb} which are assigned the least evolved instantaneous burst SED flux in a set.

Reducing Equation 6.10 shows that the flux from the burst at t_{sb} can then be written

$$F_\nu(t_{sb}) = \dot{M}_\star(0)e^{-\frac{t_{sb}}{\tau}}\int_0^{t_{sb}} e^{\frac{t'}{\tau}}F_\nu(t')dt' \quad (6.11)$$

The range of values for the decay constant τ was chosen to be broadly in line with the years at which an instantaneous burst SED was generated at τ = 0.5Myrs, 1-10Myrs at $\Delta\tau$ = 1Myrs and 20-80Myrs at $\Delta\tau$ = 10Myrs, leading to seventeen values on the decay parameter grid.

mf_{sb}, the rate at which new GMC's are forming stars per year at t_{sb} = 0 is a free parameter for which a range of values must be found that can be applied in turn to the instantaneous burst SED sets to generate each constant star formation rate approximation (CSFRA) SED for t_{sb}. Therefore the next subsection considers the range of values that it might be appropriate to assign to mf_{sb}.

Determination of the Fitting Range for mf_{sb}

mf_{sb} is the rate at which new GMC's are forming stars per year at t_{sb} = 0 and is a free parameter for which a range of values must be found. These values are then used in Equation 6.2 to find the rate at which stars are forming per year at t' = 0.

Before identifying the range for mf_{sb}, it must first be briefly mentioned that it was not feasible for this thesis work to develop a fitting procedure of sufficient complexity that clouds of *different* GMC masses could be combined together. This is despite it being unlikely that the GMCs in a ULIRG will be in similar evolutionary state (ERR00). The sheer number of potential SED combinations in the resulting starburst library would make including such a procedure highly prohibitive in computer resources and time.

For example, the starburst SED library contains over 450 explicitly calculated SEDs and when these are extended to constant star formation at all 17 values of τ discussed above, that number rises to around 7000. At the end of the AGN chapter it was noted that that library contained some 135 explicit SEDs, so pairing each starburst SED with each AGN SED in the fitting procedure results in over 9 x 10^5 possible combinations in the emergent SED library.

Therefore the parameter mf_{sb} is defined as the rate at which new GMC's of a *similar mass* are forming stars per year at t′ and the fitting is carried out for all the CSFRA SEDs in one M_{GMC} at a time. Thus, rather than determining a range of mf_{sb} appropriate to *all* M_{GMC}'s at once, four ranges were found for mf_{sb}, one each appropriate to M_{GMC} = 10^6-, 10^7-, 10^8 & 10^9 $M_\odot$ respectively.

The object of the exercise is to therefore find upper and lower limits for the rate at which GMCs are forming stars per year at t_{sb} = 0, for each GMC mass, It was decided to set these limiting mf_{sb} values as those which gave the model data only a 20% chance of belonging to the population distribution of the ULIRGS having the lowest and highest flux in the object sample. 12540+5708 (Mrk 231) has the largest flux at $S_{90\mu m}$ = 1.60 x 10^{-12}Wm$^2\mu$m^{-1} whilst 15250+3609 whose energy distribution contains the smallest flux at $S_{1100\mu m}$ = 8.08 x 10^{-17}Wm$^2\mu$m^{-1}. Therefore the range of mf_{sb} for each M_{GMC} under this criteria was found from exhaustive fitting of the model data to these two ULIRGS, using the *Miracle* supercomputer housed at University College London. The results are detailed in Table 6.5.

Having obtained an estimate of the appropriate range of mf_{sb} for each M_{GMC}, the effect of varying the starburst global star formation activity half-life τ whilst keeping t_{sb} and mf_{sb} constant can now be considered.

M_{GMC} ($M_\odot$)	Lower Limit mf_{sb} (yr^{-1})	Upper Limit mf_{sb} (yr^{-1})	Increment per run	Number of runs/η
10^9	6.250 x 10^{-7}	1.875 x 10^{-5}	6.250 x 10^{-7}	30
10^8	1.250 x 10^{-5}	3.750 x 10^{-4}	1.250 x 10^{-5}	30
10^7	6.250 x 10^{-5}	1.875 x 10^{-3}	6.250 x 10^{-5}	30
10^6	1.250 x 10^{-4}	3.750 x 10^{-3}	1.250 x 10^{-4}	30

Table 6.5: The Rate at which GMC's are forming stars per year at t′ = 0, mf_{sb}, to be included in the rigorous fitting procedure of the ULIRGs at each M_{GMC}. The first column gives the mass of the GMC from which the model instantaneous burst SEDs are derived. The second, third and fourth columns give the lower and upper fitting limits of mf_{sb} and the increment in mf_{sb} on each fitting run respectively. The final column gives the number of times the fitting procedure is therefore carried out for each of the seven star formation efficiencies η in a single M_{GMC}.

The Affect of the Half-Life τ

The extension to approximate constant star formation assumes that the star formation rate can be parameterised as a function which exponentially decays according to a range of e-folding times τ. Physically this constant might be interpreted as the decay in the number of GMCs joining the starbursting ensemble as it evolves. Essentially τ can be seen as an estimate of the time for which star formation can be sustained within an ensemble and allows implications to be made as to star formation fuelling and gas transport within a merger.

The range of τ chosen for the modelling is τ = 0.5Myrs, 1-10Myrs at $\Delta\tau$ = 1Myrs and 20-80Myrs at $\Delta\tau$ = 10Myrs. Figure 6.15 illustrates the number of GMCs to join the ensemble in a time bin, $N_{GMC}(t')\Delta t$, from Equation 6.7 whilst keeping t_{sb} = 10Myrs and mf_{sb} = 1.875 x 10^{-5} constant for τ = 1-, 5-, 10-, 30-, & 60Myrs. The appropriate instantaneous burst SED flux to assign to each $N_{GMC}(t')\Delta t$ is indicated across the top of Figure 6.15 by the straight line of values $F_\nu(t')$. As mentioned, referring to Equation 6.10 it can be seen that it is the instantaneous burst flux from the most evolved SEDs i.e., $F_\nu(t'=t_{sb}=10Myrs)$, which is given to the largest number of GMC's joining the starbursting ensemble and the least evolved SED i.e., $F_\nu(t_{sb}=0)$ which is assigned to the smallest

number of joining GMC's. At first glance this may appear counter-intuitive, but it must be remembered that this also represents the rate at which stars are forming at t′ and it is those stars, which upon decay, generate the flux seen in the appropriate instantaneous burst SED.

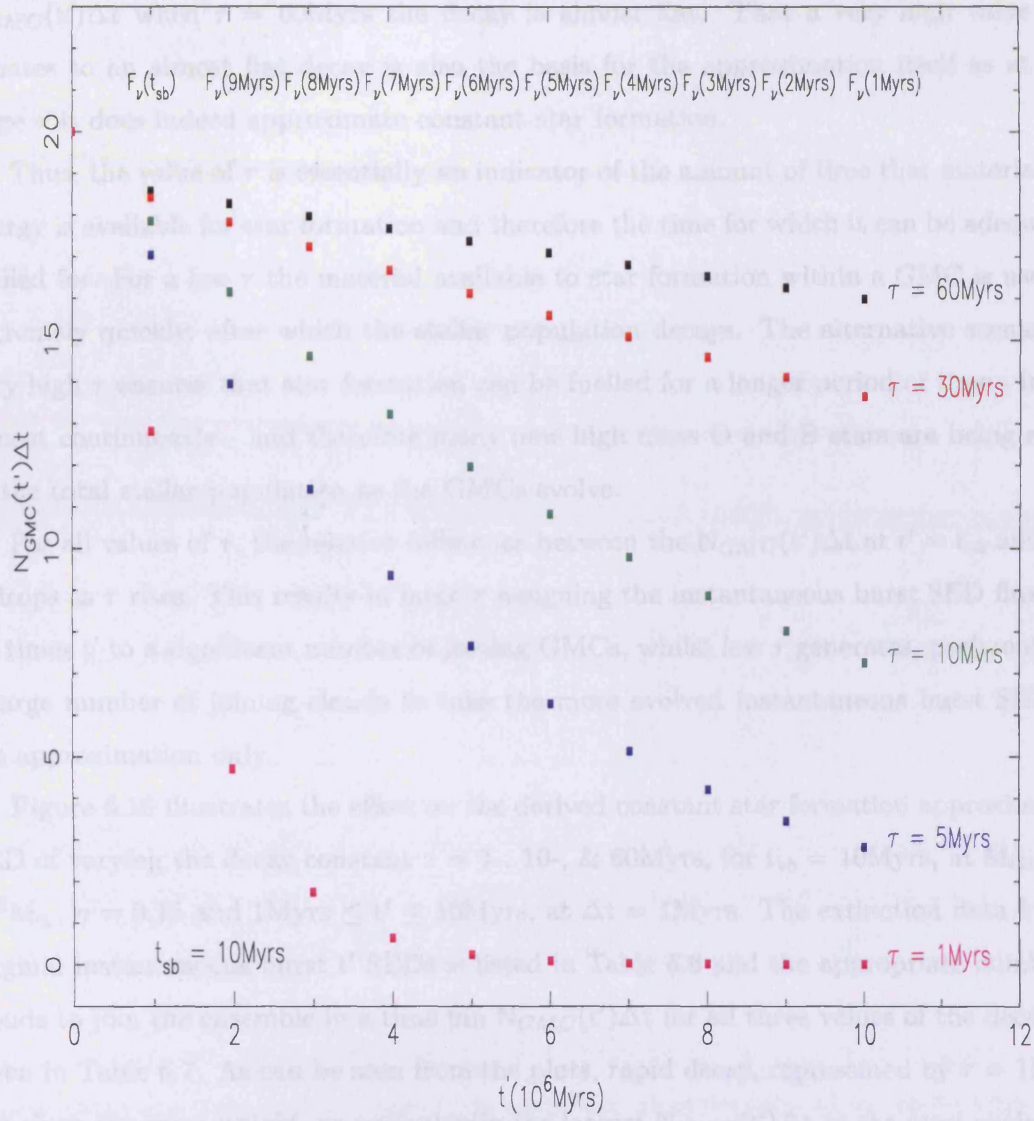

Figure 6.15: Illustration of the affect on the number of GMC's joining the ensemble in time bin $N_{GMC}(t')\Delta t$, of varying the half-life τ in the constant star formation approximation, whilst keeping t_{sb} = 10Myrs and $mf_{sb} = 1.875 \times 10^{-5}$ constant. The value of τ is indicated down the right-hand side of the plot and the time of the instantaneous burst SED to be assigned the appropriate $N_{GMC}(t')\Delta t$ is indicated across the top of the plot by $F_\nu(t')$

Referring to Figure 6.15, the lower most curve has been plotted for τ=1Myrs and as can be seen, this ensures very rapid initial decay in $N_{GMC}(t')\Delta t$, after which it flattens off at comparatively low values. However, moving to the values of $N_{GMC}(t')\Delta t$ when τ = 10Myrs, it can be seen that the decay is much more gradual and finally, looking at $N_{GMC}(t')\Delta t$ when τ = 60Myrs the decay is almost flat. That a very high value of τ equates to an almost flat decay is also the basis for the approximation itself as at very large τ it does indeed approximate constant star formation.

Thus, the value of τ is essentially an indicator of the amount of time that material and energy is available for star formation and therefore the time for which it can be adequately fuelled for. For a low τ the material available to star formation within a GMC is used up extremely quickly, after which the stellar population decays. The alternative scenario of very high τ ensures that star formation can be fuelled for a longer period of time - in fact almost continuously - and therefore many new high mass O and B stars are being added to the total stellar population as the GMCs evolve.

For all values of τ, the relative difference between the $N_{GMC}(t')\Delta t$ at $t' = t_{sb}$ and $t' = 0$ drops as τ rises. This results in large τ assigning the instantaneous burst SED fluxes at *all* times t' to a significant number of joining GMCs, whilst low τ generates, preferentially, a large number of joining clouds to take the more evolved instantaneous burst SEDs in the approximation only.

Figure 6.16 illustrates the effect on the derived constant star formation approximation SED of varying the decay constant τ = 1-, 10-, & 60Myrs, for t_{sb} = 10Myrs, at $M_{GMC} = 10^8 M_\odot$, η = 0.15 and 1Myrs $\leq t' \leq$ 10Myrs, at Δt = 1Myrs. The extinction data for the original instantaneous burst t' SEDs is listed in Table 6.6 and the appropriate number of clouds to join the ensemble in a time bin $N_{GMC}(t')\Delta t$ for all three values of the decay are given in Table 6.7. As can be seen from the plots, rapid decay, represented by τ = 1Myrs, has given the most weight, or equivalently the largest $N_{GMC}(t')\Delta t$ to the most evolved or latest t' SEDs, whilst the earlier t' SEDs have essentially been weighted down by being assigned to a low number of GMC's. Table 6.6 shows that this biases the CSFRA strongly towards the lower optical depth t' SEDs. Moving to τ = 10Myrs, a slower decay has been initiated and therefore although $N_{GMC}(t')\Delta t$ has been alloted more evenly to the entire t' instantaneous burst SED set, the later t' SEDs are still marginally favoured. Finally for τ = 60Myrs, which represents almost constant star formation, whilst the greatest number of $N_{GMC}(t')\Delta t$ have been assigned to the earlier, or least evolved and hence higher optical

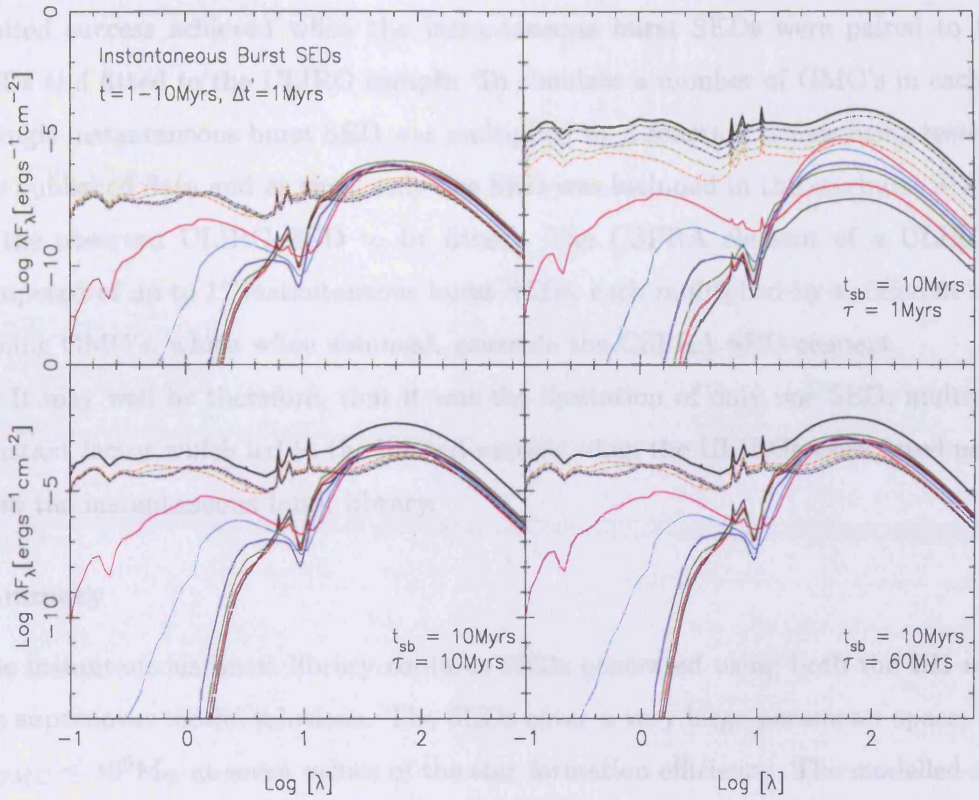

Figure 6.16: Illustration of the affect of varying the half-life, τ on the constant star formation approximation SEDs. The top right-hand plot shows the instantaneous burst SEDs for $M_{GMC} = 10^8 M_\odot$, $\eta = 0.15$ for $t' = 1$ - 10Myrs, at $\Delta t' = 1$Myrs. The remaining plots illustrate $F_\nu(t')$ where $t' = 1$, 2, 3, 4, 5 & 6Myrs for the thin solid black, red, green, turquoise and pink lines and $t' = 7$, 8, 9 & 10Myrs for the dot-dashed lines. The solid and dot-dashed lines indicate those times when the supershell temperature exceeds the dust condensation temperature whilst internal and external to $R2_W$ respectively. The thick solid black line gives the constant star formation approximation $F_\nu(t_{sb})$. t_{sb} = 10Myrs for each curve and the appropriate value of the global star formation rate activity half-life τ is indicated in bottom right-hand corner of each plot.

depth SEDs, the approximation has also assigned a significant number to the more evolved, older SEDs resulting in the constant star formation approximation with the highest overall flux magnitude.

Finally in this section it might be appropriate to suggest a reason for the somewhat limited success achieved when the instantaneous burst SEDs were paired to the AGN SEDs and fitted to the ULIRG sample. To simulate a number of GMC's in each ULIRG, a single instantaneous burst SED was multiplied by a constant before being tested against the published data and as such, only one SED was included in the starburst SED element of the observed ULIRG SED to be fitted. The CSFRA element of a ULIRG SED is composed of up to 17 instantaneous burst SEDs, each multiplied by a different number of joining GMC's, which when summed, generate the CSFRA SED element.

It may well be therefore, that it was the limitation of only one SED, multiplied by a constant factor which led to the limited success when the ULIRGs were fitted using SEDs from the instantaneous burst library.

Summary

The instantaneous burst library contains SEDs generated using both the HII region and the supernovae model solutions. The SEDs cover a very large parameter space; $10^6 M_\odot \leq M_{GMC} \leq 10^9 M_\odot$ at seven values of the star formation efficiency. The modelled extinction distributions range from systems that are optically thin for the majority of their life time to those that are totally dust enshrouded for most of their evolution.

The instantaneous burst SEDs have been extended to approximate constant star formation using 17 values of the classic time decay parameterisation. When taken together these SEDs represent a substantial sampling in parameter space and might provide an observer with a useful resource for matching to observations, without the necessity of accomplishing radiative transfer simulations.

What now remains is to test the efficacy of the emergent SED library, and the modelling approach as a whole, by comparing the library to observations.

t(Myr)	A_v^{TOT}(t)	A_v^{SH}(t)	A_v^{Wi}(t)	A_v^{n}(t)	A_v^{α}(t)	PHASE
1.00	92.21	0.00e+00	1.99e+00	8.93e+01	9.22e-01	R_W
2.00	86.24	0.00e+00	1.62e+00	8.37e+01	9.22e-01	R_W
3.00	81.65	0.00e+00	1.13e+00	7.96e+01	9.22e-01	R_W
3.81	78.98	0.00e+00	3.58e-01	7.77e+01	9.22e-01	$R_{SN}(t_{SNstart})$+1ΔR
3.91	78.13	1.04e-233	1.03e-02	7.72e+01	9.22e-01	R_{Eq}
4.00	65.92	6.43e-205	0.00e+00	6.50e+01	9.22e-01	R_W+1ΔR : R_c-1ΔR
4.81	23.72	1.61e-78	0.00e+00	2.28e+01	9.22e-01	R_c
5.00	20.02	6.03e-64	0.00e+00	1.91e+01	9.22e-01	R_c+1ΔR : $R2_W$-1ΔR
6.00	6.06	2.44e-30	0.00e+00	5.14e+00	9.22e-01	R_c+1ΔR : $R2_W$-1ΔR
6.51	0.92	5.03e-23	0.00e+00	0.00e+00	9.22e-01	$R2_W$
7.00	0.91	3.54e-21	0.00e+00	0.00e+00	9.14e-01	$R2_W$+1ΔR : R2SN-1ΔR
8.00	0.90	5.11e-18	0.00e+00	0.00e+00	8.99e-01	$R2_W$+1ΔR : R2SN-1ΔR
9.00	0.88	2.01e-15	0.00e+00	0.00e+00	8.84e-01	$R2_W$+1ΔR : R2SN-1ΔR
10.00	0.87	2.95e-13	0.00e+00	0.00e+00	8.69e-01	$R2_W$+1ΔR : R2SN-1ΔR
20.00	0.73	1.03e-02	0.00e+00	0.00e+00	7.24e-01	$R2_W$+1ΔR : R2SN-1ΔR
30.00	4.80	4.21e+00	0.00e+00	0.00e+00	5.89e-01	$R2_W$+1ΔR : R2SN-1ΔR
40.00	3.63	3.16e+00	0.00e+00	0.00e+00	4.68e-01	$R2_W$+1ΔR : R2SN-1ΔR
50.00	2.77	2.41e+00	0.00e+00	0.00e+00	3.63e-01	$R2_W$+1ΔR : R2SN-1ΔR
60.00	2.26	1.99e+00	0.00e+00	0.00e+00	2.71e-01	$R2_W$+1ΔR : R2SN-1ΔR
70.00	1.92	1.73e+00	0.00e+00	0.00e+00	1.91e-01	$R2_W$+1ΔR : R2SN-1ΔR
80.00	1.68	1.56e+00	0.00e+00	0.00e+00	1.20e-01	$R2_W$+1ΔR : R2SN-1ΔR

Table 6.6: Extinction Av^{TOT}(t) variation with time for a single M_{GMC}=$10^8 M_\odot$, η=0.15 cloud. t is the time of the instantaneous burst SED, Av^{TOT}(t) is the total extinction, A_v^{SH}(t) is the contribution from the supershell, A_v^{Wi}(t) is the extinction generated in the HII region whilst A_v^{n}(t) and A_v^{α}(t) are the extinction from the neutral and ambient regions respectively. The column entitled *PHASE* indicates the state of the system at the time the extinction was calculated.

t′ (Myrs)	$N_{GMC}(t')\Delta t$ (τ=1)	$N_{GMC}(t')\Delta t$ (τ=10)	$N_{GMC}(t')\Delta t$ (τ=60)
10	12.81	17.84	18.58
9	4.71	16.14	18.27
8	1.73	14.61	17.97
7	0.64	13.22	17.67
6	0.23	11.96	17.38
5	0.096	10.82	17.09
4	0.018	9.79	16.81
3	0.012	8.86	16.53
2	0.004	8.02	16.26
1	0.002	7.25	15.99

Table 6.7: The number of GMC's to join the ensemble in a time bin $N_{GMC}(t')\Delta t$ for t_{sb} = 10Myrs, mf_{sb} = 1.875 x 10^{-5}, M_{GMC}=$10^8 M_\odot$, η=0.15 for τ = 1-, 10- & 60Myrs. t′ is the time of the instantaneous burst SED assigned to each of the $N_{GMC}(t')\Delta t$ GMCs.

Chapter 7

Assessment of the ULIRG Model

In this chapter the veracity of the GEM modelling approach is assessed. This is be accomplished by pairing SEDs from the AGN and constant star formation approximation (CSFRA) SED libraries in turn and matching the resultant combined ULIRG SED to the published data of a small sample of nearby (z<1) ULIRGS. Having identified the combined SED which matches best, estimates for quantities such as the ULIRG luminosity, star formation rate, starburst age or dust mass can be derived for each object. Comparing these derived quantities to those already published in the literature, for the same sample, can provide a quantitative assessment of the modelling approach.

Throughout this thesis, the work of Farrah *et al.* (2003) [FH03] has been referred to extensively. For example the model used to develop the AGN SED library in Chapter 2 is essentially the same as that used by FH03 to generate their AGN SED library, whilst the HII region evolution developed here in Chapter 3 uses the same fundamental method as FH03 but then extends it to incorporate a time-dependent ionizing flux. Finally, the sample of ULIRGs to be considered in this chapter was taken from FH03, who also paired AGN and HII region emergent SEDs to find a best-fitting combined model SED for each ULIRG. FH03 published values for the ULIRG physical characteristics mentioned above and as such provides a useful resource for comparative and assessment purposes.

This chapter begins by presenting the published data for the ULIRG sample and considers the transformation of that data into the rest frame. The next section discuses issues of degeneracy and outlines the statistical methodology employed to measure the goodness-of-fit and illustrates the way in which the AGN and CSFRA SEDs are combined to produce the ULIRG SED library for testing. Identification of the best-fit ULIRG SED for each object is then considered. For simplicity model *combined* SEDs from the ULIRG

SED library will be referred to by the term GEM and the combined SED which fits each ULIRG data best will be referred to as the *best-fit GEM SED.*

Having identified the best-fit GEM SED for each ULIRG, section *Analysis I* first describes the method by which the components of that SED can be used to find the AGN, CSFRA and combined ULIRG luminosity. Extraction of the SFR's using traditional, published methods and the luminosity of the CSFRA element of the best-fit GEM SED is then discussed. The section then compares these results to those of FH03 and considers the values taken by the free parameters of the best-fit GEM SED in the context of what has been published generally in literature for the ULIRG sample.

Analysis II uses the CSFRA component of the best-fit GEM SED to find e.g., SFR's from the *free parameters* only. This method uses the GMC mass and star formation efficiency η of the single GMC which originated the instantaneous burst SEDs included in that CSFRA component. Comparison of these SFR's derived using the SED free parameters to those found in the previous *Analysis I* section from the CSFRA SED luminosity only, or to those published in the literature, can provide an independent indication of the credibility of the adopted modelling.

The final assessment section, *Analysis II* considers impact of including supernovae in the modelling and then the chapter concludes with some of the more important potential sources of error in the GEM modelling approach. Beginning then with presentation of the ULIRG sample.

7.1 ULIRG Sample

The primary criteria for the choice of which six objects, from the FH03 sample were to be modelled in this thesis was the number of data points available for each and as such, the objects chosen are amongst the richest in data from the FH03 sample.

Each best-fit ULIRG SED obtained by FH03 for the chosen sub-sample had an associated $\chi^2 \leq 3$ and a calculated rest-frame 1-1000μm luminosity $L_{1-1000\mu m} > 10^{12} L_{\odot}$; in line with the FH03 definition of a ULIRG. As mentioned in Chapter 3, several criteria exist for the ULIRG definition, but the broad wavelength range used by FH03 for selection is particularly useful as continuum shape may bias selection if luminosities are derived across a smaller wavelength ranges (FH03).

IRAS Name	Other Name	RA(2000) (hh:mm:ss)	Dec. (° ‘ “)	z	Optical Spectrum	No.Data Points
00262+4251		00 28 54.2	+43 08 15.3	0.0927	LINER	14
12540+5708	Mrk 231	12 56 14.2	+56 52 25.2	0.0422	SEYFERT 1	29
13428+5608	Mrk 273	13 44 42.1	+55 53 12.6	0.0378	SEYFERT 2	23
14348-1447		14 37 38.4	-15 00 22.8	0.0827	LINER	22
15250+3609		15 26 59.4	+35 58 37.5	0.0552	LINER	21
23365+3604		23 39 01.3	+36 21 08.7	0.0645	HII+LINER	18

Table 7.1: Ultraluminous Infrared Galaxy sample. Co-ordinates, redshifts, optical spectral classifications and number of data points, taken from FH03 and the NASA Extragalactic Data base (NED). The fluxes to be fitted are listed in Table 7.2 which also indicates at what wavelengths only upper limits are available.

7.1.1 Published Data

For convenience, Table 7.1 re-lists the observational characteristics of the six local ultraluminous infrared galaxies selected for testing. Table 7.2 gives the published fluxes from FH03, the values of which were cross-checked in NED and the appropriate originating literature. The optical and near-IR fluxes were taken from the APM and 2MASS data bases along with Carico *et al.* (1988) and Spinoglio *et al.* (1995). *IRAS* fluxes were taken from the *IRAS* Faint Source Survey and FH03 used the XSCANPI software to derive *IRAS* fluxes when only upper limits were present in the catalogues. Other infrared data were taken by FH03 from Carico *et al.* (1988), Maiolino *et al.* (1995), Klaas *et al.* (1997), Rigopoulou *et al.* (1999), Dale & Uson (2000), Zink *et al.* (2000), Klaas *et al.* (2001) and Tran *et al.* (2001). Sub-millimetre data were taken from Rigopoulou *et al.* (1996), Dunne *et al.* (2000) and Dunne & Eales (2001).

However, a **caveat** must be added as *Hubble Space Telescope (HST)* data obtained for a sample of ULIRGS by Farrah *et al.* (2001) indicated that the emission at optical wavelengths from these objects was in most cases dominated by old stellar populations rather than light from a starburst or AGN (Farrah *et al.* 2001). Emission from unobscured population II stars originating in the ULIRG merger progenitors is not included in this thesis work, as all source clusters were embedded in a dusty GMC and no 'naked' old stars were included. As the contribution from this population could lie anywhere between 0 and 100% there is the potential for a significant but unquantified contribution from the old stellar populations in the tabulated optical fluxes (FH03). It was therefore assumed by FH03 and in this thesis work, that all fluxes short-wards of 3.5μm in the rest frame were 3σ upper limits and these are indicated in Table 7.2 with the prefix '<'.

ULIRG	00262-1447	12540+5708	13428+5608	14348-1447	15250+3609	23365+3604
$\lambda(\mu m)$	$S_\lambda(Wm^2)$	$S_\lambda(Wm^2)$	$S_\lambda(Wm^2)$	$S_\lambda(Wm^2)$	$S_\lambda(Wm^2)$	$S_\lambda(Wm^2)$
0.55	-	<7.14e-14	<5.61e-15	<1.31e-15	<1.47e-15	-
0.64	-	<5.38e-14	<8.24e-15	<2.01e-15	<1.97e-15	-
1.25	<8.67e-15	<1.17e-13	<2.15e-14	<4.06e-15	<1.00e-14	<1.96e-14
1.66	<1.12e-14	<1.94e-13	<2.44e-14	<4.53e-15	<1.05e-14	<1.79e-14
2.22	<6.73e-15	<2.51e-13	<2.17e-14	<4.46e-15	<7.08e-15	<1.29e-14
3.5	-	<3.19e-13	<1.51e-14	-	<3.48e-15	-
5.9	2.85e-15	3.08e-13	3.87e-14	6.40e-15	1.42e-14	6.40e-15
7.7	2.87e-14	4.69e-13	1.14e-13	3.34e-14	6.70e-14	4.12e-14
10.0	<2.61e-14	4.27e-13	2.99e-14	<2.88e-14	<8.00e-14	<3.59e-14
12.0	1.08e-14	4.67e-13	5.87e-14	2.72e-14	5.95e-14	2.02e-14
15.0	-	5.79e-13	9.99e-14	<5.39e-14	-	2.97e-14
25.0	4.54e-14	1.03e-12	2.74e-13	5.29e-14	1.57e-13	1.13e-13
60.0	1.66e-13	1.60e-12	1.08e-12	3.43e-13	3.55e-13	3.72e-13
90.0	8.19e-14	9.10e-13	7.92e-13	2.28e-13	2.10e-13	2.13e-13
100.0	7.31e-14	9.08e-13	6.41e-13	2.12e-13	1.78e-13	2.70e-13
120.0	7.31e-14	6.08e-13	4.99e-13	1.68e-13	1.05e-13	1.70e-13
150.0	4.46e-14	2.94e-13	2.62e-13	1.04e-13	4.41e-14	8.95e-14
180.0	3.89e-14	1.62e-13	1.45e-13	6.09e-14	2.59e-14	5.43e-14
200.0	<3.08e-14	1.03e-13	1.11e-13	3.95e-14	1.71e-14	4.42e-14
450.0	-	3.42e-15	4.71e-15	1.45e-15	1.68e-15	1.13e-15
800.0	-	-	-	-	3.15e-16	-
850.0	-	-	-	8.47e-17	-	7.06e-17
1100.0	-	1.28e-16	-	4.64e-17	8.08e-17	-

Table 7.2: The observational data for the six ULIRGS in the sample, taken from FH03. All wavelengths and fluxes are quoted in the observed frame except those at 5.9- and 7.7-μm which are given in the rest frame.

7.1.2 Transformation to Rest Frame

Both the AGN and CSFRA model emergent SEDs have been generated in the rest frame, whilst almost all the fluxes listed in Table 7.2 have been published in the observed frame. Transformation of that published data into the rest frame was therefore accomplished by first accounting for flux dilution due to interstellar extinction and distance.

Galactic Interstellar Extinction

The observed fluxes are first de-reddened for the extinction experienced due to absorption by gas and dust between the stars of the Milky Way. In line with FH03, 1.5 magnitudes of V band interstellar extinction was accounted for in the data using the extinction law tabulated in Mathis (1990) which gives the absorption A(λ) in terms of that in the J bandpass ($\approx 1.2\mu$m) A(J). By setting the visual extinction at $\lambda = 0.55\mu$m to be 1.5, A_λ = A(λ)/A(J) x 1.5 and the de-reddened flux is $S_\lambda e^{A_\lambda}$. It was decided to again follow the work of FH03 in order to simplify comparison, assessment and analysis of the GEM modelling approach.

Adjustment for Flux Dilution due to Distance

The fluxes must then be adjusted for the dilution experienced over the journey to Earth. To accomplish this, first the distance D to each ULIRG, must be found in SI units and as can be seen from Table 7.1, the maximum redshift of any ULIRG in the sample is z = 0.09 so

$$D = \frac{cz}{H} \tag{7.1}$$

where c is the speed of light and H is Hubble's constant taken as 72kms^{-1}/Mpc. The observed fluxes S_λ(Obs), listed in Table 7.2 can then be transformed into those emitted in the rest frame S_λ(Em) by adjusting for the dilution due to the inverse square law, using the following simple equation

$$S_\lambda(Em) = S_\lambda(Obs)\left[\frac{D}{R2_{SN}}\right]^2 \tag{7.2}$$

where $R2_{SN}$ is the outer radius of the system. The wavelength bins also have the redshift correction applied and the flux is then re-binned appropriately. The adjustment of the flux to accommodate dilution due to redshift and distance was applied to tabulated fluxes

at all listed wavelengths except 5.9- and 7.7-μm, which have these fluxes published in the rest-frame (FH03).

Wavelength Shift due to Distance

As each of the wavelengths in Table 7.2, except 5.9- and 7.7-μm, have been quoted in the observed frame it was also necessary to de-redshift the observed wavelengths and transform them into the rest-frame. Again, due to the locality of the ULIRG sample it was not necessary to accommodate relativistic recession velocities so the wavelengths were easily de-redshifted using the following relationship

$$z = \frac{\lambda_{Obs} - \lambda_{Em}}{\lambda_{Em}} \tag{7.3}$$

where λ_{Obs} is the observed wavelength and λ_{Em} is the corresponding emitted rest frame wavelength such that

$$\lambda(Em) = \frac{\lambda(Obs)}{1+z} \tag{7.4}$$

7.2 Statistical Methodology

As mentioned at the end of Chapter 2 where the AGN prescription was summarised, the AGN emergent model SED Library contains 135 SEDs, each explicitly calculated by DaRT. The starburst instantaneous burst model SED Library contains 62 HII region and 353 supernovae model SEDs, each also explicitly calculated by DaRT. This instantaneous burst SED Library was then extended to approximate constant star formation leading to $\approx$ 7000 SEDs in the CSFRA model SED library. In the fitting, each of these CSFRA model SEDs is then paired with a model AGN SED and the combined ULIRG SEDs are tested for goodness-of-fit against the samples' observational data, resulting in over 9 x 10^5 possible combinations in the ULIRG Library.

Working with such a considerable number of SEDs immediately presents the problem of uniqueness of the best-fit as e.g., the dynamical model by which the starburst dust distributions have been derived, the scaling of the STARBURST99 central source functions used to irradiate that distribution in DaRT or the issue of equivalent cluster mass for different combinations of M_{GMC} and η, introduces degeneracy into the problem.

Four examples of degeneracy are now discussed. Degeneracy might potentially occur between the two systems $M_{GMC} = 10^8 M_\odot$, $\eta = 0.1$ and $M_{GMC} = 10^9 M_\odot$, $\eta = 0.01$ both

of which have a central cluster mass of $M_{\star} = 10^7 M_{\odot}$. This being so, it is the outer radius of the GMC, $R2_W$, which changes to accommodate the relative quantity of dust in each system, with $R2_W(10^9 M_{\odot}) >> R2_W(10^8 M_{\odot})$. However as was shown in section §5.5 where the extinction distributions $Av^{TOT}(t)$ were discussed, in some cases enter an optically thin regime early in their life-time - the GMC dust having been evacuated by the superbubble - and they remain optically thin for some considerable time until the supershell has cooled sufficiently for dust to condense out and contribute to the extinction. Thus a similar cluster mass would be revealed to the observer over the period the systems were optically thin and as such it could be difficult to distinguish the instantaneous burst SEDs generated at those times; an effect compounded by the constant star formation approximation.

In addition, degeneracy is caused by the free parameter mf_{sb} which determines the rate at which GMCs are forming stars at $t_{sb} = 0$, used in the constant star formation rate approximation, which was fully discussed in §6.1.2. mf_{sb} has been assigned a reasonably broad range (see Table 6.5) to ensure it is appropriate for *each* of the ULIRGs in the testing sample, but the large number of values this free parameter can take (30) has introduced another source of degeneracy. For example, if CSFRA SEDs for $M_{GMC} = 10^8 M_{\odot}$, $\eta = 0.1$ and $M_{GMC} = 10^9 M_{\odot}$, $\eta = 0.1$ were prepared for $t_{sb} = 3$Myrs; a time prior to the first supernova exploding and the former fit had an associated GMC star forming rate mf_{sb} ten times higher than the latter, it is likely that the resultant CSFRA SEDs would differ only slightly in e.g., flux magnitude.

Another example of degeneracy might occur between mf_{sb} and the age of the starburst t_{sb}, in a high η system as increasing the starburst age means more similarly behaved optically thin SEDs are included in the CSFRA, which raises the overall flux SED magnitude - the same affect as achieved when mf_{sb} is increased. Also, considering the degeneracy in η, $Av^{TOT}(t)$ and M_{GMC} illustrated by the scaling of the extinction distributions presented in Chapter 5, it is likely that in some circumstances e.g., an older, lower mass system could mimic the SED of a younger, but higher mass system.

Degeneracy can also apply when considering the AGN luminosity factor discussed at the end of Chapter 2. The fundamental AGN model SEDs were generated from the 9 combinations of dust temperature T_{dust} and extinction in the ultraviolet τ_{uv}, with each PG Quasar irradiating source function pre-calibrated to a luminosity of $L_{AGN} = 10^{12} L_{\odot}$ before the transfer of flux was calculated by DaRT. Obviously this presented a limitation to the luminosity of the best-fit and a free parameter by which each model AGN SED could be

multiplied, mf_{agn} was introduced, to synthesise SEDs for a range of luminosities covering a parameter space $10^{11}L_{\odot} < L_{AGN} < 10^{13}L_{\odot}$. As the AGN SEDs contribute substantially to the flux in the FIR this introduces another degeneracy as the starburst SEDs also contribute to the FIR flux, which could potentially lead to an under- or overestimation of the starburst component. The inclusion of the two multiplication factors determining the rate at which GMCs are forming stars at t_{sb}= 0, mf_{sb} and the luminosity of the AGN, mf_{agn} increases the number of possible SED combinations in the ULIRG SED Library by a factor of $\approx$ 100 with the result that the ULIRG SED Library is likely to be highly degenerate!

It was therefore decided to study this degeneracy and attempt to generate enough statistically significant data for each ULIRG that trends in values of e.g., the rate at which GMCs are forming stars at $t_{sb} = 0$, mf_{sb}, the time since the onset of star formation t_{sb}, or the associated value of the half-life τ could be obtained, thereby giving an indication of the appropriateness of the best-fit GEM SEDs for modelling each object. The data was generated by combining AGN and CSFRA SEDs in turn to produce a library of emergent ULIRG SEDs, each of which was tested against the samples' published data points and assessed using the reduced χ^2 goodness-of-fit criteria. Then, if the reduced χ^2 values are found to be e.g., scattered highly randomly in χ^2 space, as mf_{sb}, t_{sb} and τ change, it might indicate that the GEM SED achieving the absolute lowest reduced χ^2 for that object had a large *apparent* error associated with it. However, if the χ^2 values exhibited a more general trend in behaviour with varying mf_{sb}, t_{sb} and τ, perhaps a smaller apparent error, beyond that implied by e.g., the SED also achieving the lowest reduced χ^2 could be attached to the best-fit GEM SED. The assessment of this apparent error and the identification of the GEM SED most suitable for progression to analysis of each ULIRG, is carried out at the end of the next section.

7.2.1 Generation of the GEM ULIRG SED Library

This section begins by considering the reduced χ^2 test which is to be used as a measure of the goodness-of-fit of the model data points to the published ULIRG SEDs. Following this the free parameters associated with the problem and then the method by which the AGN and CSFRA SEDs are paired together to generate the ULIRG combined GEM SED Library is then illustrated.

χ^2 Goodness-of-Fit Test

Comparison of models with experimental data is a common technique in science and the reduced χ^2 test has been chosen for use in this thesis work. The value χ^2 is calculated from the square of the difference between the model data and the published data and weighted by the model data's errors (Barford 1967). Both FH03 and this work use the reduced χ^2 test, not only for comparative purposes, but also due to the small number of observational data points obtained for each object. If the published points are the actual values y_i and the model SED points are the ideal points em f(x_i)

$$\chi^2 = \sum_{i=1}^{m} \frac{[y_i - f(x_i)]^2}{\sigma_i^2} \tag{7.5}$$

where σ_i^2 is the expected error in the model SED values given by

$$\sigma_i^2 = \sum_i \frac{p_i^2}{n} \tag{7.6}$$

where n is the degrees of freedom and p_i^2 is the error relative to the published values and essentially sets a limit on how closely the model can fit the data. The error was set at 20%, based on uncertainties in the experimental data, such that $p_i^2 = 0.2y_i$. The number of degrees of freedom n, is found by subtracting the number of free parameters l, from twice the number of published data points m such that $n = 2m - l$. For example, Table 7.1 shows that 00262+4251 has $2m = 28$ whilst Table 7.3 shows that $l = 8$, so the number of degrees of freedom at which the χ^2 testing for 00262+4251 was carried out is $n = 20$.

The central concept of the χ^2 test is the acceptance or rejection of the null hypothesis. The null hypothesis is generally taken as the reverse of the result required and in this case states that the model SED points do *not* belong to the same population distribution function as the published data points. The χ^2 value calculated for each model is then used to determine the probability of that combined SED fit *not* occurring randomly using pre-determined critical values of the χ^2 distribution. For example, if a $\chi^2 = 1.36$ was determined at 8 degrees of freedom, interpolation of the critical probability values using a natural spline function finds that there is a probability of a non-random fit of 0.982 and so it could be said that that particular model SED combination has a $\approx$ 98% chance of belonging to the population distribution of the published points and a 2% chance that the fit was generated randomly - hence the fit is significant at the 2% level. Although the significance level chosen to indicate a good fit is largely subjective, many experimenters chose a level of between 1% and 5% (Barford 1967).

AGN Free Parameters	Symbol	Value Range	No. of Its. per Variable
UV Optical Depth	τ_{uv}	1000, 1250, 1500	3
Dust Temperature	T_{dust}	1000K, 1250K, 1500K	3
Viewing Angle	θ_v	$\pi \leq \theta_v \leq 90$	15
Luminosity Factor	mf_{agn}	$0.1 \leq mf_{agn} \leq 10$	40
Starburst Free Parameters	**Symbol**	**Value Range**	**No. of Its. per Variable**
Time since onset of Star Formation	t_{sb}	1-10Myrs at Δt = 1Myrs 20-80Myrs at Δt = 10Myrs	17
Global Star Formation activity Half-life	t_τ	0.5-10Myrs at Δt = 1Myrs 20-80Myrs at Δt = 10Myrs	18
Rate at which GMC's form Stars ($t_{sb} = 0$)	mf_{sb}	M_{GMC}=10^6-,10^7,10^8-,$10^9 M_\odot$ - See Table 6.5	$30/M_{GMC}$
GMC Cluster Mass ($M_{GMC}.\eta$)	$M_\star$	η=0.01,0.25,0.05,0.1,0.15,0.2,0.25	$7/M_{GMC}$

Table 7.3: The free parameters of the GEM ULIRG SED. The first column lists the free parameter and the second gives its identifying symbol. The third and fourth columns give the range of the values the variables can take and how many times each variable is iterated to complete its parameter space, respectively. The GMC central cluster mass $M_\star$ is a product of the GMC mass M_{GMC} and the star formation efficiency η

Number of Free Parameters

The iterative variables or free parameters in this problem are, for the AGN component: the optical depth at ultraviolet wavelengths τ_{uv}, the dust temperature T_{dust}, the viewing angle θ_v and the luminosity multiplier mf_{agn}. For the CSFRA starburst component the free parameters are the time since the onset of star formation t_{sb}, the global starburst activity half-life τ and the rate at which GMC's are forming stars at $t_{sb} = 0$, mf_{sb}. The mass of the GMC M_{GMC} and the efficiency with which stars are formed, η are related functions of each other via the equation $M_\star = M_{GMC}.\eta$ and so form a single free parameter. Each of these variables is listed in Table 7.3 for ease of reference.

With eight free parameters on the model grid another bespoke computer program was written to accomplish the generation of the combined ULIRG SED Library and this can now be discussed.

The Combined GEM ULIRG SED

Figure 7.1 is a colour coded flow-chart illustrating the procedure by which the AGN and CSFRA SEDs are combined together to generate the GEM ULIRG SED library for testing against the published data. The variables for the AGN element are shown on the flowchart by the series of green-toned boxes across the top of the page. Each variable box also contains in square brackets the number of values that variables takes in its parameter space i.e., T_{dust} [1-3] indicates that the AGN dust temperature T_{dust} can take three values; 1000K, 1250K & 1500K and therefore iterates three times. Similarly, the starburst SED variables are shown on the flowchart by the three lines of blue-toned boxes across the bottom of the page.

Each of these variable boxes has a Loop Number attached, indicated by L_i where i = 1-6. Across the right centre of the flowchart, a series of purple-toned ovals illustrate the data matching process and finally, the set of red-toned boxes in the centre left allow the loops and variables to be iterated.

Beginning then with the AGN loops, L_1 shows that the variable to iterate is the dust temperature T_{dust} and furthermore, that there are three iterations of that variable in the loop. So first a single SED is selected from the AGN library, e.g. T_{dust} = 1000K, τ_{uv} = 1000, θ_v=0° and the lowest value of the luminosity multiplier i.e., mf_{agn} = 0.1 is used to calibrate the flux in luminosity space. This SED is $F_v(AGN_1)$ - the AGN element of the combined ULIRG SED to be matched to the published data.

Remembering that testing is carried out for one M_{GMC} and η set at a time, a single CSFRA SED is also selected at e.g., $M_{GMC} = 10^7 M_\odot$, η = 0.1, t_{sb}=1Myrs and t_τ = 0.5Myrs. Then the lower limit of the rate at which GMCs are forming stars at t_{sb} = 0 for that M_{GMC}, mf_{sb}, is used to generate the CSFRA $F_v(SB_1)$ contribution to the ULIRG SED.

Moving to the purple-toned ovals running right to left across the centre of the flowchart, $F_v(AGN_1)$ is summed with $F_v(SB_1)$ to generate the combined GEM ULIRG SED $F_v(GEM_1)$. This GEM SED is then tested for goodness-of-fit against the published data for one ULIRG in the sample and the reduced χ^2 calculated and recorded. This first loop L_1 is then repeated 14 times for $0° < \theta_v < 90°$ whilst maintaining all other variables constant.

The second iteration of the T_{dust} loop is then carried out. The AGN SED for the first viewing angle θ_v=0° is selected at the next dust temperature e.g., T_{dust} =1250K, but the

values of $\tau_{uv} = 1000$ and $mf_{agn} = 0.1$ are kept constant. This new AGN SED, $F_v(AGN_2)$, is again summed with precisely the same CSFRA SED $F_v(SB_1)$ to give the GEM ULIRG SED $F_v(GEM_2)$ and the reduced χ^2 calculated and recorded.

In this way, AGN SEDs for all three values of T_{dust}, at all viewing angles, using a constant value for τ_{uv} and mf_{agn} have been paired with $F_v(SB_1)$ and tested against the published data. Having iterated T_{dust} the required number of times, the loop number iterates to L_2 meaning the optical depth changes to its second value $\tau_{uv} = 1500$ and the T_{dust} loop, L_1 is run again *in its entirety.* As τ_{uv} has three values on its parameter grid, L_2 is also repeated three times leading to a total of 9 runs at 15 viewing angles each, in exploring the AGN T_{dust} and τ_{uv} space.

The final AGN loop L_3 is that of the luminosity multiplier mf_{agn} which has 40 values in its parameter space. Once T_{dust} and τ_{uv} space has been tested, the luminosity multiplier increases to e.g. $mf_{agn} = 0.11$ and Loops L_1 and L_2 are re-run again *in their entirety.* Upon completion, the mf_{agn} variable increments and Loops L_1 and L_2 are again repeated, until all 40 values of mf_{agn} have been tested.

Completing the iterations for mf_{agn} means that *each* AGN SED $F_v(AGN_n)$ in the library has been paired with the *same* CSFRA SED $F_v(SB_1)$, the combined GEM ULIRG SEDs $F_v(GEM_n)$ matched to the published data and the reduced χ^2 for each calculated and recorded. However, this represents the results for testing only *one* CSFRA SED at a single value of t_{sb}, τ and mf_{sb}. The next step is to therefore iterate the starburst variables.

Loop L_4 is the first of the starburst loops, all of which are indicated by the blue-toned boxes on the bottom right of the flowchart. The L_4 variable is the time since the onset of star formation t_{sb} and whilst keeping τ and mf_{sb} constant as for $F_v(SB_1)$, t_{sb} takes its second value, $t_{sb} = 2$Myrs and CSFRA SED $F_v(SB_2)$ is generated. Having iterated the CSFRA SED by one, *each* of the AGN Loops discussed previously is re-run i.e., L_1 ; L_2,L_1 ; L_3,L_2,L_1, and the χ^2 of the resulting GEM ULIRG SEDs $F_v(GEM_n)$, recorded.

This process of iterating the starburst age, Loop L_4 and then re-running all three AGN loops, repeats for all 17 possible values of t_{sb}. This procedure results in *all* AGN SEDs being matched to $\approx$ 17 of the CSFRA SED, with each of those CSFRA SEDs still having the *same* value of τ, mf_{sb}, M_{GMC} and η.

Loop L_5 now engages, which iterates the half-life variable τ, which has 18 values in its parameter space. Once τ has risen by one, *all* previous loops are re-run, including that for t_{sb}. At the completion of the τ Loop L_5, *every* AGN SED has been paired with *every*

CSFRA SED for a *single* value of mf_{sb}; the rate at which GMCs are forming stars at t_{sb} = 0. This completes one *cycle of the program.*

Loop L_6 for mf_{sb} then iterates by one value and *every* loop run so far is re-run. Once Loop L_6 has completed its iterations and mf_{sb} has been tested at all 30 values, *every* AGN SED has been paired with *every* CSFRA SED available at a *single* M_{GMC} and a *single* star formation efficiency η and tested against the published data for one ULIRG.

Looking at the the red-toned boxes on the middle left of the flowchart in Figure 7.1 the star formation efficiency now rises by one to e.g., $\eta = 0.025$, $M_{GMC} = 10^7 M_\odot$ remains the same and *every loop* $L_1 \leq$ Loops No. $\leq L_6$ is re-run. Thus there are 30 cycles for each η in an M_{GMC}. Having completed each of the seven iterations of the variable η, the GMC mass M_{GMC} is then iterated by one and again *all* loops are re-run. Once the fourth iteration of M_{GMC} has ended, *every* possible ULIRG SED combination in the two AGN and CSFRA libraries has been tested against the published data for *one* ULIRG. As there are six ULIRGS in the object sample, the entire reduced χ^2 testing procedure detailed above is then repeated for each object.

Testing the GEM ULIRG SED Library against the published data required high end computing facilities and so the fitting program was run on the *Miracle* supercomputer, housed at University College London, which has been purposely designed to accommodate scientific problems of this nature.

7.2.2 Identification of the Best-fit

This section considers the results of the rigorous fitting of each ULIRG in the sample using the procedure outlined above. As mentioned, it was decided to collect a significant quantity of data for each object and in that way attempt to obtain an estimate of the appropriateness of the best-fit SED. As the data is collected for a single M_{GMC} and η at a time, the rate at which GMCs are forming stars at $t_{sb} = 0$, mf_{sb}, the time since the onset of star formation t_{sb} and the global star formation activity half-life τ are plotted in the next subsection against the reduced χ^2 achieved by the GEM SEDs when tested against the published data for the ULIRG sample. With eight free parameters in the modelled space, the number of degrees of freedom n in each model is high. Therefore it was decided to set the significance level at $\approx 5\%$, which generally equated to a reduced χ^2 of approximately 7, so the results for each object are truncated at this value of χ^2 to aid visual resolution of the data.

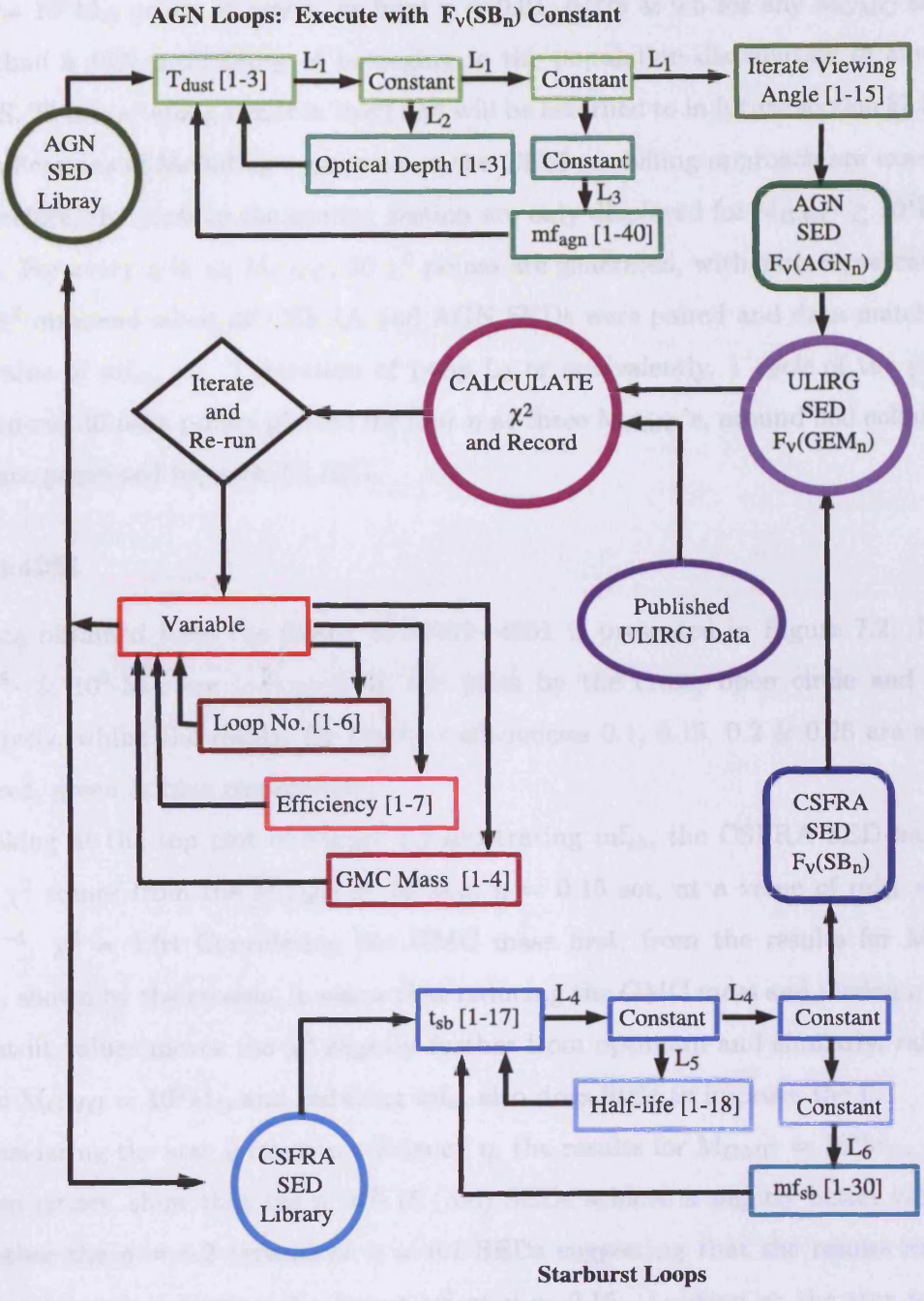

Figure 7.1: Flowchart illustration of the method by which the AGN and CSFRA are paired together to generate the combined GEM ULIRG SED, which is then tested against the published data for a ULIRG using the reduced χ^2 test as a measure of the goodness of fit.

During this ULIRG fitting it was found that no CSFRA SED originating from the $M_{GMC} = 10^6 M_\odot$ group at any η, or from $\eta = 0.01$, 0.025 & 0.5 for any M_{GMC} achieved better than a 40% probability of belonging to the population distribution of any of the ULIRGS. This is a telling result in itself and will be returned to in future section §7.5 where the ramifications of including supernova in the GEM modelling approach are examined.

Therefore, the plots in the coming section are only displayed for $M_{GMC} \geq 10^7 M_\odot$ and $\eta \geq 0.1$. For every η in an M_{GMC}, 30 χ^2 points are generated, with each representing the *lowest* χ^2 obtained when *all* CSFRA and AGN SEDs were paired and data matched at a *single* value of mf_{sb}, i.e., 1 iteration of Loop L_6 or equivalently, 1 *cycle* of the program. With around 30 data points plotted for four η at three M_{GMC}'s, around 360 colour-coded points are presented for each ULIRG.

00262+4251

The data obtained from the fitting of 00262+4251 is presented in Figure 7.2. M_{GMC}= 10^7-,10^8- & 10^9-$M_\odot$ are indicated on the plots by the cross, open circle and triangle respectively, whilst the results for the four efficiencies 0.1, 0.15, 0.2 & 0.25 are shown in black, red, green & blue respectively.

Looking at the top plot of Figure 7.2 illustrating mf_{sb}, the CSFRA SED having the lowest χ^2 comes from the $M_{GMC} = 10^8 M_\odot$, $\eta = 0.15$ set, at a value of mf_{sb} = 3.75 x $10^{-4} yr^{-1}$, χ^2 = 1.04 Considering the GMC mass first, from the results for $M_{GMC} = 10^7 M_\odot$, shown by the crosses, it seems that reducing the GMC mass and raising mf_{sb} from the best-fit values moves the χ^2 slightly further from optimum and similarly, raising the mass to $M_{GMC} = 10^9 M_\odot$ and reducing mf_{sb} also does little to improve the fit.

Considering the star formation efficiency η, the results for $M_{GMC} = 10^8 M_\odot$, given by the open circles, show that the $\eta = 0.15$ (red) SEDs achieve a slightly better value of χ^2 than either the $\eta = 0.2$ (green) or $\eta = 0.1$ SEDs suggesting that the results have been funnelled towards achieving the lowest χ^2 at $\eta = 0.15$. Looking at the star formation efficiencies for $M_{GMC} = 10^9 M_\odot$ given by the triangles across the bottom of the mf_{sb} plot, not only does the reduced χ^2 appear to improve as mf_{sb} rises within an η, but also as η itself rises from 0.1 to 0.2 yet no SED combination from any $M_{GMC} = 10^9 M_\odot$ efficiency improves on the $M_{GMC} = 10^8 M_\odot$, $\eta = 0.15$ results. Finally, looking at $M_{GMC} = 10^7 M_\odot$, given by the crosses, those for $\eta = 0.25$ (blue) & 0.2 (green) appear to plateau and then increase in χ^2 as mf_{sb} rises, but again the fits are not as good as some of those for M_{GMC}

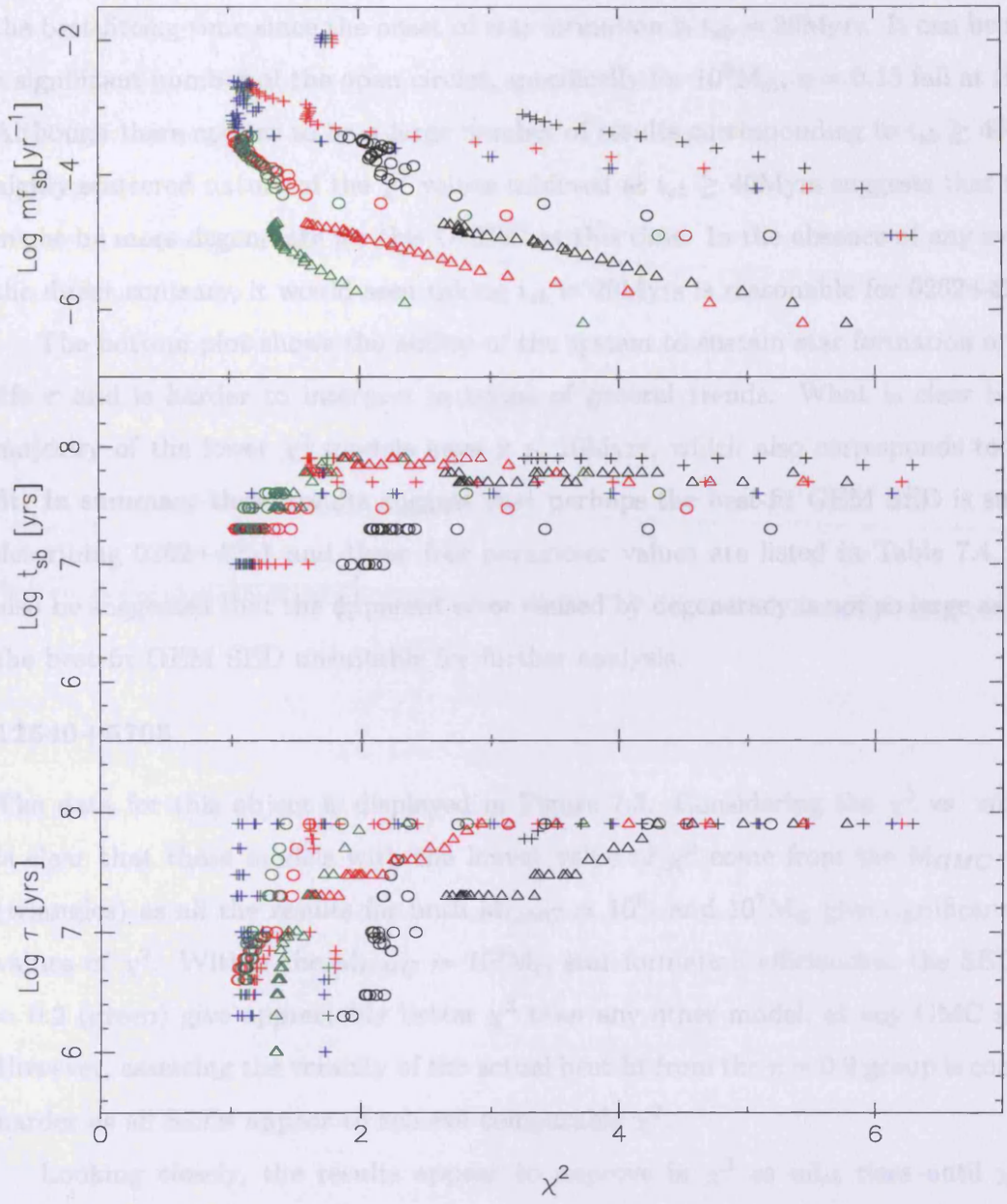

Figure 7.2: 00262+4251: The top plot gives the rate at which GMCs are forming stars at t_{sb} = 0, mf_{sb} vs. χ^2. M_{GMC}= 10^7-,10^8- & 10^9-$M_\odot$ are indicated by the cross, open circle and triangle and the results for the four efficiencies 0.1, 0.15, 0.2 & 0.25 are shown in black , red, green & blue respectively. The same colour and marker scheme is used for the middle and bottom plots which show the time since the onset of star formation t_{sb} vs. χ^2 and the starburst global star formation activity half-life τ vs. χ^2respectively

= $10^8 M_\odot$, $\eta = 0.15$. Therefore, it does not appear that increasing or decreasing M_{GMC}, η or mf_{sb} around those values which achieved the best-fit would improve the 0262+4251 fit.

Moving to the central plot of Figure 7.2 which shows the data in terms of χ^2 vs. t_{sb}, the best-fitting time since the onset of star formation is t_{sb} = 20Myrs. It can be seen that a significant number of the open circles, specifically for $10^8 M_\odot$, $\eta = 0.15$ fall at this value. Although there appear to be a large number of results corresponding to $t_{sb} \geq$ 40Myrs the highly scattered nature of the χ^2 values achieved at $t_{sb} \geq$ 40Myrs suggests that the SEDs might be more degenerate for this ULIRG at this time. In the absence of any evidence to the direct contrary, it would seen taking t_{sb} = 20Myrs is reasonable for 0262+4251.

The bottom plot shows the ability of the system to sustain star formation or the half-life τ and is harder to interpret in terms of general trends. What is clear is that the majority of the lower χ^2 models have $\tau \leq$ 10Myrs, which also corresponds to the best-fit. In summary these results suggest that perhaps the best-fit GEM SED is suitable for describing 0262+4251 and these free parameter values are listed in Table 7.4. It might also be suggested that the apparent error caused by degeneracy is not so large as to render the best-fit GEM SED unsuitable for further analysis.

12540+5708

The data for this object is displayed in Figure 7.3. Considering the χ^2 vs. mf_{sb} plot it is clear that those models with the lowest value of χ^2 come from the $M_{GMC} = 10^9 M_\odot$ (triangles) as all the results for both $M_{GMC} = 10^8$- and $10^7 M_\odot$ give significantly poorer values of χ^2. Within the $M_{GMC} = 10^9 M_\odot$ star formation efficiencies, the SEDs from η = 0.2 (green) give appreciably better χ^2 than any other model, at any GMC mass or η. However, assessing the veracity of the actual best-fit from the $\eta = 0.2$ group is considerably harder as all SEDs appear to achieve comparable χ^2.

Looking closely, the results appear to improve in χ^2 as mf_{sb} rises until χ^2 best is reached, whereupon raising mf_{sb} further pushes the χ^2 values marginally towards more unfavourable. As it would seem incontrovertible that the best-fit CSFRA SED comes from the set of $M_{GMC} = 10^9 M_\odot$, $\eta = 0.2$ SEDs, taking the value of $mf_{sb} = 1.5 \times 10^{-5} yr^{-1}$, which corresponds to the lowest χ^2 achieved of all models, appears appropriate.

Moving to the plot for t_{sb} although the largest number of data points, distributed across all η and M_{GMC}, converge on t_{sb} = 10Myrs, the average χ^2 achieved by these points is considerably higher than that achieved by the best fit. As the largest proportion

of $M_{GMC} = 10^9 M_\odot$, $\eta = 0.2$ SEDs appear to converge on t_{sb} = 20Myrs value, it seems reasonable to take this as the starburst age for 12540+5708.

Finally, the half-life τ, illustrated in the bottom plot, also does not appear to be definitive in trend, with the values scattered widely both in τ and χ^2 space. However, there does appear to be a slight funnelling effect of the χ^2 results towards τ = 10Myrs so in the absence of evidence to the contrary, this was taken as the global star forming activity half-life.

In summary then, for 12540+5708 the best-fit SED corresponds to $M_{GMC} = 10^9 M_\odot$, $\eta = 0.2$, $mf_{sb} = 1.5 \times 10^{-5} yr^{-1}$ with $\chi^2 = 0.79$. This best-fit GEM SED does therefore appear reasonable for 12540+5708, but what the plots have revealed is that whilst the best fit CSFRA SED is highly likely to have come from the $M_{GMC} = 10^9 M_\odot$, $\eta = 0.2$ SED set, the adopted values of mf_{sb}, t_{sb} and τ are subject to more considerable uncertainty.

13428+5608

The data for this object is displayed in Figure 7.4 and the best fit GEM SED comes again comes from the $10^9 M_\odot$ set of CSFRA SEDs. Considering the top χ^2 vs. mf_{sb} first, the results for $M_{GMC} = 10^7$-, 10^8- & $10^9 M_\odot$ indicated by the crosses, circles and triangles respectively, appear to each cluster in mf_{sb} quite strongly. However, clearly those results from $M_{GMC} = 10^9 M_\odot$ are an improvement on those of both $M_{GMC} = 10^7$ & $10^8 M_\odot$. The general trend in behaviour appears to be that as the value of mf_{sb} drops, the value of the giant molecular cloud M_{GMC} rises and the χ^2 achieved improves. It therefore seems reasonable that the best-fit SED for 13428+5608 does originate in the $M_{GMC} = 10^9 M_\odot$ set of SEDs.

Looking at the star formation efficiency, for $M_{GMC} = 10^7 M_\odot$ (crosses) the highest star formation efficiency at $\eta = 0.25$ (blue) achieves lower χ^2s than $\eta = 0.2$, which in turn achieves better results than $\eta = 0.15$. The points seem to exhibit a trend whereby as mf_{sb} rises, the χ^2s move towards and then reach a χ^2 best, but as mf_{sb} rises further the χ^2 again moves away from that χ^2 best, suggesting that even if the range of mf_{sb} values tested were to be extended it would not improve the fit. Similar behaviour is seen for the $M_{GMC} = 10^8 M_\odot$ ηs with the highest star formation efficiency SEDs achieving the best χ^2s. However, looking at $M_{GMC} = 10^9 M_\odot$ it appears that the best χ^2 results are achieved by $\eta = 0.15$ with both the results of $\eta = 0.1$ & 0.2 somewhat poorer. This is highly suggestive that the star formation efficiency appropriate to 13428+5608 is $\eta = 0.15$ at

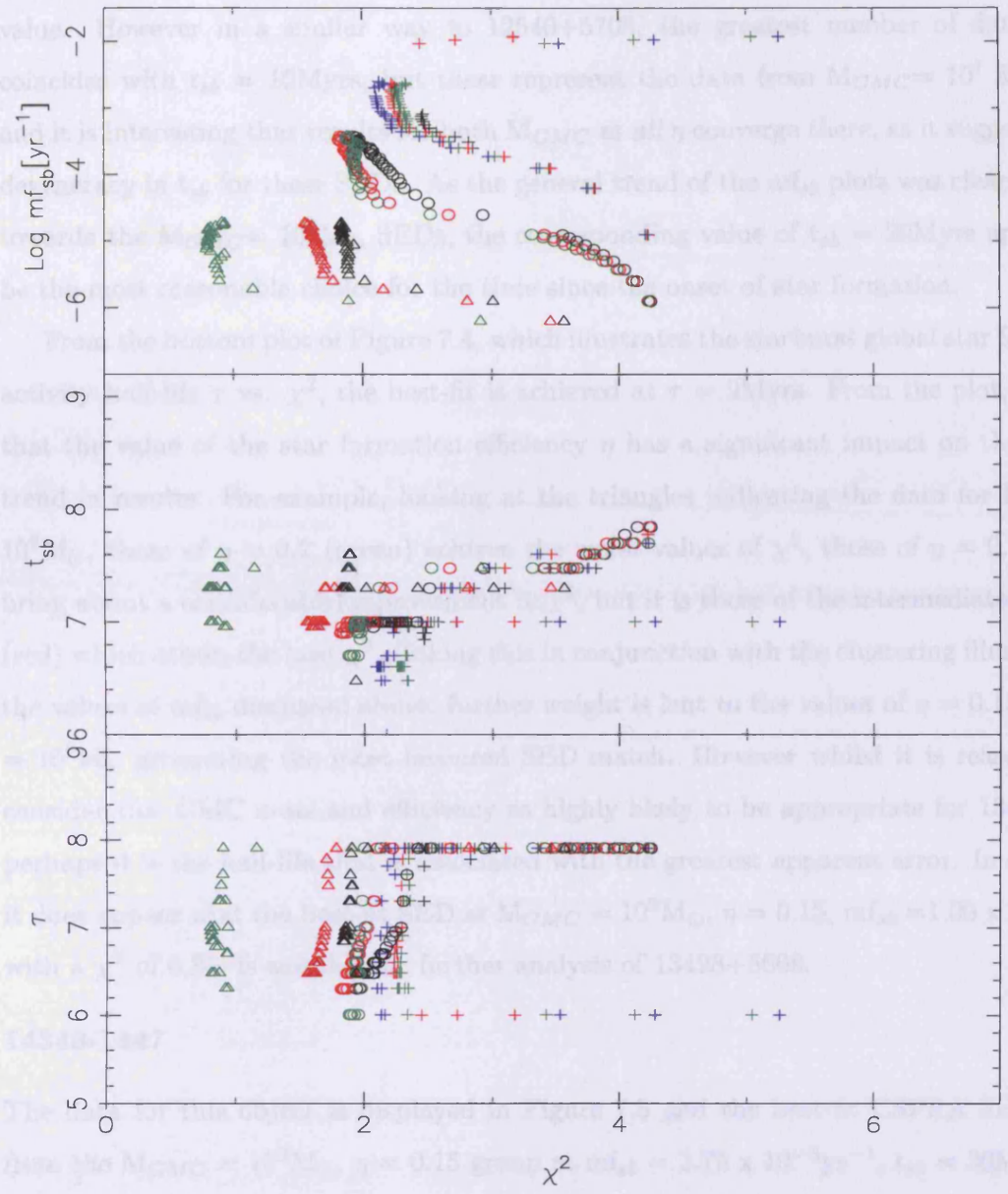

Figure 7.3: 12540+5708: The top plot gives the gives the rate at which GMCs are forming stars at $t_{sb} = 0$, mf_{sb} vs. χ^2. M_{GMC}= 10^7-,10^8- & 10^9-$M_\odot$ are indicated by the cross, open circle and triangle and the results for the four efficiencies 0.1, 0.15, 0.2 & 0.25 are shown in black , red, green & blue respectively. The same colour and marker scheme is used for the middle and bottom plots which show the time since the onset of star formation t_{sb} vs. χ^2 and the starburst global star formation activity half-life τ vs. χ^2 respectively

M_{GMC}= $10^8 M_\odot$.

Moving to the second plot in Figure 7.4 the best-fit CSFRA starburst age is t_{sb} = 20Myrs and a reasonable number of data points from M_{GMC}= $10^9 M_\odot$ converge on this value. However in a similar way to 12540+5708, the greatest number of data points coincides with t_{sb} = 10Myrs, but these represent the data from M_{GMC}= 10^7 & $10^8 M_\odot$ and it is interesting that results for both M_{GMC} at *all* η converge there, as it suggests some degeneracy in t_{sb} for these SEDs. As the general trend of the mf_{sb} plots was clearly biased towards the M_{GMC}= $10^9 M_\odot$ SEDs, the corresponding value of t_{sb} = 20Myrs appears to be the most reasonable choice for the time since the onset of star formation.

From the bottom plot of Figure 7.4, which illustrates the starburst global star formation activity half-life τ vs. χ^2, the best-fit is achieved at τ = 9Myrs. From the plot, it seems that the value of the star formation efficiency η has a significant impact on the general trend in results. For example, looking at the triangles indicating the data for M_{GMC} = $10^9 M_\odot$, those of η = 0.2 (green) achieve the worst values of χ^2, those of η = 0.1 (black) bring about a considerable improvement in χ^2, but it is those of the intermediate η = 0.15 (red) which attain the best χ^2. Taking this in conjunction with the clustering illustrated in the values of mf_{sb} discussed above, further weight is lent to the values of η = 0.15, M_{GMC} = $10^9 M_\odot$ generating the most favoured SED match. However whilst it is reasonable to consider this GMC mass and efficiency as highly likely to be appropriate for 13428+560, perhaps it is the half-life that is associated with the greatest apparent error. In summary it does appear that the best-fit SED at M_{GMC} = $10^9 M_\odot$, η = 0.15, mf_{sb} =1.00 x $10^{-5} yr^{-1}$ with a χ^2 of 0.80, is suitable for further analysis of 13428+5608.

14348-1447

The data for this object is displayed in Figure 7.5 and the best-fit CSFRA SED comes from the M_{GMC} = $10^9 M_\odot$, η = 0.15 group at mf_{sb} = 3.75 x $10^{-6} yr^{-1}$, t_{sb} = 30Myrs, τ = 50Myrs and χ^2 = 1.38. Considering the mass of the GMC first, these distributions show very similar attributes to the equivalent plot for 13428+5608 with the results for M_{GMC} = $10^7 M_\odot$ being worse than those for M_{GMC} = $10^8 M_\odot$, which in turn are poorer than those for M_{GMC} = $10^9 M_\odot$. The general trend appears to be therefore, that as mf_{sb} drops and M_{GMC} rises, χ^2 improves. This is suggestive that the most appropriate GMC mass for 14348-1447 is M_{GMC} = $10^9 M_\odot$ and that increasing the range of mf_{sb} tested would not necessarily achieve a better χ^2.

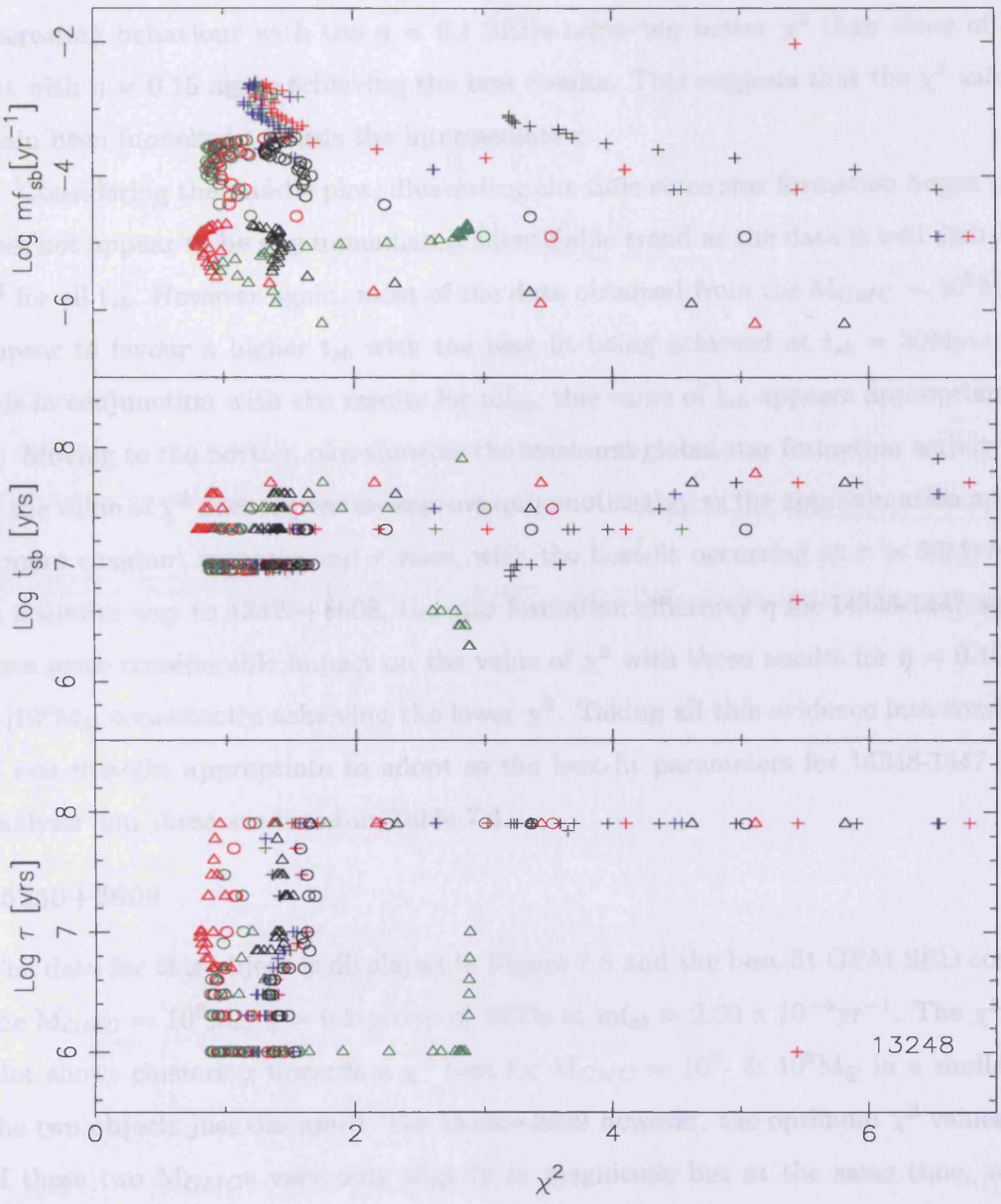

Figure 7.4: 13428+5608: The top plot gives the rate at which GMCs are forming stars at t_{sb} = 0, mf_{sb} vs. χ^2. M_{GMC}= 10^7-,10^8- & 10^9-$M_\odot$ are indicated by the cross, open circle and triangle and the results for the four efficiencies 0.1, 0.15, 0.2 & 0.25 are shown in black , red, green & blue respectively. The same colour and marker scheme is used for the middle and bottom plots which show the time since the onset of star formation t_{sb} vs. χ^2 and the starburst global star formation activity half-life τ vs. χ^2 respectively

Looking at the star formation efficiency, the same behaviour seen for 13428+5608 is again duplicated with the values of χ^2 best achieved by each η within the $M_{GMC} = 10^7$ & $10^8 M_\odot$ SEDs improving as η rises. However, the $M_{GMC} = 10^9 M_\odot$ SEDs show more interesting behaviour with the $\eta = 0.1$ SEDs achieving better χ^2 than those of $\eta = 0.2$ but with $\eta = 0.15$ again achieving the best results. This suggests that the χ^2 values have again been funnelled towards the intermediate η.

Considering the middle plot, illustrating the time since star formation began t_{sb}, there does not appear to be any immediately identifiable trend as the data is well distributed in χ^2 for all t_{sb}. However again, most of the data obtained from the $M_{GMC} = 10^9 M_\odot$ group appear to favour a higher t_{sb} with the best fit being achieved at $t_{sb} = 30$Myrs. Taking this in conjunction with the results for mf_{sb}, this value of t_{sb} appears appropriate.

Moving to the bottom plot showing the starburst global star formation activity half-life τ, the value of χ^2 does appear to improve quite noticeably as the approximation approaches a more constant scenario and τ rises, with the best-fit occurring at $\tau = 50$Myrs. Again in a similar way to 13428+5608, the star formation efficiency η for 14348-1447 appears to have some considerable impact on the value of χ^2 with those results for $\eta = 0.15$, $M_{GMC} = 10^9 M_\odot$ consistently achieving the lower χ^2. Taking all this evidence into consideration it was thought appropriate to adopt as the best-fit parameters for 14348-1447 in future analysis and these are listed in Table 7.4.

15250+3609

The data for this object is displayed in Figure 7.6 and the best-fit GEM SED comes from the $M_{GMC} = 10^8 M_\odot$ $\eta = 0.2$ group of SEDs at $mf_{sb} = 2.00 \times 10^{-4} yr^{-1}$. The χ^2 vs. mf_{sb} plot shows clustering towards a χ^2 best for $M_{GMC} = 10^7$- & $10^8 M_\odot$ in a similar way to the two objects just discussed. For 15250+3609 however, the optimum χ^2 values for each of these two M_{GMC}s vary only slightly in magnitude but at the same time, vary quite significantly in the corresponding value of mf_{sb}. The more scattered nature of the $M_{GMC} = 10^9 M_\odot$ results perhaps indicate that the most appropriate fit does not originate in that group. It is the $M_{GMC} = 10^8 M_\odot$ results which marginally achieve the very best χ^2 of all the results and as a large number of the data points from the $M_{GMC} = 10^8 M_\odot$ do appear to converge on a similar value of mf_{sb}, using $M_{GMC} = 10^8 M_\odot$ as the originating instantaneous burst GMC mass for 15250+360 seems reasonable, although the result does appear to have a reasonably large apparent associated error.

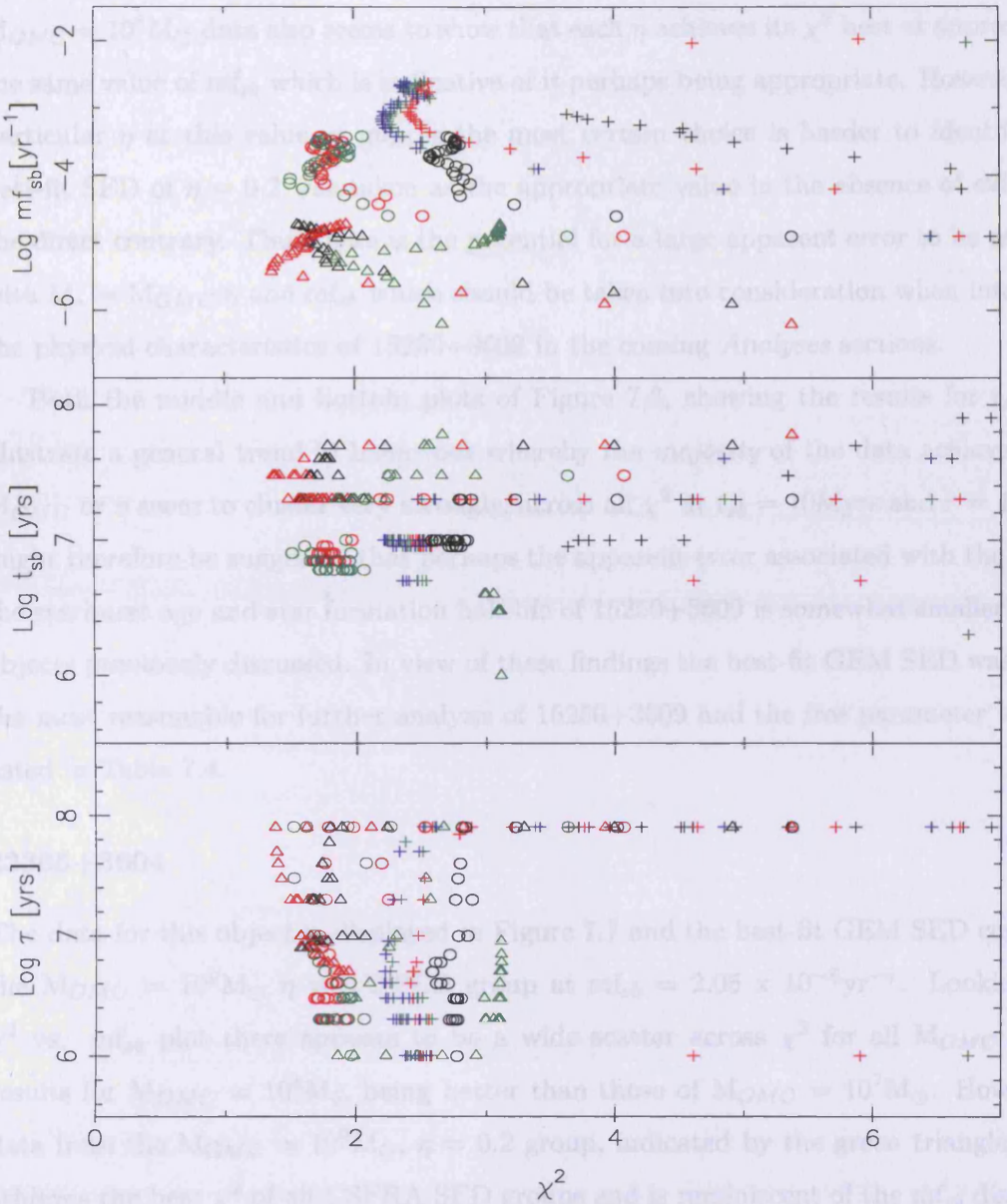

Figure 7.5: 14348-1447: The top plot gives the rate at which GMCs are forming stars at t_{sb} = 0, mf_{sb} vs. χ^2. M_{GMC}= 10^7-,10^8- & 10^9-$M_\odot$ are indicated by the cross, open circle and triangle and the results for the four efficiencies 0.1, 0.15, 0.2 & 0.25 are shown in black , red, green & blue respectively. The same colour and marker scheme is used for the middle and bottom plots which show the time since the onset of star formation t_{sb} vs. χ^2 and the starburst global star formation activity half-life τ vs. χ^2 respectively

Considering the star formation efficiency for $M_{GMC} = 10^8 M_\odot$ the behaviour of approaching a χ^2 best as mf_{sb} rises and then moving further from this optimum as mf_{sb} continues to rise (or vice versa), is again exhibited by all three $\eta = 0.1$, 0.15 & 0.2. The $M_{GMC} = 10^8 M_\odot$ data also seems to show that each η achieves its χ^2 best at approximately the same value of mf_{sb} which is indicative of it perhaps being appropriate. However, which particular η at this value of mf_{sb} is the most certain choice is harder to identify so the best-fit SED of $\eta = 0.2$ was taken as the appropriate value in the absence of evidence to the direct contrary. Thus there is the potential for a large apparent error to be associated with $M_\star = M_{GMC} \cdot \eta$ and mf_{sb} which should be taken into consideration when interpreting the physical characteristics of 15250+3609 in the coming *Analyses* sections.

Both the middle and bottom plots of Figure 7.6, showing the results for t_{sb} and τ, illustrate a general trend in behaviour whereby the *majority* of the data achieved at any M_{GMC} or η seem to cluster very strongly, across all χ^2 at $t_{sb} = 10$Myrs and $\tau = 1$Myrs. It might therefore be suggested that perhaps the apparent error associated with the values of the starburst age and star formation half-life of 15250+3609 is somewhat smaller than the objects previously discussed. In view of these findings the best-fit GEM SED was perhaps the most reasonable for further analysis of 15250+3609 and the free parameter values are listed in Table 7.4.

23365+3604

The data for this object is displayed in Figure 7.7 and the best-fit GEM SED comes from the $M_{GMC} = 10^9 M_\odot$ $\eta = 0.2$ SED group at $mf_{sb} = 2.05 \times 10^{-6} yr^{-1}$. Looking at the χ^2 vs. mf_{sb} plot there appears to be a wide scatter across χ^2 for all M_{GMC} with the results for $M_{GMC} = 10^8 M_\odot$ being better than those of $M_{GMC} = 10^7 M_\odot$. However, the data from the $M_{GMC} = 10^9 M_\odot$, $\eta = 0.2$ group, indicated by the green triangles, clearly achieves the best χ^2 of all CSFRA SED groups and is reminiscent of the mf_{sb} distribution in χ^2 of 00262+4251. It would therefore appear that whilst is it fairly certain that the best-fit SED appropriate to 23365+3604 does indeed come from the $M_{GMC} = 10^9 M_\odot$ $\eta = 0.2$ instantaneous burst SED group, it is harder to say which exact value of mf_{sb} has the smallest apparent associated error. Thus, in the absence of indicators to the contrary, the mf_{sb} of the SED combination which achieved the lowest χ^2 was taken as the relevant value for the rate at which GMCs were forming stars at $t_{sb} = 0$.

Moving to the plots of t_{sb} and τ, it does appear that most of the data in both plots

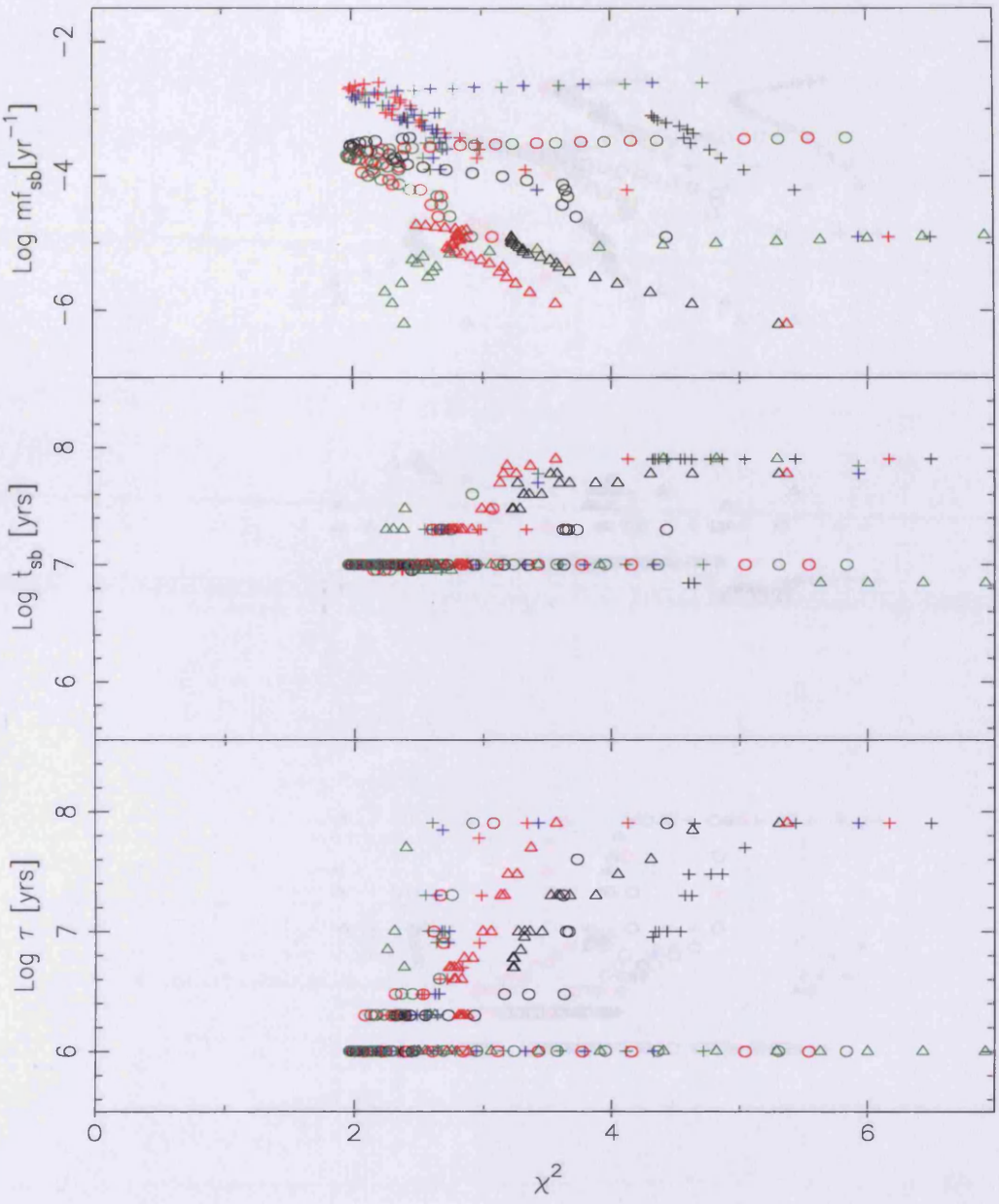

Figure 7.6: 15250+3609: The top plot gives the rate at which GMCs are forming stars at t_{sb} = 0, mf_{sb} vs. χ^2. M_{GMC}= 10^7-,10^8- & 10^9-$M_\odot$ are indicated by the cross, open circle and triangle and the results for the four efficiencies 0.1, 0.15, 0.2 & 0.25 are shown in black , red, green & blue respectively. The same colour and marker scheme is used for the middle and bottom plots which show the time since the onset of star formation t_{sb} vs. χ^2 and the starburst global star formation activity half-life τ vs. χ^2 respectively

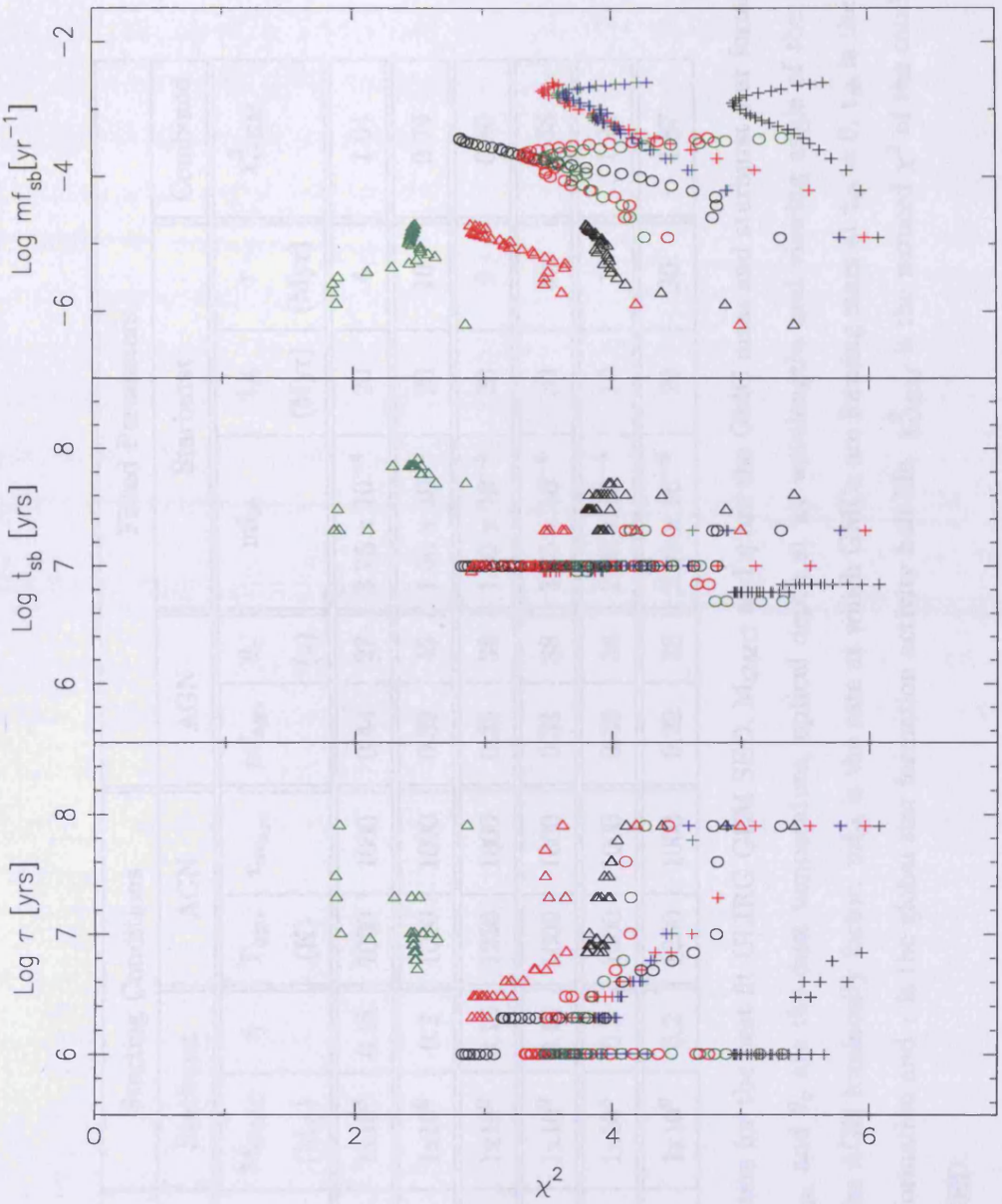

Figure 7.7: 23365+3604: The top plot gives the rate at which GMCs are forming stars at $t_{sb} = 0$, mf_{sb} vs. χ^2. M_{GMC}= 10^7-,10^8- & 10^9-$M_\odot$ are indicated by the cross, open circle and triangle and the results for the four efficiencies 0.1, 0.15, 0.2 & 0.25 are shown in black , red, green & blue respectively. The same colour and marker scheme is used for the middle and bottom plots which show the time since the onset of star formation t_{sb} vs. χ^2 and the starburst global star formation activity half-life τ vs. χ^2 respectively

	Starting Conditions				Fitted Parameters					
	Starburst		AGN		AGN		Starburst			Combined
ULIRG NAME	M_{GMC} ($M_\odot$)	η	T_{agn} (K)	$\tau_{uv_{agn}}$	mf_{agn}	θ_v (o)	mf_{sb}	t_{sb} (Myr)	τ (Myr)	χ^2_{GEM}
00262+4251	$1x10^8$	0.15	1000	1000	0.44	27	3.75×10^{-4}	20	4	1.04
12540+5708	$1x10^9$	0.2	1000	1000	0.39	49	1.50×10^{-5}	20	10	0.79
13428+5608	$1x10^9$	0.15	1250	1000	0.35	38	1.00×10^{-5}	20	9	0.80
14348-1447	$1x10^9$	0.15	1000	1000	0.31	38	3.75×10^{-6}	30	50	1.38
15250+3609	$1x10^8$	0.2	1000	1000	0.39	38	2.00×10^{-4}	10	1	1.96
23365+3604	$1x10^9$	0.2	1250	1000	0.22	38	2.05×10^{-6}	20	30	1.87

Table 7.4: Free parameters for the best-fit ULIRG GEM SED. M_{GMC} and η are the GMC mass and starburst star formation efficiency. T_{agn}(K), τ_{agn} and θ_v are the dust temperature, optical depth at uv wavelengths and viewing angle of the AGN model, whilst $mf_{agn}$is the AGN luminosity factor. mf_{sb} is the rate at which GMCs are forming stars at $t_{sb} = 0$, t_{sb} is the time since the onset of star formation and τ is the global star formation activity half-life. χ^2_{GEM} is the reduced χ^2 of the combined best-fit ULIRG GEM SED.

converges around lower values of these two free parameters than those achieved by the best-fir CSFRA SED, at t_{sb} = 20Myrs and τ = 30Myrs. However, in the final analysis the considerable improvement in the χ^2 achieved by the $M_{GMC} = 10^9 M_\odot$, $\eta = 0.2$ group, over any other result, indicates that this is perhaps the most appropriate for 23365+3604 and the corresponding free parameters are listed in Table 7.4. However a caveat must be added that there is the potential for a considerable apparent error associated with the values adopted for the time since the onset of star formation and the star formation half-life.

The most appropriate best-fit GEM SED for the ULIRG sample has now been established and an estimate made of the apparent error due to degeneracy for each. It was found that the best-fit GEM SEDs were on the whole suitable for progression to further analysis of the ULIRG sample. Looking at Table 7.4 what is immediately obvious is that these best-fit GEM SEDs have been skewed firmly towards *high* η and GMC mass. As mentioned in Chapter 5, each of the high η models show essentially the same behaviour in optical depth with the extinction plummeting to very low values ($Av^{TOT}(t) < 0.1$) early in a systems life-time and remaining there for some considerable time, until a small recovery in the extinction is seen as the supershell dust begins to contribute at large radii. This issue of results biased towards *high* η and M_{GMC} will be returned to in some depth in future section *Analysis III*, where the affect of including powerful supernova in the modelling is discussed.

7.3 Analysis I

It is now possible to discuss extraction of some of the ULIRG physical characteristics from the best-fit GEM SEDs. Comparing these values to those of FH03 and others published in the literature might give further indication of both the degeneracy issues and the suitability of the best-fit GEM SEDs for predicting ULIRG characteristics.

The section begins with derivation of the luminosity of the fractional CSFRA and AGN SEDs, along with the total luminosity of the fitted ULIRG. Following this, the prescription of Rowan-Robinson *et al.* (1997) and the Kennicutt Star Formation Law (Kennicutt 1998) are discussed to show how the observed star formation rate can be obtained from the 60μm luminosity and integrated FIR luminosity of the best-fit CSFRA SED respectively. Finally a brief synopsis of the Sanders *et al.* (1988) evolutionary model for ULIRGs is

given so that the merger and interaction state might be interpreted in the data.

The next subsection considers these results and the values taken by the CSFRA free parameters of the best-fit GEM SEDs, in light of what has already been published by e.g., FH03 and others, for the ULIRG sample. For example, the fractional luminosity contribution from the AGN and CSFRA model SEDs to the best-fit GEM SED can give insight into the dominant heating source. The time since the onset of star formation t_{sb} and the half-life of star formation activity τ can also be seen in terms of the dynamics of fuelling of star formation and give indications of whether a constant, burst or more intermediate scenario is more appropriate.

7.3.1 ULIRG Physical Characteristics I

SED Component Luminosity

The best-fit GEM SED for each ULIRG is the sum of the model AGN SED and model CSFRA starburst SED which matched the published data best. The luminosity can be found for each of these SED elements separately using

$$L_i = 4\pi R2_i^2 \int F_{i_\lambda} d\lambda \tag{7.7}$$

where the subscript i refers to either the AGN, CSFRA or best-fit GEM SED and R2 is the outer radius of the system; $R2_W$, $R2_{SN}$ and $R2_{AGN}$ for the HII region, supernova and AGN solutions respectively.

Star Formation Rate Estimation

There are several methods of estimating the SFR in galaxies, including using the UV continuum, the radio continuum or forbidden lines. However, the most relevant here is via IR continuum measurements, based on the assumption that enshrouding dust absorbs all the optical/UV continuum from the hot young stars and re-radiates it in the IR. Calibrations for converting IR luminosities to star formation rates, or bolometric corrections, have been published by several authors using different assumptions about the star formation time scale (e.g., Hunter, Gillett, Gallagher, Rice & Low 1986; Meurer, Heckman, Lehnert, Leitherer & Lowenthal 1997). FH03 however, used the prescription of Rowan-Robinson *et al.* (1997) which was derived from observations of 13 *Hubble Deep Field Galaxies* (Madau *et al.* 1996) and so this method will be employed in the thesis work. Additionally, Kennicutt (1998) developed a commonly used star formation rate correction derived by applying

the models of Leitherer & Heckman (1995) and a Salpeter IMF and this too provides good comparative material.

Star Formation Rate from CSFRA SED 60μm Luminosity

The prescription developed by Rowan-Robinson *et al.* (1997) uses the 60μm starburst luminosity

$$SFR_{RR}^{GEM} = 2.6\text{x}10^{-10}\frac{\phi}{\epsilon}\frac{L_{60}}{L_{\odot}}(M_{\odot}yr^{-1}) \tag{7.8}$$

where ϵ is the fraction of optical/UV light from the starburst that is absorbed by dust and re-emitted in the IR, assumed to be $\epsilon = 1$, L_{60} is the 60μm luminosity of the CSFRA SED element of the best-fit GEM SED and the factor ϕ incorporates a correction for the initial mass function (ϕ=1) (FH03).

Star Formation Rate from CSFRA SED Integrated FIR Luminosity

The Kennicutt Global Schmidt Star Formation Rate Law finds the bolometric correction to the FIR luminosity to be

$$SFR_{KL}^{GEM} = 4.5\text{x}10^{-44}L_{FIR}(M_{\odot}yr^{-1}) \tag{7.9}$$

where L_{FIR}(erg s^{-1}) is the IR luminosity integrated over the mid- and far-IR spectrum of the CSFRA SED element of the best-fit GEM SED, across the wavelength regime 8-1000μm (Kennicutt 1998) which was found using Equation 7.7 above with R2 = $R2_{SN}$ and the trapezium rule.

What is interesting to note from both Equation 7.9 and 7.8 is that neither include flux at short wavelengths in their estimation of the SFR, as each presume that the dust is reprocessing *all* the UV radiation emitted by e.g., the O, B and Wolf-Rayet stars in the stellar association.

Merger and Interaction State

Turning now to the connection between the merger and interaction state of the ULIRG and the time since the onset of star formation, or equivalently the starburst age t_{sb}, the global star formation activity half-life τ and the AGN and CSFRA fractional luminosities obtained from the best-fit GEM SEDs.

Perhaps one of the most pre-eminent evolutionary models for luminous infrared galaxies is that proposed by Sanders *et al.* (1988) [hereafter S88]. Using optical, IR and millimetre-wave observations of a sample of ten ULIRGs selected from the IRAS Bright Galaxy Survey, Sanders *et al.* (1988) were able to conclude that all ten were ongoing interactions between two spiral galaxies and what is more, each was powered by a combination of AGN and starburst activity. The objects were found to contain significant quantities of molecular gas and dust ($5 \times 10^9 M_\odot < M_{H_2} < 2 \times 10^{10} M_\odot$) and coupling this with the comparable space density of ULIRGs and Quasi-Stellar Objects (QSOs) in the local Universe ($z \leq 1$), S88 suggested that ULIRGs were perhaps the dust enshrouded precursors of optically selected QSOs (S88).

In this scenario, interactions between two molecular gas-rich spirals transport large quantities of gas to the central regions of a galaxy (S88). The concentration of clouds in the merger nucleus and an increased star formation efficiency due to cloud-cloud collisions initiates bursts of nuclear star formation activity *before* the merger of the two nuclei (S88). As the merger progresses, the nuclear starburst begins to subside and self gravity may then play a crucial role in the subsequent evolution of the nuclear disk and the possible feeding of a central AGN (S88). At this stage, the S88 observations indicated that the AGN contributes, perhaps dominantly, to the infrared luminosity, especially if both merger progenitors previously contained an AGN (S88). Eventually, the combined pressure of supernovae explosions and stellar winds etc. disrupt the gas and push away enough material to open up a hole along a line of sight to the AGN and the SED changes from exhibiting an excess in the infrared to an excess at optical and UV wavelengths; commensurate with a QSO (S88).

In this scenario, the starburst age t_{sb} gives an indication of when the galaxy merger was initiated, whilst the value for the star formation activity half-life τ, might be seen in terms of decay in the number of GMCs joining the starbursting ensemble and hence fuelling of star formation and transport of gas within the merger. The fractional contributions of the starburst or AGN SEDs to the GEM SED might also be used to imply the dominant heating or power source in the merger, and often the potential evolutionary state of the ULIRG at the time of observation.

Finally, referring back to §6.1.2 Equation 6.7 for the number of clouds *joining* the starbursting ensemble in a time bin $N_{GMC}(t')\Delta t$, can now be seen as physically representing the number of GMCs *within which star formation is initiated* via e.g., cloud-cloud collision,

in a time bin. Essentially, at $t_{sb} = 0$, only mf_{sb} GMCs exhibit star formation and then, as the merger progresses, more of the molecular GMC's in the two spiral progenitors are excited into star formation, meaning the absolute number of GMCs which have formed stars increases with time. This leads to expression 6.7 for the number of GMCs *joining* the ensemble per time bin Δt and Equation 6.6 for $N_{GMC}^{TOT}(t_{sb})$, the total number of GMCs forming stars with efficiency η to have joined the starbursting ensemble since the merger was initiated.

Summary of Physical Characteristics I

In the coming sections, first the general consensus in the literature regarding the physical characteristics of each ULIRG will be briefly discussed. Then the luminosity contributions from the AGN and the CSFRA SEDs to the best-fit GEM ULIRG SED will be compared to those of FH03 and the behaviour of the GEM SED discussed. These results and those obtained for the starburst age t_{sb} and the global star formation activity half-life τ will then be evaluated in terms of the dominant heating source and the merger and interaction state of the galaxy. Finally, the GEM SFRs derived above will be compared to those published by FH03 for the same ULIRG and a brief conclusion drawn on the appropriateness of each best-fit GEM SED. For easy reference the quantities to be tested, compared and assessed in this section are:

- L_{AGN}^{GEM}, L_{SB}^{GEM} & L_{TOT}^{GEM} are the log to the base ten of the luminosity of the best fitting AGN SED, constant star formation approximation SED and combined GEM SEDs respectively, in solar units.
- L_{AGN}^{FH03}, L_{SB}^{FH03} & L_{TOT}^{FHO3} are the log of to the base ten of those luminosity elements above, published by Farrah *et al.* (2003).
- SFR_{KL}^{GEM} is the SFR obtained from the CSFRA element of the best-fit GEM SED integrated 8-1000μm Luminosity using the prescription of Kennicutt (1998), via Equation 7.9
- SFR_{RR}^{GEM} indicates the SFR obtained from the CSFRA element of the best-fit GEM SED 60μm Luminosity, via the method of Rowan-Robinson *et al.* (1997) given in Equation 7.8.

- SFR_{RR}^{FH} gives the SFR published by FH03 and obtained using his best-fitting HII region element SED 60μm luminosity, along with the method of Rowan-Robinson *et al.* (1997) described in Equation 7.8.

- t_{sb} and τ are the age of the starbursting ensemble and the global star formation activity half-life respectively. t_{sb}^{FH} is the starburst age derived and published by FH03

7.3.2 ULIRG Sample Discussion I

Figures 7.8 and 7.9 display the best-fit GEM SEDs identified for each ULIRG and Table 7.5 gives the corresponding fractional luminosity contributions and the total luminosity along with the calculated reduced χ^2_{GEM}. This table also gives the equivalent luminosity and reduced χ^2_{FH} values from FH03.

Table 7.6 repeats the time since the onset of star formation t_{sb} and the global star formation activity half-life τ for easy reference. Also given are the two values for the SFR obtained from the CSFRA element of the best-fit GEM SED and the result from FH03. It is convenient to drop the prefix *best-fit* from the term 'best-fit GEM SED' as this can now be implicitly presumed.

00262+4251

This is the most distant object in the sample having a redshift z = 0.0927. The values of mf_{sb}, t_{sb} and τ obtained for the GEM SED were found to be reasonably secure when the reduced χ^2 results for this object were analyzed, with the largest apparent error being attached to the global star formation activity half-life τ.

Several authors have suggested that 00262+4251 might be classified in the evolutionary model of e.g., S88, as a remnant which had completed its merger. For example, Dasyra *et al.* (2006) used VLT observations to study the dynamical evolution of a sample of ULIRGS and determined from long-slit H and K band spectroscopy and stellar kinematics, that the nuclear separation was such that 00262+4251 was in post-coalescence (Dasyra *et al.* 2006). Downes & Solomon (1998) also used the IRAM interferometer CO mm-wave emission observations to yield a gas mass at the outer radius of the extended disc of M_{H_2} = 4 x $10^9 M_\odot$, from which they suggested that the merger was complete and that self-gravity was now playing a critical role in the evolution of the nuclear gas and the feeding of the

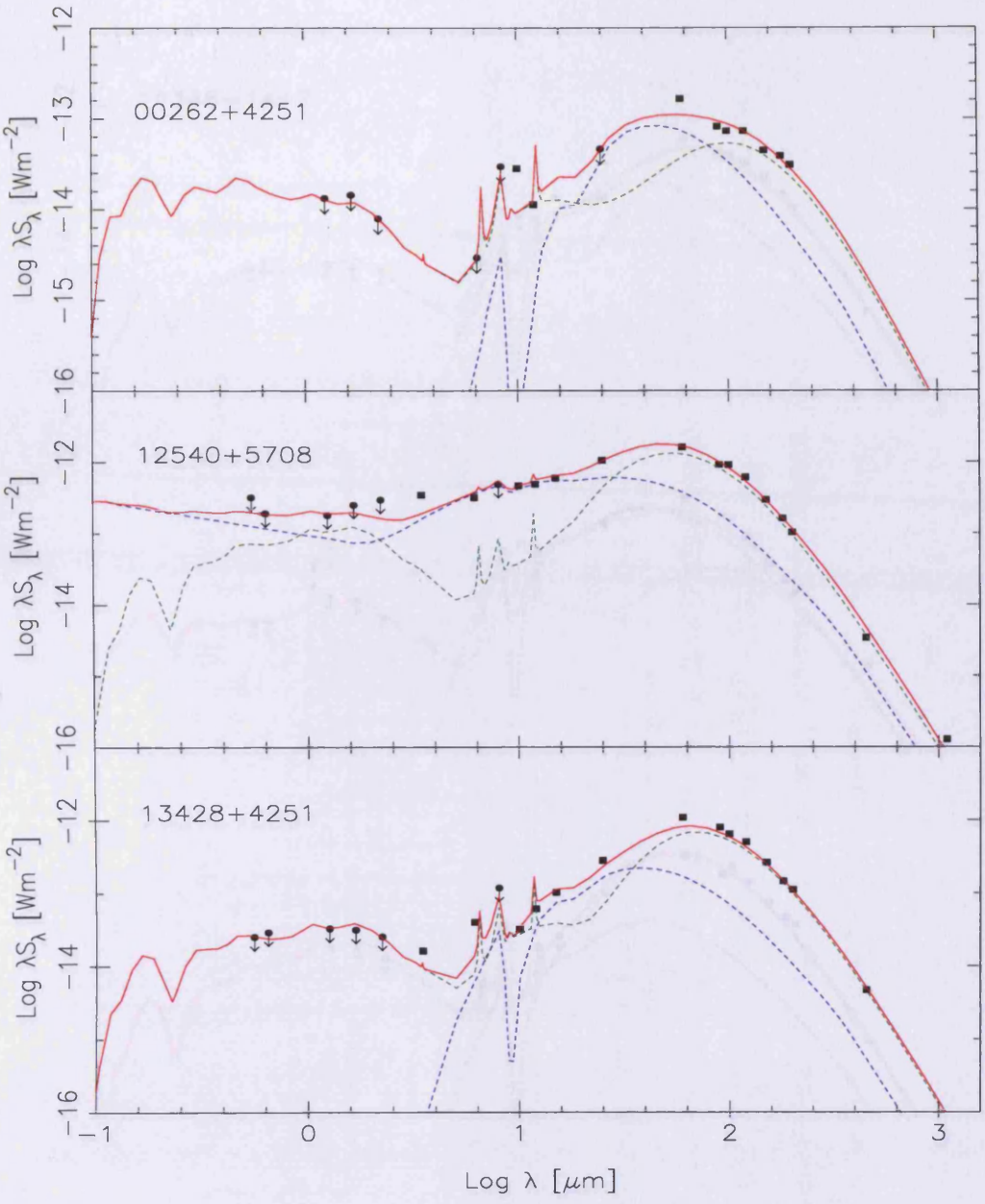

Figure 7.8: Best-Fit GEM SEDs for 00262+4251, 12540+5708 & 13248+5608. The green dashed curve gives the CSFRA starburst component, the blue dashed line gives the AGN contribution and the red solid line illustrates the combined GEM SED. The squares give the published data observed fluxes and the circles with attached downward pointing arrows indicate the upper limits.

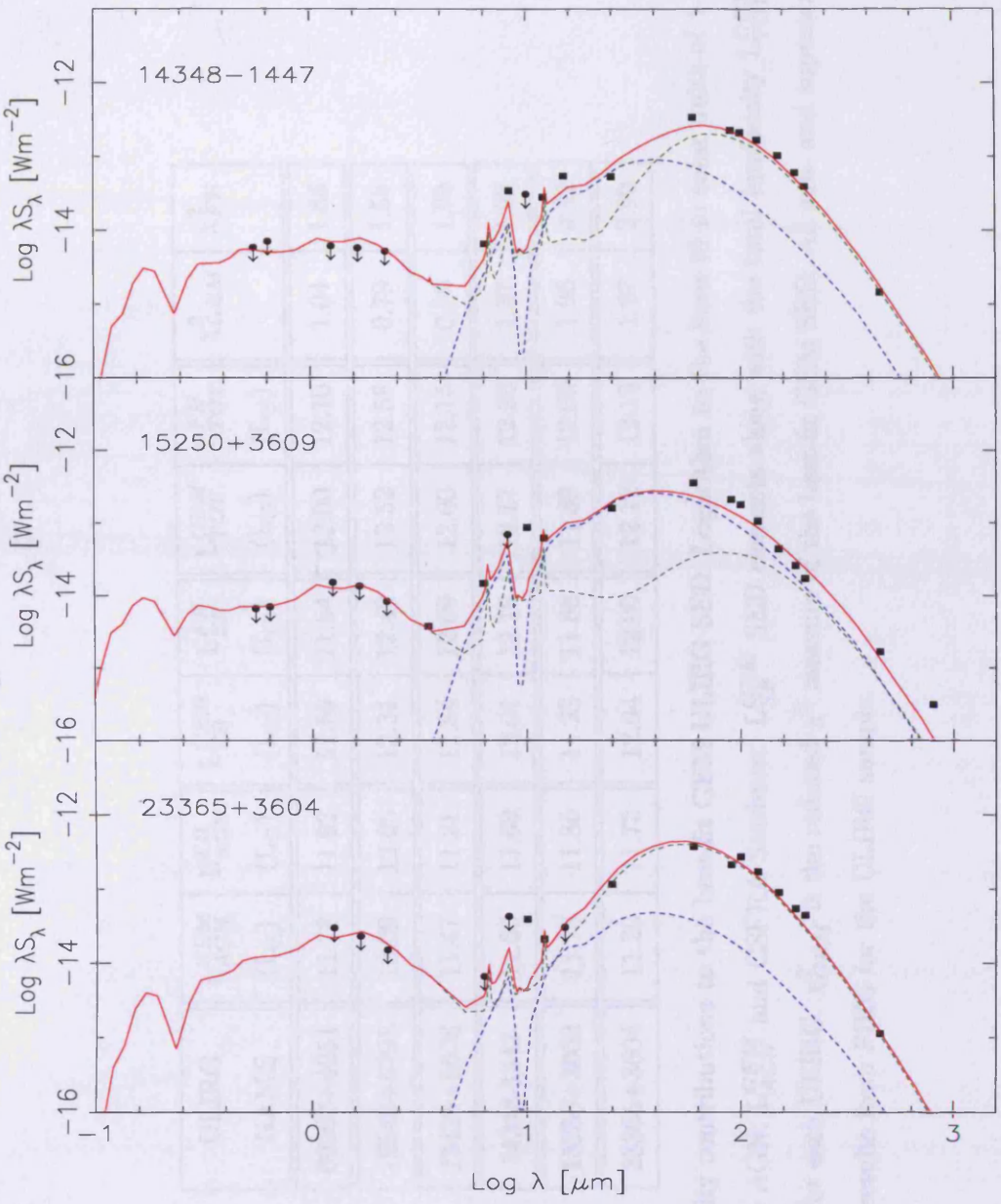

Figure 7.9: Best-Fit GEM SEDs for 14348-1447, 15250+3609 & 23356+3605. The green dashed curve gives the CSFRA starburst component, the blue dashed line gives the AGN contribution and the red solid line illustrates the combined GEM SED. The squares give the published data observed fluxes and the circles with attached downward pointing arrows indicate the upper limits.

ULIRG NAME	L_{AGN}^{GEM} ($L_\odot$)	L_{AGN}^{FH} ($L_\odot$)	L_{SB}^{GEM} ($L_\odot$)	L_{SB}^{FH} ($L_\odot$)	L_{TOT}^{GEM} ($L_\odot$)	L_{TOT}^{FH} ($L_\odot$)	χ^2_{GEM}	χ^2_{FH}
00262+4251	11.78	11.92	11.59	11.64	12.00	12.10	1.04	1.66
12540+5708	12.09	12.05	12.31	12.42	12.52	12.58	0.79	1.56
13428+5608	11.47	11.21	11.84	12.09	12.00	12.15	0.80	1.99
14348-1447	11.66	11.69	12.01	12.18	12.17	12.30	1.37	1.98
15250+3609	11.78	11.86	11.23	11.68	11.89	12.08	1.96	2.32
23365+3604	11.29	11.73	12.04	12.00	12.12	12.19	1.87	2.90

Table 7.5: Luminosity contributions to the best-fit GEM ULIRG SED. Logarithm to the base 10 in solar units of 1-1000μm luminosity from the AGN; L_{AGN}^{GEM} and CSFRA Starburst; L_{SB}^{GEM} SED elements along with the total luminosity L_{TOT}^{GEM} of the best-fit GEM SED for each ULIRG. χ^2_{GEM} is the reduced χ^2 measure of the best-fit GEM SED. All sub- and superscripts *FH* give the equivalent results from FH03 for the ULIRG sample.

ULIRG NAME	SFR_{KL}^{GEM} ($M_\odot yr^{-1}$)	SFR_{RR}^{GEM} ($M_\odot yr^{-1}$)	SFR_{RR}^{FH} ($M_\odot yr^{-1}$)	t_{sb} (Myrs)	t_{sb}^{FH} (Myrs)	τ (Myrs)
00262+4251	173	135	50	20	26-45	4
12540+5708	420	404	470	20	10-16	10
13428+5608	173	172	260	20	16-26	9
14348-1447	255	254	310	30	26-37	50
15250+3609	115	95	70	10	10-37	1
23365+3604	230	229	200	20	≈26	30

Table 7.6: Physical Characteristics of the best-fit ULIRG SEDs. SFR_{KL}^{GEM} uses the Kennicutt Global Schmidt Law of Equation 7.9, SFR_{RR}^{GEM} uses the formulation of Rowan-Robinson *et al.* (1997) given in Equation 7.8. SFR_{RR}^{FH} is the observed star formation rate from FH03 also calculated using Equation 7.8 (Rowan-Robinson *et al.* 1997). t_{sb} is the time since the onset of star formation or equivalently the starburst age, from the CSFRA component of the best-fit GEM SED and τ is the global star formation activity half-life. Also shown is t_{sb}^{FH} which is the derived starburst age from FH03

AGN (Downes & Solomon 1998). Finally, Genzel *et al.* (2001) used observations from the VLT & Keck telescope to show that 00262+4251 has gas and stellar dynamics which are strongly decoupled, potentially implying that the starburst activity has perhaps subsided, leaving a weak star formation ring (Genzel *et al.* 2001).

What evidence is there in the GEM SED to concur with this synopsis? The SED is illustrated in the top plot of Figure 7.8 where the published data, with the upper limits indicated, are also displayed. The GEM SED shows that the AGN element dominates in the FIR whilst the CSFRA SED contributes the flux at sub-mm and at shorter UV, optical and near-infrared wavelengths. Table 7.5 also shows that L_{AGN}^{GEM} is 61% of the total luminosity and L_{SB}^{GEM} is 39% of the total, which is in general agreement with FH03, who obtained 66% and 34% for the AGN and starburst components respectively.

The AGN fractional contribution to the GEM SED luminosity is perhaps indicative of a completed merger, suggesting that the AGN has come to dominance as the heating source, in line with the results of Dasyra *et al.* (2006) and Downes & Solomon (1998). The smaller fractional contribution of the CSFRA SED to the total luminosity might also be interpreted in terms of the weak starburst ring observed by Genzel *et al.* (2001). The suggestion that starburst activity has subsided is also in general agreement with the GEM free parameter results, as the time since the onset of star formation obtained from the CSFRA SED is t_{sb} = 20Myrs and the global star formation activity τ = 4Myrs (Genzel *et al.* 2001). The starburst age shows that star formation was initiated some time ago and the rapid decay in the number of GMC's within which star formation is initiated per time bin, or equivalently the star formation rate at efficiency η, indicates that star formation was somewhat limited and was perhaps localized in hotspots in the interaction (S88). In turn this is suggestive of the AGN coming to dominate sometime ago as funnelling of molecular gas into the nuclear regions allowed its fuelling to (re)commence (S88).

Considering the star formation rate, the two values obtained from the 00262+4251 CSFRA SED using the integrated 8-1000μm and 60μm luminosity are broadly in agreement with each other at SFR_{GEM}^{KL} = 173$M_{\odot}yr^{-1}$ and SFR_{GEM}^{RR}= 135$M_{\odot}yr^{-1}$. However, the value found by FH03 SFR_{FH}^{RR} = 50$M_{\odot}yr^{-1}$, also using the 60μm luminosity is considerably smaller. An explanation for this discrepancy might be found in the FH03 relative contributions of the AGN and CSFRA SEDs to the total luminosity. Looking at Table 7.5, FH03 assigns more of the total luminosity to the AGN SED and as this element dominates in the FIR it is likely that the starburst contribution was somewhat underestimated. This

may well have had a knock-on affect on the 60μm luminosity needed for the FH03 SFR calculation. Finally, the starburst age obtained from the CSFRA SED as t_{sb} = 20Myrs is within the range determined by FH03 at $t_{sb_{FH}}$ = 26-45Myrs.

In summary it would appear that the GEM result of the AGN as the dominant power source in 00262+4251, with star formation that was initiated some time ago, but is now fading, compares reasonably favourably with the literature (e.g., Dasyra *et al.* 2006; Downes & Solomon 1998; Genzel *et al.* 2001). Potentially this adds weight to the identification of the best-fit GEM SED being appropriate.

12540+5708

This object is more commonly known as Markarian 231 (Mrk 231) and has a redshift of z = 0.0422. The identification of the GEM SED found that, whilst the best-fit was *very* likely to have come from the $M_{GMC} = 10^9 M_\odot$ $\eta = 0.2$ instantaneous burst SED set, the values obtained for mf_{sb} and t_{sb} were less secure due to degeneracy of these two variables, especially in the optically thin environment of a high η model.

The general consensus in the literature appears to be that the merger in Mrk231 is complete and that the AGN is in dominance. For example, Condon *et al.* (1991) mapped Mrk 231 at 8.44 GHz with the VLA and found it was dominated by a variable (on timescales of years) radio source too compact ($\simeq$1 pc) to be an ultraluminous starburst and concluded it must be powered by an AGN 'monster'. A low resolution mid-infrared spectroscopic survey of 62 ULIRGs used the line-to-continuum ratio of the 7.7μm PAH emission as a discriminator between starburst and AGN activity and all objects were classified as a starburst, except Mrk 231 (Rigopoulou *et al.* 1999). Risaliti *et al.* (2006) presented L-band spectroscopy performed with the Infrared Spectrometer And Array Camera (ISAAC) at the VLT to suggest the dominant heating source in Mrk 231 was the AGN, a conclusion confirmed by NIR spectroscopy from Imanishi (2001). Finally, Cutri *et al.* (1984) used infrared photometry to suggest that Mrk231 has a Seyfert 1 nucleus, likely residing in a giant elliptical galaxy, indicating the merger was complete.

However, Cutri *et al.* (1984) also found that the total IR luminosity of Mrk 231 was powered by both an AGN and a starburst and Iwasawa (1999) found that the X-ray emission from Mrk 231 although weak, could not be fitted by a pure power-law or a thermal bremsstrahlung model. Finally Dasyra *et al.* (2006) used spectroscopic VLT observations to suggest that whilst Mrk 231 is an advanced merger, composed of a single compact

nucleus, its nucleus is surrounded by irregular 'rings' of more recent star formation and a small tidal arm containing blue star-forming 'knots'.

Looking at the GEM SED, illustrated in the middle plot of Figure 7.8, it can be seen that the spectral fit is considerably different to that of 00262+4251 with the AGN dominating across the shortest UV and optical wavelengths and in the MIR illustrating that the central engine is optically revealed. The shape of the FH03 best-fit SED was also similar to that of the GEM SED with the starburst element generating the dust flux at the longest FIR and sub-mm wavelengths and also across the NIR. Finally Table 7.5 shows that L_{SB}^{GEM} is 62% of the total luminosity and that FH03 found the starburst also contributed the majority of the total at 70%.

That the short wavelength flux in the GEM SED is being generated by the AGN potentially demonstrates that the enshrouding dust has been blown away under the influence of stellar winds and supernova. In the scheme of S88, this might imply the merger is complete and that the AGN has come to dominance which is in agreement with the results of e.g., Condon *et al.* (1991), Rigopoulou *et al.* (1999) or Risaliti *et al.* (2006) above.

That the starburst element is generating the longest wavelength dust flux in both the GEM and FH03 best-fit SEDs indicates that star formation is still ongoing in the clouds remaining around the central AGN. Perhaps this result can be seen in terms of the Dasyra *et al.* (2006) observations of star formation rings and blue star forming knots. In turn this lends further weight to the indication from the GEM SED that the enshrouding dust has been expelled from the galaxy.

Table 7.6 shows that the GEM SED has yielded values for the starburst age and star formation activity half-life of t_{sb} = 20Myrs and τ=10Myrs respectively. The larger value of τ in comparison to e.g., 00262+4251 possibly indicates that the fuelling for the star formation in Mrk 231 was reasonably sustained. At these values of t_{sb} and τ the star forming material is probably still being funnelled into the central AGN implying both that the gas is being moved around the galaxy on fairly large scales and that active star formation is still ongoing, albeit less vigorously. Thus if both star formation and AGN activity is observed, perhaps the relative contributions to the GEM SED luminosity from the AGN and starburst, at 62% and 38% respectively, might be appropriate.

Turning now to the star formation rates, $SFR_{KL}^{GEM} = 420 M_{\odot} yr^{-1}$ and $SFR_{RR}^{GEM} = 404 M_{\odot} yr^{-1}$ found from the CSFRA contribution to the GEM SED are comparable to that of FH03 at $SFR_{RR}^{FH} = 470 M_{\odot} yr^{-1}$ as shown in Table 7.6. That the GEM SFR's

are lower than that of FH03 might be explained by both the higher total luminosity and greater percentage of that luminosity assigned by FH03 to the starburst element SED, leading to a larger 60μm luminosity. However, Yun & Carilli (2002), who generated a library of dusty starburst templates to fit the infrared SEDs over radio-to-far-infrared wavelengths, also used the Kennicutt global Schmidt law, but found a SFR = 236$M_{\odot}yr^{-1}$ for Mrk 231. This illustrates the sensitivity of the SFR estimation to the specific best-fit synthetic spectra. Finally, the age of the starburst, calculated from the CSFRA SED, at t_{sb} = 20Myrs is also in broad agreement with that of FH03 at $t_{sb_{FH}}$ = 10-16Myrs.

Therefore in summary, the GEM SED has the AGN generating the flux at shorter wavelengths, suggesting that the merger is complete and that a dust-void along a line of sight to the AGN has been opened under the influence of strong stellar winds and supernovae (S88). This perhaps implies that the AGN is now the dominant power source in Mrk 231, in agreement with Condon *et al.* (1991), Risaliti *et al.* (2006), Imanishi (2001) and (Rigopoulou *et al.* 1999). That a starburst element in reasonably rapid decay is also required is weighed out by the Dasyra *et al.* (2006) observations and the values of t_{sb} and τ obtained

13428+5608

This ULIRG, more commonly known as Mrk 273, is located in the nearby universe at z = 0.0378. Both the values of mf_{sb} and t_{sb} obtained during the identification of the best-fit SED were considered to be reasonably firm, whilst the value of the decay in the star formation rate or equivalently, the number of GMCs joining the starbursting ensemble in a time bin, τ, was found to be subject to slightly more uncertainty.

There is considerable evidence in the literature to suggest that this ULIRG is powered by nuclear starbursts. For example, Condon *et al.* (1991) conducted radio continuum observations and found that Mrk 273 contains a diffuse radio source obeying the FIR-radio correlation, indicating it was almost certainly a starburst galaxy. Carilli & Taylor (2000) published hydrogen 21cm absorption and radio continuum emission observations at 1.4GHz made using the Very Long Baseline and Very Large Arrays to also suggest that this ULIRG was dominated by a compact starburst (Carilli & Taylor 2000). Finally, Genzel *et al.* (1998) and Lutz *et al.* (1998) both used NIR spectroscopy to reveal the PAH features indicative of a starburst.

Figure 7.8 displays the GEM SED along with the published data and illustrates that

the starburst dominates at all wavelengths except the MIR and Table 7.5 shows that L_{SB}^{GEM} is 70% of the total luminosity. Thus, the GEM results are in general agreement with the literature and the suggestion that Mrk 273 is primarily powered by a starburst. The conclusion is also in agreement with FH03 who have the starburst dominating the overall ULIRG luminosity with L_{SB}^{FH03} being 88% of the total. The values of t_{sb} = 20Myrs and τ = 9Myrs obtained from the CSFRA SED element are fairly similar to those of 12540+5708 just discussed and the star formation might also therefore be thought to have been reasonably well fuelled during the merger interaction (S88). Again in a similar way to 12540+5708, recent star formation rings have been observed by Scoville *et al.* (2000) who presented NIR images of this object obtained with the *Hubble Space Telescope* and Surace (1998) who used Optical and UV imaging to also imply its presence.

However, that an AGN element is *still* required to fit the spectrum of Mrk 273 is perhaps strengthened by the results of e.g., Knapen *et al.* (1997) who suggested that strong observed radio emission was associated with an active galactic nuclei and therefore the source of the Seyfert 2 narrow-line emission seen by Veilleux *et al.* (1999) in their NIR J- and K-band spectra. That 13428+5608 is a composite object was also indicated by the results of Levenson *et al.* (2001) who presented an X-ray imaging and spectroscopic analysis of Seyfert 2 galaxies containing starbursts and attempted classification based on their optical and UV characteristics (Levenson *et al.* 2001). The composite galaxies, which included Mrk 273, exhibited extended, soft, thermal X-ray emission which the authors attributed to the starburst component, whilst the spatial signature of the AGN was thought to be an unresolved central point source (Levenson *et al.* 2001). Mrk273 was therefore found to be a strong X-ray source with extended rather than resolved emission, which classified it as a composite Sy2/SB source (Levenson *et al.* 2001). These latter analyses appear to agree well with the general GEM result of requiring both a starburst and perhaps a less dominant AGN component to match the published ULIRG data.

Table 7.6 shows that the star formation rates derived from the GEM CSFRA SED at $SFR_{KL}^{GEM} = 173 M_{\odot} yr^{-1}$ and $SFR_{RR}^{GEM} = 172 M_{\odot} yr^{-1}$ are roughly of the same order of magnitude as that of FH03 at $SFR_{RR}^{FH} = 260 M_{\odot} yr^{-1}$. In this instance, that the FH03 value is somewhat larger than those obtained from the GEM SED might be due to FH03 attributing a greater proportion of the Mrk 273 best-fit SED luminosity to the starburst element, thereby raising the 60μm luminosity over an above what was obtained by the GEM CSFRA SED. Finally, the age of the starburst found by FH03 at $t_{sb_{FH}}$ = 16-26Myrs

is similar to the value from the GEM CSFRA SED at t_{sb} = 20Myrs.

In summary therefore, it would appear that Mrk 273 is perhaps best described in the literature as being powered by strong nuclear starbursts (e.g., Condon, Huang, Yin & Thuan 1991; Carilli & Taylor 2000; Genzel, Lutz, Sturm, Egami, Kunze, Moorwood, Rigopoulou, Spoon, Sternberg, Tacconi-Garman, Tacconi & Thatte 1998; Lutz, Spoon, Rigopoulou, Moorwood & Genzel 1998), but never-the-less, requiring an AGN component to meet the infrared luminosity. (e.g., Knapen, Laine, Yates, Robinson, Richards, Doyon & Nadeau 1997; Veilleux, Sanders & Kim 1999; Levenson, Weaver & Heckman 2001). This categorization appears to be in good agreement with the results obtained from the GEM SED and suggests that it might be suitable for predicting some of the physical characteristics of Mrk 273.

14348-1447

At z=0.082 this ULIRG is at the further end of the sample redshift distribution. In a similar way to 13428+4251, the values obtained for the number of GMCs within which star formation is active at t_{sb} = 0 and the age of the starburst in 14348-1447 are reasonably secure, but a larger apparent error might be attached to the value of the global star formation activity half-life τ.

The general consensus in the literature appears to be that 14348-1447 is powered by starbursts, with the object in pre-coalescence and therefore still in the process of merging. For example, the Rigopoulou *et al.* (1999) survey, which classified any object having $L_{PAH}/L_{FIR} > 1$ as a starburst and $L_{PAH}/L_{FIR} < 1$ as an AGN, found 14348-1447 had an L_{PAH}/L_{FIR} = 3.55 which firmly categorized it as being primarily powered by starbursts. Risaliti *et al.* (2006) used the L-band spectroscopy from the ISAAC camera at the VLT to classify 14348-1447 as a starburst based on the relative contributions to its energy output from the starburst and AGN components.

Going hand-in-hand with this starburst classification are the observations of e.g., Genzel *et al.* (2001) who suggested after analysis of high-quality near-IR spectra from VLT and Keck that the object was still merging or those of Dasyra *et al.* (2006), whose spectroscopic VLT observations showed that 14348-1447 was a binary source, the separation of which was sufficient for classification of the galaxy as pre-coalescence. Finally, Evans *et al.* (2001) used millimetre CO observations of 5 double-nucleus ULIRGs to suggest that 14248-1447 was in the intermediate stages of the merger process and that the distribution

of molecular gas suggested fuelling for both the starburst and the AGN.

Figure 7.9 displays the GEM SED which shows the CSFRA SED exerting the most influence across the FIR and sub-mm wavelengths and also at shorter UV, optical and NIR wavelengths, but in the MIR, both an AGN and a starburst are required to fit the observed silicate absorption and narrow-band emission. Table 7.5 shows that the weight of the GEM SED is given to the starburst component, which contributes some 69% of the total luminosity. This is also in agreement with the results of FH03 where L_{SB}^{FH03} is 75% of the total and the observations of Rigopoulou *et al.* (1999) and Risaliti *et al.* (2006). That the GEM AGN component does not contribute more to the total luminosity is indicative in the scheme of S88 of an object which has yet to complete its merger, in agreement with the results of Genzel *et al.* (2001), Dasyra *et al.* (2006) & Evans *et al.* (2001).

Table 7.6 shows that for 14348-1447 the time elapsed since the star formation began is t_{sb} = 20Myrs and that τ = 50Myrs; a long half-life which is in sharp contrast to the lower τ values found for the three ULIRGs already discussed. A value of τ this high might imply a more star constant formation scenario, where the fuelling is sustained and gas is still being moved around the merger on large scales in a non-local fuel delivery scenario (S88). This can again be perhaps seen in terms of the observations of Rigopoulou *et al.* (1999) and Risaliti *et al.* (2006) as the initiation of bursts of powerful star formation potentially indicates that cloud-cloud collisions are still underway, the merger nuclei have yet to form and the AGN has yet to come to dominance (Dasyra *et al.* 2006).

Considering the star formation rates, Table 7.6 shows that the rates derived from the CSFRA contribution to the GEM SED at SFR_{KL}^{GEM} = $255M_{\odot}yr^{-1}$ and SFR_{RR}^{GEM} = $254M_{\odot}yr^{-1}$, are underestimated when compared to the results of FH03 at SFR_{RR}^{FH} $310M_{\odot}yr^{-1}$. Referring to Table 7.5 this may well again be as a result of the higher proportion of the ULIRG luminosity being matched to the starburst element by FH03, raising the 60μm luminosity, compared to that of the GEM CSFRA SED. 14348-1447 was also modelled by Yun & Carilli (2002) who derived a SFR = $127M_{\odot}yr^{-1}$, again lower than, but broadly in line with, the GEM results. Table 7.6 also shows that the ages of the starburst found by FH03 and from the GEM CSFRA SED agree reasonably at 26-37Myrs and 20Myrs respectively.

In summary it would appear the GEM result that 14348-1447 is a starburst, still in the process of merging, is in good general agreement with the published observations in the literature, perhaps indicating the best-fit GEM SED is appropriate.

15250+3609

This ULIRG has a redshift of z = 0.0552. In the identification of the best-fit GEM SED, the values obtained for the starburst age t_{sb} and the decay in the star formation rate τ were found to be somewhat more secure than the value of mf_{sb}, the number of star forming GMC's in the ensemble at $t_{sb} = 0$. What was clear however, was that the best-fit CSFRA SED is made up of instantaneous burst SEDs belonging to the $M_{GMC} = 10^8 M_\odot$ $\eta = 0.2$ set.

15250+3609 was included in the Dasyra *et al.* (2006) survey, which mainly focused on sources that have coalesced in a single nucleus implying that the merger was complete. Using stellar kinematics extracted from the CO ro-vibrational band heads in their VLT H- and K-band spectroscopy and the structural and photometric properties of 15250+3609, Dasyra *et al.* (2006) were able to suggest that this ULIRG was a remnant which originated from a major merger and that the result was the formation of a system supported by random motions i.e., an elliptical galaxy. In the evolutionary model of S88 this conclusion would perhaps suggest that the AGN element of the ULIRG should be in dominance as the primary power and dust heating source.

The GEM SED is displayed in Figure 7.9 and Table 7.5 shows that this SED achieved the poorest χ^2 of the six objects in the sample. Figure 7.9 shows the AGN contributing heavily to the luminosity in the MIR and FIR and that the starburst dominates across the NIR, optical and UV as well as at sub-mm wavelengths. Both components appear to be required in the MIR to match the absorption and emission features. Table 7.6 shows that both the GEM SED and FH03 have the AGN element dominating the total luminosity at 78% and 60% of the total respectively. With the literature indicating that 15250+3609 is powered by an AGN, these results point to the central engine being heavily dust enshrouded, a suggestion made by FH03 and confirmed by GEM.

However, based on its MIR spectrum, Lutz *et al.* (1998) classified 15250+3609 as a starburst and Scoville *et al.* (2000) found it contained one central nucleus and a second dimmer nucleus, along with a large ring-like structure. The categorization of this ULIRG as a starburst was also implied by the low resolution MIR spectroscopy of Rigopoulou *et al.* (1999) who derived a PAH over infrared luminosity of $L_{PAH}/L_{FIR} = 2.880$

Looking at Table 7.6, t_{sb} = 10Myrs and τ = 1Myrs which suggests that 15250+3609 underwent a poorly fuelled merger a short time ago and that the star formation is perhaps

now subsiding. Existence of fading star formation might also be implied by the smaller fractional CSFRA contribution to the GEM SED. However a value of τ this extreme - essentially an instantaneous starbursting system - suggests that the merger was rapid, with large amounts of gas being funnelled very quickly toward the central region, initiating the localised bursts of star formation. This is perhaps in general agreement with Scoville *et al.* (2000) who suggested that bright clusters in 15250+3609 have colours and luminosities consistent with being created by collision or interactions only a relatively short time ago (10^7-10^8yr). Finally, the value for the starburst age obtained by FH03 at $t_{sb_{FH}}$ = 10-37Myrs also indicates that 15250+3609 could potentially be a young ULIRG.

Turning to the SFRs, Table 7.6 shows $SFR_{KL}^{GEM} = 115 M_{\odot} yr^{-1}$ and $SFR_{RR}^{GEM} = 95 M_{\odot} yr^{-1}$, whilst $SFR_{RR}^{FH} = 70 M_{\odot} yr^{-1}$ is somewhat lower, perhaps due to the instantaneous burst GEM classification of 15250+3609. However, Yun & Carilli (2002) obtained SFR = $82 M_{\odot} yr^{-1}$ which lies mid-way between SFR_{RR}^{GEM} and SFR_{RR}^{FH}.

In summary whilst it appears that much of the literature suggests 15250+3609 is powered by starbursts (e.g., Lutz, Spoon, Rigopoulou, Moorwood & Genzel 1998; Scoville, Evans, Thompson, Rieke, Hines, Low, Dinshaw, Surace & Armus 2000; Rigopoulou, Spoon, Genzel, Lutz, Moorwood & Tran 1999) there is evidence to propose the central engine is the dominant dust heating source in line with the GEM result (Dasyra *et al.* 2006). What is clear is that the GEM SED is similar in property to the FH03 SED and thus there is some agreement with the literature.

23365+3604

This ULIRG has a redshift of z = 0.0645. In the identification of the best-fit it was found that whilst the value of mf_{sb} was considered reasonably appropriate, the values of t_{sb} and τ contained a somewhat larger apparent error.

The classification of 23365+3604 as a starburst comes from the low resolution MIR spectroscopy of Rigopoulou *et al.* (1999), which revealed a PAH over infrared luminosity of $L_{PAH}/L_{FIR} = 4.479$, the largest ratio in their sample. As $L_{PAH}/L_{FIR} > 1$ was indicative in their scheme of a starburst galaxy, 23365+3604 was categorized as such (Rigopoulou *et al.* 1999).

Figure 7.9 displays the GEM SED which shows that the CSFRA starburst element contributes most of the flux at all wavelengths except across the MIR, where an AGN element is also required to generate the narrow-band emission and silicate absorption

features. Table 7.5 shows that the CSFRA contribution to the GEM SED generates some 85% of the total luminosity, in general agreement with the results of FH03 who have the starburst providing 65% of the total. This GEM result indicating that nuclear star bursting is the dominant dust heating source in 23365+3604 is therefore in agreement with what was available in the literature.

That a starburst classification may be appropriate is also indicated by the estimates of t_{sb} = 20Myrs, τ = 30Myrs derived from the GEM CSFRA SED, displayed in Table 7.6. This slow rate of decay is essentially bordering on a more constant scenario, with the star formation being initiated in significant numbers of GMCs in each time bin and this may well explain the greater proportion of the total luminosity assigned by GEM to the CSFRA SED as compared to FH03. At τ = 30Myrs, the sustained star formation might be indicative in the model of S88 of GMCs spiralling very slowly into the central AGN. As these fuelling GMCs are unlikely to be local in origin perhaps gas is being moved around the galaxy on very large scales, further suggesting that the object may still be in the process of merging. This GEM result - that there is a more continual evolution of the stellar population - is possibly in broad agreement with the observations of Surace & Sanders (2000), who used the UH 2.2m telescope on Mauna Kea to suggest that the total galaxy colours of 23365+3604 imply a mix of older stellar populations and new stars.

Finally, the values of the SFR obtained from the CSFRA contribution to the GEM SED at $SFR_{KL}^{GEM} = 230 M_{\odot} yr^{-1}$ and $SFR_{RR}^{GEM} = 229 M_{\odot} yr^{-1}$ agree well both with each other and with the FH03 result at $SFR_{RR}^{FH} = 200 M_{\odot} yr^{-1}$; the difference potentially being due to the larger L_{SB}^{GEM} obtained by the GEM CSFRA SED. Similarly the derived time since the onset of star formation activity at t_{sb} = 20Myrs differs only slightly to that of FH03 at $t_{sb_{FH}}$ = 26Myrs.

In therefore appears that the results obtained from the GEM SED for 23365+3604 are generally in agreement with observations published in the literature, potentially indicating that the best-fit GEM SED may well be reasonably appropriate for predicting some of this ULIRG's physical characteristics. This concludes the first assessment of the best-fit GEM SEDs.

Summary of Analysis I

In the preceding section the veracity of the GEM modelling approached was tested by comparing the results implied by the free parameters of the best-fit GEM SEDs to those

available in the literature. For all six ULIRGS in the sample, the dominant heating source indicated by the fractional contributions from the CSFRA and AGN SEDs to the total luminosity were in reasonable accord with the literature. The merger and interaction state implied for these objects by their starburst age t_{sb} and the star formation activity half-life τ, in conjunction with the fractional luminosities, were also found to be appropriate when compared to published observations of the ULIRG sample.

The sample appears to contain two objects which approximate constant star formation: 14348-1447 & 23365+3604, two objects for which an essentially bursting scenario is indicated: 00262+4251 & 15250+3609 and two objects which fall intermediate between these extremes; 12540+4251 & 13428+5608. Of the sample, only 14348-1447 was found to be still in the process of merging. The other five objects were found to have completed the merger process and further, in 12540+4251, sufficient time appears to have elapsed for the dust shroud around the AGN to be dispersed and the central engine to be optically revealed. Finally, the age of the starburst as determined from the FH03 and GEM SEDs also agreed favourably.

The star formation rates derived from the luminosity of the CSFRA contribution to the GEM SEDs, using both the Kennicutt star formation law and the prescription of Rowan-Robinson *et al.* (1997) agreed reasonably well with each other in all instances. Further, each was approximately of the same order of magnitude as those found by FH03 for the sample.

It would therefore appear that the GEM modelling approach has generated a best-fit SED for each ULIRG in this small sample which exhibits the general characteristics implied by observation and discussed in the literature. The modelling was able to replicate systems across a broad range of luminosity, starburst age and star formation activity decay and generated reasonable predictions for ULIRGs in a variety of evolutionary states. It would also appear that the degeneracy within the GEM ULIRG SED Library did not cause the derived results to vary randomly when compared to published observations and conclusions.

7.4 Analysis II

As was seen in the last section, the GEM SFRs at the current epoch, derived using the FIR integrated and the 60μm luminosity, agreed favourably both to each other and to

those obtained by FH03. However, the same flux data points for each ULIRG were used by FH03 and GEM and both FH03 and GEM were able to achieve reduced $\chi^2 \leq 3$ for the best-fit SEDs, in all cases. It is therefore relatively unsurprising that the SFRs obtained from the GEM SED luminosity match those of FH03.

Perhaps a better test of the GEM modelling approach might be to compare these star formation rates to ones obtained using only the free parameters corresponding to the best-fit GEM SED, without recourse to the SED luminosity. Comparison of these rates to those found in *Analysis I* and to those of FH03 would effectively provide an independent estimate of the appropriateness of the best-fit GEM SED and of the modelling approach as a whole. Further because the GEM models have been built entirely from scratch, the gas and dust distribution corresponding to the single GMC which originated the instantaneous burst SEDs in the CSFRA element of the GEM SED, is also available. Access to this information, when used again in tandem with the free parameters of the GEM SED, allows the dust mass of the ULIRG to be derived independently of the SED flux. Comparison of these dust masses to those of FH03 also provides a useful indication of the suitability of the GEM approach.

Therefore in the coming section, first derivation of this second set of physical ULIRG characteristics is described, whereafter a brief comparative discussion assesses the results.

7.4.1 ULIRG Physical Characteristics II

This section begins with the method by which the star formation rate at the current epoch is obtained from the GEM SED free parameters. It is also possible to generate estimates for the initial and average star formation rates, the number of GMCs to join the ensemble since the star formation began and the mass of stars formed. Taken together these values can give an indication of the star formation history of a ULIRG over and above only the observed star formation rate.

Initial Star Formation Rate

Calculation of the star formation rate from the best-fit free parameters was first discussed at the end of Chapter 5, §6.1.2, where the instantaneous burst SED library was extended to approximate constant star formation. Repeating Equation 6.3 here for convenience and re-naming it so it can be easily identified in comparison, the initial star formation rate

$\dot{M}_\star(0)$ can be written

$$SFR_{Int}^{GEM}(0) = \dot{M}_\star(0) = mf_{sb} \cdot \eta \cdot M_{GMC} \tag{7.10}$$

where mf_{sb} gives the rate at which GMCs are forming stars per year at $t_{sb} = 0$ and the product of η . M_{GMC} is the mass of stars formed in each GMC.

Observed Star Formation Rate

Similarly, the star formation rate per year at the current epoch can by found be assessing Equation 7.10 at $t' = t_{sb}$

$$SFR_{Obs}^{GEM}(t_{sb}) = \dot{M}_\star(t') = mf_{sb} \cdot \eta \cdot M_{GMC} \cdot e^{-\frac{t'}{\tau}} \tag{7.11}$$

which is essentially Equation 6.4, with τ being the star formation activity half-life.

Total Mass of Stars Formed

The trapezium rule can now be used to sum the mass of stars formed in each time bin Δt to give the total mass of stars formed

$$M_\star^{TOT}(t_{sb}) = \sum_{0}^{t_{sb}} \dot{M}_\star(t')\Delta t \tag{7.12}$$

which is Equation 6.5 from Section §6.1.2 in Chapter 5.

Average Star Formation Rate

Having obtained the total mass of stars formed it is a simple calculation to divide Equation 7.12 by the starburst age t_{sb} to find the average star formation rate SFR_{Avg}^{GEM}.

Total Number of GMCs in the Starbursting Ensemble

In a similar way to calculation of the total stellar mass, the total number of clouds to join the starbursting ensemble $N_{GMC}^{TOT}(t_{sb})$ can be found by dividing Equation 7.12 by the mass of stars each GMC has formed $M_{GMC}.\eta$.

ULIRG Dust Mass

The starburst element dust mass can be found using the properties of the single GMC which originated the instantaneous burst SED flux $F_\nu(t')$ used in the CSFRA element

of the best-fit GEM SED, along with a suitable gas-to-dust ratio gd_r. The AGN dust component then is found using torus geometry, the best-fit dust temperature T_{dust} and the optical depth at ultra-violet wavelengths τ_{uv}. When the CSFRA and AGN element dust masses are added together, the total dust mass of the ULIRG is obtained.

GEM Starburst Dust Mass

The starburst dust mass estimation begins by obtaining the dust density distribution of the single instantaneous burst GMC as it evolves with time. The method by which the GMC's neutral, ionized and ambient gas densities are combined together with the adopted gas-to-dust ratio to find the dust mass is practically the same as that used to compose the optical depth distributions in Chapters 3 & 5. An illustrative example is now derived for one GMC at a time when the supernovae have begun, but the superbubble is still trapped within the HII region

$$M_D^{SB}(t') = \frac{4\pi}{3}\Big[(Fd^{SH}(t')\rho^{SH}(t')[R_{SN}^3(t') - R_{cav}^3(t')] + Fd^{Wi}\rho^{Wi}(t')[R_W^3(t') - R_{SN^3}(t')] + Fd^n\rho^n(t')[R2_W - R_{SN}(t')]) + Fd^\alpha\rho^\alpha[R2_{SN} - R2_W]\Big]\frac{1}{gd_r} \quad (7.13)$$

where $M_D(t')$ is the mass of dust at t' and gd_r is the gas-to-dust ratio. $\rho^{SH}(t')$, $\rho^{Wi}(t')$, $\rho^n(t')$ and $\rho^\alpha(t')$ are the shell, HII region, neutral and ambient region densities respectively. $4\pi/3[R_{SN}^3(t')\text{-}R_{cav}^3(t')]$ is the shell volume, $4\pi/3[R_W^3(t')\text{-}R_{SN}^3(t')]$ is the HII region volume, $4\pi/3[R2_W^3\text{-}R_{SN}^3(t')]$ is the volume of the neutral region and $4\pi/3(R2_{SN}^3\text{-}R2_W^3)$ is the volume of the ambient region. Finally, $Fd^{SH}(t')$, $Fd^{Wi}(t)$, $Fd^n(t)$ & Fd^α are the dust condensation factors for the shell, HII region, neutral and ambient regions respectively and essentially couple the temperature of the gas to the quantity of dust that can condense. As described in the Section §3.6 $Fd^n = Fd^\alpha = 1$ in all cases as 100% of the dust contributes to the extinction in those cool regions. $Fd^{Wi} = 0.2$ is taken directly from ERR00, whilst $Fd^{SH}(t)$ is dependent on the temperature of the gas in the shell and is given by Equation 5.37, Section §5.4 Chapter 5.

The total starburst dust mass at the current epoch - i.e., at the starburst age t_{sb}, $M_D^{SB}(t_{sb})$ is then given by

$$M_D^{SB}(t_{sb}) = mf_{sb}\sum_0^{t_{sb}} e^{-\frac{t'}{\tau}} M_D(t_{sb} - t')\Delta t \quad (7.14)$$

Considering the gd_r, a mean ratio of H_2 gas to warm dust of 540 ± 290 was derived by Sanders *et al.* (1991), based on 115GHz CO spectra from 60 *IRAS* galaxies obtained

with the 12m NRAO single dish telescope. All of the galaxies in the Sanders *et al.* (1991) sample were at a sufficient distance that the 55" beam measured the total CO luminosity and therefore the total molecular gas content could be estimated. Infrared luminosities were obtained from the four *IRAS* band fluxes, using the prescription of Puget & Boulanger (1990) to approximate the luminosity from 8- to 1000μm. Whilst there are big questions over this issue, the molecular gas content was computed from the integrated CO intensities by assuming a constant conversion factor between the CO line emission and the molecular hydrogen mass ($M(H_2) = 4.78\ L_{CO}$ [K km s^{-1} pc^2]), where the constant 4.78 corresponds to a CO to H_2 conversion factor $\alpha = 3 \times 10^{20}$ cm^{-2} (K km s^{-1}). This represented a mean of the determinations found in the literature based on virial mass estimates (e.g., Sanders *et al.* 1985; Sanders *et al.* 1991). All of the *IRAS* galaxies were extremely rich in molecular gas with $M_{H_2} = 1 \times 10^9$ - $6 \times 10^{10} M_\odot$, corresponding to 0.5-30 times the mass of H_2 gas in the Milky Way (Sanders *et al.* 1991). For comparative purposes the gas-to-dust ratio in average spiral galaxies is though to be $\sim$ 500 (Devereux & Young 1990), $\sim$ 150 for the Milky Way (FH03) and $\sim$ 700 in ellipticals (Wiklind & Henkel 1995). As the ratio of Sanders *et al.* (1991) was also used by FH03 and it appears to be the most suitable for luminous infrared galaxies, a gas-to-dust ratio of 540 was used in this thesis work.

GEM AGN Dust Mass

The AGN dust mass $M_D^{AGN}(t_{sb})$ was found by considering the AGN dust temperature T_{dust}, the optical depth τ_{uv} and tori geometry of the best-fit AGN model, which gives the density and via the gas-to-dust ratio, the mass of dust in the AGN torus.

GEM ULIRG Dust Mass

Adding the AGN dust mass $M_D^{AGN}(t_{sb})$ to that found for the starburst component $M_D^{SB}(t_{sb})$ gives the total combined dust mass of the ULIRG $M_{Dust}^{GEM}(t_{sb})$.

FH03 ULIRG Dust Mass

FH03 could have calculated their starburst dust masses from the model free parameters in precisely the same way just described, as those authors also had access to the HII region evolution density distribution and hence the dust mass. However, it was noted in FH03, that with their use of an HII region evolution model only, employing an equation such as 7.14 would give the total dust mass at the current age of the starburst without accounting

for dust destroyed by shocks and supernovae and hence their dust mass $M_{Dust}^{FH}(t_{sb})$ would be overestimated. Therefore FH03 estimated their dust mass using sub-millimetre data under the assumption the system was optically thin at those wavelengths and hence all the dust was visible and then followed the prescription of Hildebrand (1983)

$$M_{Dust}^{FH} = \frac{1}{(1+z)} \frac{S_{\nu_0} D_L^2}{\kappa(\nu_r) B(\nu_r, T_{DUST})} \tag{7.15}$$

where z is the redshift, ν_0 and ν_r are the observed and rest frame frequencies, S_{ν_0} is the flux in the observed frame, D_L is the distance to the source, T_{DUST} is the dust temperature, $\kappa(\nu_r)$ is the mass absorption coefficient at frequency ν in the rest frame and $B(\nu_r, T_{dust})$ is the rest frame Planck function.

The important thing to note from Equation 7.15 is that it uses a monolithic mass-weighted dust temperature, T_{DUST} which is obtained by fitting an optically thin greybody function to the infrared best-fit combined AGN and starburst SED over the range 200-1000μm

$$S_\nu \propto \nu^\beta B(\nu, T_{DUST}) \tag{7.16}$$

A caveat should be made that deriving monolithic dust temperatures from spectral fitting can be an oversimplification as it is more likely that dust exists at various temperatures in different regions of the ULIRG.

Table 7.5 shows that both this thesis work and FH03 achieved reduced $\chi^2 \leq 3$ in all cases for the ULIRG sample and that the fractional and total luminosities derived were also reasonably similar. It is therefore highly likely that carrying out the procedure just considered on the GEM best fitting combined model SED to find the dust mass, would yield very similar values to those of FH03. Therefore, the FH03 dust masses will be discussed in the next section in comparison to the dust mass derived from the initial optical depth and free parameters of the GEM SED, via Equation 7.14.

Summary of Physical Characteristics II

For easy reference the quantities to be tested and compared in this second analysis section comprise:

- $SFR_{Int}^{GEM}(0)$, SFR_{Avg}^{GEM} and $SFR_{Obs}^{GEM}(t_{sb})$ are the initial, average and observed star formation rates, calculated using the free parameters of the CSFRA best-fit SED.

- $M_{\star}^{TOT}(t_{sb})$ and $N_{GMC}^{TOT}(t_{sb})$ are the total mass of stars formed and the total number of GMCs within which star formation has been initiated since $t_{sb} = 0$, again calculated using the free parameters of the CSFRA best-fit SED.

- $M_{Dust}^{GEM}(t_{sb})$ is the total dust mass calculated using the optical depth distribution of the instantaneous burst GMC which originated the CSFRA best-fit SED and the AGN tori geometry and best-fit free parameters.

- $M_{Dust}^{FH}(t_{sb})$ is the ULIRG dust mass derived by the best-fit SED by FH03 assuming a monolithic dust temperature.

7.4.2 ULIRG Sample Discussion II

Table 7.4.1 gives each of the values listed previously in the above section and for comparative purposes, the star formation rate SFR_{RR}^{GEM} found in *Analysis I* from the 60μm GEM SED flux using the prescription of Rowan-Robinson *et al.* (1997) in Equation 7.8. The value obtained for the star formation activity half-life τ, in *Analysis I*, is also given.

Looking at the table and considering first the free parameter $SFR_{Obs}^{GEM}(t_{sb})$ and its comparison with the 60μm luminosity rate SFR_{RR}^{GEM}. The free parameter SFR appears to be somewhat dependent on the star formation scenario for each object, as indicated by the half-life τ. For example, with the two objects that exhibited an almost instantaneous burst star formation scenario: 00262+4251 & 15250+3609, the free parameter rates, $SFR_{Obs}^{GEM}(t_{sb})$ are considerably underestimated when compared to the 60μm rate. With the two objects in the sample which indicate an intermediate star formation scenario: 12540+5708 & 13428+5608 $SFR_{Obs}^{GEM}(t_{sb})$ matches the 60μm rate SFR_{RR}^{GEM} very well and finally, the two objects which have a more constant star formation scenario: 14348-1447 & 23365+3604, the $SFR_{Obs}^{GEM}(t_{sb})$ is somewhat overestimated when compared to the 60μm rate SFR_{RR}^{GEM}. Also, it appears that the more extreme the star formation scenario is found to be, the greater the discrepancy between the free parameter and 60μm rates.

Unfortunately, this result indicates that the method by which quantities such as the observed, average and initial star formation rates are obtained from the free parameters of the best-fit CSFRA SED only appears to be reliable when considering the star formation history of ULIRGs exhibiting an intermediate star formation scenario. Where the root cause of this result lies is difficult to determine; perhaps the problem is within the GEM modelling approach itself or potentially it is within the approximation of constant star

ULIRG NAME	M_{GMC} ($M_\odot$)	η	τ	SFR_{Int}^{GEM} (0) ($M_\odot yr^{-1}$)	SFR_{Avg}^{GEM} ($M_\odot yr^{-1}$)	SFR_{Obs}^{GEM} (t_{sb}) ($M_\odot yr^{-1}$)	SFR_{GEM}^{RR} (t_{sb}) ($M_\odot yr^{-1}$)	N_{GMC}^{TOT} (t_{sb})	Log $M_\star^{TOT}$ (t_{sb}) ($M_\odot$)	Log M_{Dust}^{GEM} (t_{sb}) ($M_\odot$)	Log M_{Dust}^{FH} (t_{sb}) ($M_\odot$)
00262+4251	10^8	0.15	4	5630	1164	38	135	1552	10.36	8.42	8.42
12540+5708	10^9	0.2	10	3000	1326	406	404	132	10.42	8.04	7.95
13428+5608	10^9	0.15	9	1500	617	163	172	82	10.08	7.58	7.70
14348-1447	10^9	0.15	50	550	424	308	254	84	10.10	7.78	7.97
15250+3609	10^8	0.2	1	4000	432	2	95	216	9.64	7.73	7.43
23365+3604	10^9	0.2	30	500	366	256	229	36	9.86	7.62	7.81

Table 7.7: Results from the *Analysis II* of the ULIRG characteristics. M_{GMC} and η are the GMC mass and star forming efficiency of the cloud that originated the instantaneous burst SEDs used to generate the CSFRA element of the best-fit GEM SED. τ is the global star formation activity half-life. $SFR_{Int}^{GEM}(0)$, SFR_{Avg}^{GEM} and $SFR_{Obs}^{GEM}(t_{sb})$ are the initial, average and observed star formation rates per annum, SFR_{RR}^{GEM} is the SFR found in *Analysis I* from the 60μm luminosity using the prescription of Rowan-Robinson *et al.* (1997) given in Equation 7.8 and $N_{GMC}^{TOT}(t_{sb})$ is the total number of GMC's to have joined the ensemble to t_{sb}. Log $M_\star^{TOT}(t_{sb})$ is the Log to the base 10 of the total mass of star formed to t_{sb} and Log $M_{Dust}^{GEM}(t_{sb})$ and Log $M_{Dust}^{FH}(t_{sb})$ are the log to base 10 of the GEM ULIRG dust mass and the FH03 ULIRG dust mass respectively.

formation and the resulting equations used to derive the SFR from the CSFRA SED free parameters.

However, for the two intermediate scenario objects where the star formation rates obtained from the best-fit CSFRA SED 60μm luminosity and from the free parameters, match, it does appear that GEM generated results whereby what is essentially a snapshot of the SFR at t_{sb} i.e., that derived from the sum of a number of different instantaneous burst SEDs with varying ages, could be compared very favourably to one that assumes a power output which is entirely converted into sub-mm and IR dust radiation and uses the SED flux to obtain the SFR.

Turning now to the ULIRG combined dust mass, these values are also listed in Table 7.4.1 and it appears that they agree reasonably favourably in every instance, with the results being neither consistently over or under estimated with respect to the FH03 derived value or when considered in the light of τ. In a similar way to the SFR's obtained in *Analysis I*, it is relatively unsurprising that the dust masses obtained by GEM and FH03 match as the same optical depth is required to fit the FIR and sub-mm dust flux seen in the published ULIRG spectra. However, the question can be asked: if the GMCs joining the starbursting ensemble as the merger progresses originate in instantaneous burst systems having a low optical depth for the majority of their life-time (high η), how is the dust mass just identified built up over time?

In addition to the star formation rate at the current epoch, the GEM approach also provides an indication of the star formation history of each ULIRG via the average and initial star formation rates and the total number of clouds within which star formation has been initiated since the merger began $N_{GMC}^{TOT}(t_{sb})$. These values are also listed in Table 7.4.1 and the relatively large number of clouds joining each starbursting association in the elapsed period since $t_{sb} = 0$, along with the average star formation rates, demonstrates that star formation occurred in significant number of clouds in the past and it is via this mechanism that the dust mass builds up over time.

Summary of Analysis II

It would appear that comparison of the results obtained in *Analysis I* to those of *Analysis II* achieved reasonable consistency. Whilst it was found that the star formation rate history of a ULIRG could only be securely assessed for objects exhibiting an intermediate star formation scenario, it was clear that the free parameter dust mass did not appear to be

dependent on the assumed star formation scenario when compared to FH03, suggesting the model approach might be appropriate for its calculation.

7.5 Analysis III

This final analysis section considers the remaining result obtained during the identification of the best-fit GEM SED for each ULIRG; that no GEM SED using a CSFRA SED element which originated in the instantaneous burst SEDs of systems categorised low η, was able to achieve better than a 40% probability of non-random fit when matched to the published data. Models in the low η group are $M_{GMC} = 10^6 M_\odot$ at any efficiency η or from $M_{GMC} = 10^7$-, 10^8- & $10^8 M_\odot$ at $\eta = 0.01$, 0.025 or 0.5. Thus, the free parameters of the CSFRA SED element of the best-fit GEM SEDs have *in all cases* been skewed very firmly towards not only significant GMC mass but also to high star formation efficiency. The origin of this result was found to lie in the inclusion of powerful supernovae energy injections in the GEM modelling and the adoption of the upper limits of the short wavelength data points in the ULIRG fitting procedure.

It was mentioned in §7.1.1 that all published observational data used in the fitting at $\lambda \leq 3.5\mu$m in the rest frame, are assumed by both FH03 and this thesis work, to be 3σ upper limits. These upper limits all occur in the wavelength region of the SED where mildly attenuated direct source flux would be expected. Correspondingly, as noted in Section §5.5, where the behaviour of the instantaneous burst SEDs was described, it is models from the high star formation efficiency group which generate SEDs exhibiting the appropriate significant, only mildly attenuated source flux across UV, optical and NIR wavelengths.

Flux in the SED at these wavelengths originates with the inclusion of supernova in the modelling of the GMC density distribution as each of the systems in the high star formation efficiency group contains a powerful central source function, surrounded by a small radius of neutral dust. Once the supernova energy has been injected into the GMC, the high velocity superbubble created rapidly expands through the GMC, shocking and compressing the neutral material into a thin shell ahead of the hot superbubble interior. The dust in this shell is too hot to condense out and contribute to the extinction and the systems optical depth drops precipitously until the GMC becomes optically thin. Due in part to the high velocity of the superbubble, a significant period must elapse before the

shell temperature approaches the dust condensation temperature, and once it does, the shell volume is so vast that the condensed dust is distributed very sparsely and hence contributes little to the opacity.

Therefore in contrast to a low η system, a high η system does not experience significant recovery in its optical depth after the trough and from early times, direct, only mildly attenuated source flux is able to escape the system without interaction and generate flux across UV, optical and NIR wavelengths. It is the combination of the impact of powerful supernovae evacuating what is essentially an almost dust-free line of sight to the central source cluster and the necessity of fitting the published upper limits which has driven the best-fit CSFRA SEDs towards instantaneous burst SEDs from the high η group of models.

This conclusion presents two interesting considerations. First it might be expected that in a system where the dust did act as an enshrouding bolometer, the best-fit instantaneous burst SEDs might originate in the low η group. Secondly, fewer, high optical depth but equivalent mass GMCs might be required in the starbursting ensemble to meet the long wavelength emission, than when low optical depth clouds were used in the fit.

These hypotheses can be tested by artificially adjusting the upper limits of one object down-wards at short wavelengths to emulate potentially more realistic absolute fluxes originating in a dust-enshrouded system. The ULIRG SED library can then be tested against that adjusted flux distribution, the best-fit free parameters re-calculated and compared to those obtained when the published upper limit fluxes for the object were fitted.

Adjustment of the Short-Wavelength Upper Flux Limits

The object chosen for this thought experiment is 13428+5608 as it represents an intermediate star formation scenario with t_{sb} = 20Myrs and τ = 9Myrs. The value of the original published flux and the subsequently adjusted fluxes are listed in Table 7.8 such that Adjusted Flux = Published Flux/Divisor. In a similar way to the objects in the ULIRG sample, GEM combined SEDs were tested for goodness-of-fit using the range of the GMC star forming rate at t_{sb} = 0, mf_{sb}, listed in Table 6.5. In this instance results from the *Identification of the Best Fit* are displayed in Figure 7.10 for *all* four M_{GMC} and *all* seven η, as in contrast to the real ULIRGS in the sample, for the adjusted flux object, models from the both the low and high star formation efficiency group are able to achieve better than a 40% probability of non-random fit.

Table 7.9 lists all the results obtained using the published 13428+5608 upper limits

Wavelength μm	Upper Limit Published Flux $S_\lambda(Wm^2)$ (SED_{pub})	Divisor	Adjusted Flux $S_\lambda(Wm^2)$ (SED_{adj})
0.55	5.61e-15	10	5.61e-16
0.64	8.24e-15	10	8.24e-16
1.25	2.15e-14	5	4.30e-15
1.66	2.44e-14	5	4.88e-15
2.22	2.17e-14	5	4.34e-15

Table 7.8: Upper limit short wavelength adjusted fluxes for 13428+5608. The original published flux listed in column two are all upper limits and when divided by the value listed in column three, they become the adjusted fluxes displayed in column 4. The fluxes in column four were then joined with those published for 13428+5608 wavelengths $> 3.5\mu$m, which were not upper limits, and the fitting procedure repeated.

[hereafter SED_{pub}] and when the adjusted shortwave length 13428+5608 fluxes were fitted [hereafter SED_{adj}].

Considering the identification of the best-fit SED first, looking at all three plots on Figure 7.10 it would appear that the SED which achieved the very lowest χ^2 is appropriate as the best-fit GEM SED and that the attached apparent error is not so large as to bring the veracity of the best-fit into doubt. Perhaps the most important thing to note from Figure 7.10 is that the results for $M_{GMC} = 10^6 M_\odot$ at $\eta = 0.2$, indicated by the red squares, achieves the very best $\chi^2 = 1.5$, which is in direct contrast to the results for any ULIRG in the sample when the published upper limits were fitted. $\eta = 0.2$, $M_{GMC} = 10^6 M_\odot$ was classified in Chapter 5 as belonging to the low group of star formation efficiencies based on the dust-reformation behaviour of the optical depth distribution. Low η systems all exhibit similar extinction distributions as after reaching a small trough very early in the system's life time, the extinction undergoes a rapid recovery to more substantial values and thereafter remains optically thick, as at no time does e.g., $A_v^{TOT}(t)(\eta{=}0.2) \leq 0.1$. Another interesting result from the fitting is that no models from the $M_{GMC} = 10^9 M_\odot$, $\eta = 0.25$ and only a very few of the $M_{GMC} = 10^9 M_\odot$, $\eta = 0.15$ & 0.2 group achieved a better

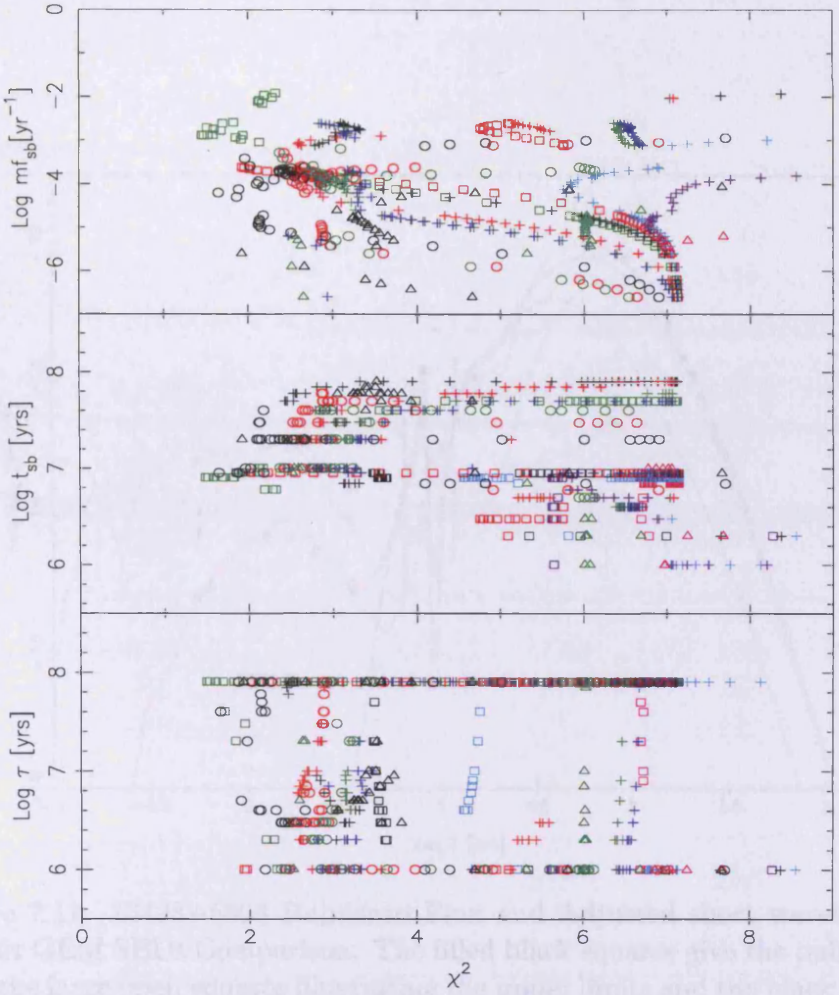

Figure 7.10: 13428+5608 Adjusted Flux χ^2 data. The top plot gives the rate at which GMC's are forming stars at $t_{sb} = 0$, mf_{sb} vs. χ^2. M_{GMC}= 10^6-, 10^7-, 10^8- & 10^9-$M_\odot$ are indicated by the square, cross, open circle and triangle and the results for the seven efficiencies 0.01, 0.025, 0.05, 0.1, 0.15, 0.2 & 0.25 are shown in pink, purple, turquoise, black , red, green & blue respectively. The same colour and marker scheme is used for the middle and bottom plots which show the time since the onset of star formation t_{sb} and the global star formation activity half-life τ respectively

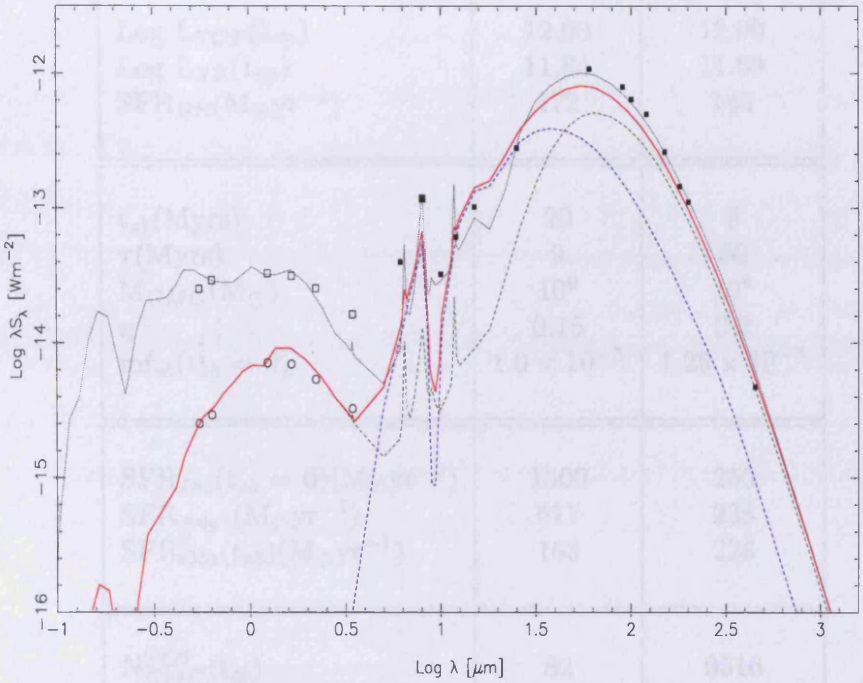

Figure 7.11: 13428+5608 Published Flux and Adjusted short wavelength Flux best-fit GEM SEDs Comparison. The filled black squares give the published data with the large open squares illustrating the upper limits and the black dashed line giving the best-fit GEM SED identified for the *published* fluxes and analysed in this thesis work. The open circles give the Adjusted Fluxes for 13428+5608 and the solid red, green dashed and blues dashed lines are the *Adjusted* Flux best-fit ULIRG, CSFRA and AGN SEDs respectively.

Quantity	SED_{pub}	SED_{adj}
Log $L_{TOT}(L_\odot)$	12.00	12.00
Log $L_{SB}(L_\odot)$	11.84	11.69
$SFR_{RR}(M_\odot yr^{-1})$	172	145
t_{sb}(Myrs)	20	8
τ(Myrs)	9	80
$M_{GMC}(M_\odot)$	10^9	10^6
η	0.15	0.2
$mf_{sb}(t_{sb} = 0)$	1.0×10^{-5}	1.25×10^{-3}
$SFR_{Int}(t_{sb} = 0)(M_\odot yr^{-1})$	1500	250
SFR_{Avg} $(M_\odot yr^{-1})$	617	238
$SFR_{Obs}(t_{sb})(M_\odot yr^{-1})$	163	226
$N_{GMC}^{TOT}(t_{sb})$	82	9516
Log $M_\star^{TOT}(t_{sb})$	10.08	9.46
Log $M_{Dust}(t_{sb})(M_\odot)$	7.58	7.44

Table 7.9: 13428+5608 Adjusted SED Results. The results derived for 13428+5608 using the *published* data (upper limits) from the best-fit GEM SED in *Analysis I & II* (SED_{pub}) are listed in the second column. The third column gives those quantities derived when the short wavelength ($\lambda \leq 3.5\mu$m) fluxes for were *adjusted* downward to emulate fluxes potentially more realistic of total dust enshroudment of the central source (SED_{adj}).

than 40% probability of non-random fit - almost precisely the reverse of the result found when the upper limits were fitted. The actual best-fit values of $M_{GMC} = 10^6 M_\odot$ and $\eta = 0.2$ firmly classify it as originating in the low η group of instantaneous burst model SEDs and the result suggests that the hypothesis that it was fitting the upper limits of the published fluxes which skewed that SED's results towards high η and large M_{GMC} is perhaps confirmed.

The best-fit SED_{pub} and SED_{adj} are displayed in Figure 7.11 for comparative purposes and first considering the luminosities obtained from those SEDs. As can be seen a higher starburst element luminosity was obtained from SED_{pub} than from SED_{adj} at Log $L_{SB} = 11.84 L_\odot$ and Log $L_{SB} = 11.69 L_\odot$ respectively. This may well be responsible for the discrepancy in SFR_{RR}s, with the higher starburst luminosity contribution generating the greater SFR_{RR}.

Moving to the starburst age and decay rate, it can be seen that the adjusted flux model is fitted best by a younger population at $t_{sb} = 8$Myrs than for the published flux model and that further, the decay attached to the adjusted flux model is essentially constant at $\tau = 80$Myrs. That the starburst is younger and contributes less to the luminosity in the adjusted flux model is also illustrated by the total mass of stars formed $M_\star^{TOT}(t_{sb})$ and the dust mass $M_{dust}(t_{sb})$, the values of which are both lower than for the published model fluxes.

The GEM SED free parameter rates $SFR_{Obs}(t_{sb})$ for the published and adjusted flux distributions are on Table 7.9 and it can be seen that the adjusted flux free parameter SFR is considerably over-estimated, not only in comparison to the 60μm luminosity rate but also to the free parameter rate when the published fluxes were fitted. Whilst it is tempting to make connections between e.g., the transmission properties of high vs. low optical depth clouds and the proposition that high optical depth clouds require more stars to illuminate the dust mass, or perhaps deliver some conclusion on the appropriateness of the bolometric corrections between the IR luminosity and the SFR, unfortunately this is not possible. As was mentioned in *Sample Discussion II*, it appears that GEM considerably overestimates the free parameter SFR when the indicated star formation scenario is constant and the adjusted fluxes are fitted by $\tau = 80$Myrs, implying the overestimation could be at a maximum. A much more rigorous testing of the GEM Library, using e.g., better estimations of the short wavelength fluxes, for a larger sample of ULIRGs, might provide more information on this issue.

Turning finally to the hypothesis that fewer, equivalent mass, optically thick GMCs would be needed to meet the long wavelength dust emission of the SED_{adj} than when the SED_{pub} was fitted. Table 7.9 shows that $N^{PUB}_{GMC}(t_{sb}) = 82$ star forming GMCs were required to fit the SED_{pub} flux whilst some $N^{ADJ}_{GMC}(t_{sb}) = 9516$ clouds were required to fit the SED_{adj} flux. However, what should be remembered is that the SED_{adj} was fitted with instantaneous burst SEDs originating at $M_{GMC} = 10^6 M_\odot$ whereas the SED_{pub} was best-fitted at $M_{GMC} = 10^9 M_\odot$ so essentially, the number of *equivalent mass* GMCs required by the SED_{adj} is only some $N^{ADJ}_{GMC}(t_{sb}) = 9$, which is considerably smaller than the number needed for the SED_{pub} fit. This conclusion is also weighed out by the values obtained for the observed dust mass at Log $M^{PUB}_{Dust}(t_{sb})(M_\odot) = 10.08$ and Log $M^{ADJ}_{Dust}(t_{sb})(M_\odot) = 9.46$, although it is likely that some of the difference in this last result is due to the relative difference in the GEM SED_{adj} and SED_{pub} CSFRA element luminosities $L_{SB}(L_\odot)$.

Summary of Analysis III

The hypothesis that a star forming ensemble exhibiting total dust enshroudment would be best-fitted using a CSFRA SED composed of instantaneous burst SEDs originating in the *low* η model GMC's is confirmed. Further, the suggestion that fewer equivalent mass, high optical depth clouds would be required in a dust enshrouded ULIRG is also confirmed.

The SFRs obtained from the 60μm luminosity of both the adjusted and published flux distributions matched reasonably well, with the discrepancy being explained by the differences in the starburst luminosity contribution to each model. As the adjusted flux model was best-fitted by a *constant* star formation scenario it was not possible to make significant comment on the difference between the SFR obtained using the CSFRA SED free parameters and that using the 60μm luminosity. This is because it was found in *Analysis II* that these SFRs only matched reliably when an *intermediate* star formation scenario was indicated.

Finally, the differences in the starburst age obtained showed that the dust-enshrouded adjusted flux model was best-fitted by a younger stellar population than the published flux ensemble, which is not surprising as it is at early times that the instantaneous burst SED systems are most optically thick.

It would appear that perhaps the wide range of the M_{GMC} & η parameter space chosen and the optical depth distributions developed in this thesis might be able to shed light on the physical characteristics of ULIRGs existing in a broad variety of evolutionary states.

What this thought experiment has made abundantly clear however is the urgency of the need to improve the upper limits to the short wavelength data.

7.6 Conclusion to the Analyses

It was found that it is possible to generate a model library of AGN and CSFRA SEDS from scratch which, when matched in pairs, produces a library of ULIRG SEDs suitable for testing against the published data for a small sample of nearby objects. A best-fit GEM SED was identified which in all cases was able to achieve a reduced $\chi^2 \leq 3$, indicating there was a good probability of non-random fit.

Degeneracy in the ULIRG SED library and the veracity of the modelling approach were examined in three Analyses sections. The first of these found that the SFRs derived using the GEM SED 60μm luminosity compared favourably with those of FH03, as did the fractional and total luminosities of the AGN and CSFRA to the GEM SED. Examination of the values taken by the starburst age t_{sb}, the global star formation activity half-life τ and the implied nuclear fuelling and merger state were also generally in good accord with observations of the sample published in the literature.

Analysis II showed that the SFRs found from the GEM SED 60μm luminosity, could be replicated using the GEM SED free parameters only when the scenario indicated by the star formation activity half-life τ was intermediate. For constant and instantaneous burst star formation scenarios the GEM SED free parameter SFRs were over and under estimated respectively when compared to the 60μm rate. However, for the two objects in the sample which exhibited an intermediate scenario, in addition to the SFR at the current epoch, the GEM approach was able to provide the initial and average star formation rates, the number of clouds within which star formation is initiated as time passes and the mass of stars formed.

Each of the dust masses calculated in *Analysis II* for the six objects in the sample, using the GEM free parameters and the gas density distribution of the single GMC originating the instantaneous burst SEDs comprising the CSFRA contribution to the best-fit GEM SED, were of similar order of magnitude to those of FH03. In all cases it was found that the dust masses derived from the GEM free parameters were the result of aggressive star formation in the past and in contrast to the SFR, the calculation did not appear to be dependent on the value of the global star formation activity half-life τ.

Analysis III considered the final result of the thesis, whereby the CSFRA component of

each ULIRG SED had been skewed very firmly towards high star formation efficiency and GMC mass. Overall the results of the thought experiment conducted perhaps implied that the GEM ULIRG SED library could be employed to model systems where the dust acts as an enshrouding bolometer, as well as systems where direct, only mildly unattenuated source flux is able to escape entirely, without interacting with the dust. It might be expected that in a system exhibiting significant short wavelength UV, optical and NIR flux, this flux can be best matched using a CSFRA SED originating in the high M_{GMC} & η model group, where powerful supernova have evacuated what is essentially a dust-free line-of-sight to the central source function. Conversely, if there is little direct short wavelength flux exhibited in the ULIRG SED, the CSFRA SED element would originate in the low M_{GMC} & η model group where the dust-evacuation impact of the very powerful supernovae is absent. Whilst it is not necessarily possible to derive the free parameter dust-enshrouded SFR or history in a ULIRG exhibiting constant or instantaneous star formation scenarios, the 60μm luminosity method of estimating the dust-enshrouded SFRs does appear to be appropriate for the adjusted flux object.

The assessment of the veracity GEM approach is now concluded. Taking everything into consideration it might be said that the method of modelling ULIRGs using a combination of AGN SEDs and CSFRA SEDs, the latter of which includes the treatment of the impact of supernovae on GMCs, might provide reasonable recourse for predicting the observed physical characteristics of some local ULIRGs.

Before the thesis can be concluded however, brief consideration must be given to some of the more obvious potential sources of error in the GEM approach so that a complete picture may be obtained.

7.7 Potential Sources of Error in the GEM Approach

In order to obtain the complete picture, a brief discourse must be made on the primary GEM error sources. Intimately linked to this discussion are improvements to the modelling approach, as many of the issues raised are theoretically solvable given sufficient time, money and inclination! 2

Temperature of the Supershell

Perhaps the error source having the most significant impact on the model results are those arising from non-equilibrium ionization affects in the calculation of the temperature of the

supershell. The GEM approach has used the equations of MK87 to model the motion of the superbubble and those authors presumed a uniform neutral density of $n_o = 1cm^{-3}$ existed ahead of the superbubble as this ensured that the assumption of steady-state ionization equilibrium was valid. This 'on-the-spot' approximation ensures that once the supershell has collapsed into isothermal motion it maintains its low temperature via e.g., forbidden line or bound-bound cooling. However, it was also noted in Chapter 5, where the method by which calculation of the supershell temperature in this thesis work was developed, using a neutral density of $n_o = 1cm^{-3}$ and the stall conditions of e.g., OY96 or DP05 led to superbubble radii which exceeded observation and resulted in a growth rate discrepancy.

Therefore in an attempt to further progress, this thesis work has used a neutral density of $n_o = n_{av_{H_2}} = 300cm^{-3}$ in the GMC and then exploded the superbubble into a medium already ionized by the stellar winds, which is consequently at a lower density. However, once the superbubble has overtaken the HII region IF it is expanding into $300cm^{-3}$ and material at this high density, when shocked and compressed into the neutral supershell, is very likely to invalidate the 'on-the-spot' approximation!

The stellar populations considered in this thesis are clusters for which the supernovae energy has been taken to be continuous and in an attempt to model multiple superbubbles catching up with one another, each new shell created in a time step is assumed to merge with any existing shells to form one single supershell. Therefore in Chapter 5 a three step method of calculating the supershell temperature was devised that took into account not only the temperature of the gas existing in the supershell at a particular time t, but also allowed for the ingress of hot shocked gas from the most recently formed shell *and* attempted to make some accommodation for the lack of heat loss from the potentially very dense supershell shell caused by non-equilibrium ionization affects. It is this approximation of the supershell temperature calculation that is perhaps the most serious source of error in the GEM modelling approach.

It is possible to suggest that if the temperature of the supershell were under-estimated it would be likely that the extinction distributions belonging to the high η group of models would exhibit more of a recovery in the opacity after reaching a trough. Potentially, that the systems would then not show the optically thin characteristics for a substantial part of their life-time needed to fit the ULIRG upper limits - perhaps the high η model extinctions would then resemble those of the low η models. This would result in the M_{GMC} and η

corresponding to the CSFRA contribution to the best-fit GEM SED potentially being lower than those achieved in the ULIRG sample fitting. It is difficult to say what affect this would have on e.g., the SFRs calculated from the CSFRA free parameters; it is possible that they would rise, as the transmission properties of low optical depth clouds perhaps require more stars to illuminate the dust mass. However, it was not possible to reach this conclusion from the thought experiment conducted in the last section due to the degeneracy of the model in τ. What is clear however, is that it is very likely that the SFRs calculated from the e.g., the 60μm luminosity would remain unchanged.

Conversely, if the supershell temperature in this work has been over-estimated, the low η models might not exhibit the recovery seen in their extinction after the trough and would potentially drop to an optically thin regime rapidly and remain there for the majority of the system's life-time. In this instance the star formation rate calculated from the free parameters might likely plummet. However, little impact would be made on the high η GMC extinction distributions due to their already low life-time extinction.

So, there is little recourse for assessing the appropriateness of the supershell temperature calculation except perhaps by comparing the results obtained here to those already published in the literature and that was carried out in *Analysis I & II* with apparently favourable results. A better test would be to compare these results to those generated across the same parameter space using a fully 3-dimensional, hydrodynamic code to model the evolution of the GMC. A hydrodynamic code makes use of Eulers Equations to trace the thermal evolution of the gas itself and would therefore model e.g., the forbidden line or bound-bound cooling in the supershell explicitly. Such a code, *Maartje*, has been developed by Lim & Mellema (2003) and this employs the Flux-Vector Splitting Method to calculate the fluxes in all three co-ordinate directions by making use of a predictor-corrector method. A ray tracer is used to follow the transfer of ionizing photons along the grid because the transport of ionising radiation from one part of the grid to the other alters its hydrodynamical properties. Importantly, the code calculates the ionization, heating and cooling rates (see Mellema *et al.* (1998)) in addition to calculating the local chemistry (Lim & Steffen 2003) and these can be used to estimate the dust density distribution via the adoption of a suitable gas-to-dust ratio. A code such as this could be used to model the expansion of stellar winds and supernova bubbles in a non-uniform density distribution and calculate the ionization along with the shock structure of the cloud/galaxy. Comparing the gas temperature distribution generated by a hydrodynamic code to that obtained

from the GEM modelling approach over a similar parameter space would give a much better idea of the error contained within the GEM supershell temperature calculation (but in the process render GEM obsolete!).

Dimensionality

Turning now to the dimensionality, clearly a 1-d model of evolution is a vast over-simplification. First, there are suggestions that IR, optical and UV flux in, for example, the SED of M82 is best explained by a clumpy interstellar medium (Siebenmorgen & Krügel 2007). In that scenario, either hard radiation is leaking out through the clumps or funnels created by supernova explosions or stars exist outside the nuclear dust clouds (Siebenmorgen & Krügel 2007). In the GEM model, this short wavelength flux in the SED is attributed to direct stellar radiation leaking out of an optically thin cloud, but never-the-less, the interstellar medium is unlikely to be uniform; something a 1-dimensional model cannot take into consideration. Further evidence that modelling in 3-d might reduce error was provided by DP05 who suggested that one reason for the growth rate discrepancy found in their supernovae model was the lack of dimensionality and the discussed effects.

The flexibility of environment provided by a 3-d code can also be used to improve the modelling approach and this was illustrated by Siebenmorgen & Krügel (2007) who had good success in fitting ULIRG SED's by including *hotspots* in addition to the central stellar clusters. These hotspots arise when a luminous star is enveloped by a cloud with a density considerably above the mean density of the nucleus. Siebenmorgen & Krügel (2007) were able to achieve a much better fit to MIR emission from the nucleus than when using stellar clusters alone . So it might well be that distributing hotspots randomly though a 3-d cloud could also improve estimations of the model SED flux. In summary, it appears that galactic-scale outflows originate from multiple sites of star formation in highly inhomogeneous media and therefore the extension of the GEM modelling approach into three dimensions is perhaps the best way to proceed.

Source Function

Another source of error in the GEM modelling approach might originate with the STARBURST99 stellar synthesis code and its evolutionary tracks and model atmospheres. As one example, enhanced mass-loss was introduced into e.g., the Meynet *et al.* (1994) stellar evolutionary tracks in order to account for rotation and match observations of e.g., Wolf-

Rayet stars (Leitherer & Heckman 1995). However, if rotation was accommodated for from first principles, there would be no need to enhance the mass-loss rates which would remove a fundamental assumption. This would no doubt improve the evolutionary tracks as the mass-loss rate of a star is the biggest single factor that governs its life-cycle.

In addition to the potential sources of error contained within the stellar synthesis code itself, there are those that arise from its application in the GEM modelling approach. For example, as mentioned in Chapter 3, the STARBURST99 source functions were generated using the instantaneous burst star formation scenario; the stellar population is formed at $t \sim 0$, whereafter is evolves passively over time, with no new stars being born. Then, rather than extending the resultant instantaneous burst model SEDs to approximate constant star formation, a better approach might be to start with source functions generated by a constant star formation scenario, also an option in STARBURST99 and to then evolve the GMC's under their influence explicitly. Not only would this allow the appropriateness of the CSFRA in a wide variety of circumstances to be assessed but would also provide an extensive model SED library for matching to ULIRG published data, in addition to the existing model instantaneous burst SED library.

Finally, it was mentioned that the Equations used to derive e.g., the SFR from the CSFRA SED were tailored particularly to the GEM modelling approach. The result that the SFR from the CSFRA SED free parameters and that from the SED's integrated 60μm luminosity only matched in an intermediate star formation scenario. Generating the SEDs using a source function in constant star formation mode explicitly would remove the necessity of derive equations to quantify the SFR and it could be obtained directly from the SED in the absence of any free parameters or approximations.

Another major source of error might be that of the assumed Initial Mass Function (IMF) of the stellar population. The IMF used in the GEM approach amounted to essentially a Salpter distribution with the improvements of Kroupa (2002) to take account of variation for the very lowest mass brown-dwarfs. The slope of the IMF, defined as the frequency distribution of stellar masses per unit logarithmic interval of mass, is a steeply decreasing function of mass which ensures that, for e.g., the Kroupa (2002) parameterization used here, all the stellar mass is concentrated into low-mass stars, whilst the steep stellar mass-luminosity relation compensates for the downward-weighting affect (DP05).

Considering the prescription of Kennicutt (1998), Equation 7.9, which uses the integrated 8-1000μm luminosity and the assumption that the dust shell is wrapped around

the star formation region so that the IR emission acts like a stellar bolometer. With this assumption, for a stellar population with age 1 Myr having a solar abundance, DP05 calculated that each solar mass of *massive stars* produces an IR flux of log $[L_{IR}/ergs^{-1}]$ = 47.41 for the Kroupa (2002) parametrisation. However, the IR flux per solar mass of *all stars* is very different at $\log[L_{IR}/ergs^{-1}] = 46.70$. This shows that assumptions about the IMF can introduce a potential uncertainty of a factor of two in inferred star formation rates when calculated using e.g., the integrated IR luminosity. Whilst it is currently unknown what form of the IMF might apply in ULIRGs or if the IMF varies from galaxy to galaxy, STARBURST99 offers the option for user-defined IMFs composed of up to five power laws with individual exponents to cover the wavelength region, so the possibility exits of varying the IMF space and comparing the results to further observations.

Considering now the metallicity of the stellar population which is extremely important to the mass-loss rates and hence the stellar winds needed to drive the HII region evolution. As far back as 1926, Milne proposed that radiation pressure applied force to the ions in the atmospheres of stars, pushing them outwards to create a wind. Massive stars have almost opaque winds and as O stars emit strongly in the UV where many atomic species can have thousands of lines, the wind is line driven (Norris 2003). The photon momentum transfer is proportional to the number of optically thick lines which can interact with the wind. The metallicity of the stellar population therefore has enormous influence over the number of heavy element lines and the balance of optically thick to optically thin lines (Norris 2003). Thus, the chemistry of the wind has an affect on the radiative forces working on it and hence the mass-loss rate.

Theoretically the mass-loss rate $\dot{M}$ is expected to be proportional to the metallicity Z of the environment, to a power law exponent such that $\dot{M} \propto Z^m$. From studies of Castor *et al.* (1975), Abbott (1982) and Kudritzki *et al.* (1987) m ranges from 0.5 (Kudritzki *et al.* 1987) to 0.94 (Abbott 1982). All the GEM models followed ERR00 and were calculated in STARBURST99 using solar metallicity (Z=1, m=0.5 (Meynet *et al.* 1994) as it was felt that including this as a further free parameter was outside the scope of the thesis work. However, there are five individual parameterizations of the metallicity available for use in STARBURST99 so incorporating this parameter at a later date would be eminently possible and would be particularly important if modelling galaxies at higher red-shifts.

Turning to the star formation efficiency parameter, which defines the amount of gas

in each GMC available for star formation, the maximum limit was chosen as $\eta = 0.25$. However, in Chapter 3 it was mentioned that for e.g., M82, Hughes *et al.* (1994) used ISO spectroscopy to estimate an implied gas consumption rate of between 0.2-0.39, so clearly the parameter space for the star formation efficiency could be expanded to test higher values. That the lowest values of η, when coupled to the lower GMC masses reverted to the HII region solution because the superbubbles created were not powerful enough to escape the HII region ionization front with their supershells intact, perhaps illustrates that there is no need to investigate further at the lower end of the star formation efficiency parameter space. Obviously the possibility of broadening the parameter space by choosing smaller increments in the star formation efficiency might also improve the ULIRG fits.

In a related area, Chapter 5 discussed the use of a constant supernova luminosity function and it was found that in this particular instance it was appropriate. However, it was also mentioned that DP05 published an equation to describe a time-dependent supernova luminosity which could be numerically integrated. Although this equation was not incorporated into the GEM approach it would be interesting to change the form of the supernovae luminosity function from time-dependent to time-independent in future work and to assess the impact of the time varying function on the results.

Short Wavelength Data

Better estimates of the absolute values of the short wavelength fluxes that are currently assigned as upper limits, might greatly improve the ability of the GEM model to predict ULIRG physical characteristics. As was mentioned earlier in this chapter, all the published data at $\lambda \leq 3\mu$m were assumed to be upper limits, as the contribution from old red Population II stars could dominate the emission at NIR and optical wavelengths and this contribution is currently unquantified. Including the emission from these stars would be a considerable step forward but due to the large size of the attached errors, it would have been essentially fruitless to model the emission from this population in the thesis. However, attempts to improve the estimation of these short wavelength fluxes are currently being undertaken by e.g., the UKIDSS next generation near-infrared sky survey which is the successor to 2MASS. The UKIDSS deep survey began in May 2005 and aims to survey around 7500 square degrees of the Northern sky, extending over both high and low Galactic latitudes, in JHK to K=18.3 and will be a true NIR counterpart to the Sloan survey. The survey instrument is WFCAM on the UK Infrared Telescope (UKIRT) in Hawaii and

amongst its principal targets are high-redshift dusty starburst galaxies and more local elliptical galaxies (UKIDSS homepage: http://www.ukidss.org/).

Also appropriate for improving the short wavelength data points will be observations from the James Webb Space Telescope (JWST) which has a 6.5m primary mirror and is planned for launch in 2013. There will be four science instruments on JWST: a NIR camera, a NIR multi-object spectrograph, a MIR instrument, and a tunable filter imager covering 0.6 - 27μm in wavelength (JWST homepage: http://www.jwst.nasa.gov/). The JWST has therefore been designed to work principally in the IR range with some capability in the visible. Observations with the JWST might lead not only to better estimates of the star formation rate and dust mass, as old red stars contribute to the emission with out contributing to the dust mass, but also to potentially removing the biasing of the best-fit CSFRA SEDs towards high η and M_{GMC}.

The Dusty GMC

Moving now to the physical circumstances of the GMCs themselves, using four bracketed GMC masses - $M_{GMC} = 10^6$-, 10^7-, 10^8- & $10^9 M_\odot$ is an oversimplification. As mentioned in Chapter 3 this is weighed out by the likes of Solomon *et al.* (1987) who used the CO luminosity of 273 molecular clouds in the Milky Way to show that the mass distribution varied with index γ = -1.5 or Dame *et al.* (1986) who use the Columbia CO survey to determine an equivalent slope from clouds in a section of the Perseus spiral arms. Whilst it is not necessarily the case that GMC mass distribution in ULIRGS varies in the same way as the Milky way, it is much more likely that the GMCs would form a distribution of masses rather than a series of discrete values.

Considering the assumption of a uniform density, both in the neutral region and in the supershell. This is likely to be a considerable over-simplification which a fully HD code could dispense with.

The dust model used in this thesis work has the same properties as those thought to exist in the Milky Way, yet it is uncertain that this model is totally appropriate. For example, two well studied local dwarf galaxies: the Large and Small Magellanic Clouds, are deficient in heavy elements by factors of about 2.5 (LMC) and 7 (SMC) (Whittet 2003). Consequently it is likely that both the quality and quantity of dust in these galaxies' interstellar mediums is somewhat different to the Milky Way. In the LMC for example, whilst variation from Milky Way extinction is found in e.g., the FUV rise and the 2175$\AA$

bump in the vicinity of the 30 Doradus complex, the general form of the extinction in the LMC is reasonably similar to that of the Milky Way. However, the extinction curve derived for the SMC seems to be radically different as it displays a steep continuum and extremely weak or even absent 2175$\AA$ bump absorption . This latter result has been linked to the low metallicity of the SMC and its effect on grain production (Whittet 2003). The ingredients and quantity of dust which therefore leads to the bump absorption or FUV extinction in galactic extinction curves must vary from galaxy to galaxy.

One group which has successfully utilized a dust recipe other than that thought to exist in the Milky Way is Gordon *et al.* (1997) who showed from colour-colour plots of the dust in starburst galaxies that they had an extinction curve lacking the 2175$\AA$ bump, like the SMC curve, but a steep FUV rise intermediate between the LMC and SMC curves. Gordon *et al.* (1997) modelled starbursts using both Milky Way and SMC extinction type dust and found that the dust was unlikely to have formed with these properties and more likely acquired them as a result of massive star formation occurring in the starburst . Clearly then, varying the quantity and type of dust in the recipe and carrying out a comparative analysis with observations might improve the ULIRG fits.

Finally, regarding the component species of the starburst dust model, new prescriptions have appeared more recently in the literature, containing a broader range of elements - particularly for the Polycyclic Aromatic Hydrocarbon content so important in fitting the prominent mid-infrared features characteristic of a starburst galaxy. For example Piovan *et al.* (2005) presented a detailed study of the extinction properties of dusty interstellar mediums including graphites, silicates and PAHs and found good global agreement between theory and the ISM extinction and emission data of the Milky Way, LMC and SMC.

Radiative Transfer

It is now appropriate to briefly consider DaRT, the radiative transfer code used in this thesis work. DaRT was written as part of a Ph.D. project and published in its spherically symmetric form in 1990 (Efsthathiou & Rowan-Robinson 1990*b*). Whilst DaRT is suitable for the 1-d semi analytic approach taken in this thesis work, it would be unsuitable for the complex radiative transfer calculations needed in a fully hydrodynamic model. A 3-d radiative transfer code has been published more recently which would be capable of carrying out these complex calculations, *MOCASSIN* (Ercolano *et al.* 2003).

MOCASSIN uses the MPI parallel programming approach and has successfully modelled ionized and dusty nebular with complex geometries and inhomogeneous media and is one of the few codes which could incorporate more than one internal illumination source which would be needed to include hotspots. *MOCASSIN* includes non-equilibrium emission from small particles such as PAHs, vital for modelling the MIR emission feature of starbursts as well as the atomic processes which dominate heating and cooling within the neutral region. As the code calculates the dust emission in all four Stokes vectors and the atomic FIR fine-structure lines, as well as from atomic and ionic transitions, it is a power diagnostic tool for interpreting the emission from hot, dusty, dense, ionized and neutral regions.

χ^2 Fitting

Finally in this section rather than simply multiplying the AGN SEDs by mf_{agn} to expand the luminosity space they cover, it would no doubt be better if models were run through the radiative transfer code individually calibrated to the required luminosity.

Considering the rate at which GMCs are forming stars at $\mathrm{t}_{sb} = 0$, mf_{sb} the parameter space over which the models were tested could perhaps be extended and sampled more closely in $\Delta\mathrm{mf}_{sb}$. However, the major source of error in the χ^2 fitting is likely to be the restriction of the starbursting ensemble GMCs to one individual mass per fit. ULIRGS probably exist in a wide variety of evolutionary states and the inclusion of the GMC mass, whilst introducing a further free parameter, might considerably improve the ULIRG best-fits.

This concludes the discussion on the major potential sources of error in the GEM modelling approach. The next chapter presents the conclusions to this thesis and ends with a short discussion on a potential program of future research.

Chapter 8

Conclusions & The Future

This chapter presents the main conclusions from the thesis, paying particular attention to the new advancements. A short program of future work which might benefit the research field is then considered before the thesis closes with some brief concluding remarks.

8.1 Conclusions

The thesis generated a new semi-analytical treatment of the effects of supernovae on ULIRG SEDs. Three source elements were developed to accomplish this: an AGN, HII region and supernovae model.

AGN Model

The AGN model was based on the successful method of FH03. A PG Quasar source function was embedded in a dusty torus, the radiative transfer of flux calculated and the emergent SEDs generated. The parameter space of FH03 was considerably extended by using three values for the dust temperature and three for the equatorial optical depth at ultra-violet wavelengths. With fifteen viewing angles in each model, this resulted in 135 explicitly calculated SEDs. These were then extended in luminosity space to cover the range $10^{11}L_{\odot} \leq L_{AGN} \leq 10^{13}L_{\odot}$ for use in the ULIRG fitting.

The radiative transfer code DaRT, was received from its authors ERR90 in a totally uncommented form. The method by which calculation of the radiative transfer of flux is accomplished in DaRT was divined and the code throughly benchmarked. It was found that due in part to the shell indexation being out of step, DaRT missed approximately 30° in angle when integrating, which resulted in a serious lack of flux in the emergent spectra. The root of the fault was eventually located and repaired and ERR00 notified

(2004). Having ascertained the code was working correctly, values for the grid integration parameters were identified which allowed temperature convergence of a dusty system in a minimum time whilst also using the minimum of computer resources (See Appendix A).

HII Region Solution

The first element of the starburst solution; the HII region model, was based on the scheme developed by ERR00 for a GMC evolving under the influence of a stellar ionizing flux. ERR00 utilized a constant stellar flux source function and choose as that constant value the flux emitted by a cluster at t = 3.3Myrs. At this time, most of the OB supergiants in the association are still on the main sequence and the value of the ionizing flux is high. Using such a large value of the ionizing flux at all times meant that ERR00 essentially modelled a single ionized bubble which maintained its ionization rate and therefore distorted the affect of a varying flux. In reality a series of slower and slower bubbles might actually be generated and this is better modelled with a time-dependent ionizing photon flux.

The thesis therefore advanced the work of ERR00 by incorporating a time-dependent ionizing stellar flux into the HII region evolution. The central source functions were generated using the stellar evolutionary synthesis code STARBURST99 (Leitherer & Heckman 1995) and a new equation to describe the time-dependent expansion of the HII region was developed. This used a Taylor series expansion to the second order of the classic Spitzer (1978) equation for the radial evolution of an HII region. The equations defining the evolution of the GMC were then programmed into the bespoke computer code GEM.

ERR00 were able to assume, using MK87, that all superbubbles which would be generated by the source cluster would remain in trapped inside the HII region ionization front for all times t and it was therefore unnecessary to incorporate the effect of supernovae energy injection on the dusty GMC. This is indeed the case if a high value constant ionizing flux is employed as in ERR00. However, as the thesis employed a time-dependent flux, the magnitude of which decayed in time, most superbubbles generated as the massive stars exploded, quickly overtook the HII region ionization front to become the driving force behind the system's evolution.

However, for six of the lowest stellar cluster mass models in the thesis parameter space, the velocity of the superbubble generated by the source cluster dropped below the sound speed in the HII region whilst the bubble was still trapped within the ionization front. Es-

sentially these superbubbles have insufficient momentum to continue their progress though the ionized sphere as random motions in the upstream gas cause them to lose their integrity. In this instance a model reverts to the HII region solution and the supernovae solution is not invoked. It was found that all systems with a central stellar mass $M_\star \leq 10^5 M_\odot$ invoked the HII region solution for all t.

Supernovae Model

The supernovae solution was developed using the standard-pressure driven expansion model of MK87 and MM88. This simulated the evolution of a GMC under the influence of a continuous supernovae energy injection. Previous application of the standard-pressure drive model to supernovae systems, for example OY96 & DP05, used embedding densities more representative of the interstellar medium and a pressure equilibrium, or stall condition, to signal the change from adiabatic to isothermal motion. However, both OY96 and DP05 generated superbubbles with expanded to too large a diameter without reaching the stall condition and a growth rate discrepancy with observations was identified.

The thesis used an average embedding density $n_{av_{H_2}} = 300\text{cm}^{-1}$ which is more representative of a GMC and a specific cooling radius and time (MM88) at which the approximated adiabatic supershell collapsed into a fully radiative zone. In contrast to ERR00, OY96 & DP05, simple shock physics were employed to trace the gas density enhancement across the shock in both the adiabatic and isothermal phases. However, expanding the superbubble into a density of $n_{av_{H_2}} = 300\text{cm}^{-1}$ meant that the supershell was likely to be very dense and hence the assumption that the shell was in ionization-equilibrium was likely invalidated. A new three-step process was therefore developed to estimate the gas temperature of the supershell. This attempted to not only take into account the lack of radiative heat loss from the very dense shell, but also the temperature of the gas existing in the shell at a particular time-step, the ingress of hot gas overtaken and the cooling effect of volume dilution as the supershell expands.

The gas temperature was linked to the quantity of dust which could condense out of the shell to contribute to the extinction by a temperature dependent dust condensation factor. New expressions were then developed to quantify the evolution of the optical depth along a line of sight and these, along with the motion equations and the relationships required for the DaRT radiative transfer code initial inputs, were also programmed into GEM.

As the shell sweeps up all the mass ahead of it during expansion, at the point it ap-

proaches the dust condensation temperature it often provides the majority of a system's extinction. It was found that the extinction distributions could be divided into high and low star formation efficiency η with the break occurring at $\eta \approx 0.1$. Using the approximation $M_\star = M_{GMC}.\eta$, low η systems had supershells with gas temperatures below the dust condensation temperature at the GMC boundary $R2_W$, whereas high η models had supershell temperatures in excess of the dust condensation temperature at $R2_W$.

Whilst the extinction of a low η system initially experienced a decline as the superbubble expanded through the system accumulating the upstream gas into a shell too hot for dust to exist, as time went on, the extinction reached a trough and then recovered to more substantial values in a dust reformation scenario. Thus a low η model essentially remained optically thick for its entire lifetime. Evidence from the literature (e.g., Barlow, Sugerman, Fabbri, Meixner, Fisher, Bowey, Panagia, Ercolano, Clayton, Cohen, Gledhill, Gordon, Tielens & Zijlstra 2005; Sugerman, Ercolano, Barlow, Tielens, Clayton, Zijlstra, Meixner, Speck, Gledhill, Panagia, Cohen, Gordon, Meyer, Fabbri, Bowey, Welch, Regan & Kennicutt 2006) supported this scenario with observations of dust shells around supernovae.

In a high η model, where the supershell exceeds the dust condensation temperature at $R2_W$, the extinction dropped extremely rapidly to reach a minimum of $A_v^{TOT} \leq 2$ at $R2_W$ where it remained for some time as the superbubble expanded through the ambient region. Eventually, the supershell is able to cool to the condensation temperature, but as the shell volume at this point is so vast, the extinction does not exhibit substantial dust reformation and the optical depth remains low for the system's life-time.

GEM was then run 28 times to obtain the dust density distribution for all parameter combinations on the model grid. The distributions were then irradiated by the appropriate STARBURST99 stellar cluster SED, the radiative transfer of flux calculated and the emergent SEDs obtained.

The instantaneous burst SEDs calculated by DaRT for the supernovae solution could be similarly categorised as high or low η based on their spectral behaviour, primarily at short UV, optical and NIR wavelengths. The low η models appeared to be representative of a dust enshrouded source function where most it not all UV and optical radiation was reprocessed and re-emitted into the infrared - the dust acts like a bolometer. Conversely, those models classified high η tended to be optically revealed and exhibited substantial, only mildly attenuated source flux at short wavelengths.

A table of the generalised predicted spectral characteristics which might be observed in low and high η systems was presented. Behaviour was considered over the three wavelengths regimes: UV & Optical, NIR & MIR and the FIR & sub-mm at early ($t \leq 10$Myrs) and late ($t > 10$Myrs) times.

ULIRG SED Library

The SEDs generated by DaRT for the supernovae and HII region solution were paired in turn with those generated by the AGN solution and the resulting combined ULIRG SED was matched to the published data from six nearby ULIRGs. It was found that none of the ULIRG SEDs tested were able to achieve a better than 40% probability of belonging to the same population distribution as the published SEDs. This was likely because a ULIRG does not consist of a single GMC but rather more likely consists of an ensemble of GMCs. This was accounted for in the matching process by multiplying the emergent supernovae or HII region SEDs by a constant factor to simulate multiple clouds. It was thought that this restriction was responsible for the limited success achieved when matching the instantaneous burst SEDs to the ULIRG published flux.

Therefore the instantaneous burst library was extended to approximate constant star formation (CSFRA), using the classic decay parameter τ and the ULIRG sample re-fitted. The primary difference when simulating constant star formation is that many different GMCs and hence SEDs, are assumed to join the starbursting ensemble as it evolves. Therefore, rather than the emergent CSFRA SEDs being the sum of many equivalently shaped SEDs, they are the sum of many GMC SEDs, each representative of a different evolutionary state.

Significantly greater success was obtained when re-fitting the ULIRG sample using the AGN SEDs paired to the CSFRA SEDs. For all six ULIRGs in the sample a combined SED from the model library achieved a better than 5% probability of non-random fit to the published data. As it is currently unknown if instantaneous or more continuous star formation fits ULIRGs best (e.g., Kewley *et al.* (2002), the thesis result is indicative that a more constant star formation scenario for ULIRGs.

ULIRGs Results

It was found during the testing process just discussed that the thesis modelling approach appeared to provide a suitable means of processing GMC material so that ULIRG evolution

could be examined.

The best-fitting combined GEM ULIRG SEDs were able to generate star formation rates, using both the integrated infrared and 60μm luminosity of the CSFRA SED, which in every case matched very favourably with those published in the literature. Further it was found that the power source implied by the fractional contributions of the AGN and CSFRA SEDs to the total luminosity were also in agreement with the literature. Finally, the ULIRG age and the merger and interaction state implied by the free parameters of the CSFRA SED were in good agreement with published observations and conclusions.

It was found that the sample contained two objects which exhibited an instantaneous burst star formation scenario (00262+4251 & 15250+3609), two which exhibited approximately constant star formation (14347-1447 & 23365+3604) and two which were intermediate between these two extremes (12540+4251 & 13428+5608).

These results demonstrate that the thesis has generated a synthetic ULIRG SED library which can be successfully used to predict the physical characteristics of a small sample of nearby ULIRGs. This library could be made available on the world wide web, allowing the research community to obtain ULIRG SEDs which match other observations. These SEDs could then be used to infer a range of physical conditions in the observed object, *without* the necessity of conducting the radiative transfer simulations explicitly. This would provide a useful resource for better understanding the local universe.

An attempt was also made to use the free parameters of the CSFRA contribution to the GEM ULIRG SED to find the star formation rate, dust mass and total stellar mass independently of the SED luminosity. The star formation history of the ULIRG was also obtained using the initial and average star formation rates along with the number of GMC's to join the starbursting ensemble over the ULIRG's life-time.

Unfortunately, it was only in the ULIRGs which were found to exhibit an intermediate star formation scenario that the derived star formation rate from the free parameters and from the 60μm luminosity matched. In the two constant star formation cases the free parameter SFRs appeared to be somewhat overestimated whilst for the instantaneous burst star formation objects, the SFRs were underestimated. However, the dust masses estimated from the mass, efficiency and dust density distribution of the instantaneous burst SEDs contained within the best fitting CSFRA SED, matched those of FH03 reasonably well.

As was mentioned at the end of Chapter 5, there is very little information available

in the literature on generating the constant star formation rate approximation and most of the equations were derived by the author of the thesis for specific application to the GEM modelling approach. As the derived dust masses appear to be appropriate there is the possibility that it is Equation 7.11 for the observed CSFRA SFR which might be inappropriate. Alternatively if the error lies in the GEM modelling approach it is most likely in the calculation of the temperature of the supershell.

Perhaps one of the most important results obtained when testing the ULIRG sample was that each of the best-fitting CSFRA SEDs were generated from the high η set of models. As mentioned the extinction of these models remains very low for the majority of a system's life time and the SEDs generated tend to have source functions which are optically revealed. It was therefore thought this high η result was a direct effect of using the upper limits to the flux data points at short wavelength ($\lambda \leq 3\mu$m) in the fitting as these models generate significant flux in that region of the spectrum.

This hypothesis was tested in a thought experiment whereby the short wavelength fluxes for one ULIRG were artificially adjusted downwards. This simulated more realistic fluxes in that regime potentially generated by old population II stars originating in the merger progenitors. It was found that the adjusted spectra was best-fitted ($\chi^2 = 1.5$) by a model from the low η group as in these systems the dust acts as a bolometer.

Ultimately this thought experiment demonstrated unequivocally that a co-ordinated multi-wavelength approach, specifically at short wavelengths, is perhaps the only way to develop more robust conclusions. However it was also demonstrated that the GEM ULIRG SED library could be applied to a very broad range of astrophysical environments, from essentially optically thin to optically thick, and reasonable fits to observed spectra obtained.

8.2 The Future

Notwithstanding the difficulties with the short wavelength data, amongst the sources of error identified in the last chapter, it is the adoption of a fully hydrodynamic (HD) three-dimensional code to trace the evolution of the core of the GMC and model the affect of both winds and supernova on the surrounding ISM which would perhaps have the most impact on research and results. Coupling the output of a 3-d HD code to a radiative transfer code capable of calculating the emission from small grains and PAHs, in addition to the more traditional grain components, would provide a useful resource which could

be employed to study a wide range of astrophysical processes in at a variety of scale and environment.

For example, a program of work using an HD code might first consider the influence of a single high mass core evolving in a GMC. Varying input parameters such as core and ambient density or metallicity and stellar mass, would allow their effect on the dynamical and chemical evolution of the system to be gauged and might provide an appropriate library of solutions to aid interpretation of survey data from e.g., UKIDSS.

Moving to larger scales, collective effects might also be modelled whereby several high mass star formation sites could be distributed randomly within a GMC and the impact on its evolution of colliding and merging winds and superbubbles, or mutually overlapping HII regions along a line of sight might be determined. The effect of stellar mass, SFR and metallicity on the density, temperature and velocity structure of a GMC could also be examined by reproducing observations of young clusters e.g., NGC346 in the Small Magellenic Cloud; a wealth of new data exists for this cluster through ongoing collaborative AAT & ESO projects, in addition to HST data. Research such as this might be used to identify key quantities such as what combination of parameters allow triggered star formation to occur and under what physical circumstances is star formation suppressed?

Building on this kind of understanding of the effect of high mass stars evolving in complex environments, the model might be applied to massive ellipticals. These galaxies are dominated by old stellar populations e.g., Bower *et al.* (1992) and the abundance ratio of alpha element to iron - which are synthesized in supernovae with different onset timescales - reveal a remarkably strong and short-live burst of star formation lasting around $\approx$ 1Gyr (Thomas *et al.* 1999). Typical early-type galaxies have $\approx 10^{12}M_{\odot}$ so SFR's as high as $\approx 1000M_{\odot}yr^{-1}$ have been inferred - far greater than any local starburst galaxies. Such SFR's have a phenomenal feedback on the ISM so it is important the the interplay between wind, gas cooling and the effect of the metallicities of the stellar population is understood. There has also been suggestion, e.g., Bell *et al.* (2004) or Ferreras *et al.* (2005), that the decrease in the co-moving number density of early-type galaxies with redshift might be explained by these objects disappearing from optical/NIR surveys, so a better model of the evolution of the dusty phase in early-type galaxies would be a valuable tool to furthering understanding.

Finally at the opposite end of galactic scales, dwarf galaxies are also extremely sensitive to both stellar feedback and environmental affects and this is responsible for the

complexity of the star formation histories of local dwarf galaxies seen on their resolved colour-magnitude diagrams e.g., Mateo (1998). A 3-d HD code could study the formation history of dwarf elliptical, spheroidal and irregular galaxies and the connection between morphology and intrinsic or external factors. A good test laboratory for a program of research such as this might be APPLES 1, which is the smallest (half-life radius $\approx$ 100pc), least massive (8 x $10^7 M_\odot$) and the most isolated galaxy ever observed. Located $\approx$ 10Mpc away, its spectral energy distribution reveals a complex mixture of stellar populations formed over several Gyr, implying a remarkably low SFR e.g., Tosi *et al.* (1991). A comparative analysis of these results and those from elliptical galaxies to available observations could again be used to establish constraints on the mass dependence of the SFR and the mode of galaxy formation as a function of environment and time.

8.3 Concluding Remarks

This work has demonstrated that it is possible to incorporate the effects of supernovae on ULIRG evolution and achieve results very favourable in comparison to observations. It is clear that further effort would be well invested in advancing these modelling techniques and thereby improving our understanding of these remarkable, cosmologically significant objects.

Appendix A

Sampling in Dart

As mentioned in Chapter 2 the DaRT radiative transfer code was obtained from its authors, ERR90, in a totally uncommented form. It was therefore important to check carefully that the transfer code worked as published and did indeed produce results according to the users specification of the model system. The first task was to therefore ascertain exactly how the integration grid was initialized and defined

A.1 Initialization of the DaRT System

When modelling dusty structures, easy convergence, in a minimum number of iterations, is of paramount importance. A fine geometric grid, consisting of a large number of segments, may well converge in a small number of iterations, but could use a prohibitively large amount of computational resource. On the other hand, a coarse grid, containing only a small number of segments may take a long or even infinite time to converge due to large discontinuities in e.g., temperature or dust density between the grid elements. Some balance must therefore be achieved between the number and the size of grid elements to create optimum grid sampling and ensure convergence in a reasonable number of iterations. This question was considered in some depth by ERR90 and a grid containing segments of equal optical depth to ultraviolet (UV) radiation was found to meet this criteria (ERR90).

A.1.1 The Radial Grid

Calculation of the shells of equal optical depth is dependent not only on the value of the optical depth itself but also on the radial density distribution $R^{-\beta}$. The optical depth τ_ν(R,Θ) to the centre of the star at frequency ν can be defined as

$$\tau_\nu\left(R,\Theta\right) = \int_{R_1}^{R_2} \pi a^2 n_{gr}\left(R',\Theta\right) Q_{\nu,ext} dR' \tag{A.1}$$

where n_{gr} is the number density of grains, a is their radius, the extinction efficiency $Q_{\nu,ext}$ = $Q_{\nu,abs}$ + $Q_{\nu,scat}$, R_1 and R_2 are the inner and outer edge of the dust cloud respectively and Θ is the azimuthal angle. Having defined the optical depth at UV wavelengths along the equator, the initial grid is generated by calculating the radii of consecutive points that provide shells of equal optical depth. The number of shells is determined by the user-defined input parameter *NRAD* along with the definition of inner and outer dust radii, R_1 and R_2, discussed in §2.5.1). Each of these shells is further separated into eight linear divisions, a value which was found to promote easy convergence in a minimum number of iterations (ERR90). The radial grid at this stage can therefore be pictured as a dust-free cavity internal to R_1 and a series of logarithmically spaced nested shells, surrounding a central source, with each shell presenting equivalent optical depth to ultraviolet radiation and sub-divided within itself into eight linear sections.

A.1.2 The Azimuthal & Angular Grids

Having set up the radial grid, the azimuthal grid is defined by specifying the total number of ϕ directions in radians, *NPHII*. This value is determined between $0 \leq \phi \geq \pi/2$ due to the symmetry of the system. Not all of these directions however will be through the dusty disc and the variable *NBDISC* controls the number of viewing angles within the disc. Thus if *NPHII* = 15 and *NBDISC* = 11, four of the viewing angles will be external to the disc, distributed over the region 90°-Θ_{max}, where Θ_{max} is the disc opening angle. The remaining 11 viewing angles will be distributed through the disc between Θ_{max}-0°. As the disc must be sampled more closely near to its plane, where more rapid changes in intensity might be expected, the number of degrees between each viewing angle increases as θ_v increases (ERR90).

The angular (θ) grid is defined by drawing tangents to the radial shells, centered on the origin, which divide the grid into a series of curved, wedge-shaped segments, each of equal dust volume and optical depth. These tangents represent the rays of the system and integrations are carried out by adding contributions to the integrals of the radiative transfer equation from material at the intersections of the ray with the radial shells centered at the origin. The number of tangents in a particular system is given by the user-defined parameter *NTH*.

Thus, if there were 32 radial shells (e.g., *NRAD* = 32), each divided into eight linear sections, an integration along a particular line-of-sight would consist of a maximum of 352

x 2 steps - the displacement along the tangential ray *ds* and the value of the integrand at that step (ERR90).

A.1.3 First-Guess Temperature Distribution

Finally a first-guess blackbody temperature distribution is applied across the grid to determine the Planck function of the grains. The temperature distribution is defined by the dust sublimation radius R_1 and the dust sublimation temperature T_{dust}, which is interpolated across the grid from R_1 using a power law of roughly $R^{-0.4}$ dependence - the optically thin limit (ERR90).

A.1.4 User-Defined Grid Variables

NRAD, *NPHII* and *NTH* describe the boundary limits of the integration grid variables and the appropriate values these variables must take to achieve good convergence in an axi-symmetric system were found during a substantial sampling and testing analysis. This is included later in this Appendix in §A.4

A.2 The Radiative Transfer Equation

Having discussed the initialization of the system to form the integration grid, the radiative transfer equation can now be considered. For a system of spherical polar coordinates centered at the geometrical centre of the system, the equation of radiative transfer at the general point $P(R,\Theta)$ in the torus is

$$\frac{dI_\nu}{ds} = -C_{\nu,ext} n_{gr}(R,\Theta) I_\nu + C_{\nu,abs} n_{gr}(R,\Theta) B_\nu[T(R,\Theta)] + \frac{n_{gr}(R,\Theta)}{r\pi} \int I'_\nu C_{\nu,scat}(\theta') d\omega' \quad \text{(A.2)}$$

where $I_\nu(R,\Theta,\theta,\phi)$ is the specific intensity of the radiation field in the direction defined by θ and ϕ, s is the distance along a ray passing through point P in the same direction, n_{gr} is the number density of grains at P and $C_{\nu,ext}$, $C_{\nu,abs}$ and $C_{\nu,scat}$ are the extinction, absorption and scattering cross-sections respectively and θ is the scattering angle. Equation A.2 can be solved numerically by ray tracing the intensity at each integration point $P(R,\Theta)$ and that solution can now be considered (ERR00).

Total Intensity

Assuming that the system is in radiative equilibrium there are three ways in which energy can contribute to the total intensity (I_ν) in a given direction. These are; radiation from

the central source $I_\nu^{(1)}$, thermal radiation from grains $I_\nu^{(2)}$ and scattering from grains $I_\nu^{(3)}$. Hence the total intensity I_ν, is given by

$$I_\nu = I_\nu^{(1)} + I_\nu^{(2)} + I_\nu^{(3)} \tag{A.3}$$

Radiation from the Central Source $I_\nu^{(1)}$

The first term in Equation A.3 is the contribution to the intensity from direct radiation emitted by the central source and has the solution

$$I_\nu^{(1)}(R,\Theta,\theta,\phi) = B_\nu(T_s)\, exp\left[-\tau_\nu(R,\Theta)\right] \tag{A.4}$$

for $\theta \leq \sin^{-1} R_{AGN}/R_2$, where R_{AGN} is the radius of the central source and in all other cases equals 0. $B_\nu(T_s)$ is the Planck function of the central source radiating at temperature T_s(K) and τ_ν(R,θ) is the optical depth at frequency ν to the centre of that source given by Equation A.1.

Thermal Radiation from Grains $I_\nu^{(2)}$

The second term in Equation A.3, the contribution to the intensity of thermal radiation from the dust grains in the cloud has the solution

$$I_\nu^{(2)}(R,\Theta,\theta,\phi) = \int_0^S exp\left[-\int_0^{S'} Q_{\nu,ext} ds'\right] \pi a^2 Q_{\nu,abs} n_{gr}(R',\Theta') \cdot B_\nu\left[T(R',\Theta')\right] ds \tag{A.5}$$

where S is the distance from the integration point P to the edge of the cloud along s, S' is the distance of the point with co-ordinates (R',Θ') from the integration point and B_ν[T(R',Θ')] is the grain source function at that point (ERR90).

Scattered Light from Grains $I_\nu^{(3)}$

The final term in Equation A.3 is the contribution to the intensity of scattered light from dust grains and has the solution

$$I_\nu^{(3)}(R,\Theta,\theta,\phi) = \int_0^S exp\left[-\int_0^{S'} Q_{\nu,ext} ds'\right] \pi a^2 Q_{\nu,abs} n_{gr}(R',\Theta') \cdot J_{scat}(R,\Theta,R',\Theta',\theta) \tag{A.6}$$

where

$$J_{scat}(R,\Theta,R',\Theta',\theta) = \frac{1}{4\pi} \int I'_\nu \xi(\theta')\, d\omega'$$

is the average scattering intensity over all solid angles and $\xi(\theta')$ is the phase function. Comparing Equation A.6 with the solution for thermal grain radiation in Equation A.5, it can be seen that the only difference is in the final source term (ERR90). The phase function can be expanded as a series of Legendre polynomials in θ' which in the first two terms gives

$$\xi\left(\theta'\right) = 1 + b_1 \cos\theta' \tag{A.7}$$

where b_1 is the scattering anisotropy factor which takes a value of 0 in the case of fully isotropic scattering used in this thesis. Further defining the mean intensity as

$$J_\nu\left(R,\Theta\right) = \frac{1}{2\pi}\int_0^\pi \int_{-1}^1 I_\nu\left(R,\Theta,\mu,\phi\right) d\mu d\phi \tag{A.8}$$

and the observed flux as

$$H_\nu\left(R,\Theta\right) = \frac{1}{2\pi}\int_0^\pi \int_{-1}^1 I_\nu\left(R,\Theta,\mu,\phi\right) \mu d\mu d\phi \tag{A.9}$$

where μ=cosθ, the scattering source term can then be re-written in terms of these moments as

$$J_{scat}\left(R,\Theta,R',\Theta',\theta\right) = J_\nu\left(R',\Theta\right) - b_1 cos\psi H_\nu\left(R',\Theta'\right) \tag{A.10}$$

where ψ is the angle R′ makes with the ray. Substitution of Equation A.10 back into Equation A.6 yields the solution for $I_\nu^{(3)}$, the contribution to the emergent spectrum from scattering.

The Integration Loop

The code first identifies a grid point by entering the nested loops in R and Θ along a ray originating from that point. The Planck function of the central source at that point is then attenuated by multiplication with the negative exponential of the optical depth to the source centre allowing $I_\nu^{(1)}$ in Equation A.4 to be calculated. A similar procedure is then carried out to find the Planck function of the grains at that point, using their extinction and absorption efficiencies and Equation A.5 for $I_\nu^{(2)}$ is solved. Geometric quantities such as cos θ, cos ψ are then identified, allowing the mean intensity given in Equation A.8 and the flux given by Equation A.9 to be evaluated over ϕ and θ. For the purposes of the grid integration it is convenient to split J_ν and H_ν into two parts; J_ν^+ and H_ν^+ in the outward direction and J_ν^- and H_ν^- in the inward direction such that $J_\nu = J_\nu^+ - J_\nu^-$ and $H_\nu = H_\nu^+ -$

H_ν^-. Finally, the scattering term J_{scat} given by Equation A.10 is determined, allowing $I_\nu^{(3)}$ to be calculated and hence the total intensity I_ν, given by Equation A.3 at that integration point is obtained.

Once all the integration points on the model grid have been evaluated the solution is checked using the conditions of radiative equilibrium and balance. Temperature corrections are then determined and applied across the grid to bring it closer to satisfying these radiative conditions. The integration process is then re-started and continues iteratively until the conditions are satisfied to better than 1% at all grid points (ERR90). These radiative conditions and the process by which temperature corrections are determined and convergence achieved can now be discussed.

A.2.1 Validity of the Solution

Due to uncertainties in, for example, grain absorption and scattering efficiencies or the exact condensation temperature for a particular grain species, major inaccuracies in the integrated solution can be introduced. To check the validity of a solution it is tested against the conditions of radiative equilibrium and balance.

Radiative Equilibrium

The condition of radiative equilibrium or flux constancy can be written for a conservative problem in the first instance as

$$\mathrm{div}H = 0 \qquad \text{where} \qquad H = \int_0^\infty H_\nu d\nu \tag{A.11}$$

such that in integral form

$$\int_\nu \mathrm{div}H dV = C \tag{A.12}$$

where V is the volume and C is a constant corresponding to the bolometric luminosity of the central source. Using the divergence theorem Equation A.12 can be evaluated

$$\int_\nu H dV = \int_S H dS = C \tag{A.13}$$

where S denotes surface so that

$$\int_0^{\frac{\pi}{2}} \int_0 H R_2 cos\Theta d\Theta d\Phi = C \tag{A.14}$$

where Φ is the azimuthal angle. However, H has no density dependence on Φ so Equation A.14 reduces to

$$R^2 \int_0^{\frac{\pi}{2}} H cos\Theta d\Theta = \frac{C}{2\pi}. \tag{A.15}$$

DaRT evaluates the right-hand side of Equation A.15 for $C/2\pi$ at $R = R_1$ and in this way checks the solution for conservation of the net flux out of the sphere of radius R_1 around the central source (ERR90). However this condition can only be tested over the entire surface R_1 and it can not be solved for a particular value of θ on that surface so it can not be used in the axi-symmetric case to evaluate a solution at a specified point. In turn this means the corrections needed to the temperature distribution after each iteration to bring the solution of the next iteration closer to convergence can not be calculated using it. In addition, DaRT was based on the original program of Rowan-Robinson (1980) which published an RT code that calculated flux transfer in a simple spherically symmetric system (in which case Equation A.15 reduces to $HR^2 = C$) and it was found that even in this instance, computing temperature corrections using flux constancy only led to poor satisfaction of the equilibrium condition. However, radiative equilibrium is theoretically equivalent to radiative balance at every point in the cloud and using this as a condition for calculating the temperature corrections, in addition to flux constancy, leads to much better convergence (ERR90).

Radiative Balance & Temperature Corrections

Radiative balance at every point in the cloud can be expressed

$$\int_0^\infty Q_{\nu,abs} J_\nu (R,\Theta)\, d\nu = \int_0^\infty Q_{\nu,abs} B_\nu [T(R,\Theta)]\, d\nu \tag{A.16}$$

The temperature distribution which produces radiative equilibrium is not generally known and initially the condition check will not normally find that the radiation field satisfies Equations A.15 and A.16 (ERR90). But, it is possible to use the information from the previous iteration to estimate a change $\Delta T(R,\Theta)$ that will cancel the errors found in the flux and allow the conditions to be more closely met in the next iteration. When the current approximation of $T(R,\Theta)$ does not satisfy Equation A.16, performing a Taylor series expansion on B_ν and re-arranging, provides the temperature correction to be applied across the grid

$$\Delta T(R,\Theta) = \frac{\int_0^\infty Q_{\nu,abs} \left(J_\nu (R,\Theta) - B_\nu [T(R,\Theta)]\right) d\nu}{\int_0^\infty Q_{\nu,abs} \frac{\partial B_\nu}{\partial T} d\nu} \tag{A.17}$$

Thus, at the end of each iteration the system is tested for radiative balance and flux constancy and based on these data, DaRT corrects the temperature distribution accross the grid and writes out the new flux array for the next iteration. In this way the system

is brought closer to convergence with each iteration until the Equation A.17 is satisfied to within 0.1% and convergence is achieved (ERR90).

The Emergent AGN Spectrum

In an axi-symmetric system, emergent SEDs are required for a number of viewing angles through the disc. To obtain these individual spectra DaRT calculates the flux H_ν at a radius R_3, which is located a substantial distance from the edge of the cloud external to R_2. Calculating the flux at this radius rather than at R_2 prohibits any distortions which might be introduced due to cloud geometry and a value of $R_3 = 100R_2$ was found to be suitable. This calculation is carried out after convergence of the temperature distribution has been achieved and SEDs for each viewing angle specified by the user are obtained.

A.3 Input & Output

The code is laid out in four programs, each of which handles a different aspect of the transfer problem. The primary program *.main* is responsible for such things as initializing the physical parameters of the system and orchestrating the integrations needed for the solution. *.main* calls sub-routines from program *.setup* to define quantities such as the dust density distributions and grain cross-sections. The actual integration is handled using subroutines from the program *.rayall* and finally, sub-routines from the program *.aux* are called to test for radiative balance and calculate temperature corrections after each iteration.

In the first instance, the DaRT code reads in the user-defined model parameters such as the ratio of the inner to outer dust radii $ERAT = R_1/R_2$, the dust sublimation temperature (T_{Dust}) or the source luminosity ($L_\star$) from the input file *in.par* using the two subroutines *flinp.main*(real) and *inpig.main* (integers). The radial, azimuthal and zenith angle grids are then generated by the subroutines *rad.main*, *phi.main* and *theta.main* - it is these user-defined grid variables which will be fully considered in the next section. Finally, the subroutine *wave.main* sets up the wavelength grid which, following ERR90, was chosen for this thesis to contain 84 points, over the range $0.07\mu\text{m} \leq \lambda \leq 1450\mu\text{m}$, with the grid being more closely sampled at short wavelengths to accommodate the potentially significant variation that can occur in that part of the emergent spectral energy distribution.

Having defined the grid initialisation parameters, the grain abundances, absorption and scattering properties supplied to DART are used by the routine *xsflux.setup* to calculate

the extinction cross-sections across the wavelength grid. The subroutine *tscale.setup* then determines the location of the inner dust radius from the ratio of the inner to outer dust radii, the dust sublimation temperature and the source luminosity and makes a first guess at the temperature grid by interpolating the temperature at the inner dust radius - the sublimation temperature - across the basic integration grid using a power-law of roughly $R^{-0.4}$ dependence; the optically thin limit.

Having initialised the system and defined the integration grid, the solution to the transfer equations can now be considered. First the wavelength intervals needed for the integrations in Equations A.6, A.8 and A.9 are calculated by sub-routine *xsflux.setup.* Having accomplished that, the flux and first moment (J_ν) arrays are initialised from the user-defined input file *in.flux* which contains the PG Quasar derived source function flux. Following that the grain source function ($B_\nu[T(R',\Theta')]$) for every integration point within the system is calculated, also by the sub-routine *xsflux.setup.*

The integration loop now begins by first identifying a grid point by entering nested loops in R and Θ, along a ray originating from that grid point. The routine *raylot.main* then calls the sub-routine *raylot2.rayall* which calculates the Plank function of the central source at the integration point and then multiplies it by the negative exponential of the optical depth to the centre of the source - the attenuation factor. These values are the quantities needed for Equation A.4, the contribution of the radiation from the central source $I_\nu^{(1)}$. *raylot2.rayall* then orchestrates the calculation of $\mu = \cos\theta$ which is needed for the integrations in Equations A.5, A.6, A.8 and A.9 along with $\cos\psi$ needed for Equation A.10. Subroutine *rayfun.rayall* then organizes the calculation of the displacement along the ray *ds* and other geomteric detils of the integration point, along with the optical depth between the current grid point and the edge of the cloud (*ds'* needed for the attenuation factors in Equations A.5 & A.6). Finally, these details are fed back into *rayfun.rayall* which is than able to calculate $J_\nu(R'.\Theta)$, $H_\nu(R'.\Theta)$ and $Q_{\nu,abs}J_\nu$ (R',Θ) over ϕ and ν, again needed for Equations A.5, A.6, A.8 and A.9. The scattering term J_{scat} is then calculated along with $d\mu = d[\cos\theta]$. Finally $J_\nu(R'.\Theta)$, $H_\nu(R'.\Theta)$ and $Q_{\nu,abs}J_\nu$ (R',Θ) are evaluated over $d\mu$ and $d\lambda$ and the intergrals totalled before continuing to the next grid point and repeating the process.

Once all integration points have been evaluated along all lines of sight, $J_\nu(R'.\Theta)$ and $H_\nu(R'.\Theta)$ are divided by 2π to solve equations A.8 and A.9. These, along with the totals for I_ν^2; thermal radiation from grains and I_ν^3; scattered light from grains, are are used to

solve Equation A.3 for that particular iteration.

At the end of each iteration *gutter.aux* is called to test the system for radiative balance and *ratter.aux* tests for radiation equilibrium. Based on these data *corrtt.aux* calculates the temperature correction itself and then *corrtt.main* corrects the distribution accross the grid and writes out the new flux array for the next iteration. This completes one iteration of the code and the entire procedure is them repeated until satisfaction of Equations A.16 and 1.35 to better that 1% at all grid points (Efsthathiou & Rowan-Robinson 1990*b*) is achieved. The number of iterations this takes is also investigated in a following subsection.

A.4 Grid Integration Variables

The interpolation characteristics of the axi-symmetric code, especially for the longer wavelength absorption dominated calculations, were benchmarked by its author (ERR90) against the finite difference code DUSTY (Ivezic, 1997) and were found to be accurate. However, this concept was thoroughly tested by the author of this thesis and additional benchmarking revealed it was incorrect. Due in part to the shell indexation being out of step, for values of the ratio $R_\star/R_1 \geq 0.1$, the code missed approximately 30° in angle when integrating, which resulted in a serious lack of flux in the emergent spectra. As this thesis' author was, at that early time in the Ph.D, unable to program in any language and as DaRT was their very first experience with scientific computing, the root of the fault found was located and repaired by Dr. Jeremy Yates of University College London (UCL) in 2004 and appropriate notification was made to the code's author, Andreas Efstathiou.

Having adapted the DaRT radiative transfer code to correctly integrate over all angles in a model system, the problem of sufficient grid definition can be split into two individual considerations. The first is to identify the minimum total number of points which will allow the radiative transfer equations to be reasonably integrated, and second, the minimum number of points across the grid at which the temperature corrections should be derived to coax the system into radiative balance after the minimum number of iterations.

As will be seen in the following subsections, the total number of integration points required to achieve radiative balance was obtained by testing a range of values for the ϕ division parameter, NPHII. Then, the same range of values for the θ division parameter, NTH, was tested for convergence, whilst holding NPHII constant. Following that, the radial parameter NSUB was tested, which not only defines the total number of grid segments to be used as default, but also confirms that the number of points at which the

temperature correction is applied is suitable. Convergence was tested after only one iteration as it is the underlying grid that is being tested rather than the solution itself. Having obtained reasonable values for NPHII, NTH and NSUB, DaRT was run for successively more iterations, using the convergence measure of 1%, to find the minimum number which produced convergence at a single solution.

The code integrates the equations of radiative transer using the trapezium rule which divides the area to be integrated - in this case $-\pi/2 < \phi < \pi/2$ and $0 < \theta < \pi/2$ over radius R - into sequences of abutting trapezia. The area of each trapezia is then estimated and the equations of radiative transfer integrated over those areas. Obviously, the more trapezia that are used, the better the approximation of the area to be integrated and the smaller the error between the true solution and the estimation. But, as mentioned, the aim of this section is to find the smallest, error limited, value for each grid parameter.

The model chosen for all the testing in this section has a central blackbody source of temperature 40,000K with the dust in the surrounding cloud made up of a single grain type - Silicate (Draine & Lee) - with a common radii of $a = 0.1\mu$m. Silicate was chosen because of its strong scattering dominated feature at 0.25μm (Log λ = -0.6) as it is here, at the shorter wavelengths, that the interpolation between segments in the code may be the least reliable.

Each model was run with an R and θ dust density index of $\beta = \gamma =$ -1 and an equatorial optical depth $A_v^{TOT} = 1$. Although all the models were set up to be spheres, with the number of viewing angles equalling the number of θ divisions, the models were run through the axi-symmetric code so this density distribution ensured that there was significantly more dust at the equator than at the poles. This was done to provide distinct differences, and therefore additional monotoring, on the expected spectra from e.g., the viewing angles 0°, 45° and 90°.

A.4.1 The ϕ Grid

As mentioned, the azimuthal grid is defined by specifying the number of directions in ϕ, using the parameter NPHII. As this was the first of the sampling runs, reasonable values of the θ and radial parameters, NTH and NSUB respectively, had to be chosen to be held constant. The value of NTH was chosen to be 15, whilst NSUB was held at 2; a parameter which will be thoroughly explained in the coming subsection entitled *The Radial Grid.*

First the limits for the ϕ investigation were set at $\text{NPHII}_{min} = 11$ and $\text{NPHII}_{max} =$

45 and models were run for NPHII = 11, 15, 17, 19, 21, 23, 25, 27, 29, 35 and 45 whilst keeping all other grid parameters constant. Having extracted emergent spectral energy distributions for the three viewing angles $\theta_v = 0°$, 45° & 90° from each model solution, they were normalised to NPHII = 45. Representative normalized spectra for NPHII = 11, 15 & 25 are shown on the left-hand-side of Figure A.1 by the green stars, blue circles and pink triangles respectively. On the right-hand-side of Figure A.1, the *maximum* deviation of each of the 10 NPHII spectra from the normalised curve, or the maximum variance, is also illustrated for $\theta_v = 0°$, 45° and 90°.

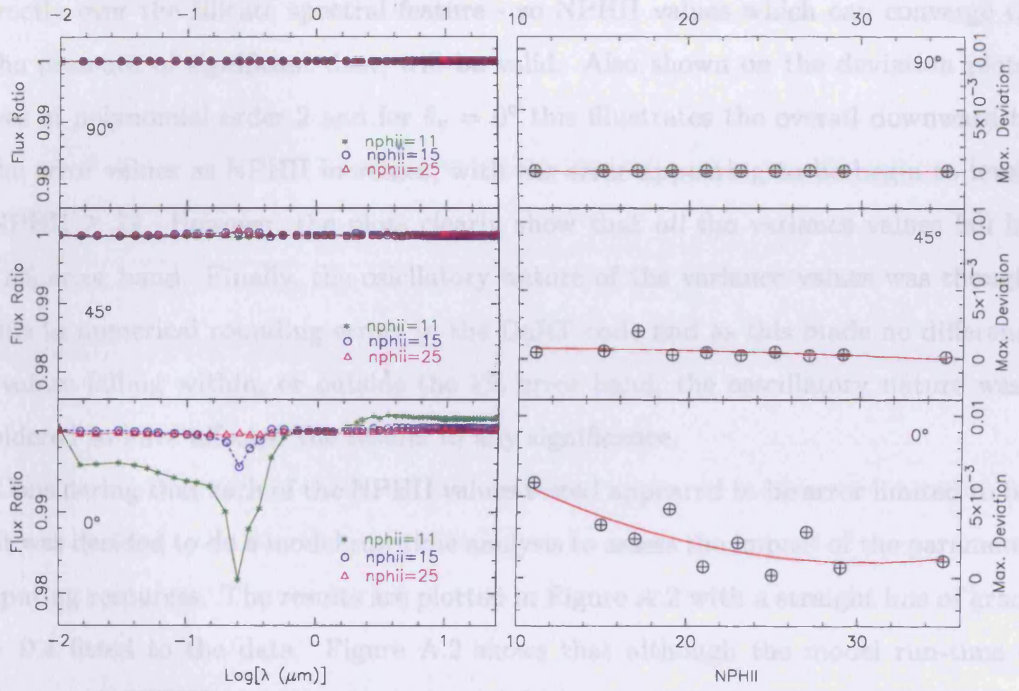

Figure A.1: Representative normalized spectra for NPHII = 11, 15 & 25 are shown on the left-hand-side of the figure by the green star, blue circles and pink triangles respectively. On the right-hand-side, the maximum variance of the normalised curve (to NPHII = 45) are shown by the black crossed circles and the red curves show polynomial fits to the data of order 2. Data is shown for θ_v = 90°, 45° & 0°, top to bottom.

Perhaps the most obvious result from the normalized spectra is the discrepancy between the results for $\theta_v = 90°$ compared to those of $\theta_v = 0°$. At 90°, NPHII = 11 concurs almost perfectly with that of NPHII = 45 indicating that the code converges equally well with either value. However as the viewing angle closes on the equator, the discrepancy between the normalised spectra increases, until at $\theta_v = 0°$ there are significant differences.

This is just as expected due to the dust density indexes used for the models and the equatorial optical depth specified. Essentially, these results indicate that the code has increasing difficultly converging as NPHII drops, in the presence of large amounts of dust, at short wavelengths.

The right-hand-side of the plot shows the maximum deviation of the NPHII spectra and as with the spectral energy distribution plots, the values for $\theta_v = 90°$ lie on nearly a straight line at 0, whilst the values for $\theta_v = 0°$ show the widest variation of all. For each of the normalised spectra the maximum deviation occurs at Log λ = -0.6 ($\lambda = 0.25\mu$m) - directly over the silicate spectral feature - so NPHII values which can converge there, in the presence of significant dust, will be valid. Also shown on the deviation plots are curves of polynomial order 2 and for $\theta_v = 0°$ this illustrates the overall downward trend in the error values as NPHII increases, with the error appearing to be begin to level out at NPHII $\geq$ 29. However, the plots clearly show that *all* the variance values fall below the 1% error band. Finally, the osicllatory nature of the variance values was thought to be due to numerical rounding errors in the DaRT code and as this made no difference to the values falling within, or outside the 1% error band, the osscillatory nature was not considered to have affected the results to any significance.

Considering that each of the NPHII values tested appeared to be error limited to below 1% it was decided to do a model run-time analysis to assess the impact of the parameter on computing resources. The results are plotted in Figure A.2 with a straight line of gradient m = 0.4 fitted to the data. Figure A.2 shows that although the model run-time does increase with NPHII, the increase is not inhibiting over all the values of NPHII tested. As an aside, the variation of NPHII = 21 and 23 is caused by the unintended sharing of central processor time with other user's models.

It therefore appears that in the presence of large quantities of dust, at e.g., $\theta_v = 0°$, the deviation of the lowest value of NPHII = 11 tested, is the largest of all and further the model did not properly converge at *any* wavelength. NPHII = 15 on the other hand was able to converge both at long and short wavelengths whilst the maximum deviation, located across the silicate scattering feature, at $\Delta\text{NPHII}_{15} = 0.003$ was found to be well within any observational error that might be expected at 20%. As NPHII = 15 did not incur any particular penalty in the model-run time analysis, this was chosen as the smallest possible error limited value for the ϕ grid parameter that also ensured convergence of the code at all wavelengths.

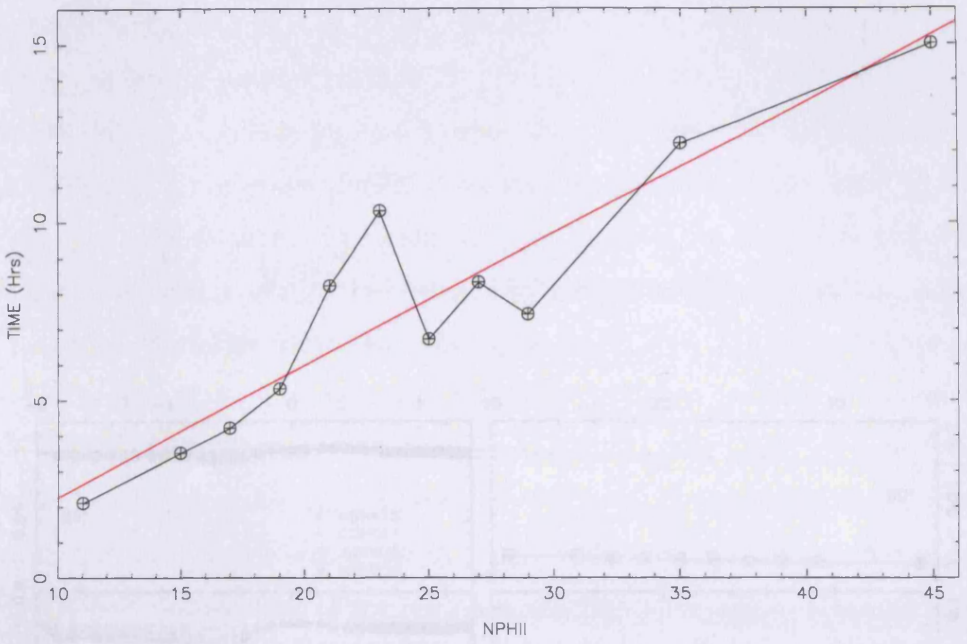

Figure A.2: Model run-time analysis for integration grid variable NPHII. The red line shows the best-fit to the data, which has a slope of m = 0.4.

A.4.2 The θ Grid

Having obtained a suitable value for the azimuthal angle parameter, the zenith angle θ can be considered. The θ grid is defined between $0 < \theta < \pi/2$ due to the symmetry of the system and it is the parameter NTH which defines the number of slices to be integrated within that quarter sphere. In the same way as for the azimuthal grid, models were run for NTH = 11, 15, 17, 19, 21, 23, 25, 27, 29, 35 and 45, whilst keeping NPHII = 15 and NSUB = 2 constant. Having extracted the relevant viewing angle spectra for $\theta_v = 0°$, 45° & 90°, each model was again normalised to the spectra from the largest value of NTH = 45. Figure A.3 shows on the left-hand-side representative normalised spectra for NTH = 15, 21, 25 & 35 whilst the right-hand-side shows the maximum deviation of the normalised spectra.

Figure A.3 shows again that the code experiences the most difficulty converging at short wavelengths, especially in the presence of considerable amounts of dust, as illustrated by the normalized spectra for $\theta_v = 0°$. In a similar way to the NPHII testing, the maximum deviation of the normalised spectra occurs for all values of NTH directly over the silicate scattering feature at Log λ = -0.6. The polynomial order 2 curves illustrated on the right-hand-side of Figure A.3 show a much more prominent downward trend of the error values

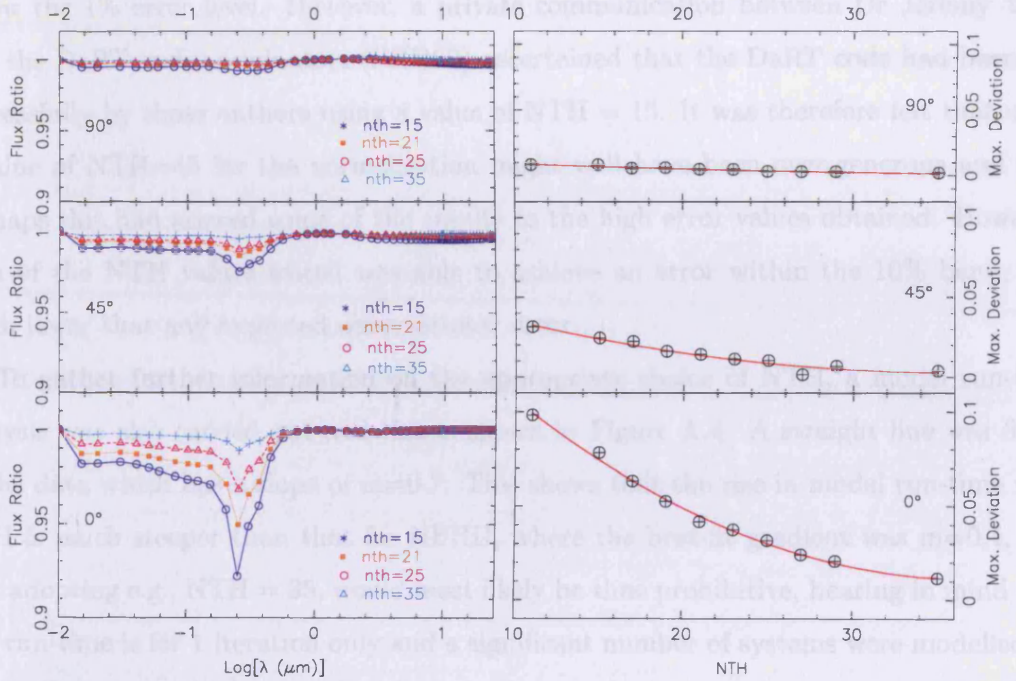

Figure A.3: Representative normalized emergent spectra for NTH = 15, 21, 25, 35 are shown on the left-hand-side of the figure by the blue circles, orange squares, pink triangles and turquoise pluses respectively. On the right-hand-side, the maximum variance of each of the normalised spectra (to NPHII = 45) are shown by the black crossed circles whilst the red curves show polynomial fits to the data of order 2. Data is shown for $\theta_v = 90°$, 45° & 0°, top to bottom.

towards NTH = 45, than that of NPHII, particularly for $\theta_v = 0°$, which only appear to be levelling out from a value of NTH $\approx$ 27.

However, unlike the results for $\theta_v = 0°$ when the ϕ parameter NPHII was tested, which showed that most of the values produced an error below the 1% band, *none* of the NTH values achieved this low error. The difficulty here becomes the maximum and minimum limits set for the investigation. For example, had the results been normalised to eg: NTH = 25, maximum deviation values for NTH = 21 or NTH = 23 may well have occured below the 1% error level. However, a private communication between Dr Jeremy Yates and the DaRT codes originators (ERR90) ascertained that the DaRT code had been run successfully by those authors using a value of NTH = 15. It was therefore felt that using a value of NTH=45 for the normalisation might well have been over-generous and that perhaps this had skewed some of the results to the high error values obtained. However, each of the NTH values tested was able to achieve an error within the 10% band, still much lower that any expected observational error.

To gather further information on the appropriate choice of NTH, a model run-time analysis was also carried out and this is shown in Figure A.4. A straight line was fitted to the data which has a slope of m=0.7. This shows that the rise in model run-time with NTH is much steeper than that for NPHII, where the best-fit gradient was m=0.4, and that adopting e.g., NTH = 35, would most likely be time prohibitive, bearing in mind that this run-time is for 1 iteration only and a significant number of systems were modelled for the Ph.D.

Taking all this evidence into consideration, it was felt that a value of NTH = 21 was perhaps appropriate as the default value for NTH - it being neither overly prohibitive in computing time or associated with a very large deviation. Although this value gives an error on NTH of 0.04, as can be seen in later Section *'Errors on the DaRT Grid'*, the combined error value on both the parameters NPHII & NTH is still only 5% - well within any minimum observational error that may be expected. As such, NTH = 21 was used in conjunction with NPHII = 15 in the third stage of the sampling investigation - the radial grid.

A.4.3 The Radial Grid

Having determined suitable, error limited, values for the θ and ϕ parameters, an appropriate value for the radial parameter NSUB can be established.

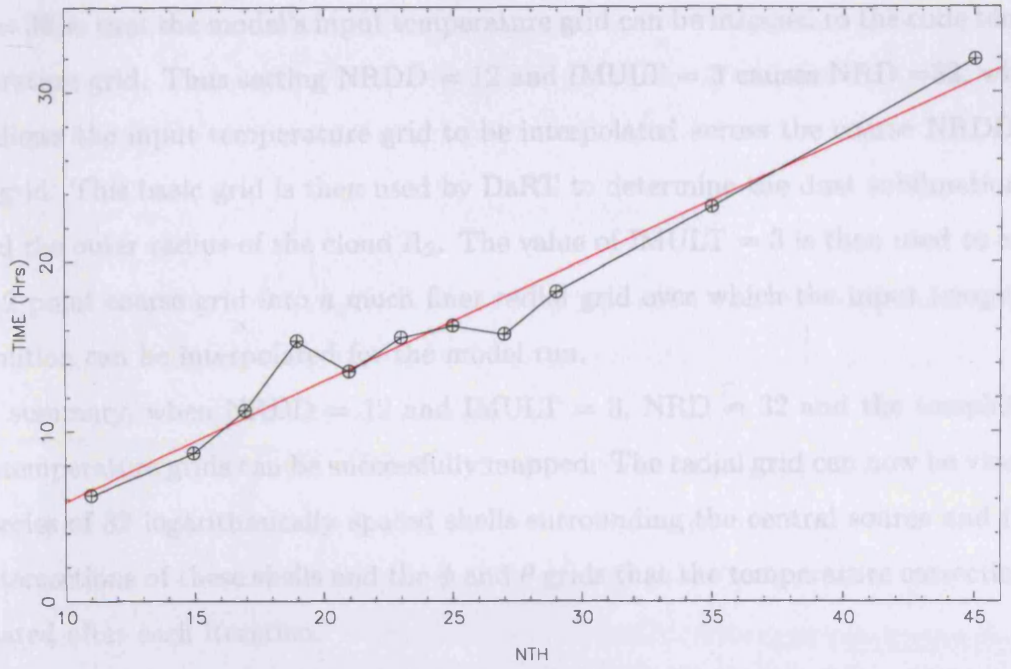

Figure A.4: Model run-time analysis for integration grid variable NTH. The red line shows the best-fit to the data, which has a slope of m = 0.7.

As mentioned at the start of this Appendix, in DaRT the system gradually converges towards radiative balance with the local radiation field, at all points in the grid, as the necessary temperature corrections are calculated after each iteration. The radiative transfer equation is an integro-differential equation, with the intensity, or its moments, at any grid point determined by the intensities at all other grid points. However, having ascertained that the interpolation characteristics of the code are good, unlike for the transfer equation, the temperature corrections do not have to be found at *every* grid point but can be calculated more sparsely and then interpolated across the grid.

In order to understand the importance of the user-defined parameter NSUB, it is convenient to begin with the other radial parameters used by DaRT which are hard wired as default, having been found appropriate during the codes initial construction by ERR90. First, the parameter NRD describes the total number of basic grid points, which is also the total number of points at which the temperature corrections after each iteration are calculated and applied:

$$NRD = [(NRDD - 2) \cdot (IMULT + 2)] \tag{A.18}$$

In this equation, NRDD is the minimum number of basic grid points and IMULT is the desired expansion multiple of NRDD. The parameter NRD has to be set by default at

NRD = 32 so that the model's input temperature grid can be mapped to the code template temperature grid. Thus setting NRDD = 12 and IMULT = 3 causes NRD =32, which in turn allows the input temperature grid to be interpolated across the coarse NRDD = 12 point grid. This basic grid is then used by DaRT to determine the dust sublimation radii R_1 and the outer radius of the cloud R_2. The value of IMULT = 3 is then used to expand that 12 point coarse grid into a much finer radial grid over which the input temperature distribution can be interpolated for the model run.

In summary, when NRDD = 12 and IMULT = 3, NRD = 32 and the template and input temperature grids can be successfully mapped. The radial grid can now be visualised as a series of 32 logarithmically spaced shells surrounding the central source and it is at the intersections of these shells and the ϕ and θ grids that the temperature corrections are calculated after each iteration.

However, in contrast to the temperature corrections, the integro-differential equations of radiative transfer must be calculated at many more grid points than 32 to forestall large discontinuities in e.g., the dust density which would ultimately prevent the code converging. Thus the basic, 32 point temperature interpolated grid discussed above is further divided into a subgrid for the integration of the transfer equations. The division of the basic grid is controlled by the parameter NSG which is the total number of grid points.

$$NSG = [(NRD - 2) \cdot 8 \cdot (NSUB + INNER)] \tag{A.19}$$

As can be seen, Equation A.19 includes the user defined parameter to be tested in this section; NSUB, which is the number of subdivisions in the subgrid, INNER is the number of radial points set aside for the dust free cavity surrounding the central source and NRD = 32 as discussed.

Considering Equation A.19 in its entirety, first the default value '8' divides each of the 32 logarithmically spaced radial 'temperature correction' shells, described by NRD, into 8 linearly spaced sections that then describe the subgrid. The value of INNER is set by default at INNER = 50 which allows the dust sublimation radii of any model to be encompassed. It should be mentioned at this point that a private communication from the codes' authors to Dr Jeremy Yates of UCL, confirmed that the values of NRD = 32, INNER = 50 and the '8' used for the linear interpolation were found during the code's construction to be suitable for *any* user-defined model system.

Moving now to the parameter NSUB, this parameter describes how the 8 linear sections of the subgrid are then further subdivided. Using the example described in the previous paragraph, with NRD = 32 and INNER = 50, NSG is found to be

$$NSG = [(30 \cdot 8 \cdot NSUB) + 50] = [(240 \cdot NSUB) + 50] \tag{A.20}$$

So a value of NSUB = 2 would produce a total number of points across the model radius of NSG = 580, with the radiative transfer equations calculated at *each* point and the temperature corrections calculated at roughly every *16th* point.

The total number of radial points in the grid, NSG, is very sensitive to the value of NSUB, which must therefore be chosen with some care to ensure the system converges in a minimum amount of time. Thus, for the purposes of assessing the radial grid sampling, the relatively low values of NSUB = 2, 5 and 9 were tested. The optimum values of NPHII = 15 and NTH = 21 obtained in the previous sections were held constant throughout the radial grid testing. The results of the radial sampling are presented in Figure A.5 which shows the emergent spectra $\theta_v = 0°$ for NSUB = 2 & 5, normalised to the spectra for NSUB = 9. Whilst not shown, the maximum deviations of these two normalised curves are $\Delta\text{NSUB}_2 = 0.02$ and $\Delta\text{NSUB}_5 = 0.007$.

With the radial parameter NSUB, the run-time and the memory needed for the model to complete 1 iteration increases dramatically as NSUB increases. For example; NSUB = 2 has a memory requirement of 80Mb and 1 iteration takes around 7 hours. However, NSUB = 9 requires a memory allocation of 300Mb and upwards of 20 hours to run 1 iteration. This could suggest that a value of NSUB = 9 run through perhaps 5 successive iterations to achieve convergence, would take over 100 hours. Considering this and the fact that the error value on NSUB = 2 is only some 2% it was decided to use NSUB = 2 as the default parameter for the radial grid.

A.4.4 Summary of Integration Grid Variables

The values obtained for all the parameters discussed in this section are summarised in Table A.1

A.4.5 Errors on the DaRT Grid

As mentioned the error on the azimuthal parameter NPHII = 15 is 0.003, the error on the zenith parameter NTH = 21 is 0.04 and that of the radial grid parameter NSUB = 2 is

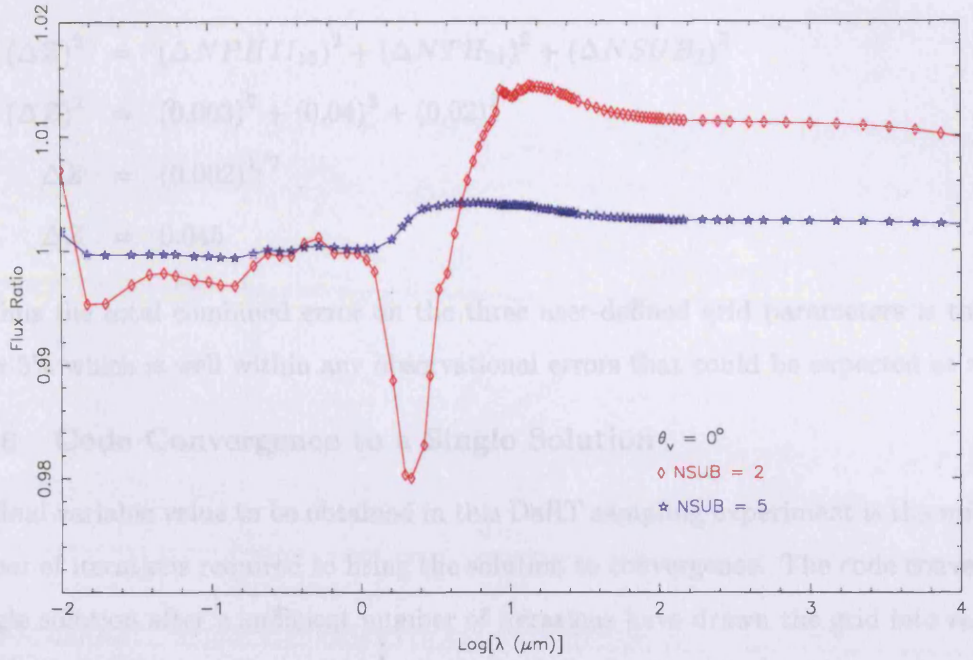

Figure A.5: Emergent spectra at $\theta_v = 0°$ for NSUB = 2 & 5, normalised to NSUB = 9, are shown by the red diamonds and blue stars respectively. The maximum variance for NSUB = 2 is 0.02, whilst that of NSUB = 5 is 0.007.

DESCRIPTION	PARAMETER	VALUE
Azimuthal Grid Variable ϕ	**NPHII**	**15**
Zenith Grid Variable θ	**NTH**	**21**
Total No. Basic Radial Points	NRD	32
Minimum No. Basic Radial Points	NRDD	12
Expansion Multiple of NRD	IMULT	3
No. Radial Points in Central Dust Cavity	INNER	50
No. Subdivisions in the Sub-Grid	**NSUB**	**2**
Total No. Radial Grid Points	**NSG**	**580**

Table A.1: Summary of DaRT Integration Grid Variables used in the modelling. Those values obtained from the sampling exploration are emboldened, whilst those set as default by ERR90 are not.

0.02. Adding these errors linearly generates a total error ΔZ on the DaRT GRID such that

$$\begin{aligned}(\Delta Z)^2 &= (\Delta NPHII_{15})^2 + (\Delta NTH_{21})^2 + (\Delta NSUB_2)^2 \\ (\Delta Z)^2 &= (0.003)^2 + (0.04)^2 + (0.02)^2 \\ \Delta Z &= (0.002)^{1/2} \\ \Delta Z &= 0.045 \end{aligned} \tag{A.21}$$

Thus the total combined error on the three user-defined grid parameters is therefore ΔZ $\approx$ 5% which is well within any observational errors that could be expected at $\approx$ 20%.

A.4.6 Code Convergence to a Single Solution

The final variable value to be obtained in this DaRT sampling experiment is the *minimum* number of iterations required to bring the solution to convergence. The code converges to a single solution after a sufficient number of iterations have drawn the grid into radiative balance through successive temperature corrections. So to test the minimum number of iterations after which the code has settled down to a single solution, the same model was employed as that used to test the integration grid parameters, with the same convergence measure of 1%. The system was then run through DaRT for 1, 2, 3, 4, 5 and 6 iterations, the emergent spectra for $\theta_v = 0°$ extracted and then normalized using the spectra obtained from 6 iterations.

The results of the iteration number testing are shown in Figure A.6 and the graph nicely illustrates the λ-iteration convergence problem. Looking first at the normalized curves for 1, 2 and 3 iterations, there appears to be significant discrepancy with the curve for 5 iterations. In the shorter wavelength region, which corresponds to the inner hotter dust, the solution settles down relatively quickly as the temperature corrections affect the inner grid almost immediately. However, in the longer wavelength region, which corresponds to cooler dust in the outer areas of the grid, the solution takes longer to settle as the temperature corrections applied in the inner grid propagate outwards.

As the curve for 5 iterations has an error of 0.02 it was decided to use this value as the minimum number of iterations required in each modelling run to attain a single converged solution.

As to be expected the number of iterations to produce convergence roughly scales with the optical depth. The models just tested were assigned an optical depth of $\mathrm{Av}^{TOT} = 1$,

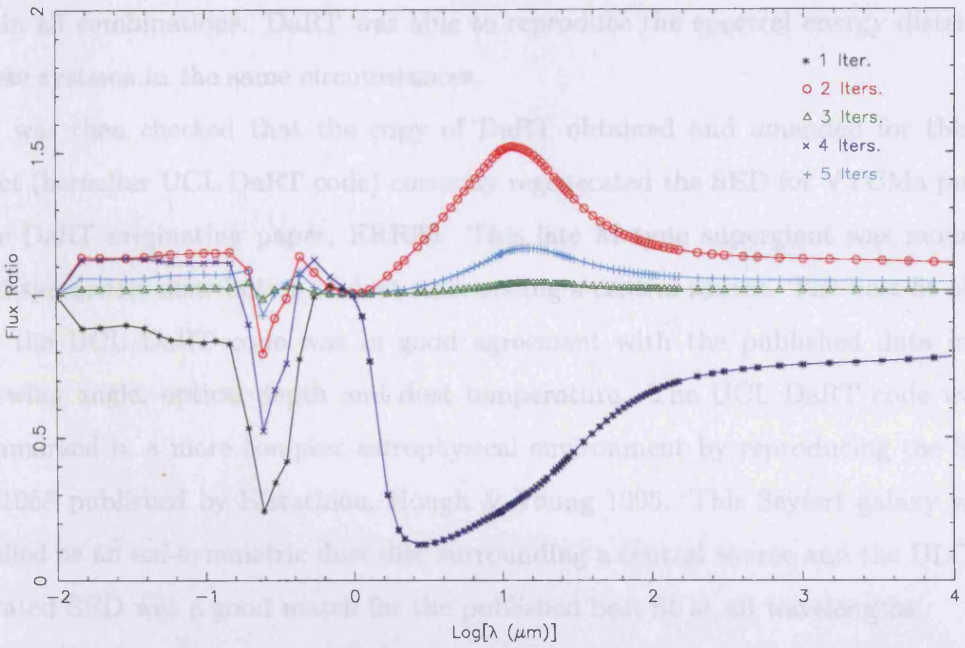

Figure A.6: Emergent Spectra for 0° after 1, 2, 3, 4 & 5 iterations, normalised to the spectra from 6 iterations. 1, 2, 3, 4 & iterations are indicated by the black stars, red circles, green triangles, blue crosses and turquoise pluses respectively.

but many of the systems used in the Ph.D. starburst and AGN modelling have significantly higher optical depths. Therefore the DaRT code was altered, again by Dr. Jeremy Yates of UCL to automatically halt once convergence had been achieved, regardless of the number of iterations greater than 6 which had been completed. As default the models were run for 100 iterations and often converged in many less. However, some of the most dust dense systems at very early times required more than 100 iterations so the DaRT code was also altered to register the solution from the 100th iteration so that the code could be re-started from that solution and continued to convergence. This completes the discussion on grid sampling in DaRT.

Independent Benchmarking

Having obtained suitable error limited values for the DaRT grid input variables and evaluated the number of iterations needed for a solution to converge, DaRT was independently benchmarked using the dust radiative transfer code DUSTY (Nenkova *et al.* 2000). In *Benchmark Problems for dust Radiative Transfer*, Nenkova *et al.* (2000) presented solutions for a simple spherically symmetric model system calculated using two radially dependent density distributions; R^o and R^{-2} and four optical depths at 1μm; 1, 10, 100 &

1000 in all combinations. DaRT was able to reproduce the spectral energy distributions of these systems in the same circumstances.

It was then checked that the copy of DaRT obtained and amended for this thesis project (hereafter UCL DaRT code) correctly regenerated the SED for VYCMa published in the DaRT originating paper, ERR90. This late M type supergiant was modelled as an axi-symmetric distribution of dust surrounding a central source. The best fit obtained using the UCL DaRT code was in good agreement with the published data in terms of viewing angle, optical depth and dust temperature. The UCL DaRT code was then benchmarked in a more complex astrophysical environment by reproducing the SED for NGC1068 published by Efstathiou, Hough & Young 1995. This Seyfert galaxy was also modelled as an axi-symmetric dust disc surrounding a central source and the ULC DaRT generated SED was a good match for the published best-fit at all wavelengths.

Concluding Remarks

As mentioned, although the author of this thesis did not re-program DaRT, either to fix the 30° interpolation fault or to ensure the code halted once convergence had been achieved, *all* other elements discussed in this Appendix were divined by the thesis's author, directly from the uncommented *Fortran77* code itself. These include: identifying that the interpolation fault existed, the process by which DaRT integrates the equations of radiative and generates the temperature corrections, the input and output files and subroutines and the method by which the grain extinction profiles are incorporated into the model system.

Finally, it should also be noted that the author of this thesis did solely design, develop and write, in its entirety, the *C* language computer code GEM which generated the Giant Molecular Cloud dust density distributions - fully discussed in Chapters 3, 4 and 5 - and used as input starting conditions for DaRT radiative transfer code, when modelling the starburst systems.

Appendix B

Gas Dynamics

As mentioned in §4.3.1 where the equations governing the superbubble motion and supershell width were considered, the Rankine-Hugoniot conditions are integral to determining the compression undergone by the gas as it crosses a shock. These conditions show how the flow variables of pressure, density and velocity on either side of the shock to conserve mass, energy and momentum.

Having obtained the conditions they can be used to determine the density compression across a shock in both the adiabatic and isothermal phases. Once these factors are determined, they can be used in conjunction with the mass of overtaken gas to estimate the width and hence the density of gas in the shell, eventually leading to an estimation of extinction generated by the shell.

B.1 The Rankine-Hugoniot Conditions

Because the flow variables are time-independent, the jump conditions do not have to be derived in a frame of reference where the shock is moving, but rather are more easily established in a frame of reference where the shock is stationary and the gas is moving. Although unnecessary for specifically determining the compression ratio, the velocity ratio will be transformed into the proper frame of reference for use later in the model.

Figure B.1 is a schematic showing the flow variables into and out of the shock. Using the standard notation of Dyson & Williams (1997*d*) the upstream variables are gas at pressure P_o and density ρ_o entering the stationary shock at velocity u_o. The gas exits the shock at pressure P_1, density ρ_1 and velocity u_1 - the downstream variables. As with the derivation of the equation of motion for the superbubble, the Rankine-Hugoniot conditions assume that the first shell forms instantaneously at and that all material interior to the

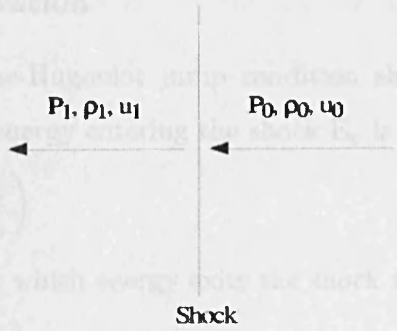

Figure B.1: The flow variables on either side of a shock. Velocities are given in the rest frame of the shock. (Dyson & Williams 1997*d*).

shock at that time then resides in the shell. Having made this assumption it is possible to neglect the pressure interior to the shell i.e., in the superbubble, allowing the derivation to commence (Dyson & Williams 1997*c*).

B.1.1 Mass Conservation

The first Rankine-Hugoniot jump condition describes how the gas mass is conserved across the shock and its derivation is a simple procedure as the rate of mass entering the shock per unit area must be equal to the rate at which mass exits per unit area. Thus

$$\rho_o u_o = \rho_1 u_1 = \phi \tag{B.1}$$

where ϕ is the constant mass flux.

B.1.2 Momentum Conservation

The momentum conservation condition also derives simply as the forces acting on the gas are not balanced and the acceleration of it is a function of the gas mass and the pressure acting upon it. Newton's Second Law therefore applies so if the momentum of the mass entering the shock front is $(\rho_o u_o)u_o$ and the momentum of the mass exiting the shock is $(\rho_o u_o)u_1$, the change can be expressed as the impulse given by the pressure difference and substituting from Equation B.1 leads to

$$\rho_o u_o^2 + P_o = \rho_1 u_1^2 + P_1 = \zeta \tag{B.2}$$

where ζ is the constant momentum flux. Equation B.2 is the second Rankine-Hugoniot condition showing how momentum is conserved across the shock.

B.1.3 Energy Conservation

The third and final Rankine-Hugoniot jump condition shows how energy is conserved across the shock. First the energy entering the shock E_o is written as

$$E_o = \rho_o u_o \left(\frac{1}{2} u_o^2 + \frac{3}{2} \frac{P_o}{\rho_o} \right) \tag{B.3}$$

and similarly, the rate E_1 at which energy exits the shock and enters the shell is

$$E_1 = \rho_1 u_1 \left(\frac{1}{2} u_1^2 + \frac{3}{2} \frac{P_1}{\rho_1} \right) \tag{B.4}$$

with the difference between Equations B.3 and B.4 being the rate at which work is done on the gas by the change in pressure across the discontinuity

$$E_o - E_1 = P_o u_o - P_1 u_1 \tag{B.5}$$

By definition energy is conserved across the shock but it is worth considering what changes in the energy balance facilitate this conservation. The primary source of loss from the entry energy is its kinetic energy which is almost entirely given over to the translational energy of the shocked gas so although this energy input causes the gas pressure to increase and kinetic energy to be lost, internal energy has risen to compensate and the energy across the shock is conserved (Dyson & Williams 1997*d*). E_o and E_1 in Equation B.5 can now be substituted with Equations B.3 and B.4 respectively and using mass continuity and momentum conservation gives the energy conservation condition

$$\frac{1}{2} u_o^2 + \frac{5}{2} \frac{P_o}{\rho_o} = \frac{1}{2} u_1^2 - \frac{5}{2} \frac{P_1}{\rho_1} = \xi \tag{B.6}$$

where ξ is a constant specific total energy.

B.1.4 Summary of the Rankine-Hugoniot Conditions

It is now convenient to drop the subscripts from the conservation conditions and express Equation B.1 for mass continuity as

$$\phi = \rho u \tag{B.7}$$

Equation B.2 for momentum conservation as

$$\zeta = P + \rho u^2 \tag{B.8}$$

and the specific total energy from Equation B.6 is

$$\xi = \frac{1}{2} u^2 + \frac{1}{2} \frac{P}{\rho} \tag{B.9}$$

and these expressions have been included in the main body of Chapter 4, §4.3.2. Having obtained these conditions describing the relationships between the flow variables across the shock they can be used to find the velocity ratio across the shock and hence the compression factor needed to calculate the shell width.

B.2 Density Ratio in Adiabatic Phase

Beginning with the velocity ratio, the energy balance equation can be transformed into a quadratic equation whose roots are the up- and downstream gas velocities. The sum of those roots can then be used in conjunction with the upstream Mach Number to obtain the velocity ratio across the shock.

B.2.1 Up- and Downstream Gas Velocity

First defining a reference velocity $\bar{u}$ such that

$$\bar{u} = \frac{\zeta}{\xi} \tag{B.10}$$

Substituting Equations B.7 and B.8 for ζ and ξ gives P/ρ in terms of the reference velocity. Another expression for P/ρ can be found by defining the local sound speed a_0 as

$$a_0^2 = \frac{5}{3}\frac{P}{\rho} \tag{B.11}$$

where 5/3 is the ratio of specific heats for atoms. Equating these expressions gives

$$\frac{P}{\rho} = u\bar{u} - u^2 = \frac{3}{5}a_0^2 \tag{B.12}$$

Re-writing the energy conservation condition in terms of the reference velocity $\bar{u}$ and substituting from Equation B.12 leads to the quadratic equation

$$u^2 - \frac{5}{4}u\bar{u}u + \frac{\xi}{2} = 0 \tag{B.13}$$

and it is the roots of this equation which are the up and downstream gas velocities. Returning now to the use of subscripts, the algebraic relationship for solving a quadratic equation can be used to evaluate the roots, but in this instance it is sufficient to only consider their sum $u_o + u_1$ = -b/a, where b = 5/4 and a = 1. From Equation B.13 the reference velocity can now be expressed in terms of the entry and exit velocities such that

$$\bar{u} = \frac{4}{5}(u_o + u_1) \tag{B.14}$$

B.2.2 Up and Downstream Mach Numbers

Now considering the up and downstream Mach numbers; M_o and M_1 respectively. Defining M_o as the ratio of the velocity with which the gas enters the shock u_o, to the adiabatic sound speed ahead of the shock a_o gives

$$M_o = \frac{u_o}{a_o} \tag{B.15}$$

Using Equation B.12 to substitute for a_o and the energy balance equation to eliminate the reference velocity, the ratio of the velocity across the shock u_1/u_o, can be found in terms of the upstream Mach number

$$\frac{u_1}{u_o} = \frac{3 + M_o^2}{4M_o^2} \tag{B.16}$$

If the shock were weak then by definition $M_o \leq 1$. This is clearly not the case but nevertheless, that the shock is strong defined by $M_o \gg 1$, should be confirmed before final evaluation of B.16. This is most easily accomplished by transforming the velocity variables back into the stellar frame of reference and then considering what values M_o might have in modelling.

B.2.3 Velocity Ratio

Transforming u_o and u_1 is begun by defining V_s as the shock velocity in the fixed frame with v_o and v_1 being the up (pre-shock) and down (post-shock) velocities respectively. Thus

$$u_o = v_o - V_s \qquad \text{and} \qquad u_1 = v_1 - V_s$$

The up-steam velocity v_o is that in the ionized HII region or a short time later in the neutral cloud, as the superbubble expands. V_s is given by the adiabatic shock velocity $v_{SN}(t)$ from Equation 4.17 derived in the previous section. As both the ionized HII region and the neutral velocity are considerably less than the shock velocity it is only necessary to consider the case where $V_s \gg v_o$, so in the stellar frame, $u_o = v_{SN}(t)$.

Now considering the upstream adiabatic sound speed given by Equation B.11. As the jump conditions show, this is not given by the sound speed in the shocked gas ahead of the shell, as might be surmised from comparison with $u_o = v_{SN}(t)$, but rather is the sound speed of the pre-shocked gas; that in the HII region or the neutral region, depending on how far the superbubble has advanced into the cloud. In the former case, although

passage of the ionization front has increased the pressure in the HII region, its sound speed remains small in comparison to $v_{SN}(t)$ and in the later case, the pressure ahead of the shock is negligible. Thus, the upstream Mach number $M_o = v_{SN}(t)/a_o \gg 1$ and the shock is confirmed as strong. Evaluation of Equation B.16 under this assumption shows it can be reduced to

$$4u_1 = u_o \tag{B.17}$$

which is the velocity ratio across the shock (Dyson & Williams 1997*d*).

B.2.4 Density Ratio

The density ratio across the shock in the adiabatic phase can now be found by re-arranging the mass continuity Equation B.1 for u_1/u_o and substituting it into Equation B.17

$$\rho_1 = 4\rho_o \tag{B.18}$$

This is obviously still valid in the stellar frame so for an adiabatic shock, the post-shock compression is limited to four times the pre-shock density. This limitation is a function of the pressure in the post-shocked gas as even if $u_o = v_o = v_{SN}(t)$ is made extremely large, there is a corresponding exchange of kinetic energy into the translational energy of the post-shocked gas. The high pressure resulting from that exchange then opposes the compression and limits the density ratio to 4 (Dyson & Williams 1997*d*).

B.3 Density Ratio in the Isothermal Phase

In a similar way to the adiabatic phase, the thickness of the shells formed in the isothermal phase are also inversely dependent on the compression across the shock.

An isothermal shock can be thought of as an adiabatic shock coupled to a cooling region and the key fact to understanding shocked gas radiating in this way is that the upstream gas entering the shock wave at temperature T_o, is heated to temperature T_s where $T_s \gg T_o$ and then exits the cooling region at temperature T_2 where $T_2 \approx T_o$. The distance the gas has to flow through the cooling region to return to its original temperature is the cooling length l_{cool} whilst the surface at which it reaches that temperature is the cooling surface C. This scheme is illustrated in Figure B.2 below. As l_{cool} is small with respect to the size of the system, surfaces C and S are very close together and can be thought of as one surface. The gas therefore flows very quickly through the cooling region

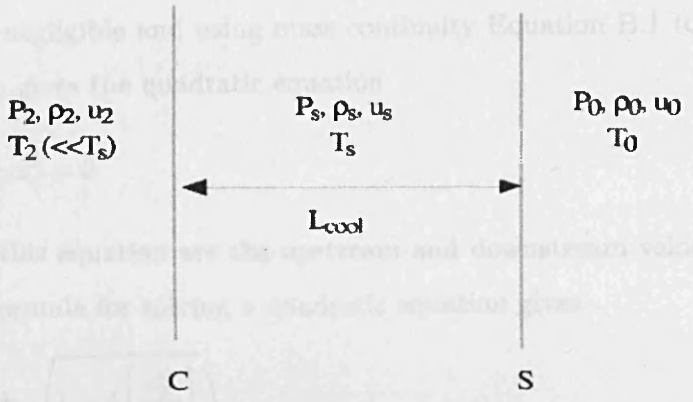

Figure B.2: Schematic illustration of a radiating shock wave (Dyson & Williams 1997*d*).

and the flow variables are again time-independent, so crucially, the Rankine-Hugoniot conservation conditions apply across the entire expanse - shock plus cooling region (Dyson & Williams 1997*d*). The assumption that the temperature does not change across the shock allows the energy balance condition to take into consideration all forms of energy, including that radiated from the cooling region, with the simple statement $T_o \approx T_2$, rather than explicitly summing over all energy sources and sinks. The jump conditions for mass and momentum do not change so those relations can now be re-cast for the isothermal phase (Dyson & Williams 1997*d*).

Deriving the factor by which the upstream gas is compressed is again most easily accomplished by starting in a frame of reference where the gas is moving and the shock is stationary. Therefore in the coming discussion the upstream pressure, density and velocity in the pre-shock region are P_o, ρ_o and u_o and the downstream pressure, density and velocity in the shocked, but cooled gas are P_2, ρ_2 and u_2 respectively. First defining the square of the isothermal sound speed c_o in the upstream gas as the ratio of the up-steam pressure and density and using the energy balance or isothermality condition $T_o = T_2$ across the discontinuity gives

$$c_o^2 = \frac{P_o}{\rho_o} = \frac{P_2}{\rho_2} \tag{B.19}$$

Balancing the change in momentum with the change in pressure gives

$$u_o^2 \rho_o + P_o = P_s u_2^2 + P_2 = \zeta \tag{B.20}$$

which expresses momentum conservation for the isothermal phase. Taking the upstream pressure P_o to be negligible and using mass continuity Equation B.1 to substitute for ρ_o and dividing by ρ_2 gives the quadratic equation

$$u_2{}^2 - u_o u_2 + c_o^2 = 0 \tag{B.21}$$

The two roots of this equation are the upstream and downstream velocities so using the simple algebraic formula for solving a quadratic equation gives

$$u_2 = \frac{u_o}{2}\left(1 \pm \sqrt{1 - 4\left[\frac{c_o^2}{u_o{}^2}\right]}\right) \tag{B.22}$$

In assuming that the upstream pressure is negligible, the sound-speed c_o must also be small. The upstream Mach number M_o defined as the ratio of the gas velocity to the sound speed is given by

$$M_o = \frac{u_o}{c_o} >> 1 \tag{B.23}$$

as $u_o \gg c_o$ and the shock is strong. Taking the first term in the series expansion, using the negative solution as the gas is compressed by the shock and re-arranging the mass conservation condition, the density ratio across the shock is obtained

$$\frac{\rho_o}{\rho_2} = \frac{u_o^2}{c_o^2} \tag{B.24}$$

which is the upstream Mach number squared and in a fixed stellar frame of reference this relationship does not change. Equation B.24 can be found in terms of the GMC system variables using the transformation $u_o = v_o - v_{SN}(t)$, where v_o is the upstream gas velocity, assumed to be at rest in the neutral region and $v_{SN}(t)$ is the shock velocity given by Equation 4.46, $u_o = v_{SN}(t)$ in the limit $v_{SN}(t) \gg v_o$. Assuming that R_c is located in the neutral region leads to $\rho_o = \rho^n$ being the neutral density, $\rho_2 = \rho^{SH}$ as the shell density and $c_o = c_n$ the neutral sound speed

Bibliography

Abbott, D., 1982, *ApJ*, **259**, 282

Alexander, D. M., Efstathiou, A., Hough, J. H., Aitken, D. K., Lutz, D., Roche, P. F. & Sturm, E., 1999, *MNRAS*, **310**, 78

Allamandola, L. J., Tielens, A. G. G. M. & Barker, J. R., 1985, *ApJ*, **290**, L25

Antonucci, R., 1993, *ARA&A*, **31**, 473

Antonucci, R. & Miller, J., 1985, *ApJ*, **297**, 621

Barford, N., 1967, *Experimental Measurements: Precision, Error and Truth* (Addison-Wesley Published Co. Inc.), chapter 3, p. 1

Barlow, M. J., Sugerman, B. E. K., Fabbri, J., Meixner, M., Fisher, R. S., Bowey, J. E., Panagia, N., Ercolano, B., Clayton, G. C., Cohen, M., Gledhill, T. M., Gordon, K., Tielens, A. G. G. M. & Zijlstra, A. A., 2005, *ApJ*, **627**, L113

Bell, E. F., Wolf, C., Meisenheimer, K., Rix, H.-W., Borch, A., Dye, S., Kleinheinrich, M., Wisotzki, L. & McIntosh, D. H., 2004, *ApJ*, **608**, 752

Bicknell, G. V., Dopita, M. A., Tsvetanov, Z. I. & Sutherland, R. S., 1998, *ApJ*, **495**, 680

Bohlin, R., Savage, B. & Drake, J., 1978, *ApJ*, **224**, 132

Bowen, G., 1988, *ApJ*, **329**, 299

Bower, R. G., Lucey, J. R. & Ellis, R. S., 1992, *MNRAS*, **254**, 589

Bowers, R. & Deeming, T., 1984, *Astrophysics I; Stars* (Jones & Bartlett Publishers), chapter 6, p. 115

Brown, A., Hartman, D. & Fritzinger, J., 1995, *A&A*, **300**, 903

Bruzual, A. & Charlot, S., 1993, *ApJ*, **405**, 538

Bruzual, A. & Charlot, S., 1995, *ftp://gemini.tuc.noao.edu/pub/charlot/bc95*

Cardelli, J., Clayton, G. & Mathis, J., 1989, *ApJ*, **345**, 245

Carico, D., Sanders, D., Soifer, B., Elias, J., Matthews, K. & Neugebauer, G., 1988, *AJ*, **95**, 356

Carilli, C. & Taylor, G., 2000, *ApJ*, **532**, L95

Castor, J., Abbott, D. & Klein, R., 1975, *ApJ*, **195**, 157

Charbonnel, C., Meynet, G., Maeder, A., Schaller, G. & Schaerer, D., 1993, *A&AS*, **101**, 415

Chase, M., Davies, C., Downey, J., Frurip, D., McDonald, R. & Syverud, A., 1985, *J.Phys. Chem. Ref. Data*, **14**, Suppl.No.1

Clements, D., Sutherland, W., Saunders, W., Efstathiou, G., McMahon, R., Maddox, S., Lawrence, A. & Rowan-Robinson, M., 1996, *MNRAS*, **279**, 459

Colbert, J., 1999, *ApJ*, **511**, 721

Condon, J., Huang, Z.-P., Yin, Q. & Thuan, T., 1991, *ApJ*, **378**, 65

Coziol, R., 1996, *A & A*, **309**, 345

Cutri, R., Rieke, G. & Lebofsky, M., 1984, *ApJ*, **287**, 566

Dale, D. A. & Uson, J. M., 2000, *AJ*, **120**, 583

Dame, T., Elmgreen, B., Cohen, R. & Thaddeus, P., 1986, *ApJ*, **507**, 615

Dasyra, K. M., Tacconi, L. J., Davies, R. I., Naab, T., Genzel, R., Lutz, D., Sturm, E., Baker, A. J., Veilleux, S., Sanders, D. B. & Burkert, A., 2006, *ApJ*, **651**, 835

Devereux, N., Tanigughi, Y., Sanders, D., Nakai, N. & Young, J., 1994, *ApJ*, **107**, 2006

Devereux, N. & Young, J., 1990, *ApJ*, **359**, 42

Dopita, M., Groves, B., Fischera, J., Sutherland, R. S., Tuffs, R., Popescu, C., Kewley, L., Reuland, M. & Leitherer, C., 2005, *ApJ*, **619**, 755

Dopita, M. A., Groves, B. A., Sutherland, R. S., Binette, L. & Cecil, G., 2002, *ApJ*, **572**, 753

Downes, D. & Solomon, P., 1998, *ApJ*, **507**, 615

Draine, B., 1985, *ApJS*, **57**, 587

Draine, B., 1989, *IAU Symposium*, **135**, 313

Draine, B. & Lee, H., 1984, *ApJ*, **285**, 89

Dunne, L. & Eales, S., 2001, *MNRAS*, **327**, 697

Dunne, L., Eales, S., Edmunds, M., Ivison, R., Alexander, P. & Clements, D. L., 2000, *MNRAS*, **315**, 115

Dyson, J. & Williams, D., 1997*a*, *The Physics of the Interstellar Medium* (Institute of Physics Publishing Ltd), chapter 3, p. 32

Dyson, J. & Williams, D., 1997*b*, *The Physics of the Interstellar Medium* (Institute of Physics Publishing Ltd), chapter 5, p. 64

Dyson, J. & Williams, D., 1997*c*, *The Physics of the Interstellar Medium* (Institute of Physics Publishing Ltd), chapter 7, p. 112

Dyson, J. & Williams, D., 1997*d*, *The Physics of the Interstellar Medium* (Institute of Physics Publishing Ltd), chapter 6, p. 87

Edoh, O., 1983, *Optical Properties of Carbon from the Far Infrared to the Far Ultraviolet*, Ph.D. thesis, University of Arizona

Efstathiou, A., Rowan-Robinson, M. & Siebenmorgen, R., 2000, *MNRAS*, **313**, 734

Efsthathiou, A., Hough, J. & Young, S., 1995, *MNRAS*, **277**, 1134

Efsthathiou, A. & Rowan-Robinson, M., 1990*a*, *MNRAS*, **273**, 649

Efsthathiou, A. & Rowan-Robinson, M., 1990*b*, *MNRAS*, **245**, 275

Efsthathiou, A. & Rowan-Robinson, M., 1994, *MNRAS*, **266**, 212

Elmegreen, B., 1997, *ApJ*, **486**, 944

Elvis, M., Green, R. F., Bechtold, J., Schmidt, M., Neugebauer, G., Soifer, B. T., Matthews, K. & Fabbiano, G., 1986, *ApJ*, **310**, 291

Emerson, D., 1996, *Interpreting Astronomical Spectra* (John Wiley & Sons), chapter 5, p. 144

Ercolano, B., Morisset, C., Barlow, M. J., Storey, P. J. & Liu, X.-W., 2003, *MNRAS*, **340**, 1136

Evans, A., 1994*a*, *Dusty Universe* (John Wiley & Sons), chapter 3, p. 39

Evans, A., 1994*b*, *Dusty Universe* (John Wiley & Sons), chapter 8, p. 182

Evans, A., Surace, J., J.M., M. & Sanders, D., 2001, in *A.S.P. Conference Series*, volume 235, p. 313

Farrah, D., 2001, *Ultra-Luminous Infrared Galaxies*, Ph.D. thesis, Imperial College London

Farrah, D., Alfonso, J., Rowan-Robinson, M., Fox, M. & Clements, D., 2003, *MNRAS*, **343**, 585

Farrah, D., Rowan-Robinson, M., Oliver, S., Serjeant, S., Borne, K., Lawrence, A., Lucas, R. A., Bushouse, H. & Colina, L., 2001, *MNRAS*, **326**, 1333

Farrah, D., Serjeant, S., Efstathiou, A., Rowan-Robinson, M. & Verma, A., 2002, *MNRAS*, **335**, 1163

Ferreras, I., Lisker, T., Carollo, C. M., Lilly, S. J. & Mobasher, B., 2005, *ApJ*, **635**, 243

Fioc, M. & Rocca-Volmerange, B., 1997, *A & A*, **326**, 950

Franco, J., Tenorio-Tagle, G. & Bodenheimer, P., 1990, *ApJ*, **349**, 126

Genzel, R., Lutz, D., Sturm, E., Egami, E., Kunze, D., Moorwood, A. F. M., Rigopoulou, D., Spoon, H. W. W., Sternberg, A., Tacconi-Garman, L. E., Tacconi, L. & Thatte, N., 1998, *ApJ*, **498**, 579

Genzel, R., Tacconi, L., Rigopoulou, D., Lutz, D. & Tecza, M., 2001, *ApJ*, **563**, 527

Gordon, K., Calzetti, D. & Witt, A., 1997, *ApJ*, **487**, 625

Gusten, R., 1989, in *IAU Symposium*, volume 136, p. 89

Halpern, M., Benford, R., Meyer, S., Muehlner, D. & Weiss, R., 1988, *ApJ*, **332**, 596

Heckman, T., 1998, in *A.S.P.Conference Series*, volume 148, p. 127

Heisler, M., 1998, *PASA*, **15**, 167

Hughes, D., Gear, W. & Robson, E., 1994, *MNRAS*, **270**, 641

Hunter, D. A., Gillett, F. C., Gallagher, III, J. S., Rice, W. L. & Low, F. J., 1986, *ApJ*, **303**, 171

Imanishi, M., 2001, *ApJ*, **121**, 1927

Iwasawa, K., 1999, *MNRAS*, **302**, 96

Jenkins, E. & Meloy, D., 1974, *ApJ*, **193**, L121

Kennicutt, R., 1998, *ApJ*, **498**, 541

Kennicutt, Jr., R. C., Roettiger, K. A., Keel, W. C., van der Hulst, J. M. & Hummel, E., 1987, *AJ*, **93**, 1011

Kewley, L. J., Dopita, M. A., Sutherland, R. S., Heisler, C. A. & Trevena, J., 2001, *ApJ*, **556**, 121

Kewley, L. J., Dopita, M. A., Sutherland, R. S., Heisler, C. A. & Trevena, J., 2002, *ApJS*, **142**, 35

Klaas, U., Haas, M., Heinrichsen, I. & Schulz, B., 1997, *A & A*, **325**, L21

Klaas, U., Haas, M., Müller, S. A. H., Chini, R., Schulz, B., Coulson, I., Hippelein, H., Wilke, K., Albrecht, M. & Lemke, D., 2001, *A & A*, **379**, 823

Knapen, J. H., Laine, S., Yates, J. A., Robinson, A., Richards, A. M. S., Doyon, R. & Nadeau, D., 1997, *ApJ*, **490**, L53

Krätchmer, W. & Huffman, D., 1979, *Astrophys. Space Sci.*, **61**, 195

Kroupa, P., 1995, *ApJ*, **453**, 350

Kroupa, R., 2002, *Science*, **295**, 82

Kudritzki, R. P., Pauldrach, A. & Puls, J., 1987, *A & A*, **173**, 293

Laor, A. & Draine, B., 1993, *ApJ*, **401**, 99

Leger, A. & Puget, J., 1984, *A & A*, **137**, L5

Leger, A., Verstraete, L., d'Hendecourt, L., Defourneau, D., Dutuit, D., Schmidt, W. & Lauer, J., 1989, *IAU Symp.*, **135**, 173

Leitherer, C. & Heckman, T., 1995, *ApJS*, **96**, 9

Leitherer, C., Schaerer, D., Goldader, J.D. Delgado, R., Robert, C., Kune, D., de Mello, D., Devost, D. & Heckman, T., 1999, *ApJS*, **123**, 3

Leitherer, C., Walborn, N., Heckman, T. & Norman, C., 1991, *Massive Stars in Starburst Galaxies* (Cambridge University Press), chapter 1, p. 1

Levenson, N., Weaver, K. & Heckman, T., 2001, *ApJ*, **550**, 230

Lim, A. & Mellema, G., 2003, *A & A*, **405**, 189

Lim, A. & Steffen, W., 2003, *MNRAS*, **233**, 166

Lutz, D., Spoon, H. W. W., Rigopoulou, D., Moorwood, A. F. M. & Genzel, R., 1998, *ApJ*, **505**, L103

Mac Low, M.-M. & McCray, R., 1988, *ApJ*, **324**, 776

Madau, P., Ferguson, H. C., Dickinson, M. E., Giavalisco, M., Steidel, C. C. & Fruchter, A., 1996, *MNRAS*, **238**, 4

Maeder, A., 1983, *A & A*, **120**, 113

Maeder, A. & Meynet, G., 1987, *A & A*, **182**, 243

Maiolino, R., Ruiz, M., Rieke, G. & Keller, L., 1995, *ApJ*, **446**, 561

Massey, P., 1998, in *A.S.P.Conference Series*, volume 142, p. 17

Mateo, M., 1998, *ARA&A*, **36**, 435

Mathis, J., 1990, *A & A*, **28**, 37

Mathis, J. & Whiffen, G., 1989, *ApJ.*, **341**, 808

McCray, R. & Kafatos, M., 1987, *ApJ*, **317**, 190

McCray, R. & Weaver, R., 1975, *ApJ (Letters)*, **200**, L110

Mellema, G., Raga, A. C., Canto, J., Lundqvist, P., Balick, B., Steffen, W. & Noriega-Crespo, A., 1998, *A & A*, **331**, 335

Meurer, G. R., Heckman, T. M., Lehnert, M. D., Leitherer, C. & Lowenthal, J., 1997, *Astron.J*, **114**, 54

Meynet, G., Maeder, A., Schaller, G., Schaerer, D. & Charbonnel, C., 1994, *A & AS*, **103**, 97

Mèra, D., Chabrier, G. & Baraffee, I., 1996, *ApJ*, **459**, L87

Mie, G., 1908, *Ann. Phys. Lpz.*, **25**, 377

Miller, G. & Scalo, J., 1979, *ApJS*, **41**, 513

Mouhcine, M. & Contini, T., 2002, *A & A*, **389**, 106

Nenkova, M., Ivezić, Ž. & Elitzur, M., 2000, *Thermal Emission Spectroscopy and Analysis of Dust, Disks, and Regoliths*, **196**, 77

Nenkova, M., Ivezić, Ž. & Elitzur, M., 2002, *ApJ*, **570**, L9

Nicholson, K., Reichert, G., Mason, K., Puchnarewicz, E., Ho, L., Shields, J. & Filippenko, A., 1998, *MNRAS*, **300**, 893

Norris, R. P. F. N., 2003, *The Role of Massive Stars in Young Starburst Galaxies*, Ph.D. thesis, University College London

Oey, M., 1996, *ApJ*, **467**, 231

Oey, M. & Massey, P., 1995, *ApJ*, **462**, 210

Oliver, S. J., Rowan-Robinson, M., Broadhurst, T. J., McMahon, R. G., Saunders, W., Taylor, A., Lawrence, A., Lonsdale, C. J., Hacking, P. & Conrow, T., 1996, *MNRAS*, **280**, 673

Omont, A., 1986, *A & A*, **164**, 159

Osterbrock, D., 1989, *Astrophysics of Gaseous Nebulae and Active Galactic Nuclei* (University Science Books Sausalito, California), chapter 12, p. 350

Pier, E. & Krolik, J., 1993, *Apj*, **401**, 99

Piovan, L., Tantalo, R. & Chiosi, C., 2005, in *A.I.P.Conference Series*, volume 761, p. 91

Planesas, P., Colina, L. & Pérez-Olea, D., 1997, *A & A*, **325**, 81

Puget, J.-L. & Boulanger, F., 1990, *From Ground-Based to Space-Borne Sub-mm Astronomy*, 271

Purcell, E., 1969, *ApJ*, **206**, 685

Reike, G., Lebofsky, M., Thompson, R., Low, F. & Tokunaga, A., 1980, *ApJ*, **238**, 24

Rigopoulou, D., Lawrence, A. & Rowan-Robinson, M., 1996, *MNRAS*, **278**, 1049

Rigopoulou, D., Spoon, H., Genzel, R., Lutz, D., Moorwood, A. & Tran, Q., 1999, *AJ*, **118**, 2625

Risaliti, G., Maiolino, R., Marconi, A., Sani, E., Berta, S., Braito, V., Ceca, R. D., Franceschini, A. & Salvati, M., 2006, *MNRAS*, **365**, 303

Roche, P., Aitken, D., Smith, C. & M.J., W., 1991, *MNRAS*, **248**, 606

Rowan-Robinson, M., 1980, *ApJ*, **44**, 403

Rowan-Robinson, M., 1986, *MNRAS*, **238**, 523

Rowan-Robinson, M., 1992, *MNRAS*, **258**, 787

Rowan-Robinson, M., 1995, *MNRAS*, **272**, 1000

Rowan-Robinson, M. & Crawford, J., 1989, *MNRAS*, **238**, 523

Rowan-Robinson, M. & Efsthathiou, A., 1993, *MNRAS*, **263**, 673

Rowan-Robinson, M. & Harris, S., 1982, *MNRAS*, **200**, 197

Rowan-Robinson, M. & Harris, S., 1983, *MNRAS*, **202**, 797

Rowan-Robinson, M., Lock, T., Walker, D. & Harris, S., 1986, *MNRAS*, **222**, 273

Rowan-Robinson, M., Mann, R. G., Oliver, S. J., Efstathiou, A., Eaton, N., Goldschmidt, P., Mobasher, B., Serjeant, S. B. G., Sumner, T. J., Danese, L., Elbaz, D., Franceschini, A., Egami, E., Kontizas, M., Lawrence, A., McMahon, R., Norgaard-Nielsen, H. U., Perez-Fournon, I. & Gonzalez-Serrano, J. I., 1997, *MNRAS*, **289**, 490

Ruiz, M., Alexander, D. & Hough, J., 2001, *MNRAS*, **325**, 995

Saken, J., Shull, J., Garmany, C., Nichols-Bohlin, J. & R.A., F., 1992, *ApJ*, **397**, 537

Salpeter, E. E., 1955, *ApJ*, **121**, 161

Sanders, D. B., Phinney, E., Neugebauer, G., Soifer, B. & Matthews, K., 1989, *ApJ*, **347**, 29

Sanders, D. B., Scoville, N. & Soifer, B., 1991, *ApJ*, **370**, 158

Sanders, D. B., Scoville, N. & Solomon, P., 1985, *ApJ*, **289**, 373

Sanders, D. B., Soifer, B. T., Elias, J. H., Madore, B. F., Matthews, K., Neugebauer, G. & Scoville, N. Z., 1988, *ApJ*, **325**, 74

Saunders, W., Rowan-Robinson, M., Lawrence, A., Efstathiou, G., Kaiser, N., Ellis, R. S. & Frenk, C. S., 1990, *MNRAS*, **242**, 318S

Savage, B. & Mathis, J., 1979, *Ann. Rev. Astr. Astrophys.*, **17**, 73

Scalo, J., 1998, in *A.S.P.Conference Series*, volume 142, p. 201

Schaerer, D., Charbonnel, C., Meynet, G., Maeder, A. & Schaller, G., 1993, *A&AS*, **102**, 339

Schaller, G., Schaerer, D., Meynet, G. & Maeder, A., 1992, *A&AS*, **96**, 269

Schmutz, W., Leitherer, C. & Gruenwald, R., 1992, *PASP*, **104**, 1165

Schönberg, M. & Chandrasekhar, S., 1942, *ApJ*, **96**, 161

Schwarzschild, M., 1965, *Structure and Evolution of the Stars* (Dover Publications Ltd.), chapter 29, p. 271

Scoville, N. Z., Evans, A. S., Thompson, R., Rieke, M., Hines, D. C., Low, F. J., Dinshaw, N., Surace, J. A. & Armus, L., 2000, *ApJ*, **119**, 991

Seyfert, C., 1943, *ApJ*, **97**, 28S

Shull, J. & Saken, J., 1995, *ApJ*, **444**, 663

Siebenmorgen, R. & Krügel, E., 1992, *A & A*, **259**, 614

Siebenmorgen, R. & Krügel, E., 1994, *A & A*, **282**, 407

Siebenmorgen, R. & Krügel, E., 2007, *A & A*, **461**, 445

Siebenmorgen, R., Krügel, E. & Mathis, J., 1992*a*, *A & A*, **266**, 501

Siebenmorgen, R., Krügel, E. & Mathis, J., 1992*b*, *A & A*, **266**, 501

Siebenmorgen, R., Krügel, E. & Spoon, H., 2004, *A & A*, **414**, 123

Silva, L., Granato, G. L., Bressan, A. & L., D., 1998, *ApJ*, **509**, 103

Soifer, B. T., Boehmer, L., Neugebauer, G. & Sanders, D. B., 1989, *AJ*, **98**, 766S

Solomon, P., Rivolo, A. & Barrett, J. Yahil, A., 1987, *ApJ*, **322**, 101

Sorrell, W., 1990, *MNRAS*, **214**, 89

Spinoglio, L., Malkan, M., Rush, B., Carrasco, L. & Recillas-Cruz, E., 1995, *ApJ*, **453**, 616

Spitzer, L., 1968, *Diffuse Matter in Space* (Wiley-Interscience, New York)

Spitzer, L., 1978, *Physical Processes in the Interstellar Medium* (Wiley-Interscience, New York)

Steidel, C., 1996, *AAS*, **189**, 3301S

Steigman, G., Strittmatter, P. A. & Williams, R., 1975, *ApJ*, **198**, 575

Sugerman, B. E. K., Ercolano, B., Barlow, M. J., Tielens, A. G. G. M., Clayton, G. C., Zijlstra, A. A., Meixner, M., Speck, A., Gledhill, T. M., Panagia, N., Cohen, M., Gordon, K. D., Meyer, M., Fabbri, J., Bowey, J. E., Welch, D. L., Regan, M. W. & Kennicutt, R. C., 2006, *Science*, **313**, 196

Surace, J., 1998, *A High-Resolution Near-Infrared Study of the Evolutionary Link Between Ultraluminous Infrared Galaxies and Optical QSOS*, Ph.D. thesis, University of Hawaii

Surace, J. & Sanders, D., 2000, *ApJ*, **120**, 604

Sutherland, R. & Dopita, M., 1993, *ApJS*, **88**, 253

Tenorio-Tagle, G. & Bodenheimer, P., 1988, *ARA&A*, **26**, 145

Thomas, D., Greggio, L. & Bender, R., 1999, *MNRAS*, **302**, 537

Toomre, A. & Toomre, J., 1972, *ApJ*, **178**, 623

Tosi, M., Greggio, L., Marconi, G. & Focardi, P., 1991, *ApJ*, **102**, 951

Tran, Q. D., Lutz, D., Genzel, R., Rigopoulou, D., Spoon, H. W. W., Sturm, E., Gerin, M., Hines, D. C., Moorwood, A. F. M., Sanders, D. B., Scoville, N., Taniguchi, Y. & Ward, M., 2001, *ApJ*, **552**, 527

Veilleux, S., Sanders, D. & Kim, D.-C., 1999, *ApJ*, **522**, 139

Voit, G., 1991, *ApJ*, **379**, 121

Weaver, R., McCray, R., Castor, J., Shapiro, R. & Moore, R., 1977, *ApJ*, **218**, 377

Whittet, D., 2003, *Dust in the Galaxtic Environment* (Institute of Physics Publishing Ltd), chapter 2, p. 58

Whittle, M., 1992, *ApJ*, **387**, 121

Wiklind, T. & Henkel, C., 1995, *A & A*, **297**, 1206

Woltjer, L., 1972, *Ann. Rev. Astr. and Ap.*, **129**, 10

Yun, M. & Carilli, C., 2002, *ApJ*, **568**, 88

Zeilik, M. & Gregory, S., 1998, *Introductory Astronomy & Astrophysics* (Saunders College Publishing), chapter 18, p. 366

Zink, E., Lester, D., Doppmann, G. & Harvey, P., 2000, *ApJS*, **131**, 413